

THE CATHOLIC UNIVERSITY OF AMERICA

Numerical Simulation of Nonlinear Internal Solitary Wave Interactions with
Submarine Topographic Features

A DISSERTATION

Submitted to the Faculty of the
Department Of Civil Engineering
School Of Engineering
Of The Catholic University of America
In Partial Fulfillment of the Requirements

For the Degree
Doctor of Philosophy

©

Copyright
All Rights Reserved

By
Michael Peter Lee

Washington, D.C.

2011

Numerical Simulation of Nonlinear Internal Solitary Wave Interactions with Submarine Topographic Features

Michael Peter Lee, Ph.D.

Director: Hsien-Ping Pao, Ph.D.

Approximately 120 computer simulations were conducted to evaluate how a mode-1-type internal wave would interact with a variety of submarine topographic (physiographic) obstacles likely to be found in a marine setting. A total of seven obstacle geometries were selected for evaluation – shelf, slope-shelf, extended slope, short-slope, reverse-shelf, a single (isolated) rectangular obstacle, and a single triangular obstacle. Internal waves of ‘depression’ as well as ‘elevation’ were formed using a two-layered, stratified numerical model based on the Navier-Stokes and continuity equations. The governing equations assumed Boussinesq conditions. Output data from the FORTRAN-based computer code were post-processed using MATLAB-based computer programs that calculated internal wave amplitudes and energies. These data were compared to published data associated with experimental wave tank studies and found generally to be in good agreement. Data from the numerical simulation trials were also used to generate figures illustrating various hydrodynamic features (pycnocline, streamlines, and velocity vectors) of an internal wave as it forms as well as when it interacts with different types of obstacle geometries.

The types of features and processes observed included the formation of Kelvin-Helmholtz or K-H-like vortices and various stages of the classically-recognized wave-breaking progression (“wash-down,” “breaking,” “bore,” and “surge”). When considering a stratified fluid system, it was confirmed that internal wave characteristics are influenced in large measure by the relative depths of the two fluids defining the system as well as the effects of viscous decay (damping). It was also confirmed that the nature of the interaction between an internal wave and a topographic obstacle is influenced by the magnitude of either the nonlinear parameter or the blocking parameter. The numerical simulation trials also allowed for the interrogation of the modeling domain to determine the nature of the stability conditions (static vs. dynamic) in time and space. In this regard, evaluation of both the Richardson number and the normalized density gradient provided additional insights into the hydrodynamics of the system when topographic obstacles are present. Three instability states were evaluated: K-H, buoyant, and static.

This research contributes to a basic understanding of internal wave phenomena and includes some general conclusions regarding the effects of obstacle geometry on internal wave behavior and properties.

This dissertation by Michael Peter Lee fulfills the dissertation requirement for the doctoral degree in Philosophy approved by H.-P Pao, Ph.D., as Director, and by S. Nieh, Ph.D., and S.-C Ling, Ph.D., as Readers.

Hsien Ping Pao, Ph.D., Director

Sen Nieh, Ph.D., Reader

Shyang-Chin Ling, Ph.D., Reader

... To my wife Kathleen, for her long-standing patience and encouragement,
and to our daughter Fiona, whose future is without limits

CONTENTS

LIST OF ILLUSTRATIONS	viii
LIST OF TABLES	xxii
LIST OF ABBREVIATIONS.....	xxiii
ACKNOWLEDGEMENTS	xxvii
CHAPTER I INTRODUCTION	1
1.1 Internal Solitary Waves	1
1.2 Scope of Work and Objectives	10
1.3 Contribution and Originality	11
1.4 Organization	12
CHAPTER II BACKGROUND	14
2.1 The Study of Internal Solitary Waves	14
2.1.1 Scott-Russell “Wave of Translation”	24
2.1.2 The K-dV Equation.....	28
2.1.3 Early Reports of ISW Phenomena	31
2.1.4 More “Recent” Developments	36
2.2 Internal Wave Mechanics.....	44
2.2.1 Key Internal Wave Forming Factors (Sources)	53
2.2.1.1 Stratification	54
2.2.1.2 Tidal Influences	59
2.2.1.3 Topographic Influences	62

2.2.1.4	Perturbing and Restoring Forces	71
2.2.2	Internal Waves and Topography (Sinks)	78
2.2.2.1	Shoaling	80
2.2.2.2	Breaking.....	81
2.2.2.3	Summary.....	89
CHAPTER III COMPUTATIONAL METHODOLOGY.....		93
3.1	Background.....	93
3.2	Governing Equations.....	95
3.3	Computational Approach	99
3.3.1	Finite Difference Approximations.....	103
3.3.2	Numerical Scheme.....	105
3.3.3	Key Modeling Assumptions.....	109
3.3.4	Specification of Time-step	113
3.4	Boundary Conditions.....	115
CHAPTER IV NUMERICAL SIMULATIONS.....		120
4.1	Internal Solitary Wave Parameters	120
4.1.1	Wave Speeds, c_o and C	122
4.1.2	Wave Amplitude, a_i	122
4.1.3	Wavelength, L_w	123
4.1.4	Wave Energy, E	124
4.2	Benchmark Trials.....	125
4.2.1	Computational Domain	127
4.2.2	Key System Parameters and Initial Conditions.....	130

4.2.3	Results of Benchmark Simulations	132
4.2.3.1	General Observations	136
4.2.3.2	Detailed Observations	141
4.2.3.3	Comparison to Chen (2006) Data.....	150
4.2.3.4	Other Observations and Comparisons.....	151
4.3.1	Simulations Involving Topographic Obstacles.....	170
4.3.1.1	Shelf-Like Obstacle.....	175
4.3.1.2	Slope-Shelf Scenario	185
4.3.1.3	Slope-Only Scenario.....	193
4.3.1.4	So-called Short-Slope Scenario	205
4.3.1.5	Reverse Shelf-Only Scenario.....	215
4.3.1.6	Isolated Topographic Obstacles	223
4.3.2	Quantitative Effects of Topographic Obstacles on ISWs	251
4.3.3	Static Stability vs. Dynamic Instability	268
CHAPTER V CONCLUSIONS AND RECOMMENDATIONS		281
5.1	Conclusions	281
5.2	Recommendations.....	284
APPENDIX A EXAMPLE MATHCAD® SPREADSHEET		288
APPENDIX B DETAILS OF NUMERICAL SIMULATION INVOLVING A SHELF-LIKE TOPOGRAPHIC OBSTACLE.....		289
APPENDIX C DETAILS OF NUMERICAL SIMULATION INVOLVING A SLOPE-SHELF TOPOGRAPHIC OBSTACLE		309
APPENDIX D DETAILS OF NUMERICAL SIMULATION INVOLVING AN EXTENDED SLOPE-TYPE TOPOGRAPHIC OBSTACLE.....		325

APPENDIX E	DETAILS OF NUMERICAL SIMULATION INVOLVING A SHORT SLOPE-TYPE TOPOGRAPHIC OBSTACLE	337
APPENDIX F	DETAILS OF REFLECTED INTERNAL WAVE	378
APPENDIX G	DETAILS OF NUMERICAL SIMULATION INVOLVING AN ISOLATED TRIANGULAR TOPOGRAPHIC OBSTACLE	390
REFERENCES	411

LIST OF ILLUSTRATIONS

- Figure 1.** Scale of internal waves shown in relation to other types of physical and biological upper ocean processes. Taken from Dickey (1990, 1991). Reproduced by permission of the American Geophysical Union (AGU). www.agu.org/pubs/authors/usage_permissions.shtml. 4
- Figure 2.** Thorpe's (1975) depiction of physical processes and conditions thought to contribute to the formation of internal waves. Reproduced by permission of the AGU..... 20
- Figure 3.** Briscoe's (1975) “simplified” depiction of the basic physical processes thought to contribute to the generation of ISWs. Letters are described in the text. Reproduced by permission of the AGU..... 21
- Figure 4.** Aqua MODIS (or Moderate Resolution Imaging Spectroradiometer) is true-color satellite image of ISW trains around the island of 'Abd-al-Kūrī (12° 11' N, 52° 14' E), located between the Gulf of Oman and the Indian Sea. Internal waves of depression can be identified by the presence of dark contours (lines) in the image; internal waves of elevation can be identified by the presence of light contours. Image dated August 27, 2003. Image credit: NASA..... 39
- Figure 5.** European Remote-Sensing Satellite (or ERS-2) SAR image showing large-amplitude ISWs around the Dongsha atoll (20° 31' N, 116° 44' E), in the South China Sea. Internal waves of depression can be identified by the presence of dark contours (lines) in the image; internal waves of elevation can be identified by the presence of light contours. Image dated June 23, 1998. Orbit 16598. Frame 0387-423. Copyright © 2010 European Space Agency. Reproduced by permission..... 40
- Figure 6.** Locations of observed ISW phenomena. Based on data compiled by Jackson (2004) who identified more than 50 locations globally where ISWs and ISW wave trains occur. Some locations experience multiple ISW occurrences over time..... 42

- Figure 7.** Percent distribution of Earth’s surface area by type and by latitude. Data are for both the Northern (N) and Southern (S) hemispheres. About 39 percent of the Northern Hemisphere is covered by the continental land mass compared to 19 percent in the Southern Hemisphere. Overall, the land to ocean ratio in the Northern Hemisphere is about 1:1.5; in the Southern Hemisphere, the ratio is about 1:4. Data obtained from *United Nations Atlas of the Oceans*. Available at www.oceansatlas.org. 43
- Figure 8.** Sinusoidal orbital pattern characteristic of an internal wave. Arrows indicate flow patterns around dashed streamlines. Small rectangles define areas of surface-roughness or slicks that can be observed in photographs and satellite images. From LaFond (1959). 50
- Figure 9.** Examples of internal wave observations *in situ*. Vertical axis is depth in meters and horizontal axis is time (hours). Image internal wave of depression in the top 1000 m of the water column revealed using acoustic scattering Strength using a 48-kilohertz (kHz) hydrograph Doppler sonar. Contours are isolines of equal acoustic scattering strength corrected for spherical spreading showing downward displacement of scattering layers. Image recorded in the Luzon Strait at 119.6°E, 20.5°N from April–May 2005. Taken from Lui et al. (2005). Reproduced by permission of the AGU. (b) Internal wave train in the top 250 m of the water column revealed using spectral echogram. Image acquired using an EK500 Echo-sounder operating at frequency of 38 kHz in the Lombok Strait at 115.75°E, 8.47°S. Higher backscatter values indicate higher plankton concentration or large schools of fish. Colors represent relative backscatter strength in decibels. Taken from Susanto, Mitnik, and Zhang (2005, Figure 4). Copyright © 2005 The Oceanography Society. Reproduced by permission. 52
- Figure 10.** Deep ocean pycnoclines. From Ingmanson/Wallace. *Oceanology: An Introduction*. 1E. Copyright © 1973 Brooks/Cole, a part of Cengage Learning, Inc., Reproduced by permission. www.cengage.com/permissions. 56
- Figure 11.** Frequency of reported ISW phenomena at those locations depicted in Figure 6. Bar graphs illustrate how thermal stratification of ocean waters can influence the formation of ISWs in the respective hemispheres. Figure 11a shows a waning in ISW behavior in ocean waters of the Southern Hemisphere during the Summer months while a waxing in ISW behavior can be observed in ocean waters occupying the Northern Hemisphere during the same time period. See Figure 11b. Overall, Jackson’s (2004) compilation reports that marine environments in the Equatorial Region of the ocean have the largest number of reported ISW sightings (473) followed by the Northern Hemisphere (343) and the Southern Hemisphere (54). Not included in this

figure are certain locations recognized as “hot spots” for ISW formation. They include the Norwegian Shelf (130 annual sightings), the Strait of Messina (77 annual sightings), and the Strait of Gibraltar (91 annual sightings)..... 58

Figure 12. Physiographic maps of the ocean floor. (a) “World Ocean Floor Panorama” shaded relief map prepared by H.C. Heezen and M. Tharp (1977). Copyright © Marie Tharp 1977/2003. Reproduced by permission Marie Tharp LLC, 8 Edward St., Sparkill, NY, 10976..... 63

Figure 12. Continued. (b) Digital seafloor relief map prepared by Amante and Eakins (2009). Image generated by NOAA/National Geophysical Data Center..... 64

Figure 13. Physiographic map illustrating an example the continental shelf-continental slope transition. Taken from Cacchione and Pratson (2004). Reproduced by permission of *American Scientist*, magazine of Sigma Xi, the Scientific Research Society..... 65

Figure 14. Progression of Kelvin-Helmholtz stability in a two-layered system. Taken from Gregg (1973) based on an unpublished study by S.A. Thorpe/National Institute of Oceanography (UK). Copyright © 1973 *Scientific American*, a division of Nature America, Inc. All rights reserved..... 77

Figure 15. Representation of streamlines for a developing (dynamically unstable) internal wave in a two-layered system. **IIA** — Upper and lower fluid layers moving in the same direction. **IIB** — Upper and lower fluid layers moving in opposite directions. Taken from Defant (1961a) citing Bjerknes and others (1933). Reprinted from *Physical Oceanography*, vol. 2, A. Defant (ed.), Fig. 236, p. 566, Copyright © 1961 Pergamon Press..... 78

Figure 16. Major surface features for shoaling ISWs. Figure (Lui et al. 1998) shows photographic as well as SAR signatures for a theoretical internal wave in a two-layered system passing from relatively deep water ($h_1 < h_2$) to relatively shallow water ($h_1 > h_2$). Reproduced by permission of the AGU... 80

Figure 17. Breaking progression for a plunging-type surface wave. Taken from Mason (1952). 83

Figure 18. Principal surface wave breaker types as defined by Galvin (1968). Reproduced by permission of the AGU. 84

Figure 19. Seven internal wave breaking classes proposed by Emery and Gunnerson (1973). Class type is designated by numbers in the respective boxes. 86

Figure 20. Non-dimensional numerical simulation of solitary wave showing profiles of bolus formation and surge (run-up). Exhibit shows surface wave profile on a sloping beach (1:10) and internal velocity distributions at various time steps n . Taken from Heller, Unger, and Hagar (2005). Reproduced by permission of the American Society of Civil Engineers.	88
Figure 21. Steps in Roache's (1972, 1998a) recommended approach for solving the Navier-Stokes equations.	101
Figure 22. Finite difference grid.	108
Figure 23. Depiction of computational domain used in this study. This figure shows the pycnocline in relation to the location of the step or potential wells used to artificially generate internal waves for the purposes of the numerical simulation. “ EW ” means elevation well whose density is ρ_2 . “ DW ” means depression well whose density is ρ_1 . This figure is not to scale and the proportions are approximate.	110
Figure 24. Boundary condition designations corresponding to Table 10. This figure is not to scale and the proportions are approximate.	116
Figure 25. Internal Solitary Wave Features. Elevation-type ISW shown. Parameters depicted in this figure are described elsewhere in this dissertation.	121
Figure 26. Example MATLAB worksheet used to calculate measurable ISW properties. Top figure illustrates a depression-type ISW measured at location 1101 following a simulated encounter with an isolated topographic obstacle. Computational arrangement is for a simulated dimensional depth ratio of 10 cm/40 cm. Other system parameters for the simulation are listed in the shaded box. Top figure is not to scale and the proportions are approximate.	133
Figure 27. Density-height curve showing example of pycnocline profiles. The solid line is the undisturbed pycnocline profile at time zero before the start of the numerical simulation. The dashed line shows how the profile of the pycnocline has evolved through the course of the simulation at some subsequent time t . A dimensionless Boussinesq parameter of -0.03 was used in the simulation. Arrows indicate the magnitude of the wave amplitude a_i . (a) Depression-type ISW. (b) Elevation-type ISW.	134
Figure 28a. Non-dimensional numerical simulation showing the evolution of a depression-type ISW. Shaded area highlights step well used to artificially	

generate an ISW. Arrow indicates the direction of wave propagation at the start of the numerical simulation.....	137
Figure 28b. Continued.....	138
Figure 29a. Non-dimensional numerical simulation showing the evolution of an elevation-type ISW. Shaded area highlights step well used to artificially generate an ISW. Arrow indicates the direction of wave propagation at the start of the numerical simulation.....	139
Figure 29b. Continued.....	140
Figure 30. Sequence of events leading to the evolution of a depression-type ISW. Multiple isopycnals are shown with the pycnocline highlighted.	143
Figure 31. Sequence of events leading to the evolution of an elevation-type ISW. Multiple isopycnals are shown with the pycnocline highlighted in blue. Streamlines are shown by dashed lines. Non-dimensional numerical simulation shows clockwise overturning of the step well.	144
Figure 32. Example of K-H-like features associated with the formation of an ISW during a non-dimensional numerical simulation. The pycnocline is highlighted in red.....	146
Figure 33. Non-dimensional simulation showing streamlines, internal flow field direction, and pycnocline for a mode-1 depression-type ISW. Example corresponds to one time step from simulation depicted in Figure 28. Arrows indicate clockwise flow pattern. Insets A and B show details of clockwise flow field direction.	147
Figure 34. Non-dimensional simulation showing streamlines, internal flow field direction, and pycnocline for a mode-1 elevation-type ISW. Example corresponds to one time step from simulation depicted in Figure 29. Arrows indicate counter-clockwise flow pattern. Insets A and B show details of counter-clockwise flow field direction.	148
Figure 35. Examples of normalized velocity vectors for an ISW. (a1) Depression-type ISW. Above the pycnocline (dotted line), the profile illustrates a flow pattern consistent with a clockwise flow regime as the velocity vectors occupy those quadrants designated I and III. The simulation depicts fluid flow from the right-to-the-left above the pycnocline. Below the pycnocline, the flow is left-to-right. See earlier Figure 30. (a2) Elevation-type ISW. Above the pycnocline, the profile illustrates a flow pattern consistent with a counter-clockwise flow regime as the velocity vectors occupy those quadrants	

designated II and IV. The simulation depicts fluid flow from the left-to-the-right above the pycnocline. Below the pycnocline, the flow is flow from the right-to-left. Also see earlier Figure 31. Exhibits “b” and “c” display, respectively, the horizontal and vertical components of the normalized velocity vectors. 149

Figure 36. Benchmark trials showing the effect of grid density on potential well depth η_0 and ISW amplitude a . (a) Dimensionless benchmark trials for five different grid densities. (b) Benchmark trial data shown in relation of median and range of Chen (2006) data. 151

Figure 37. Benchmark trials showing the relationship between potential well depth η_0 and ISW amplitude a . (a) Non-dimensional trials for 40 cm-deep tank scenarios. (b) Non-dimensional trials for 50 cm-deep tank scenarios. 152

Figure 38. Normalized wave speed vs. normalized wave amplitude for simulated dimensional 40 cm-deep wave tank trials. Plot shows simulation data for 48 trials corresponding to four measurement locations once the ISW had reached steady-state. Solid symbol represents a mean value for a particular simulation. 155

Figure 39. Normalized wave speed vs. normalized wave amplitude for simulated dimensional 50 cm-deep wave tank trials involving elevation-type ISWs. Plot shows simulation data for 32 trials corresponding to four measurement locations once the ISW had reached steady-state. Solid symbol represents a mean value for a particular simulation. 156

Figure 40. Normalized wave speed vs. normalized wave amplitude for simulated dimensional 50 cm-deep wave tank trials involving depression-type ISWs. Plot shows simulation data for 48 trials corresponding to four measurement locations once the ISW had reached steady-state. Solid symbol represents a mean value for a particular simulation. 157

Figure 41. Comparison of normalized wave speed vs. normalized wave amplitude data for data reported the literature as well as the benchmark trial simulations. 159

Figure 42. Comparison between benchmark trial simulations and Chen (2006) data. (a) Scatter diagram. (b) MATLAB-generated regression lines corresponding to respective data sets. (c) Break-down of benchmark trials results by simulated dimensional depths. 160

Figure 43. Rates of viscous damping for four different depression-type ISW amplitudes in three different depth configurations. Plots show data for 80 trials (simulations).....	164
Figure 44 Effects of viscous damping on amplitudes of ISWs of depression for three different depth configurations as a function of distance traveled from the generation point. Plots show data for 80 trials (simulations).....	165
Figure 45. Rate of normalized energy decay for ISWs of depression for three different depth configurations as a function of distance traveled from the generation point. Plots show data for 80 trials (simulations) energy as a function of $\eta(t)$	169
Figure 46. Digital Images of submarine topography characteristic of the continental slope/continental shelf transition. Example is for the vicinity Monterey Canyon, California. (a) Black-white shaded relief image. (b) False-color image of bathymetry. Figures illustrate an example of the shelf and slope-shelf topographic obstacle scenarios modeled in this research. Investigators (i.e., Carter, Gregg, and Lien 2005) have long-recognized this area as representative of one for which the formation of ISWs is favorable. Images generated by the U.S. Geological Survey/Menlo Park.....	171
Figure 47. Examples of types of topographic/physiographic analogs considered in the numerical simulations. These geometries were numerically introduced into the computation domain depicted earlier in Figure 23. Figures are not to scale and are intended only for illustrating the approximate location of the pycnocline defining this two-layered fluid system relative to the obstacle..	172
Figure 48. Principal physiographic features found in the ocean. The relative proportions of these features in a marine setting is summarized in Table 8. Source MOS.org.....	174
Figure 49a. Non-dimensional numerical simulation showing an encounter between a depression-type ISW and a shelf-like obstacle. The vertical dashed line corresponds to the position of the theoretical turning point defined by $h_1 = h_2$. $Re = 9.372e4$ and $Fn = 0.085$	176
Figure 49b. Continued.....	178
Figure 49c. Continued.....	179
Figure 49d. Continued.	181

- Figure 50.** Selected details of the non-dimensional numerical simulation depicted in Figure 49 showing an encounter between a depression-type ISW and a shelf-like obstacle. The vertical dashed line corresponds to the position of the theoretical turning point plane defined by $h_1 = h_2$. Velocity vector field is shown as are streamline contours (dashed lines). (a) “Wash-down” associated with shoaling. (b) “Bore” formation. Also see Appendix B. 182
- Figure 51.** Time series plots of normalized velocity vector profiles for a depression-type ISW at ten uniformly-spaced locations during an encounter with a shelf-type obstacle. Horizontal velocity vectors are blue (or solid) lines. Vertical velocity vectors are red (or dashed) lines. The pycnocline elevation is depicted by a dotted line. 183
- Figure 52.** Detailed time series plots of normalized velocity vector profiles for a depression-type ISW transitioning to an elevation-type ISW. Figure shows uniformly-spaced time series plots beginning at the Probe 9 location depicted in Figure 51. The pycnocline elevation is depicted by a dotted line. 185
- Figure 53a.** Non-dimensional numerical simulation showing an encounter between a depression-type ISW and a slope-shelf obstacle. The dashed line corresponds to the vertical position of the theoretical turning point defined by $h_1 = h_2$. $Re = 9.372e4$, $Fn = 0.085$, and $Q = 24$ corresponding to a slope of about 2.4° 187
- Figure 53b.** Continued..... 189
- Figure 54.** Selected details of the non-dimensional numerical simulation depicted in Figure 53 showing an encounter between a depression-type ISW and a slope-shelf obstacle. The vertical dashed line corresponds to the position of the theoretical turning point plane defined by $h_1 = h_2$. Vectors in the velocity field are shown as are streamlines (dashed lines). (a) Well-developed vortex along the slope face after the ISW has passed the theoretical turning point plane. (b) Upwelling field located in the vicinity of slope crest as a secondary ISW of elevation is passing. Additional details of this particular numerical simulation can be found in Appendix C. 191
- Figure 55.** Time series plots of normalized velocity vector profiles for a depression-type ISW at ten uniformly-spaced locations during an encounter with a slope-shelf obstacle. Horizontal velocity vectors are blue (or solid) lines. Vertical velocity vectors are red (or dashed) lines. The pycnocline elevation is depicted by a dotted line. 192
- Figure 56.** Detailed time series plots of normalized velocity vector profiles for a depression-type ISW transitioning to an elevation-type ISW. Figure shows

uniformly-spaced time series plots beginning at the Probe 9 location depicted in Figure 55. The pycnocline elevation is depicted by a dotted line.	193
Figure 57a. Non-dimensional numerical simulation showing an encounter between an elevation-type ISW and an extended slope-type obstacle. The vertical dashed line corresponds to the position of the theoretical turning point defined by $h_1 = h_2$. $Re = 2.303e5$, $Fn = 0.074$, and $Q = 50$ corresponding to a slope of about 1°	195
Figure 57b. Continued.....	196
Figure 57c. Continued.....	198
Figure 57d. Continued.	200
Figure 58. Selected details of the non-dimensional numerical simulation depicted in Figure 57 showing an encounter between a depression-type ISW and an extended slope-type obstacle. The vertical dashed line corresponds to the position of the theoretical turning point plane defined by $h_1 = h_2$. Insets within each figure show the relative location of the ISW to the obstacle at the time step indicated. (a) Internal solitary wave approaching the theoretical turning point plane. (b) Onset of polarity reversal and early formation of multiple, secondary elevation-type ISWs. (c) Wave train of elevation-type ISWs approaching obstacle slope. Static pycnocline is indicated. (d) Wave train advancing (or marching) up the slope.....	203
Figure 59. Time series plots of normalized velocity vector profiles for a depression-type ISW at ten uniformly-spaced locations during an encounter with an extended slope obstacle. Horizontal velocity vectors are blue (or solid) lines. Vertical velocity vectors are red (or dashed) lines. The pycnocline elevation is depicted by a dotted line.	204
Figure 60. Detailed time series plots of normalized velocity vector profiles for a depression-type ISW transitioning to an elevation-type ISW. Figure shows uniformly-spaced time series plots beginning at the Probe 8 location depicted in Figure 59. The pycnocline elevation is depicted by a dotted line.	205
Figure 61a. Non-dimensional numerical simulation showing an encounter between a depression-type ISW and a so-called short-slope obstacle. $Re = 2.096e4$, $Fn = 0.075$, and $Q = 22.9$ corresponding to a slope of about 2.5°	207
Figure 61b. Continued.....	209
Figure 61c. Continued.....	211

Figure 61d. Continued.	212
Figure 62. Selected details of the non-dimensional numerical simulation depicted in Figure 61 showing an encounter between an elevation-type ISW and a so-called short-slope obstacle. The vertical dashed line corresponds to the position of the theoretical turning point plane defined by $h_1 = h_2$. Vectors in the velocity field are shown as are streamline contours (dashed lines). (a) Onset of shoaling/breaking first defined by “wash-down.” (b) “Breaking” of ISW defined by the overturning of the pycnocline. Additional details of this particular numerical simulation can be found in Appendix E.	213
Figure 62. Continued. (c) Example of bolus (or bore) advancing up slope at a point beyond the plane of the theoretical turning point (vertical dashed line). (d) Maximum run-up elevation of breaking ISW defined by pycnocline surge up the face of the obstacle.	214
Figure 63a. Non-dimensional numerical simulation showing an encounter between an elevation-type ISW and a reverse-self obstacle. The vertical dashed line corresponds to the position of the theoretical turning point defined by $h_1 = h_2$. $Re = 3.314e4$ and $Fn = 0.085$	216
Figure 63b. Continued.	217
Figure 63c. Continued.	219
Figure 63d. Continued.	220
Figure 63e. Continued.	221
Figure 64. Time series plots of normalized velocity vector profiles for a depression-type ISW at ten uniformly-spaced locations during an encounter with a reverse-shelf obstacle. The pycnocline elevation is depicted by a dotted line.	222
Figure 65. Detailed time series plots of normalized velocity vector profiles for an elevation-type ISW transitioning to a depression-type ISW. Figure shows uniformly-spaced time series plots beginning at the Probe 11 location depicted in Figure 64. The pycnocline elevation is depicted by a dotted line.	223
Figure 66. Examples of isolated topographic obstacles. (a) U.S. Navy fathometer recorder trace of unnamed seamount located at $14^\circ 20' N$, $165^\circ 55' W$, in the vicinity of the Marshall Islands. Fathometer orientation trace is 059° true North. Image taken from Hess (1946, Figure 8). (b) Digital Image	

of the so-called Healy Seamount ($81^{\circ} 31.57' \text{ N}$, $134^{\circ} 28.80' \text{ W}$). Located about 1100 km north of Alaska, in the Arctic Ocean, this recently-discovered seamount is approximately 30 km long and 13 km wide. The seamount rises from the abyssal plain at a depth of more than 3800 m to a least depth of 2622 m. The view is from the northeast looking southwest. In the far background (approximately 440 km) away is the Chukchi Plateau, in Siberian Russia. False-color image generated by NOAA and the Center for Coastal & Ocean Mapping Joint Hydrographic Center (Durham, NH).....225

Figure 66. Continued. (c) Example of MOR bathymetry profile for the East Pacific Rise. The MOR can be found at the $\text{km} = 0$ position in the profile. Exact profile location not reported. Vertical exaggeration is 20:1. Adopted from Small and Sandwell (1994, Figure 1). (d) Shipboard multi-beam bathymetry image of the East Pacific Rise from 9° to 11° N , at 104° W . Bird's-eye (3D) perspective of a MOR looking North shows a transform fault running from the Pacific plate on the left to the North American plate on the right. False-color image generated by NOAA/Woods Hole Oceanographic Institute. See Ryan et al. (2009).....226

Figure 67a. Non-dimensional numerical simulation showing an encounter between a depression-type ISW and an isolated rectangular obstacle. The vertical dashed line corresponds to the position of the theoretical turning point defined by.....230

Figure 67b. Continued.....232

Figure 67c. Continued.....234

Figure 67d. Continued.235

Figure 68. Time series plots of normalized velocity vector profiles for a depression-type ISW at ten uniformly-spaced locations during an encounter with an isolated rectangular obstacle. Horizontal velocity vectors are blue (or solid) lines. Vertical velocity vectors are red (or dashed) lines. The pycnocline elevation is depicted by a dotted line.....236

Figure 69. Selected details of a non-dimensional numerical simulation between an elevation-type ISW and an isolated rectangular obstacle depicted in Figure 67 showing “full interaction” (Table 14). The vertical dashed line corresponds to the position of the theoretical turning point plane defined by $h_1 = h_2$. Insets within each figure show the relative location of the ISW to the obstacle at the time step indicated. Vectors in the velocity field are shown as streamline contours (dashed lines). (a) Onset of shoaling/breaking first

defined by “wash-down.” (b) “Breaking” of the ISW defined by the overturning of the pycnocline.....	238
Figure 69. Continued. (c) Example of bolus/bore-like feature advancing beyond the plane of the theoretical turning point (vertical dashed line). (d) Example of an elevation-type ISW taking form.	239
Figure 70. Selected details of a non-dimensional numerical simulation between an elevation-type ISW and an isolated rectangular obstacle showing “moderate interaction” (Table 14). The vertical dashed line corresponds to the position of the theoretical turning point plane defined by $h_1 = h_2$. Insets within each figure show the relative location of the ISW to the obstacle at the time step indicated. Vectors in the velocity field are shown as are streamline contours (dashed lines). (a) Onset of shoaling/breaking first defined by “wash-down.” (b) “Breaking” of the ISW defined by the overturning of the pycnocline.	240
Figure 71a. Non-dimensional numerical simulation showing an encounter between a depression-type ISW and an isolated triangular obstacle. The vertical dashed line corresponds to the position of the theoretical turning point defined by $h_1 = h_2$. $Re = 6.247e4$, $Fn = 0.075$, and $Q = 24$	242
Figure 71b. Continued.....	244
Figure 71c. Continued.....	246
Figure 71d. Continued.	247
Figure 72. Time series plots of normalized velocity vector profiles for a depression-type ISW at 12 uniformly-spaced locations during an encounter with an isolated triangular obstacle. Horizontal velocity vectors are blue (or solid) lines. Vertical velocity vectors are red (or dashed) lines. The pycnocline elevation is depicted by a dotted line.....	248
Figure 73. Selected details of a non-dimensional numerical simulation between an elevation-type ISW and an isolated triangular obstacle depicted in Figure 71 showing “full interaction” (Table 14). The vertical dashed line corresponds to the position of the theoretical turning point plane defined by $h_1 = h_2$. Vectors in the velocity field are shown as are streamline contours (dashed lines). (a) Onset of shoaling/breaking defined by “wash-down.” (b) “Breaking” of the ISW defined by the overturning of the pycnocline.	249
Figure 74. Selected details of a non-dimensional numerical simulation between an elevation-type ISW and an isolated triangular obstacle displaying	

“moderate interaction” (Table 14). The vertical dashed line corresponds to the position of the theoretical turning point plane defined by $h_1 = h_2$. Vectors in the velocity field are shown as are streamline contours (dashed lines). (a) Onset of shoaling/breaking defined by “wash-down.” (b) “Breaking” of the ISW defined by the overturning of the pycnocline.251

Figure 74. Continued. (c) Example of likely bolus/bore-like feature advancing beyond the plane of the theoretical turning point (vertical dashed line). (d) Example of likely ISW surge.252

Figure 75. Selected details of a non-dimensional numerical simulation between an elevation-type ISW and an isolated triangular obstacle showing "weak interaction" (Table 14). The vertical dashed line corresponds to the position of the theoretical turning point plane defined by $h_1 = h_2$. Vectors in the velocity field are shown as are streamline contours (dashed lines). (a) Onset of shoaling/breaking defined by “wash-down.” (b) “Breaking” of the ISW.253

Figure 76. Normalized amplitude for a transmitted ISW vs. nonlinear parameter α_{NL} for simulated 50 cm-deep wave tank trials involving an isolated triangular obstacle. Plots show data for 36 numerical simulation trials. (a) Comparison to Kuo (2005), Chen (2006), and Cheng (2006) experimental wave tank trials. (b) Comparison to MATLAB-generated best-fit curve of Kuo (2005) Chen (2006), and Cheng (2006) data. (c) Numerical simulation trials differentiated by magnitude of potential well depth η256

Figure 77. Normalized wave speed for a transmitted ISW vs. nonlinear parameter α_{NL} for simulated 50 cm-deep wave tank trials involving an isolated triangular obstacle. Plots show data for 36 numerical simulation trials. (a) Comparison to Cheng (2006) experimental wave tank trials. (b) Comparison to MATLAB-generated best-fit curve of Cheng (2006) data. (c) Numerical simulation trials differentiated by magnitude of potential well depth η259

Figure 78. Normalized energy for a transmitted ISW vs. nonlinear parameter α_{NL} for simulated 50 cm-deep wave tank trials involving an isolated triangular obstacle. Plots show data for 36 numerical simulation trials. Simulation results are compared to Cheng (2006) experimental wave tank trials that involved both triangular and trapezoidal obstacles. (a) MATLAB-generated best-fit curve of Cheng (2006) data depicted by solid line; dashed line corresponds to MATLAB-generated best-fit curve for simulations

performed for this study. (c) Numerical simulation trials differentiated by magnitude of potential well η .	261
Figure 79. Normalized transmitted wave energy for an ISW vs. blocking parameter ζ for simulated 50 cm-deep wave tank trials involving an isolated triangular obstacle. (a) Simulation results are compared to experimental wave tank trials Kuo (2005), Chen (2006), and Cheng (2006). (b) Comparison to MATLAB-generated best-fit curve of Kuo (2005) and Cheng (2006) data.	264
Figure 80. Wave energy transmission coefficient vs. blocking parameter ζ for simulated 50 cm-deep wave tank trials involving an isolated triangular obstacle. (a) Simulation results are compared to Kuo (2005), Chen (2006), and Cheng (2006) experimental wave tank trials. (b) Comparison to MATLAB-generated best-fit curves. (c) Numerical simulation trials differentiated by magnitude of potential well depth η .	267
Figure 81. Spatial distribution of localized instability resulting in “full interaction” (Table 14) between an isolated rectangular obstacle and an ISW. (a) “Wash-down” phase. (b) “Breaking” phase. $Fn = 0.68$. Exhibit corresponds to numerical simulation trial shown earlier in Figure 67.	272
Figure 81. Continued. (c) “Bore formation” phase. (d) “Surge” phase.	273
Figure 82. Spatial distribution of localized instability resulting in “weak interaction” (Table 14) between an isolated rectangular obstacle and an ISW. Solid line corresponds to the pycnocline. (a) “Wash-down” phase. (b) “Breaking” phase. $Fn = 0.68$.	274
Figure 83. Spatial distribution of localized instability resulting in “full interaction” (Table 14) between an isolated triangular obstacle and an ISW. Solid line corresponds to the pycnocline. (a) “Wash-down” phase. (b) “Breaking” phase. $Fn = 0.68$. Exhibit corresponds to numerical simulation trial shown earlier in Figure 73.	275
Figure 84. Spatial distribution of localized instability resulting in “moderate interaction” (Table 14) between an isolated triangular obstacle and an ISW. (Solid line corresponds to the pycnocline. (a) “Wash-down” phase. (b) “Breaking” phase. $Fn = 0.68$. Exhibit corresponds to numerical simulation trial shown earlier in Figure 74.	276
Figure 84. Continued. (c) “Bore formation” phase. (d) “Surge” phase.	277

Figure 85. Spatial distribution of localized instability resulting in “weak interaction” (Table 14) between an isolated triangular obstacle and an ISW. Solid line corresponds to the pycnocline. (a) “Wash-down” phase. (b) “Breaking” phase. $Fn = 0.68$. Exhibit corresponds to numerical simulation trial shown earlier in Figure 75.278

LIST OF TABLES

Table 1. Physical Processes and Conditions Considered Responsible for Internal Wave Generation. Compiled from Thorpe (1975) using headings suggested by Garrett and Munk (1979).....	19
Table 2. Internal Wave Parameters and Qualitative Observations. Taken from Roth, Briscoe, and McComas (1981, Table 1).....	23
Table 3. Outline of Water Wave Theories.	27
Table 4. Summary of Surface and ISW Properties in a Two-layered Fluid System. Taken from Bogucki and Garrett (1993) citing Ostrovsky and Stepanyants (1989) and Whitman (1974). Surface ISW shown for the purposes of comparison. Assumes $h_2 > h_1$, first order theory.....	35
Table 5. Physiographic Settings for Internal Wave Generation.	47
Table 6. Typical Scales for Mid-latitude Continental Shelf-Type Internal Waves. Assumes a stratified (two-layered) fluid system. Derivations from the values listed in this table can be large. Adopted from Apel et al. (2006, p. 63) unless otherwise noted.	48
Table 7. Amplitude Functions for Principal Constituents of Tidal Harmonic Forcing. Taken from Wahr (1995).	61
Table 8. Hypsometry and Bathymetry of the Earth's Surface. Taken from Wyllie (1971) citing Scheidegger (1963), Menard and Smith (1966), and Ronov and Yaroshevsky (1969).	66
Table 9. Definition of Select System Parameters.	99
Table 10. Boundary Conditions for Computational Domain.	116
Table 11. Summary of Experimental Investigations of ISW Phenomena using Wave Tanks.....	126
Table 12. System Parameters Selected for the Numerical Simulations.	131

Table 13. Estimated Rates of Amplitude Decay for ISWs in Experimental Settings as a Function of Distance as Reported by Various Investigators...	168
Table 14. Suggested ISW Blocking Parameter Values and Effects.	228

LIST OF ABBREVIATIONS

a	wave amplitude
B	blocking parameter: elevation-type wave
c	linear wave speed (velocity)
c_0	wave celerity
CFD	computational fluid dynamics
Cr	Courant number
D	undisturbed reference depth of the modeling domain (in the z direction)
D_m	mass diffusivity
E_D	normalized density gradient
E_P	transmitted wave energy
E_T	wave energy transmission coefficient
ERS	European Remote-Sensing Satellite or ERS
ERTS	Earth Resources Technology Satellite
ETUDE	<u>E</u> xplicit in <u>T</u> ime <u>U</u> p-stream <u>D</u> ifference <u>E</u> stimate
Fn	Froude number
g	gravitational constant of acceleration

h_1	depth of upper fluid layer
h_2	depth of lower fluid layer
J	Joules
K-H	Kelvin–Helmholtz
kHz	kilohertz
HOT	higher-order terms
ISW	internal solitary wave
K-dV	Korteweg-de Vries (equation)
L	length of modeling domain (in the x direction)
L_{PW}	potential well length
L_w	characteristic ISW wavelength
m	slope
MAC	marker-in-cell
MODIS	Moderate Resolution Imaging Spectroradiometer
MOR	mid-ocean ridge
N^2	Brunt-Väisälä frequency
N_{ISW}	number of internal solitary waves
NAS	National Academy of Sciences (USA)
NOAA	National Oceanographic and Atmospheric Administration
ONR	Office of Naval Research
PDE	partial differential equation

Q	stretched coordinate coefficient $\left(Q = \frac{L}{D}\right)$
R	correlation coefficient (of regression)
Re	Reynolds number
Ri	Richardson number
RV	Reflected internal wave
s	internal wave steepness
Sc	Schmidt number
SAR	synthetic aperture radar
t	time
T	wave period
\tan_b	slope of uniform incline
TS	time-step
u	horizontal (x) component of the fluid velocity vector
w	vertical (z) component of the fluid velocity vector
2D	two-dimensional
3D	three dimensional
α	K-dV nonlinear coefficient
α_d	false diffusion constant
α_{NL}	nonlinear parameter
β	K-dV dispersion coefficient

γ	mass density (Boussinesq parameter)
Δ	characteristic wavelength
ρ_1	density of the upper fluid layer
ρ_2	density of the lower fluid layer
η_0	potential well depth
$\eta(t)$	interfacial displacement of the ISW
ν	kinematic fluid viscosity
∇^2	Laplacian operator
φ	stream function
λ	wavelength
ξ	vorticity
ξ_{in}	Iribarren number
ζ	blocking parameter: depression-type wave
ω	tidal frequency

ACKNOWLEDGEMENTS

First, I would like to thank my thesis advisor, Professor Hsien-Ping Pao. I will always be grateful for his patience, encouragement, and long-standing commitment to my academic ambitions. He alone deserves the greatest share of credit for helping to shepherd me through my research project and the subsequent preparation of the dissertation. I would also like to thank Professors Sen Nieh and Shyang-Chin Ling for their thoughtful review comments on my dissertation as well as their participation as jurors in my research defense.

The FORTRAN computer code that forms the basis of my research was initially developed at the Catholic University of America's (CUA's) School of Civil Engineering by Professor Pao, Professor (Emeritus) Timothy W. Kao, Kamal Saffarinia, and He Xiao. When working with this computer code, I was very fortunate to have the acquaintance of certain engineers with extensive numerical modeling experience. Dr. Richard B. Codell (Nuclear Regulatory Commission — NRC) provided invaluable assistance in resolving (debugging) some of the programming challenges that arose with modifications made to the original FORTRAN computer code with my research. Dr. Alper Ucak (CUA)

provided essential guidance and support with the development of the original MATLAB® programs used to post-process the data obtained from the computer trials. Dr. Norman A. Eisenberg (NRC) was a constant source of expert advice on all things fluid mechanics and was frequently consulted when questions arose — and I had many. When approached, all of these gentlemen were especially generous in sharing both their time and their unique expertise.

Neil Coleman (NRC), Charles Gorday (NRC), and Keith Martin (National Institute of Science and Technology) deserve my thanks for their assistance in successfully locating some of the more obscure references cited in my dissertation.

Lastly, I am grateful for the editorial advice and review comments provided periodically by Drs. Codell, Eisenberg, and Michael T. Ryan (NRC Advisory Committee on Reactor Safeguards).

Financial assistance from the NRC in connection with my doctoral studies is acknowledged.

CHAPTER I

INTRODUCTION

1.1 Internal Solitary Waves

The existence of surface and internal solitary waves (ISWs or solitons) in oceans and other large water bodies has been well-established in the scientific literature for more than 150 years (Fedorov and Ginsburg 1992). As with many other types of natural phenomena that are infrequent or difficult at first to recognize, historic accounts of internal wave-like behavior are reported to extend back even farther if the scientific literature was to be re-evaluated (Malandain 1988). Internal waves have also been observed in the atmosphere as lee waves as well as waves propagating along inversion layers. They are also associated with wind sheers at the lower boundary of the high-altitude jet stream (Abdullah 1954, Rottman and Einaudi 1993).

Internal waves in the ocean constitute a major form of hydrodynamic phenomena. They are not rouge waves (Smith 2006) nor might they be considered “extreme oceanic events” (White and Fornberg 1998, Garrett and Müller 2007). As their name implies, internal waves travel within the interior of

the sea. Researchers have found that they occur in a variety of marine environments and form when stratified layers of water, of different densities (either salinity or temperature) meet. Midorikawa (1977) and Ostrovsky and Stepanyants (1989) suggest that ISWs can sometimes form under the influence of tidal processes when barotropic tides produce baroclinic motions. Reported observations of internal wave phenomena are generally limited to certain months of the year suggesting a seasonal (temporal) aspect to their behavior (Apel et al. 1975). Based on their review of temperature records, Carsola and Callaway (1962), for example, note that internal wave phenomena appear to peak during the spring-summer months based on the presence of a well-developed thermocline, and are poorly-defined or generally absent in the thermocline during the neap (weak) tidal phase.

Internal wave formation can take place when stratified ocean water is disturbed and mixed in the presence of irregular or abrupt topographic (physiographic) features commonly observed on the ocean floor such as the continental shelf, seamounts, or submarine rises (Maxworthy 1979, St. Laurent et al. 2003). Once formed, these (downwind) waves maintain their coherence through non-linear (hydrodynamic) processes. They appear as a quasi-linear collection of waves (wave trains) in high-altitude aerial photography or satellite imagery as a result of interactions with surface waves (Gargett and Hughes

1972). Recently, reports of internal wave phenomena have been described in the “Science Section” of the *New York Times* when reference was *New York Times* when reference was made to the association of Kelvin-Helmholtz (K-H) billows with breaking internal waves off the coast of the Azores Islands, in the Atlantic Ocean. See Broad (2010).

As a class, ISWs are nonlinear and non-sinusoidal. They typically have wavelengths that can vary from hundreds of meters (m) to tens of kilometers (km), and periods from several minutes to several hours (Figure 1). Wave amplitudes (pycnocline displacements from peak to trough) can sometimes exceed 100 m and are not uncommon. Hence, they may be considered to be mesoscale ocean phenomena. The orbital motions of internal wave water particles have the largest radius at the pycnocline depth. From this location, their orbitals decrease vertically in both directions. The horizontal velocities do not decay with depth, as would be the case with surface (gravity) waves. Also, as illustrated later in this dissertation, the horizontal and vertical velocities of the water particles in the respective fluid layers are opposite to each other.

The importance of internal wave behavior cannot be underestimated. Anything that is in or near a body of water is subject to wave motion (Pretor-Pinney 2010). The study of pycnocline displacements and currents associated

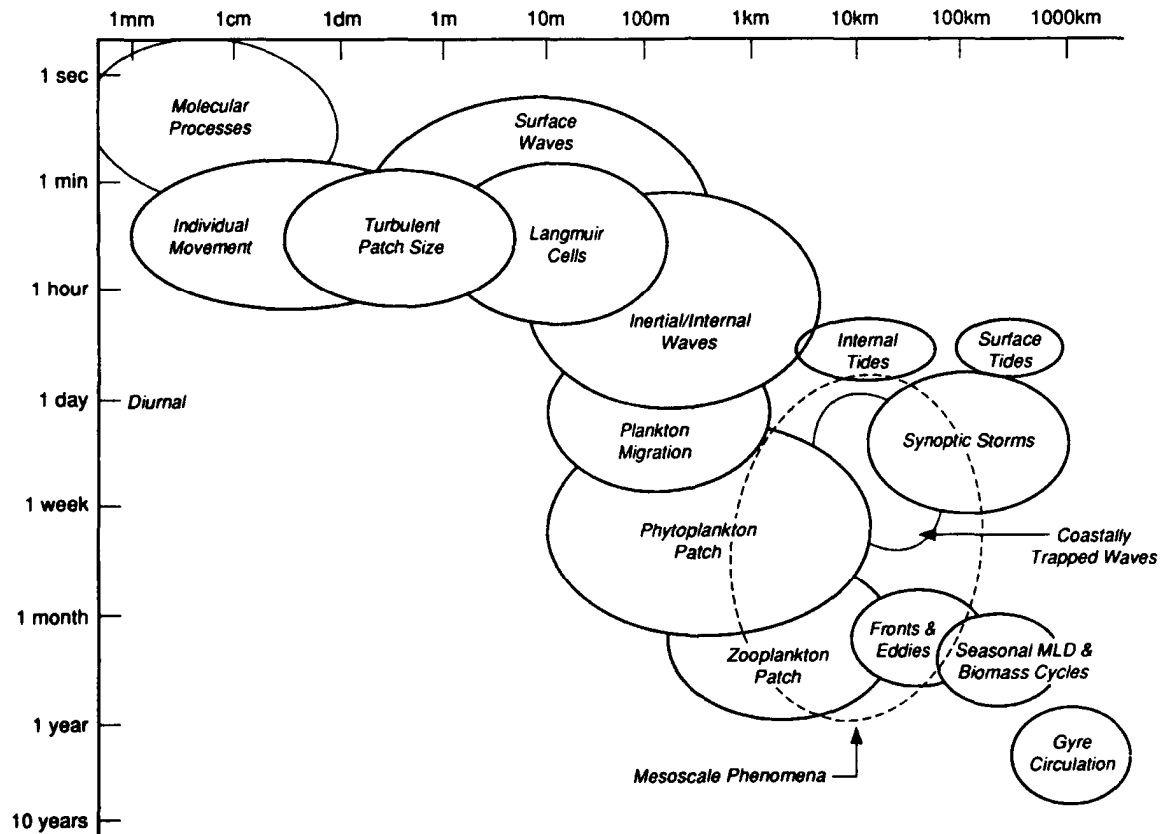


Figure 1. Scale of internal waves shown in relation to other types of physical and biological upper ocean processes. Taken from Dickey (1990, 1991). Reproduced by permission of the American Geophysical Union (AGU). www.agu.org/pubs/authors/usage_permissions.shtml.

with internal waves has many practical applications including applied oceanography, hydraulic engineering, deep-water construction and structure performance, and sediment and environmental pollutant transport. An early motivation in the study of internal waves was practical. The desire was to better understand what effects this class of waves might have on the stability of deep ocean drilling platforms (Osborne, Burch, and Scarlet 1978, Osborne and Burch

1980). Some physical oceanographers, though, considered internal wave phenomena annoyances as they introduced “background noise” into the data they were collecting (El-Sabh, Glombitza, and Johannessen 1971, Colton 1972). Nevertheless, the significance of ISW phenomena has grown as they are now thought to be responsible for a significant portion of oceanic mixing of heat, salt, and other nutrients by virtue of breaking phenomena (Briscoe 1984, Gregg 1991, Munk and Wunsch 1998). In particular, turbulent mixing may lead to nutrient pumping which is considered especially relevant to controlling the dispersal of nutrients important to marine communities present in the water column (Bourgault and Kelly 2003, Stevick et al. 2008). Nutrient pumping (upwelling) has also been found to correlate to reports of internal tidal bores associated with the spring-to-neap lunar cycle (Pineda 1991, 1994).

For their part, Egbert and Ray (2000) concluded that internal tidal and wave phenomena radiated into the deep ocean can provide enough energy to maintain abyssal stratification. A recent compilation by Wunsch and Ferrari (2004), for example, indicates that internal waves represent about 24 percent of the ocean energy reservoir or about 14 exajoules (EJ) or 10^{18} J.¹ Moreover, it has been recently suggested that internal wave-like phenomena might also

¹ Based on an earlier estimate by Munk (1981). The total ocean energy reservoir has been estimated by Wunsch and Ferrari to be about 53 EJ. Uncertainties in that estimate are reported to range between a factor of 2 and possibly as large as 10.

represent geomorphic agents that can shape the gradients of continental slopes (Cacchione, Pratson, and Ogston 2002, Zhang, King, and Swinney 2008). As discussed later in this dissertation, internal waves are not uncommon in nature. Rather, despite being nonlinear phenomena, their occurrence appears to fit into a certain predictable pattern suggesting that they are more common than once thought.

However, despite increased recognition of both their occurrence and importance, the study of internal waves has not benefited from the same level of study as surface or wind-generated waves have historically enjoyed (i.e., National Research Council 1963, Kinsman 1965). Although there have been several decades of study and research, certain fundamental aspects of internal wave behavior are still poorly understood such as their exact formation methods and propagation properties (Helfrich and Melville 2006). A particular challenge to researchers has been to develop a parameterization scheme (e.g., Pierson et al. 1958) that can be used to help explain the behavior of internal waves when they shoal in response to changing topographic conditions. See Emery and Gunnerson (1973). To this end, researchers have found it useful to rely on the use of experimental wave tanks to recreate the *in situ* or field observations reported by oceanographers as well as test mathematical theories that can be used to describe their behavior.

Compared to the number of published field studies and observations, there are fewer published studies of internal wave behavior based on wave tank experiments and even fewer published numerical simulations. When performed, the primary focus of many past wave tank experiments has primarily been on investigating the shoaling behavior of internal waves with topographic features (obstacles) of moderate slope (Kao and Pao 1980, Saffarinia and Kao 1996). These studies have provided additional insights into the hydrodynamic behavior of solitary wave-like forms as well as help to validate the so-called K-dV equation, derived by Korteweg and de Vries (1895), which has been widely used to describe internal waves. In recent years, however, there has been a growing interest in improving the understanding of behavior between internal waves and more discrete topographic features such as submarine seamounts (Lui et al. 1998, Hsu, Liu, and Liu 2000).

One of the challenges to oceanographers has been to capture real-time data on internal waves as they occur *in situ*. Field data are expensive to collect. Research ships need to be chartered, staffed, and outfitted with the scientific instrumentation. Once underway, the research expedition needs to locate an internal wave in anticipation of where and when one might occur, and then collect the data on its properties in real time. Moored (stationary) data arrays are an alternative to ship-borne surveys but these methods still suffer from the

limitation that they need to be properly located and operational to document the phenomena of interest (e.g., Dickey 2003) — in the case of this research, the occurrence of a passing internal wave. Even when collected, some investigators have called into question the temporal as well as spatial representativeness of the physical data themselves collected in a marine setting (National Academy of Sciences — NAS 1993).

In many fluid mechanic/hydrodynamic studies, an acceptable alternative research technique to field investigations is laboratory experimentation (e.g., Rouse 1976, Mutel 1998). Although relatively less expensive, laboratory experiments are still both labor and resource intensive. Another issue to consider concerns the physical representativeness of the experimental results themselves which have been the subject of considerable academic discussion as well as advice for improvement (Coleman and Steele 1995, Stern et al. 1999). Despite the best attempts of investigators to achieve physical representatives and accuracy, Monaghan and Kos (2000) and, more recently, Bourgault and Richards (2007) have called into question the value of wave tank experiments involving internal waves owing to questions about the exactness of the results relative to actual field data (i.e., scaling effects) and/or recognized theories. In wave tank experiments conducted by Wessels and Hutter (1996), for example, they estimated some of their measurement errors to be as large as 25 percent.

In an effort to improve the physical representativeness and accuracy of internal wave investigations, researchers have employed computational fluid dynamics (CFD) techniques to the study of internal waves. Computational fluid dynamics is a branch of fluid mechanics dealing with the simulation of fluid flows through the use of numerical methods. The numerical methods implement certain (universal) governing equations, and are used to obtain detailed results of the flow field such as velocities, pressures, densities, and temperatures. A CFD simulation requires that the physical geometry, fluid properties, initial and boundary conditions, and external (forcing) conditions be defined for some computational domain for which the governing equations are solved in both time and space.

In the years following its development, the digital computer has been widely used to model complex physical phenomena (e.g., Davis and Herzfeld 1993, Kaufman, and Smarr 1993), including those phenomena involving ocean dynamics (NAS 1975). In this regard, CFD methods have been developed and proven to be an acceptable research alternative to wave tank experiments when it can be demonstrated that certain fluid mechanics validation and verification issues are addressed (Stern et al. 2001, Oberkampf and Trucano, 2002). Moreover, because it has been recognized that visually-displayed information can convey additional information on both the temporal and spatial variations in

scientific data (Tufte 1983, 1990, 1997), many of the commercial CFD programs available — e.g., FLUENT, FLOW-3D, COMSOL, MODFLOW² — now have integrated graphics packages that allows for a virtual rendering of the fluid behavior being investigated which have led to improvements (at least academically) in the study of hydrodynamic phenomena generally (Fraser et al. 2007).

1.2 Scope of Work and Objectives

This research numerically simulates the two-dimensional (2D) behavior of large-amplitude ISWs within a shallow, canal-like basin. For convenience, the basin is closed at both ends. As an initial condition for the modeling exercises, the basin is stratified and comprised of two layers of fluid with different densities. This is the simplest idealization for the modeling of internal wave propagation. When perturbed, the difference in densities and the tendency of the system to restore itself is a key factor contributing to the formation of an interfacial internal wave. Rather than using the K-dV equation, which is only valid for moderate-amplitude solitons, this research relied on certain governing equations represented by the Navier-Stokes and the continuity equations. The numerical method used to solve these equations was a one-step explicit finite

² ANSYS FLUENT (2010), FLOW-3D (2010), COMSOL Multiphysics (1998), and Visual MODFLOW (2010).

difference scheme. This method possesses both the transportive and conservative properties described by Roache (1972, 1998a). To address any truncation errors associated with the calculations at each time step (i.e., numerical dispersion, false diffusion), an explicit numerical method described by Valentine (1987) was used. The calculating environment was FORTRAN-95. Computational results were processed using the student version of MATLAB®-software (MATLAB® and SIMULINK® 2008).

A key focus of the research was to examine how simulated internal waves interact with topographic obstacles and quantify how their properties change (vary) when different obstacle geometries are encountered. The computational results obtained were compared against the experimental results reported by other researchers.

1.3 Contribution and Originality

There has been a long-standing scientific interest in understanding the hydrodynamic behavior of stratified fluids (e.g., Long 1953, 1954, 1955; Yih 1969, and Imberger 1987). In the case of internal waves, based on observations from aerial photographs and satellite images, earlier studies *in situ* focused primarily on their shoaling behavior in response to an encounter with the continental slope/continental shelf transition. In an experimental setting such

as a wave tank, prior researchers have attempted to recreate the interactions observed in the field and quantify them. This research contributes to an improved understanding of the behavior between nonlinear internal waves and other certain types of submarine topographic features by evaluating these interactions numerically and then graphically presenting the results. In particular, this research is unique in that it has been possible to employ graphics software to depict the small-scale features of internal wave dynamics that have not been readily observable in a traditional wave tank setting through the use of dye layers, hot film probes, particle seed methods or other such techniques. These features include the velocity fields, a prescribed density interface [or pycnocline – from the Greek *pyknós* (πυκνός), for dense], streamlines, and even the spatial distribution of the Richardson number. Moreover, the research contributes to a basic understanding of internal wave phenomena and will include some general conclusions regarding the effects of obstacle geometry on internal wave behavior and properties.

1.4 Organization

In the remaining chapters, this dissertation is organized as follows. *Chapter 2* provides some background on the historical study of internal wave phenomena, and reviews the physical mechanisms generally responsible for ISW generation, propagation, and dissipation. *Chapter 3* identifies the governing

equations that form the basis for this research and describes the computational approach employed in the numerical simulations. *Chapter 4* presents and analyzes results from the numerical simulation trials themselves. These trials include numerical simulations of internal wave encounters with topographic analogues for seven types of submarine features likely to be found on the seafloor. Higher graphic resolution figures reveal additional details from some of these simulations. These figures are presented in appendices to this dissertation. Last, *Chapter 5* presents some concluding remarks and recommendations for future research bearing on the study of internal wave phenomena.

CHAPTER II

BACKGROUND

2.1 The Study of Internal Solitary Waves

Much of what is known about internal waves can be attributed to observations made at sea as well as the results of theoretical studies and experimental models. As a result, there is a rich (and growing) literature with respect to the study of internal wave behaviour. In the United States, funding particularly by both the Office of Naval Research (ONR) as well as the National Science Foundation over the last half-century has done much to advance oceanic science in this research area as well as other areas of physical oceanography. Sapolsky (1990) and the NAS (2000) describe some of the major programs and projects benefiting from this support.

An early motivation behind the development of remote sensing technology was to observe the Earth, its resources, and its physical processes (Fischer 1975). Conventional aerial photographs were already used routinely to study both geologic features (Simmons 1952, Ray 1960) as well as ocean phenomena (Dietz 1947, Cox and Munk 1954, McKenzie 1958). 70-mm color photographs

taken as part of the Gemini manned space flight program in the 1960s were instrumental in promoting the subsequent use of unmanned satellites to map and catalogue the Earth's surface and the physical processes acting thereon (Lowman 1999).

Some of this imagery – initially acquired from the Gemini program and later from the ERTS-1 satellite³ – revealed wave-like features on the ocean surface that were different from those commonly associated with wind-driven surface waves. When observed, these solitary wave-like features were frequently found to be associated with the deep ocean/continental shelf topographic transition (Apel et al. 1975). Russian investigators were also aware of the occurrence of these features from photographs/imagery acquired in connection with their own National programs (Babkov 1973). Researchers at the time had already begun to independently propose that the continental shelf had some overall influence on their formation based on field measurements of primarily density and temperature data (Ichiye 1950, Defant 1959, Rattray, 1960, Lee 1961, Yasui 1961). Zeilon (1913, 1934), for example, had previously demonstrated experimentally that topographic sills or sill-like features at the bottom of a glacially-carved fjord could give rise to the occurrence of internal

³ Landsat, originally named the 'Earth Resources Technology Satellite' or ERTS-1, was first launched in 1972 (Williams and Carter 1976).

wave phenomena. Sandström (1991, p. 438) has suggested that Zeilon's pioneering work in this area deserves more credit (i.e., recognition) in the literature that it has received.

In the years following their identification in imagery, internal wave behaviour has been investigated extensively by physical oceanographers. Published studies include investigations focused on the origins and characteristics (amplitudes, wavelengths, speeds, and energies) of internal waves and how these properties evolve once they encountered prominent topographic features commonly found along the seafloor. Most studies reported that some type of high-relief topographic feature such as a continental shelf/continental sill needed to be present to allow for this type of wave to form. Recent studies such as those conducted by Garrett and Kunze (2007) suggest that less prominent topographic features such as a mid-ocean ridge or MOR associated with seafloor spreading centers can, under certain conditions, also factor into internal wave generation.

To better understand the current state-of-knowledge concerning internal wave behavior, the *Annual Reviews of Fluid Mechanics* series, select proceedings

of the University of Hawaii's *'Aha Huliko'a Winter Workshops* ⁴, and certain issues of *Geophysical Research Letters* ⁵, were found to be excellent sources of information on this subject and thus good places to start when canvassing the literature. Over the last 40 or so years, published reports of marine observations of internal waves have been complemented with experimental investigations intended to recreate what was observed *in situ* as well as numerical simulations performed more recently that rely on the use of digital computers.

One of the earliest published literature surveys bearing on internal wave phenomena was an annotated bibliography prepared by Ichiye (1966) with ONR support. He identified close to 160 papers and reports on this subject. About a decade later, another review was published by Garrett and Munk (1979) in *Annual Reviews of Fluid Mechanics*. In that paper, the authors cited Defant (1961), Briscoe (1975), Roberts (1975), and Philips (1977) as key sources of then-current information on internal waves. Other useful references include Philips (1966), Lighthill (1978), Miles (1980), Munk (1981), Baines (1986), Huthnance (1989), and Farmer and Armi (1999). A short list of more-recently published papers would include Staquet and Sommeria (2002), Moum et al. (2003), and St.

⁴ Specifically, proceedings for the 1984, 1991, 1995, and 1999 workshops. See Müller and Pujalet (1984) and Müller and Hendersen (1991, 1995, and 1999).

⁵ Volume 30, number 3, for example. See Briscoe (1975).

Laurent et al. (2003). Miles (1980) and Helfrich and Melville (2006) are also important for they provide comprehensive assessments of relevant literature during the preceding years. A literature review that is contemporaneous with this research has been prepared by Berntsen (2008). That bibliography is limited primarily to internal wave studies and investigations published over the last two decades. The Berntsen bibliography contains more than 150 citations that are both annotated and indexed.

In general, what the literature has reported is that internal waves are now generally considered to be more ubiquitous oceanic phenomena than once thought. They can be generated in multi-parameter space by many different processes and mechanisms that vary both temporally and spatially (Levine 1983). The most common internal wave generation scenario relies on tidal-topographic interactions involving some type of stratified fluid system. When considering the growing body of literature that now exists on the subject, perhaps two papers deserve special recognition. First, Thorpe (1975) and later Briscoe (1975) identified key physical processes and conditions considered responsible for the formation of internal waves. Table 1 identifies the some of those key processes and conditions. The relationships between some of the processes and conditions identified by Thorpe (1975), in time and in space, are depicted in Figure 2.

Table 1. Physical Processes and Conditions Considered Responsible for Internal Wave Generation. Compiled from Thorpe (1975) using headings suggested by Garrett and Munk (1979).

← Increasing Water Depth	SURFACE GENERATION	
	Travelling pressure fields	Variable wind stress
	Variable buoyancy flux	Surface wave energy flux
	Rainfall-induced surface turbulence	Shallow diurnal thermocline
	Rainfall-induced halocline	
	INTERNAL GENERATION	
	Steep density gradient	Stratigraphic stability
	Diapycnal eddy diffusivity	Kinematic diffusivity
	Internal energy fluxes	Horizontal tidal currents
	Coriolis frequency	"Fossil" turbulence
	BOTTOM GENERATION	
	Variable/irregular topography	Horizontal tidal currents
	Weak density gradient	

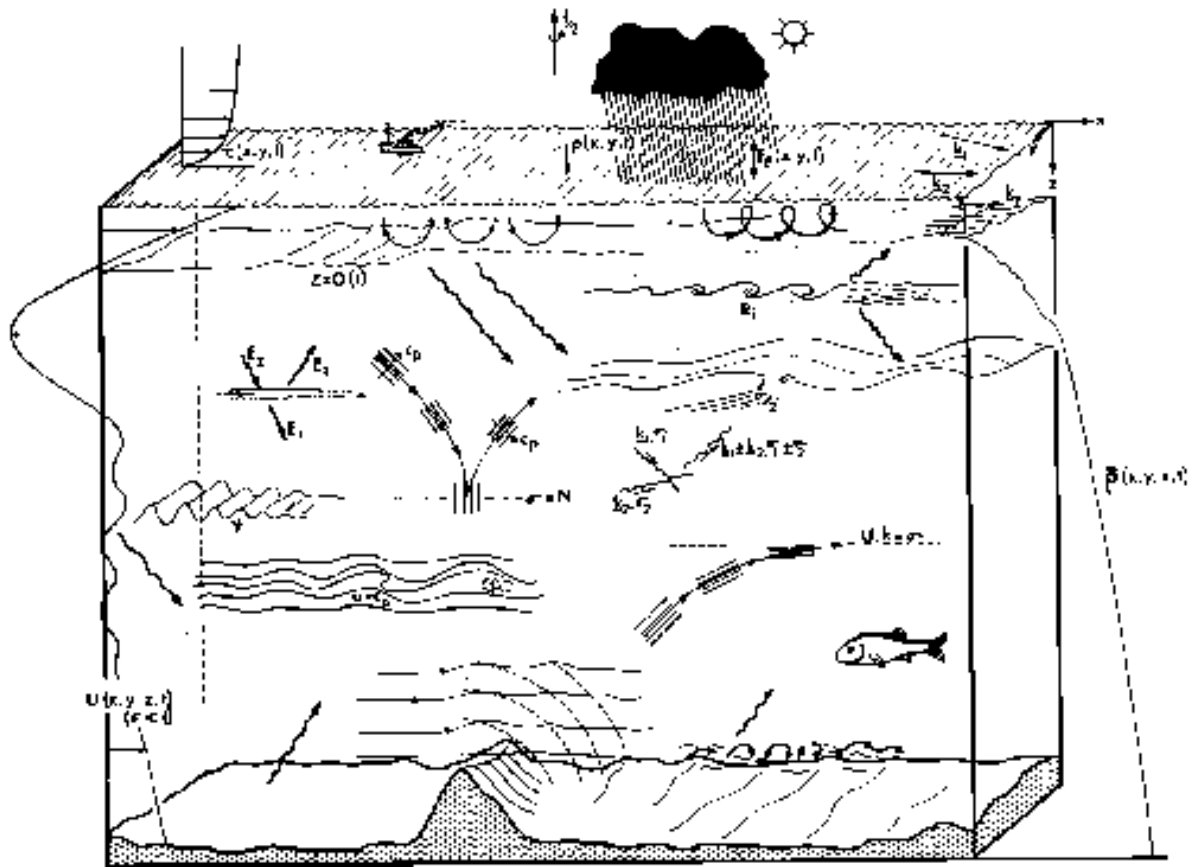


Figure 2. Thorpe's (1975) depiction of physical processes and conditions thought to contribute to the formation of internal waves. Reproduced by permission of the AGU.

Briscoe (1975) has suggested a more simplistic interpretation of the physical environment responsible for the generation of an internal wave. As illustrated in Figure 3, the internal wave generation environment would consist of five major elements. Unranked, these elements would include:

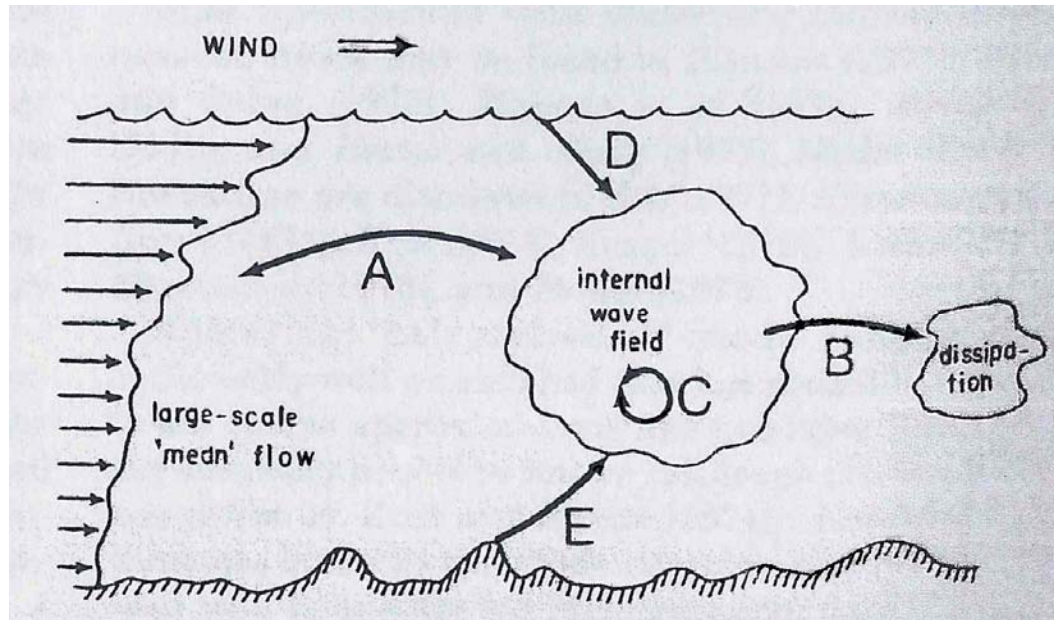


Figure 3. Briscoe's (1975) “simplified” depiction of the basic physical processes thought to contribute to the generation of ISWs. Letters are described in the text. Reproduced by permission of the AGU.

- A system of interactions with a large scale flow system, such as baroclinic tides (**A**)
- A series of losses due to energy dissipation (**B**)
- The effects of interactions within the internal wave field itself (**C**)
- The influence of hydrostatic effects such as stress, pressure, and buoyancy (**D**)
- The influence of submarine topography (**E**)

Other internal wave generation scenarios have been proposed that include one or more of the processes listed in Table 1 and depicted in Figure 2. They include:

- Relaxation of internal hydraulic flows (Maxworthy 1979, Apel et al. 1985)
- Intrusions created by collapsing mixed layers (Maxworthy 1980)
- Upstream influences (Baines 1984, Melville and Helfrich 1987, and Grue et al. 1997)

An important step in advancing the phenomenological understanding of internal waves, though, was achieved by Garrett and Munk (1972, 1975) when they synthesized existing internal wave data and developed a universal kinematic model for solitary wave behaviour. Their so-called *Garrett-Munk Spectra* describes variations in internal wave energy as a function of wave frequency and wave number. When they do occur, Roth, Briscoe, and McComas (1981) have suggested that the characteristics of internal waves found to occur in the upper reaches of the ocean (depths generally less than 200 m) are qualitatively different from those internal waves found to occur at depths greater than 200 m as the later are subject to fewer state fluctuations. See Table 2.

Table 2. Internal Wave Parameters and Qualitative Observations. Taken from Roth, Briscoe, and McComas (1981, Table 1).

PARAMETER	UPPER OCEAN	DEEP OCEAN
Energy Sources	Atmosphere, winds, surface waves	Many, none dominant
Spectral Shape	Variable	Constant
Level	Variable	Constant
Directionality	Sometimes	None, except for internal tides
Energy Loss	Rate uncertain	Rate uncertain
Internal Oscillations	Strong, variable	Variable, often energy propagation down
Internal Tides	Very strong, variable	Variable
Coherence	Low, but high in some bands	Low
Geographical Specificity	Yes	None
Space Variability	Unknown	None
Critical Issues	General description, cause of variability	Energy sources, losses

Lastly, it is worth noting that prior to *glasnost*, Russia investigators were also a significant source of information concerning internal waves. Monin, Kamenkovich, and Kort (1977) are cited as a major reference concerning Soviet research on the subject through the year 1974. Briscoe (1975) estimated that Russian researchers have accounted for about 15 percent of the overall literature

pertaining to internal wave phenomena. Several of the more recent studies conducted by Russian researchers are described in Apel et al. (2006).

2.1.1 Scott-Russell “Wave of Translation”

The first solitary wave observed was not an internal wave; rather, it was a report of a solitary surface wave in an inland water body. When reviewing the literature, one will find that most papers begin with some causal reference to the Scottish naval engineer John Scott-Russell (1806-1882) and his chance encounter near Edinburgh in 1834. While working at the *Union Canal*, Scott-Russell happened to observe a solitary wave traveling along the free surface of the in-land canal. In his subsequent accounts of the event, Scott-Russell (1838, 1845) reported that a well-defined mound or hump of elevated water was generated on free-surface when a canal barge being towed came to an abrupt stop. This early observer also reported that he was able to follow the wave-like structure for a mile or two before losing sight of it. He estimated that the amplitude of the elevated wave was 1-to-2 feet (or about less than a meter) in height with associated wave length of about 30 feet (or about 10 m). Scott-Russell later referred to this wave-like structure that formed at the bow of the boat as a “wave of translation.”

After much experimental work, Scott-Russell developed two key observations concerning solitary wave behavior that continue to prove to be

valid. In his first observation, he was able to describe the wave speed (velocity) for a solitary wave as a function of wave height using the following expression:

$$c = [g(D + \eta)]^{\frac{1}{2}} \quad (2.1)$$

where g , D , and η are, respectively, the gravitational constant of acceleration, the undisturbed water depth, and the maximum height of the solitary wave, as measured from the undisturbed water level (Newell 1983, p. 1127). In the second observation (Miles 1980, p. 12), Scott-Russell determined that wave breaking occurs when $D \approx \eta$. Additional details concerning the Scott-Russell discovery can be found in Emmerson (1977), Bullough (1988), Craik (2004), and Darrigol (2003).

What was especially intriguing about this discovery was that the type of wave observed by Scott-Russell was inconsistent with prevailing linear wave theory first advanced by George Biddell Airy (1801-1892) and later expanded upon by George Gabriel Stokes (1819-1903). Moreover, Scott-Russell's wave was reported to have retained its shape as it traveled along the shallow canal. Airy/Stokes wave theory, on the other hand, argued that a wave of finite amplitude cannot propagate any substantial distance without a change in its form – that is to say, the wave's amplitude would decay in favor an increase in its wavelength. Moreover, surface waves were believed to travel as a collection

or group of waves or wave trains and not as lone entities as observed by Scott-Russell. See Craik (2004).

Although Scott-Russell was able to later recreate his wave of translation experimentally in wave tank, his published account was met with skepticism within the broader scientific community at the time, and it was several years before there was a plausible mathematical explanation for what was observed in Scotland. Craik (2005, pp. 32-33) suggests that the publication of Stoke's seminal paper on water theory in 1847 (Stokes 1847) may have eclipsed early recognition of the significance of Scott-Russell's discovery as there were any number of investigators contemporaneously engaged in hydrodynamic wave research. See Table 3. Also see Wehausen and Laitone (1960). Boussinesq (1872, 1877) and Lord Rayleigh (1876) later introduced mathematical proofs demonstrating theoretical existence of a "wave of translation." They demonstrated that a wave of finite amplitude could propagate without changing form due to the balance between nonlinearity and dispersion. Nonlinearities, it has been found, tend to steepen the wave front owing to the increase in wave speed and amplitude.

Table 3. Outline of Water Wave Theories.

THEORY	DESCRIPTION	REFERENCES
Airy Waves (sinusoidal)	Waves of small amplitude in deep water	Laplace (1776), Airy (1845)
Stokes and Gerstner Waves (trochoidal)	Waves of finite amplitude in deep, intermediate, and shallow water	Gerstner (1802), Stokes (1847), Froude (1862), Rankine (1863), Rayleigh (1877)
Cnoidal Waves	Waves of finite amplitude in intermediate to shallow water	Korteweg and deVries (1895), Keller (1949)
Solitary Waves (nonlinear)	Solitary or isolated waves of finite amplitude in shallow water	Scott-Russell (1844), Boussinesq (1871), Rayleigh (1876), McCowan (1891)

Ernshaw (1847) was the first (albeit unsuccessfully) attempt to provide a mathematical explanation for solitary waves whereas Bazin (1865) later reported that he was successfully in his efforts to recreate Scott-Russell's wave tank experiments in a long branch of the *Canal de Bourgogne*, near Dijon. More recently, Monaghan and Kos (2000) reconstructed the Scott-Russell experimental wave tank apparatus and later used computer simulations to clarify as well as independently confirm certain details of the reconstructed experiment.

2.1.2 The K-dV Equation

In 1895, D.J. Korteweg (1848-1941) and G. de Vries (1866-1934) derived a mathematical proof validating the plausibility of Scott-Russell's observed wave. Based on their own wave tank experiments, Korteweg and de Vries (K-dV) also observed that waves similar to those of Scott-Russell's, when they occurred in shallow rectangular canals, demonstrated lower wave frequencies and higher wave amplitudes than a "typical" surface wave. In 1895, they formulated the so-called K-dV equation which bears their names and is today considered a critical turning point in the modern study of nonlinear wave behavior for it serves as a prototypical mathematical model for solving nonlinear partial differential equations (PDEs – Bais 2005).

In simplified dimensional form (Osborne and Burch 1980), the K-dV equation can be expressed as a third order PDE:

$$\frac{\partial \eta}{\partial t} + c_i \frac{\partial \eta}{\partial x} + \alpha \eta \frac{\partial \eta}{\partial x} + \beta \frac{\partial^3 \eta}{\partial x^3} = 0 \quad (2.2)$$

where x and t denote position and time, and $\eta(x, t)$ defines the displacement of the surface of the liquid or, alternatively, the interface displacement between the two liquid layers, c_i is the linear wave speed, α is a coefficient of nonlinearity, and β is the dispersion coefficient. The K-dV equation assumes a weakly nonlinear wave under inviscid conditions, and is unique for it has as its periodic solution (which they named "cnoidal wave") in the form of:

$$\eta = \eta_0 \cdot \text{sech}^2 \left[\frac{(x - c_0 t)}{\Delta} \right] \quad (2.3)$$

where η_0 is the maximum soliton amplitude, t is time, and Δ is the characteristic wave length, defined as:

$$\Delta^2 = \frac{12\beta}{\alpha\eta_0} \quad (2.4)$$

Equation 2.3 is valid as long as the total water depth is significantly larger than two times the crest-to-trough distance (characteristic width) of the internal wave. Under certain conditions, the nonlinear and dispersive terms found in equation 2.2 – α and β – are in balance and, as discussed later, when this happens, the physical circumstances are stable enough for the formation of internal waves, including solitary waves. Although mathematically cumbersome, the K-dV equation has proven to be a fairly robust tool for first-order qualitative modeling and prediction of small-to-moderate amplitude wave behavior. See Miles (1990). Since publication of the K-dV equation, other mathematical solutions for nonlinear wave PDEs have been derived to help explain the existence of solitary waves. Newell (1983) and Apel et al. (2006) examine a variety of alternatives to the K-dV equation (model).

When investigating internal wave behavior, researchers have found it convenient to rely on a simplified (shallow-water) model of stratification consisting of two fluid layers. The upper fluid layer has a thickness and a

density designated, respectively, h_1 and ρ_1 whereas h_2 and ρ_2 correspond to the same properties of the lower fluid layer.⁶ Here, the density variation between the two fluid layers is given as $\frac{\Delta\rho}{\rho}$. Thus, when considering the K-dV equation, the nonlinear and dispersion coefficients α and β can be expressed in terms of h_1 and h_2 as:

$$\alpha = \frac{3c_0}{2} \cdot \frac{h_1 - h_2}{h_1 h_2} \quad (2.5)$$

and

$$\beta = \frac{c_0}{6} \cdot h_1 h_2 \quad (2.6)$$

When taking into account the densities of the respective fluid layers, the wave celerity can be defined as:

$$c_0 = \left(\frac{g(\rho_2 - \rho_1) h_1 h_2}{\rho_2 h_1 + \rho_1 h_2} \right)^{\frac{1}{2}} \quad (2.7)$$

Lastly, the linear wave speed c_i can be expressed as a function of β , the wavelength λ , and the phase speed c_0 :

$$c_i = c_0 + \frac{4\beta}{\lambda^2} \quad (2.8)$$

⁶ Alternatively, some of the literature refers to h_1 and h_2 as, respectively, d_+ and d_- .

2.1.3 Early Reports of ISW Phenomena

The first deep-water observation of an “internal” wave of translation is reported by Maury (1861). He described the presence of a strong “tide rip” in the absence of any perceptible current at the entrance of the *Malacca Straits* in the Indonesian Seas. Although there was no additional description of the event to be found in the literature, the occurrence of internal waves in the area today is well documented (Susanto, Mitnik, and Zheng 2005).

In 1893, there was a second report of an internal wave occurrence which did receive detailed scientific follow-up. At the time, the Norwegian explorer Fridtjof Nansen (1861-1930) was leading the so-called *Fran Expedition of 1893-1896* in an attempt to reach the geographic North Pole. As the expedition approached Russia’s Taimyr Peninsula, along the Kara Sea coastal region of the Arctic Ocean, near Siberia, it was reported that his ship encountered some type of invisible force impeding its forward progress in the water – hence the presence of “dead water” as later defined by Bascoum (1980). Subsequent study by Ekman (1904) suggested that the hydrodynamic scenario encountered by the *Fran* was one in which a thin layer of fresh water from a melting glacier had come to rest on top of a denser layer of sea water without mixing. Following recreation of this stratified density scenario in a wave tank, Ekman demonstrated experimentally that a ship’s wake could create an “invisible”

(internal) wave at the boundary of the two fluid layers. His experiment revealed that the ship's forward progress had been hindered from below the water surface by an internal wave that had formed at the salt water/fresh water boundary. Ekman also learned that the amount of flow resistance introduced by the wave's presence increased in proportion to the size of its amplitude. The growing internal wave would continue to slow the ship's progress until the wave's celerity allowed it to overcome and pass the ship. Ekman found that the process of wave generation is particularly efficient when the ship's draught is comparable to the depth of the upper fluid layer. Long (1972) provides an illustration of how dead water phenomena can occur in a stratified fluid system similar to that first investigated by Ekman.

A much recognized but less-studied example of a solitary wave is the tidal bore. A tidal bore is a tidally-generated solitary wave that occurs on the free surface and generally occurs at the mouth of shallow rivers. The bore forms when the incoming tide is forced into the narrowing river mouth, and the bore grows in height until a single wave forms and moves upstream. Tidal bores are analogous to hydraulic jumps and can be modeled as such (Tricker 1965). They are important to consider as their formation have been shown to be sensitive to the magnitude of the Froude number – the inverse of the Richardson number (Lynch 1982) – which happens to be an area of interest to this research.

Chanson (2009, 2010) describes the properties and behaviors of bore-like phenomena associated with surface waves. Wei et al. (1995) presents a numerical model describing the formation of an undular bore using shallow-water-wave equations.

Malandain (1988) reports that there are multiple references to tidal bores in the literature, the earliest being on the *Qiantang River*, near Hangzhou, in China sometime during the 7th Century B.C. See Zuosheng, Emery, and Yui (1989). About 70 localities in 16 countries world-wide are reported to experience some form of tidal bore phenomena to varying degrees. Bartsch-Winkler and Lynch (1988) have compiled an extensive catalog of these locations.

Researchers periodically report evidence of internal wave phenomena during the 1930s-1960s in conjunction with the study of ocean currents. Sverdrup, Johnson, and Fleming (1949) provide a summary of observations made by physical oceanographers in the 1930s. Other reports are described by Munk (1941), Ufford (1947), Emory (1956), and Lafond (1961a). These and other studies and investigations are summarized in Ichiye (1966). However, it is worth noting that internal wave phenomena captured in data recordings were not recognized by oceanographers as such at the time. Measurements of oscillating phenomena below the ocean surface were frequently confused with

some type of aberrant tidal turbulence rather than an example of internal wave-like phenomena (Gould 1971).

When evaluating the observational data described in some of these studies, researchers generally relied on internal wave theories developed by Fjeldstad (1933) which set forth the following depth-density relationship used to define the wave speed in a shallow fluid system as:

$$c = \left(\frac{g h_1 h_2}{h_1 + h_2} \cdot \frac{\rho_1 - \rho_2}{\rho_1} \right)^{\frac{1}{2}} \quad (2.9)$$

Fjeldstad's depth-density formulation assumes that $\frac{\rho_1 - \rho_2}{\rho_1}$ is small, on the order of about 0.01 percent, and that the ISW wavelength is large relative to the total depth of the fluid system. Consequently, the density term can and is often dismissed reducing equation 2.9 to:

$$c = \left(g \frac{h_1 h_2}{h_1 + h_2} \right)^{\frac{1}{2}} \quad (2.10)$$

The generally small velocities observed for internal waves *in situ* are attributed to the influence of the density term.

When considering internal waves in the context of water depth, Roth, Briscoe, and McComas (1981) suggest there are some differences between ISWs that form in waters deeper than 200 m compared to those ISWs that form in shallow waters (e.g., less than 200 m). Recognizing these differences, Bogucki

Table 4. Summary of Surface and ISW Properties in a Two-layered Fluid System. Taken from Bogucki and Garrett (1993) citing Ostrovsky and Stepanyants (1989) and Whitman (1974). Surface ISW shown for the purposes of comparison. Assumes $h_2 > h_1$, first order theory.

WAVE PROPERTY	WAVE TYPE		
	SURFACE	SHALLOW WATER	DEEP WATER
Phase speed c_o of an infinitely long, infinitesimally small wave	$[g'(h_1+h_2)]^{\frac{1}{2}}$	$\left(g' \frac{h_1 h_2}{h_1+h_2}\right)^{\frac{1}{2}}$ $(g'h_1)^{\frac{1}{2}*}$	$(g'h_1)^{\frac{1}{2}}$
Velocity, c	$c_o \left(1 + \frac{1}{2} \cdot \frac{a}{h_1+h_2}\right)$	$c_o \left[1 + \frac{1}{2} \cdot \frac{a(h_2-h_1)}{h_1 h_2}\right]$ $c_o \left(1 + \frac{1}{2} \cdot \frac{a}{h_1+h_2}\right)^*$	$c_o \left(1 + \frac{3}{8} \cdot \frac{a}{h_1+h_2}\right)$
Amplitude and wavelength	$a \left(\frac{L_w}{2}\right)^2 = \frac{4}{3} \cdot (h_1+h_2)^2$	$a \left(\frac{L_w}{2}\right)^2 = \frac{4}{3} \left[\frac{(h_1 h_2)^2}{h_2-h_1}\right]$ $a \left(\frac{L_w}{2}\right)^2 = \frac{4}{3} \cdot h_1^2 \cdot h_2^*$	$a \left(\frac{L_w}{2}\right)^2 = \frac{4}{3} \cdot h_1^2$
Shape $\eta(x,t)$	$a \cdot \text{sech}^2 \left[\frac{(x-ct)}{0.5 \cdot L_w} \right]$	$a \cdot \text{sech}^2 \left[\frac{(x-ct)}{0.5 \cdot L_w} \right]$	$\frac{a}{1 + \left[\frac{(x-ct)}{0.5 \cdot L_w} \right]^2}$

* if $h_2 \gg h_1$

and Garrett (1993) also suggest that some of the major ISW properties (i.e., phase speed, wave speed) can likewise be differentiated. See Table 4, above.

2.1.4 More “Recent” Developments

It would be more than fifty years before there was widespread interest once again in the study of internal waves. Helfrich and Melville (2006) suggest that there were two key developments responsible for changing perceptions regarding the study of internal waves from hydrodynamic curiosities to areas of greater scientific interest. The first development concerned the publication of a 1965 paper in *Physical Review Letters* by Kruskal and Zabusky. These two researchers had been using a digital computer to evaluate non-linear wave phenomena such as the collision of two solitary waves. Prior to performing their computer simulations, there was the expectation that the two colliding solitary waves would consume and cancel each other upon impact. However, the computer simulations revealed just the opposite. Kruskal and Zabusky demonstrated that two solitary waves could collide without any subsequent change in either of their respective wave speeds or amplitudes. In their later paper on the subject, Kruskal and Zabusky also coined the term "soliton" in recognition that the solitary wave obeyed the principal of superposition. Another outcome of the Kruskal and Zabusky study was that they independently derived the 1895 K-dV equation. [Hirt, Nichols, and Romero (1975) later used the Marker-in-Cell or MAC numerical technique, perfected by Welch et al. (1965), to produce a computer-generated animation of two solitary waves colliding and yielding the same outcome predicted by Kruskal and Zabusky.]

Gardner et al. (1967) soon thereafter demonstrated that a soliton was a dominant solution to the K-dV equation.

The second key development identified by Helfrich and Melville (2006) was the confluence in the 1960s-1970s of three independent scientific endeavors – the exploration of the ocean, advances in applied mathematics, and the introduction of remote sensing techniques, as noted earlier.

- Perry and Schimke (1965), for example, are cited for being the first to instrumentally measure an internal wave in the *Andaman Sea*, near the Bay of Bengal, rather than infer its existence indirectly from scientific observations (i.e., field data). They documented groups of internal waves with amplitudes as large as 80 m and wavelengths 2000 m long on the main thermocline at a depth of 500 m in 1500 m-deep water. [These observations were later confirmed by Osborne and Birch (1980).]
- In the area of remote sensing, Ziegenbein (1969) is recognized for first demonstrating that the presence of internal waves below the ocean surface can be detected by measuring subtle variations in the texture of the water surface by measuring the scatter of radar signals.

Previously, it had been possible to identify internal waves only from aerial photographs (Shand 1953) based on a surface expression (or footprint) first referred to as a “slick” (Ewing 1950). However, from low-Earth orbit (generally less than 2000 km), it became possible to observe and photograph the Earth’s surface, including the oceans, remotely from vantage points greater than those previously possible using aircraft (Colvocoresses 1974). Internal waves were first observed from space as part of the 1975 Apollo-Soyuz mission (Apel 1979) and later, using Landsat satellite imagery (Apel et al. 1975). In 1978, synthetic-aperture radar or SAR was placed on the SEASAT satellite. Unlike Landsat, SEASAT was the first satellite specifically designed to collect data on oceanic phenomena (Fu and Holt 1982). The SAR allowed for the acquisition of higher-resolution images necessary for the measurement of key ocean attributes. In this regard, the SEASAT imagery was particularly well-suited for recording the subtle variations produced on the ocean’s surface by internal wave orbitals occurring at depth. Since then, internal waves have been observed regularly from space. Examples of Landsat and SAR imagery can be found in Figures 4 and 5, respectively.⁷

⁷ LaFond (1959) later described the existence of ripples (turbulence) due to shearing velocities in the water created by alternating up-welling and down-welling flow streams. The orbital motion of water particles associated with an internal wave causes areas of divergent and

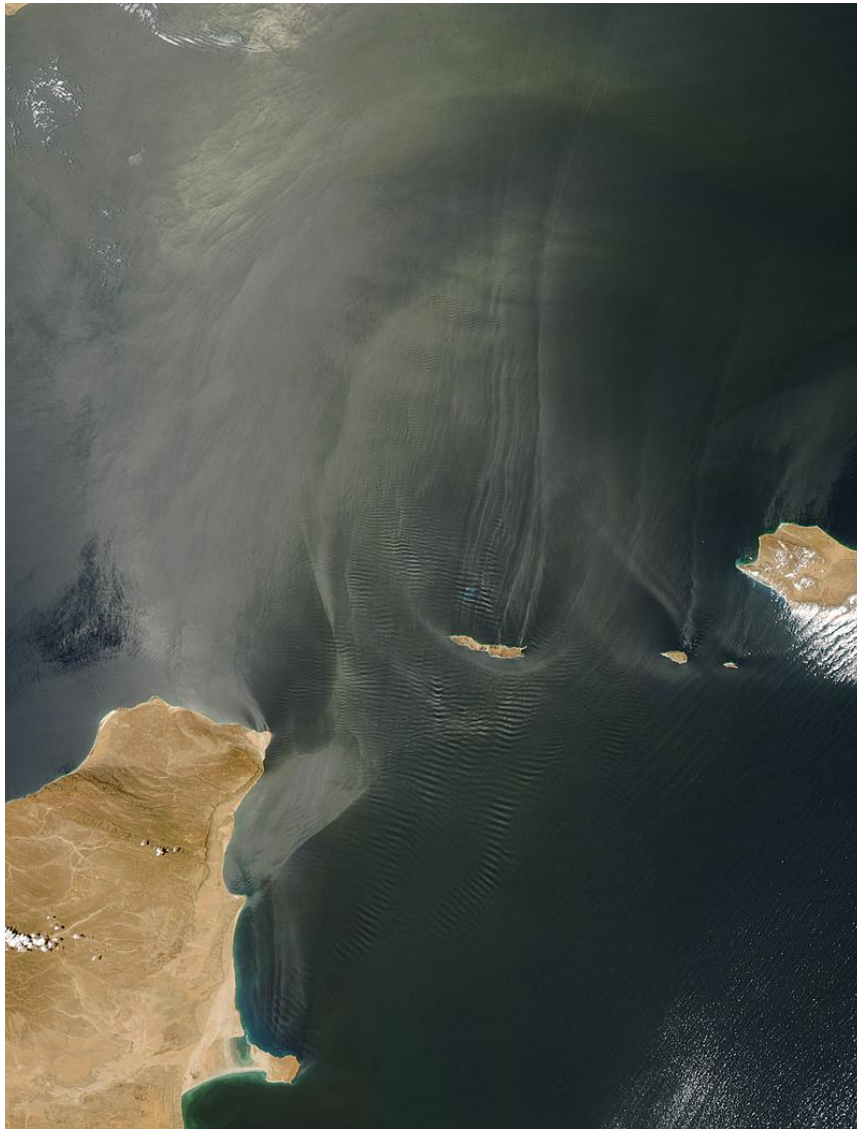


Figure 4. Aqua MODIS (or Moderate Resolution Imaging Spectroradiometer) is true-color satellite image of ISW trains around the island of 'Abd-al-Kūrī ($12^{\circ} 11' \text{ N}$, $52^{\circ} 14' \text{ E}$), located between the Gulf of Oman and the Indian Sea. Internal waves of depression can be identified by the presence of dark contours (lines) in the image; internal waves of elevation can be identified by the presence of light contours. Image dated August 27, 2003. Image credit: NASA.

convergent motion at the sea surface. These features are visible in a SAR image as bands of low and high backscatter (dark and bright bands) due to a decrease and an increase of the surface roughness, respectively. See Figure 5.

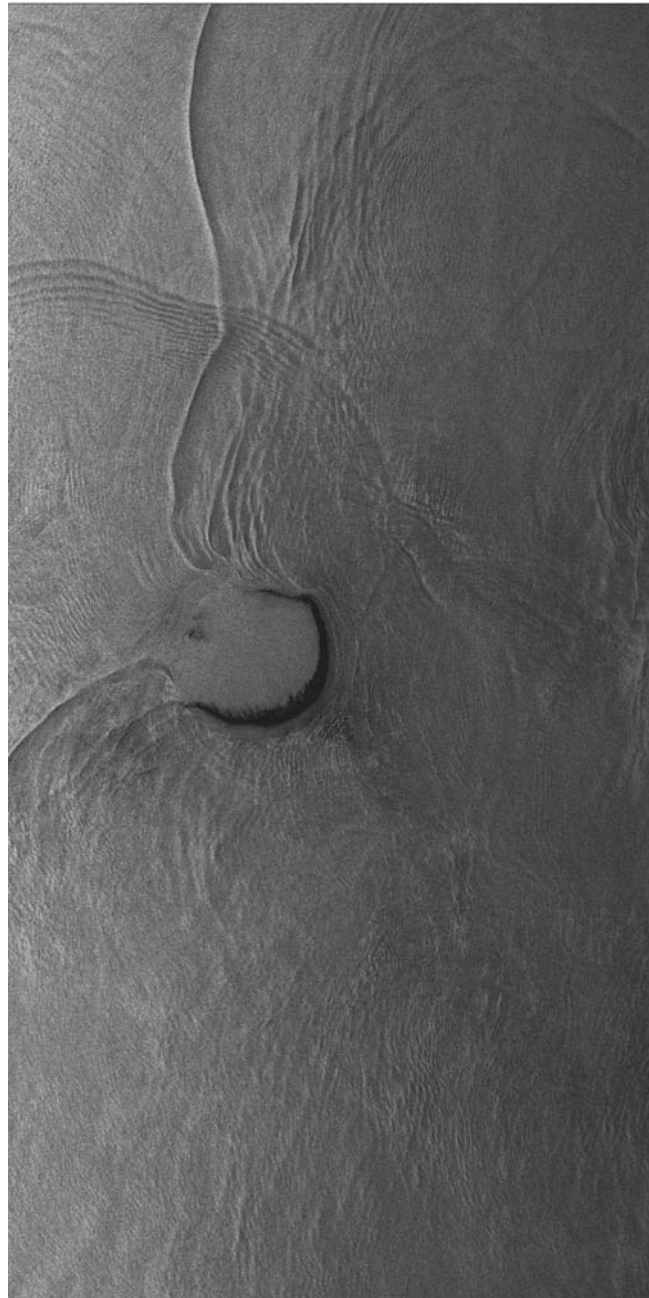


Figure 5. European Remote-Sensing Satellite (or ERS-2) SAR image showing large-amplitude ISWs around the Dongsha atoll ($20^{\circ} 31' \text{ N}$, $116^{\circ} 44' \text{ E}$), in the South China Sea. Internal waves of depression can be identified by the presence of dark contours (lines) in the image; internal waves of elevation can be identified by the presence of light contours. Image dated June 23, 1998. Orbit 16598. Frame 0387-423. Copyright © 2010 European Space Agency. Reproduced by permission.

- Last, Helfrich and Melville give credit to Gardner et al. for providing an exact analytical solution to the K-dV equation.

In recent years, researchers have also been evaluating alternative methods for investigating ISWs through the use of acoustical techniques. These techniques generally rely on measuring the acoustic energy or back-scatter generated by the passing wave front. See, for example, Sandström, Elliott, and Cochrane (1989) and Warn-Varnas et al. (2003).

With assistance from Apel, Jackson (2004) compiled a catalog of about 300 images, taken mostly from space, that show evidence of ISW phenomena occurring at more than 50 locations around the globe (Figure 6). Most of the ISW reports occur in the Northern Hemisphere, where there is the largest percentage of the continental land mass, or some extension thereof (Figure 7). Jackson's compilation also suggests that the occurrence this type of wave form is more frequent in nature than previously thought⁸ — on the order of about 1100 occurrences in any year.

⁸ To illustrate this point, the occurrence of a catastrophic 1700 tsunami, another type of internal wave, in Japan was never fully accounted for until the early 2000s with the discovery of geologic evidence of the same event in Washington State. See Atwater et al. (2005). Extensive reviews of the literature by Weigel (2006), for example, suggest that tsunamis are geologically rare events (i.e., Ager 1993) that are seldom reported historically. However, the advent of remote sensing technology has demonstrated that the occurrence of internal wave-like phenomena is not as rare as once thought.

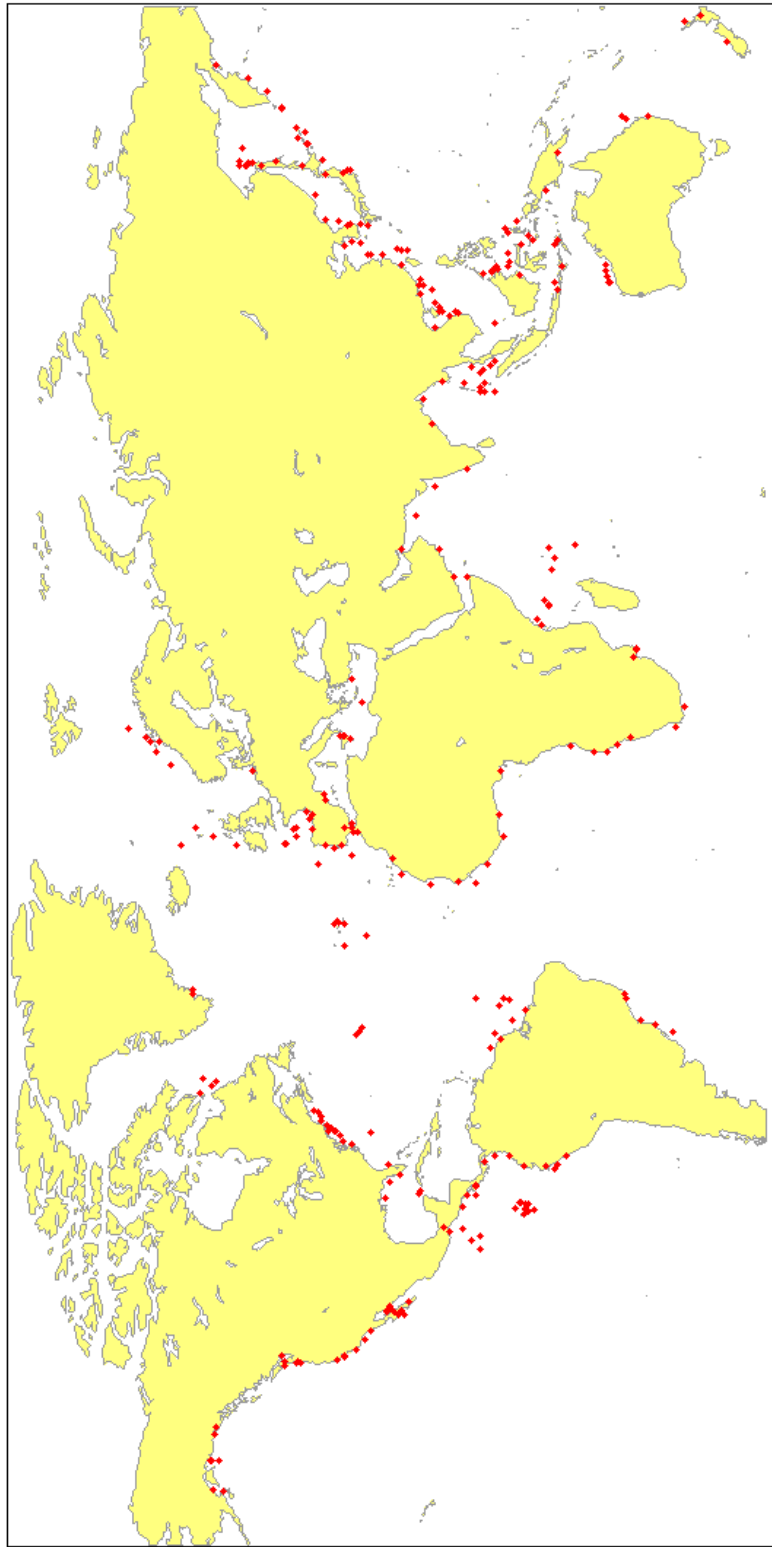


Figure 6. Locations of observed ISW phenomena. Based on data compiled by Jackson (2004) who identified more than 50 locations globally where ISWs and ISW wave trains occur. Some locations experience multiple ISW occurrences over time.

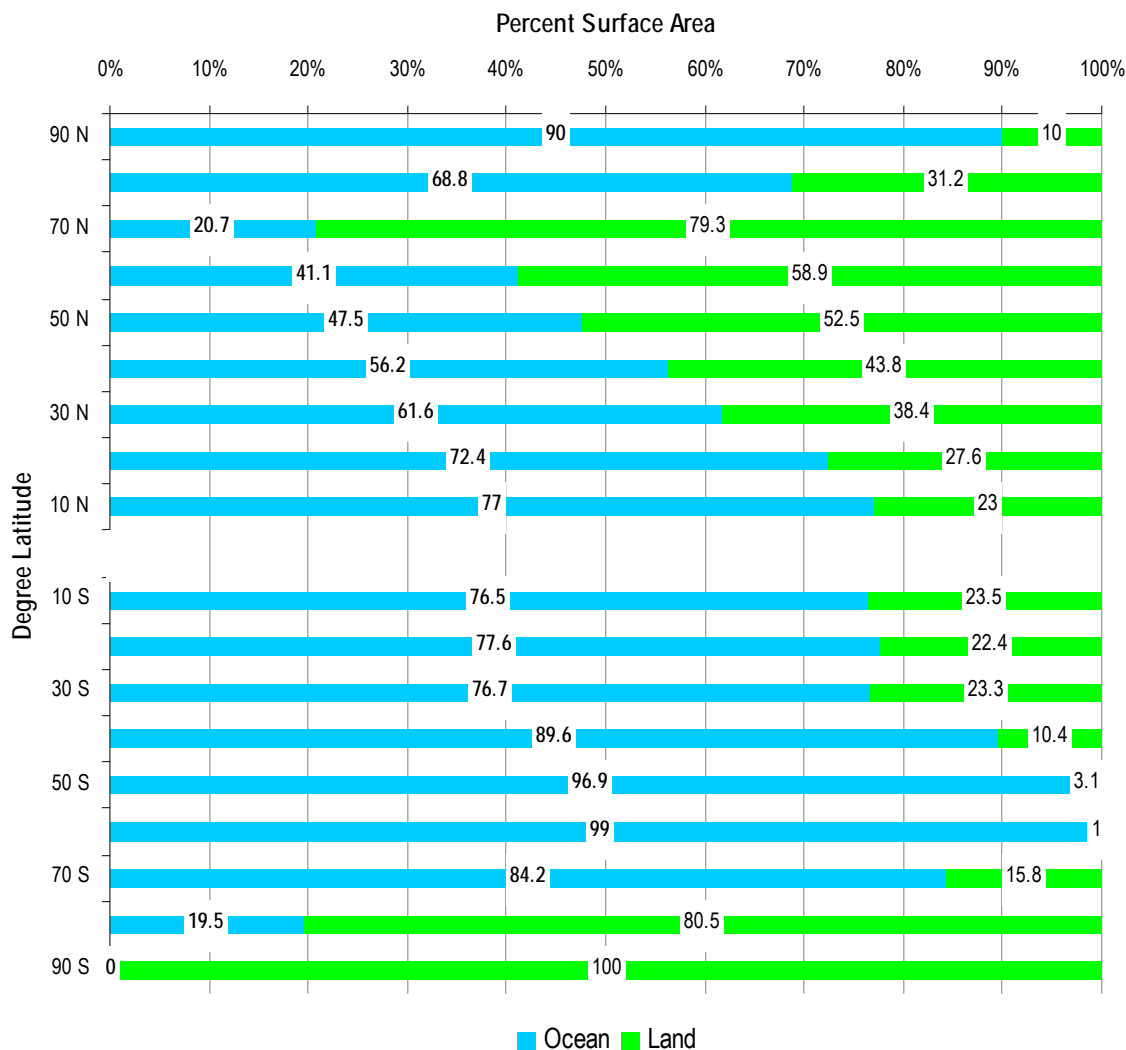


Figure 7. Percent distribution of Earth's surface area by type and by latitude. Data are for both the Northern (N) and Southern (S) hemispheres. About 39 percent of the Northern Hemisphere is covered by the continental land mass compared to 19 percent in the Southern Hemisphere. Overall, the land to ocean ratio in the Northern Hemisphere is about 1:1.5; in the Southern Hemisphere, the ratio is about 1:4. Data obtained from *United Nations Atlas of the Oceans*. Available at www.oceansatlas.org.

Although Jackson (2009) recently proposed an empirical model for estimating the frequency of internal wave occurrence at a particular geographic location, accurate annual frequency estimates of ISW occurrences in nature generally do not exist (Ostrovsky and Stepanyants 1989).⁹ Nevertheless, as discussed later in this dissertation, closer examination of the Jackson (2004) compilation reveals that there is a temporal influence to the occurrence of ISWs.

2.2 Internal Wave Mechanics

Recalling the processes and conditions depicted in Figure 2, researchers generally agree that the prevailing environment for the generation of internal waves can be attributed to the interaction between stratified waters and local variations in seafloor topography. In the open ocean, the motion of surface waves is generally unaffected by the ocean floor. The orbital motions of water particles at the ocean's surface decay with depth, well-before reaching the seafloor. However, as is the case with surface waves, most researchers

⁹ Because the recording ISW behavior in real-time can at times be impractical, developing order-of-magnitude-level frequency estimates for internal waves might be possible through the use of expert judgment. As suggested by its name, the opinions (views) of recognized subject matter experts can be obtained through a formal elicitation process. Questions cannot be answered by more traditional lines of scientific inquiry so the opinions of qualified individuals can be used as a substitute for data when subject to quantification (Dalkey and Helmer 1963). The elicitation technique, in general (Meyer and Booker 1990), has found wide use in both engineering (Hora and Iman 1989, Chhibber, Apostolakis, and Okrent 1992) and earth science applications (Hunter and Mann 1989, Senior Seismic Hazard Analysis Committee 1995).

acknowledge that irregularities in the seafloor topography, in the form of a prominent physiographic feature, are a key factor influencing the formation of internal waves. See Bell (1975) and Ivey, de Silva, and Imberger (1995), for example. Thorpe (2001) is another useful reference to consult. Munk (1941) and LaFond and Rao (1954) previously argued that when topographic conditions permit, internal tides are likely the principal forcing function responsible for the formation of an internal wave. They also found that internal tides introduce instabilities into the density profile which lead to turbulent mixing. See Garrett and Kunze (2007) and LaFond and Roa (2007).

As mentioned above, when the surface expression of internal wave-like phenomena were first identified in satellite imagery, it was frequently in proximity to the ocean-continental slope/shelf transition zone (Apel et al. 1975). Closer to shore, submarine canyons or glacial scours are now recognized as secondary generating mechanism for internal wave formation (Shepard and Marshall 1973, Hotchkiss and Wunsch 1982). These V-shaped topographic features are common along the continental shelf/continental slope transition (Daly 1936, Shepard and Dill 1966). Some canyons are associated with the mouths of major river systems whereas some are not. Hickey (1995) has estimated that submarine canyons and canyon-systems incise between 20 and 50 percent of the North American continental shelf between the equator and

Alaska. Improvements in sonar mapping techniques and computer processing of the data obtained there from have led to higher-resolution images of this major marine physiographic feature (Pratson and Haxby 1997).

Ambient hydrostatic equilibrium, in which every water particle in the water column is in a state of neutral buoyancy, may be perturbed by a combination of the factors cited in Table 1, to produce an internal wave. Since tides, stratification, and irregular topography are common marine features, internal waves and solitary wave-like features have been found to be ubiquitous across the globe wherever stratified waters and shallow bathymetry coincide. In the Jackson (2004) compilation, at least marine 54 sites associated with the formation of internal waves were identified, not all of which are coincident with the continental shelf/continental slope. Researchers have identified other marine settings where internal waves can form. These settings are listed Table 5. Once formed, the ensuing internal waves can be defined as a single wave or, more commonly, as groups of waves (or wave trains) — usually 3 to 10 in number — that can be seen on the ocean's surface. Typical magnitudes for selected internal wave parameters formed along the continental shelf are given in Table 6. The internal wave that occurs at depth generates almost no surface manifestation — that is to say, there is almost no variation in the free surface water elevation to suggest that an internal wave, at depth, is present. Any

Table 5. Physiographic Settings for Internal Wave Generation.

SETTING	CONTEXT	REFERENCES
Sill/Shelf	Topographic transition from a deep to shallow-sea environment at the continental slope-shelf leads to the breaking of internal waves	Baines (1973, 1974), Hibiya (1986)
Submarine Canyon	Narrow steep-walled incisions within the continental shelf characterized by turbulent tidal currents	Kunze et al (2002)
Strait	Geographically narrow stretch of sea connecting two larger water bodies subject to strong tidal currents	Gargett (1976)
Island-like	Active volcanoes, coral islands and reefs, banks, atolls, and guyots subject to the to and fro of ocean currents	Bell (1975), Holloway and Merrifield (1999), Niwa and Hibiya(2001)
Fjord, Loch	Steep-walled, deep topographic feature subject to stratified mixing involving continental fresh water and oceanic saline water	Smith and Farmer (1977) Farmer and Smith (1978, 1980)
Closed Water Bodies	Large standing body of stratified water such as a lake or small ocean which temporal changes in temperature and/or density can take place when subjected to wind stress.	Mortimer (1952), Hunkins and Fleigel (1973), Farmer (1978), Boegman et al. (2003)
Mid-ocean Ridge	Tidal flow in association with weakly-stratified water over seafloor spreading ridge in abyssal ocean leading to internal wave breaking	Ledwell et al. (2000), Rudnick et al. (2003), Thurnherr et al. (2005)
River	Gravity current from river discharges into coastal waters causing wave convergence between the two systems	Nash and Moum (2005)

Table 6. Typical Scales for Mid-latitude Continental Shelf–Type Internal Waves. Assumes a stratified (two-layered) fluid system. Derivations from the values listed in this table can be large. Adopted from Apel et al. (2006, p. 63) unless otherwise noted.

PARAMETER	VALUE
Wave Front Length (km) [†]	1 – 5
η_0 (m)	0 – 30
h_1 (m)	5 – 25
h_2 (m)	100
Wavelength (m)	50 – 500
Distance Between ISW Fronts (km) ^{††}	15 – 25
Relative Density Difference	0.001
Wave Phase Speed, c (m/s)	0.20 – 1.0
Current Velocity (m/s)	0.10 – 1.0
Wave Packet Lifetime (hr)	24 – 48
Potential Wave Energy Yield (Jm^{-2})	~ 4 ^{†††}

[†] Group of waves.

^{††} Distance between two ISW trains.

^{†††} Estimated by Pielou (2001). For the purposes of comparison, the potential energy yield associated with a surface wave of equal height in the open ocean is approximately 1256 Jm^{-2} (Pond and Prichard 1983). An internal wave has much less energy than a surface wave of equal height because the density difference along the pycnocline is very slight compared to the air-water interface (i.e., a surface wave). However, by virtue of potentially greater amplitude, the potential energy yield of an internal wave can be substantially larger than that of a surface wave.

surface expression that might occur would take place when the wave orbitals were sufficiently close to the free surface to allow them to interact with surface waves commonly as groups of waves or wave trains. The wave trains were usually comprised of waves in groups numbering from 3 to 10. Although they can vary both spatially and temporally, internal waves and internal wave trains can be seen in imagery and photographs, and their properties indirectly estimated using those sources (Li, Clemente-Colón, and Friedman 2000).

The ocean surface interruption that ultimately gives rise to a surface-roughness is generally thought to result in a modulation that allows internal waves to be identified in imagery (Gargett and Alpers 1985). The association between the orbital patterns responsible for the surface appearance observed was first suggested by LaFond (1959). LaFond's hypothetical rendition of an orbital path for an internal wave (Figure 8), in turn, appears to be based on Defant (1961) crediting Bjerknes and others (1933). Moreover, the geometry of the orbital path itself based a mathematical expression developed by Lamb (1847). This expression describes the motion of progressive waves forming between two fluids of different densities.

As depicted in Figure 8, the wave-particle orbitals are ellipsoidal rather than circular, as would be the case typically with a linear-type wave commonly

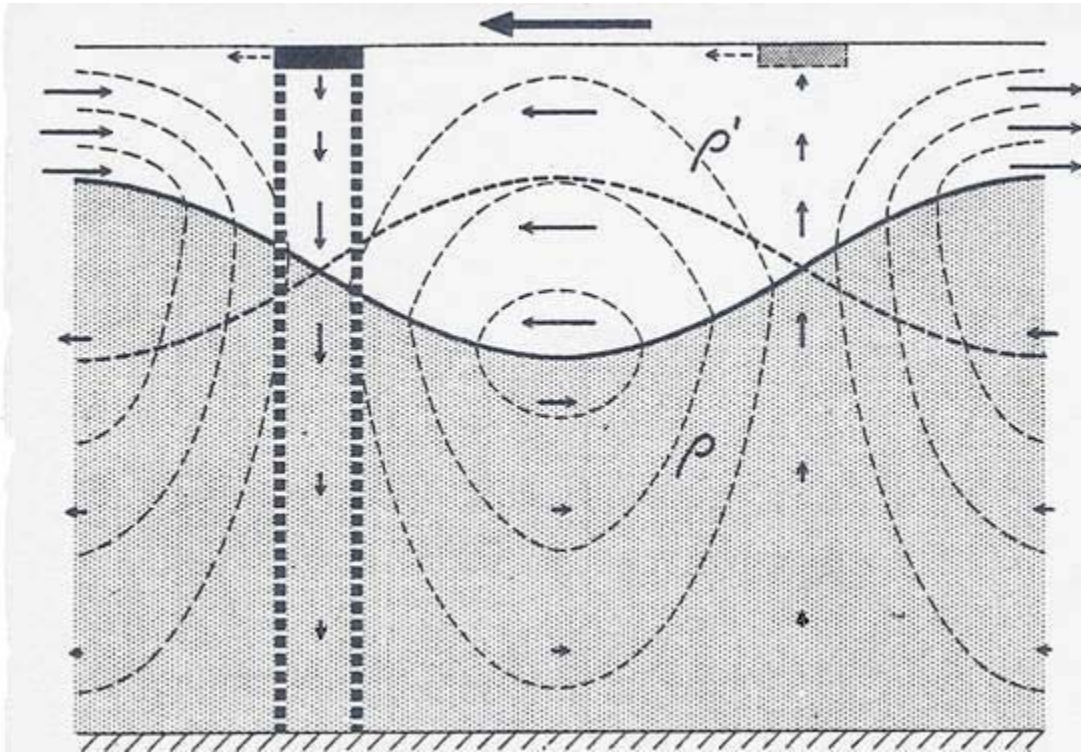


Figure 8. Sinusoidal orbital pattern characteristic of an internal wave. Arrows indicate flow patterns around dashed streamlines. Small rectangles define areas of surface-roughness or slicks that can be observed in photographs and satellite images. From LaFond (1959).

seen on the water surface. LaFond (1961b) also established that the movement of water particles, in adjacent fluid layers immediately above and below the pycnocline, are in directions opposite to that of each other.¹⁰ LaFond's

¹⁰ According to Lamb (1847), the vertical displacement at the interface of a two-layered system can be expressed as:

$$\eta = \alpha \cos(kx - \sigma t)$$

and the horizontal velocity flow u' in the upper layer h_1 is:

conceptualization, depicted in Figure 8, comports well with observations of internal wave phenomena *in situ*. See Figure 9.

The question thus arises as to what combination of physical processes and/or conditions cited in Table 1 might lead to the generation of an internal wave? Moreover, once they form, how do internal waves behave? In answering these questions, the reader is reminded that internal waves are recognized as non-linear phenomena. As discussed in Campbell (1989), for any given set of physicochemical conditions (generating mechanisms), one cannot predict which specific set of conditions are necessary to produce a specific outcome (response), as is the case with linear systems — specific examples being the prediction of the force between two masses. Given a specific outcome (response), one cannot describe the specific set of initial and boundary conditions that will produce the desired response. In a linear system, such as a linear spring-mass-damping system, for example, a given subsequent trajectory of motion may be obtained by solving for the required time-varying force input to the system. However, some researchers (e.g., Thorpe, Briscoe) have identified certain environmental conditions (Table 1) considered to be favorable for the generation of internal

$$u' = -\left(\frac{a}{h_1}\right)c \cos(kx - \sigma t)$$

where a is the wave amplitude at the pycnocline.

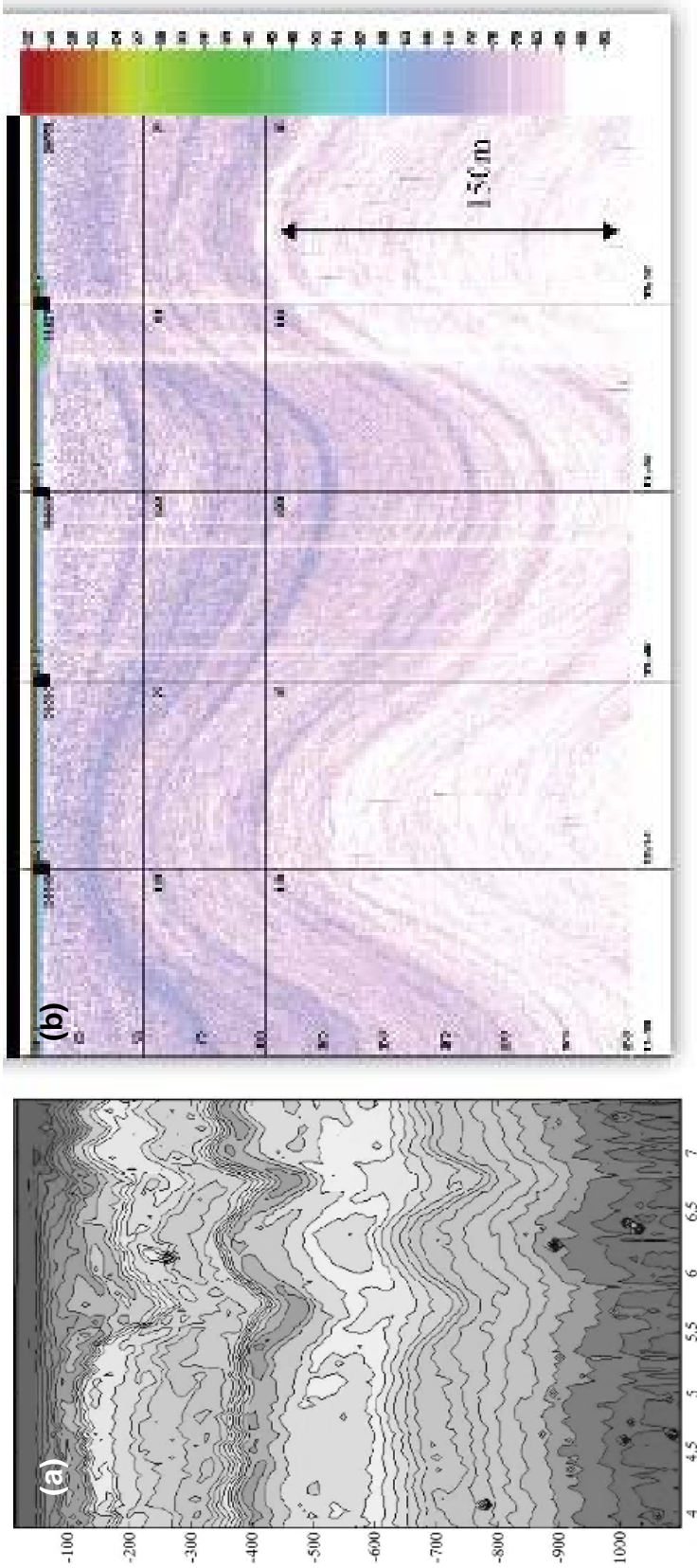


Figure 9. Examples of internal wave observations in situ. Vertical axis is depth in meters and horizontal axis is time (hours). Image internal wave of depression in the top 1000 m of the water column revealed using acoustic scattering strength using a 48-kilohertz (kHz) hydrograph Doppler sonar. Contours are isolines of equal acoustic scattering strength corrected for spherical spreading showing downward displacement of scattering layers. Image recorded in the Luzon Strait at 119.6°E, 20.5°N from April–May 2005. Taken from Lui et al. (2005). Reproduced by permission of the AGU. (b) Internal wave train in the top 250 m of the water column revealed using spectral echogram. Image acquired using an EK500 Echo-sounder operating at frequency of 38 kHz in the Lombok Strait at 115.75°E, 8.47°S. Higher backscatter values indicate higher plankton concentration or large schools of fish. Colors represent relative backscatter strength in decibels. Taken from Susanto, Mitnik, and Zhang (2005, Figure 4). Copyright © 2005 The Oceanography Society. Reproduced by permission.

waves. It is likely that the non-linear interactions among these conditions locally play an important role in the forcing of larger marine systems.

When considering the physical processes and conditions identified in Table 1, collectively, and then attempting to establish their relative contributions to the formation of an internal wave, this effort can prove to be problematic as the coupling between the respective processes is poorly understood. Because of the cascading effects of nonlinear interactions among these conditions, it is often not possible to reconstruct the exact origin of observed internal waves (Staquet and Sommeria 2002). Gerkema and Zimmerman (1995), though, have attempted to reduce the complexity of this problem by proposing a simple progression (sequence) consisting of the following processes to account for internal wave phenomena:

baroclinic tide → topographic interaction → internal tides → internal solitary waves

An alternative, still more simplistic approach might be to consider internal wave behavior in the context of sources and sinks.

2.2.1 Key Internal Wave Forming Factors (Sources)

Internal waves are generated in regimes where the barotropic tidal current encounters irregularities in bottom topography. The topography acts as

a wave-maker owing to oscillatory “to and fro” motions associated with tidal cycles. The individual elements comprising this internal wave-forming scenario are described briefly below.

2.2.1.1 Stratification

Internal waves form at depth and propagate in any fluid where the vertical stratification is strong and well-defined (Lighthill 1978). Stratification can be due to vertical temperature or salinity gradients in the water column. Internal waves are generated when the density interface is disturbed. Disturbances are often caused by tidal flows that propagate along (parallel to) the density interface. In freshwater environments, the variation in density is caused primarily by temperature (a thermocline). In brackish marine environments, the variation in density is due to salinity (a halocline). Two water masses having the same density may have different temperatures and salinities, as varying values of each can result effectively in the same density. As a rule, therefore, temperature is more important than salinity when determining fluid density. Because temperature and salinity can vary spatially, it is not unusual to find warmer waters below cooler waters, or less saline waters below more saline waters. See Sverdrup, Johnson, and Fleming (1949).

A strong vertical density gradient is referred to as a “pycnocline.” Areas where freshwater and saltwater bodies meet, such as estuaries and river deltas,

have well-defined pycnoclines. Depending on the season and the latitude, the thickness and depth of the pycnocline below the water surface can vary. In the open ocean, the pycnocline generally extends from about 120 to 270 meters below the surface (LaFond 1962). Pycnoclines are most prevalent in the lower latitudes of the open ocean as the temperature- and salinity-based density variations are usually the greatest in comparison to the higher latitudes. At the higher latitudes (50 to 60 degrees), the thickness of the pycnocline begins to lessen or becomes almost non-existent owing to the lack of variation in the density of the water column. A permanent halocline usually coincides with the top of the permanent thermocline. See Figure 10. As noted earlier in this dissertation, when a pycnocline begins encounter or “feel” the seafloor, there is the potential for the formation of an internal wave. Using SAR imagery, some researchers (Zheng, Yan, and Klemas 1993, Li, Clemente-Colón, and Friedman 2000) have been able to indirectly estimate the depth of the pycnocline by calculating the group velocity of internal wave packets.

The properties of the pycnocline appear to influence the form and location of internal waves (Apel et al 2006). For example, returning to equation 2.2 and the non-linear parameter α and the dispersion parameter β , the sign of the dispersion parameter β is always positive for oceanic internal waves whereas the sign of the non-linear parameter α may be both positive and negative. The

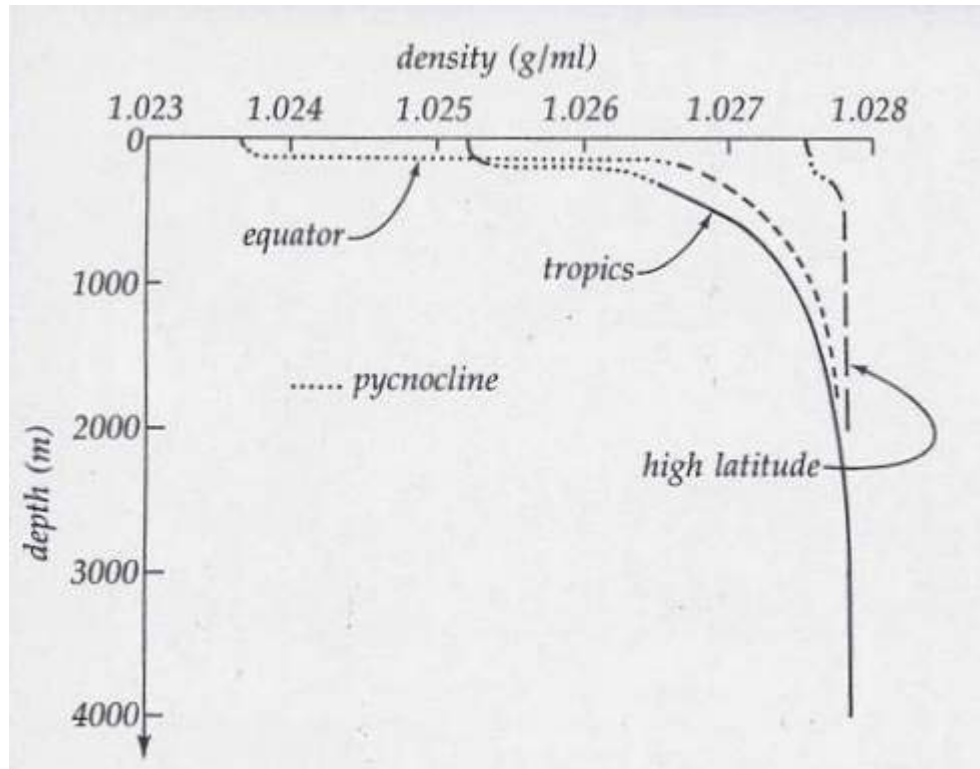


Figure 10. Deep ocean pycnoclines. From Ingmanson/Wallace. *Oceanology: An Introduction*. 1E. Copyright © 1973 Brooks/Cole, a part of Cengage Learning, Inc., Reproduced by permission. www.cengage.com/permissions.

combination of the α and the β parameters determine the polarity of the internal wave. For example, if α is negative so will the polarity of η_0 , and the internal wave corresponds to an internal wave of depression. Depression-type internal waves tend to favor marine scenarios where a shallow pycnocline overlies a deeper layer of water, as might be the case during the Spring-Summer months. Conversely, if α is positive so will the polarity of η_0 , and the ensuing internal wave is a wave of elevation. Elevation-type internal waves tend to favor a scenario in which there is a shallow sea with strong mixing and a deep

pycnocline near the seafloor, as might be the case during the Winter months. Recalling equation 2.5 and the non-linear wave parameter α , internal waves propagating in a system defined by a thin upper fluid layer resting over a deeper fluid layer ($h_1 < h_2$) always produce a depression-type internal wave. When internal waves form on a thin, near-bottom fluid layer ($h_1 > h_2$), the resulting internal wave is a wave of elevation.¹¹ Recalling Figure 8, the flow direction for water particles in a depression wave is clockwise; the flow direction for an elevation wave is counter clockwise. The seasonal influence on thermal stratification of ocean waters, and thus ISW formation, appears to be well-supported by the distribution (timing) of ISW reports in imagery. See Figure 11.

When considering a variable (sloping) topography, Kaup and Newell (1978) suggest that the polarity of the incident interfacial wave — i.e., either an internal wave of elevation or depression — can be reversed at some vertical plane defined as $h_1 = h_2$. At this so-called “turning point,” there is a corresponding change in the sign of the difference between h_1 and h_2 . Once an internal wave advances to a location where this difference becomes negative, that is to say $h_1 < h_2$, the incident wave will experience a reversal in its polarity. Knickerbocker and Newell (1980) numerically examined polarity reversal whereas Helfrich and

¹¹ This dissertation focuses primarily on the breaking behavior of internal waves of depression in a two-fluid system. Long (1972), on the other hand, has examined some of the factors influencing the behavior internal waves of elevation in a two-fluid system.

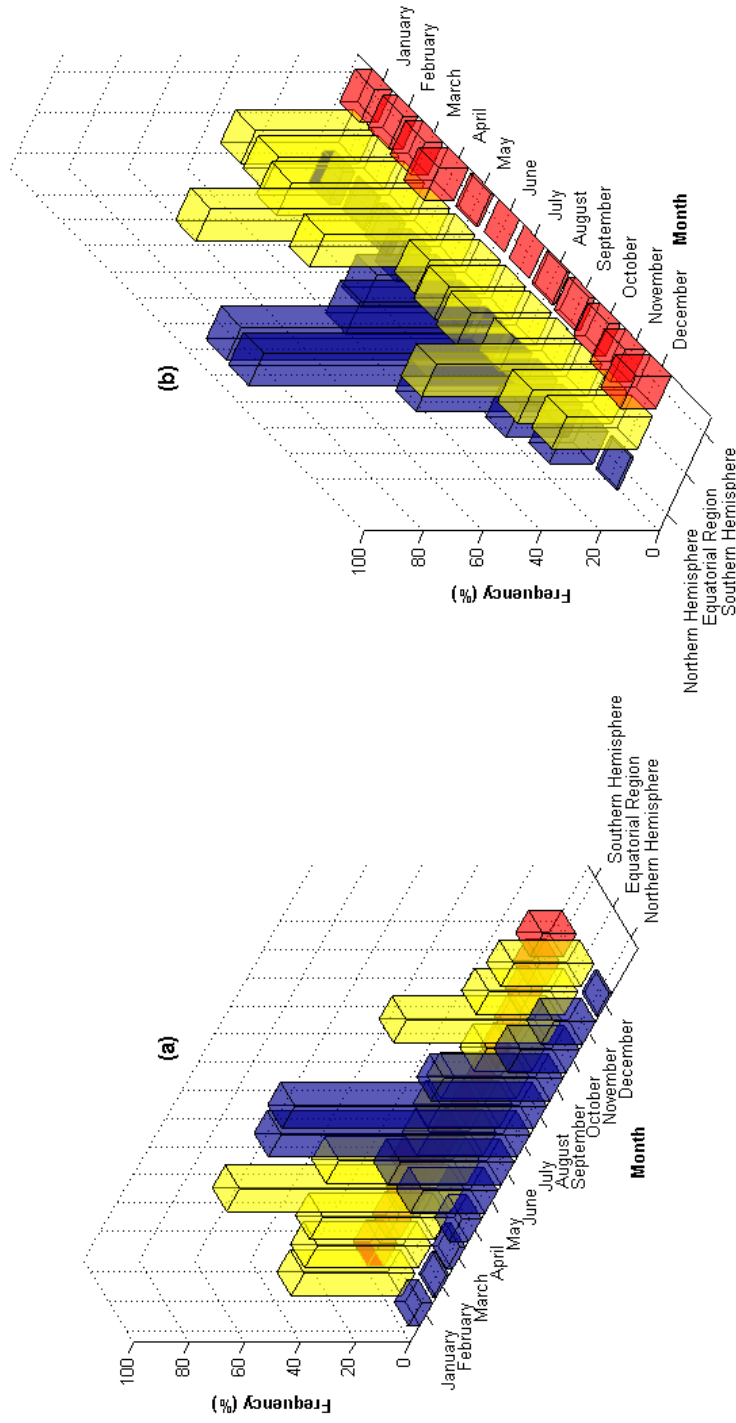


Figure 11. Frequency of reported ISW phenomena at those locations depicted in Figure 6. Bar graphs illustrate how thermal stratification of ocean waters can influence the formation of ISWs in the respective hemispheres. Figure 10a shows a waxing in ISW behavior in ocean waters of the Southern Hemisphere during the Summer months while a waxing in ISW behavior can be observed in ocean waters occupying the Northern Hemisphere during the same time period. See Figure 10b. Overall, Jackson's (2004) compilation reports that marine environments in the Equatorial Region of the ocean have the largest number of reported ISW sightings (473) followed by the Northern Hemisphere (343) and the Southern Hemisphere (54). Not included in this figure are certain locations recognized as 'hot spots' for ISW formation. They include the Norwegian Shelf (130 annual sightings), the Strait of Messina (77 annual sightings), and the Strait of Gibraltar (91 annual sightings).

Melville (1986) demonstrated this transition experimentally. Vlasenko and Hutter (2002) produced a numerical simulation that shows the evolution of an internal wave through the turning point theoretically used to define this change in polarity. Reported observations of this particular aspect of internal wave behavior, though, are particularly rare in nature. Lui et al. (1998) report that phase shifts seen in the SAR images of internal waves in the South China Sea are evidence of a shift (a reversal) in the polarity of the internal wave orbital. More recently, Orr and Mignerey (2003) and Shroyer, Moum, and Nash (2009) were able to document the reversal of an internal wave's polarity *in situ*. Zhao et al. (2003) were able to observe to polarity reversal in satellite imagery.

2.2.1.2 Tidal Influences

Many of the physiographic environments identified earlier in Table 5 rely on the influence of tides as forcing function contributing to the development of an internal wave. A number of investigators (Helland-Hansen and Ekman 1909, Ufford 1947, Arthur 1954, and Reid 1956) have previously commented on the close correlation between the fluctuating thermocline and tidal periodicity. Haurwitz (1954), though, previously questioned the correctness of some of these correlations and hence the implied synchronicity between tidal variations and internal wave generation. Jackson's (2004) compilation showing the geographic distribution of reported ISW occurrences have identified certain marine settings around the globe — the Norwegian Shelf, the Strait of Messina, and the Strait of

Gibraltar — as ISW “hot spots” owing to the important influence of tidal forces in internal wave formation. Nevertheless, most researchers continue to endorse the notion that the waxing and waning of tidal currents act as a wave-maker capable of producing internal waves (Farmer and Smith 1980, Haury, Briscoe, and Orr 1979, Hibiya 1986 and 2004, Lamb 1994).

Tidal behavior has been the subject of intense study by both mariners and scientists for several millennia (Cartwright 1999, Reidy 2008). Tide-generating forces present in the ocean arise primarily from the differential attraction between the Earth, the Moon, and the Sun, in a manner consistent with Newton’s law of universal gravitation. Small differences in the direction and magnitude of these forces give rise to tides. As the Earth rotates about its axis, tidal-generating forces produce two maxima (high water) and two minima (low water) — or semidiurnal waters — about every 24 hours. The fluctuation (oscillation) between maxima and minima levels is responsible for the alternating currents and displacements typically associated with tidal behavior.

Estimating these levels (i.e., the ocean’s response to tidal forces) is essentially algebraic. Sea level changes at any given geographical location in the ocean can be expressed as the sum of the cosine functions for the principal tidal-forcing constituents — M_2 , K_1 , S_2 , etc. (Pugh 1987). See Table 7. The principal

Table 7. Amplitude Functions for Principal Constituents of Tidal Harmonic Forcing. Taken from Wahr (1995).

NAME	ORIGIN	AMPLITUDE FUNCTION (cm)
M_2	Principal lunar	63.19
S_2	Principal solar	29.40
N_2	Larger lunar elliptic	12.10
K_1	Luni-solar declinational	36.88
O_1	Principal declinational	26.22
P_1	Principal declinational	12.20

tidal-forcing constituents can be amplified by diurnal and semidiurnal fluctuations of the pycnocline. Since in many places, tidal-generated sea level changes can be several meters it is clear that significant tidal amplification occurs in many marine settings due to topographic effects encountered along the seafloor. The strongest internal waves generated are in the tidal amplification range of around 0.4 to 0.5 m. They are mostly attributed to the M_2 tidal component.

2.2.1.3 Topographic Influences

As a supplement to the June 1968 issue of its magazine, the *National Geographic Society* published its famous shaded-relief map of ocean floor showing prominent topographic features to the underlying geology. The 1:30,412,800-scale map reflected a stylized interpretation of seafloor bathymetry information first presented by Bruce Heezen and Mary Tharp of the *Lamont Geological Observatory of Columbia University* (now the *Lamont-Doherty Earth Observatory*) during the 1950s is shown in Figure 12a. See Lawrence (1999) and Doel, Levin, and Marker (2006). Upon inspection, what the Heezen-Tharp map revealed was that the ocean floor had several distinct physiographic features – foremost among these were the abyssal plains, rift valleys in association with sea-floor spreading centers, and the continental margins defined by the continental shelves and the transitional continental slopes. A less stylized interpretation of these features, based on improved subsea mapping techniques, has been prepared by Amante and Eakins (2009) for the National Oceanographic and Atmospheric Administration (NOAA) and can be found in Figure 12b.

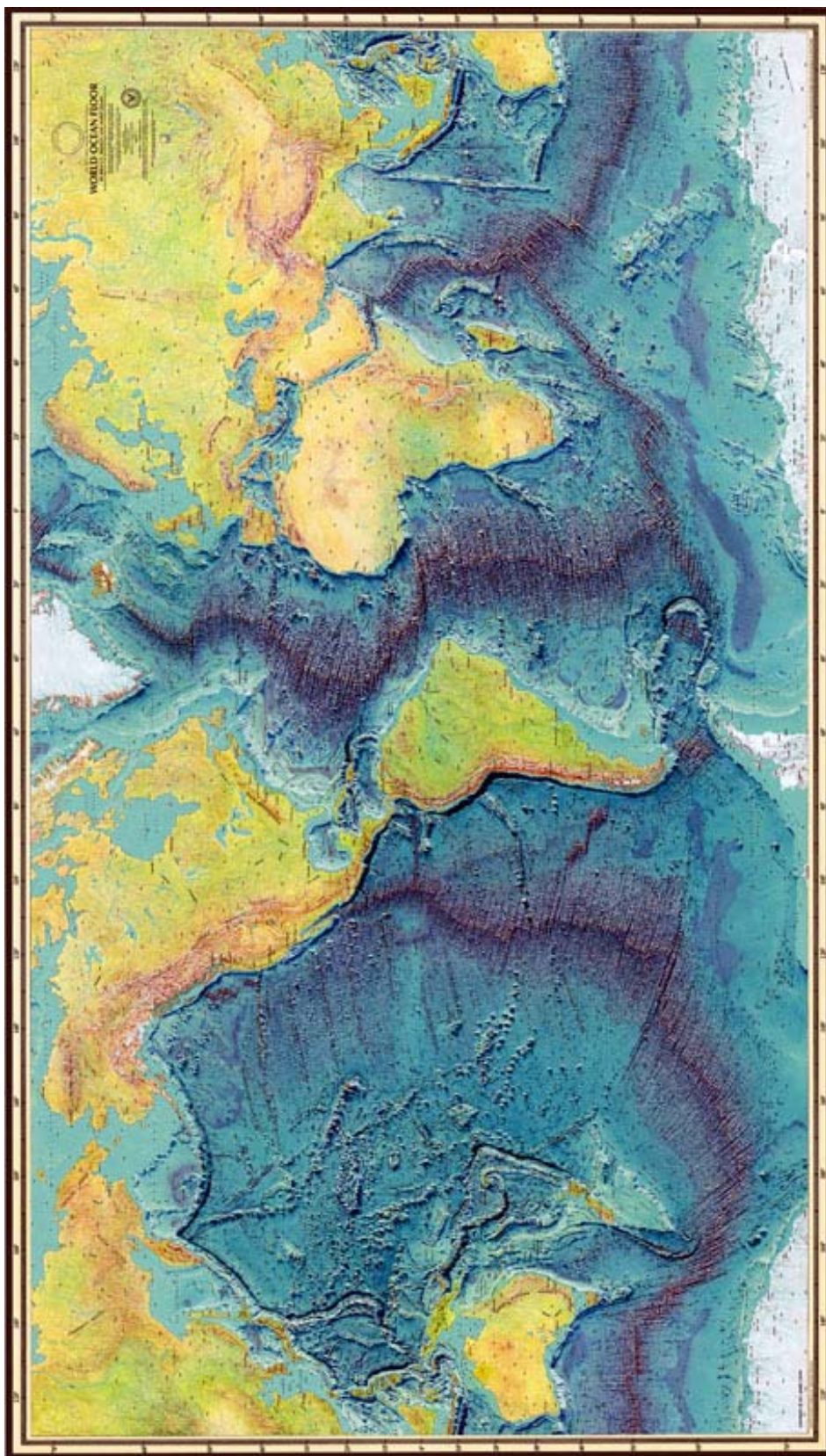


Figure 12. Physiographic maps of the ocean floor. (a) “World Ocean Floor Panorama” shaded relief map prepared by H.C. Heezen and M. Tharp (1977). Copyright © Marie Tharp 1977/2003. Reproduced by permission Marie Tharp LLC, 8 Edward St., Sparkill, NY, 10976.

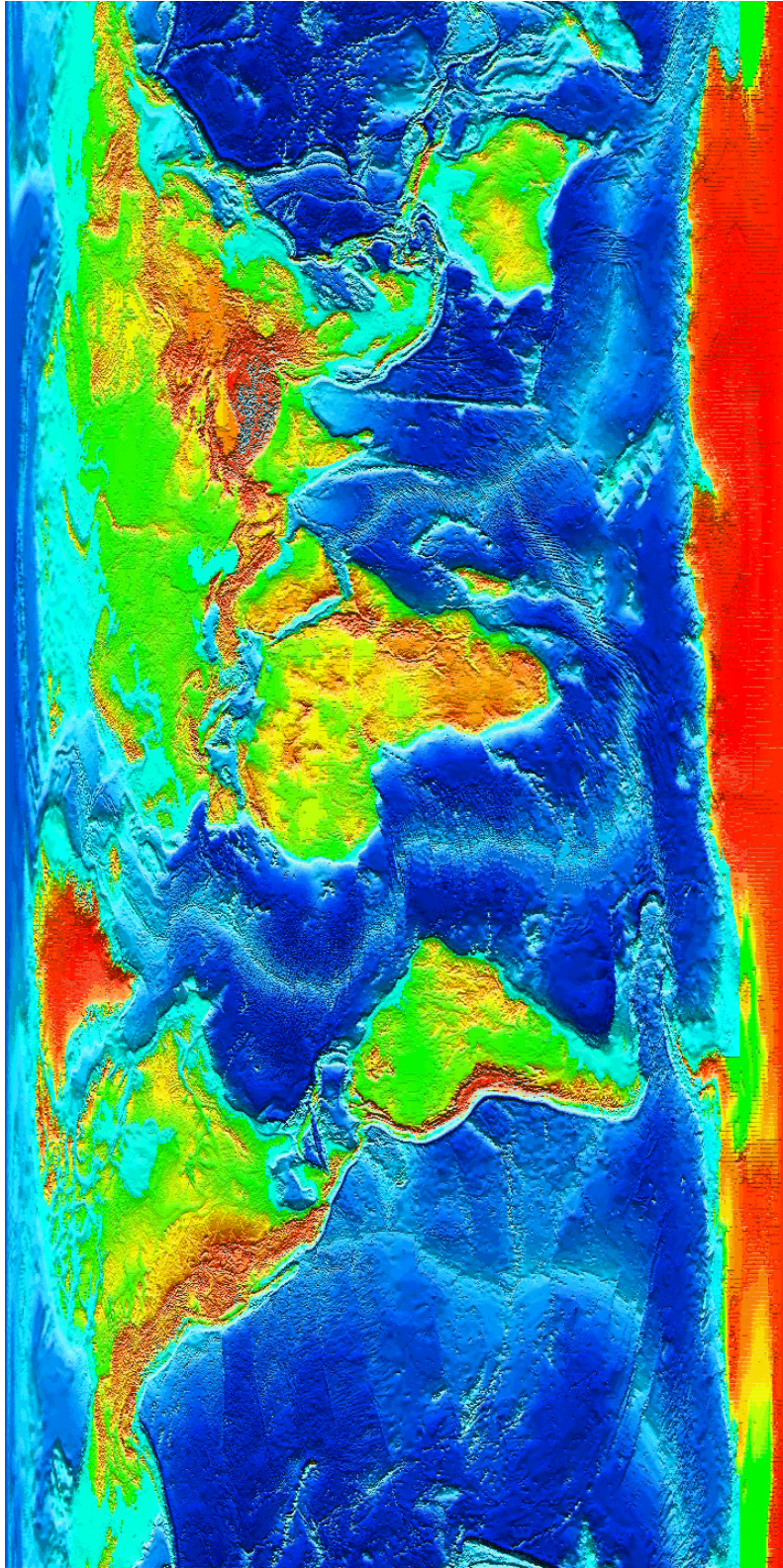


Figure 12. Continued. (b) Digital seafloor relief map prepared by Amante and Eakins (2009). Image generated by NOAA/National Geophysical Data Center.

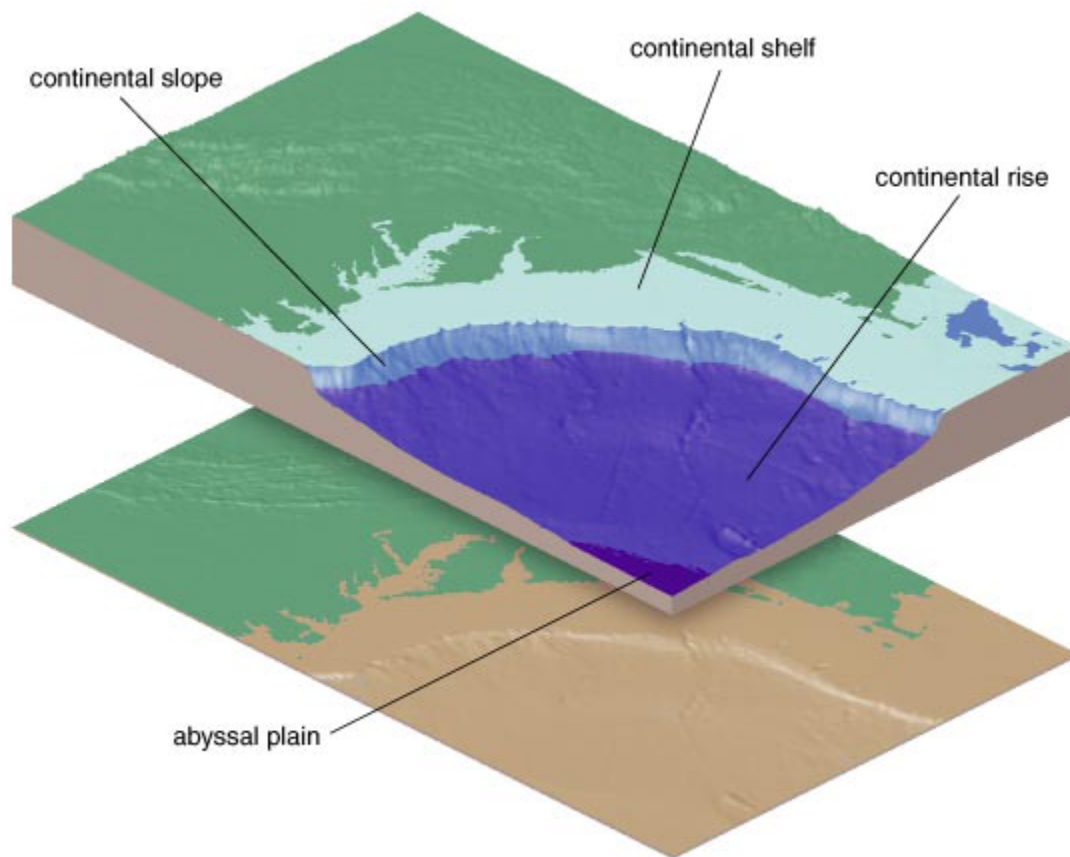


Figure 13. Physiographic map illustrating an example the continental shelf-continental slope transition. Taken from Cacchione and Pratson (2004). Reproduced by permission of *American Scientist*, magazine of Sigma Xi, the Scientific Research Society.

Garrett (2003) has referred to the continental shelf/continental slope transition as the “great [internal] wave maker” owing to their geographic extensiveness. The continental shelf is a shallow, sea-floor platform that, although submerged, is clearly an extension of the continental land mass (Figure 13). This topographic feature represents about 15 percent of the ocean floor surface area. See Table 8. Globally, the continental shelves range in depth from about 20 m to about 550 m below sea level with an average depth of about

Table 8. Hypsometry and Bathymetry of the Earth's Surface. Taken from Wyllie (1971) citing Scheidegger (1963), Menard and Smith (1966), and Ronov and Yaroshevsky (1969).

PHYSIOGRAPHIC FEATURE	AREA (10 ⁶ km ²)	% LAND OR OCEAN	% EARTH SURFACE	
			INDIVIDUAL	CUMULATIVE
Continental Land Mass	149.0	100	29.1	29.1
Continental Shelf/Continental Slope	55.4	15.3	10.9	40
Ocean: <i>Abyssal Ocean Basin Floor*</i>	151.5	41.8	29.7	63.3
<i>Mid-Ocean Ridges and Rises</i>	118.6	32.7	23.3	169
<i>Continental Rise</i>	19.2	5.3	3.8	120.8
<i>Island Arc and Trench</i>	6.1	1.7	1.2	120
<i>Volcanoes</i>	5.7	1.6	1.1	117.1
<i>Other Submarine</i>	5.4	1.5	0.9	100

* including seamounts

133 m (Emery 1965). Horizontally, they can vary in width from slightly less than 1 km to almost 15,000 km with an average width of about 78 km (*Op cit.*). Slopes are generally about 1° with the exception being the land mass surrounding the Philippines archipelago where the angle of the continental slope is about 11°. Most of the continental shelf surface area was exposed during the waxing and waning of Pleistocene-age glaciation (2.588 million to 11,550 years before present) which helps to account for its generally irregular topography.

The limits of the continental shelf are abruptly defined by the continental slope. Topographically, the continental slope is described as a narrow 20 km-band of submerged land whose average grade is about 4° and extending to a depth of about 130 m vertically below sea level. Shepard (1973) provides a description of how these features vary globally from continent to continent. The abrupt change in grade of the continental shelf/continental slope occurs over a relatively short distance – about 20 km – and is considered by most researchers as a key factor contributing to internal wave formation in this particular marine setting.

There literature indicates that there are other topographic features depicted in Figure 12 besides the continental shelf/continental slope also known to influence the formation of internal waves in the ocean. They include MORs, seamounts, and islands.

Mid-ocean ridges. Close inspection of both the Heezen-Tharp map (Figure 12a) and the NOAA map (Figure 12b) indicates that most dominant physiographic feature in each of the ocean basins are MORs. The data compilation in Table 8 indicates that MORs, and their associated transform fault systems, account for nearly a quarter (about 23 percent) of the earth's surface and even a higher proportion of the ocean floor – nearly a third. The geologic significance of MORs was first highlighted when their discovery helped to unify plate tectonic theory

by establishing the geodynamic forcing mechanism believed to be responsible for continental drift (Heezen, Tharp, and Ewing 1959). MORs represent areas where the earth's crust forms and spreads (Wilson 1963 and 1965, Heirtzler 1968, Jacoby 1981). Globally, the collective length of the MOR system is about 65,000 km and in some places, its elevation can rise as much as 500 m above the ocean floor (Heezen 1960).

In recent years, MORs have gained attention once again for helping to explain mixing in the deep ocean. Researchers concluded that some mixing of abyssal waters takes place beyond the continental margins and is likely attributed to internal wave phenomena (Munk and Wunsch 1998, Wunsch and Ferrari 2004). Independently, Polzin et al. (1997) and Ledwell et al. (2000) found that the MOR, by virtue of its high elevation relative to the abyssal plane (Small 1998), can induce enhanced tidal mixing in the deep ocean which, in turn, has led to studies evaluating the influence of these features on internal wave formation (Bell 1975, Balmforth, Ierley, and Young 2002, Garrett and Laurent 2002, Nycander 2005, Vlasenko and Alpers 2005, and Legg and Huijts 2006).

Seamounts. When they were first discovered in the Pacific Ocean, just prior to the Second World War, seamounts were considered natural curiosities as there was no clear geologic explanation for their occurrence (Murray 1941, Betz and

Hess 1942, Hess 1946). Following years of study, though, they are now recognized as extinct submarine volcanoes that formed over so-called “hot spots” on the ocean floor closely associated with sea-floor spreading centers (McBirney 1963, 1971; and Staudigel and Clague 2010). Early estimates first placed the number of seamounts globally at close to 10,000 (Menard 1964) followed by an update some years later by Rogers (1994) whose estimated their numbers to be around 30,000 based on additional mapping of the ocean floor. Current estimates based on both additional subsurface mapping and statistical theory suggest that the global seamount population ranges from between 100,000 to as many as one million (Wessel, Sandwell, and Kim 2010). As a result, seamounts represent a significant areal fraction defining the abyssal ocean floor — estimated to be about 28.8 million km² or about 8 percent of the ocean floor surface area (Etnoyer, Wood, and Shirley, 2010). Based on these numbers, seamounts may also be considered to be an important source of internal wave generation.

The significance of seamounts hydrodynamically rests with the fact that they do not protrude above the ocean surface. Topographically, they are they have near-vertical relief which, in some areas, can be as much as 4 km above the seafloor (Heitzler et al. 1977). Because of their somewhat extreme relief and the fact that they are generally isolated, investigators report that seamounts can

influence the hydrodynamics of the open ocean by modifying currents (Vastano and Warren 1976) and producing variations in local flow fields (Roden, Taft, and Ebbesmeyer 1982). This is achieved through a combination of steady-forcing (i.e., Taylor columns¹²) as well as periodic tidal forcing that can stratigraphically trap currents¹³ (White and Mohn 2002, Brink 1989, Chapman 1989, Lavelle and Mohn 2010).

Islands. The Jackson (2004) atlas reveals that many internal wave observations are in close proximity to islands. There are many thousands of islands globally (Arnberger and Arnberger 2001) and most of these occur as extensions of the continental landmass. There are also islands that are not associated with the continents that have formed as a result of either diastrophic or volcanic forces (Keating et al. 1987). They number close to 900 (Menard, 1986) and include active yet isolated volcanic islands, coral islands, banks, atolls, and guyots at or above sea level.

When considering the formation of internal waves, it is these more remote islands that are of research interest for it is believed that they influence internal wave formation in a manner somewhat differently than seamounts. For

¹² Based on theories first proposed by Proudman (1917) and Taylor (1917).

¹³ In a manner not unlike that of coastally-trapped waves. See Brink (1989, 1991).

example, because islands protrude above sea level, there is no opportunity for the onset of Taylor column phenomena, as is the case for seamounts. Alternatively, Heywood, Barton, and Simpson (1990) have suggested that the flow past isolated islands can be likened to the flow around a circular cylinder in a laboratory tank used to study the influence of the Reynolds numbers on the formation of rotating eddies and wake effects leading to the generation of a classic “vortex street.” In addition to these rotation effects (Gerkema 1996), other local environmental factors recognized to influence internal wave formation in proximity to islands generally include stratification, baroclinic tides, bathymetric variations, and buoyancy-induced instabilities (Stevens et al. 2005). Also see, for example, Wolanski and Deleersnijder (1998), Wolanski et al. (2004), and Zhao and Alford (2006).

2.2.1.4 Perturbing and Restoring Forces

Despite its extensive nature (~70 percent of the Earth’s surface), with few variations, the ocean demonstrates nearly stable and uniform stratification (Pedlosky 1979). Only rarely and sporadically does one encounter statically neutral or unstable regions in the stratification of the oceans and major seas (Wunsch and Ferrari 2004). When perturbations occur in the stratification take place, there is the potential for internal waves to form. As noted at the beginning of Section 2.2.1 of this dissertation, there are many physical factors capable of producing the perturbations that lead to ISW formation.

Internal gravity waves resemble surface or gravity waves in that they rely on gravity as a restoring force. When a fluid parcel is displaced in a stably-stratified water column, it will attempt to return to its equilibrium position under the influence of gravity in a manner that is (theoretically) well-understood (Cushman-Roisin and Beckers 2009). Small density differences between the respective fluid layers in the ocean lead to small buoyancy forces acting on a perturbed water particle at the interface. The resistance of the fluid parcel to external perturbations can be expressed in terms of the dimensionless Richardson number Ri . This parameter generally defines the stability of a 2D stratified fluid system dominated by shear flow. Physically, the Richardson number is the ratio of stabilizing buoyant forces to destabilizing shear forces, in the presence of a velocity gradient, that varies with depth. Mathematically, it can be calculated using either of the following expressions:

$$Ri(z) = -\frac{1}{Fn^2} \cdot \frac{\frac{\partial \gamma}{\partial z}}{\left(\frac{\partial u}{\partial z}\right)^2} \approx -\frac{g \left(\frac{\partial \gamma}{\partial z}\right)}{\rho \left(\frac{\partial u}{\partial z}\right)^2} \quad (2.11)$$

where Fn is the densimetric Froude number:

$$Fn = \frac{u_{horizontal}}{\sqrt{g'H}} \quad (2.12)$$

where g' is the reduced gravity or $g \cdot \frac{\rho_1 - \rho_2}{\rho_2}$. Typically, the horizontal velocities

are induced by tidal motions. A decrease in the density gradient or an increase in the velocity gradient within the water column can cause the pycnocline to

become locally unstable. Miles (1961, 1963) and Howard (1961) found that transition to turbulent flow can be achieved theoretically when Ri locally falls below 0.25 anywhere within the water column.¹⁴ Conversely, stability within the system is assured when $Ri(z)$ exceeds 0.25 — the likelihood of turbulent mixing is small and stratified shear flow dominates.¹⁵

The restoring buoyancy force acting on a vertically-displaced fluid particle within the water column can be characterized by the Brunt-Väisälä or buoyancy frequency. Physically, the Brunt-Väisälä frequency N^2 is a measure of the strength of system stratification and is generally a function of depth. This parameter can be defined as:

$$N^2(z) = -\frac{g}{\rho_0} \frac{\partial \rho}{\partial z} \quad (2.13)$$

and it represents the intrinsic frequency of oscillations of a fluid parcel about its equilibrium position. Depending on the strength of the stratification, the fluid parcel will require any number of cycles to restore itself to equilibrium. Buoyant

¹⁴ Howard and Maslowe (1973) note that instability also depends (to a limited extent) on the local velocity and density profiles.

¹⁵ In more recent studies of this topic, there have been suggestions of the existence of both “global” (Ri) as well as “local” Richardson numbers (Ri_c). For example, there is a growing body of experimental and observational data that indicates that turbulence can survive when $Ri \gg 1$ (Galperin, Sukoriansky, and Anderson 2007). Under such an arrangement, and to ensure continuity with the Miles-Howard criterion, $Ri > Ri_c$ where $Ri_c > 0.25$. Also see Zaron and Moum (2009)

forces thus mechanically drive or damp the restoring oscillations based on the properties of the pycnocline.

The Richardson number can also be used to understand the influence of buoyant forces on pycnocline equilibrium by considering an alternative formulation to equation 2.11 in the form of:

$$\text{Ri}(z) = \frac{N^2}{\left(\frac{\partial u}{\partial z}\right)^2} \quad (2.14)$$

When considering shear flow in the context of equation 2.14, when it exceeds twice the (Brunt-Väisälä) stratification or

$$\left|\frac{\partial u}{\partial z}\right| > 2N \quad (2.15)$$

then internal waves can break to produce turbulence and turbulent mixing via a progression in K-H instability progression, as discussed below. Criminale (1973) discusses the role of critical shear flow in internal wave formation and breaking in more detail.

More strongly-stratified fluids (i.e., $\rho_1 \ll \rho_2$) have higher frequency oscillations, because the restoring force for vertical displacements is larger; for weakly stratified fluids, the opposite is true. Internal waves can occur at frequencies less than the Brunt-Väisälä frequency. Philips (1966) notes that N^2 represents a maximum value when the thermocline is at its greatest variation,

and decreases above and below it. When N^2 is a maximum, there are a finite number of modes. In the first mode, the pycnocline has a single vertical maxima (node). In the second mode, there are two maxima (nodes) that are 180° out-of-phase. Mode-2 is also known as a “varicose waves” (Lamb 1932, Moum, Nash, and Klymak 2008).

If conditions are such that $Ri(z) < 0.25$, then the basic flow regime is unstable and can encourage the development of K-H-like rolls or billows owing to the growth in the amplitude of the disturbance. This phenomenon has been widely studied by Chandrasekhar (1961), Turner (1973), Drazin (2002), and others. These features begin as a collection of vorticity “kernels” within some water parcel (Batchelor 1967) and can be conducive to the onset of internal wave formation (Defant 1961) as they can grow into zones of dynamic instability that can support both linear and non-linear tendencies, as suggested by earlier equation 2.2.

Wave breaking can be defined as the production of turbulence and the irreversible dissipation of energy. In the case of internal waves, breaking corresponds to the occurrence of pycnocline overturning. Thorpe (1987, 2004)

suggests that the transition to K-H instability (and ultimately breaking¹⁶) can take place in a series of discrete stages, as depicted in Figure 14, and can ultimately produce an internal wave with a remnant of the “cat’s eye” as illustrated in Figure 15. The vertical scale over which breaking can physically occur is relatively small compared to the amplitude of the internal wave — on the order of several meters (Eriksen 1978, Smyth and Moum 2000). The “cat’s eye” commonly associated with K-H turbulence/breaking transition have been identified *in situ* by several internal wave researchers (Thorpe and Hall 1974, Matsuno et al. 1997, Li and Yamazaki 2001, Moum et al. 2003).

The change in internal wave properties (and behavior) in many ways is similar that of a surface wave in open water approaching shallow water. As the deep water originated-wave enters shallow water, it begins to “feel” the bottom. As this happens, the wave undergoes a transformation in a series of steps that involve changes to its amplitude, wave length, and energy. This transformation

¹⁶ Thorpe (1994) also notes that pycnocline overturning such as that suggested by these exhibits does not always imply internal wave breaking but it is a necessary condition. A physical state under which isopycnal overturning can take place can be defined as

$$s \equiv \frac{u_{\max}}{c} > 1$$

where s corresponds to the internal wave steepness.

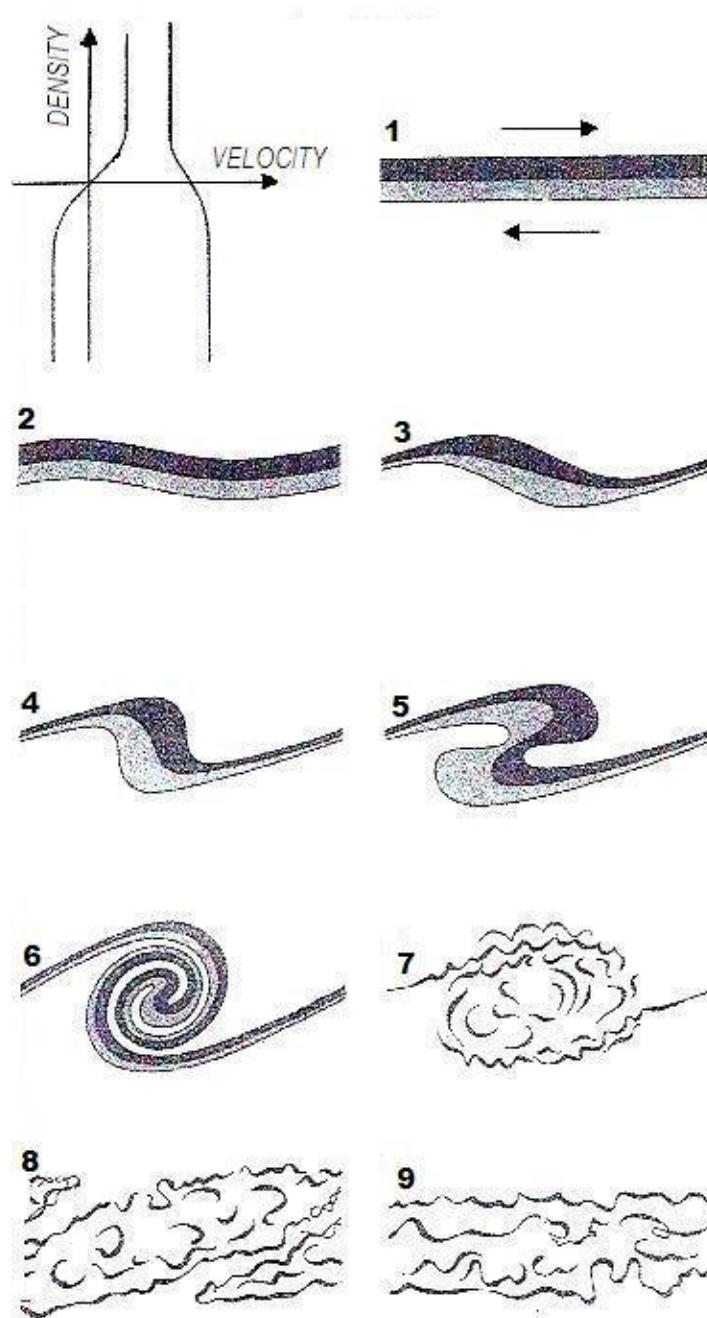


Figure 14. Progression of Kelvin-Helmholtz stability in a two-layered system. Taken from Gregg (1973) based on an unpublished study by S.A. Thorpe/National Institute of Oceanography (UK). Copyright © 1973 *Scientific American*, a division of Nature America, Inc. All rights reserved.

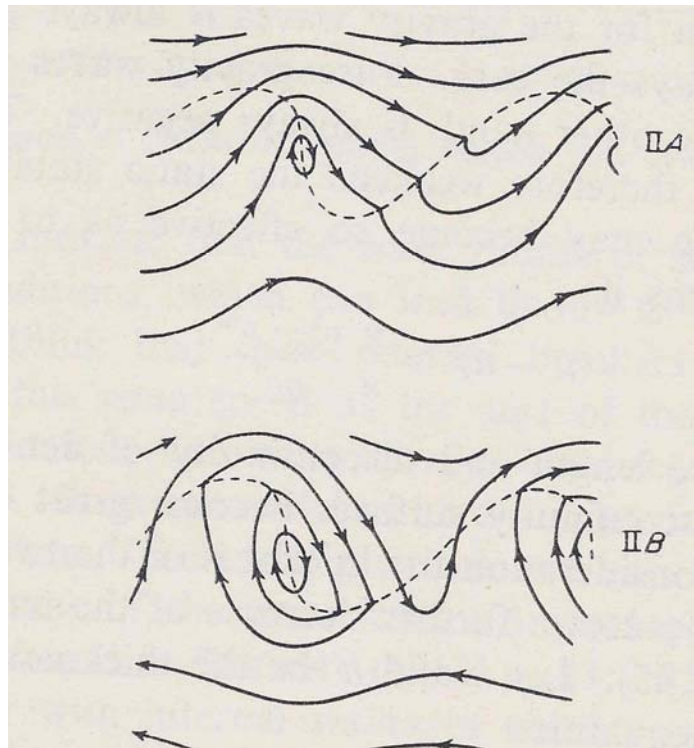


Figure 15. Representation of streamlines for a developing (dynamically unstable) internal wave in a two-layered system. **IIA** — Upper and lower fluid layers moving in the same direction. **IIB** — Upper and lower fluid layers moving in opposite directions. Taken from Defant (1961a) citing Bjerknes and others (1933). Reprinted from *Physical Oceanography*, vol. 2, A. Defant (ed.), Fig. 236, p. 566, Copyright © 1961 Pergamon Press.

is generally referred to as “shoaling” in its earliest stages and ultimately leads to the wave “breaking.”

2.2.2 Internal Waves and Topography (Sinks)

Once formed in the ocean, internal waves can travel considerable distance without any appreciable change in character. Although not all internal waves require the influence of topography to form at the onset, when they do encounter

(significant) variations in submarine topography, their properties can be altered. As mentioned earlier in this dissertation, this alteration/transformation typically manifests itself on the ocean surface through subtle variations in the texture of surface waves and can be observed, albeit indirectly, by evaluating high-altitude photographs and/or satellite imagery. As is the case with surface waves, internal waves have been found to shoal and break (Emery and Gunnerson 1973). The shoaling/breaking process for an internal wave has been depicted schematically by Lui et al. (1998) in Figure 16.

Different types of surface waves break differently and there have been many studies over the years to better understand shoaling and breaking as these phenomena are recognized as serving an important role in shoreline ecology. Key studies in the past include Iversen (1951), Biesel (1952), Patrick and Wiegel (1955), Wiegel (1964), and Galvin (1968, 1972). A more recent synopsis of wave breaking phenomena was prepared by Peregrine (1983). Nagashima (1971) suggests that the examination of breaking surface waves represents a reasonable analog against which the results of experimental investigations and numerical simulations of internal wave shoaling and breaking can be compared.¹⁷

¹⁷ Elmore and Heald (1969) note that waves behave in fundamentally the same manner subject to the properties of the fluid medium they occur in. It can be argued that surface waves also represent internal waves as air is also a type of fluid, albeit the density of air is much less

exists the possibility that the wave will ultimately undergo a change in its polarity owing to a landward decrease in the depth of the seafloor. As is the case with surface waves, an internal wave would be expected to shoal when its orbital paths encounter the seafloor. And again, like surface waves, shoaling would be expected to reduce the internal wave's forward velocity and in doing so lead to a reduction in wavelength while producing an increase in wave amplitude.

Although a satisfactory theoretical explanation exists describing shoaling and a subsequent change in internal wave polarity, observation of this phenomenon *in situ* is rare for internal waves and has proven difficult to validate. Shroyer, Moum, and Nash (2009), and others, have been able to document the reversal of polarity in the field for an internal wave off of the coast of New Jersey.

2.2.2.2 Breaking

Following shoaling, the next major stage in wave evolution, and the one typically associated with the greatest expenditure of energy is wave breaking. Wave energy is adsorbed and converted to heat. The gentler the slope of the obstacle (seafloor) the more wave energy is converted. The forward motion of an advancing wave is slowed as it encounters waters of declining depth. Wave particle speeds are slowed-down slightly more at the bottom of wave orbitals than at the top as a result of changing seafloor slope. The resulting differential

forward movement in combination with the increased wave steepness causes the wave to become vertically unstable. It is generally recognized that waves break because the velocity of particle motion at the crest of the wave front exceeds the internal wave's overall phase velocity. Because the quantity of water preceding the wave front is insufficient to fill the wave crest, thereby allowing for a symmetric wave form, the crest consequently topples forward, collapsing the wave thereby causing it to "break." For surface waves, breaking generally occurs when the wave amplitude is about 1.3 times the wave depth. Once breaking commences, it occurs quickly. An example of a breaking surface wave in profile and progression is depicted in Figure 17.

Galvin (1968) suggests that there are four types of breaking waves – *spilling*, *plunging*, *collapsing*, and *surging*. Quantitatively, this taxonomy is based on the natural slope of the beach m , wave period T , and either deep-water or breaker height, H_0 or H_T . Qualitatively, though, the Galvin taxonomy relies subjectively) on the characteristics of the wave crest to classify the breaking type morphology. As illustrated in Figure 18, spilling breakers can be distinguished by an unstable wave crest that cascades down the shoreward face of the wave producing a foamy surface of the face of the wave and cascades down the shoreward face of the wave producing a foamy water surface. In the case of plunging breakers, the crest curls over the shoreward face of the wave and falls

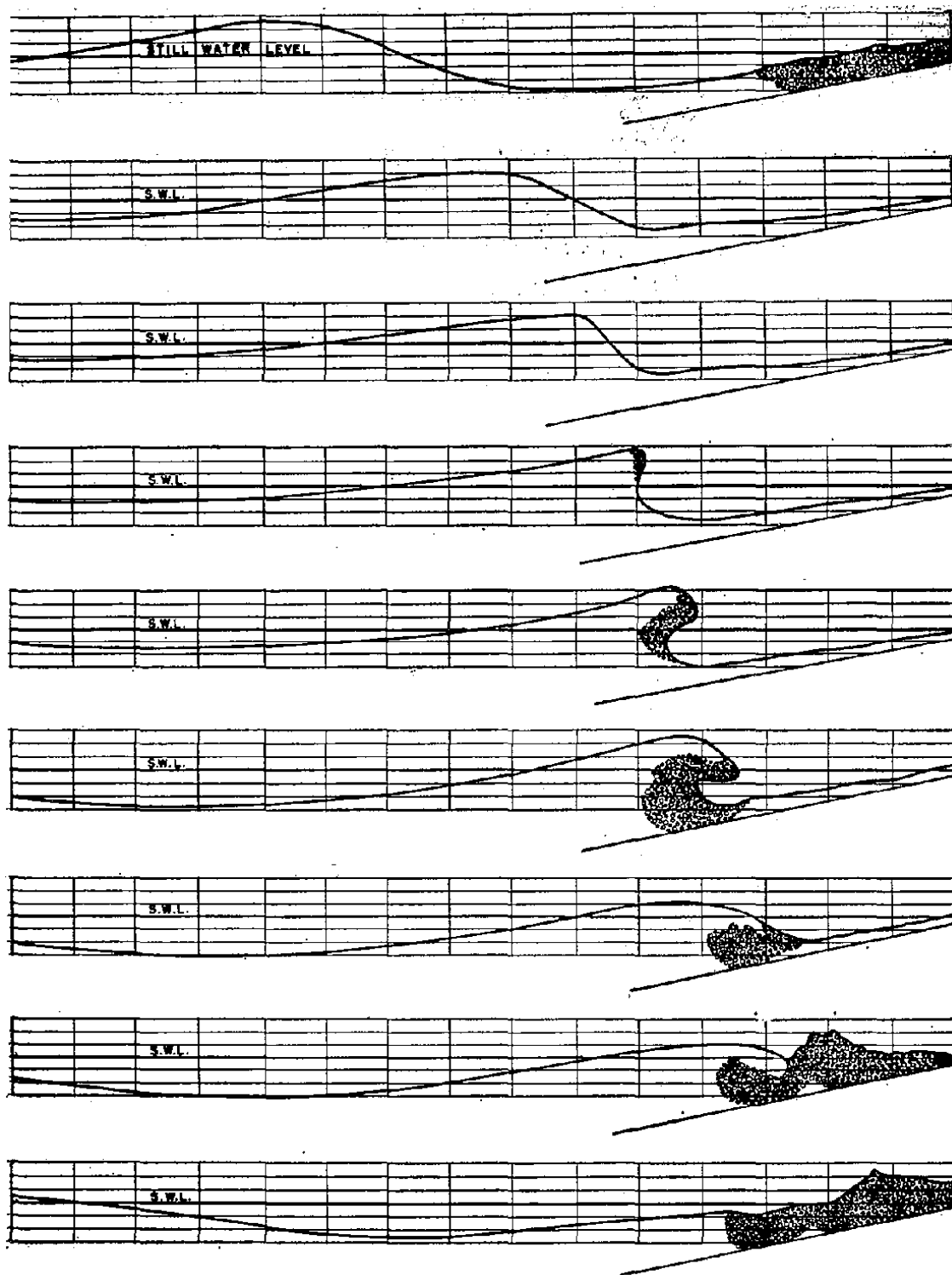


Figure 17. Breaking progression for a plunging-type surface wave. Taken from Mason (1952).

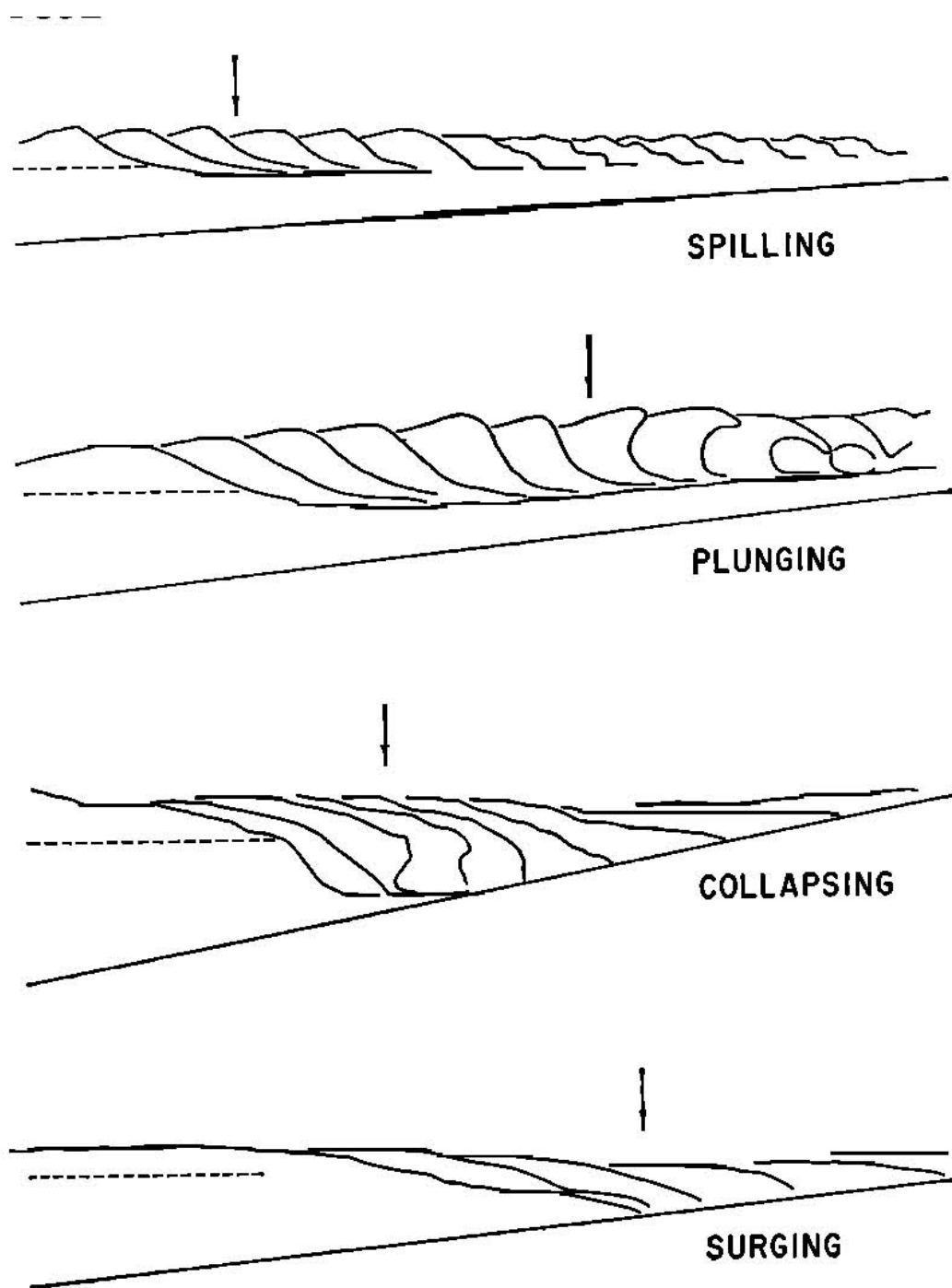


Figure 18. Principal surface wave breaker types as defined by Galvin (1968).
Reproduced by permission of the AGU.

over onto the beach, resulting in a high splash. In collapsing breakers, the crest remains unbroken while the lower part of the shoreward face steepens and then collapses, producing an irregular turbulent water surface. Lastly, the wave crest remains unbroken in the case of surging breakers and the front face of the wave advances up the beach with minor breaking.

When considering internal waves as a separate wave class, Emery and Gunnerson (1973), recommended a somewhat different taxonomy for describing breaking behavior. These researchers examined 114 thermal isotherms in the *Santa Monica Bay area* of California and suggested that internal wave breaking could be qualitatively organized into seven classes. These classes are described below and illustrated in Figure 19:

- Class 1.* Internal waves with no effect by shoaling bottom: isotherms similar at different depths.
- Class 2.* Internal waves with no effect by shoaling bottom: wave pattern superimposed on general temperature slope due to upwelling.
- Class 3.* Internal swash: shallower isotherms precede deeper ones; marked steepening of wave front.
- Class 4.* Strong internal swash: definite wave run-up.

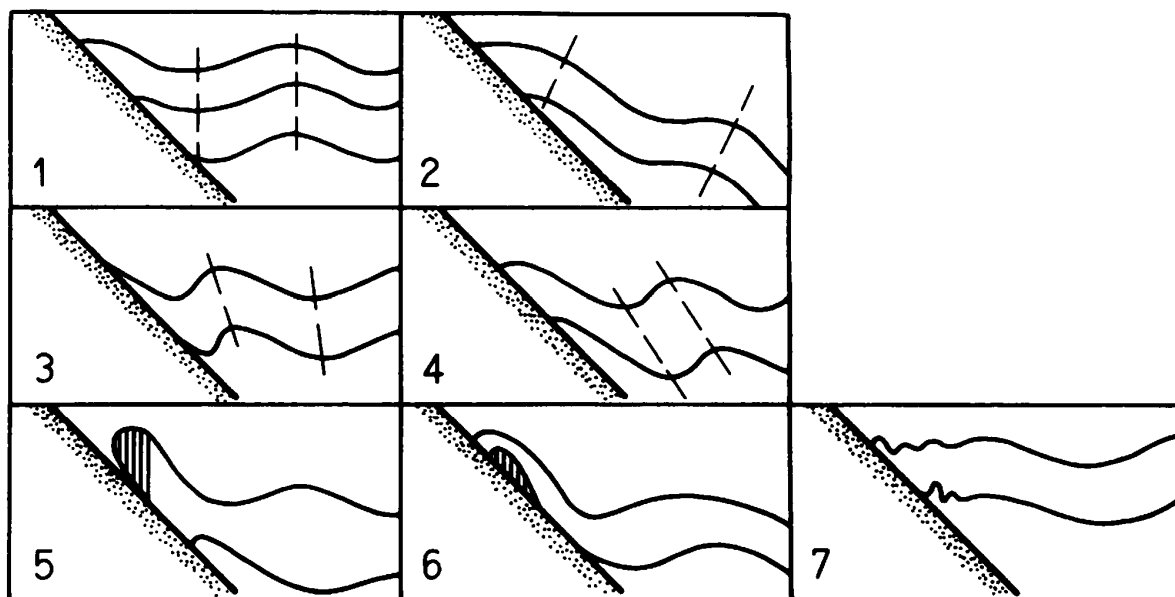


Figure 19. Seven internal wave breaking classes proposed by Emery and Gunnerson (1973). Class type is designated by numbers in the respective boxes.

Class 5. Internal surf: temperature inversion.

Class 6. Internal surf: discrete bolus of cold water along the bottom.

Class 7. Internal surf: extreme irregularity in wave form near the bottom.

In terms of the relative frequency of occurrence, Emery and Gunnerson found that of the 114 thermal sections reviewed, 40 percent could be designated Classes 1 or 2 (no effect of shoaling bottom), 39 percent could be designated Classes 3 and 4 (internal swash up the bottom slope), and 21 percent designated Classes 5, 6, or 7 (breaking internal waves – internal surf). As an area of future

scientific inquiry, Emery and Gunnerson recommended that attempts be made to quantify the respective breaking classes.

Boluses can either be transmitted landward or reflected seaward depending on the angle of the incident ISW and/or obstacle slope. Using a tsunami-type wave as a hydraulic model, Heller, Unger, and Hagar (2005) examined the basic features of bolus formation, including run-up, in connection with wave breaking. See Figure 20. Wallace and Wilkinson (1988), Helfrich (1992), Michallet and Ivey (1999), Bourgault and Kelly (2003), Venayagamoorthy and Fringer (2006), Bourgault, Kelley, and Galbraith (2008) have investigated the formation and behavior of boluses, motivated by interest in understanding the role of such features in inducing boundary mixing in coastal systems. These studies indicate, in the case of Leichter et al. (1996), for example, that internal bores may be particularly important in redistributing cool water, suspended particles, dissolved nutrients, and plankton. To better understand how far-reaching bolus effects might be experienced, Synolakis (1987) has investigated the run-up features of solitary waves.

For the purpose of completeness, it is worth noting that tidal bores are another example of a breaking solitary wave. For a tidal bore to form, two conditions must be met. First, the tides in the adjoining tidal body must be

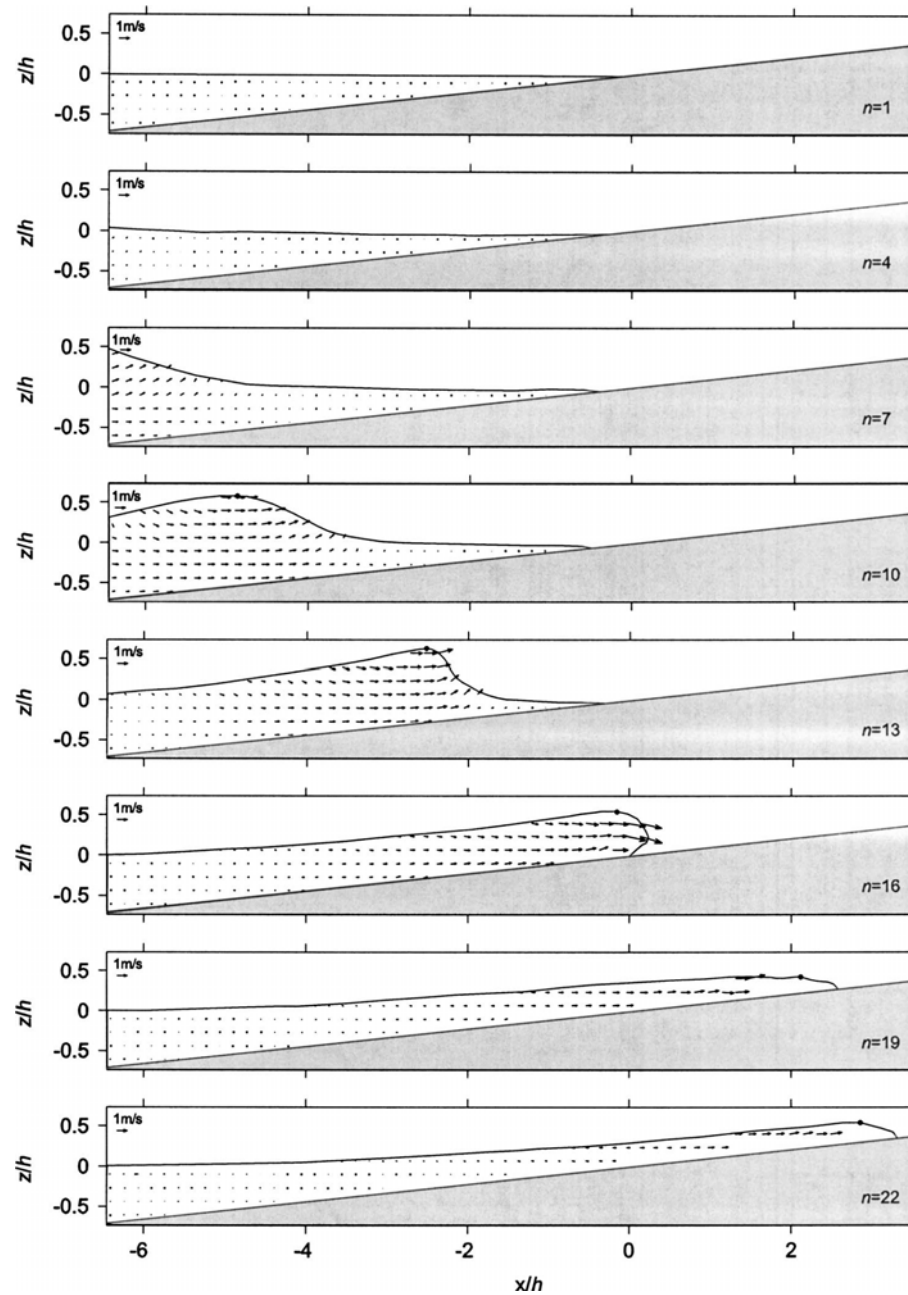


Figure 20. Non-dimensional numerical simulation of solitary wave showing profiles of bolus formation and surge (run-up). Exhibit shows surface wave profile on a sloping beach (1:10) and internal velocity distributions at various time steps n . Taken from Heller, Unger, and Hagar (2005). Reproduced by permission of the American Society of Civil Engineers.

exceptionally high. Second, the receiving inlet (a river) must be shallow, with a gently-sloping bottom and have a funnel-shaped estuary. The bore forms when the incoming tide is forced into the narrowing river mouth, and grows in height until a single wave forms and moves upstream (Lynch 1982). Tidal bores can reach up to 6 m in height above the standing water level. The earliest reported reference in the literature to tidal bores is about 1837, almost a decade before the Scott-Russell discovery.

2.2.2.3 Summary

What the literature reports is that as a wave (or wave train) approaches the continental land mass, it begins to shoal by virtue of the wave particle orbitals intersecting a progressively-rising continental slope and/or continental shelf. Once shoaling begins to take place, there is a predictable series of steps which result in the breaking of the wave as the depth of the water is now insufficient to sustain the wave's form (as well as its properties).

For the purposes of this research, it is useful to establish a terminology that can be used later to describe the simulated behavior of an internal wave as it shoals and breaks. As noted earlier in this dissertation, there is the possibility (theoretically) for a reversal in the internal wave's polarity to occur when the water depth condition corresponding to $h_1 = h_2$ is satisfied. The breaking of an internal wave can be divided into four distinct phases effectively representing its

life-cycle: *shoaling*, *breaking*, *bore*, and *run-up*. As discussed below, these designations are primarily subjective and based in large measure on observed changes in pycnocline geometry as the wave shoals through the course of the numerical simulation.

Shoaling Phase. Shoaling represents the initial phase of the internal wave transformation. The onset of shoaling is first evident when there are changes in the geometry of the internal wave streamline contours as the wave moves from deep to shallow water. Recalling Figure 8, the geometry of the streamline contours in open water is primarily elliptical. However, that geometry changes when the seafloor (or a submarine obstacle) is encountered. The streamline contours at the leading edge of the internal wave will refract or bend parallel to the slope of the seafloor. Soon thereafter, the geometry of the pycnocline (the density discontinuity) itself will begin to change. It will become less sinusoidal, more asymmetric, and the pycnocline will steepen while its wavelength decays. The leading edge of the internal wave will also refract in such a way as to mirror the seafloor slope. At some point later in this phase of the progression, the pycnocline will appear to become entrained by the seafloor and behaves as if it is washing down the seafloor slope, in a direction opposite to that of the internal wave trains' forward momentum. This phenomenon is generally referred to as "backrush" or "wash-down."

Breaking Phase. At some point in the progression, the backrush of the leading face of the internal wave will cease although the trailing face of the internal wave will continue to progress up-slope. This creates a situation in which the trailing portion of the internal wave is advancing ahead whereas the leading portion appears to be retreating in the opposite direction — down-slope. From inspection of Figure 15, it can be observed that the internal wave will steepen to some point where it ultimately develops a crest-like feature that becomes unstable. This instability leads to increased shear at the face of the density discontinuity after which the wave essentially rolls over on itself, throwing its mass forward and downward, and in doing so, forming K-H-like features. This overturning event corresponds to “breaking.”

Bore Phase. Internal wave breaking is followed by phase where the ISW essentially decomposes as a recognizable form. The once well-defined, sinusoidal internal wave has now devolved into a non-symmetric wave-like feature characterized by turbulence and turbulent mixing. Tidal bore forms can range from a single, wave front in the shape of a “roller” or “bolus,” not unlike that typically associated with a hydraulic jump, to a collection of undular bores (Small, Sawyer, and Scott 1999) followed by a train of secondary whelps; all of these forms demonstrate positive elevation. That is to say the elevation of the bore, as defined by the pycnocline, is not trough-like. Regardless of their form,

these ISW remnants are essentially confined to sub-pycnocline waters (or the h_2 layer) and mix with ambient waters as they surge up-slope. Experimental observations of tidal bores indicate a rapid deceleration of wave speed as well as large variations in localized velocities. An example of the bore phase in wave breaking is illustrated at time step $n = 16$ in Figure 20. Also see Koch and Chanson (2008, 2009).

Run-up Phase. This phase corresponds essentially to the end of the ISW life-cycle. The remnants of the ISW, in the form of a bore, continue to advance or wash upslope. For surface waves, run-up is generally defined to be the maximum vertical extent of wave up-rush on a beach above the still water level (Sorensen 1997). For ISWs, run-up would correspond to the elevation of the pycnocline in the h_1 layer relative to its' quiescent (undisturbed) position at $t = 0$. An example of the run-up phase associated with wave breaking corresponds to time step $n = 22$ in Figure 20.

CHAPTER III

COMPUTATIONAL METHODOLOGY

3.1 Background

Numerical simulations of physical phenomena provide a useful means for evaluating those phenomena not readily measurable or amendable to measurement *in situ*. Following the introduction of the high-speed digital computers, researchers have been able to simulate hydrodynamic phenomena at will through the use of mathematical models employing numerical methods applied to a structured grid. In fact, some of the earliest studies (Fromm 1963)¹⁸ focused on the finite approximation of the Navier-Stokes equation for viscous, incompressible fluids.

¹⁸ Preliminary results of this and other experimental work is described in Fromm and Harlow (1963) and Harlow, Shannon, and Welch (1965).

Over the years, CFD techniques have reached a level of maturity that permits increased accuracy in modeling predictions.¹⁹ As a consequence, there are a number of texts on the subject in particular as well as some of the ancillary issues associated with those calculations whose intent is to provide useful advice to CFD practitioners. To name a few, they include, Chow (1983), Ferziger and Perić (2002), Hildebrand (1968), Lapidus and Pinder (1982), Scannapieco and Harlow (1995), Roache (1998b), and Wesseling (2004).

In seeking numerical solutions to hydrodynamic equations, researchers nevertheless have been confronted by a common set of computational challenges (Harlow and Fromm 1965, Harlow and Amsden 1970) including questions concerning:

- how the hydrodynamic problem is to be computationally represented;
- how the governing equations are to be mathematically approximated;
- the degree of accuracy expected in the calculation;
- how numerical instabilities in the calculation will be addressed; and
- the appropriateness of the computational technique in relation to the type of hydrodynamic problem.

¹⁹ Subject to certain conditions (Oberkampf, Blottner, and Aeschliman 1995, Roache 1997, and Oberkampf and Blottner 1998).

To address these as well as other issues facing CFD practitioners, Roache (1972, 1998a), for example, outlined a basic computational methodology for solving incompressible flow problems in a rectilinear (Eulerian) reference domain with regular boundaries. Roaches' recommended computational approach also included guidance on how to numerically solve Navier–Stokes derivations of the vorticity-stream function equations – equations which as discussed below – provide the mathematical foundation of this research. The simplest model that supports the formation of an internal solitary wave can be defined as a stratified two-fluid system with a small density discontinuity (i.e., a pycnocline). This model can provide a qualitative description of the dominant internal wave of mode-1. Under such a paradigm, it is possible to study of the time-dependent motion of a viscous, incompressible fluid in 2D Cartesian coordinates using an Eulerian mesh. Roaches' guidance is still both appropriate and useful for this type of modeling arrangement, and key elements of that guidance have been employed, as discussed in the following pages.

3.2 Governing Equations

The fundamental equations for 2D incompressible flow of a Newtonian fluid with no body forces and constant properties are the Navier–Stokes momentum equations and the continuity equation (Lamb 1932, Schlichting 1968). The Navier–Stokes equations, equations 3.1 and 3.2 below, describe how

fluid velocity changes with time. Equation 3.3 is the continuity equation expressing the conservation law for fluid flow. These equations are written in an Eulerian frame of reference – that is to say one in which the fluid moves through a space-fixed reference domain. In their primitive, dimensional form (as indicated by the over bars) these partial differential equations (PDEs) are:

$$\frac{\partial \bar{u}}{\partial \bar{t}} + \bar{u} \cdot \frac{\partial \bar{u}}{\partial \bar{x}} + \bar{w} \cdot \frac{\partial \bar{u}}{\partial \bar{z}} = - \left(\frac{1}{\bar{\rho}} \cdot \frac{\partial \bar{p}}{\partial \bar{x}} \right) + \bar{\nu} \cdot \left(\frac{\partial^2 \bar{u}}{\partial \bar{x}^2} + \frac{\partial^2 \bar{u}}{\partial \bar{z}^2} \right) \quad (3.1)$$

$$\frac{\partial \bar{w}}{\partial \bar{t}} + \bar{u} \cdot \frac{\partial \bar{w}}{\partial \bar{x}} + \bar{w} \cdot \frac{\partial \bar{w}}{\partial \bar{z}} = - \left(\frac{1}{\bar{\rho}} \cdot \frac{\partial \bar{p}}{\partial \bar{z}} \right) + \bar{\nu} \cdot \left(\frac{\partial^2 \bar{w}}{\partial \bar{x}^2} + \frac{\partial^2 \bar{w}}{\partial \bar{z}^2} \right) \quad (3.2)$$

$$\frac{\partial \bar{u}}{\partial \bar{x}} + \frac{\partial \bar{w}}{\partial \bar{z}} = 0 \quad (3.3)$$

where \bar{u} and \bar{w} are, respectively, the horizontal x and vertical z components of the fluid velocity vector [L/T], and p , ρ , and ν correspond respectively to the fluid properties of pressure [M/T·L²], mass density [M/L³], and kinematic viscosity [L²/T].

Past CFD experience suggests that successful numerical solution of the governing equations can be achieved using a vorticity–stream function approach. Following mathematic manipulation, including the elimination of the pressure term p and the introduction of other variables (described below), it is possible to

transform these equations into dimensionless Boussinesq forms²⁰ expressed with respect to vorticity ξ and the stream function φ :

$$\frac{\partial \gamma}{\partial t} + \frac{1}{Q} \cdot \frac{\partial}{\partial x}(\gamma u) + \frac{\partial}{\partial z}(\gamma w) = \left(\frac{1}{\text{Re} \cdot \text{Sc}} \right) \cdot \nabla^2 \gamma \quad (3.4)$$

$$\frac{\partial \xi}{\partial t} + \frac{1}{Q} \cdot \frac{\partial}{\partial x}(\xi u) + \frac{\partial}{\partial z}(\xi w) = \left(\frac{Q}{\text{Fr}^2} \cdot \frac{\partial \gamma}{\partial x} \right) + \left(\frac{1}{\text{Re}} \cdot \nabla^2 \xi \right) \quad (3.5)$$

$$\nabla^2 \varphi = \frac{\xi}{Q^2} \quad (3.6)$$

Equation 3.4 is the diffusive transport equation for the density anomaly γ defined as $\frac{\rho_1 - \rho_2}{\rho_2}$. Equation 3.5 describes the parabolic vorticity transport equation. Equation 3.6 is the Poisson equation that relates the stream function to the vorticity within the flow field. The dimensionless Schmidt number Sc , defines the ratio of the kinematic viscosity ν to the mass diffusivity D_m [L²/T], is introduced in Equation 3.4. Equation 3.4 also introduces the dimensionless Reynolds number Re describing the ratio of inertial fluid forces to viscous fluid forces. In equation 3.5, Fn refers to the Froude number for the system – another dimensionless parameter that compares inertial forces to gravitational forces.²¹

²⁰ The Boussinesq (1903) approximation is often used to simplify the Navier-Stokes equations to allow for both theoretical analysis and numerical computation. The basis for this approximation is that there are some fluid systems in which the temperature varies little and the density therefore can be considered to be relatively constant. Consequently, the density term can be neglected in the analysis with the exception of the buoyancy term. In the study of internal waves, the Boussinesq approximation has proven to be useful (Long 1965).

²¹ For the purposes of this research and consistent with the earlier-referenced Boussinesq approximation, the Froude number used is actually a “densimetric” Froude number.

Equations 3.4 through 3.6 also make reference to a dimensionless normalizing parameter Q defined as:

$$Q = \frac{L}{D} \quad (3.7)$$

The rectilinear coordinate form of the Laplacian operator ∇^2 referenced in equations 3.4 through 3.6 is defined as:

$$\nabla^2 = \frac{1}{Q^2} \frac{\partial^2}{\partial x^2} + \frac{\partial^2}{\partial z^2} \quad (3.8)$$

Other parametric relationships in the equations above include the following:

$$\left. \begin{aligned} \xi &= Q^2 \cdot \frac{\partial u}{\partial z} - Q \cdot \frac{\partial w}{\partial x} \\ u &= \frac{\partial \varphi}{\partial z}, \quad w = -\frac{1}{Q} \cdot \frac{\partial \varphi}{\partial x} \\ \text{Fn} &= \frac{c_0}{\sqrt{g \cdot D_m}}, \quad \text{Re} = \frac{c_0 \cdot D_m}{\nu}, \quad \text{Sc} = \frac{\nu}{D_m} \end{aligned} \right\} \quad (3.9)$$

where c_0 describes the wave celerity [L/T] and g is the gravitational acceleration constant [L/T²] at sea level (9.8 m/s² or 32 ft/s²).

Finally, to further simplify the analysis, it is useful to express all of the system parameters described in the aforementioned equations in non-dimensional forms by applying certain mathematical transformations. These transformations are listed in Table 9.

Table 9. Definition of Select System Parameters.

PARAMETER	DESCRIPTION
$x = \frac{\bar{x}}{L}$	x coordinate [Dimensionless]
$z = \frac{\bar{z}}{D}$	z coordinate [Dimensionless]
$u = \frac{\bar{u}}{c_0}$	Velocity vector in the x direction [Dimensionless]
$w = \frac{\bar{w}}{c_0}$	Velocity vector in the z direction [Dimensionless]
$t = \frac{\bar{t} \cdot c_0}{d}$	Time [Dimensionless]

3.3 Computational Approach

As was the case with the previously-described Navier-Stokes and continuity equations, equations 3.4 through 3.6 are also written in a space-fixed reference frame through which the fluid moves as a function of time. The solutions for the vorticity and stream function are obtained through an explicit time-marching numerical integration process. By graphing the numerical solutions at each successive time-step (using MATLAB), it is possible to generate a simulation that represents the translation of the internal wave through the modeling domain — in effect, a “virtual” internal wave.

Roache (1972, 1998a) has recommended a mathematical approach for solving the time-dependent Navier-Stokes equations for an isothermal, homogeneous fluid. This approach relies on a “computational cycle” with well-defined steps. This approach, depicted in Figure 21, is summarized below and described in more detail in the following paragraphs.

Step No. 1 in Roache’s recommended approach begins with the definition of a computational domain over which a mesh or grid is superimposed. The mesh (or grid) discretizes the spatial domain for the analysis and in doing so defines the locations for which solutions to the finite-difference analogs of the Navier-Stokes equations are obtained. The second step (Step No. 2) in the recommended approach is to specify those initial and boundary conditions for the vorticity and the stream function that apply to this domain.

Having defined the computational domain as well as the applicable initial and boundary conditions, Step No. 3 in Roache’s recommended approach is to obtain a solution to the vorticity transport equation – one of the governing equations underpinning this research. This equation estimates the rate of fluid circulation or $\frac{\partial \xi}{\partial t}$ – for the interior points of the computational domain.

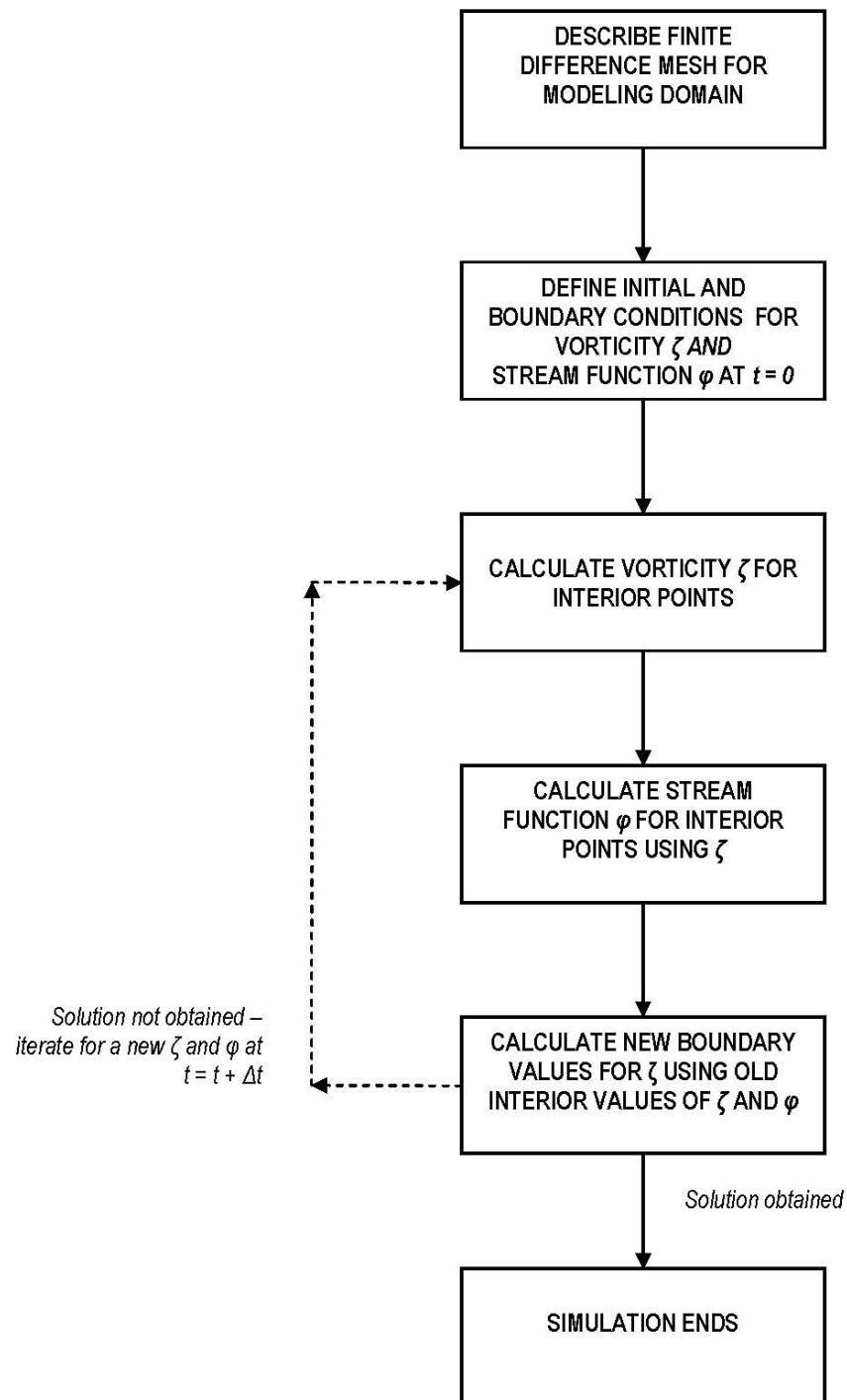


Figure 21. Steps in Roache's (1972, 1998a) recommended approach for solving the Navier-Stokes equations.

Following the calculation of vorticity, the solution of the finite difference analog of the Poisson equation is obtained in Step No. 4. As mentioned earlier in this dissertation, this equation relates vorticity to the stream function, thereby describing the mass-rate of fluid flow through the system. Using the most recent values of ξ and φ obtained for all interior points of the computational domain, the last step in the process (Step No. 5) is one in which updated (source) values of vorticity are calculated for use in the next time step Δt .

The calculation cycle described above is repeated by advancing to the next time step by some specified time increment $t + \Delta t$, thereby “marching” the vorticity solution ahead in time. Mathematically, this is called an explicit method, solution of which can be expressed as:

$$\xi_{new} = \xi_{old} + \Delta t \cdot \frac{\partial \xi}{\partial t} \quad (3.10)$$

The computational procedure ends when the pre-defined number of time steps has been completed or some convergence criterion (also pre-defined) has been satisfied.

The mathematical approach outlined above was developed by Roache (1972, 1998a) for a homogenous isothermal fluid. However, the system model considered in this research relies on a density-stratified fluid. Spatial variations in the density stratification will take place over time as a result of advective and

dispersive forces. Consequently, there is the need to computationally account for these variations by introducing a PDE that can be solved simultaneously with vorticity and the stream function equations.

3.3.1 Finite Difference Approximations

When employing the finite difference method, the PDEs are replaced by difference equations which must be satisfied for a finite set of locations (or nodes) on a grid that defines the computational domain. At each node location in the computational domain, the numerical solution to the equations of interest relies on an algebraic approximation obtained from adjacent grid nodes representing an averaged value. Solutions to these equations are thus obtained through a succession of closely-spaced time increments in which the solution will evolve or asymptotically approach steady-state subject to both initial and boundary conditions. The finite differences, therefore, apply to both time and space variations. If both the time and space increments are sufficiently small, then the calculated results can be expected to generally match the true solution to the original (governing) PDEs. Using a digital computer, Harlow and Welch (1965) were the first successfully to employ this type of numerical method to obtain solutions to the Navier-Stokes equations.

To understand how this mathematical method works, consider for example, some flow field property $f(a)$ for some fluid. The first derivative of $f(a)$ corresponding to some small sampling interval h is:

$$f'(a) = \frac{f(a+h) - f(a)}{h} + HOT(h) \quad (3.11)$$

Neglecting $HOT(h)$ or the higher-order terms of h , for a properly behaved function the forward Taylor Series expansion of $f'(a)$ at some arbitrary point x_0 is:

$$\begin{aligned} f(x_0) + \frac{f'(x_0)}{1!} \cdot (a - x_0) + \frac{f''(x_0)}{2!} \cdot (a - x_0)^2 + \\ \dots \frac{f^n(x_0)}{n!} \cdot (a - x_0)^n + R_n(a) \end{aligned} \quad (3.12)$$

By neglecting the $HOTs$ once again as well as the residuals $R_n(a)$, the expansion of $f'(a)$ with some minor algebraic manipulation reduces to:

$$f'(a) \approx \frac{f(a+h) - f(a)}{h} \quad (3.13)$$

Through the introduction of nodal subscripts i , the finite difference form of equation 3.13 can be expressed as:

$$\frac{\partial f_i}{\partial h} \approx \frac{(f_{n+i} - f_i)}{\Delta h} \quad (3.14)$$

This formulation corresponds to the “forward” (or “upwind”) finite difference approximation of $f'(a)$ because it involves the values of the function at the i location (node) as well as the $n+i$ location.

The truncation or local error associated with the approximation depicted in equation 3.14 is on the order of Δh or a first order accuracy in space.²² This error represents the difference between the PDE solution and the finite difference equation approximation. If the computational mesh were infinitely small, then an exact solution of the PDE could be obtained irrespective of the finite differencing scheme employed. However, in practice only a limited number of difference cells can be introduced into any computational domain. Thus, the resulting truncation error generated in the calculation is a function of grid quality (spacing or coarseness) and flow gradient — or how rapidly the flow field property changes in space. Because local truncation errors can be transported, advected, and diffused throughout the computational domain, it is important to select a numerical method that minimizes the transmission of those errors while at the same time demonstrating numerical stability.

3.3.2 Numerical Scheme

One of the challenges in CFD studies is the need to manage the uncertainties and errors that cause mathematical simulations to differ from the true or exact values of the phenomena that might be observed in nature. When the vorticity-stream function equations are discretized into finite difference

²² Other finite difference analogs of $f'(a)$ can be obtained by expanding backwards to the preceding point $n-i$, which also is first order accurate, or by subtracting the “forward” and the “backward” expansions to obtain a centered-difference approximation which has a truncation error on the order Δh^2 which is second-order accurate in space.

equations, the reduced algebraic expressions are generally more diffuse (dispersive) than the original PDEs so that the simulated system appears to behave differently in comparison to the physical system being modeled. The amount and character of the differences depends on the complexity of the particular system being simulated and the type of discretization method used. Mathematically, numerical or false diffusive errors can be introduced into the simulation as a result of discretizing the advection-dispersion equations. Numerical dispersion errors are generally proportional to the magnitude of the ratio between the inertial forces to the frictional forces or the non-dimensional Reynolds number. See, for example, Kao, Pao, and Park (1978).

The numerical method selected for use in this study is a one-step explicit finite difference scheme. This scheme possesses both the transportative and conservative properties described by Roache (1972, 1998a). Central differencing in space and forward differencing time are used, except for the non-linear terms of the governing equations, for which a special upwind method was applied. The special upwind method was introduced by Torrance and Rocket (1969) and has truncation errors that appear as false viscosity²³ and false diffusion²⁴.

²³ Another source of error in CFD concerns numerical stability. It is also associated with the time-stepping scheme. These errors can cause the solutions to ‘oscillate’ about some solution. Roache (1972, 1998a) refers to this oscillatory tendency to overshoot or undershoot some mathematical solution as ‘dynamic instability.’

As mentioned above, as the Reynolds number increases, these false computational effects begin to mask both the real viscosity and diffusion. In order to limit these effects, an explicit numerical scheme possessing zero numerical diffusion was adopted in this research. This numerical scheme was first introduced in one-dimensional form by Valentine (1987) as ETUDE – Explicit in Time Up-stream Difference Estimate. The 2D version of ETUDE was subsequently developed by Tannous and Valentine (1989) under the general title of the “transportative upwind scheme.” ETUDE is accurate to second order so that it reduces the numerical viscosity and false diffusion to zero.

The finite grid structure shown in Figure 22 can be used to illustrate how the 2D version of the ETUDE numerical scheme works in the context of any generic finite difference cell. Once again consider some flow field property $f(a)$. The subscripts i and j denote the locations of the nodes in the x and z directions, respectively. Along some vertical face z of any generic grid cell in the computational domain, a value of $f(a)$ can be expressed as follows:

²⁴ False diffusion can arise when an upwind differencing method is used to discretise CFD equations. Although this differencing method provides results closer to analytical ones, when the fluid flow is not aligned with grid system, the upwind differencing method causes the transported properties to appear to be ‘smeared.’ The resulting numerical error has a diffusion-like appearance; hence false diffusion. Higher-order finite differencing schemes may be more accurate than upwind differencing but the numerical solution may become unstable. False diffusion is discussed in more detail by Patankar (1980) and Ferziger and Perić (2002).

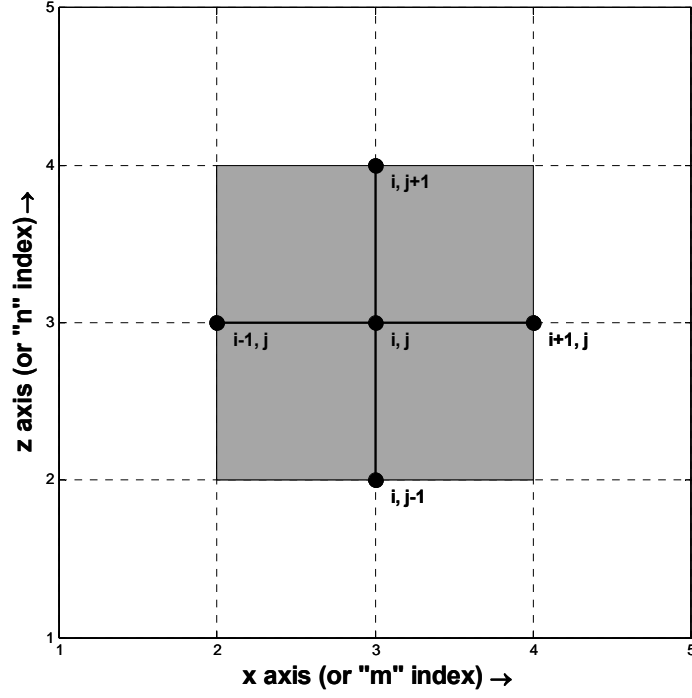


Figure 22. Finite difference grid.

$$f(a) = f_2(a) - \left(\frac{f_2(a) - f_1(a)}{\Delta x} \right) \cdot \left(\frac{\Delta x}{2} + \Delta x' \right) \quad (3.15)$$

where

$$\left. \begin{aligned} f_1(a) &= f(a)_{i-1,j+1} - \left(\frac{f(a)_{i-1,j+1} - f(a)_{i-1,j}}{\Delta z} \right) \cdot (\Delta z + \Delta z') \\ f_2(a) &= f(a)_{i,j+1} - \left(\frac{f(a)_{i,j+1} - f(a)_{i,j}}{\Delta z} \right) \cdot (\Delta z + \Delta z') \end{aligned} \right\} \quad (3.16)$$

for which $\Delta x' = \frac{1}{Q} \cdot \alpha_d \cdot u_a \cdot \Delta t$ and $\Delta z' = \alpha \cdot w_a \cdot \Delta t$, where u_a and w_a are the averaged

face velocities, and α_d is a dimensionless constant that controls false diffusion

within the numerical scheme. It is worth noting that for equation 3.16 to be

valid, $w_a < 0$. Similar expressions for equations 3.15 and 3.17 were derived for the other three faces of the generic finite difference cell (Figure 22). For example, along the lower horizontal x face of these cells, a value for $f(a)$ can similarly be expressed as:

$$f(a) = f_2(a) - \left(\frac{f_2(a) - f_1(a)}{\Delta z} \right) \cdot \left(\frac{\Delta z}{2} + \Delta z' \right) \quad (3.17)$$

where

$$\left. \begin{aligned} f_1(a) &= f(a)_{i,j-1} - \left(\frac{f(a)_{i,j-1} - f(a)_{i-1,j-1}}{\Delta x} \right) \cdot (\Delta x') \\ f_2(a) &= f(a)_{i,j} - \left(\frac{f(a)_{i,j} - f(a)_{i-1,j}}{\Delta x} \right) \cdot (\Delta x') \end{aligned} \right\} \quad (3.18)$$

Again, for equation 3.18 to be valid, $u_a < 0$. The value of α necessary for achieving zero numerical diffusion has been determined by Valentine (1987) to be 0.5 and is the same value selected for this research.

3.3.3 Key Modeling Assumptions

As mentioned earlier, the modeling domain (computing region) for this research is a stratified, two-layered system defined within an x - z coordinate system similar to that depicted in Figure 23. Upon inspection, it can be seen that this 2D arrangement, in profile, is geometrically not unlike that of a three-dimensional (3D) wave tank or flume commonly used to experimentally study hydrodynamic behavior, including internal waves. This idealized system

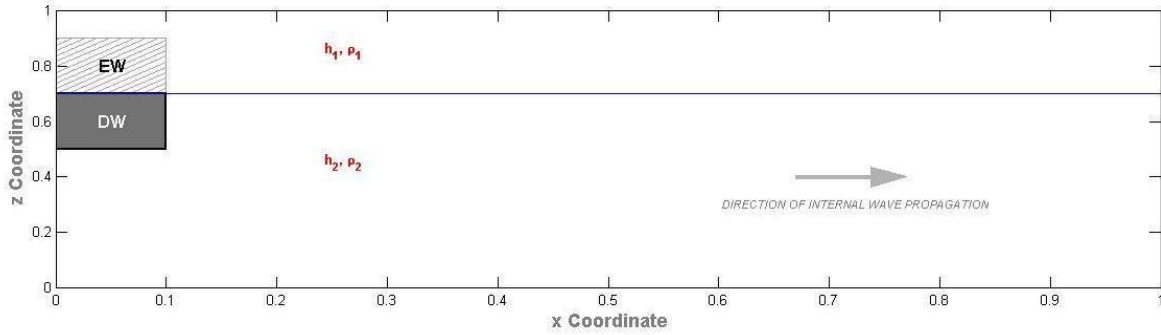


Figure 23. Depiction of computational domain used in this study. This figure shows the pycnocline in relation to the location of the step or potential wells used to artificially generate internal waves for the purposes of the numerical simulation. “**EW**” means elevation well whose density is ρ_2 . “**DW**” means depression well whose density is ρ_1 . This figure is not to scale and the proportions are approximate.

consists of a homogenous fluid of density ρ_1 and depth h_1 overlying another homogenous fluid of density $\rho_2 > \rho_1$ and depth h_2 . The two fluids are assumed to be immiscible. A system configured in this manner is frequently used to evaluate the dynamics of internal wave behavior (Long 1956, Yih 1974). Numerically, it is also possible to simulate an internal wave and observe its behavior as it propagates through this virtual domain. Obstacles with various geometries can also be introduced into the modeling domain that are topographically analogous to what might be found in a marine setting. Such features typically include seamounts, ridges, shelves, and continental slopes. As part of the simulations, the internal wave encounters these computational analogues, resulting in changes to its behavior. That is to say, the solutions to the governing equations will vary owing to the introduction of additional boundary conditions besides those already defining the physical limits of the

computational domain. Reporting on and quantifying what those changes comprise the core of this research.

The physical dimensions of the modeling domain used in this research can be represented by a reference length L horizontally and a reference depth D vertically corresponding, respectively, to the x - z coordinate plane. Consistent with the aforementioned wave tank analogue, L is about an order of magnitude greater than D (e.g., $L \gg D$). To predict the temporal variation of the flow field properties, this modeling domain can be discretized by subdividing the two axes into a finite number of uniformly-spaced nodes. The resulting nodal mesh resembles a rectilinear matrix comprised of individual computational cells where the governing equations are solved. The dimensions of this computational mesh can be defined using the indices m and n , consistent with the number of subdivisions assigned to the respective axes. The local distance between the adjacent nodes (computational cells) on this mesh is Δx and Δz where $\Delta x = \frac{L}{m}$ and $\Delta z = \frac{D}{n}$. The dimensions L and D can also be used to define an aperture coefficient or aspect ratio Q that is useful in normalizing those equations that form the numerical basis for this study.

With the computational domain defined, it is possible to obtain solutions to the governing equations by solving them on a digital computer. By introducing the subscripts i and j (Figure 22), corresponding to number of subdivisions assigned to each axis, it is possible to create a unique identifier (a doublet pair) for each computational cell that can be used to identify both the location and the sequencing for the required calculations, consistent with the specified number of time steps. By convention, the first computational cell occurring in the lower left-hand corner of the mesh is treated as the origin and is assigned the coordinates (1, 1).

Reports of internal waves in nature are commonly associated with the existence of a well-defined pycnocline. By convention, this is the interface defining the respective fluid layer densities; the less-dense, fresh water on top and the denser, more-brackish water layer on the bottom. Hence, $\rho_2 > \rho_1$. The fresh water layer is assigned a reference depth h_1 [L] and a density ρ_1 [M/L³] whereas the brackish water layer below the interface has a reference depth h_2 and a density ρ_2 . Also, $D = h_1 + h_2$. The fluids are incompressible, but can mix through mass transfer processes.

Computationally, generation of an internal wave within this system can be achieved in at least two ways. The first way is to use a “step” or “potential”

well containing fresh water at density ρ_1 that extends into the lower fluid with density ρ_2 . See Figure 23. At time $t = 0$, the barrier between the two fluids is assumed to disappear instantaneously. A second internal wave generation method is to force fluid flow through the computational domain (Dirichlet boundary conditions) in a manner analogous to tidal motion. The ensuing ISW produced by either generating method has a wave celerity defined as:

$$c_0 = \sqrt{\left[\frac{g \cdot (\rho_1 - \rho_2)}{\rho_2} \right] \cdot \left[\frac{(h_1 \cdot h_2)}{(h_1 + h_2)} \right]} \quad (3.19)$$

In conducting this research, certain simplifying assumptions were adopted when performing the numerical simulations:

- The two fluids are initially of densities ρ_1 and ρ_2 , but are miscible and will mix with time; and
- The system boundary for the free surface is rigid, but frictionless (i.e., slip boundary condition applies).

3.3.4 Specification of Time-step

It is important to recognize that governing equations 3.4 through 3.6 are coupled and need to be solved simultaneously. However, in achieving parallel solutions for time-marching computer simulations, there is the potential for non-convergence if the time-step Δt selected is too large.

Numerical stability in finite differencing schemes can be achieved by imposing so-called Courant stability conditions. Courant conditions (Courant, Friedrichs, and Levy 1967) are best explained by considering some flow field property $f(a)$ at some point (x_i, y_i) . As explained above, the finite difference solution being sought at (x_i, y_i) depends on information obtained from contiguous computational cells located at adjoining nodes $i - 1$ and $i + 1$. To achieve numerical stability, it is important that the physical property being transported (vorticity and/or the density anomaly) does not move to the next computational cell at (say $i + 2$) at a rate faster than the magnitude of the time-step Δt specified in the calculation. The time step must be small enough so that the distance the property in question is transported in one time step is less than the physical dimensions of the cell. In the 2D case presented here, a differencing scheme is said to be Courant stable when the following condition is satisfied:

$$Cr > \frac{u_x \cdot \Delta t}{\Delta x} + \frac{u_y \cdot \Delta t}{\Delta y} \quad (3.20)$$

where Cr is the dimensionless Courant number. Courant stability is thus maintained when $Cr \leq 1$. Alternatively, the Courant stability condition can be expressed as follows:

$$\Delta t < \min \left[\frac{\Delta x_i}{u_{i,j}}, \frac{\Delta y_j}{v_{i,j}} \right] \quad (3.21)$$

To minimize the round-off error associated with this numerical scheme and facilitate numerical convergence of the calculations, the dimensionless time increment Δt selected for this study was set as 1.0×10^{-3} .

3.4 Boundary Conditions

To obtain a unique solution to the governing PDEs, additional information about the physical state of the modeling domain is required. It is necessary to complement the system of governing equations previously described in Section 3.2 with a set of boundary conditions. These boundary conditions mathematically define the confines (and hence the geometry) of the modeling domain as well as the values to be applied to the dependent variables of interest (e.g., φ and ξ) at these margins. The initial conditions are simply the values of the dependent variable specified everywhere within the computational domain.

The modeling domain for which the governing equations are to be solved was illustrated earlier in Figure 24. The boundaries that define the limits of this system are all solid interfaces in that there are no mass or volume fluxes across them. These boundaries have received designations **B1** through **B4**. See Figure 24. The boundary conditions for the stream function, density anomaly, and vorticity are given in Table 10. The floor (or “base”) of the modeling domain at **B2**, defined by the plane $z = 0$. A “no-slip” or zero velocity boundary condition

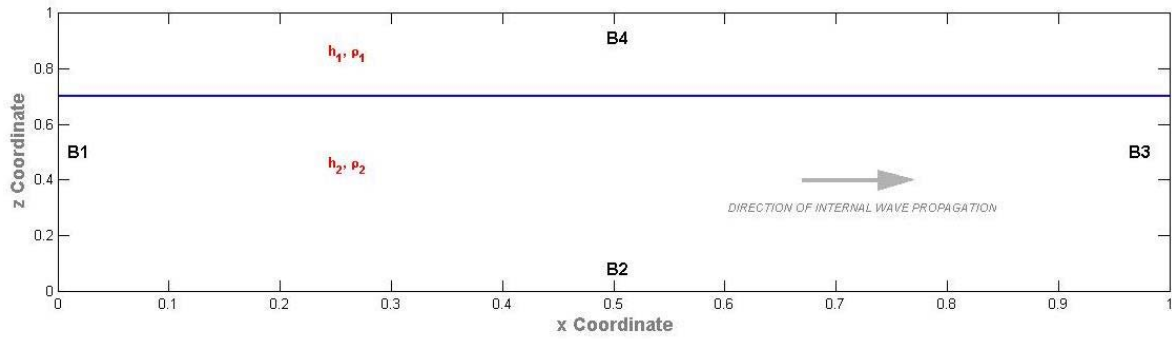


Figure 24. Boundary condition designations corresponding to Table 10. This figure is not to scale and the proportions are approximate.

Table 10. Boundary Conditions for Computational Domain.

BOUNDARY (Figure 24)	x PLANE	z PLANE	STREAM FUNCTION φ	DENSITY γ	VORTICITY ξ
B1	$x = 0$	$0 < z < 1$	$\varphi = 0$	$\frac{\partial \gamma}{\partial x} = 0$	$\xi = \frac{\partial^2 \varphi}{\partial x^2}$
B2	$0 < x < 1$	$z = 0$	$\varphi = 0$	$\frac{\partial \gamma}{\partial z} = 0$	$\xi = Q^2 \cdot \frac{\partial^2 \varphi}{\partial z^2}$
B3	$x = 1$	$0 < z < 1$	$\varphi = 0$	$\frac{\partial \gamma}{\partial x} = 0$	$\xi = \frac{\partial^2 \varphi}{\partial x^2}$
B4	$0 < x < 1$	$z = 1$	$\varphi = 0$	$\frac{\partial \gamma}{\partial z} = 0$	$\xi = 0$

is applied along this plane which ensures that both the horizontal and vertical components of the velocity vector are zero. By convention, the stream function along the base is also defined as zero. However, as suggested by equation 3.4, wall vorticity along a no-slip surface will be generated. Diffusion and the subsequent advection of wall-produced vorticity can alter the fluid flux through the modeling domain (Roach p. 140). No-slip conditions would also apply to any obstacle contiguous to the **B2** boundary surface.

The free surface of the modeling domain at **B4**, is defined by the plane $z = 1$. This particular type of boundary introduces an additional level of numerical complexity to hydrodynamic simulations owing to the need to consider the kinematic effects created by an air-liquid interface. However, the need to consider free surface effects in the simulation can be obviated by imposing a so-called “rigid lid” condition or approximation. First described by Fromm (1963) and Fromm and Harlow (1963), a “free-slip” condition is one in which it is assumed that the free surface boundary coincides with the outermost (most distal) streamline. Vorticity, vertical velocity, and other kinematic effects are understood to become asymptotic along this particular streamline by assuming there are no shear stresses. Consequently, with the normal velocity vector w

assumed to be zero, only the tangential velocity vector u can (numerically) develop as the simulation progresses towards a solution.²⁵

The **B1** (upstream) boundary corresponds to the plane along which the internal wave initially forms and from where it subsequently propagates through the modeling domain.

The downstream (outflow) boundary at the **B3** location corresponds to the computational terminus of the modeling domain. Although most researchers agree that if the length of the modeling domain L is sufficiently long – that is to say as x approaches infinity, the boundary conditions specified at this location would essentially have no influence on the numerical solution being sought. Modeling at the outlet will generally have only a local effect on the flow field. Nevertheless, as this site might be computationally unimportant, researchers have been particularly concerned with how to specify boundary conditions at the **B3** location to ensure that realistic free-flow or open conditions at the modeling terminus are maintained as part of any simulation.²⁶

²⁵ The rigid lid condition refers to the assumption that the solution to the two-layered system can be modeled by also assuming that the system depth D remains constant. Moreover, the rigid lid condition is generally valid so long as the thickness of the upper fluid layer h_l is greater than the maximum wave amplitude a_i for an elevation-type ISW.

²⁶ Roache (1972, 1998a) describes several approaches reported in the literature that have been used to define boundary conditions at this computational terminus without endorsing any particular treatment. One common approach is to equate the computational cells along the

vertical **B3** boundary m to values calculated in the cells in the preceding column — e.g., at the $m-1$ location. Nevertheless, most researchers are unanimous in the view that the outflow boundary conditions need to be specified in such a way as to not either introduce errors or numerical instabilities into the simulation.

CHAPTER IV

NUMERICAL SIMULATIONS

4.1 Internal Solitary Wave Parameters

Researchers have found that an experimental wave-tank system defined by a shallow, two-layered (stratified) fluid is the simplest physical model that can be used to support the formation of an ISW. Interfacical waves can be mechanically-generated and evolve into ISWs as a result of advective and dispersive forces. A computational (numerical) model analogous to this arrangement can allow for a straightforward comparison of the calculations obtained using a digital computer with both analytical and experimental results.

Like other types of waves, the key parameters used to describe an ISW are generally its amplitude a_i and its wavelength L_w . A convenient way to compare experimental data to theoretical predictions is to utilize these relationships. Another important parameter is the total water depth D through which the ISW propagates. In a two-layered system defined by h_1 and h_2 , the displacement parameter $\eta(t)$ represents the ISW profile and is the interfacial

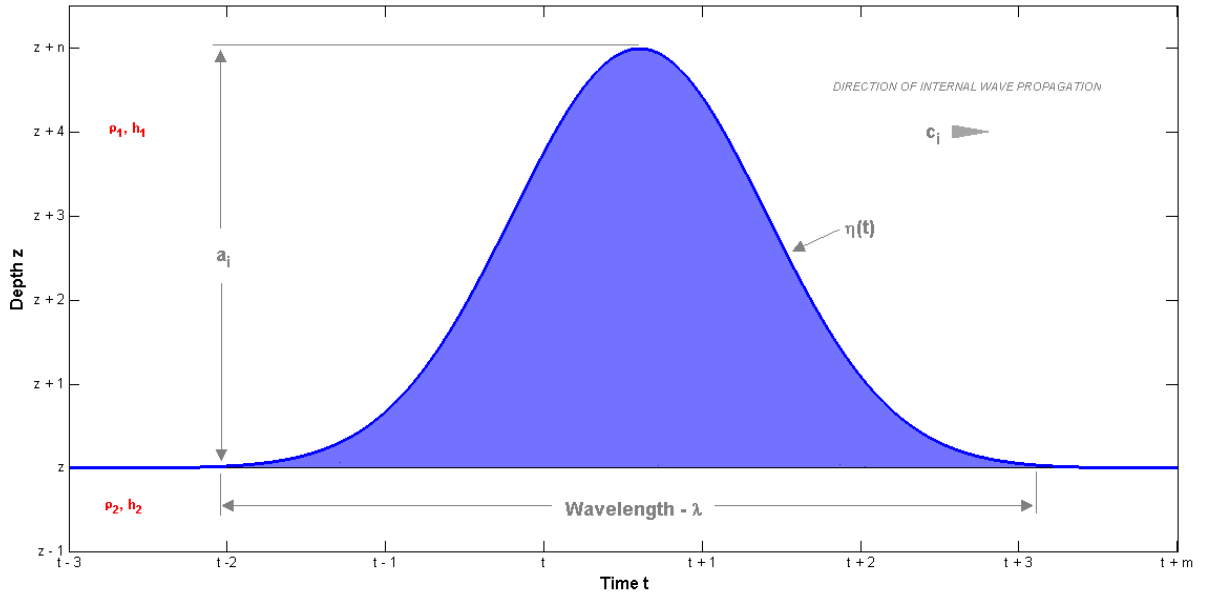


Figure 25. Internal Solitary Wave Features. Elevation-type ISW shown. Parameters depicted in this figure are described elsewhere in this dissertation.

surface along which the two fluid layers meet. In profile, the incipient ISW can be either a wave of depression or a wave of elevation. Internal waves of elevation are typically associated with depth scenarios defined by $h_1 > h_2$; the respective fluid layers have densities ρ_1 and ρ_2 . Internal waves of depression usually form when the depth scenario is such that $h_2 > h_1$. Figure 25 shows some of these properties graphically in relation to the profile for a hypothetical ISW of elevation within a two-layered stratified system.

As discussed below, it is possible to estimate ISW properties using established mathematical theories (e.g., Michallet and Barthélemy 1998). By

applying these theories, ISW properties can be measured and calculated at fixed locations in a pre-defined computational domain such as that depicted in Figure 17 by post-processing the data obtained from this research with MATLAB-based worksheets.

4.1.1 Wave Speeds, c_o and C

The ideal ISW speed or celerity c_o can be calculated for any particle located along the interfacial density surface based on the following relationship, assuming a small infinitesimal difference in density:

$$c_o = \sqrt{\left[\frac{g \cdot (\rho_2 - \rho_1)}{\rho_2} \right] \cdot \left[\frac{(h_2 \cdot h_1)}{h_2 + h_1} \right]} \quad (4.1)$$

An (actual) ISW phase velocity c that results from the numerical simulation can also be calculated by selecting a fixed particle location along the density interface (pycnocline) and measuring the time differential Δt or $t_2 - t_1$ it takes for that particle to travel some defined distance Δx or $x_2 - x_1$. In this manner, the ISW phase velocity can be expressed as $c = \frac{\Delta x}{\Delta t}$.

4.1.2 Wave Amplitude, a_i

As suggested by the pycnocline geometry shown in Figure 25, the most distinguishing feature of an ISW is its form – typically a single sinusoidal wave

either of elevation or depression. As is the case with other types of water waves, the ISW amplitude a_i corresponds to the maximum vertical displacement of a particle measured at the wave crest or, alternatively, the wave trough from its initial undisturbed (horizontal) position to some new position $\eta(t)$ along the pycnocline surface (Figure 25). As discussed in the paragraphs that follow, the wave amplitude is a key property that can be used to derive other important ISW parameters.

4.1.3 Wavelength, L_w

Unlike gravity or surface waves, that have finite wavelengths, the wavelength of an ISW is theoretically infinite (asymptotic). As a practical matter, though, the wavelength of the ISW can be defined as the horizontal distance between two corresponding yet opposing locations along its profile, as represented by the pycnocline (Figure 25). A characteristic wavelength L_w can thus be approximated (Koop and Butler 1981) by either of the following equations:

$$L_w = \frac{1}{a} \int_{-\infty}^{\infty} \eta(x) dx \quad (4.2)$$

$$L_w \approx \frac{c}{a} \int_{t_0}^{t_1} \eta(t) dt \quad (4.3)$$

where $\eta(t)$ is the interface displacement between the respective fluid layers, the horizontal coordinate x corresponding to $\eta(t)$, and t_0 and t_1 defining an

incrementally small time increment such that $\eta(t_0) \approx \eta(t_1) \approx 0$. This relationship has also been referred to as the “integral length scale.”

4.1.4 Wave Energy, E

Wave energy is generally proportional to the square of the wave amplitude. The total energy E_T for an ISW is the sum of its potential energy and kinetic energy. Once it has reached steady-state, Bogucki and Garrett (1993) have estimated the total energy contained within an ISW as:

$$E_T = C g \Delta \rho \int_{t_0}^{t_1} \eta^2(t) dt \quad (4.4)$$

where $\Delta \rho = \rho_2 - \rho_1$ and t_0 and t_1 are time estimates such that $\eta(t_0) \approx \eta(t_1) \approx 0$.

For the purposes of the numerical simulations, equation 4.4 can be used to estimate the energy of the ISW after it has encountered an obstacle. It is possible to contrast this estimate with a potential energy value for the system before the simulation is initiated. The potential energy for the system at t_0 can be expressed as a function of the length of the potential well, as suggested by Saffarinia (1991):

$$E_P = \left(\frac{\Delta \rho}{2} \right) \left(\frac{L_{PW} \cdot \eta_0^2}{Q \cdot D^3} \right) \quad (4.5)$$

4.2 Benchmark Trials

As mentioned earlier, researchers have traditionally relied on 3D wave tanks (or flumes) to study ISWs. The tanks have been fitted with cameras or instrumented with electronic probes to allow the wave's properties to be measured as it propagates through the experimental apparatus. Obstacles of different types have also been introduced along the floor of these setups to allow researchers to observe under how a propagating wave interacts with these obstructions under controlled conditions. Some earlier wave tank studies are listed in Table 11.

The experimental configuration just described can be achieved “virtually” using computer programs that employ numerical methods solving hydrodynamic equations. As is the case with an experimental wave tank, it is possible to introduce different topographic features into the computational domain by specifying additional boundary conditions that correspond to the obstruction's geometry. Through the course of the computer simulation, a “mathematical response” is evoked resulting in a numerical solution different from that obtained when the obstacle is absent. In this manner, it is possible to take a snap-shot of the ISW at any time during the numerical simulation and in doing so, record its properties as they evolve following the wave-obstacle interaction.

Table 11. Summary of Experimental Investigations of ISW Phenomena using Wave Tanks.

	BOUSSINESQ PARAMETER	$\frac{h_1}{h_2}$	c [cm/sec]	$\frac{a_i}{D}$
Kao, Pan, and Renouard (1985)	0.01	$\frac{0.95}{33} - \frac{7.6}{27.9}$	0.85	0.01 — 0.2
	0.017	$\frac{11}{22.5}$	16	
Helfrich and Melville (1986)	0.033	$\frac{11}{24}$	15.3	0.056 — 0.1
	0.053	$\frac{11}{22.5}$	15.9	
Wallace and Wilkinson (1998)	0.013 — 0.051	$\frac{37}{13}$	11 — 22	0.015 — 0.14
Martin, Walker, and Easson (1998)	0.025	$\frac{7.5}{40} - \frac{10}{20}$	9.71 — 12.61	0.5 — 0.14
Michallet and Barthélemy (1997, 1998)	0.025	$\frac{0.54}{12.94}$	13.52 — 23.78	0.002 — 0.22
		$\frac{7.27}{2.97}$		
		$\frac{8.29}{1.95}$		
Ariyaratnam (1998) Hsu and Ariyaratnam (1998)	0.028	$\frac{3}{35} - \frac{20}{20}$	10.85 — 15.5	0.06 — 0.25
Michallet and Ivey (1999)	0.012 — 0.044	$\frac{3}{35} - \frac{20}{20}$	5.6 — 11	0.1 — 0.2
Kuo (2005) Cheng (2006)	0.025	$\frac{10}{40} - \frac{40}{10}$		0.054 — 0.432
Chen (2006)	0.024 — 0.03	$\frac{10}{30} - \frac{35}{5}$	9.23 — 14.78	0.04 — 0.25

4.2.1 Computational Domain

A key CFD issue is whether the numerical simulation produces results that match physical reality. By their very nature, mathematical models are abstractions of physical systems based on numerous assumptions and simplifications. The standard computational method for achieving this “reality” determination is to perform multiple computational trials (or realizations) based on a progressively increasing grid density. That is to say, the computer simulations are repeated at using a finer mesh until it is found that there is no significant change in a particular outcome as a result of increased computational resolution. Stated differently, the simulation results have been found to converge to the same results. The results can then be compared to actual field records or experimental data collected by other researchers, to establish the accuracy (and predictability) of the numerical simulation tool.

To establish the numerical accuracy of the computer simulations that form the foundation of this research, it was first necessary to conduct a series of production trials (or benchmark simulations) of the computer code and compare those results with experimental data collected by other researchers. Experimental data were available from earlier published studies that relied on mechanically-generated ISWs. The wave tanks were usually configured to be either 40 cm- or 50 cm-deep and were up to 12 m long. A two-fluid system was

generally created by using two liquids with different specific gravities such that $\rho_2 > \rho_1$. A solitary interfacial wave was induced either by using a vertical sluice gate that would mechanically-produce step-like conditions that would later evolve downstream into an ISW or by tilting the entire experimental apparatus at one end until the desired ISW evolved. Previously, Kao, Pan, and Renouard (1985) provided some practical advice on how to mechanically-generate ISWs in an experimental setting so as to minimize the dispersive wave train associated with an artificially-generated internal wave that typically occurs as an artifact of the generation process.²⁷

For the purposes of this research, a virtual “step or potential well” was used as a surrogate for the sluice gate used by some researchers to artificially generate an ISW. A review of past research associated with wave tank experiments (Chen et al. 2007) has revealed that the gravity collapse of a step well produces a wake that transitions into an ISW of elevation — a potential well

²⁷ When mechanically generating internal waves in an experimental apparatus, Kao, Pan, and Renouard (1985) derived an equation that proportioned the dimensions of the step well depth η_0 to its length L_{PW} . Their intent was to minimize the magnitude of the dispersive wave train typically found to be associated with mechanically-generated internal waves. As a rule of thumb, suggest the following algorithm:

$$L_{PW} \simeq 2 \left[\frac{1}{\eta_0} \cdot \frac{4}{3} \left(\frac{(h_1 h_2)^2}{|h_1 - h_2|} \right) \right]^{\frac{1}{2}}$$

of depression yields an ISW of depression whereas a potential well of elevation yields an ISW of the same polarity.

Two computational scenarios (domains) were selected for use in the comparison with experimental data – one series of trials corresponding to a 40 cm-deep configuration (in the z direction) and the other configuration corresponding to a dimensional 50 cm-deep configuration (in the x direction). The length of the computational domain was 500 cm as this distance was considered to be sufficient to allow for the formation and measurement of an ISW that had essentially reached steady-state. Various combinations of h_1 to h_2 were selected to evaluate how different stratification scenarios influence ISW properties. It was possible to calculate certain system-specific input parameters for the simulations (e.g., Re , Fn) based on fixed values of h_1 , h_2 , ρ_1 , and ρ_2 . These parameters were calculated using a Mathcad®-based engineering spreadsheet (Parametric Technology Corporation 2007). An example spreadsheet used to make these calculations and derive the specific parameter values is shown in Appendix A.

To ensure the numerical simulation trials were converging with reported experimental data, a variable finite-difference mesh (grid) was imposed over the

computational domain encompassing five different grid densities. These grid densities were multiples of 1, 2, 3, 4, and 5.

The basic numerical calculations were performed using a FORTRAN-95-based computer programs²⁸ compiled using a Lahey compiler (Lahey Fortran 90 1997). Initially, the compiled programs were executed on a Hewlett-Packard (HP) Pavilion dv8000 computer. Later, a Dell Inspiron 1545 computer with expanded computing capability (3.46 GB of RAM vs. 2GB of RAM for the HP) was used. Computational results from the FORTRAN programs were processed with original programs written using the student version of MATLAB programming software.

4.2.2 Key System Parameters and Initial Conditions

Table 12 summarizes the initial conditions and system parameters used for both the benchmark trials and simulations involving topographic obstacles. Inspection of this table shows that eight different stratification scenarios (i.e., dimensional depth ratios) were selected at simulated depths of 40 cm and 50 cm. Four potential well depths η_0 – dimensional depths of 5 cm, 10 cm, 15 cm, and 20 cm – were selected for producing a wake-generated ISW in the various

²⁸ The computer program used was originally developed by H.-P. Pao, T.W. Kao, K. Saffarinia, and H. Xiao of the Catholic University of America, and was subsequently modified by this investigator for the purposes of this research.

Table 12. System Parameters Selected for the Numerical Simulations.

h_1 [cm]	h_2 [cm]	ISW TYPE	Re	Fn	Sc	C_0 [cm/sec]
40 cm Simulated Depth						
35	5	Elevation	4.454	0.56	833	11.2
30	10	Elevation	3.857	0.06	833	11.1
10	30	Depression	3.857	0.06	833	11.1
50 cm Simulated Depth						
10	40	Depression	7.528	0.068	833	15.1
15	35	Depression	8.624	0.078	833	17.3
20	30	Depression	9.22	0.084	833	18.5
40	10	Elevation	7.528	0.068	833	15.1
30	20	Elevation	9.22	0.084	833	18.5

depth configurations. Inspection of this Table 12 indicates that eight different stratification scenarios (i.e., dimensional depth ratios) were selected corresponding to simulated wave tank depths of 40 cm and 50 cm. When different step-well depths were combined with different stratification scenarios, the result yielded about 32 permutations available for the simulation trials. Each simulation or “production run” was performed for about 8000 time steps, and the size of each non-dimensional time step Δt was 0.001 to ensure that the Courant condition was maintained – that is to say the Courant number was

small compared to unity (based on particle velocities and the local mesh spacing). To achieve the differences in density necessary for generating an ISW, the density of the upper fluid layer ρ_1 was set to 999 kg/m³ (corresponding to fresh water) whereas the density of the lower fluid layer ρ_2 was assigned a value of 1030 kg/m³ (corresponding to brine). These differences yield a value for $\Delta\rho$ of 31 kg/m³. The equivalent dimensionless Boussinesq parameter γ is -0.03 and corresponds to the pycnocline interface defined by $\eta(t)$. When $\eta(t)$ either achieves either maxima or minima, the wave amplitude a_i corresponds, respectively, to either an ISW of elevation or depression.

4.2.3 Results of Benchmark Simulations

Results from the 32 benchmark simulations associated with this research are discussed below. Following completion of the production trials, ISW amplitudes, wavelengths, and energies were calculated by post-processing the data with MATLAB-based programs in the form of worksheet. The MATLAB-worksheet calculated these measurable ISW properties at specific locations and time-steps at four fixed locations in the computational domain. An example worksheet is shown in Figure 26. The worksheet can estimate the parameters of interest by first evaluating the density variation relative to the dimensionless Boussinesq parameter γ at a particular location in the computational domain. The maximum vertical distance the parameter remains unchanged relative to

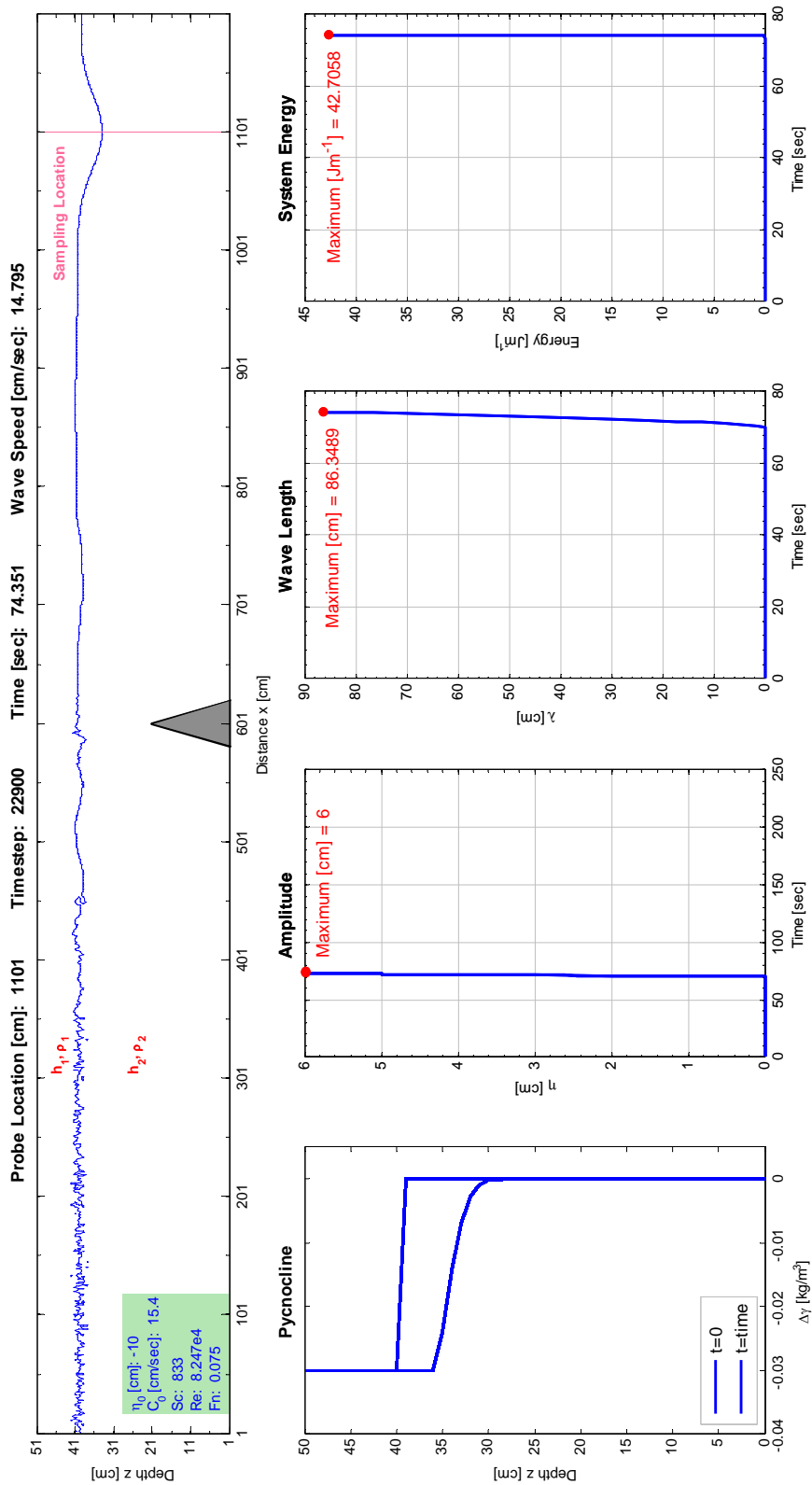


Figure 26. Example MATLAB worksheet used to calculate measurable ISW properties. Top figure illustrates a depression-type ISW measured at location 1101 following a simulated encounter with an isolated topographic obstacle. Computational arrangement is for a simulated dimensional depth ratio of 10 cm/40 cm. Other system parameters for the simulation are listed in the shaded box. Top figure is not to scale and the proportions are approximate

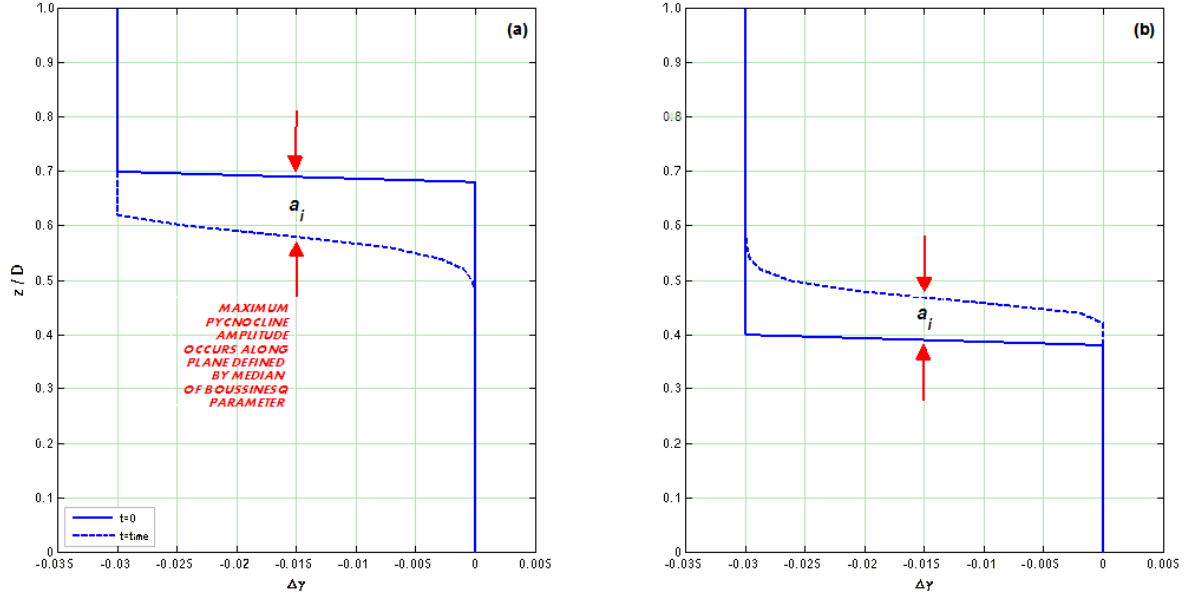


Figure 27. Density-height curve showing example of pycnocline profiles. The solid line is the undisturbed pycnocline profile at time zero before the start of the numerical simulation. The dashed line shows how the profile of the pycnocline has evolved through the course of the simulation at some subsequent time t . A dimensionless Boussinesq parameter of -0.03 was used in the simulation. Arrows indicate the magnitude of the wave amplitude a_i . (a) Depression-type ISW. (b) Elevation-type ISW.

quiescent $h_1 - h_2$ fluid interface; this vertical distance corresponds to the ISW amplitude a_i . The parameter is later used subsequently in equations 4.3 and 4.4 to calculate the wavelengths and energies. Figure 27 shows the vertical distribution of the density profile along the pycnocline. The figure shows the undisturbed pycnocline profile (solid line) at time zero, when the system is at rest. The figure also shows how the pycnocline profile changes through the course of the computer simulation (dashed line). The vertical displacement in the profile corresponds to the ISW amplitude a_i . As indicated by this figure,

depression-type ISWs (Figure 27a) tend to lower the elevation of the pycnocline whereas elevation-type ISWs (Figure 27b) tend to raise it. Lamb (1932) and Defant (1961b) suggest that the amplitude of an internal wave is a maximum at the depth corresponding to the maximum vertical density gradient.

Following completion of the benchmark simulations, the results were then compared to experimental data collected by Chen (2006). That researcher performed a series of wave tank experiments evaluating ISW properties following their interaction with different types of obstacles. In connection with that research, he performed approximately 180 wave tank trials. Chen relied on a two-layered fluid system consisting of an upper fresh-water layer and a lower brine layer. The experimental apparatus was instrumented with a series of ultrasonic probes that electronically measured the density variations in the system as the mechanically-generated wave traversed the horizontal length of the tank.²⁹ Before analyzing the results, though, Chen (2006) pre-processed the raw data using an unspecified Fourier transformation method to, in effect, “de-noise” them. The impact, if any, of the Fourier transformation on the data (measurements) was never assessed by this particular investigator. The Chen

²⁹ The trials included obstacles representing a uniform slope, a single triangular barrier, two triangular barriers, a single semicircular barrier, and two semicircular barriers.

(2006) data set nevertheless is considered to be a reasonable benchmark against which this research can be compared.

4.2.3.1 General Observations

As expected, a depressed step well yields an ISW of depression (Figure 28). Conversely, an elevated step well yields a similar-type ISW (Figure 29). At the beginning of the computer simulations, an ISW would evolve and form from a step well as the governing equations were solved at each time-step in the calculation. Both sets of figures show an ISW of mode-1 followed by a lesser ISW of an opposite polarity as well as a wave train representing transient dispersion.

For this phase of the research, only information on a well-developed ISW was sought. Hence, this series of trials did not include evaluating the interaction of the propagating wave with an obstacle. The only criterion applied at this point in the research was that duration of the simulation needed to be of a sufficient number of time-steps to allow the ISW to achieve what might be considered a steady-state form (profile) so that its properties might be measured and its interaction with a particular obstacle quantitatively evaluated. In this regard, Michallet (1988) reported that there is a need for a mechanically-generated ISW to travel some distance from the generation point down-stream until the pycnocline-defined wave has reached a steady state form. As indicated by Figures 28 and 29, several hundred time-steps in the computer simulations

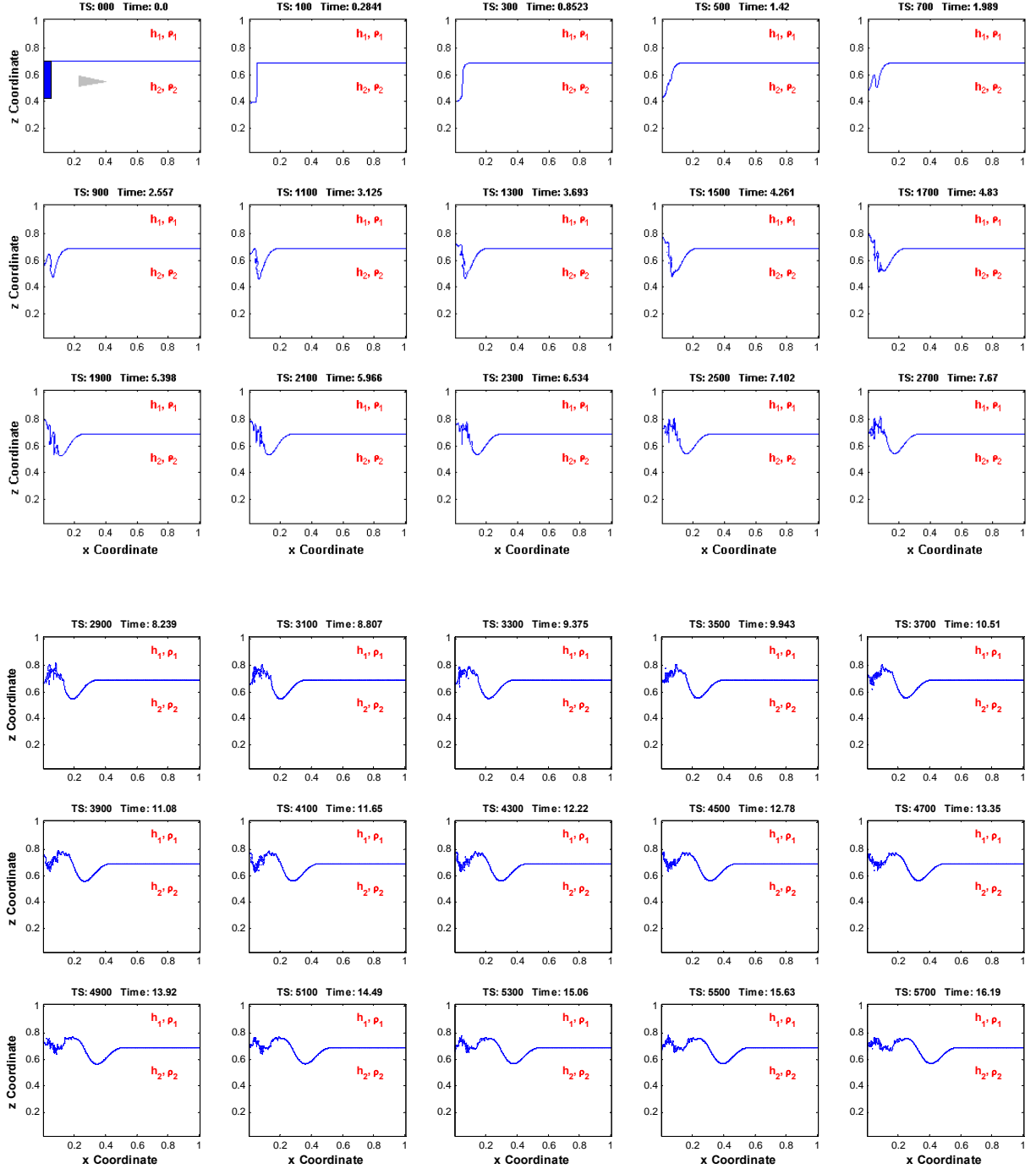


Figure 28a. Non-dimensional numerical simulation showing the evolution of a depression-type ISW. Shaded area highlights step well used to artificially generate an ISW. Arrow indicates the direction of wave propagation at the start of the numerical simulation.

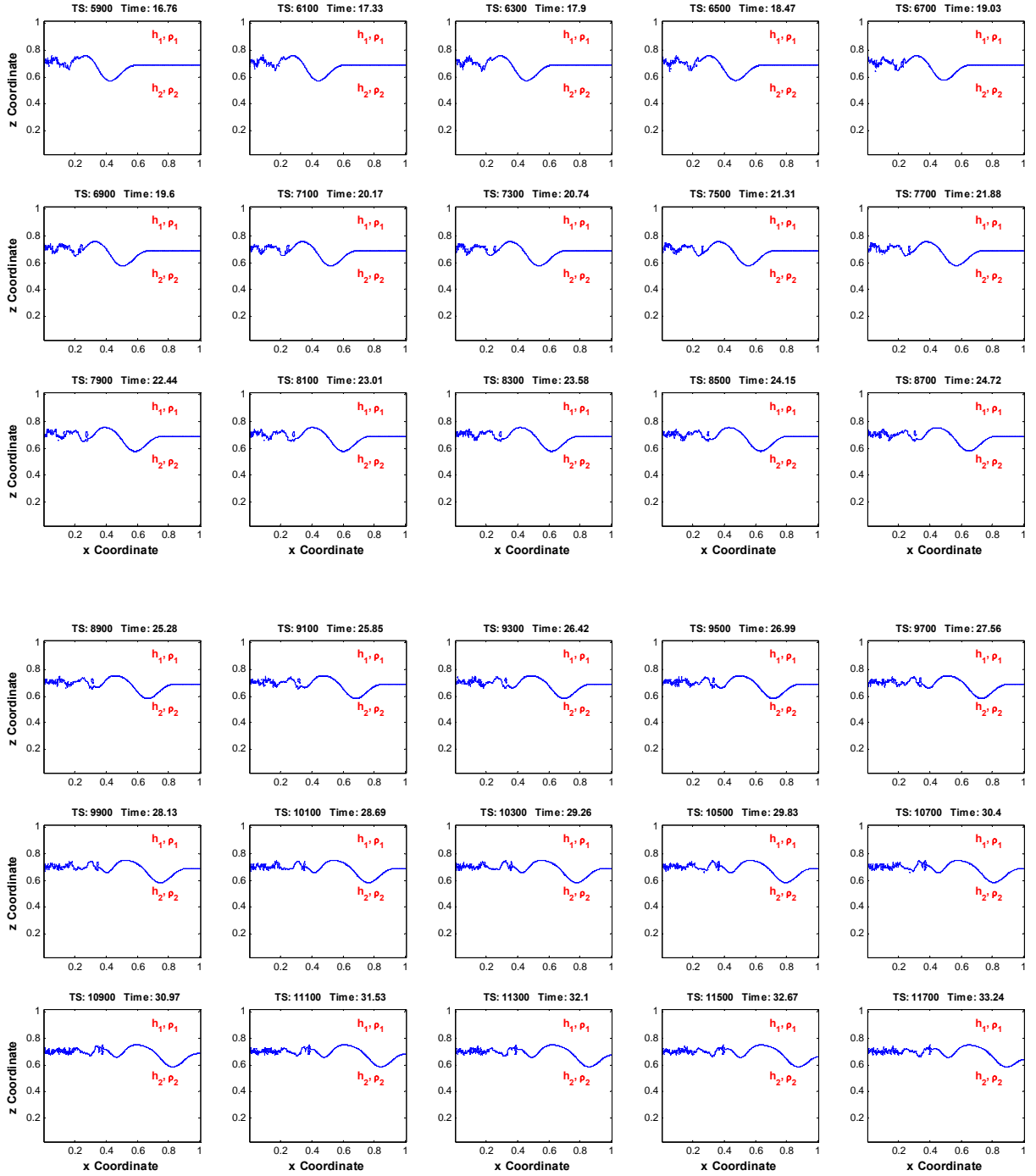


Figure 28b. Continued.

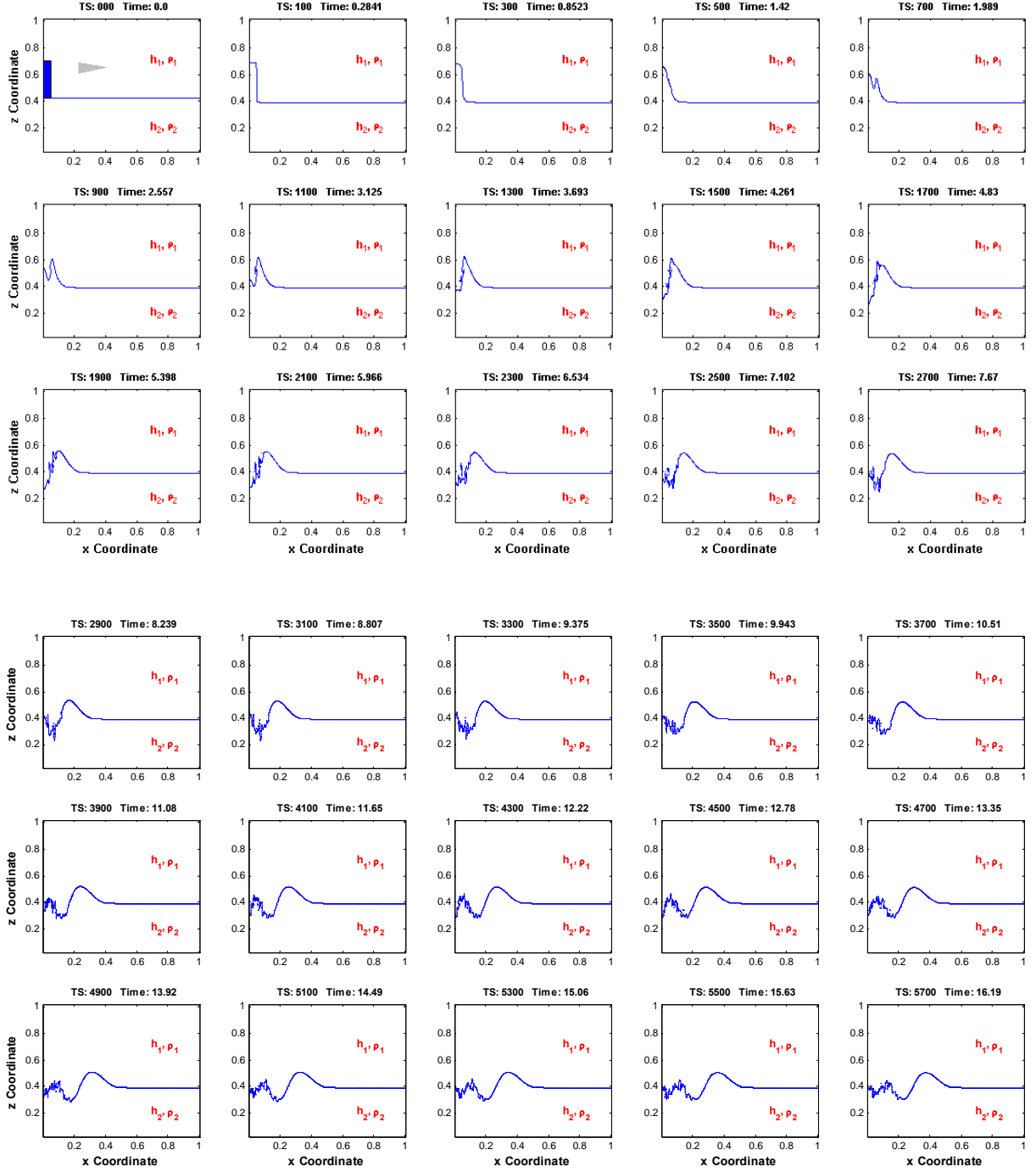


Figure 29a. Non-dimensional numerical simulation showing the evolution of an elevation-type ISW. Shaded area highlights step well used to artificially generate an ISW. Arrow indicates the direction of wave propagation at the start of the numerical simulation.

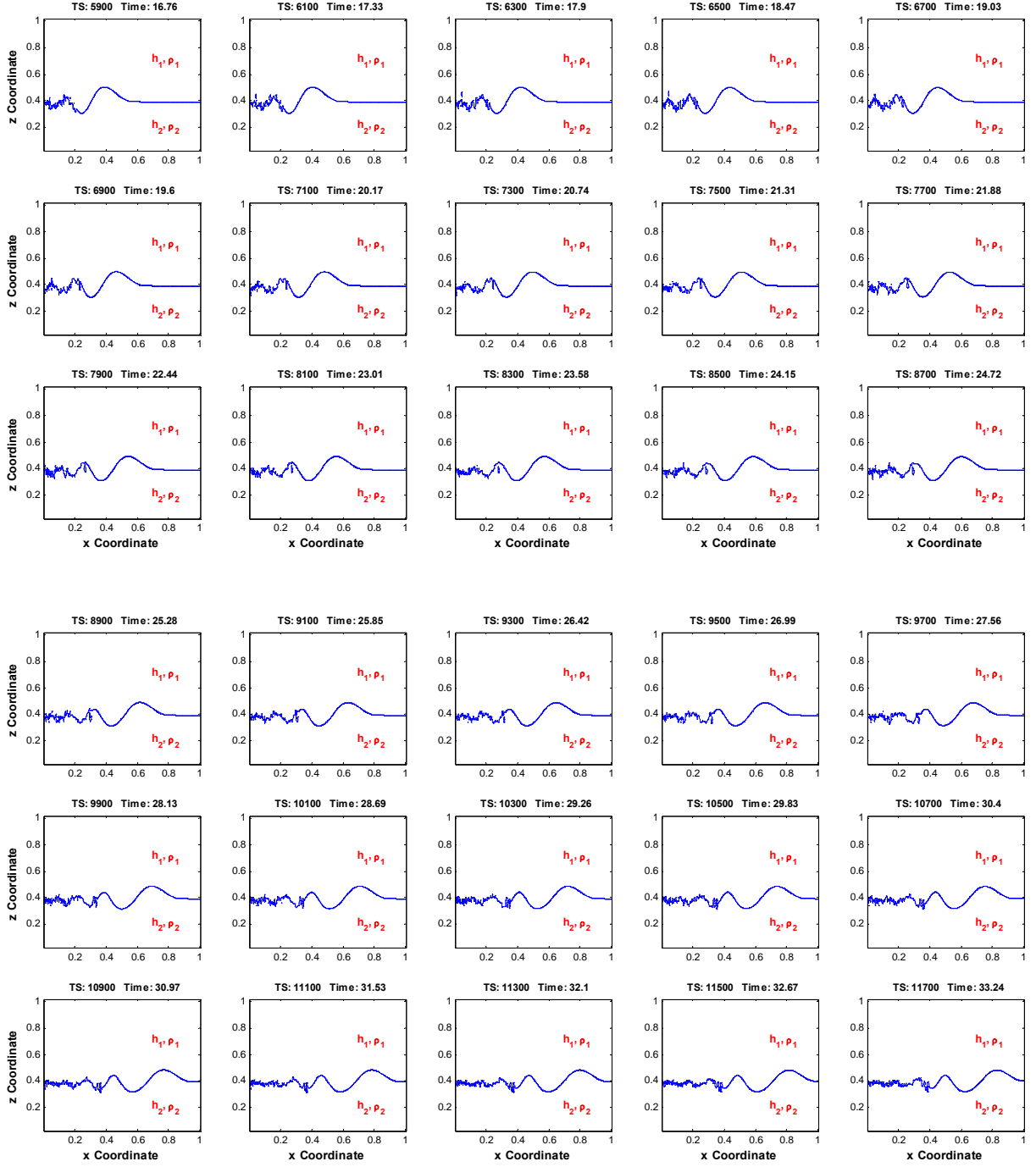


Figure 29b. Continued.

were usually required before an internal wave demonstrating a well-defined (steady-state) form was produced. However, slightly more time-steps were needed for an elevation-type wave to reach steady-state than for a depression-type wave. These differences can be attributed to slight variations in the respective Reynolds numbers for the two systems — $8.767 \times 10^{-4} \big|_{DEPRESSION}$ vs. $9.372 \times 10^{-4} \big|_{ELEVATION}$ — suggesting that the formation of an ISW of elevation is dominated by turbulent (restoring) forces. For the purposes of the benchmark trials, the number of time steps (i.e., the duration of the simulation) needed to achieve steady-state was thus determined by trial and error.

4.2.3.2 Detailed Observations

Four aspects of the numerical simulation trials associated with the benchmark simulations thus far deserve some limited discussion.

Internal Solitary Wave Development. The first detailed observation concerns how the ISW evolves in a wave tank from a step well. This issue was first explored by Kao, Pan, and Renouard (1985) who were able to empirically relate the number of solitons N_{ISW} experimentally-generated to the potential well depth η_0 as:

$$N_{ISW} \leq \frac{L_{PW}}{\pi} \sqrt{\frac{3}{2} \left| \frac{h_1 - h_2}{h_1^2 h_2^2} \right|} \eta_0 + 1 \quad (4.6)$$

Chen et al. (2007) later used video imagery to document the event sequence leading to ISW formation by varying the magnitude of η_0 . As part of their investigations, Kao, Pan, and Renouard attributed the mechanical formation of an ISW in an experimental apparatus to gravity “wave collapse.” Upon further review, Chen et al. (2007) found that overturning motions, similar to K-H vortices, producing internal bores (also known as “rollers” or “gyres”) during the transient phase of wave formation, were responsible for the mechanically-generated ISWs once the sluice gate was removed. Chen et al. also found that clockwise overturning of the pycnocline produces ISWs of the depression-type whereas a counter-clockwise overturning produces ISWs of the elevation type. After a transient phase of wave formation, the primary ISW develops into a leading wave (front) followed by a dispersive wave train. The sequence of events leading to the overturning motion of the potential well and the subsequent formation of both a depression-type and elevation-type ISW as illustrated, respectively, in Figures 30 and 31. These simulations comport with the photographic observations reported by Chen et al. (2007).

Kelvin–Helmholtz Features. The second detailed observation is that inspection of Figures 30 and 31, at the early (transient) stages in the simulations (specifically time steps 500 to 900), reveal what appears to be the formation of K–H–like features. These features occur along the pycnocline, in the vicinity of

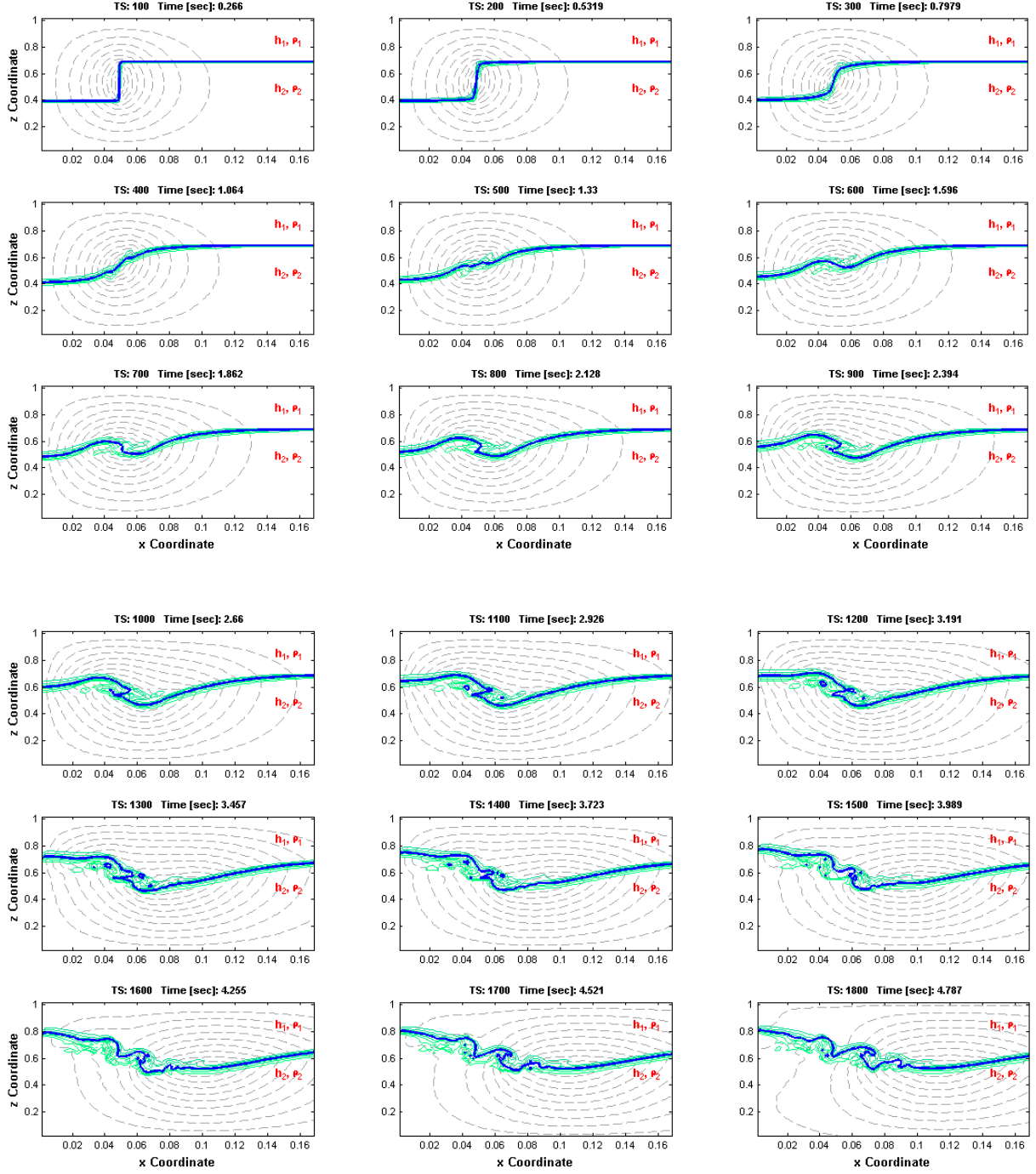


Figure 30. Sequence of events leading to the evolution of a depression-type ISW. Multiple isopycnals are shown with the pycnocline highlighted.

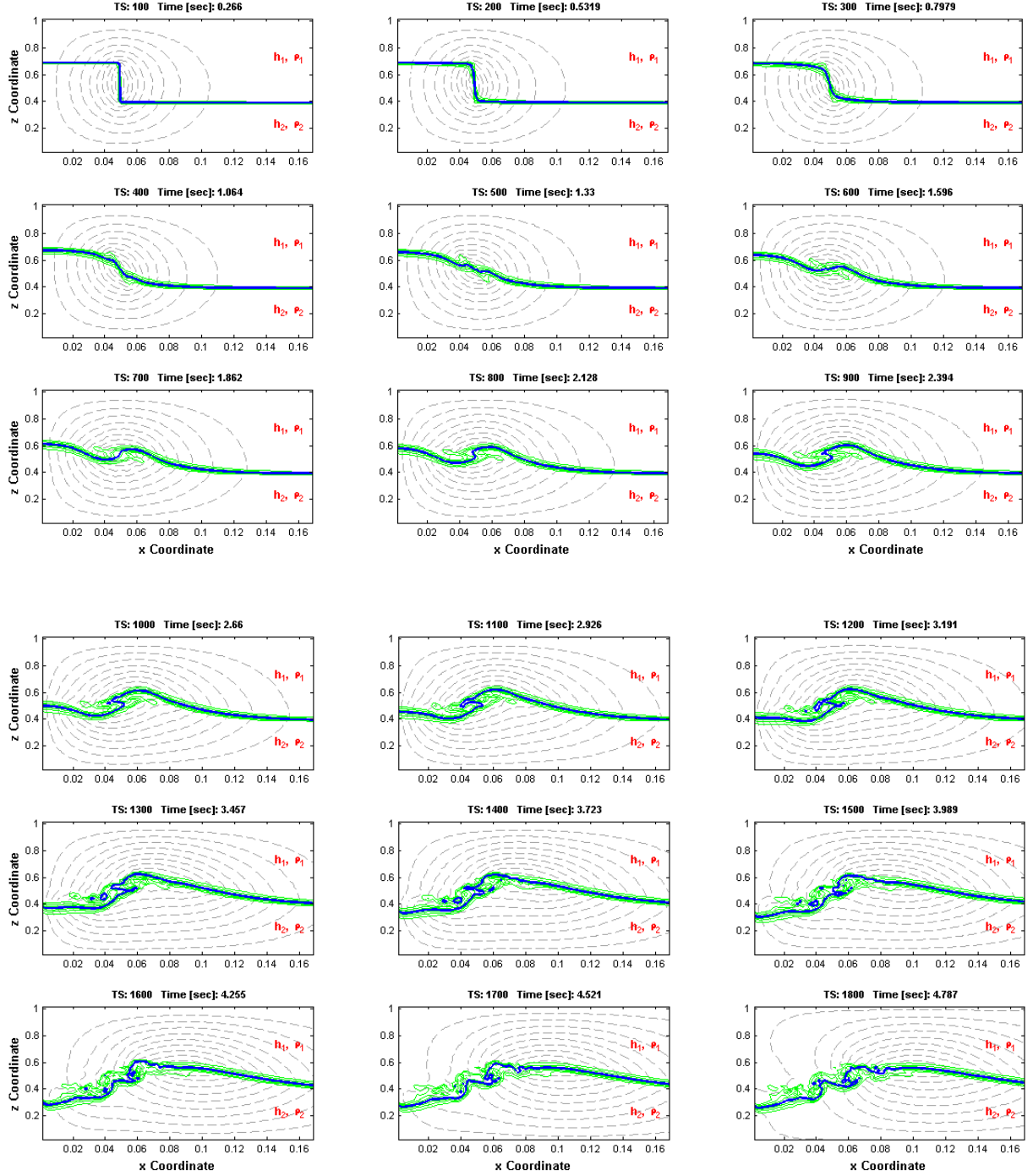


Figure 31. Sequence of events leading to the evolution of an elevation-type ISW. Multiple isopycnals are shown with the pycnocline highlighted in blue. Streamlines are shown by dashed lines. Non-dimensional numerical simulation shows clockwise overturning of the step well.

the step well. When the resolution of the simulation is increased with additional isopycnals along the pycnocline (Figure 32), the K-H-like features become more pronounced and appear analogous to those features described in the literature by researchers and illustrated earlier in Figures 14 and 15.

Sinusoidal Profile. The third detailed observation is that once the ISW achieves a steady-state profile, the sinusoidal shape characteristic of such waves becomes evident. Figures 33 and 34 correspond, respectively, to one time step in each of the simulations depicted in earlier Figures 30 and 31. Figures 33 and 34 depict the pycnocline, streamlines (or the trajectory of the velocity field), and flow-field orientation for a mode-1 type ISW of elevation and depression, respectively. The features captured in these simulations are consistent with the ISW features reported in the literature. The pycnocline (or density interface) is shown by the solid blue line. Streamlines are shown by dashed lines. Non-dimensional numerical simulation shows clockwise over-turning step well first hypothesized by Defant (1961a) who cited Bjerknes and others (1933). See earlier Figure 15. Careful inspection of the figures also indicates that the directions of the velocity vectors in the simulation above and below the pycnocline are opposite to each other, consistent with reports by LaFond (1961).

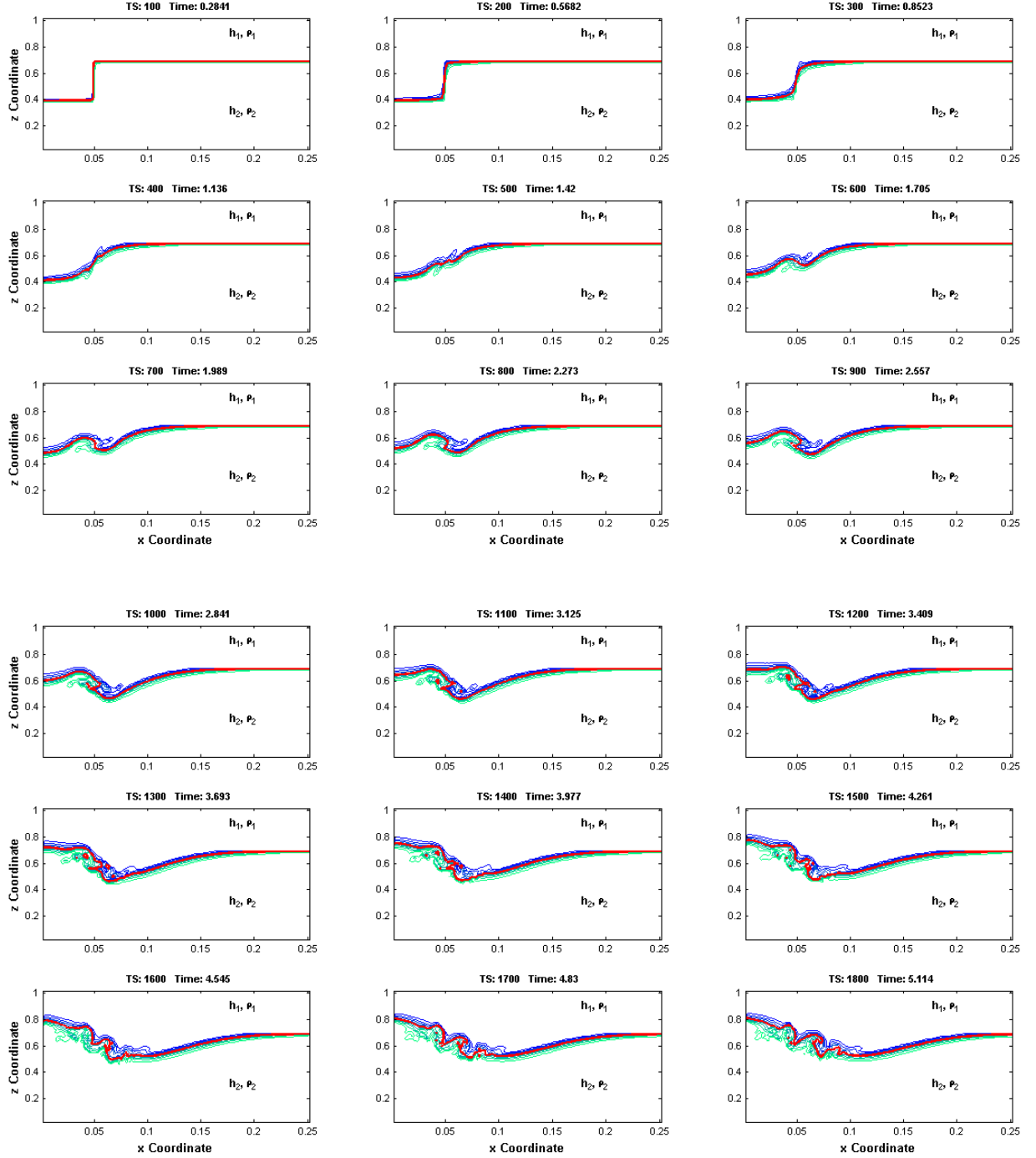


Figure 32. Example of K-H-like features associated with the formation of an ISW during a non-dimensional numerical simulation. The pycnocline is highlighted in red.

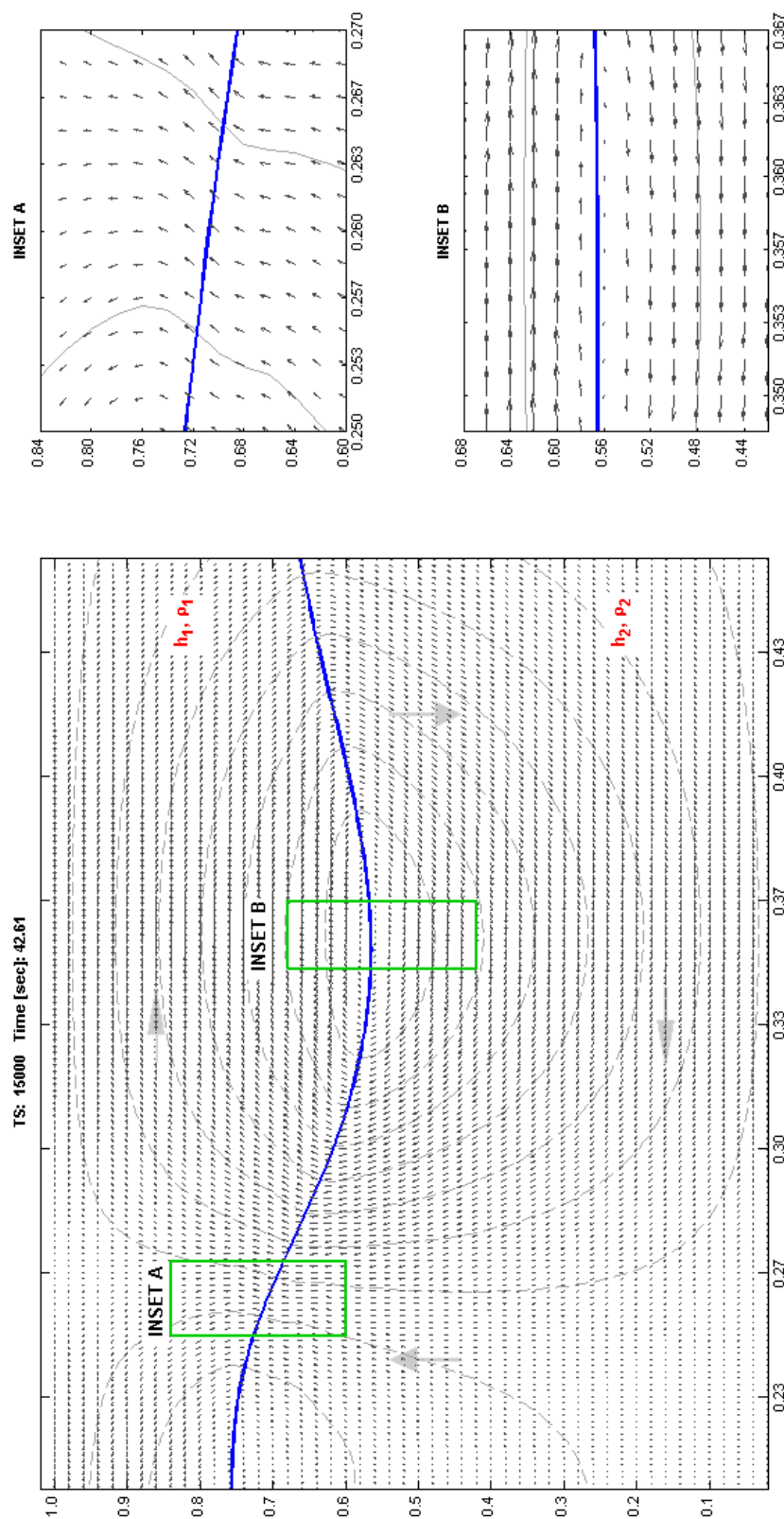


Figure 33. Non-dimensional simulation showing streamlines, internal flow field direction, and pycnocline for a mode-1 depression-type ISW. Example corresponds to one time step from simulation depicted in Figure 28. Arrows indicate clockwise flow pattern. Insets **A** and **B** show details of clockwise flow field direction.

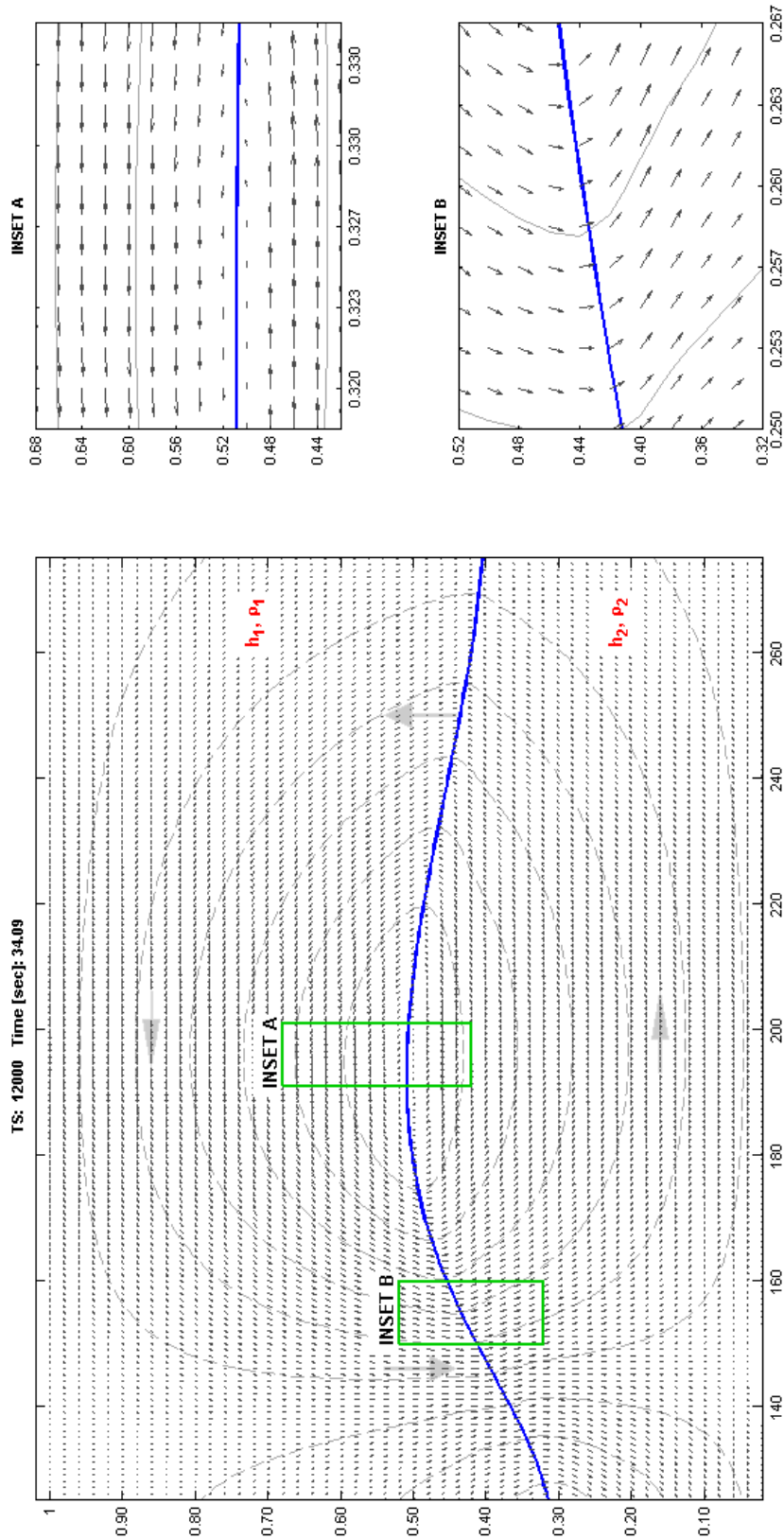


Figure 34. Non-dimensional simulation showing streamlines, internal flow field direction, and pycnocline for a mode-1 elevation-type ISW. Example corresponds to one time step from simulation depicted in Figure 29. Arrows indicate counter-clockwise flow pattern. Insets **A** and **B** show details of counter-clockwise flow field direction.

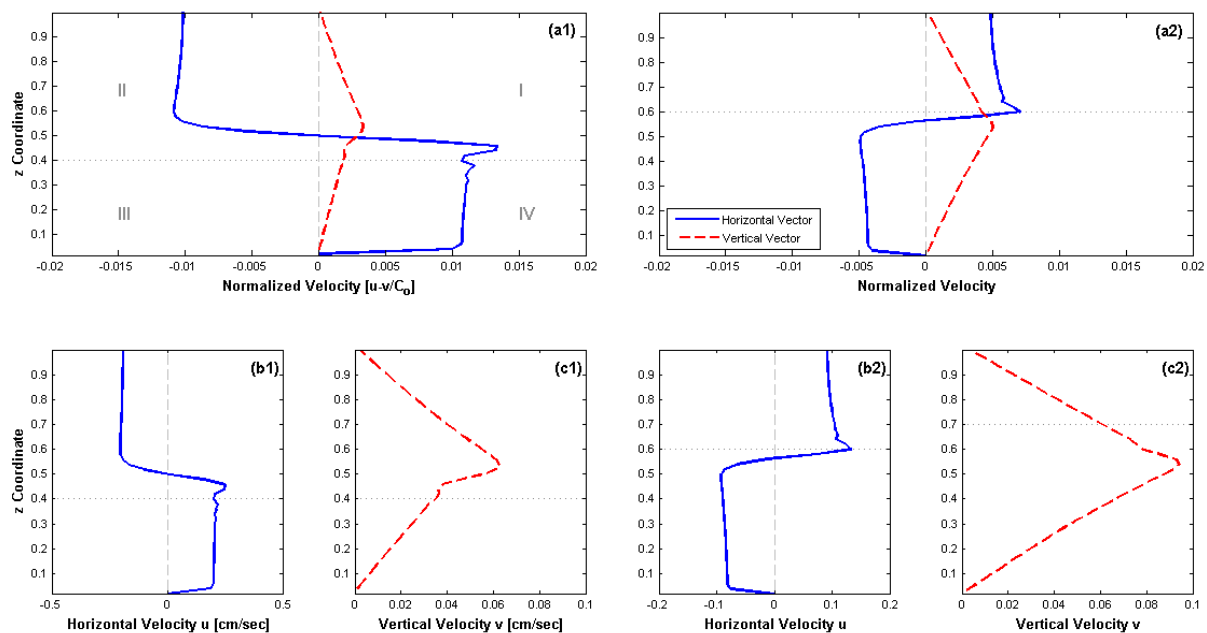


Figure 35. Examples of normalized velocity vectors for an ISW. (a1) Depression-type ISW. Above the pycnocline (dotted line), the profile illustrates a flow pattern consistent with a clockwise flow regime as the velocity vectors occupy those quadrants designated **I** and **III**. The simulation depicts fluid flow from the right-to-the-left above the pycnocline. Below the pycnocline, the flow is left-to-right. See earlier Figure 30. (a2) Elevation-type ISW. Above the pycnocline, the profile illustrates a flow pattern consistent with a counter-clockwise flow regime as the velocity vectors occupy those quadrants designated **II** and **IV**. The simulation depicts fluid flow from the left-to-the-right above the pycnocline. Below the pycnocline, the flow is flow from the right-to-left. Also see earlier Figure 31. Exhibits “b” and “c” display, respectively, the horizontal and vertical components of the normalized velocity vectors.

Velocity Profiles. The last detailed observation concerns the velocity vectors.

Figure 35 shows the normalized velocity components for both depression-type and elevation-type ISWs. Profiles include both the horizontal and vertical velocity vectors. Two points are noteworthy with respect to this figure. The first point is that both profiles in the exhibit show strong horizontal velocity in the vicinity of the pycnocline. The second point is that the profiles themselves

comport with the respective polarity orientations of the velocity vectors for the two internal wave types. For example, the velocity vectors for a depression-type ISW (Figure 35a) demonstrate a clock-wise flow pattern about the pycnocline consistent with the detailed simulation results shown in Figure 32. When examining the velocity profiles for an elevation-type ISW (Figure 35b), those profiles are consistent with the detailed simulation results shown in Figure 34 — in this case, the velocity vector orientation reflects a counter-clockwise flow pattern.

4.2.3.3 Comparison to Chen (2006) Data

Figure 36 shows the results of the production trials for five different grid densities and four different values of η_0 . Previous ISW experiments involving a stratified, two-layered system generally demonstrate a linear relationship between the depth of the step well η_0 and the magnitude of the incipient internal wave amplitude a_i . The results of the production trials shown in Figure 36a confirm this correlation. This figure also reveals how local errors associated also the finite difference method affected the magnitude of the simulated wave amplitude. For example, for small values of η_0 (5 cm), the benchmark trial results are generally clustered (closely-spaced). However, for larger values of η_0 (20cm), the results of the benchmark trial results are more widely-spaced, suggesting more dispersion (error) in the calculated results. Figure 36b

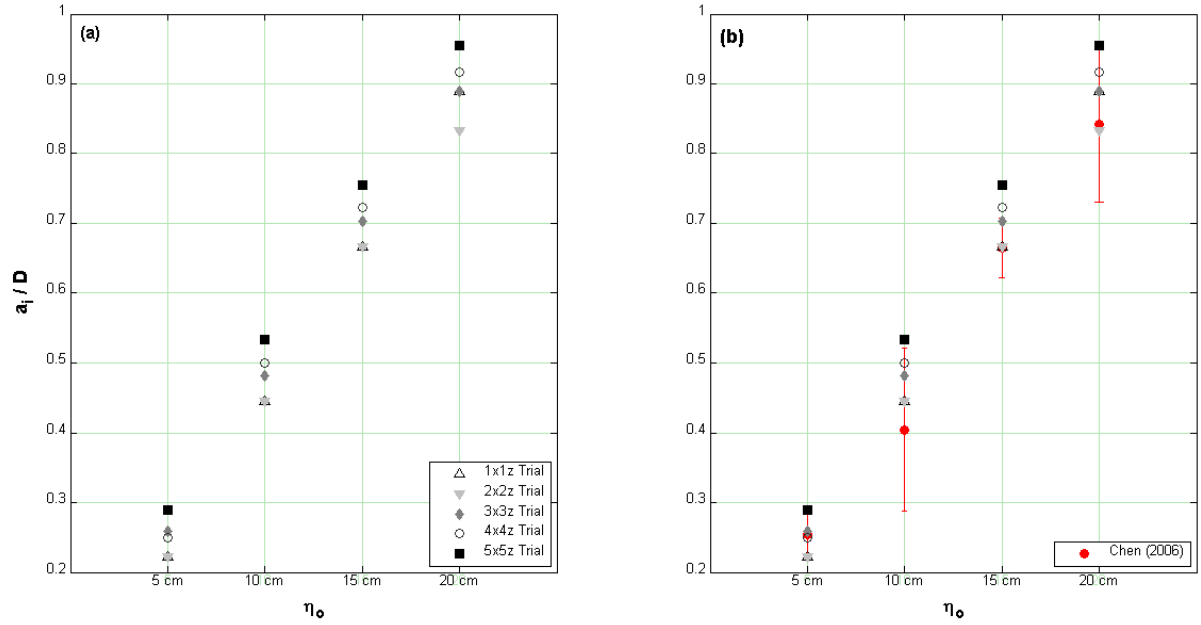


Figure 36. Benchmark trials showing the effect of grid density on potential well depth η_0 and ISW amplitude a . (a) Dimensionless benchmark trials for five different grid densities. (b) Benchmark trial data shown in relation of median and range of Chen (2006) data.

illustrates how well the results of the numerical simulation trials with respect to grid size compare with the mean and range of experimental data collected by Chen (2006). The experimental variation in the Chen (2006) data is evident by virtue of the magnitude (length) of the variance bars about the mean (Figure 36b).

4.2.3.4 Other Observations and Comparisons

Four additional aspects of the numerical simulation trials associated with the benchmark trials thus far deserve some limited discussion.

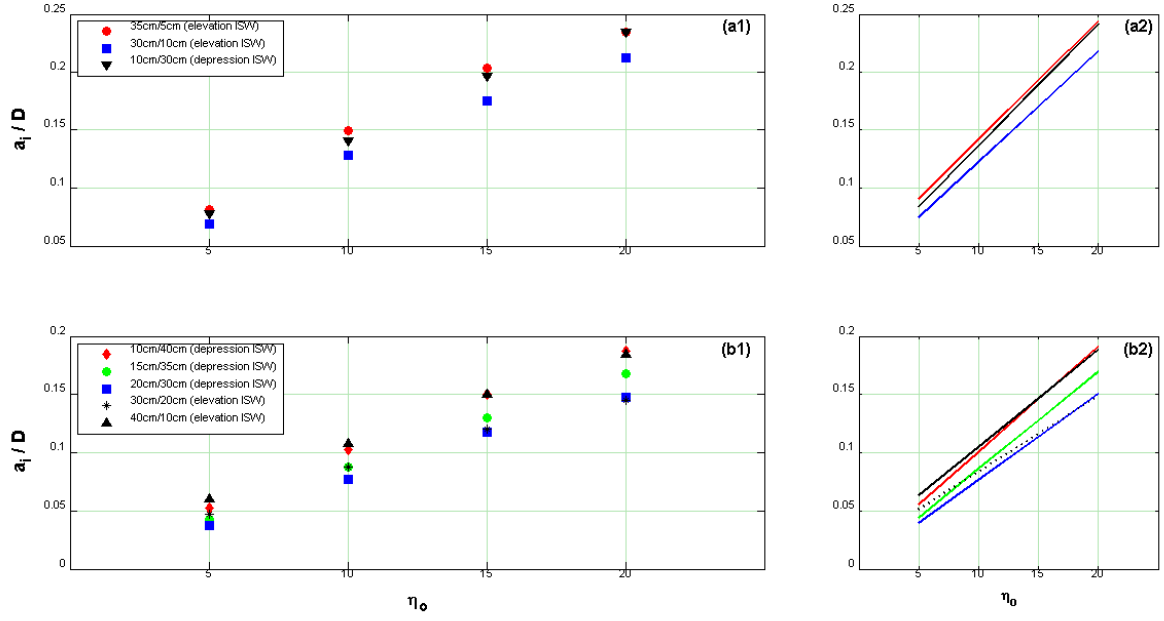


Figure 37. Benchmark trials showing the relationship between potential well depth η_0 and ISW amplitude a . (a) Non-dimensional trials for 40 cm-deep tank scenarios. (b) Non-dimensional trials for 50 cm-deep tank scenarios.

Relative Fluid Layer Depths. Another parameter affecting wave amplitude appears to be the depth configuration of the computational environment as defined by the two fluid layers h_1 and h_2 . Figure 37 shows the results of the wave tank trials for eight simulated dimensional depth configurations — either 40 cm or 50 cm — for both elevation- and depression-type ISWs. Overall, the results indicate that the normalized wave amplitude increases more rapidly for the 40 cm-simulated depth configuration than for the 50 cm-simulation depth configuration. A second overall observation is that for different values of η_0 , the normalized wave amplitude generally increases as the ratio of the two fluid layers increases. The exhibits also show that when the two fluid layers are

approximately of equal thickness, the rate of increase in the wave amplitude height tends to be less than when other depth configurations are evaluated (i.e., $h_1 \ll h_2$ or $h_1 \gg h_2$). This trend is more clearly revealed when MATLAB-generated trend (regression) lines for the data are plotted.³⁰ The trend lines for the simulated dimensional depth ratio of 35 cm/5 cm and 30 cm/10 cm (scenario generally defined to be $h_2 > h_1$) correspond to an elevation-type ISW; these regression lines are nearly parallel to each other. By contrast, the trend line for the simulated depth ratio of 10 cm/30 cm (scenario defined as $h_2 < h_1$) corresponds to a depression-type ISW; this particular trend line is the steepest of the three. Upon inspection of Figure 37, it can be observed that the same overall positive data trends are repeated. It may be concluded that elevation-types of ISWs appear to be affected by advective/dispersive forces following their formation more so than depression-type waves.

Wave Speed. Differences in the relative proportions of the fluid layer depths can provide additional insights regarding ISW properties. Equations 2.7, 2.9, and 2.10 (as well as similar equations found in Table 4) indicate that speed of an ISW is influenced by both the depth and density of the respective fluid layers.

³⁰ Although there are several mechanical (long-hand) procedures for doing so (e.g., Daniel, Wood, and Gorman 1971), it was found that the EzyFit 2.30 curve-fitting package developed for MATLAB (Ezyfit 2009) could infer (approximate) rates of change of the variables of interest depicted in the figures more efficiently.

Because the density differences between the two fluids was defined to be fairly small for the purpose of this research, the next series of exhibits were are intended to examine the influence of fluid depth on wave speed.

Martin, Walker, and Easson (1998) proposed a binary classification system for ISWs based on wave speed. They suggest that an internal wave may be classified as *supercritical* if its wave speed c_i is greater than the phase velocity c_o (or greater than one). Conversely, the ISW can be classified as *subcritical* if the wave speed is less than the internal wave phase velocity — $c_i < c_o$ — or less than one.

The simulation results depicted in Figure 38 highlight the binary nature of the wave speed classification system. These results have been normalized to the depth of the upper fluid layer h_l . The results illustrate that the normalized wave speed is proportional to the magnitude of the wave amplitude. The trials corresponding to a simulated dimensional wave tank depth ratio of 35 cm/5 cm (an elevation-type ISW) all demonstrate *supercritical* wave speeds where $c_i > c_o$. Wave speeds for the trials involving simulated dimensional wave tank depth ratios of 10 cm/30 cm and 30 cm/10 cm are mostly *supercritical* with some of the simulations in the *sub-critical* range where $c_i < c_o$. Overall, the trends of the simulation results depicted in the plots show how normalized

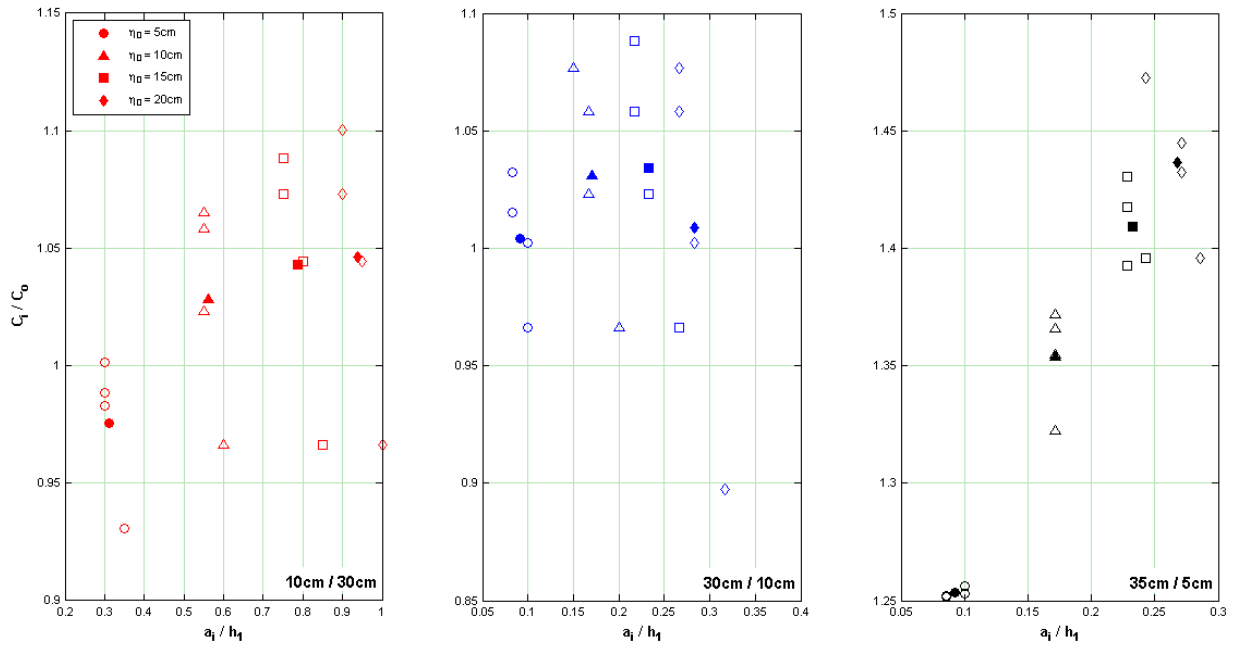


Figure 38. Normalized wave speed vs. normalized wave amplitude for simulated dimensional 40 cm-deep wave tank trials. Plot shows simulation data for 48 trials corresponding to four measurement locations once the ISW had reached steady-state. Solid symbol represents a mean value for a particular simulation.

increases in the size of the potential well depth lead to corresponding increases in wave speed.

Figure 39 shows results of the numerical simulation trials for the 50 cm-deep configuration involving only elevation-type ISWs. These results generally comport with the 40 cm dimensional configuration just described. The trends of the simulation results continue to illustrate that wave speed is proportional to magnitude of the wave amplitude. Wave speeds for the 30 cm/20 cm simulated dimensional wave tank depth configuration are all *subcritical* whereas the wave

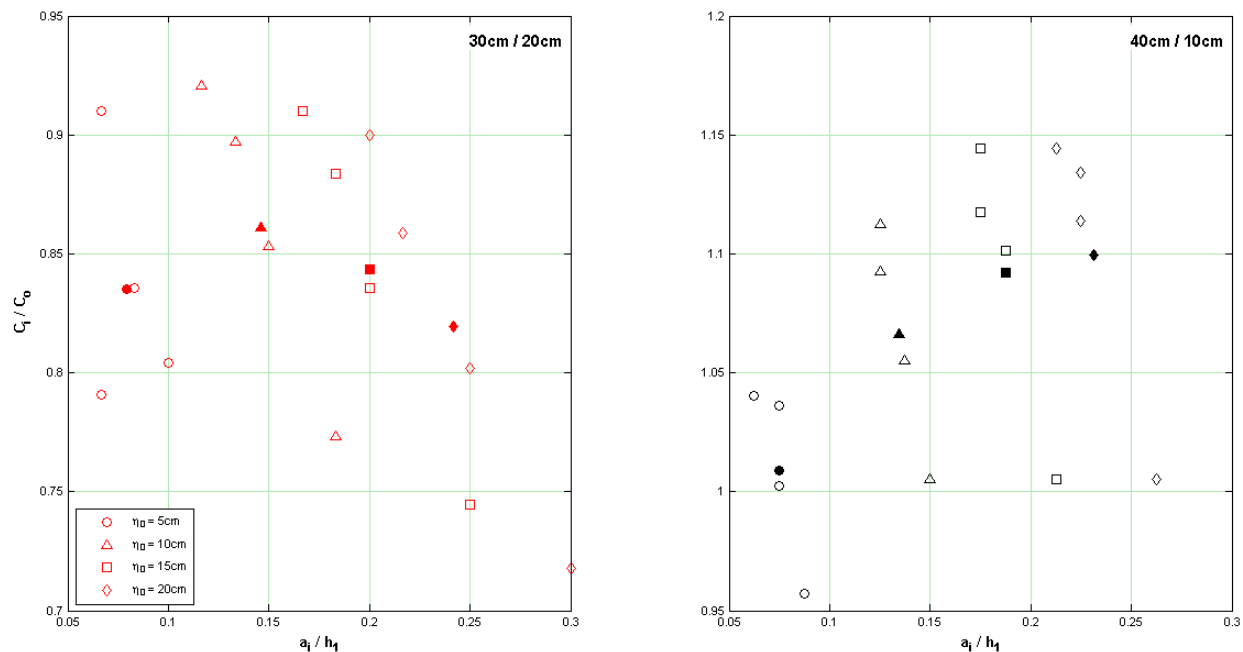


Figure 39. Normalized wave speed vs. normalized wave amplitude for simulated dimensional 50 cm-deep wave tank trials involving elevation-type ISWs. Plot shows simulation data for 32 trials corresponding to four measurement locations once the ISW had reached steady-state. Solid symbol represents a mean value for a particular simulation.

speeds for the 40 cm/10 cm simulated dimensional wave tank depth configuration are all essentially *supercritical* according to the Martin, Walker, and Easson (1998) speed classification scheme. Figure 40 shows results of the numerical simulation trials for the 50 cm-deep dimensional configuration but now involving only depression-type ISWs. The simulation results continue to be in general agreement with the 40 cm dimensional configuration when it comes to the influence of wave amplitude on wave speed. Two of the simulation configurations — dimensional depth ratios 15 cm/35 cm and 20 cm/30 cm — produced ISWs whose wave speeds were *subcritical*. The computer trials

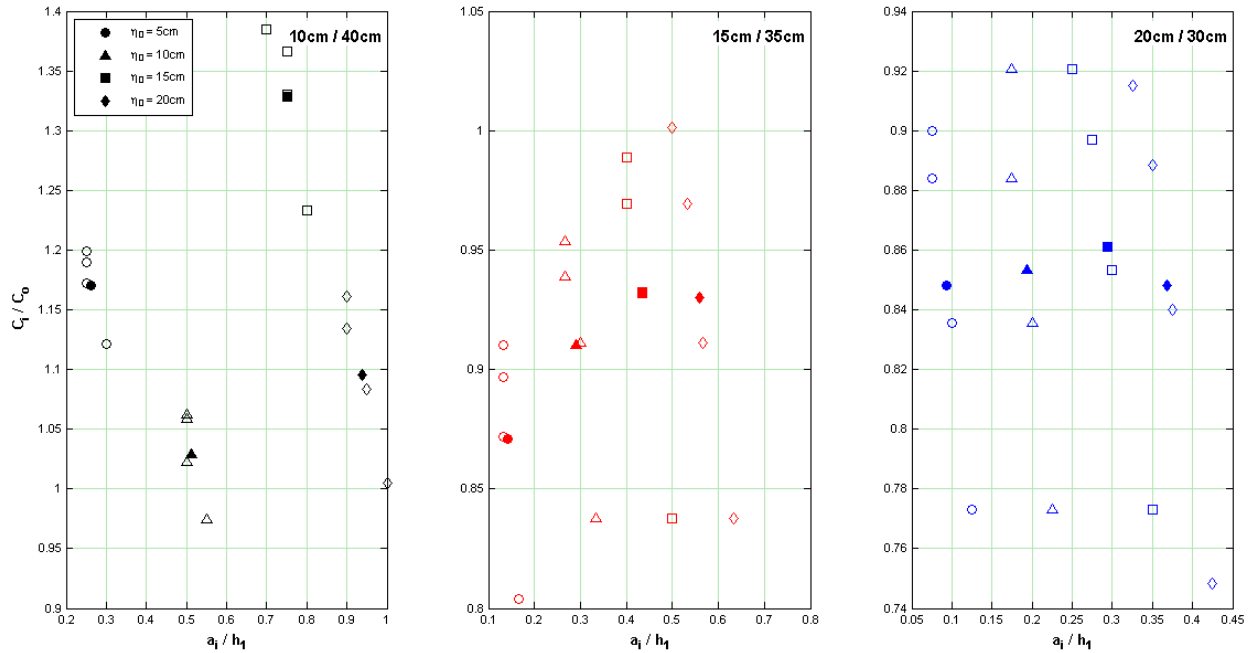


Figure 40. Normalized wave speed vs. normalized wave amplitude for simulated dimensional 50 cm-deep wave tank trials involving depression-type ISWs. Plot shows simulation data for 48 trials corresponding to four measurement locations once the ISW had reached steady-state. Solid symbol represents a mean value for a particular simulation.

involving simulated dimensional depth ratio of 10 cm/40 cm produced ISWs whose wave speeds were *supercritical*. An important observation that can be made from this aspect of the research thus far is that *supercritical* ISW wave speeds ($c_i > c_o$) were produced when one of the fluid layers' depths was large in proportion to the other.

Other researchers have conducted wave tank studies to evaluate ISW behavior. Several of these studies were summarized earlier in Table 11. To understand how the simulations described above compare to other

experimentalists' work listed in that table, the normalized wave speeds for the benchmark trials just described were compared against more than 250 sets of normalized wave amplitude data reported in the literature. This comparison is depicted graphically in Figure 41. Upon inspection of this scatter diagram, it appears that the data are self-organized into two groups. The first group is a large cluster of data that can be described as falling predominantly in the *subcritical* wave speed range ($c_i < c_o$). The second group corresponds to what can be described as a more positively-trending, set of data, that are slightly detached from and located above the so-called *subcritical group*, which demonstrate greater correlation (physical association) and appear to fall predominantly in the *supercritical* wave speed range ($c_i > c_o$). Figure 41 also shows that the data from the benchmark trials are well-nested within the distribution of experimental data reported in the literature. The Chen (2006) data have been highlighted in this figure as have the benchmark trials data. Overall, both sets of data compare favorably with the literature. This exhibit also indicates that the Chen (2006) data tend to favor the lower margin of the distribution defined by data published in the literature whereas the benchmark trials data tend to favor upper margin of that distribution.

An additional figure of merit that can be used to evaluate the data and provide further insights into the simulation results is regression analysis. In

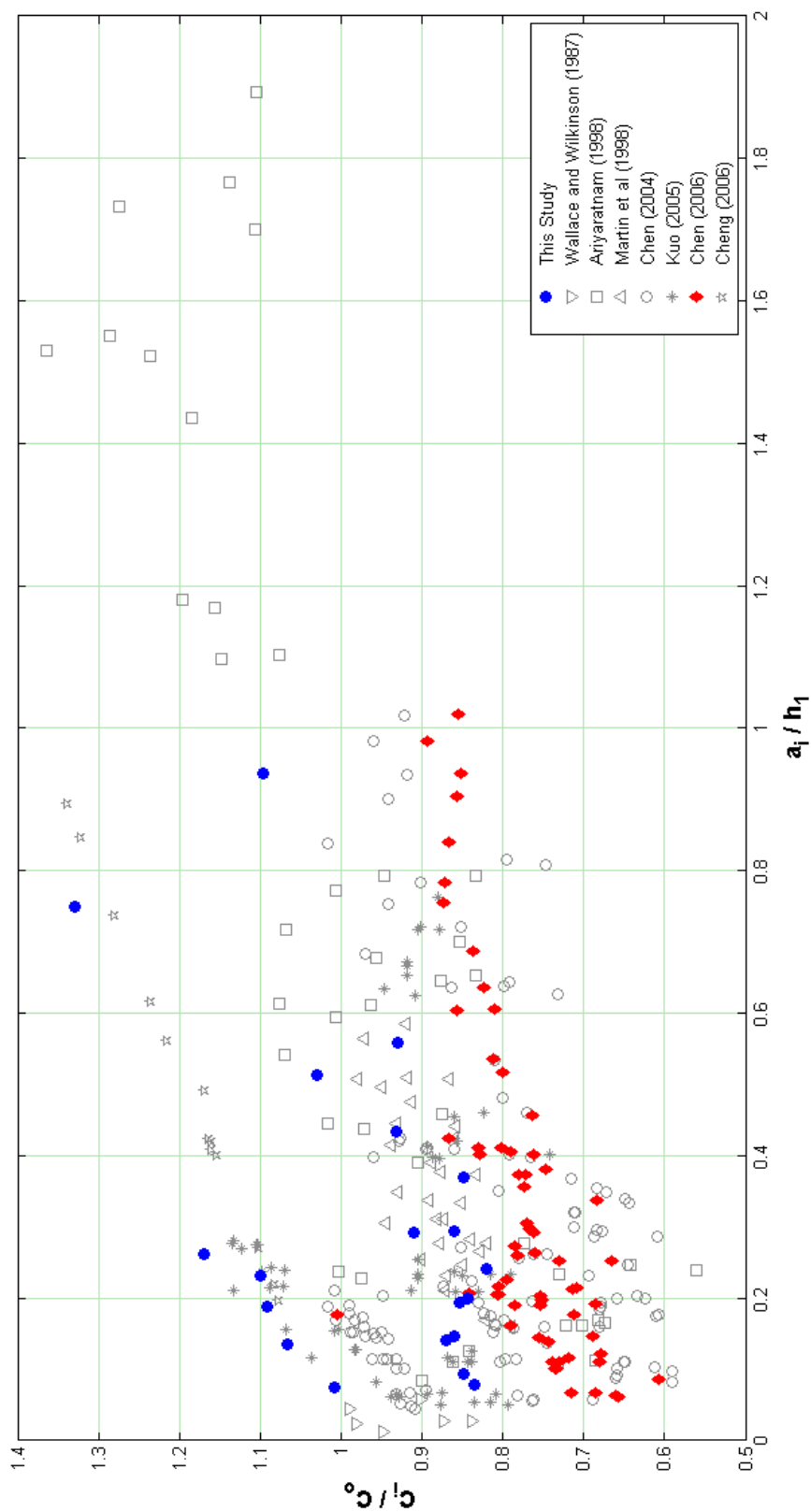


Figure 41. Comparison of normalized wave speed vs. normalized wave amplitude data for data reported the literature as well as the benchmark trial simulations.

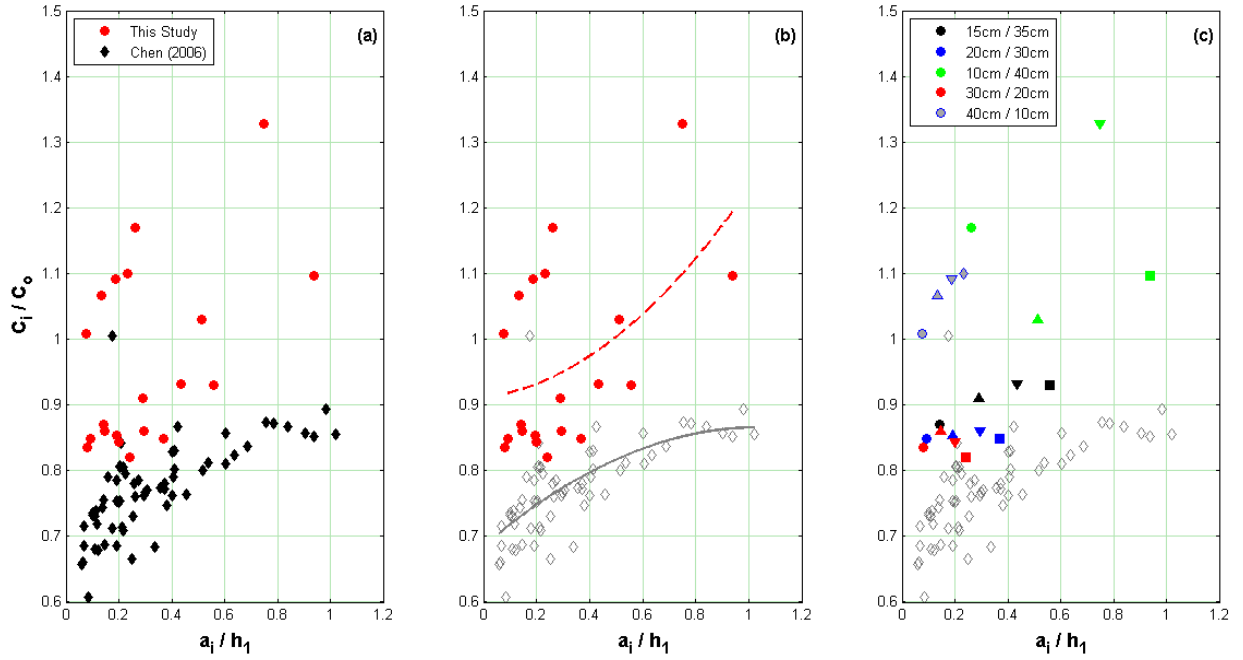


Figure 42. Comparison between benchmark trial simulations and Chen (2006) data. (a) Scatter diagram. (b) MATLAB-generated regression lines corresponding to respective data sets. (c) Break-down of benchmark trials results by simulated dimensional depths.

Figure 42(a), the Chen (2006) data and the benchmark trials data have been isolated in a separate scatter diagram to illustrate the relationship between normalized wave amplitude and normalized wave speed in more detail. Figure 42(b) shows how both data sets compare against their respective regression lines (2nd order polynomials). The linear correlation coefficient R associated with these regression lines can be used to evaluate how well the simulation results account for the relationship between the internal wave amplitude and the wave speed. MATLAB-derived R coefficients for the Chen (2006) data and the trials data are, respectively, 0.67979 and 0.5024, suggesting “moderate” correlation

between wave amplitude and wave speed. By way of comparison, a MATLAB-derived composite R coefficient for the data reported in the literature (Figure 41) is 0.47435, which is generally considered to reflect “weak” correlation between these two variables. Figure 42(c) illustrates how the respective benchmark trial results compare to the Chen (2006) data when taking into account the depth configuration used in the numerical simulation trials. The R coefficients for the individual benchmark trials are as follows:

<i>Depth Configuration</i>	<i>R Coefficient</i>	<i>Correlation</i>
15 cm/35 cm	0.99896	“strong”
20 cm/30 cm	0.82137	“strong”
10 cm/40 cm	0.14569	“weak”
30 cm/20 cm	0.99068	“strong”
40 cm/10 cm	0.99989	“strong”

As indicated in the summary table above, all of the benchmark trials demonstrated “strong” correlation with the exception of the trial whose simulated dimensional depth ratio was 10 cm/40 cm.

What is particularly noteworthy about Figure 41 is that the exhibit shows how pervasive experimental variation can be among the respective studies by graphically displaying the normalized results. In a generic sense, Fisher (1932) was the first to examine the influence of experimental design on experimental

outcomes. The exhibit clearly shows this relationship. In this context, these differences represent fixed sources of error, and can correspond to the design or configuration of the experimental wave tank apparatus itself including its dimensions, the physical properties of the respective fluids used, the influence of side effects (reflection) on internal wave properties (e.g., 3D effects), and instrumentation methods. The other source of variation in experimental outcomes can be attributed to random sources. Simply stated, there inevitably is some variation in the measurement of any particular physical property (Taylor 1987). When considering the spread in the data depicted in Figure 41, some of the variation in the results shown will reflect, to varying degrees, measurement errors.

Viscous Decay (Damping). In nature, waves cannot travel indefinitely without some change in amplitude as they will attenuate owing to the effects of viscous damping (as well as other factors). Keulegan (1948, 1959) was one of the first researchers to experimentally investigate the role of viscous damping in the decay of long infinitesimal waves. From Keulegan's work, Leone, Segur, and Hammack (1982) subsequently derived an expression that could be used to predict how an ISW would decay in a two-layered fluid system as a result of viscous damping. In dimensionless form, this equation is:

$$\left[\frac{(h_1 - h_2)a_i}{h_1 h_2} \right]^{\frac{1}{4}} - \left[\frac{(h_1 - h_2)\eta_0}{h_1 h_2} \right]^{\frac{1}{4}} = K \left[\frac{S}{(h_1 h_2)^{\frac{1}{2}}} \right] \quad (4.7)$$

where S is the distance between some downstream observation station $i+1$ and the preceding observation station i . Physically, the decay factor K describes the rate of viscous damping attenuates the wave amplitude a_i . The non-dimensional equation relating the decay constant K to other system parameters described elsewhere in this dissertation is:

$$K = \left[\frac{\nu^{\frac{1}{4}}}{12(g\Delta\rho)(h_1 + h_2)} \right] \left[\left(\left\{ 1 + \frac{2h_2}{w} \right\} \frac{h_1}{h_2} \right) + \frac{2h_2}{w} + \frac{(h_1 + h_2)^2}{2h_1 h_2} \right] \quad (4.8)$$

where w defines the width of the wave experimental tank.

The next two figures in this dissertation examine the influence of viscous damping effects on ISW amplitudes using different types of normalized parameters. Four different potential well wave depths η_0 are evaluated — dimensional depths of 5 cm, 10 cm, 15 cm, and 20 cm. This series of exhibits also depict simulation results for three different depth/stratification configurations — 10 cm/40 cm, 15 cm/35 cm, and 20 cm/30 cm. To aid in the visualization of the simulation results, MATLAB-generated best-fit curves have been fitted to the data points to illustrate trends. Through trial and error, it was found that the mathematical function that best-fits the data from the numerical

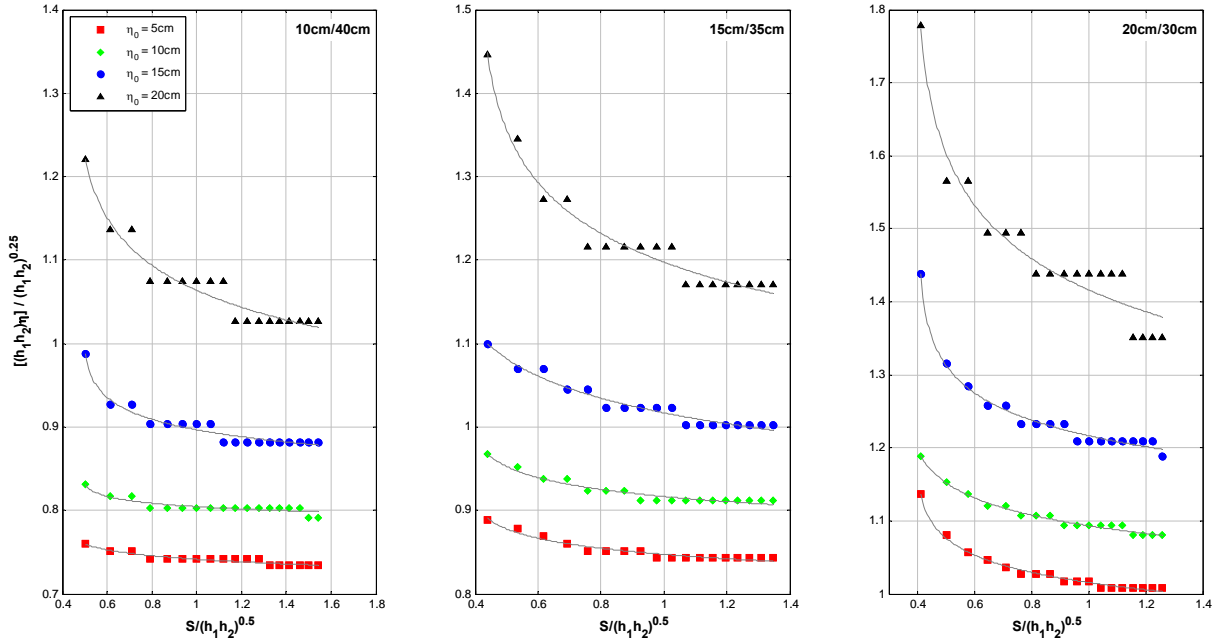


Figure 43. Rates of viscous damping for four different depression-type ISW amplitudes in three different depth configurations. Plots show data for 80 trials (simulations).

simulations depicted in this series of exhibits was a power function in the general form of $y(n) = a(x+b)^n$. See Spanier and Oldham (1987).

Figure 43 examines the rate of viscous damping in terms of equation 4.7. Consistent with that equation, the MATLAB trend lines fitted to the data suggest a strong tendency for ISWs to decay as a function of the distance traveled from the generation point. When considering the different depth configurations, the data trends in Figure 43 also show that when the depth configuration is such that $h_1 \approx h_2$ (i.e., simulated 20 cm/30 cm depth), the rate of viscous damping appears to be greater than for depth configurations that might

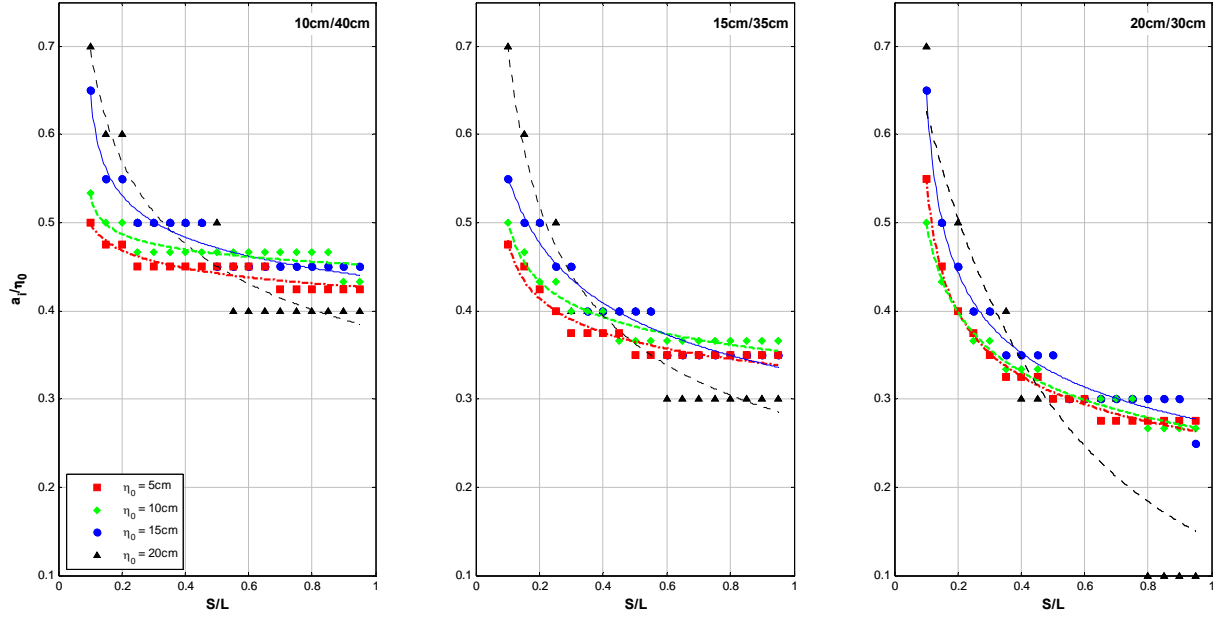


Figure 44 Effects of viscous damping on amplitudes of ISWs of depression for three different depth configurations as a function of distance traveled from the generation point. Plots show data for 80 trials (simulations).

be considered analogous to a shallow pycnocline where $h_1 \ll h_2$ (i.e., the simulated 10 cm/40 cm depth). One conclusion that might be drawn this figure is that once formed, ISWs decay more rapidly in stratified waters of approximately equal depth (i.e., a depth configuration similar to that corresponding to a 10 cm/40 cm depth scenario). Moreover, the simulation results suggest that the rate of viscous damping is greater for larger amplitude ISWs ($\eta_0 = 20$ cm) than for ISWs with smaller amplitudes ($\eta_0 = 5$ cm).

The influence of stratification — or the relative proportions of the two fluid layer depths — on viscous damping behavior can be seen in Figure 44. The figures

show the normalized decay of ISW amplitude as a function of the distance the ISW has traveled from the point of generation. From inspection of Figure 44 it is possible once again to draw some conclusions concerning the behavior of wave amplitude in a stratified fluid system. Recalling Michallet (1988), that researcher previously noted that mechanically-generated ISWs need to travel some (unspecified) distance from their generation point before achieving what could be considered a steady-state profile. When considering Michallet (1988), the first observation that can be drawn from Figure 44 is that viscous damping appears to influence the simulation more rapidly in a fluid configuration defined by $h_1 \ll h_2$ — or what might be considered to be a (relatively) shallow, near-surface pycnocline. The second observation is that the normalized amplitudes for all trials appear to reach steady state earlier in the simulation (i.e., closer to the generation point) when the pycnocline is at a shallow depth. For example, in the 10 cm/40 cm simulations, viscous damping effects were found to preserve at least 40 percent of the normalized ISW amplitude. By contrast, in the 20 cm/30 cm collection of simulations, the percentage of normalized ISW amplitude preservation dropped to about 30 percent.

The third observation is that the rate of decline in the normalized internal wave amplitude occurs over a greater distance for those simulations whose depth configurations are such that the two fluid depths are essentially equal. Stated

differently, the influence of viscous damping on ISW amplitude decay appears to extend over the full extent of the simulation (i.e., a longer period of time) when the depth configuration resembles $h_1 \approx h_2$ (20 cm/30 cm) — or what might be considered to be a (relatively) deep pycnocline. By contrast, for those simulations where $h_1 \ll h_2$ (a shallow pycnocline), most of the trial results indicate that the normalized wave amplitude reached steady state well before the mid-point of the simulation. This observation would suggest that the effects of viscous damping on the amplitude of a propagating ISW are minimized when the depth configuration resembles that of a shallow, near-surface pycnocline. Overall, the decay rates associated with the numerical simulation trials were found to compare favorably with earlier published studies summarized in Table 13.

Table 13. Estimated Rates of Amplitude Decay for ISWs in Experimental Settings as a Function of Distance as Reported by Various Investigators.

INVESTIGATOR	PERCENT AMPLITUDE DECAY [DISTANCE]
Koop and Butler (1981)	30% [7 m]
Michallet and Barthélemy (1997, 1998)	50% [3.56 m]
Ariyaratnam (1998)	20% [8 m]
Chen (2006)	12-14% [6 m]
This Study	30- 40% [6 m]

Another perspective on the influence of viscous damping on the numerical simulation trials can be obtained by examining the change in ISW energy as the wave propagates away from the generation point. Equation 4.4 expresses total ISW energy in terms of $\eta(t)$. Consistent with the decay trends illustrated in earlier Figures 43 and 44, Figure 45 shows that the rate of wave energy decline ΔE is greatest for a deeper pycnocline ($h_1 = h_2$) and the least for a shallow, near-surface pycnocline ($h_1 \ll h_2$). The decay in ISW energy does not exceed 30 percent for the simulations associated with a shallow, near-surface pycnocline whereas the simulations associated with a deeper pycnocline can generally expect to experience a more progressive decline internal energy as a result of viscous damping. Once again, the effects of the rigid lid assumption,

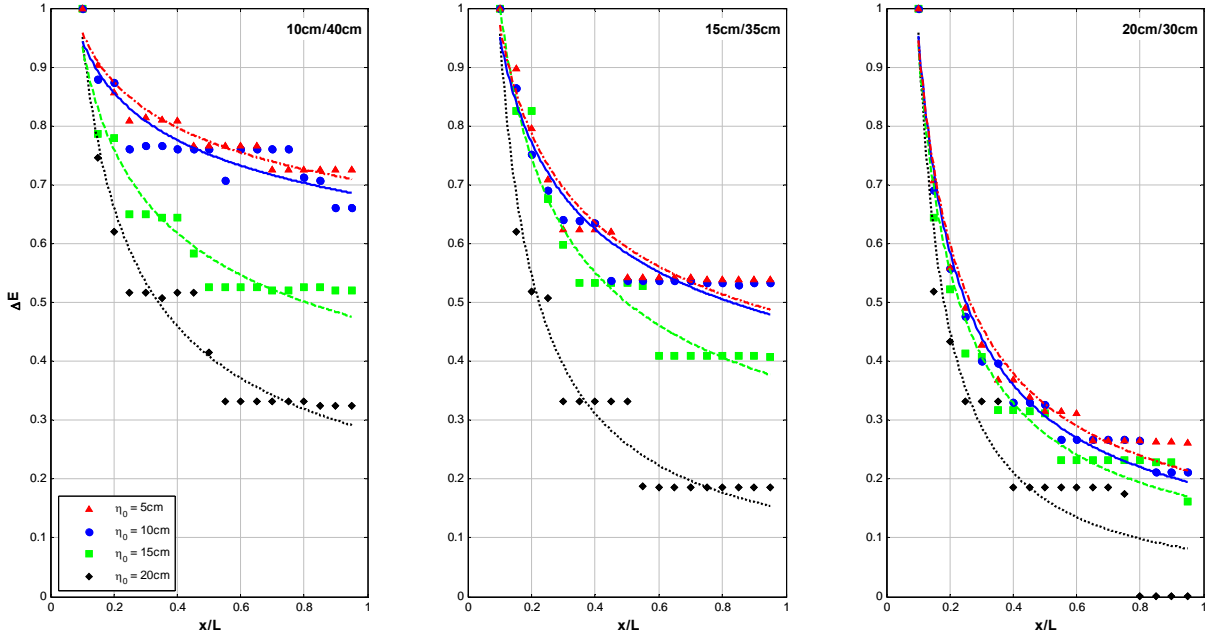


Figure 45. Rate of normalized energy decay for ISWs of depression for three different depth configurations as a function of distance traveled from the generation point. Plots show data for 80 trials (simulations) energy as a function of $\eta(t)$.

as applied to this simulation scenario, may be more pronounced when the pycnocline is located close to the top of the computational domain.

Overall, Figures 43 through 45 show that the rate of viscous decay for simulated ISWs with higher initial potential well amplitudes ($\eta_0 = 20$ cm) is more rapid than for simulated ISWs with smaller initial potential well amplitudes ($\eta_0 = 5$ cm). This series of figures show is that the rate of amplitude decay itself

appears to be influenced by the relative depths of the two fluid layers or the ratio of $\frac{h_1}{h_2}$.

4.3.1 Simulations Involving Topographic Obstacles

As noted earlier in this dissertation, researchers have frequently observed the occurrence of ISW phenomena in proximity to the continental slope/continental shelf transition. At this location, deep oceanic waters transitions into relatively shallower continental waters. Moreover, this location generally corresponds to the point where ISWs are breaking below the water surface, in the presence of a well-defined pycnocline, owing to the theoretical turning point condition of $h_1 = h_2$ being met.

The continental land mass is surrounded by an extensional yet submerged shelf that is nearly horizontal. At some point seaward, this feature segues into the continental slope whose grade is very slight — in the range of 1° to 4° . At some locations, the continental slope is essentially absent resulting in a near vertical (shear) bluff that segues into the continental rise that ultimately merges with the abyssal plane. A “bird’s-eye” perspective of this physiographic feature can be found in Figure 46. For the purposes of the numerical simulation trials, this type of obstacle can be modeled in one of two ways. It can be modeled simply as a horizontal shelf-like feature, as represented in Figure 47a, or as a

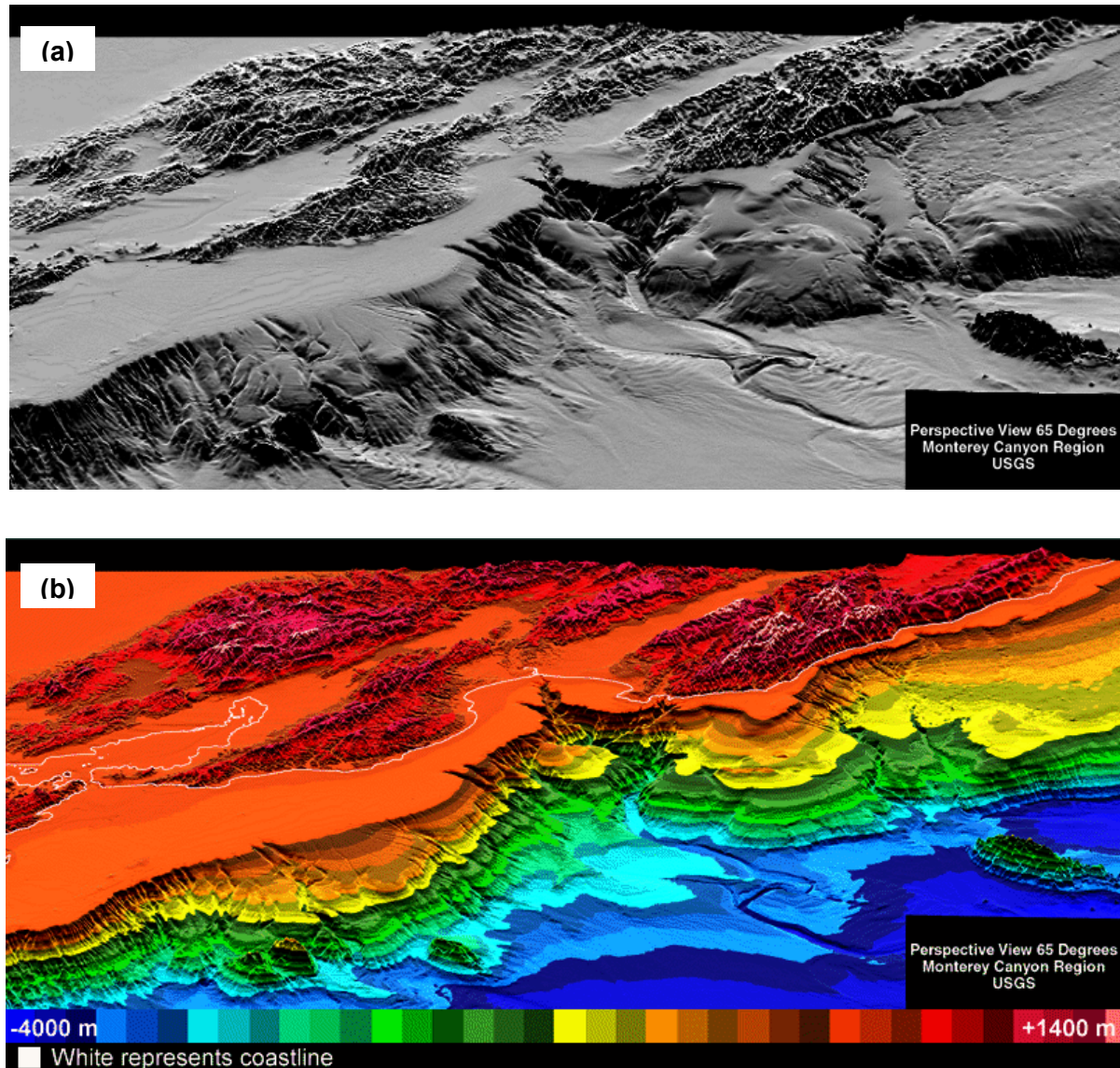


Figure 46. Digital Images of submarine topography characteristic of the continental slope/continental shelf transition. Example is for the vicinity Monterey Canyon, California. (a) Black-white shaded relief image. (b) False-color image of bathymetry. Figures illustrate an example of the shelf and slope-shelf topographic obstacle scenarios modeled in this research. Investigators (i.e., Carter, Gregg, and Lien 2005) have long-recognized this area as representative of one for which the formation of ISWs is favorable. Images generated by the U.S. Geological Survey/Menlo Park.

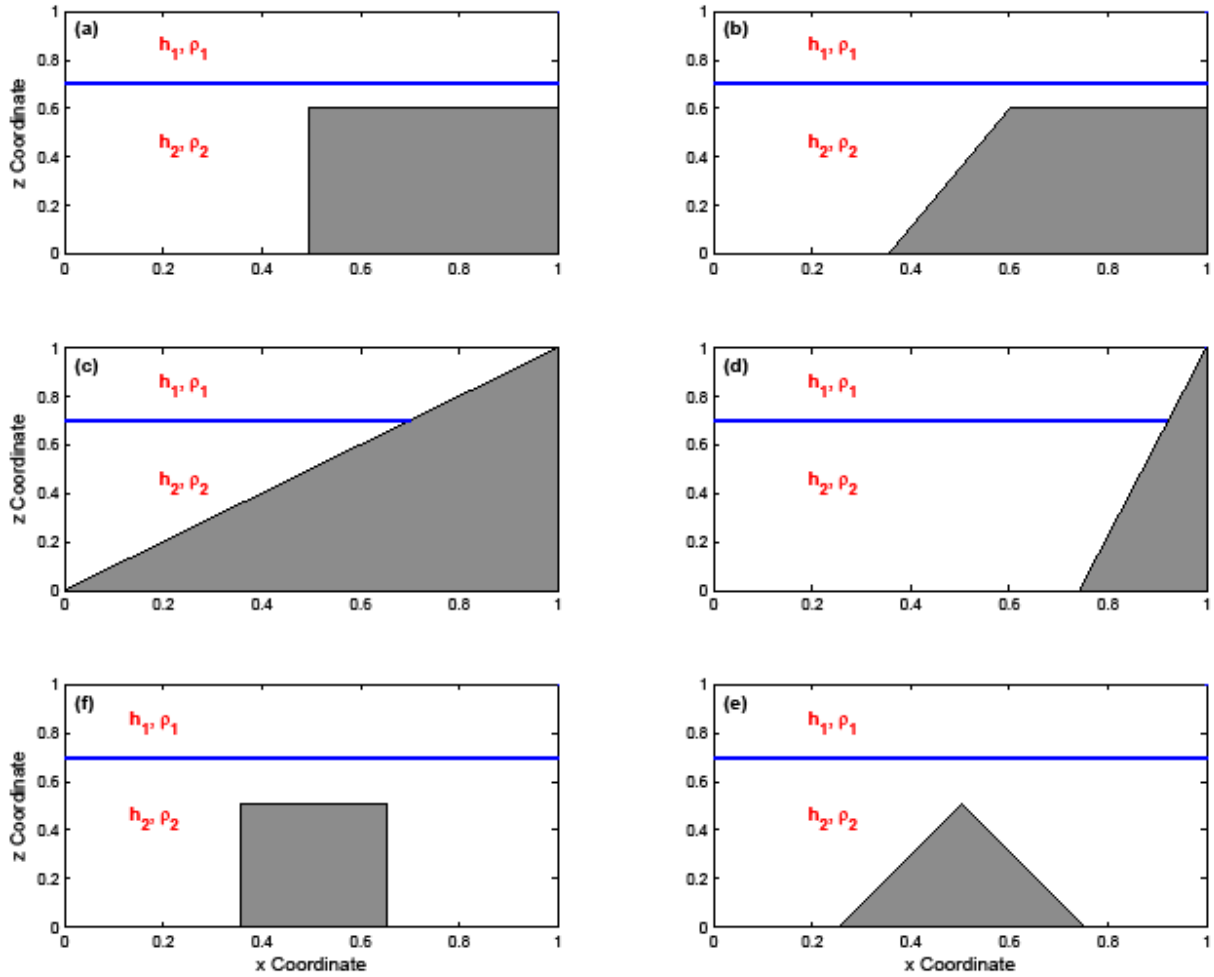


Figure 47. Examples of types of topographic/physiographic analogs considered in the numerical simulations. These geometries were numerically introduced into the computation domain depicted earlier in Figure 23. Figures are not to scale and are intended only for illustrating the approximate location of the pycnocline defining this two-layered fluid system relative to the obstacle.

short slope transitioning into a horizontal shelf, as depicted in Figure 47b.

Either of these modeling scenarios is useful for demonstrating ISW breaking as the location of the turning point can be precisely plotted and the polarity of the ISW evaluated as it passes through this position.

Overall, six simulations corresponding to specific topographic analogs of submarine features likely to be encountered on the ocean floor were evaluated. The modeling analogs selected were considered representative of the types of physiographic features (Figure 48) the literature (Table 5) suggests can affect ISW behavior in a marine setting. They are illustrated in Figure 47a-f. In addition to the two modeling scenarios described in the preceding paragraph, internal wave interactions with four other topographic/physiographic analogs were evaluated. They included an extended or long slope scenario (Figure 47c), a so-called “short” slope scenario (Figure 47d), a scenario involving a triangular-like obstacle (Figure 47e), and a scenario involving a table-like topographic feature of limited horizontal extent type (Figure 47f). Whereas the modeling configurations depicted in Figures 47a and 47b are intended to represent the transition from deeper oceanic waters to shallow continental waters, the configuration depicted in Figure 47c is intended to represent the continental margin of a marine system characterized by a long gradual slope. As noted earlier in this dissertation, these topographic shapes are also useful analogues for evaluating changes how ISW properties observed in marine settings change following an encounter with different types of topographic features.

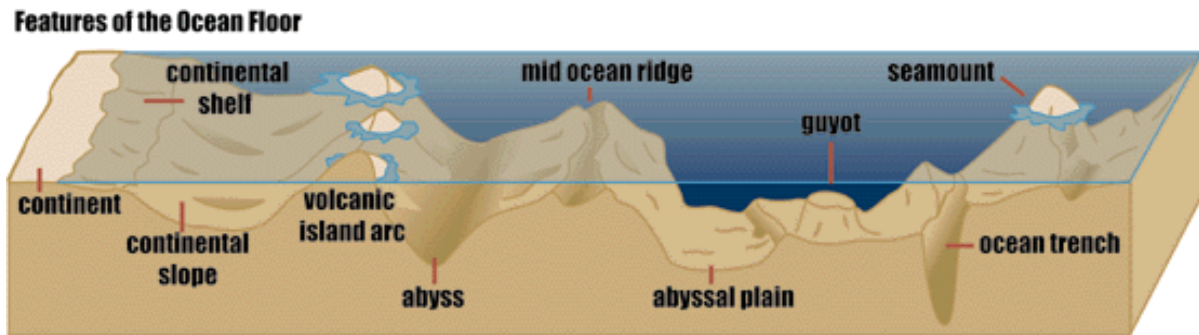


Figure 48. Principal physiographic features found in the ocean. The relative proportions of these features in a marine setting is summarized in Table 8. Source MOS.org.

The introduction of physiographic analogs such as those illustrated in Figure 47 required the specification of additional boundary conditions besides those listed earlier in Table 10. Such numerical amendments are necessary as the presence of these obstacles would, in reality, produce different physical outcomes. Just as there are likely to be differences in how an internal wave would interact with different types of submarine obstacles in nature, the numerical solution to any particular computer simulation is also likely to change when the boundary conditions are modified. Roache (1972, 1998a) provides recommendations on how to specify additional boundary conditions corresponding to the outlines of new surface shapes illustrated in Figure 47.

4.3.1.1 Shelf-Like Obstacle

Figure 49 shows a non-dimensional, simulation between an advancing ISW and a shelf-like topographic obstacle (Figure 47a). The simulation involves a depression-type ISW of the first mode that formed in open water and advances shoreward. As indicated in the Figure 49a, the ISW is well-formed and generally symmetric by about TS 10,200 of the simulation. The time series shows a leading depression-type ISW followed immediately by a lesser elevation-type ISW. A trailing dispersive wave train is also present in this exhibit.

Contrary to what might be expected, evidence of the encounter between the ISW and the topographic obstacle is first revealed by streamline contours rather than by the pycnocline. The streamline contours show the first signs of distortion in their geometry about TS 10,800, well-before there is any apparent change in the geometry of the pycnocline. Later in the simulation, though, the pycnocline does begin to show some signs of asymmetry in its profile suggesting the hydrodynamic influence of the obstacle for the first time. By TS 12,000, the ISW has become less sinusoidal. The leading edge of the pycnocline is now “v-like” in profile suggesting that the ISW has begun to shoal as a result of its encounter with the obstacle. Shortly thereafter, by about TS 12,400, the trough of the ISW has reached the approximate location of the theoretical turning point (the vertical dashed line in the figure) and the pycnocline profile is now clearly

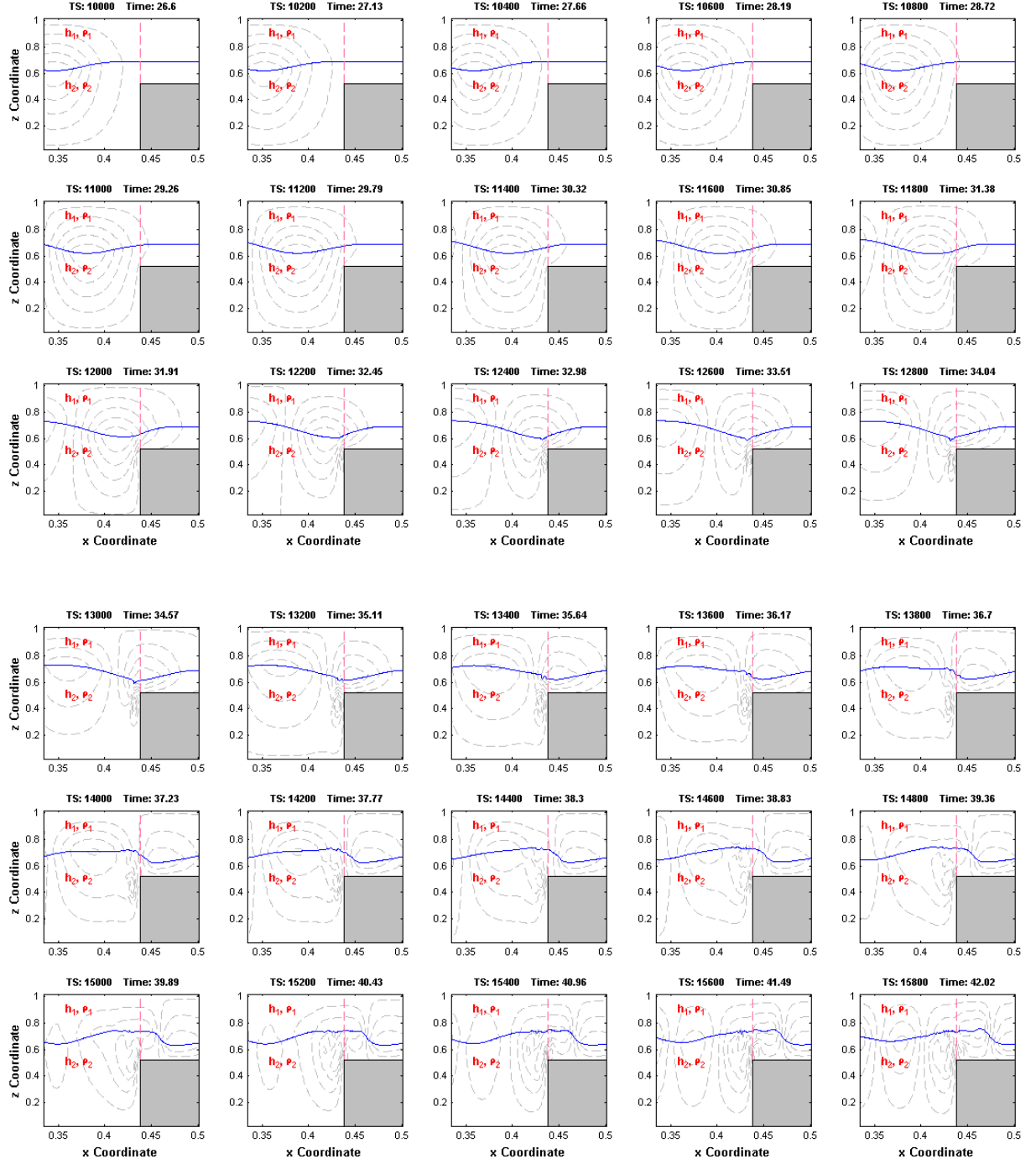


Figure 49a. Non-dimensional numerical simulation showing an encounter between a depression-type ISW and a shelf-like obstacle. The vertical dashed line corresponds to the position of the theoretical turning point defined by $h_1 = h_2$. $Re = 9.372e4$ and $Fn = 0.085$.

asymmetric. The demonstration of asymmetry by the internal wave has also been extended to the streamlines whose distribution now silhouettes the outline of the obstacle's vertical face.

Internal wave shoaling is a term of art, and in this dissertation it is defined to be topographic entrainment of the pycnocline. In this particular numerical simulation, shoaling appears to have reached its greatest vertical extent by about TS 12,600. Later, by about TS 13,400 (Figure 49a), the simulation shows evidence of the growth of a bolus in the trailing-end of the ISW for the first time.³¹ Subsequent time steps in the simulation show progressive growth in this bolus. By about TS 14,000 or so, there appears to be sufficient development (and likely momentum) in the bolus to laterally advance what now might be considered to be an elevation-type ISW. This new elevation-type ISW originates from a location beyond that defined by the turning point plane. At about TS 16,200 (Figure 49b), a bore-like feature, defined by the pycnocline, now appears to have transformed itself into a well-developed, elevation-type ISW. Figure 49c shows additional time steps in the polarity transformation. By about

³¹ An alternative explanation of this type of feature is suggested by Wessels and Hutter (1996), who identified the formation of a 'gyre' or vortex along the near side of a topographic obstruction as the internal wave encounters the obstacle. They suggest that the gyre represents a zone of strong localized turbulence that provides a mechanism for internal wave energy dissipation. As discussed later in this dissertation, the height of this obstacle relative to the height of the two fluid layers can be used to define the amount of energy dissipation likely to take place following an encounter.

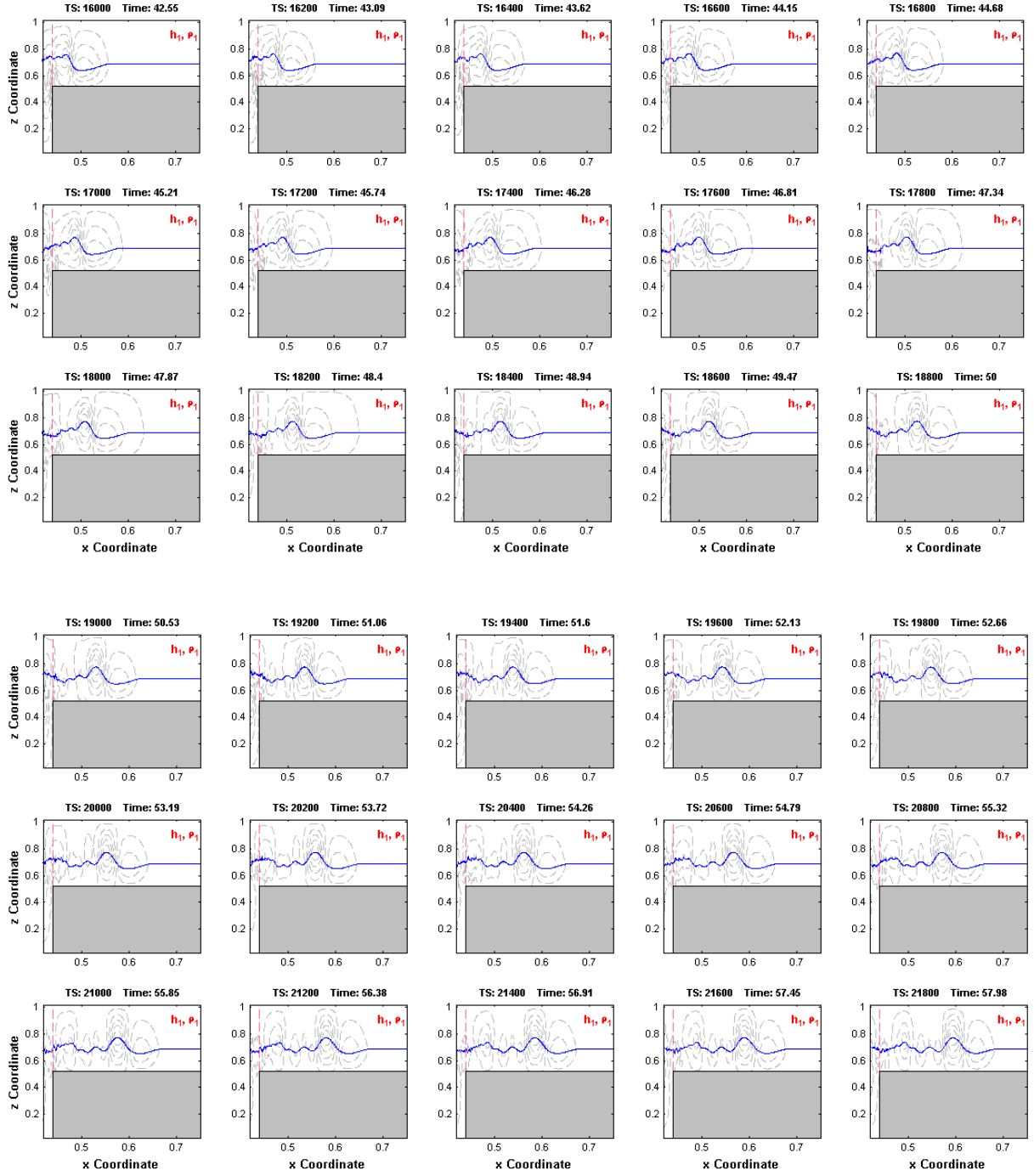


Figure 49b. Continued.

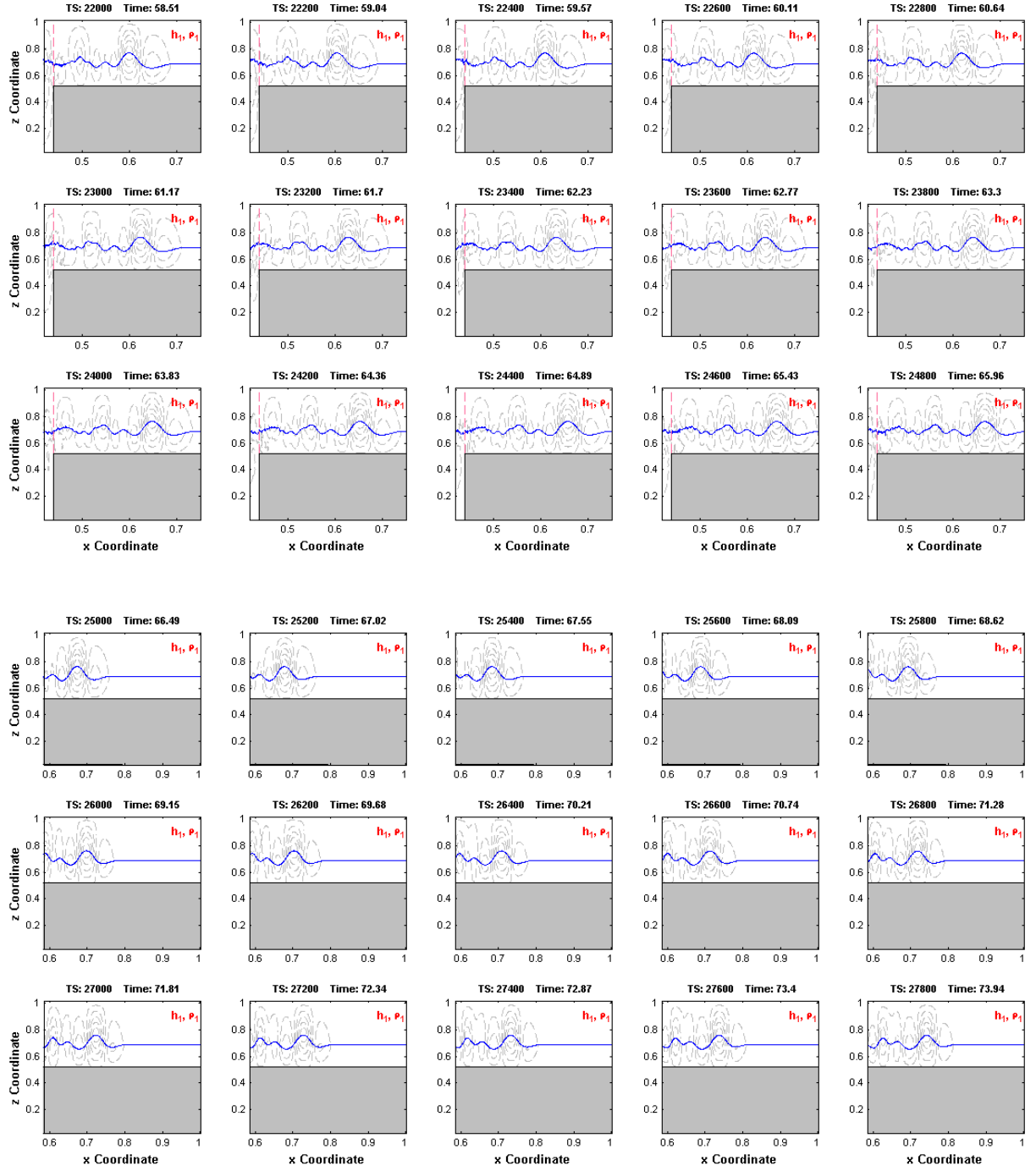


Figure 49c. Continued.

TS 27,800, all earlier evidence of the depression-type ISW appears to have disappeared from the simulation, leaving only an ISW of elevation in its place suggesting that a change (reversal) in polarity is complete. However, the simulation still shows the persistence of a single elevation-type ISW. See Figure 49d.

Additional insights concerning the interaction between the ISW and the shelf-like obstacle can be obtained from examination of higher-resolution figures. From inspection of the numerical wave simulation depicted in Figure 49, it appears that the shoaling process begins at about TS 10,600 or so. Moreover, only two aspects of the breaking progression were produced as part of the simulation — namely, the demonstration of wash-down associated with shoaling (at about TS 12,800) and the formation of the ISW into a bore (at about TS 14,800). These two wave breaking features are depicted in detail in Figure 50. Appendix B also contains higher-resolution figures of this particular modeling scenario beginning at about TS 14,800, prior to the onset of shoaling/breaking, and continuing through TS 16,400.

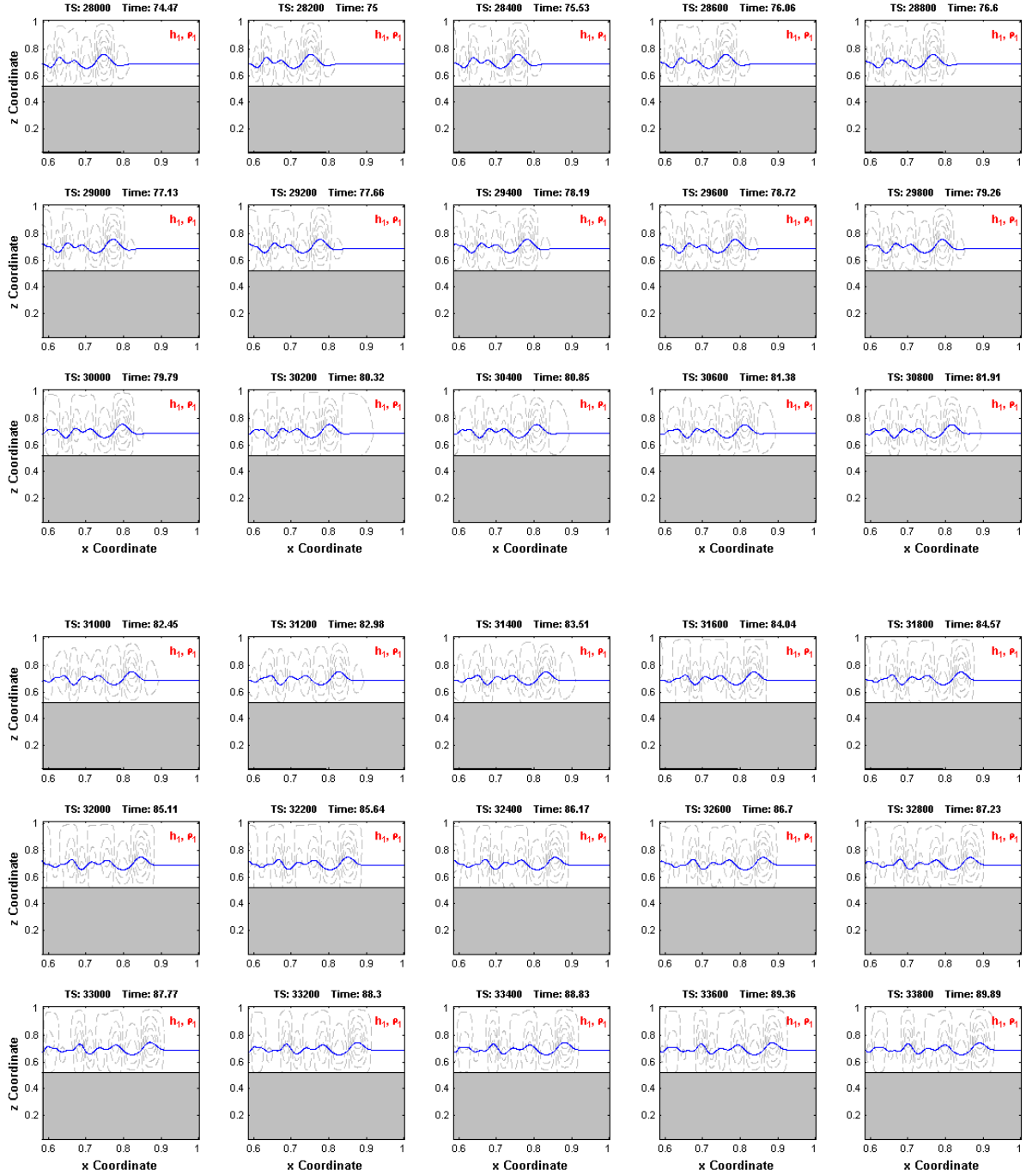


Figure 49d. Continued.

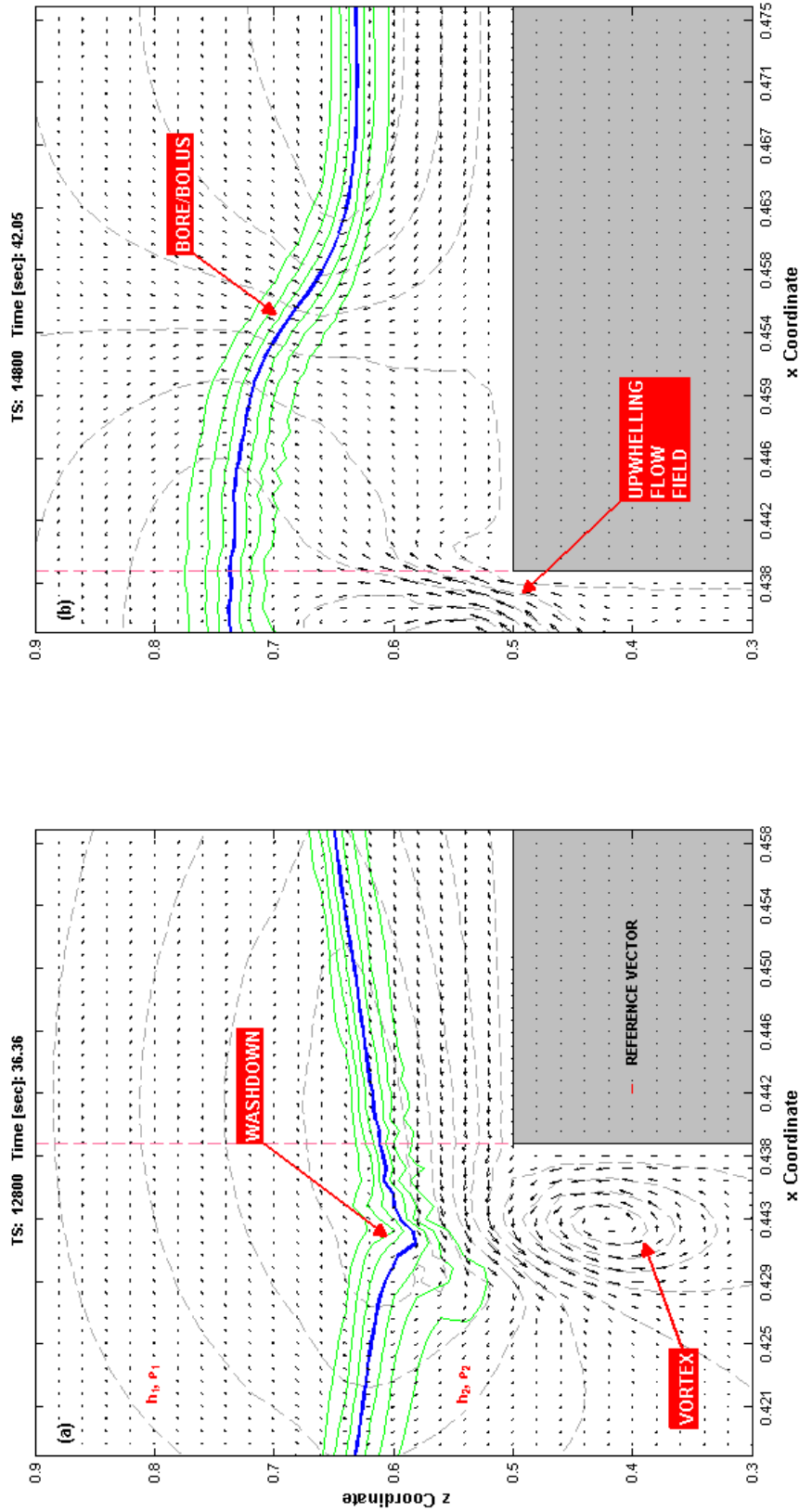


Figure 50. Selected details of the non-dimensional numerical simulation depicted in Figure 49 showing an encounter between a depression-type ISW and a shelf-like obstacle. The vertical dashed line corresponds to the position of the theoretical turning point plane defined by $h_1 = h_2$. Velocity vector field is shown as streamlines contours (dashed lines). (a) “Wash-down” associated with shoaling. (b) “Bore” formation. Also see Appendix B.

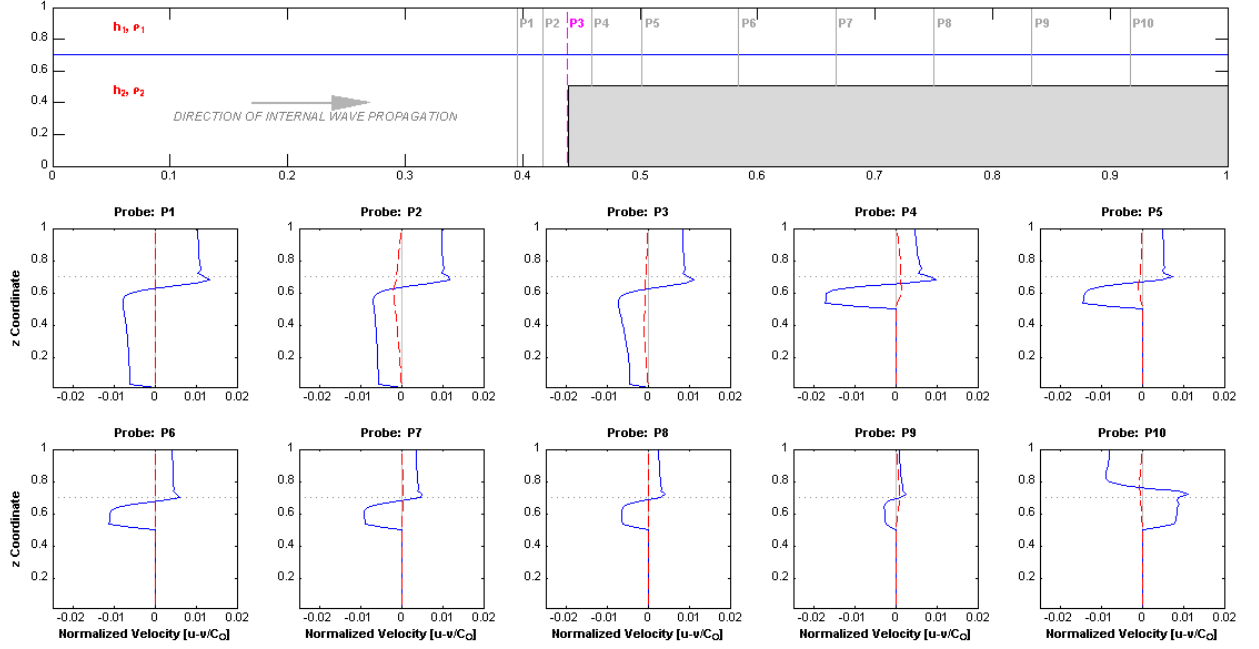


Figure 51. Time series plots of normalized velocity vector profiles for a depression-type ISW at ten uniformly-spaced locations during an encounter with a shelf-type obstacle. Horizontal velocity vectors are blue (or solid) lines. Vertical velocity vectors are red (or dashed) lines. The pycnocline elevation is depicted by a dotted line.

Recalling Figure 35, another perspective on the ISW polarity transformation can be obtained by plotting profiles of the velocity vectors. Figure 51 shows the non-dimensional profiles of the horizontal and vertical velocity vectors at several locations before and after the plane of the theoretical turning point. These profiles are consistent with the example of a depression-type ISW depicted in earlier Figure 35. Figure 51 shows that the ISW speed is generally dominated by the horizontal velocity component at the locations sampled with the exception of the location defined by the plane of the theoretical

turning point. At this location, there is also a strong vertical velocity component likely attributable to the wave's encounter with the vertical face of the obstacle which happens to be coincident with the turning point plane. What is interesting about this collection of velocity profiles is that examples characteristic of an elevation-type ISW profile are absent until the wave has travelled well-beyond the location of the theoretical turning point. The velocity profiles reveal that a complete change in polarity is achieved at a time step occurring somewhere between probe locations P9 and P10. This location generally corresponds to TS 31,400 in the simulation (Figure 49d).

To better understand how the polarity transformation takes place, a second time series of evenly-spaced velocity profiles is presented in Figure 52. These profiles are uniformly-spaced between probe locations 9 and 10 identified earlier in Figure 51. This figure shows that as the simulation proceeds in time, the horizontal velocity vectors migrate from locations associated with a depression-type internal wave (Quadrants II and IV) to locations expected to be associated with an elevation-type wave (Quadrants I and III). This figure also shows that there is a progressive increase in the magnitude of the vertical velocity vector component relative to the horizontal velocity vector until the former exceeds the magnitude of the later. After the transformation in polarity is complete — that is to say the horizontal velocity vectors have migrated to new

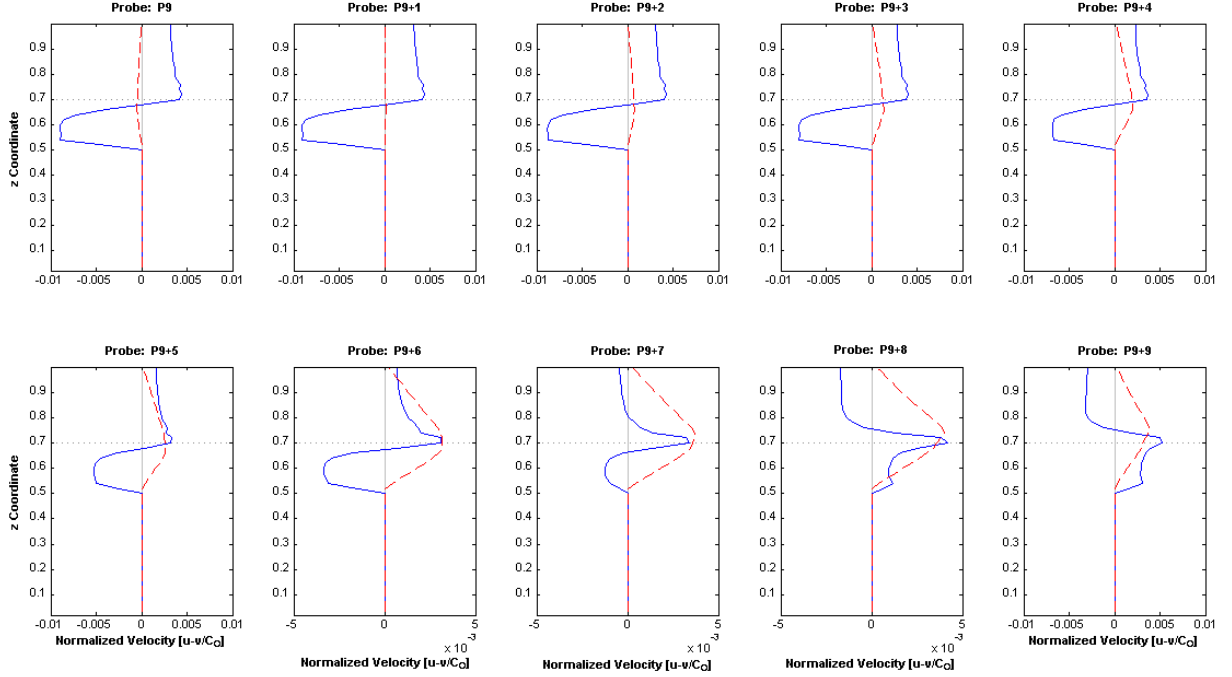


Figure 52. Detailed time series plots of normalized velocity vector profiles for a depression-type ISW transitioning to an elevation-type ISW. Figure shows uniformly-spaced time series plots beginning at the Probe 9 location depicted in Figure 51. The pycnocline elevation is depicted by a dotted line.

locations in opposite quadrants (specifically Quadrants I and III), the magnitude of the vertical velocity vector once again becomes small relative to the horizontal velocity vector.

4.3.1.2 Slope-Shelf Scenario

This non-dimensional simulation begins once again with an already-formed depression-type ISW of mode-1 advancing in open water and after a fashion, advancing to a position where it encounters a short incline whose slope is about 2° . At its' crest, this incline segues onto an elevated plateau that is horizontal for its full extent. The theoretical turning point is located along the

face of the incline between its toe and its crest. Physically, this modeling scenario is the same as the shelf-only scenario described in the previous section of this dissertation in all ways with one exception — the introduction of a short incline at the face of the shelf. According to investigations conducted by Pratson and Haxby (1996), the geometry of this modeling scenario is similar to that which might be encountered at a number of locations along the margins of the continental United States (see Figure 46). The time-series numerical simulation for this so-called “slope-shelf” scenario (earlier Figure 47b) is depicted in Figure 53.

Unlike the shelf-only scenario (Section 4.3.1.1), the slope-shelf scenario shows evidence of interaction between the advancing ISW and the obstacle much earlier in the simulation by virtue of when changes in the symmetry of the pycnocline can be first observed — in this case, at TS 4100 (Figure 53a). Later, at about TS 6200, the trough of the ISW has already crossed the theoretical turning point plane and the pycnocline is now beginning to demonstrate asymmetry in its profile. By about TS 8000 in the simulation (Figure 53a), there is visual evidence (albeit slight) of the formation of an ISW bore not unlike the bore that is commonly associated with a breaking surface wave previously illustrated in Figure 20. However, as the simulation proceeds, there is no overturning of the bore, suggesting that the system parameters for this

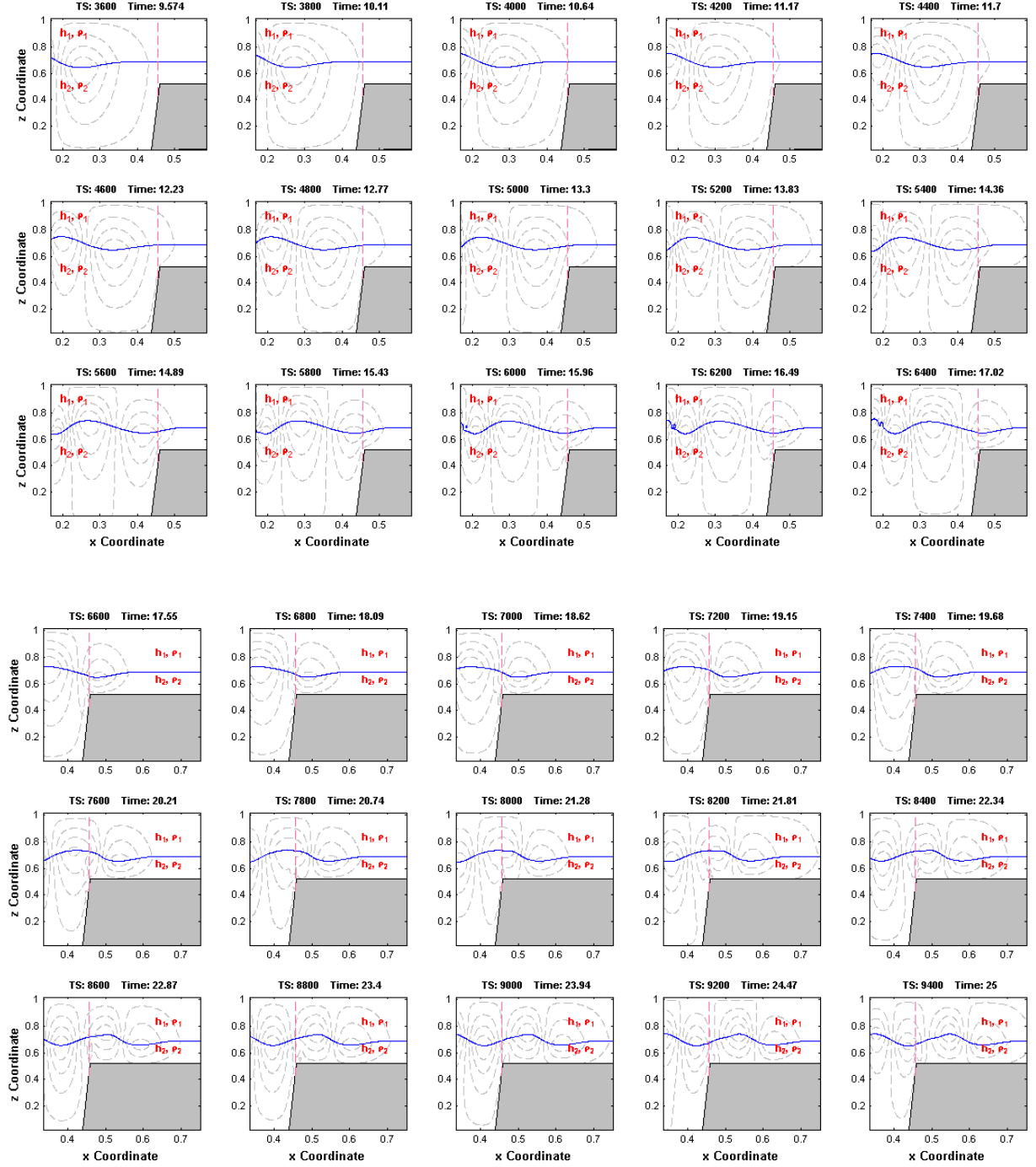


Figure 53a. Non-dimensional numerical simulation showing an encounter between a depression-type ISW and a slope-shelf obstacle. The dashed line corresponds to the vertical position of the theoretical turning point defined by $h_1 = h_2$. $Re = 9.372e4$, $Fn = 0.085$, and $Q = 24$ corresponding to a slope of about 2.4° .

simulation satisfy a condition of weak non-linearity (Vlasenko and Hutter 2002).³² In subsequent time steps (TS 11000 – Figure 53b), this bore has begun to form roughly into an elevation-type ISW. By TS 13,200, an ISW of elevation is clearly evident in the simulation. However, as was the case with the shelf-only numerical simulation trial, visual evidence of the original ISW persists until well-after the wave train has passed the turning point location as suggested by a single residual stream line at TS 15,200 (Figure 53b).

³² There are two other plausible explanations for the absence of bore formation. The first is that the grid spacing may be too wide to simulate this hydrodynamic feature as it passes. A grid spacing that was too large would tend to average-out or ‘smear’ or what might be sharper pycnocline profile. More sophisticated (commercial) CFD programs can compensate for this lack of resolution by making the grid or finite element net much finer in the vicinity of a shock wave or bore.

The other possible explanation could be due to the numerical scheme itself. Once the wave breaks, or even close to the time before it breaks, the finite difference scheme might be inadequate to capture the physical details of wave breaking and overturning. For example, if the two fluids in question were immiscible (oil and water), the numerical results would show a distinct oil phase and water phase completely connected and not oil particles dispersed in water as you would expect in the reality. Special CFD numerical techniques like ‘particle-in-cell’ (Harlow 1955, 1987) might be better suited for simulating this type of phenomenon. In summary, at the time of wave breaking, the finite difference technique appears to be adequate, although the phenomena might demand a higher grid resolution in the vicinity of the breaking wave.



Figure 53b. Continued.

Additional insights concerning the interaction between the ISW and the slope-shelf obstacle can be obtained from the examination of higher-resolution figures. From inspection of the numerical wave simulation depicted in Figure 53, it appears that the shoaling process begins at about TS 3800 or so. However, this sequence of figures also reveals that not all aspects of the breaking progression occurred through the course of the simulation. Appendix C contains higher-resolution figures of this particular modeling scenario beginning about TS 3800. The figures in this appendix reveal that the pycnocline does not appear to shoal or break. What does appear is the formation of a vortex or gyre along the face of the obstacle. This feature forms as the trough of the pycnocline approaches the vertical plane corresponding to the location of the theoretical turning point. Subsequent figures from the simulation sequence show that the vortex does not become well-defined until after the trough has passed beyond the turning point plane. Later in the simulation sequence, the higher-resolution figures in Appendix C show that this vortex transitions into a plane or zone of strong upwelling flow. These two aspects of the numerical simulation are depicted in detail in Figure 54.

Figure 55 shows the normalized velocity profiles for both the horizontal and vertical velocity vectors at various probe positions in the computation domain as the ISW passes those locations. Once again, these profiles are

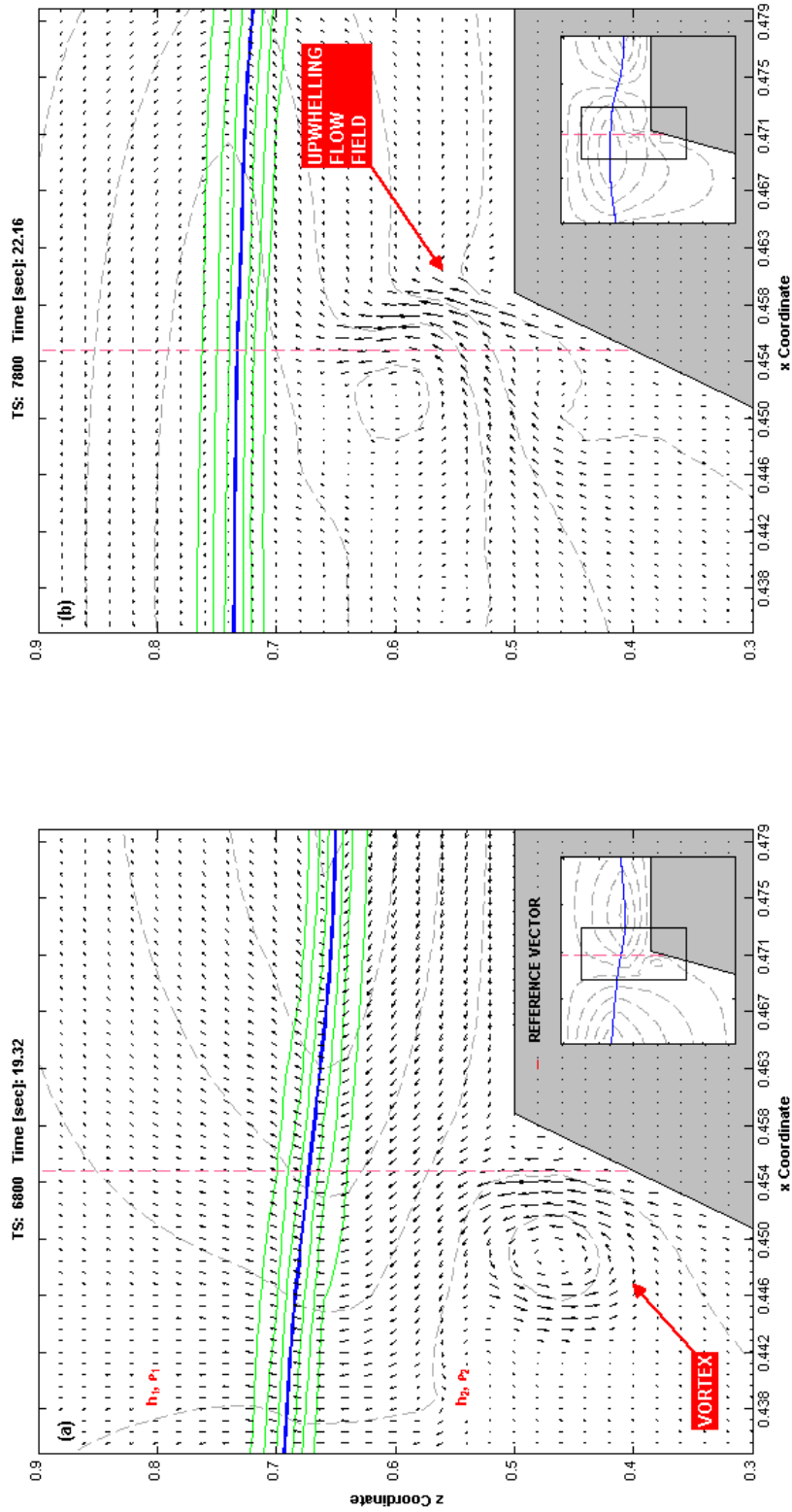


Figure 54. Selected details of the non-dimensional numerical simulation depicted in Figure 53 showing an encounter between a depression-type ISW and a slope-shelf obstacle. The vertical dashed line corresponds to the position of the theoretical turning point plane defined by $h_1 = h_2$. Vectors in the velocity field are shown as streamlines (dashed lines). (a) Well-developed vortex along the slope face after the ISW has passed the theoretical turning point plane. (b) Upwelling field located in the vicinity of slope crest as a secondary ISW of elevation is passing. Additional details of this particular numerical simulation can be found in Appendix C.

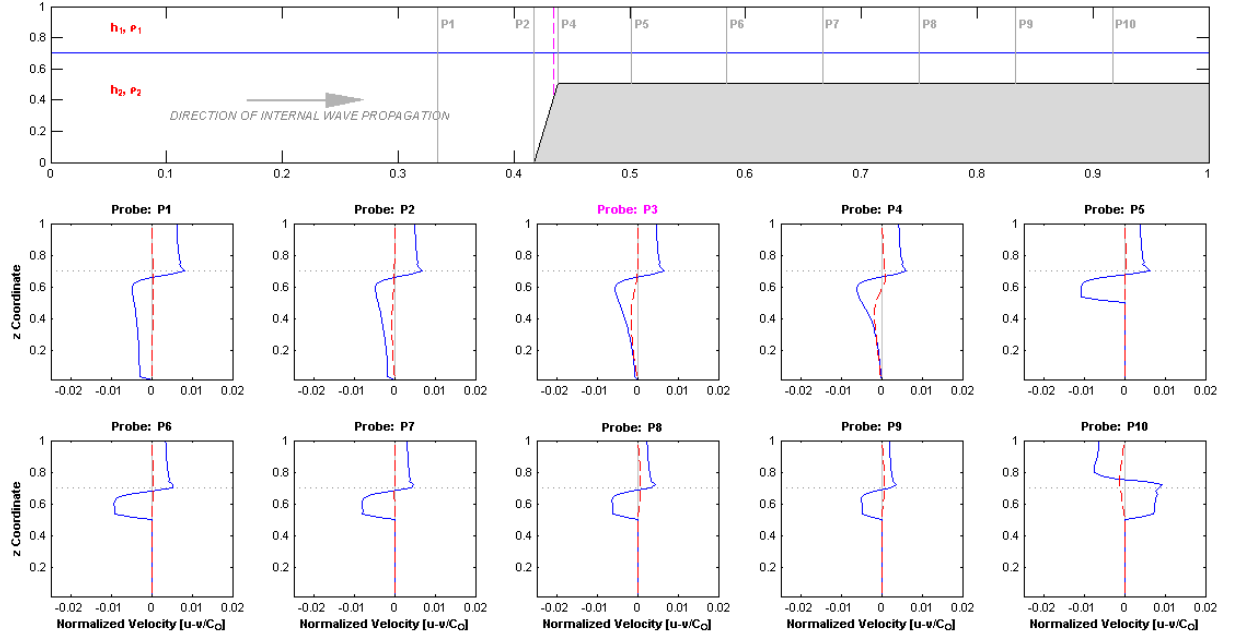


Figure 55. Time series plots of normalized velocity vector profiles for a depression-type ISW at ten uniformly-spaced locations during an encounter with a slope-shelf obstacle. Horizontal velocity vectors are blue (or solid) lines. Vertical velocity vectors are red (or dashed) lines. The pycnocline elevation is depicted by a dotted line.

consistent with profiles for a depression-type ISW depicted earlier in Figure 35. This figure shows that the wave speed continues to be dominated by the horizontal velocity component at the locations sampled. However, unlike the shelf-only trial, the change in polarity from a depression-type ISW to a wave of elevation occurs earlier in the slope-shelf simulation. This change can be observed between probe Locations P4 and P5. Figure 56 shows the details of the polarity reversal in the context of the velocity vector profiles.

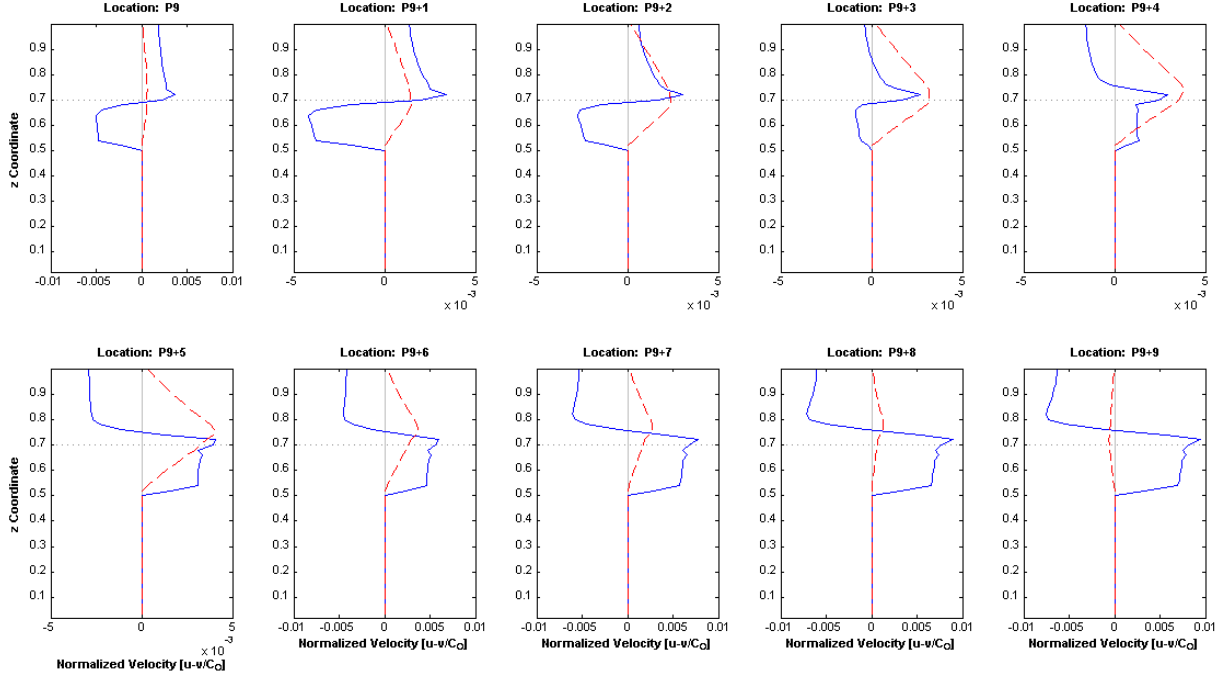


Figure 56. Detailed time series plots of normalized velocity vector profiles for a depression-type ISW transitioning to an elevation-type ISW. Figure shows uniformly-spaced time series plots beginning at the Probe 9 location depicted in Figure 55. The pycnocline elevation is depicted by a dotted line.

4.3.1.3 Slope-Only Scenario

The first two numerical simulation trials described in this dissertation demonstrated how a mode-1 type ISW interacts with obstacles representing analogues to the continental shelf/continental slope. Those simulations confirmed a key ISW property concerning the onset of wave polarity reversal. Theoretically, an ISW will undergo a reversal in polarity when topographic conditions on the seafloor relative to the water depth are such that $h_1 = h_2$, corresponding to when the vertical plane defining the turning point has been encountered.

Another useful scenario to evaluate is the interaction between an ISW and an obstacle best described as a uniform slope. Unlike the earlier two trials, though, under this modeling scenario, a mature fully-developed ISW experiences a constantly changing (diminishing) depth condition for the duration of the simulation. That is, h_1 remains essentially constant during the course of the simulation while the depth of h_2 decreases, approaching zero owing to the existence of the uniform slope. As the ISW approaches and traverses the theoretical turning point plane, it is possible to observe the evolution of breaking-like phenomena. The simulation also reveals the ultimate fate of the ISW once it has reached the terminus of the computational domain. In this case, the simulation shows what happens to the advancing ISW when the depth of the h_2 layer approaches zero.

Figure 57a shows the non-dimensional numerical simulation in progress at about TS 20,000. The ISW is a depression-type of mode-1. Also apparent in the simulation is the lesser trailing elevation wave followed by the dispersive wave train. At this point in the simulation, the streamlines associated with the leading ISW are well-developed. Moreover, the streamline contours are also beginning to reveal the effects of the obstacle as their orientation (geometry) are already parallel to the face of the slope. By about TS 26,000 (Figure 57b), the simulation shows signs of interaction between the ISW, as represented by the

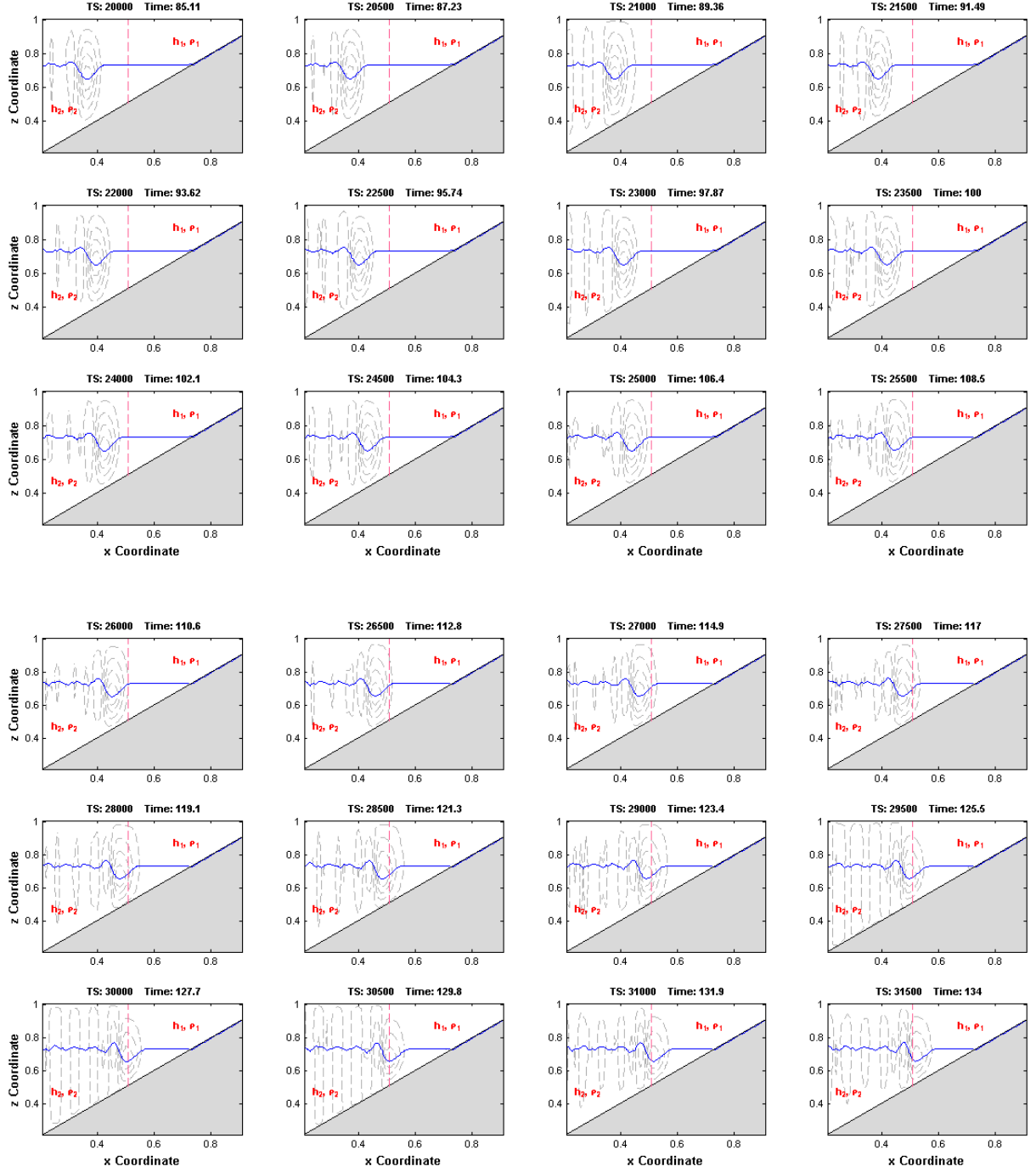


Figure 57a. Non-dimensional numerical simulation showing an encounter between an elevation-type ISW and an extended slope-type obstacle. The vertical dashed line corresponds to the position of the theoretical turning point defined by $h_1 = h_2$. $Re = 2.303e5$, $Fn = 0.074$, and $Q = 50$ corresponding to a slope of about 1° .

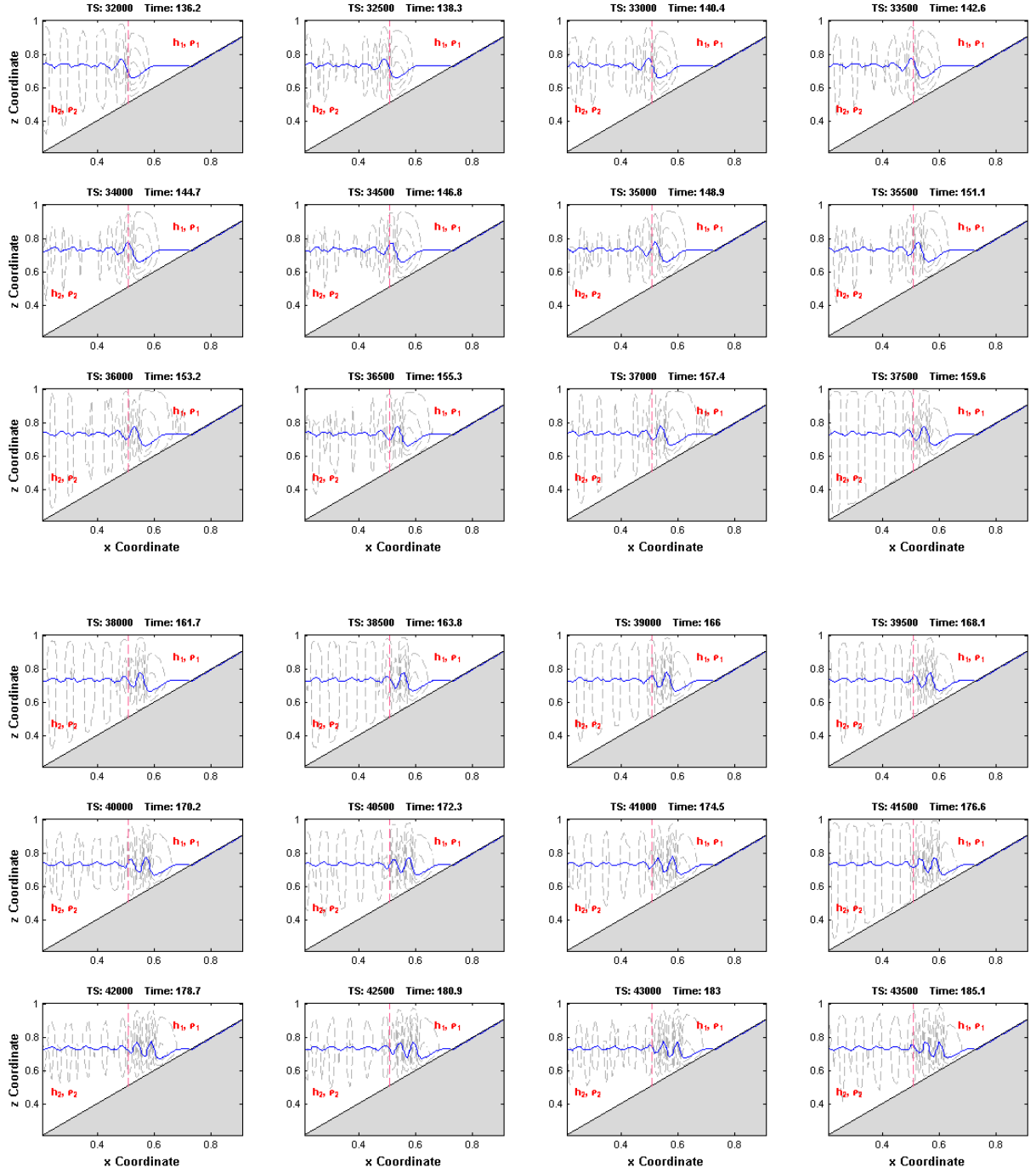


Figure 57b. Continued.

pycnocline, and slope. The ISW appears to be less sinusoidal and more asymmetric in form. As part of the interaction process, the downwind face of the internal wave pycnocline has become aligned with the gradient of the slope.

By about TS 29,500, the trough of the pycnocline has reached the plane of the theoretical turning point and the profile of the ISW is clearly asymmetrical. Moreover, the trailing face of the ISW is beginning to rotate forward and is increasing in height (elevation) suggesting that a polarity transition is underway. However, there is no evidence of the formation of a bolus, as had been the case with the previous two trials. What is also noteworthy about this simulation is that the streamline contours at the front of the ISW are beginning to separate (i.e., spread apart) whereas the streamline contours at the back of the wave, in the vicinity of the theoretical turning point plane, are increasing in density suggesting greater (vertical) fluid particle velocities in the back of the wave than in the front. By about TS 37,500 (Figure 57b), there is a well-formed elevation-type internal present in the simulation.

A short time later, at about TS 39,500, a second well-developed elevation ISW has appeared in the simulation (Figure 57b). Successive time steps in the numerical simulation show that a train of multiple ISWs have developed beyond the location of the theoretical turning point plane (Figure 57c). Also present now

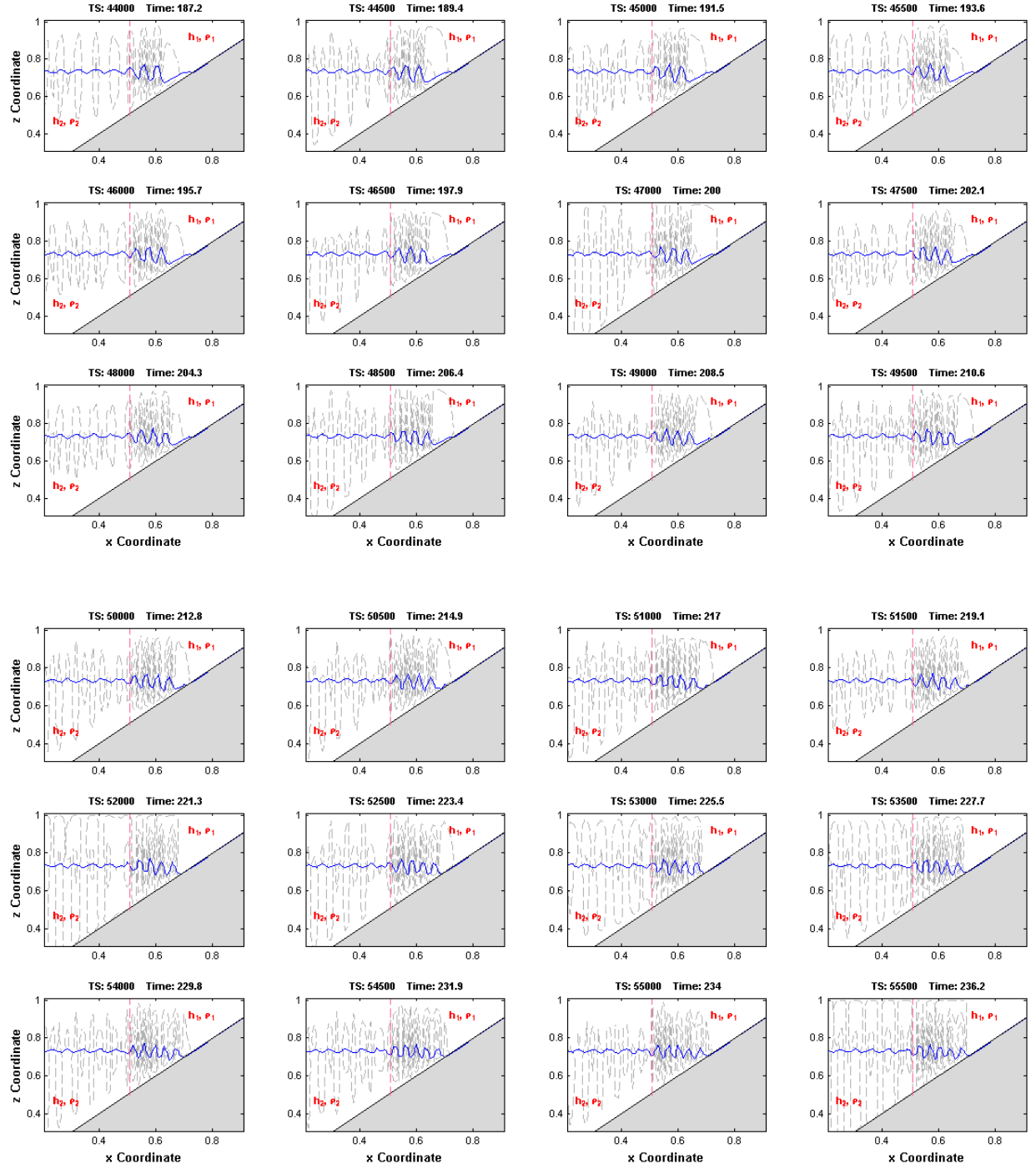


Figure 57c. Continued.

is a collection of densely-packed streamline contours. At about TS 56,000 (Figure 56d), the simulation reveals that the wave train is comprised of a collection of uniformly-spaced ISWs progressing up the face of the slope. The wave train appears to reach its maximum horizontal extent (up the face of the slope) at about TS 69,000 (Figure 57d). After this time, the wave train appears to be defined by a quasi-stationary collection of small boluses. In a field study by Bourgault et al. (2007), they observed the occurrence of these boluses. Upon review of the details of this simulation, found in Appendix D, this collection of boluses appear to be a collection small elevation-type ISWs whose origin appears to be attributed to the dispersive wave train.

Additional insights concerning the interaction between the ISW and an extended slope-type obstacle can be obtained from the examination of higher-resolution figures. From inspection of the numerical wave simulation depicted in the series of exhibits comprising Figure 57, the shoaling process appears to begin at about TS 21,000, as this is the approximate time in the simulation that the streamline contours begin to encounter the obstacle. However, unlike the previous two simulations described earlier in this dissertation, Figure 57 reveals that breaking progression for an internal wave encountering an extended slope-type obstacle manifests itself somewhat differently. To evaluate the details of this breaking progression in more detail, Appendix D contains higher-resolution

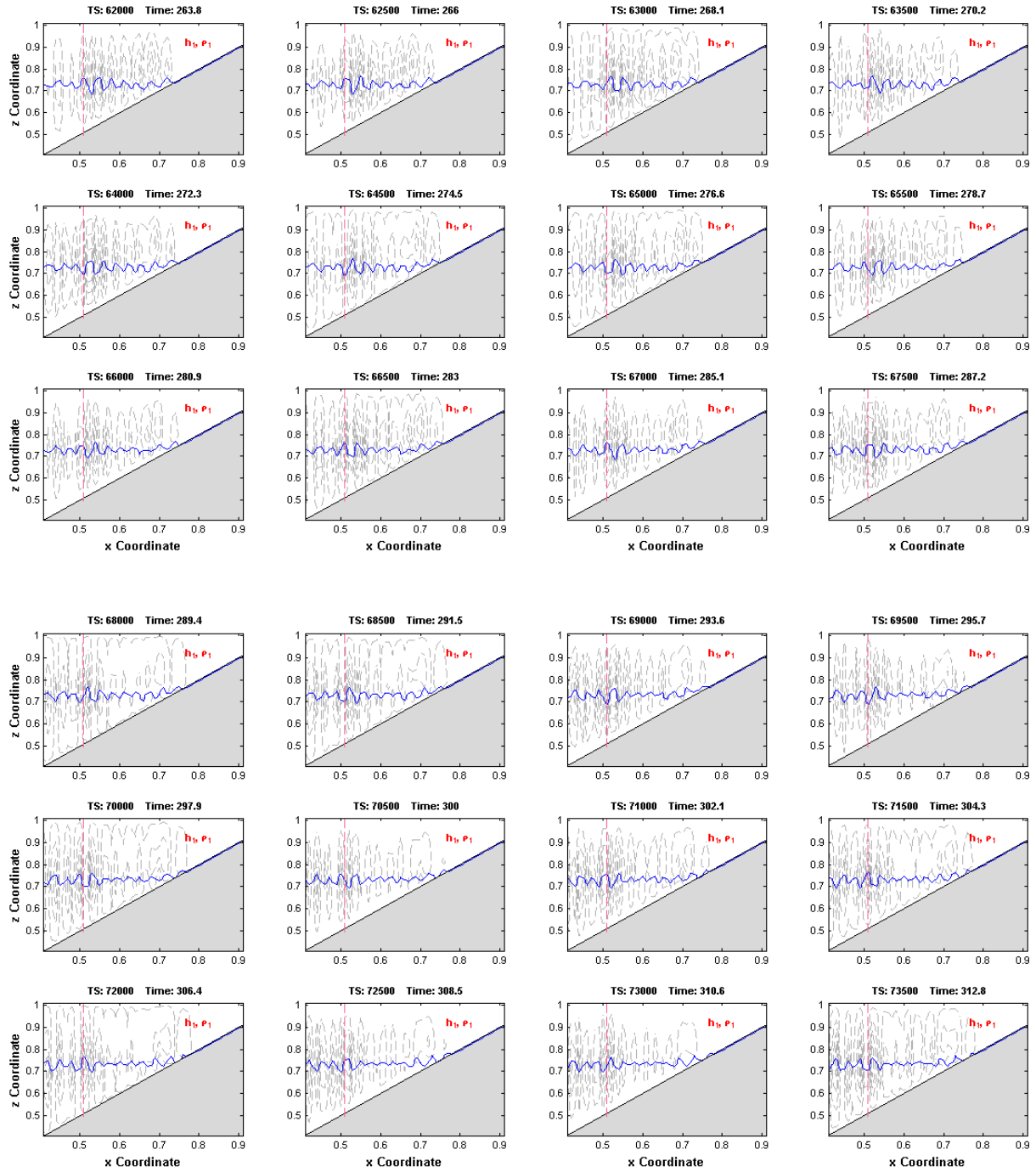


Figure 57d. Continued.

figures of this particular modeling scenario beginning about TS 18,000 in the simulation. Based on an inspection of the figures in this appendix, it can be observed that the ISW does appear to shoal and break, but in a manner slightly different from the first two simulations. By about TS 29,000, the profile of the ISW is visibly asymmetric at this point in the simulation as its trough has reached the approximate location of the theoretical turning point plane (defined as $h_1 = h_2$). Because of shoaling, the pycnocline associated with the incoming depression-type internal wave now appears to have evolved into a wash-down like feature usually considered to be a precursor to wave breaking. At least two elevation-type ISWs also now appear in the numerical simulation behind the leading wave.

As the simulation progresses, the wave-front continues to advance. Subsequent figures from the simulation sequence show additional elevation-type ISWs evolve as the wave train passes through the theoretical turning point plane. By TS 48,000, about six elevation-type waves (or boluses) appear in the simulation. Later in the simulation sequence, the exhibit shows that the collection of elevation-type waves/boluses grow in number and appear to “march” up the face of the slope. Recalling the ISW breaking classes proposed by Emery and Gunnerson (Figure 19), this simulation appears to be characteristic of the

“internal surf” class in that the computational scenario has produced multiple boluses. Selected details of this simulation are depicted in Figure 58.

Figure 59 shows the non-dimensional profiles for the horizontal and vertical velocity vectors at several locations before and after the location of the theoretical turning point. When compared to the other trials described in this dissertation, this figure shows an exceedingly strong horizontal velocity component for the ISW, through the course of the simulation, as it advances up the slope. Inspection of Figure 59 also shows that the reversal in ISW polarity appears to occur at some point in the numerical simulation between Probe locations 8 and 9. This transition in polarity is captured when the velocity profiles are plotted, as illustrated in Figure 60. Unlike the earlier trials, what is conspicuous about this particular modeling scenario is that there is a persistence of a much larger vertical velocity component, at most of the probe locations, for longer in the simulation.

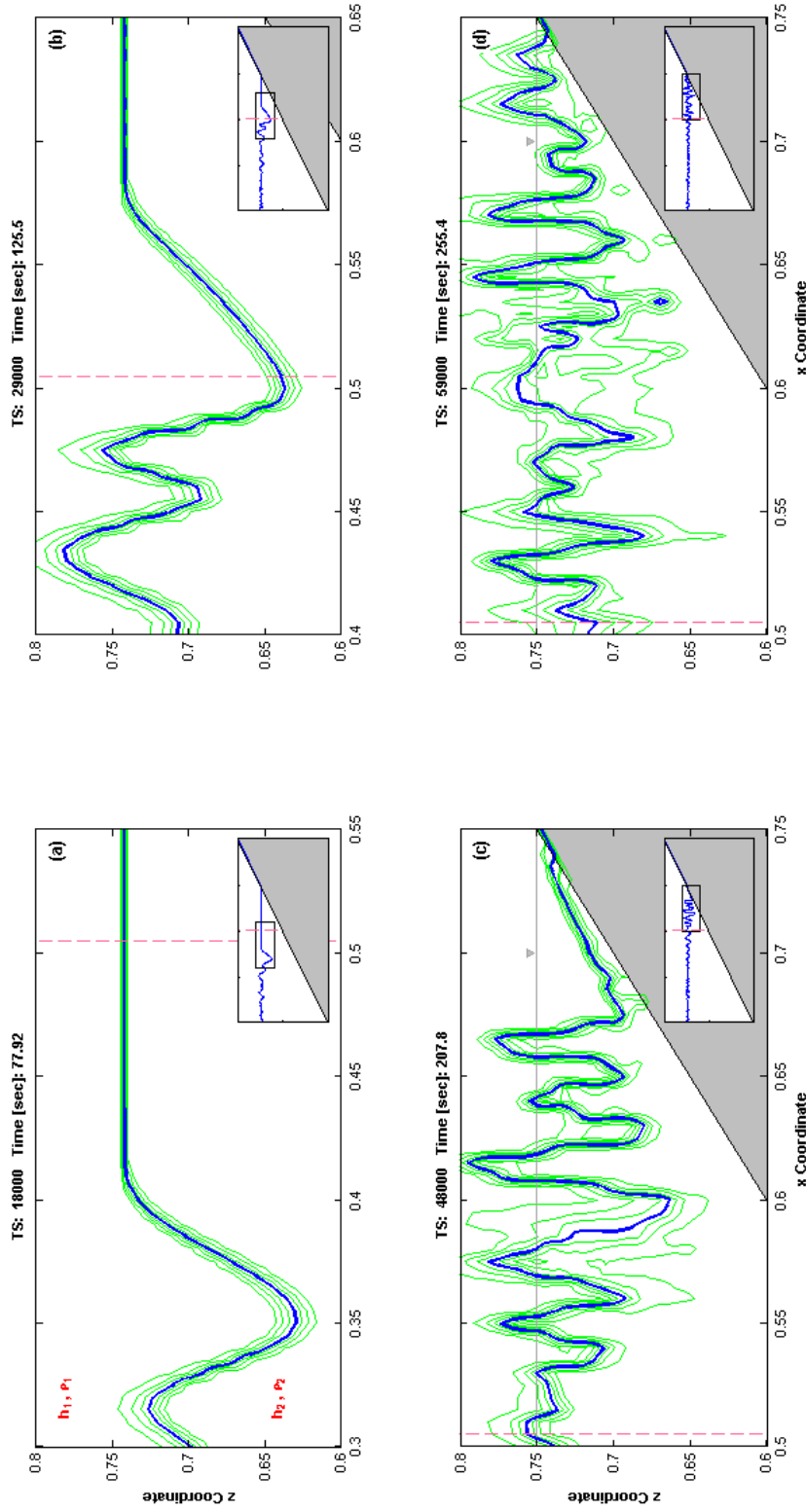


Figure 58. Selected details of the non-dimensional numerical simulation depicted in Figure 57 showing an encounter between a depression-type ISW and an extended slope-type obstacle. The vertical dashed line corresponds to the position of the theoretical turning point plane defined by $h_1 = h_2$. Insets within each figure show the relative location of the ISW to the obstacle at the time step indicated. (a) Internal solitary wave approaching the theoretical turning point plane. (b) Onset of polarity reversal and early formation of multiple, secondary elevation-type ISWs. (c) Wave train advancing (or marching) up the slope. Static pycnocline is indicated. (d) Wave train advancing (or marching) up the slope.

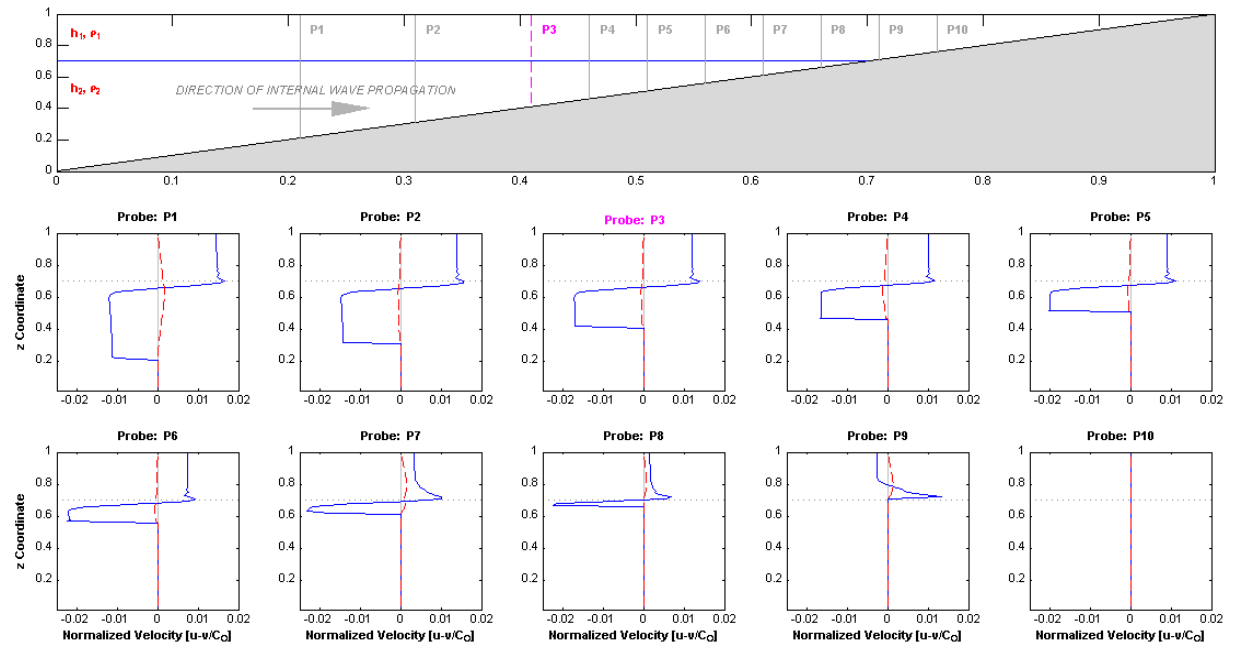


Figure 59. Time series plots of normalized velocity vector profiles for a depression-type ISW at ten uniformly-spaced locations during an encounter with an extended slope obstacle. Horizontal velocity vectors are blue (or solid) lines. Vertical velocity vectors are red (or dashed) lines. The pycnocline elevation is depicted by a dotted line.

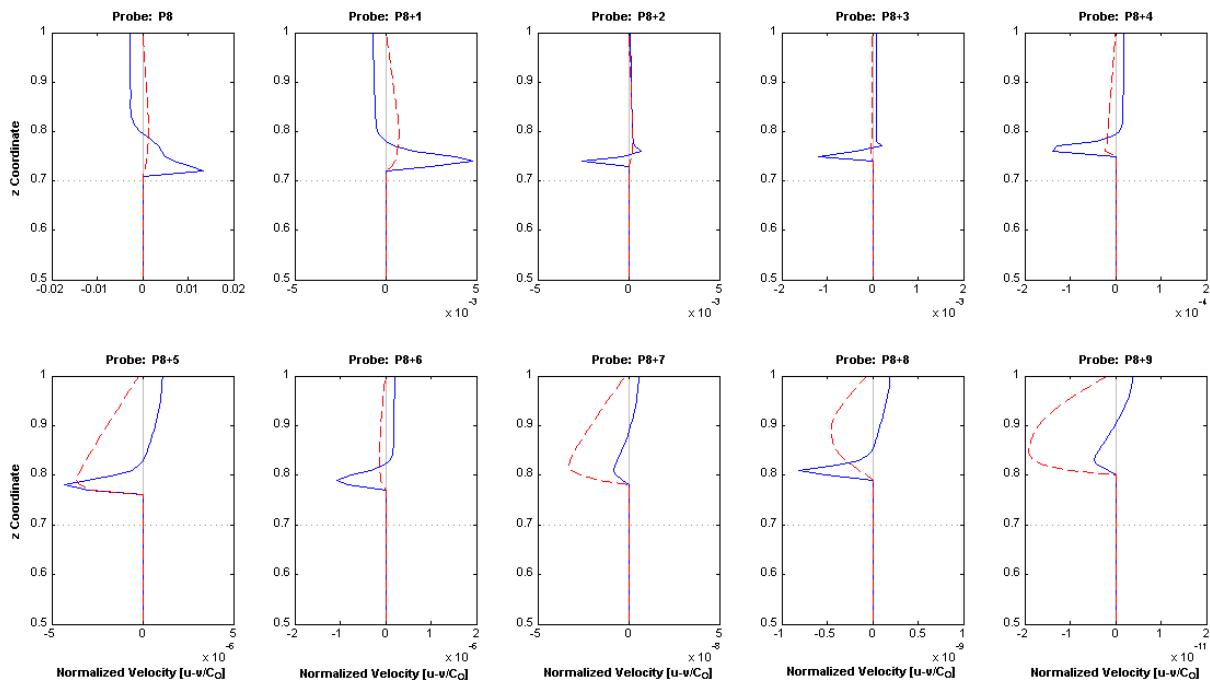


Figure 60. Detailed time series plots of normalized velocity vector profiles for a depression-type ISW transitioning to an elevation-type ISW. Figure shows uniformly-spaced time series plots beginning at the Probe 8 location depicted in Figure 59. The pycnocline elevation is depicted by a dotted line.

4.3.1.4 So-called Short-Slope Scenario

The first series of numerical simulations described in Sections 4.3.1.1 and 4.3.1.2 (respectively, the shelf and the slope/shelf simulations) successfully demonstrated how a depression-type ISW is transformed into an elevation-type ISW when the plane of the theoretical turning point is traversed. Examples of the wave breaking classes produced during these simulations were limited to the so-called “internal swash” classes – Classes 3 and 4 as suggested by Emery and Gunnerson (1973) in Figure 19. Two of the simulations demonstrated quasi-

breaking phenomena associated with the theoretical turning point, including the production of a bolus (albeit limited). However, a simulation capable of producing a wave-breaking progression that demonstrated all four phases in the sequence is sought. To this achieve the full wave-breaking progression, a numerical simulation involving a much-shorter slope was evaluated.

The numerical simulation depicting the interaction between an ISW and the so-called short-slope obstacle can be found in Figure 61. This particular computational arrangement comports with the experimental wave tank set-up used by Michallet and Ivey (1999) to successfully evaluate ISW breaking on a uniform slope. For this trial, the aspect ratio Q is equal to about 23, producing an incline whose slope was about 2.5° degrees. Unlike the previous numerical simulation trials, evidence of shoaling appears well-before the ISW has reached the face of the obstacle. Figure 61a shows a well-developed ISW of a mode-1 type at about TS 18,500 in the simulation. The ISW has yet to encounter the obstacle as the geometry of the streamlines are ellipsoidal, consistent with an unfettered ISW advancing through open water. By about TS 19,300, the streamlines are now showing signs of deformation as the orientation of the outermost streamline contours of the ISW are beginning to parallel to the obstacles' face. By about TS 20,300, the elevation of the pycnocline has begun to recede down the face of the slope. This decline takes place while the trough of

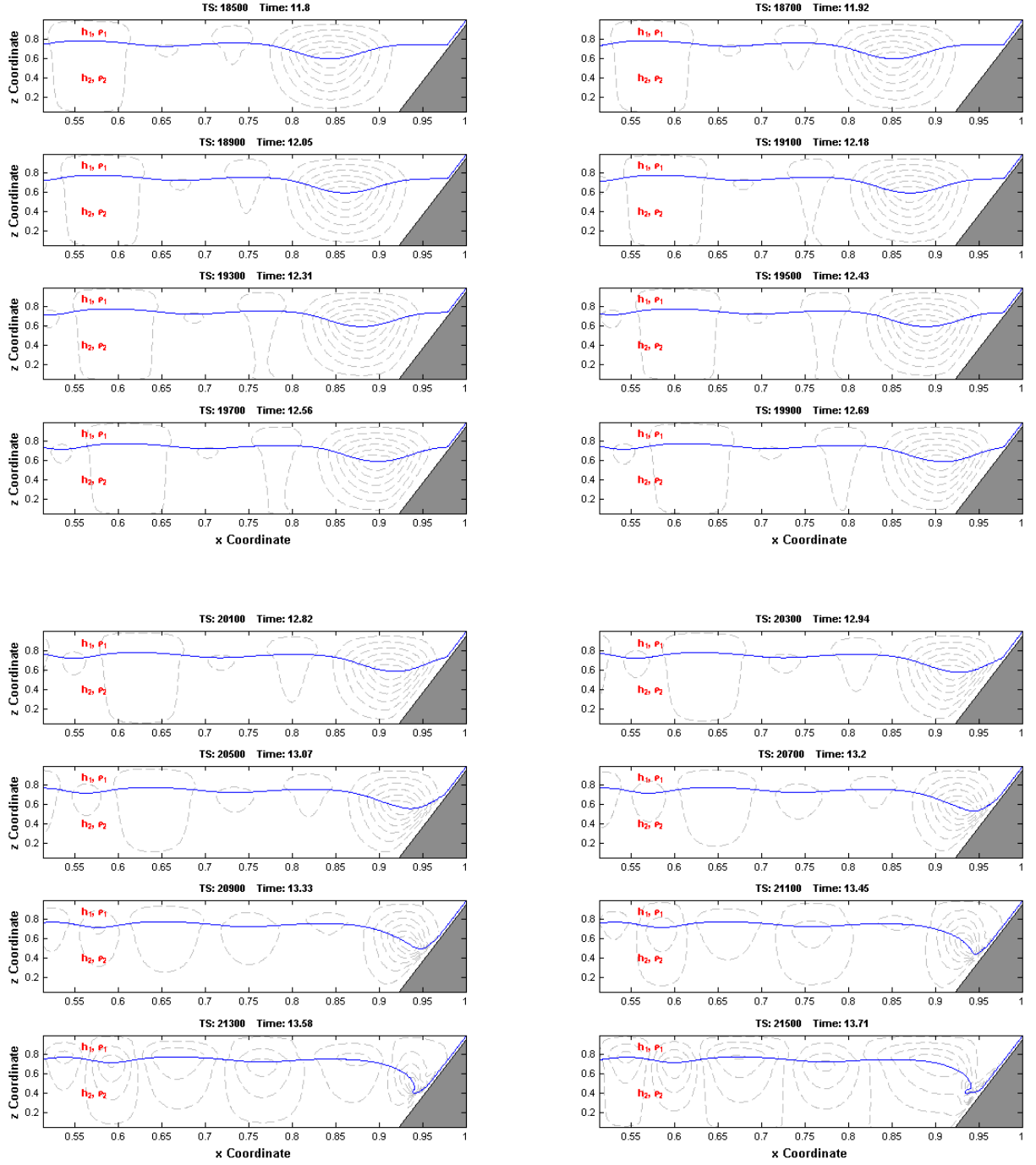


Figure 61a. Non-dimensional numerical simulation showing an encounter between a depression-type ISW and a so-called short-slope obstacle. $Re = 2.096e4$, $Fn = 0.075$, and $Q = 22.9$ corresponding to a slope of about 2.5° .

the ISW itself is still distal relative to the face of the obstacle. In subsequent time series, as the internal wave continues to approach the obstacle, the elevation of the pycnocline continues to decline demonstrating a precursor feature of wave breaking generally referred to as “backrush” or “wash-down.” The simulation also shows that the advance of the ISW is accompanied by a compliment of streamline contours whose geometry mirrors the face of the slope as the time series progresses.

By about TS 21,100, the decline (decay) in the ISW’s amplitude has reached its lowest vertical extent in the simulation. Figure 61b shows a depression-type ISW shoaling (breaking) at about TS 21,500 is evident by virtue of an overturning wave front. In subsequent time steps, the simulation shows that there is a reversal in the decline of the pycnocline’s elevation and the density interface is now beginning rise and regain some of its original elevation (Figure 61b). By TS 9400, an outline of a bolus is now apparent in the simulation. What is also interesting about this particular portion of the numerical simulation is that from about TS 21,700 to TS 22,500, the location of the streamline orbital foci are quasi-stationary. Moreover, as the bolus grows in subsequent time steps (TS 22,500 to TS 24,700), the streamline contours appear to both migrate in a direction opposite to that of the wave’s forward motion as well as diminish in intensity by virtue of a decline in their relative density. By

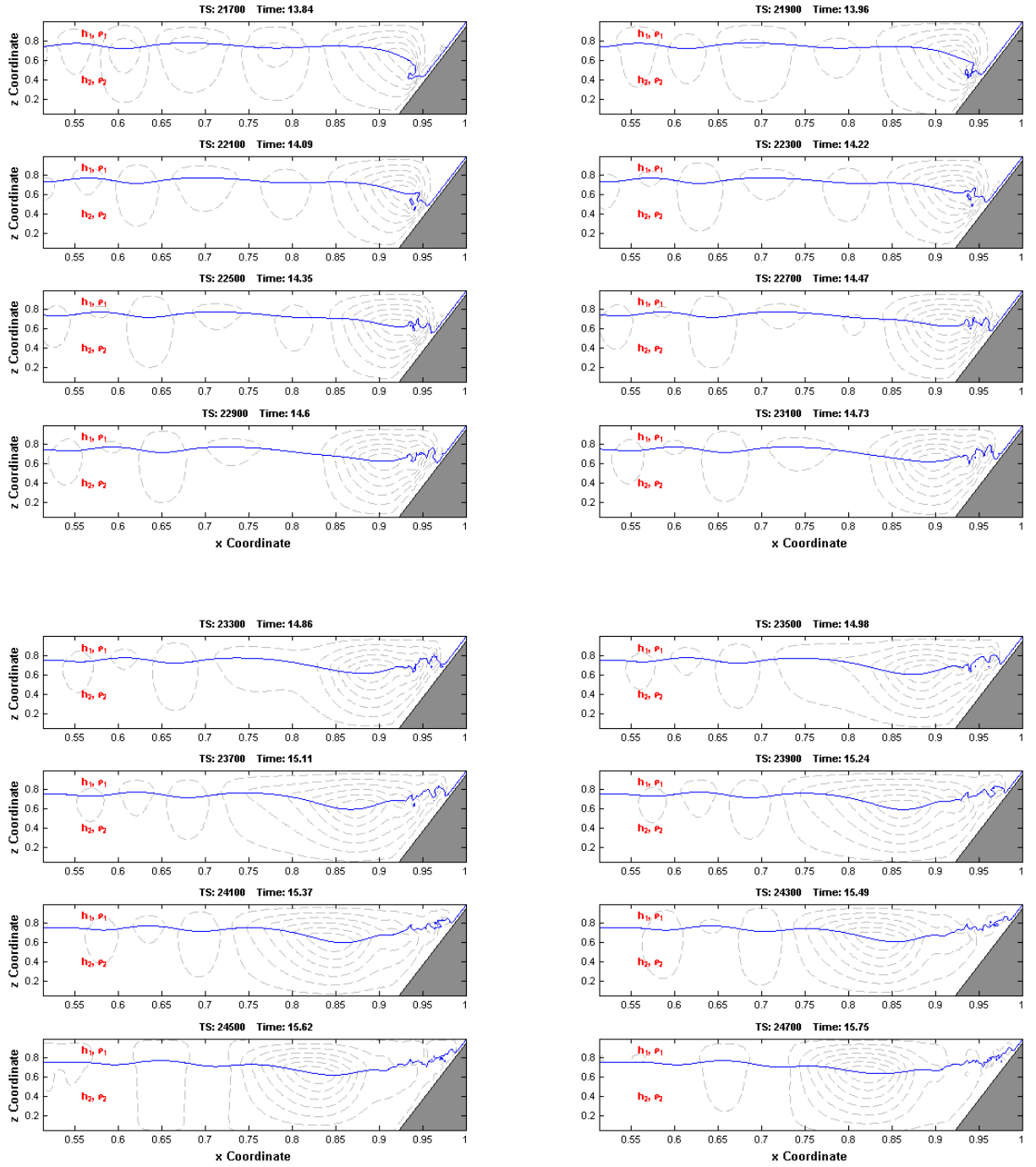


Figure 61b. Continued.

about TS 25,700 (Figure 61c), the bolus appears to have reached its greatest extent of advancement up the slope.

The progression in the wave-breaking sequence depicted in the series of exhibits comprising Figure 61 is not unlike that generically described by Galvin (1968), Lynch (1982), and others, but also the experimental demonstration by Helfrich (1992) Michallet and Ivey (1999). Additional insights concerning the interaction between the ISW and this type of obstacle can be obtained from the examination of figures possessing higher-resolution details of the simulation. Appendix E contains a higher-resolution sequence of the time series plots of the wave breaking sequence depicted in Figure 61. These plots also include the introduction of velocity vectors. In general, the four principal phases in the ISW-breaking progression are shown in Figure 62. These phases include the initial entrainment of the ISW demonstrated by “wash-down” at about TS 21,100 (Figure 62), “wave breaking” and overturning of the pycnocline at about TS 21,600 (Figure 62b), the formation of a “bolus” or bore-like feature at about TS 23,100 (Figure 62c), and ultimately “run-up” or wave surge up the obstacle slope at about TS 25,000 (Figure 62d). At several steps in the simulation, K-H-like features are also evident. These details are revealed in the higher-resolution exhibits found in Appendix E.

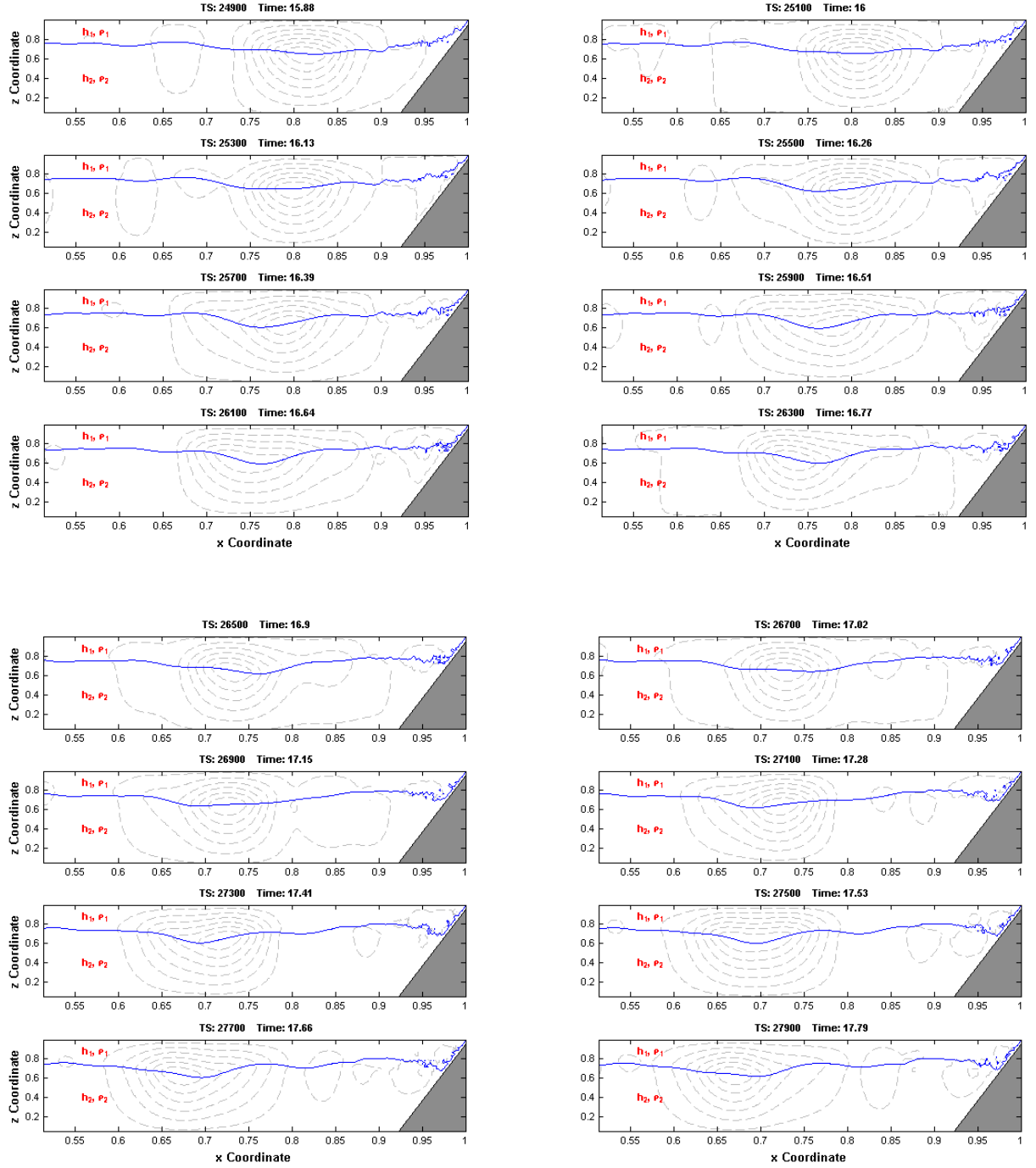


Figure 61c. Continued.

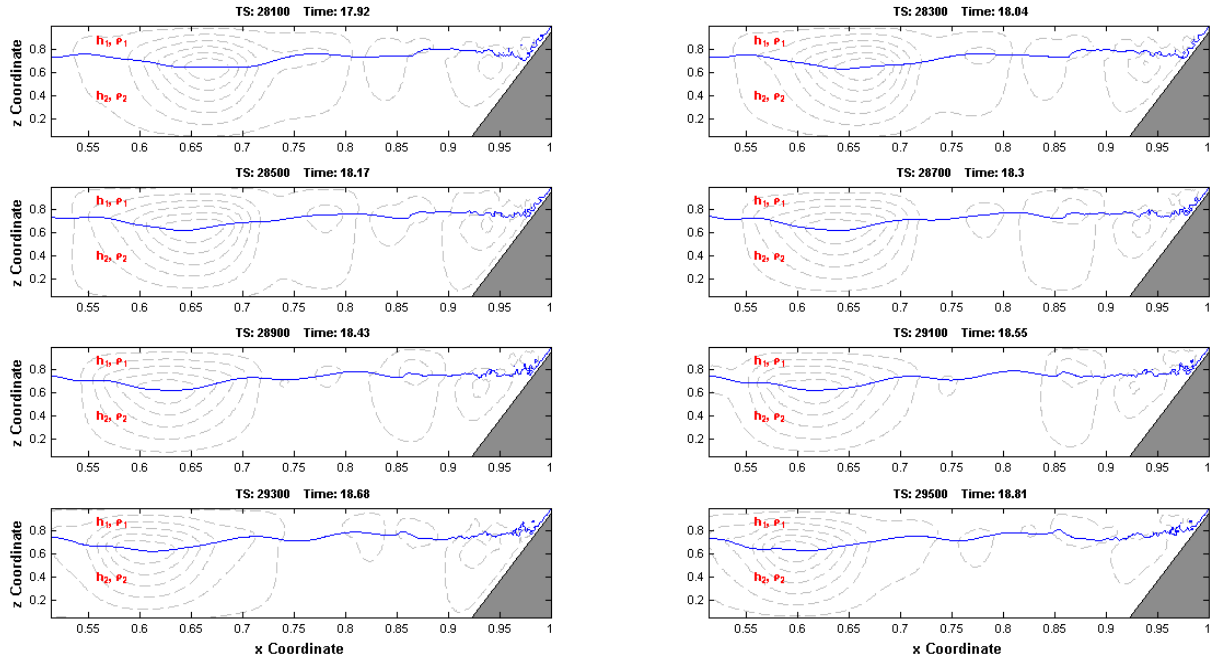


Figure 61d. Continued.

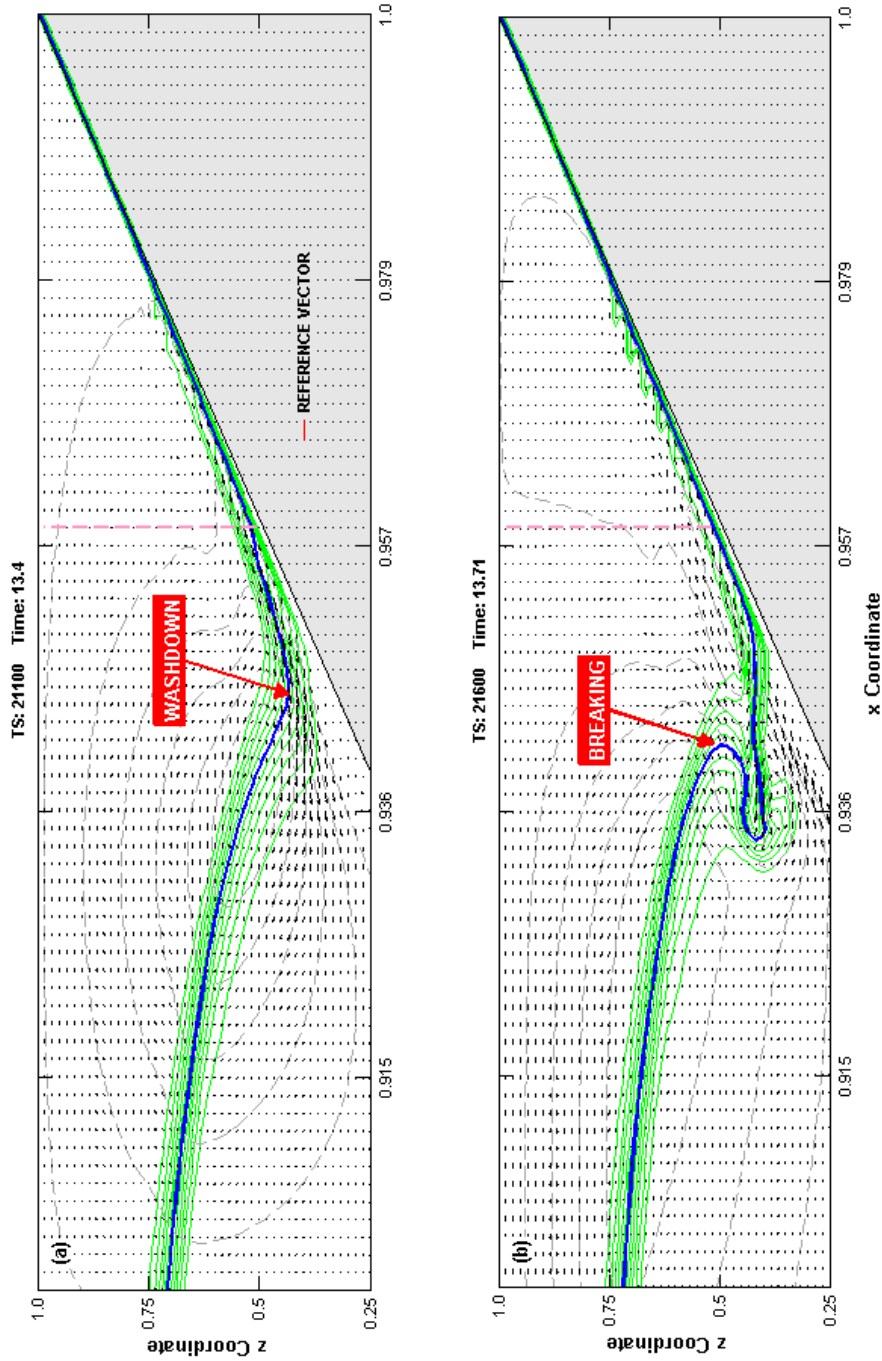


Figure 62. Selected details of the non-dimensional numerical simulation depicted in Figure 61 showing an encounter between an elevation-type ISW and a so-called short-slope obstacle. The vertical dashed line corresponds to the position of the theoretical turning point plane defined by $h_1 = h_2$. Vectors in the velocity field are shown as are streamline contours (dashed lines). (a) Onset of shoaling/breaking first defined by “wash-down.” (b) “Breaking” of ISW defined by the overturning of the pycnocline. Additional details of this particular numerical simulation can be found in Appendix E.

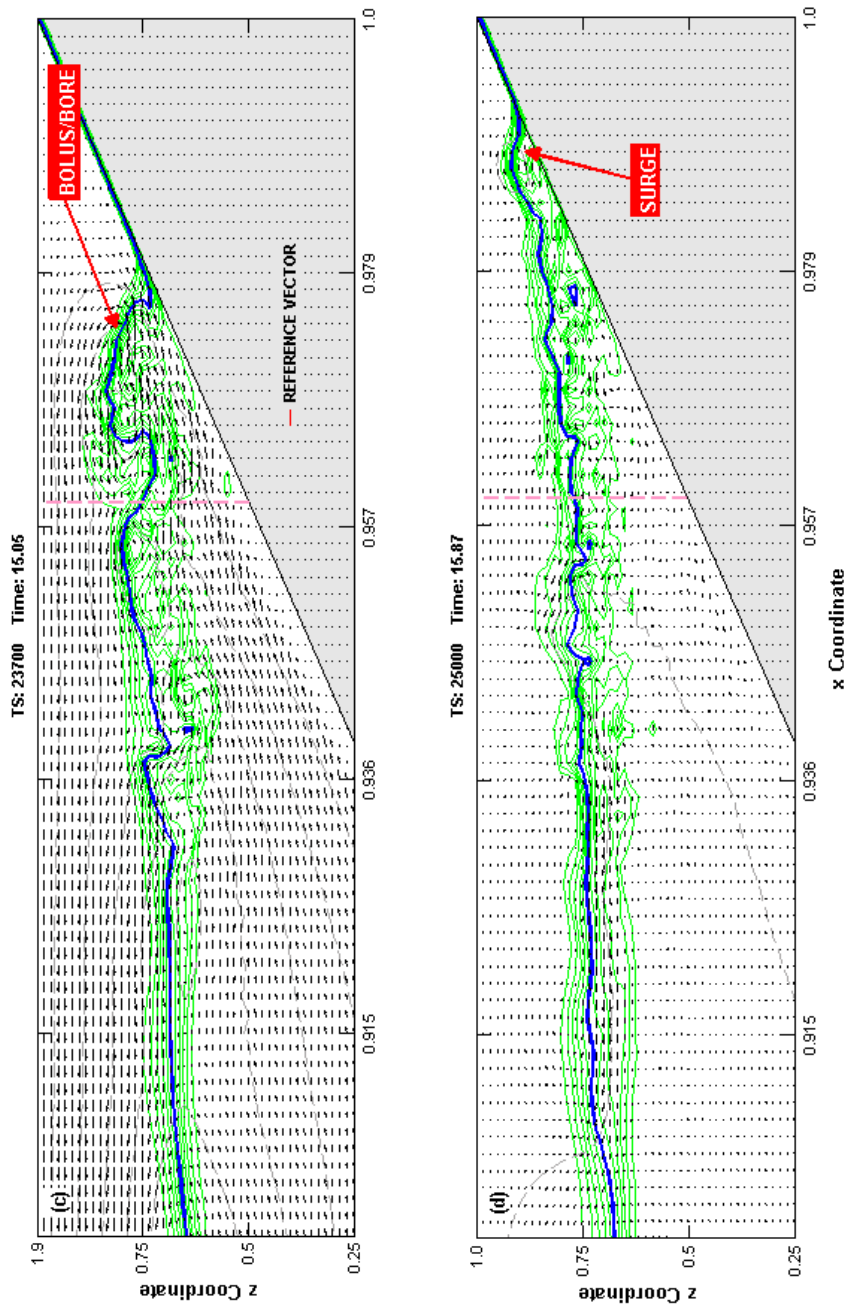


Figure 62. Continued. (c) Example of bolus (or bore) advancing up slope at a point beyond the plane of the theoretical turning point (vertical dashed line). (d) Maximum run-up elevation of breaking ISW defined by pycnocline surge up the face of the obstacle.

4.3.1.5 Reverse Shelf-Only Scenario

The simulations described thus far in this dissertation begin with an ISW forming in deep water, travelling some distance, and then entering shallow water where it shoals. Once the theoretical turning point — the vertical plane defined by $h_1 = h_2$ — has been traversed by the advancing ISW, a reversal in wave polarity can be observed. A question that naturally arises is whether a change in wave polarity can be observed assuming a somewhat different modeling scenario — one that begins with the ISWs originating in shallow water and from there, traveling into deeper water. This scenario would not be unlike that described by Nash and Moum (2005) when they investigated the formation of an ISW associated with a river discharging into the Pacific Ocean.

Figure 63a shows a time-series of simulations involving a reverse shelf type of topographic obstacle and an ISW of elevation. Once the simulation is underway, the time series shows that the streamline contours associated with the ISW respond to changes in the obstacle geometry well-before the pycnocline passes the location of the theoretical turning point plane. At about TS 17,200, the streamline contours appear to “pour” down the face of the shelf (Figure 63b). This topographic feature corresponds to the plane of the theoretical turning point. The crest of the ISW does not encounter the turning point plane location until a short time later, at about TS 19,800 (Figure 63a). Later, at about TS 20,800, (Figure 63b), there is evidence of the formation of a “reverse” bore

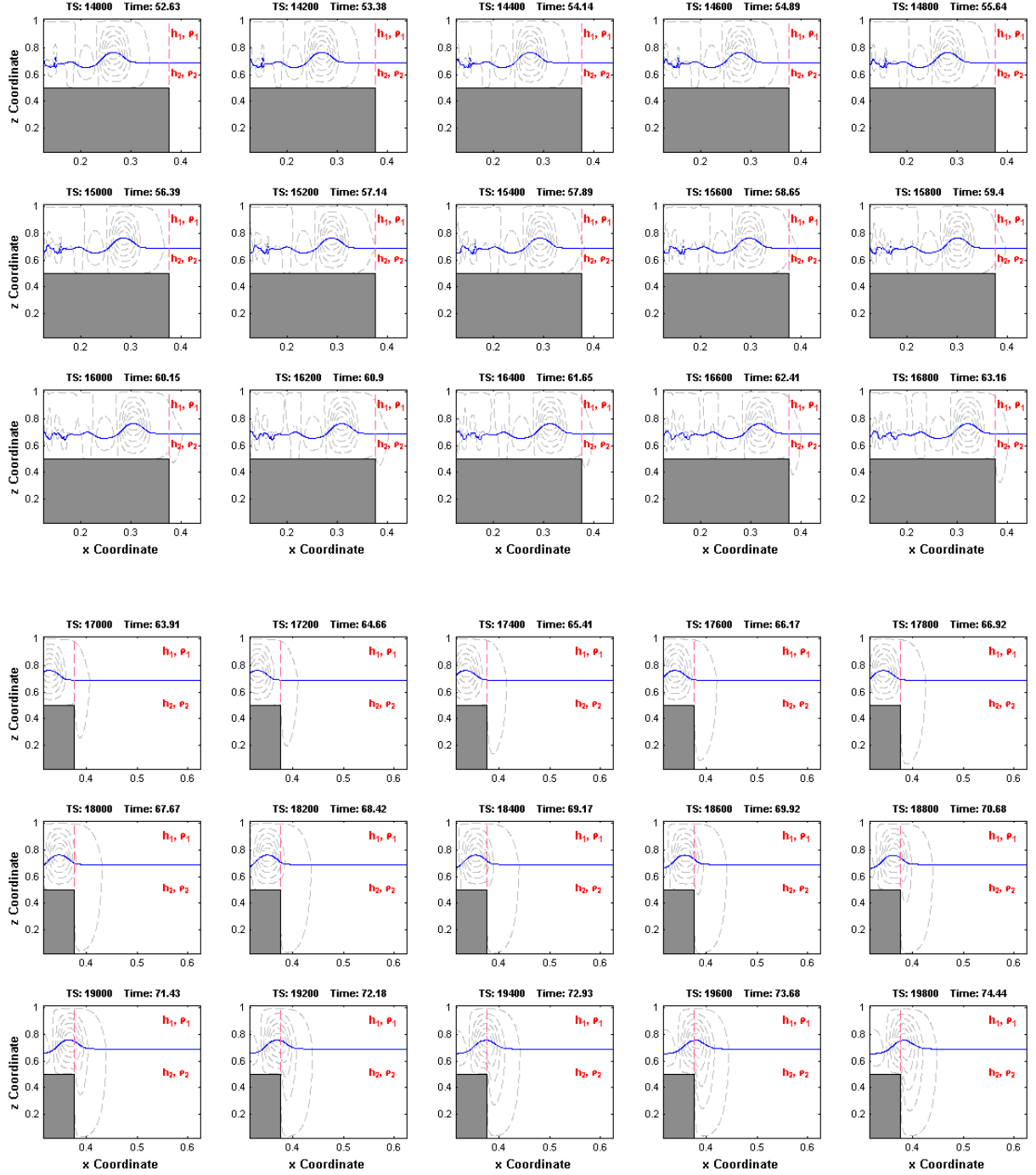


Figure 63a. Non-dimensional numerical simulation showing an encounter between an elevation-type ISW and a reverse-self obstacle. The vertical dashed line corresponds to the position of the theoretical turning point defined by $h_1 = h_2$. $Re = 3.314e4$ and $Fn = 0.085$.

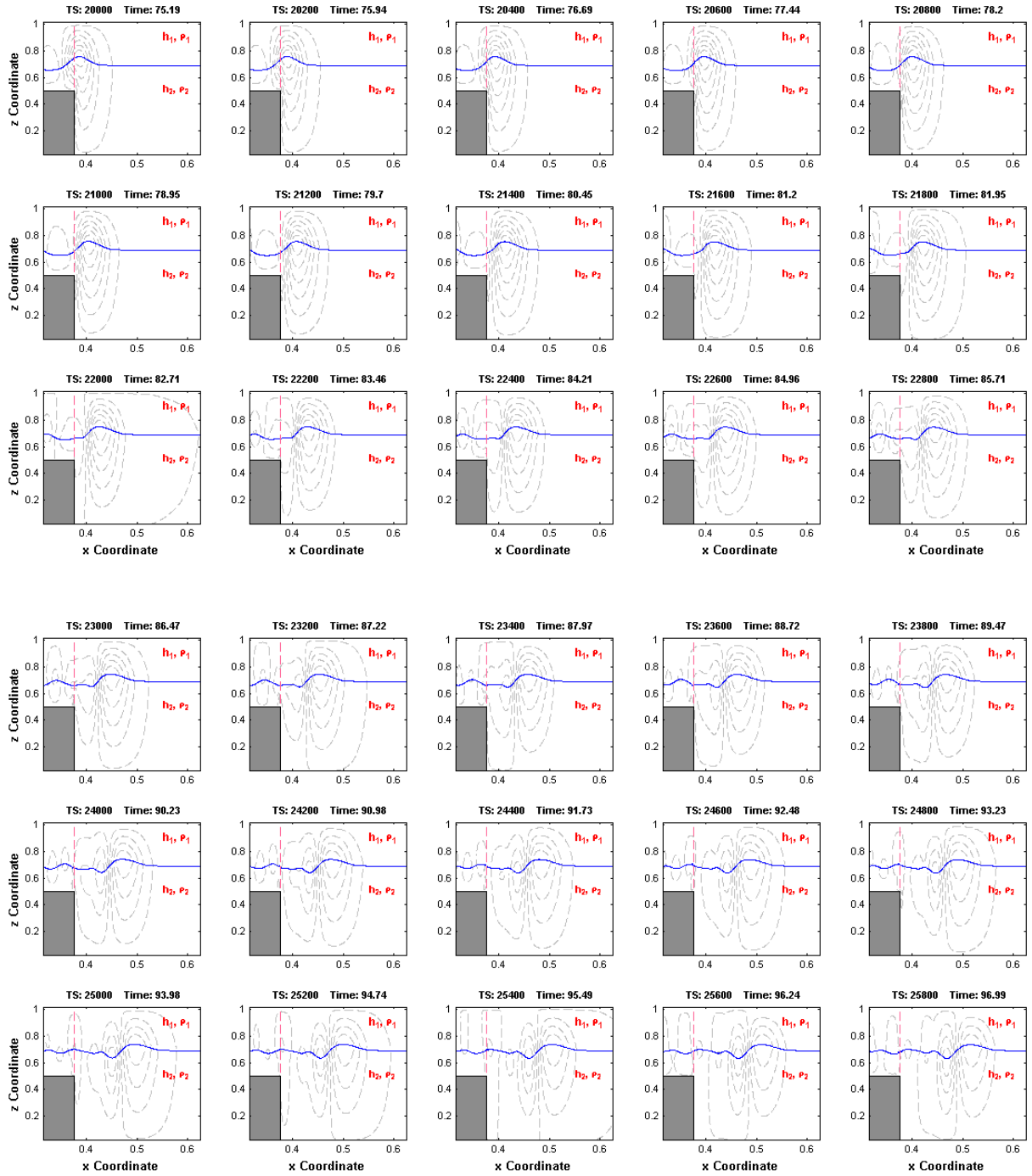


Figure 63b. Continued.

which, by TS 24,800 (Figure 63c), is now a clearly-formed depression-like ISW. The evolution in ISW polarity reversal proceeds for about another 15,000 time steps in the simulation (Figure 63e) until about TS 40,400 at which time the streamline contours associated with the leading elevation wave disappears leaving only a depression-type ISW.

Figure 64 shows the normalized velocity profiles of the horizontal and vertical velocity vectors associated with the reverse shelf-only simulation. These velocity profiles are consistent with profiles for an elevation-type ISW until the polarity transformation is complete — somewhere between Probe Locations 9 and 10. Figure 65 also shows that the wave speed continues to be dominated by the horizontal velocity component at the locations sampled.

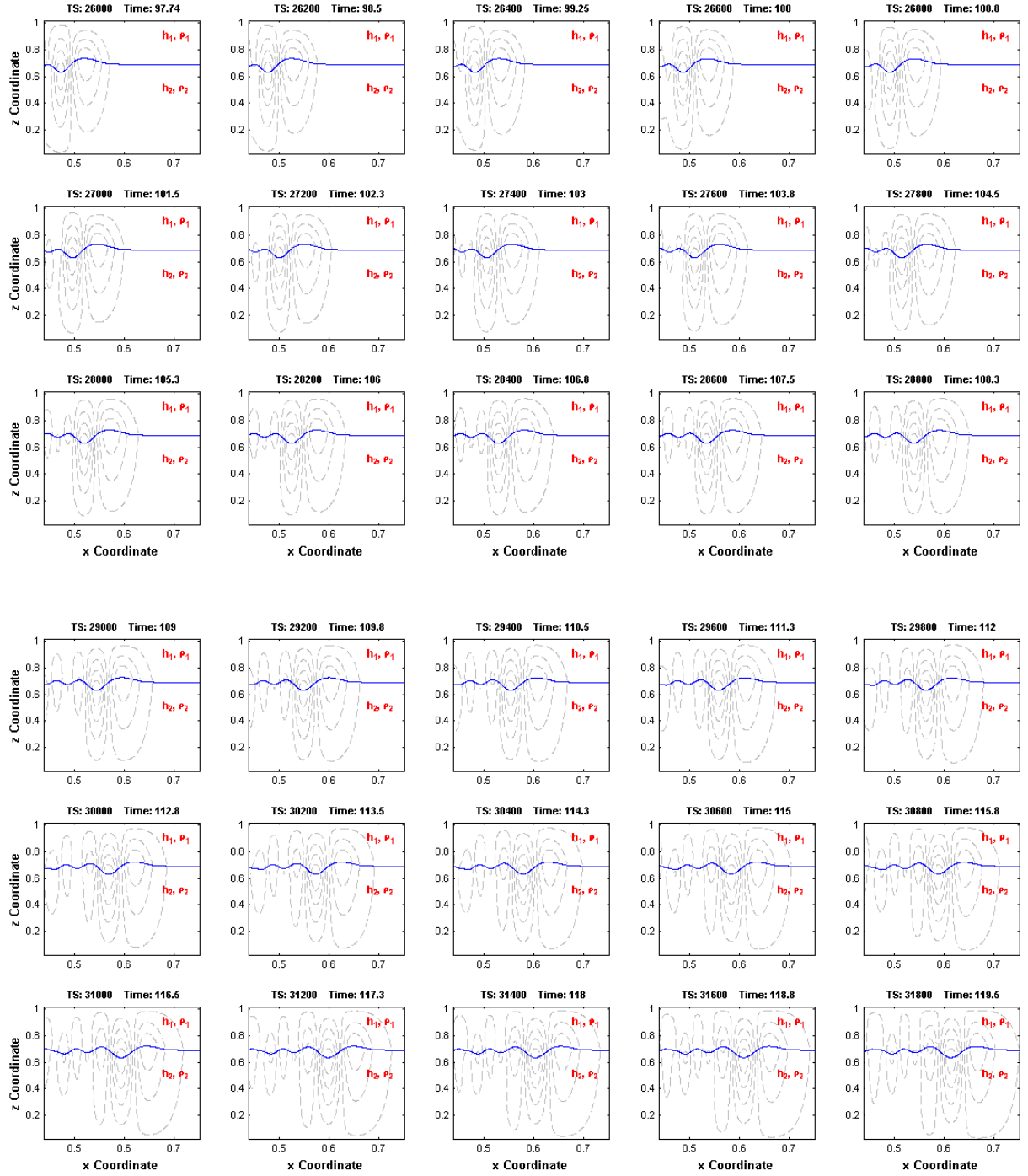


Figure 63c. Continued.

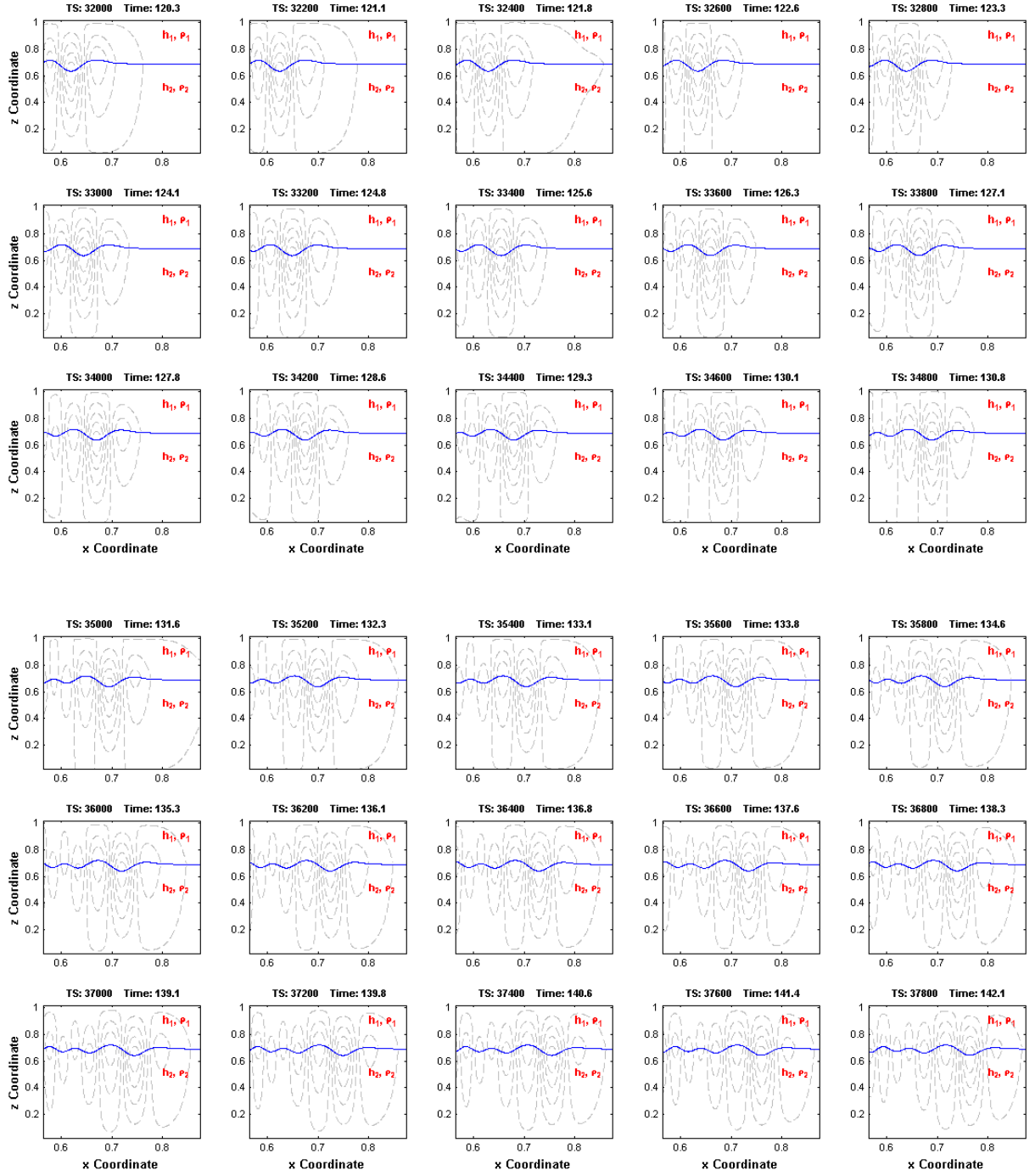


Figure 63d. Continued.

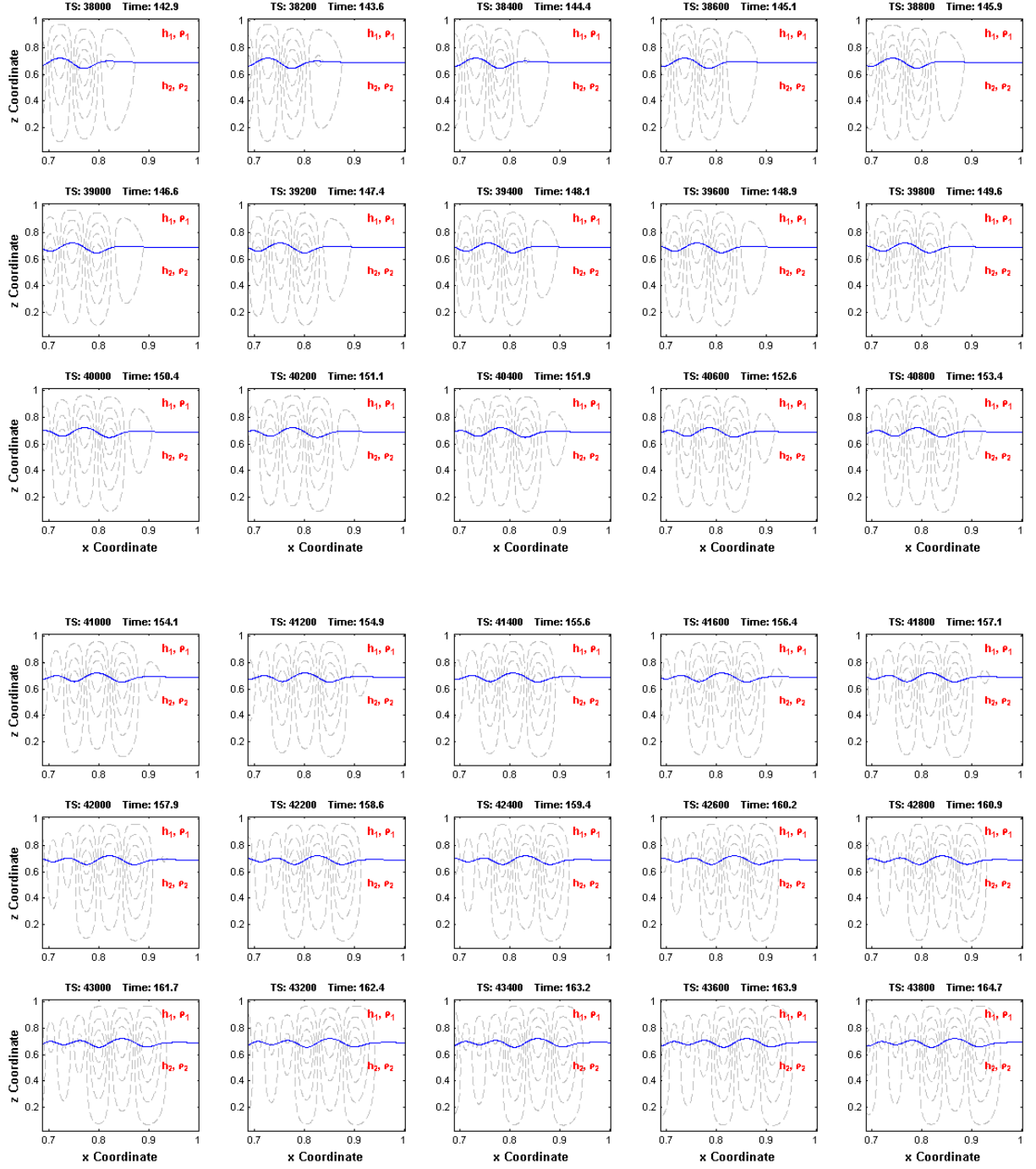


Figure 63e. Continued.

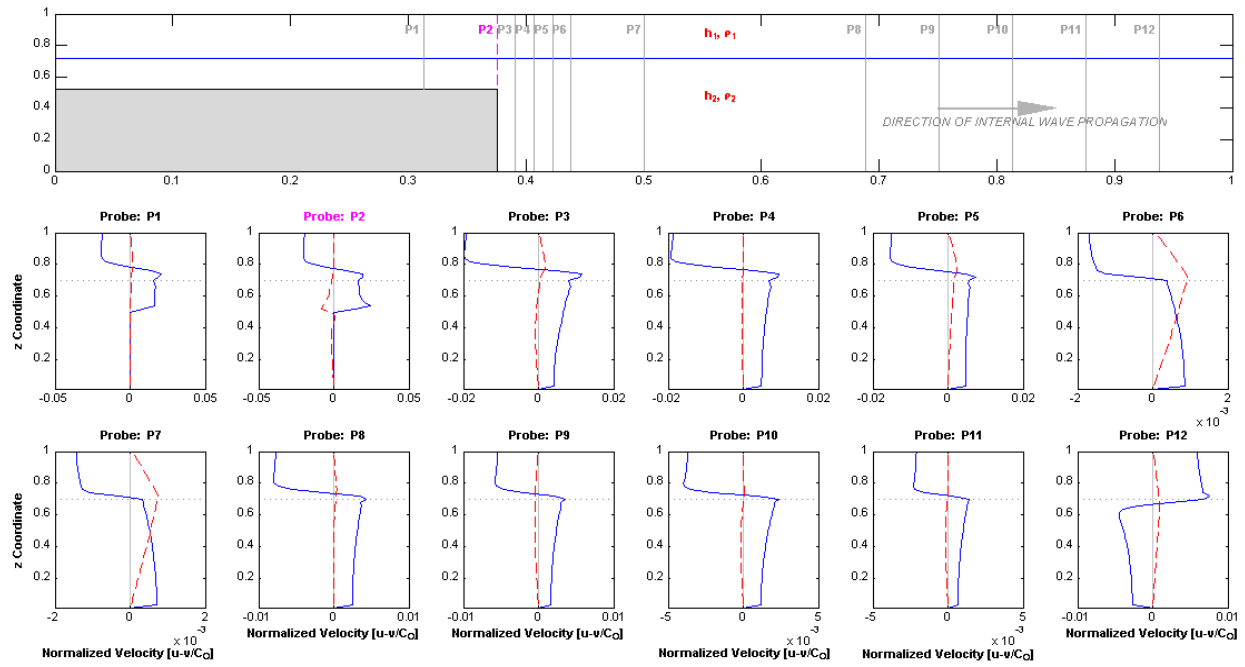


Figure 64. Time series plots of normalized velocity vector profiles for a depression-type ISW at ten uniformly-spaced locations during an encounter with a reverse-shelf obstacle. The pycnocline elevation is depicted by a dotted line.

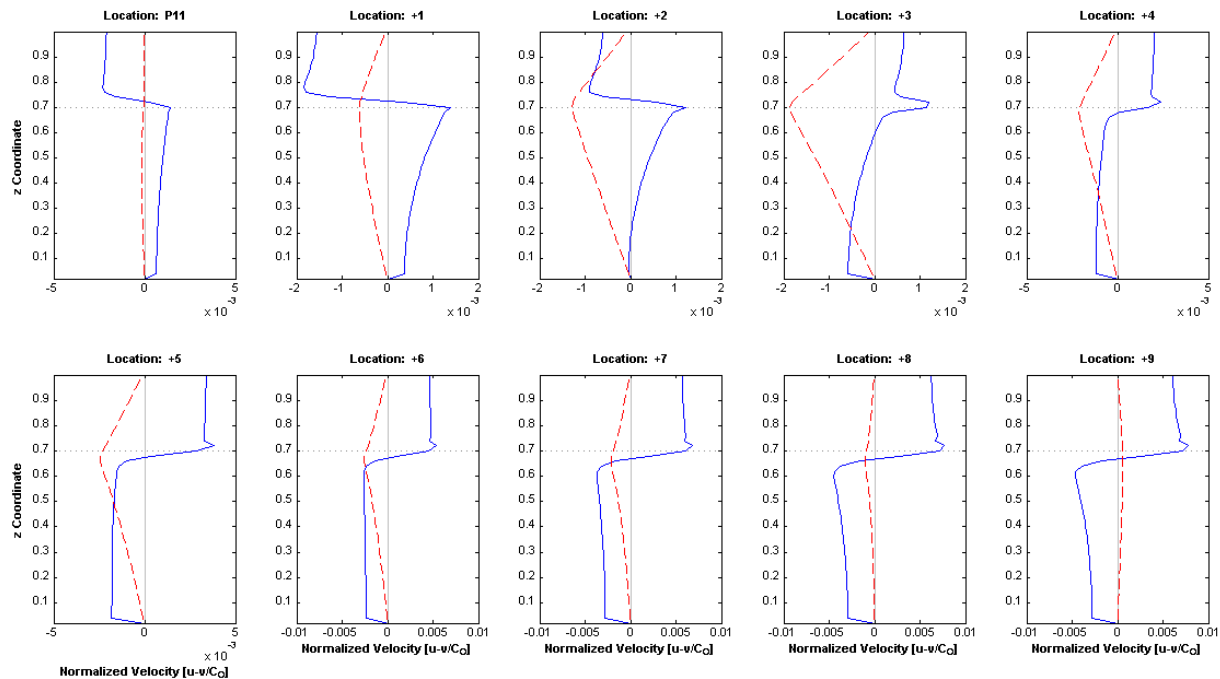


Figure 65. Detailed time series plots of normalized velocity vector profiles for an elevation-type ISW transitioning to a depression-type ISW. Figure shows uniformly-spaced time series plots beginning at the Probe 11 location depicted in Figure 64. The pycnocline elevation is depicted by a dotted line.

4.3.1.6 Isolated Topographic Obstacles

The Heezen-Tharp map and subsequent spin-off maps revealed that one of the most ubiquitous features along the ocean floor are the many submarine volcanoes, seamounts, guyots, coral atolls, and banks. As mentioned earlier in this dissertation, current estimates (Wessel, Sandwell, and Kim 2010) nominally place the number of these features at around 100,000. In terms of surface area, these features account for about 8 percent of the ocean's surface area (earlier Table 8). Although they may never breach the surface, the many isolated topographic obstacles on found along the seafloor interrupt what can generally

be a uniform (flat) abyssal landscape by virtue of their near vertical topographic relief. Figure 66a illustrates how quickly the seafloor topography can change when this type of topographic feature is encountered. The Healy Seamount, for example (Figure 66b), rises approximately 1000 m nearly vertically above the ocean floor. It is this striking change in elevation relative to the otherwise uniform abyssal topography that researchers cite (earlier Table 1) as one of the key factors contributing to the formation of ISWs, including solitary waves in the deep ocean. Figure 66c illustrates an example of a MOR. Figure 66d provides a birds-eye perspective of the same type of feature that also highlights the off-setting transform fault as well as some lesser submarine volcanic vents commonly associated with a MOR.

For the purposes of this series of numerical simulations, these prominent yet isolated topographic features can be modeled in either of two ways — as analogues of rectangles (Figure 47e) or as triangles (Figure 47f). For example, several researchers have used an isolated triangle to model an internal wave's encounter with a MOR-like feature (e.g., Guo et al. 2004, Aguilar and Sutherland 2006, and Petrelis, Llewellyn-Smith, and Young 2010). A third potential modeling scenario would involve elliptical- or hemispherical-shaped obstacles. Some researchers (i.e., Chen 2006) have examined ISW encounters with this particular type of geometric form in an experimental tank setting.

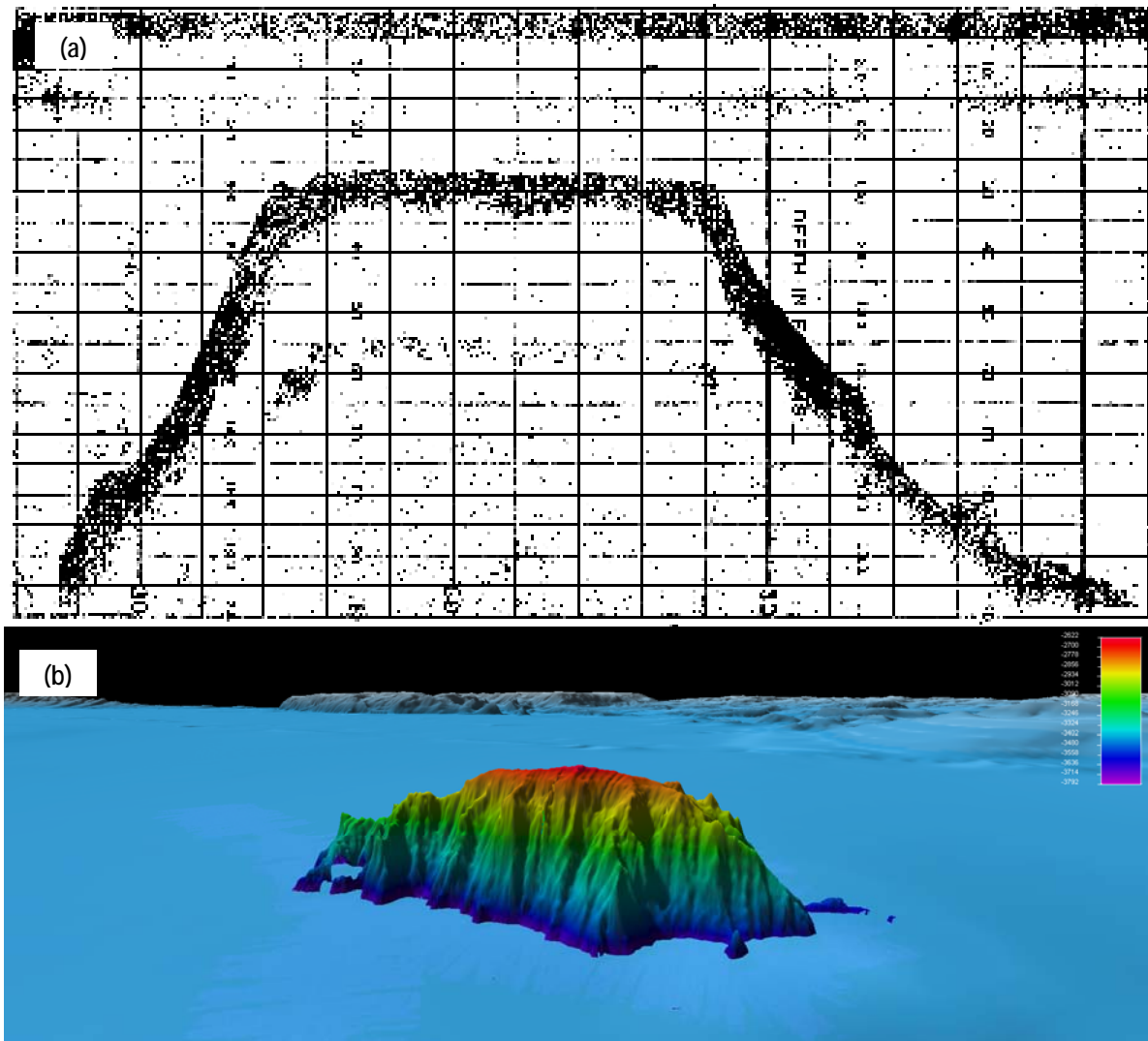


Figure 66. Examples of isolated topographic obstacles. (a) U.S. Navy fathometer recorder trace of unnamed seamount located at $14^{\circ} 20' \text{ N}$, $165^{\circ} 55' \text{ W}$, in the vicinity of the Marshall Islands. Fathometer orientation trace is 059° true North. Image taken from Hess (1946, Figure 8). (b) Digital Image of the so-called Healy Seamount ($81^{\circ} 31.57' \text{ N}$, $134^{\circ} 28.80' \text{ W}$). Located about 1100 km north of Alaska, in the Arctic Ocean, this recently-discovered seamount is approximately 30 km long and 13 km wide. The seamount rises from the abyssal plain at a depth of more than 3800 m to a least depth of 2622 m. The view is from the northeast looking southwest. In the far background (approximately 440 km) away is the Chukchi Plateau, in Siberian Russia. False-color image generated by NOAA and the Center for Coastal & Ocean Mapping Joint Hydrographic Center (Durham, NH).

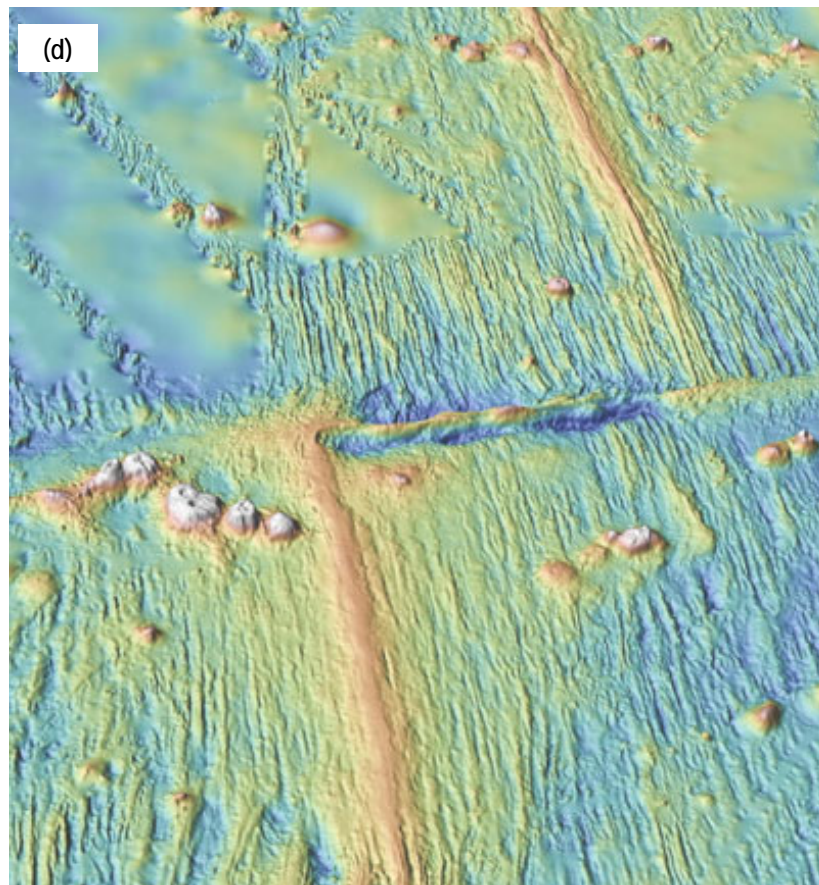
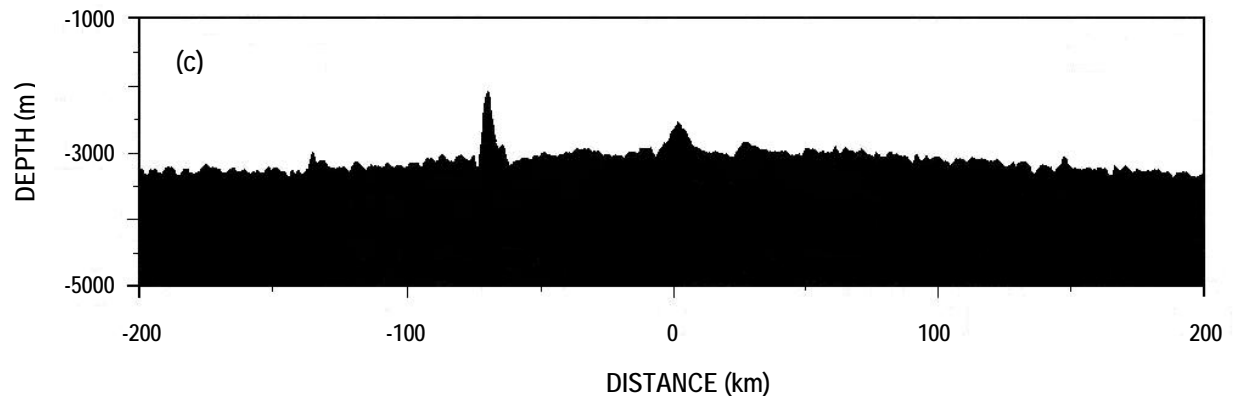


Figure 66. Continued. (c) Example of MOR bathymetry profile for the East Pacific Rise. The MOR can be found at the $\text{km} = 0$ position in the profile. Exact profile location not reported. Vertical exaggeration is 20:1. Adopted from Small and Sandwell (1994, Figure 1). (d) Shipboard multi-beam bathymetry image of the East Pacific Rise from 9° to 11° N, at 104° W. Bird's-eye (3D) perspective of a MOR looking North shows a transform fault running from the Pacific plate on the left to the North American plate on the right. False-color image generated by NOAA/Woods Hole Oceanographic Institute. See Ryan et al. (2009).

This investigator, though, considers such topographic forms unlikely in nature and thus an unrealistic modeling scenario given information to the contrary on the likely physical forms for submarine features reported in the literature (Menard 1984 and 1996, Shepard 1973).

Introduction of isolated obstacles into a numerical simulation provides another opportunity for evaluating the behavior of ISWs. It also allows provides the opportunity to better understand the role of the so-called “blocking parameter.” Described previously by Wessels and Hunter (1996) and Sveen et al. (2002), the blocking parameter is used to understand what influence an obstacle’s (barrier’s) height might have on the transmission properties of an ISW. The literature distinguishes between blocking parameters that apply to either an elevation- type or depression-type ISW. In the case of elevation-type ISWs, Wessels and Hunter (1996) defined the blocking parameter B as:

$$B = \frac{h_s}{h_2} \quad (4.9)$$

where h_s is the obstacle’s height. When a depression-type ISW is involved, Sveen et al. (2002) suggest that the blocking parameter ζ , describing the degree of interaction between an ISW and an obstacle, can be expressed as:

$$\zeta = \frac{(a_i + h_1)}{(h_1 + h_2 - h_s)} \quad (4.10)$$

Table 14. Suggested ISW Blocking Parameter Values and Effects.

ELEVATION-TYPE ISW (Wessels and Hunter 1996)		DEPRESSION-TYPE ISW		
		Sveen et al. (2002)		Kuo (2005)
$B \leq 0.6$	ISW generally not affected	$\zeta < 0.45$	ISW generally not affected	“weak interaction”
$0.8 \leq B \leq 1.2$	ISW demonstrates reflection and limited transmission	$0.45 < \zeta < 0.55$	ISW demonstrates (limited) breaking phenomena	“moderate interaction”
$B \geq 1.2$	ISW demonstrates almost full refraction	$\zeta > 0.55$	ISW demonstrates full breaking phenomena and complete energy dissipation	“full interaction”

The blocking effects imposed by a submarine obstacle on the transmission of an ISW have been evaluated by a few investigators, and their findings are described in Table 14. For his part, Kuo (2005) investigated the blocking parameter ζ , and characterized ISW interaction as either “weak,” “moderate,” or “strong.”

According to Kuo (2005), weak interaction means that the ISW is not affected by the obstacle’s presence. In evaluating the behavior between ISWs and vertical wall-like obstacles, Sugimoto, Hosokawa, and Kakutani (1987) found that for a barrier of moderate height in relation to the lower fluid layer h_2 ,

an ISW could pass over it as if it were transparent whereas if the barrier was more than moderate in height, the transmission of the ISW is suppressed yielding a reflected ISW and wave train.

Rectangular Obstacle. Figure 67 shows a non-dimensional numerical simulation involving a depression-type internal wave and an isolated rectangular obstacle. The rectangular form can be used as an analogue for an isolated seamount. For the purposes of this particular numerical simulation, the obstacle dimensionally is about twice as long (in the x direction) as it is high (in the z direction). The blocking parameter ζ is equal to 1.5 so “full interaction” (Table 14) between the obstacle and the oncoming internal wave can be expected during the simulation. The simulation shows a well-developed internal wave at about TS 8500 (Figure 67a). The plane of the theoretical turning point is defined by the front face of the rectangular obstacle.

At approximately TS 10,100, the streamline contours of the internal waves begin to encounter the obstacle. The encounter is revealed by the deflection of the leading edge of the outer-most (downwind) streamline. By TS 10,700, the simulation shows that the ISW has become entrained and the pycnocline has been draw down-ward along the face of the obstacle — the location corresponding to the plane of the theoretical turning point. The

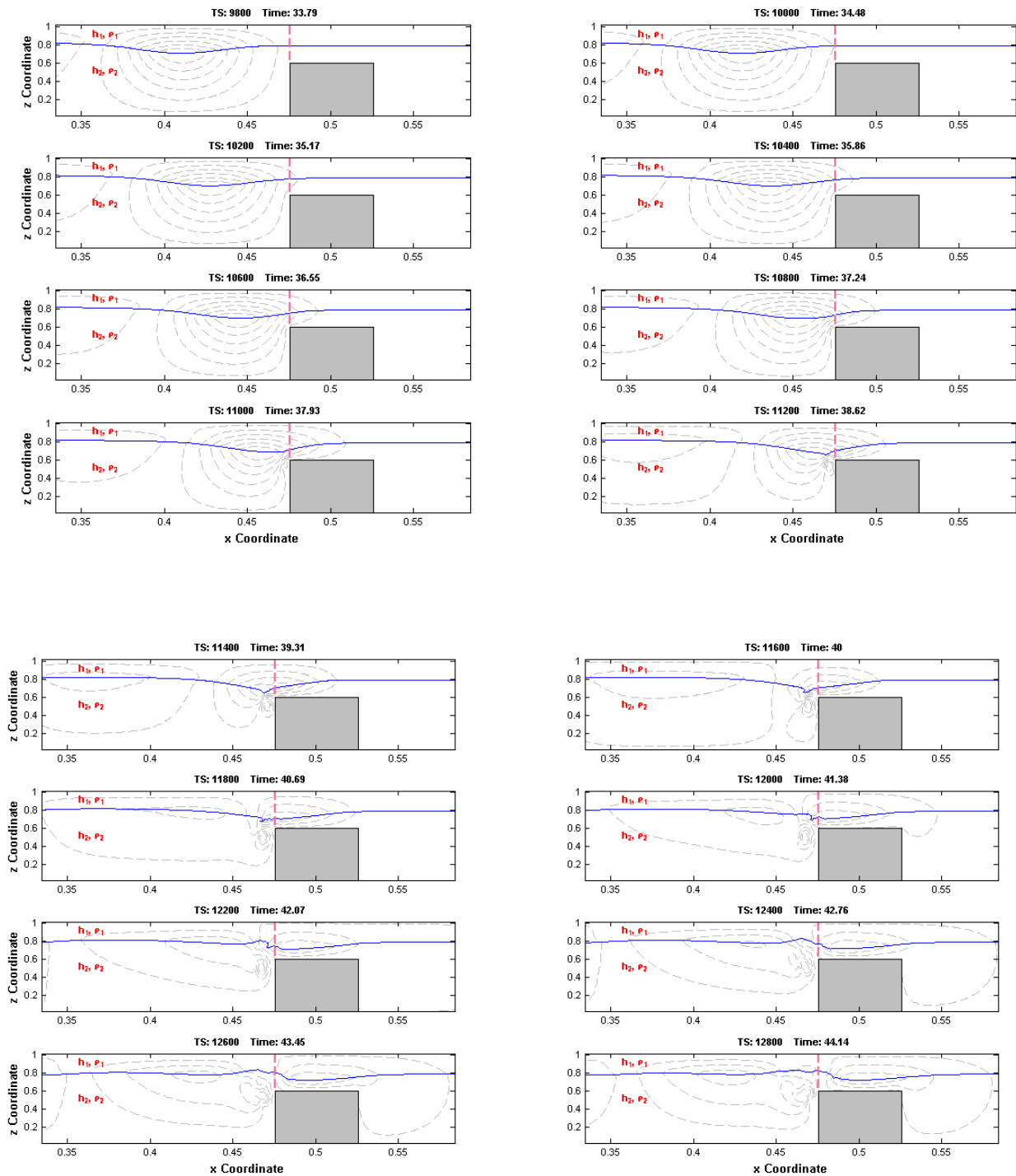


Figure 67a. Non-dimensional numerical simulation showing an encounter between a depression-type ISW and an isolated rectangular obstacle. The vertical dashed line corresponds to the position of the theoretical turning point defined by $h_1 = h_2$. $Re = 7.528e4$ and $Fn = 0.068$.

entrainment/shoaling process becomes more pronounced in subsequent time steps as suggested by what now appears to be a “jump” in the elevation of the pycnocline at about TS 11,700 (Figure 67b). In numerical simulations conducted by Legg and Klymak (2008), they report the formation of these hydraulic jumps when:

$$\frac{dh_s}{dx} \cdot \frac{N}{\omega} > 1 \quad (4.11)$$

where ω is the tidal frequency.

Following the entrainment sequence depicted in Figure 67a, the simulation (at about TS 12,500) shows that a portion of the advancing internal wave has been suppressed by the obstacle as a result of the encounter, and is reflected back in the direction from whence it came as predicted by Sugimoto, Hosokawa, and Kakutani (1987). In subsequent time steps, a collection of streamline contours are present in the simulation suggesting the presence of this reflected internal wave. The streamline contours associated with this reflected internal wave can be observed retreating back in the direction of the initial generation point. This hydrodynamic aspect of the numerical simulation is depicted in more detail in the higher resolution exhibits found in Appendix F.

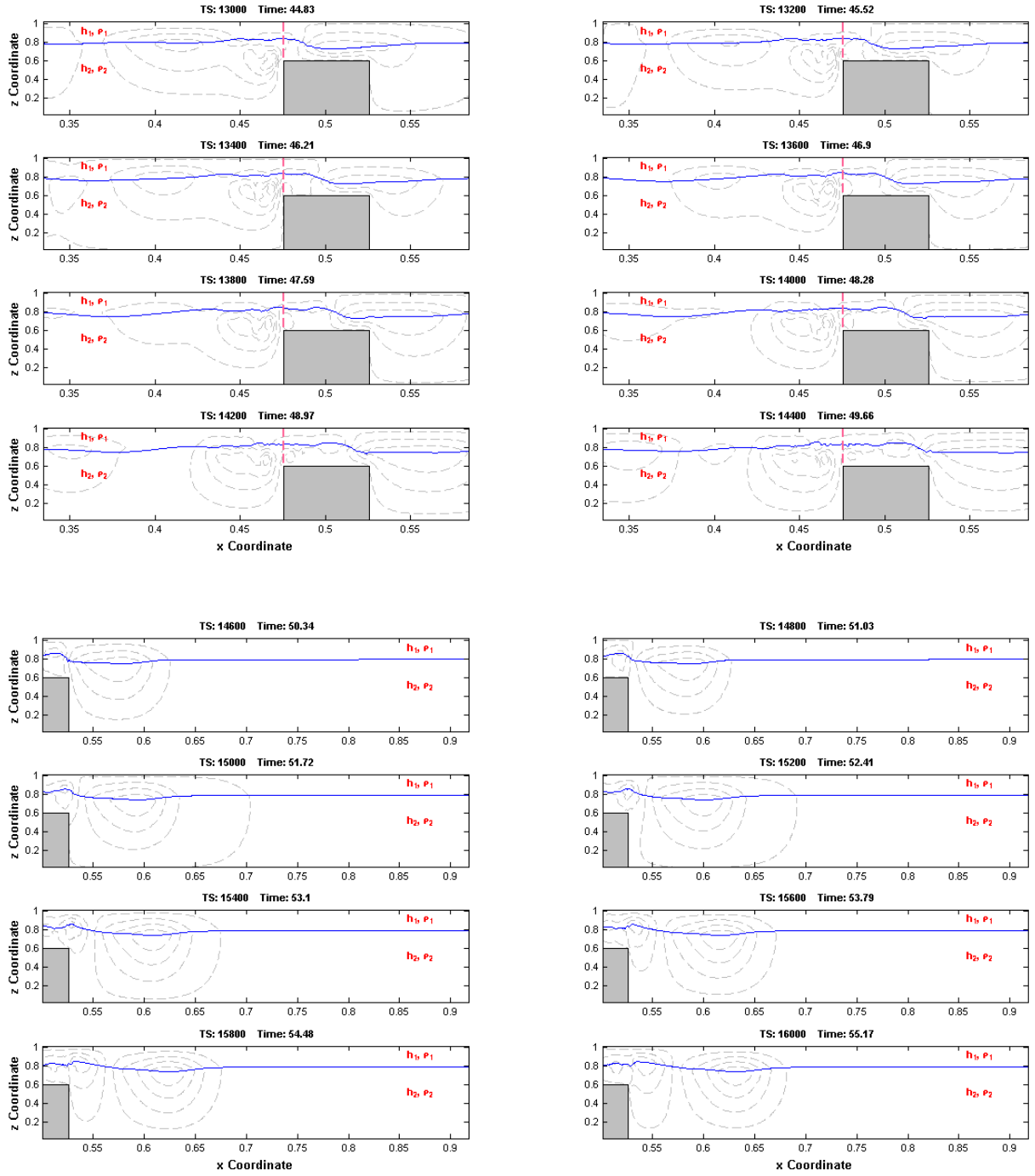


Figure 67b. Continued.

As the internal wave/obstacle interaction continues to progress, there is an apparent reduction in the number of streamline contours associated with the transmitted internal wave suggesting a decline in both wave speed and wave energy. By about TS 16,500 (Figure 67c), the outline of the earlier depression-type ISW has reappeared in the simulation. Moreover, a second elevation-type ISW has now appeared. This lesser wave becomes more distinct by TS 192,000 (Figure 67d), the last frame shown in this particular simulation sequence.

The sequence of exhibits corresponding to the later stages of this numerical simulation also reveal that there has been some decay in the speed of the wave transmitted beyond the obstacle. The wave speed decay is evident by virtue of a decline in both the number of streamline contours as well as an increase in the relative spacing of those contours. Plots of the normalized velocity vectors shown in Figure 68 confirm the decline in wave speed, which is estimated to be about 40 percent as a result of the encounter with the obstacle. However, these plots also show that there is no evidence of ISW polarity reversal following the encounter. Despite the decline in wave speed, the plots of the velocity vector profiles confirm that the ISW polarity remains unchanged.

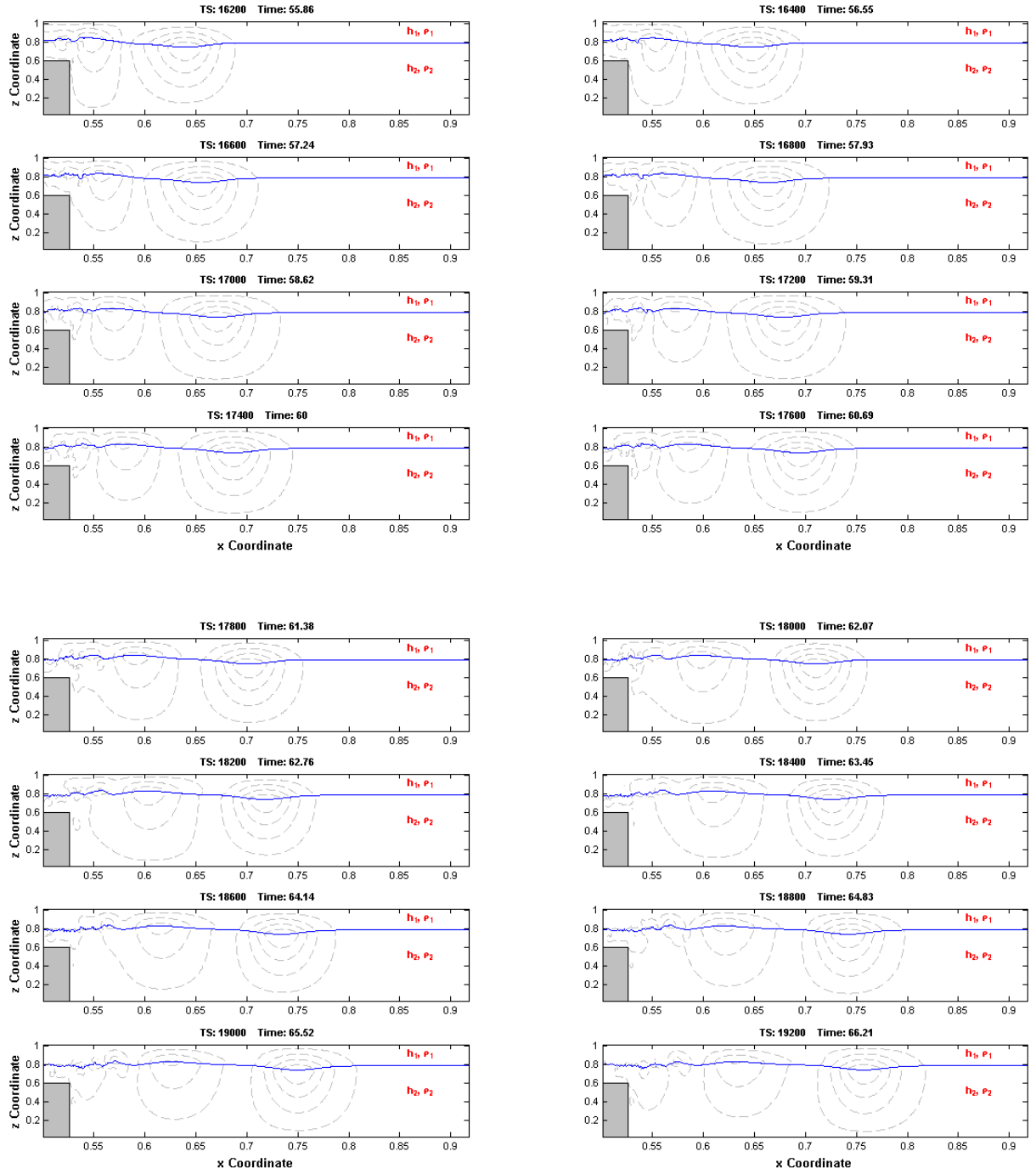


Figure 67c. Continued.

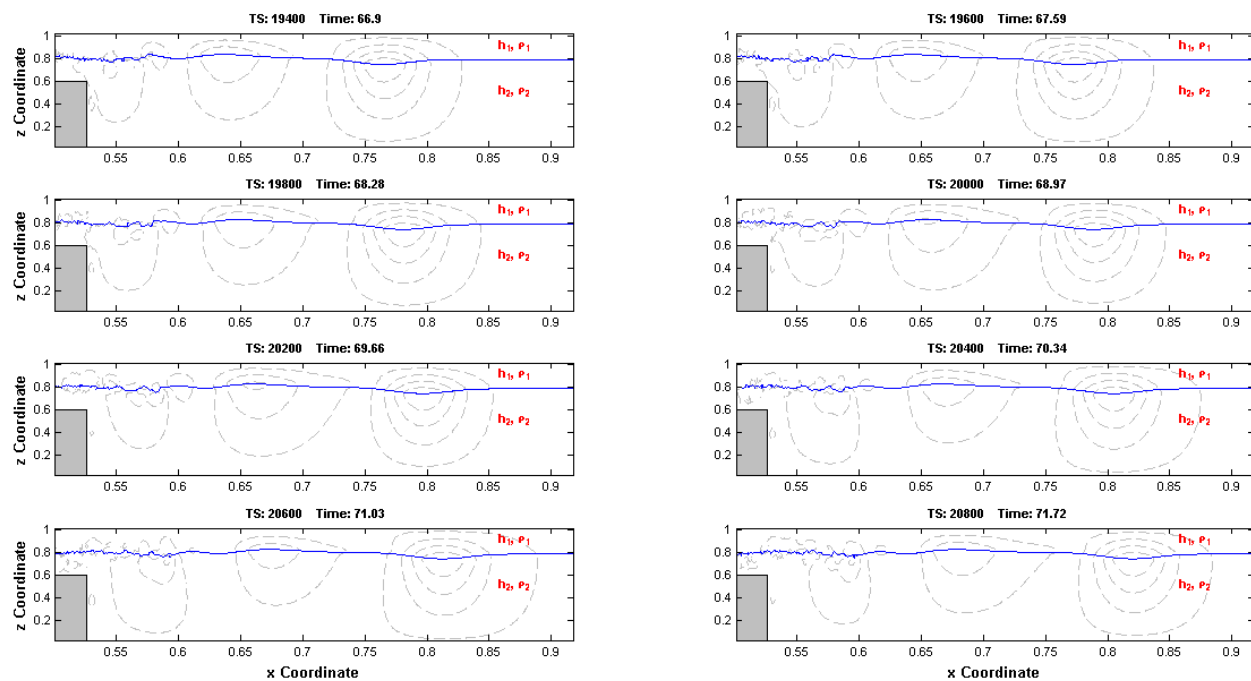


Figure 67d. Continued.

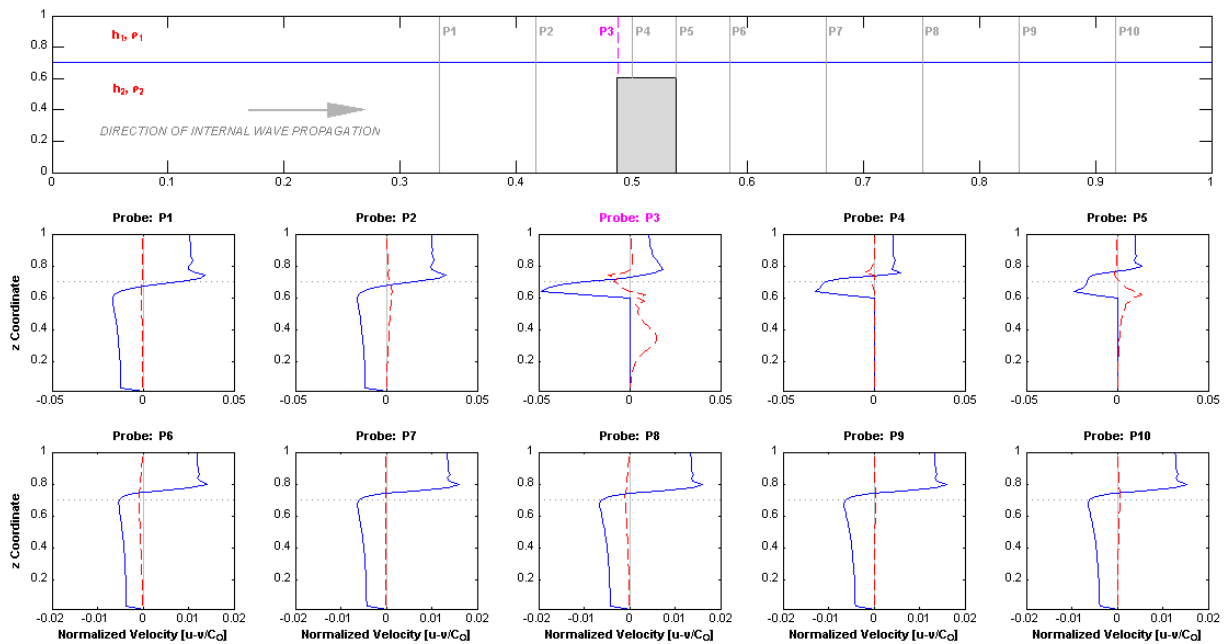


Figure 68. Time series plots of normalized velocity vector profiles for a depression-type ISW at ten uniformly-spaced locations during an encounter with an isolated rectangular obstacle. Horizontal velocity vectors are blue (or solid) lines. Vertical velocity vectors are red (or dashed) lines. The pycnocline elevation is depicted by a dotted line.

The physical configuration of the numerical simulation depicted in Figure 68 was devised in such a way that the encounter between the ISW and the rectangular obstacle resulted in full interaction between the two — that is to say the non-dimensional blocking parameter ζ was approximately 0.76 implying that the internal wave demonstrates full breaking. The principal features of the wave-breaking progression associated with an isolated rectangular obstacle, reflecting full interaction, are shown in Figure 69 including the demonstration of “wash-down,” “wave breaking,” and “bore formation.”

To provide another hydrodynamic perspective on how an ISW would interact with this particular topographic form, the simulation was repeated but under a different physical configuration so as to yield a different value for the blocking parameter ζ . Figure 70 shows essentially the same non-dimensional simulation depicted in Figure 69 but configured in such a way as to evoke “moderate interaction” between the internal wave and the rectangular topographic obstacle. The moderate interaction simulation (blocking parameter $\zeta = 0.5$) produced only two phases of the wave breaking progression — “wash-down” and the formation of a “bore” (Figure 70). A simulation intended to demonstrate “weak interaction” (Table 14) between a rectangular submarine topographic obstacle and an ISW produced no discernable wave-breaking features.

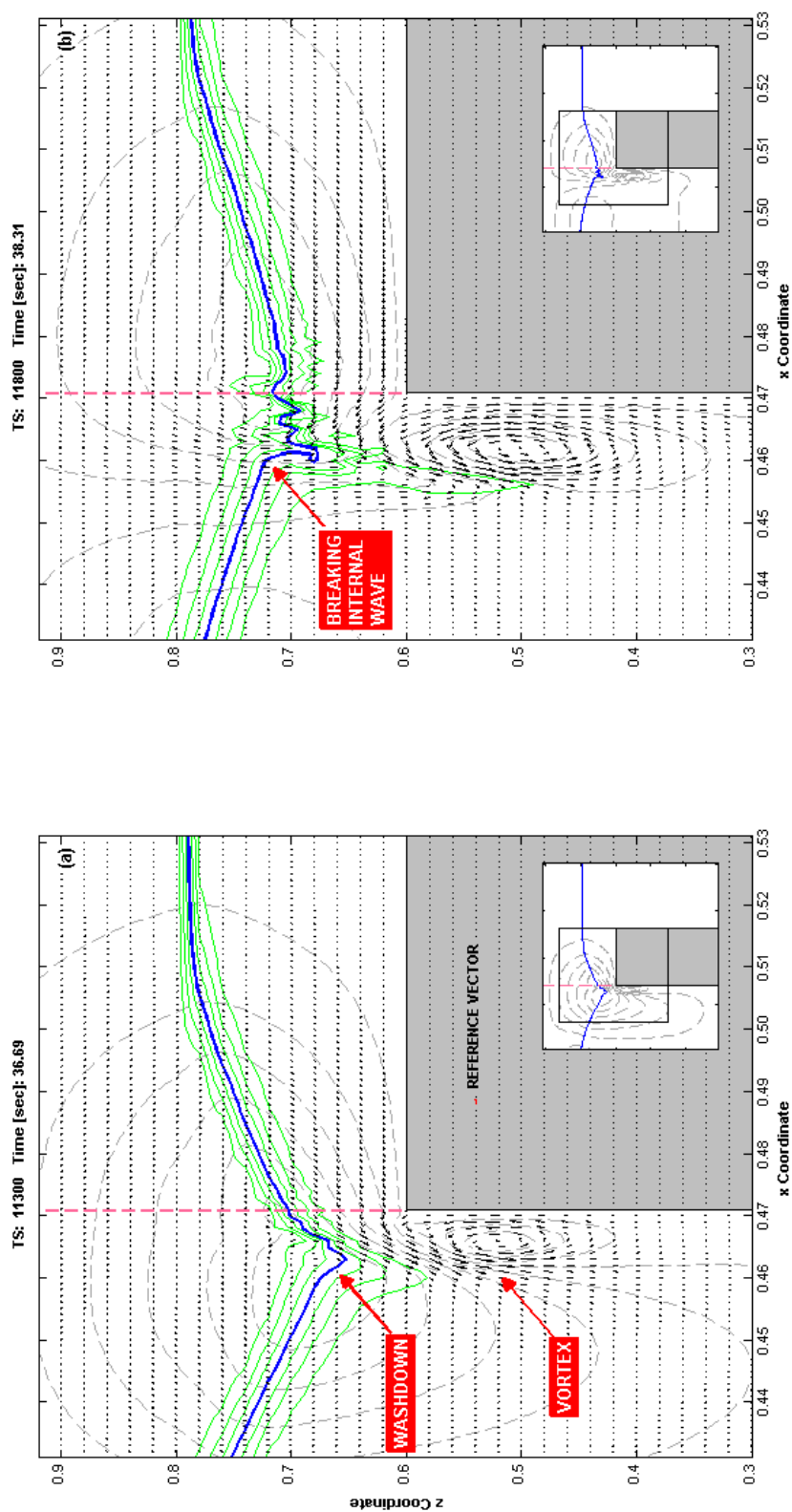


Figure 69. Selected details of a non-dimensional numerical simulation between a depression-type ISW and an isolated rectangular obstacle depicted in Figure 67 showing “full interaction” (Table 14). The vertical dashed line corresponds to the position of the theoretical turning point plane defined by $h_1 = h_2$. Insets within each figure show the relative location of the ISW to the obstacle at the time step indicated. Vectors in the velocity field are shown as streamlines contours (dashed lines). (a) Onset of shoaling/breaking first defined by “wash-down.” (b) “Breaking” of the ISW defined by the overturning of the pycnocline.

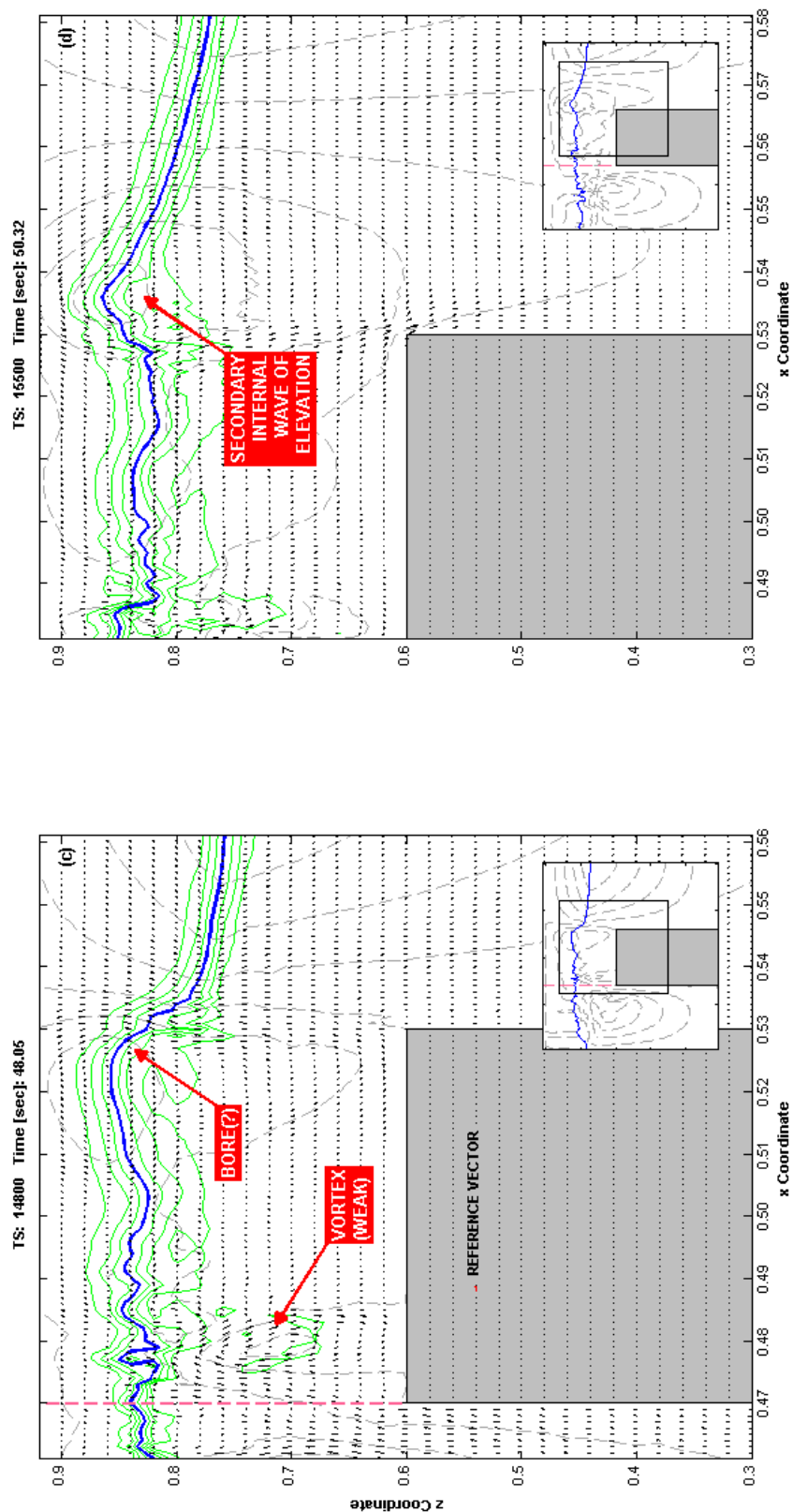


Figure 69. Continued. (c) Example of bolus/bore-like feature advancing beyond the plane of the theoretical turning point (vertical dashed line). (d) Example of an elevation-type internal wave taking form.

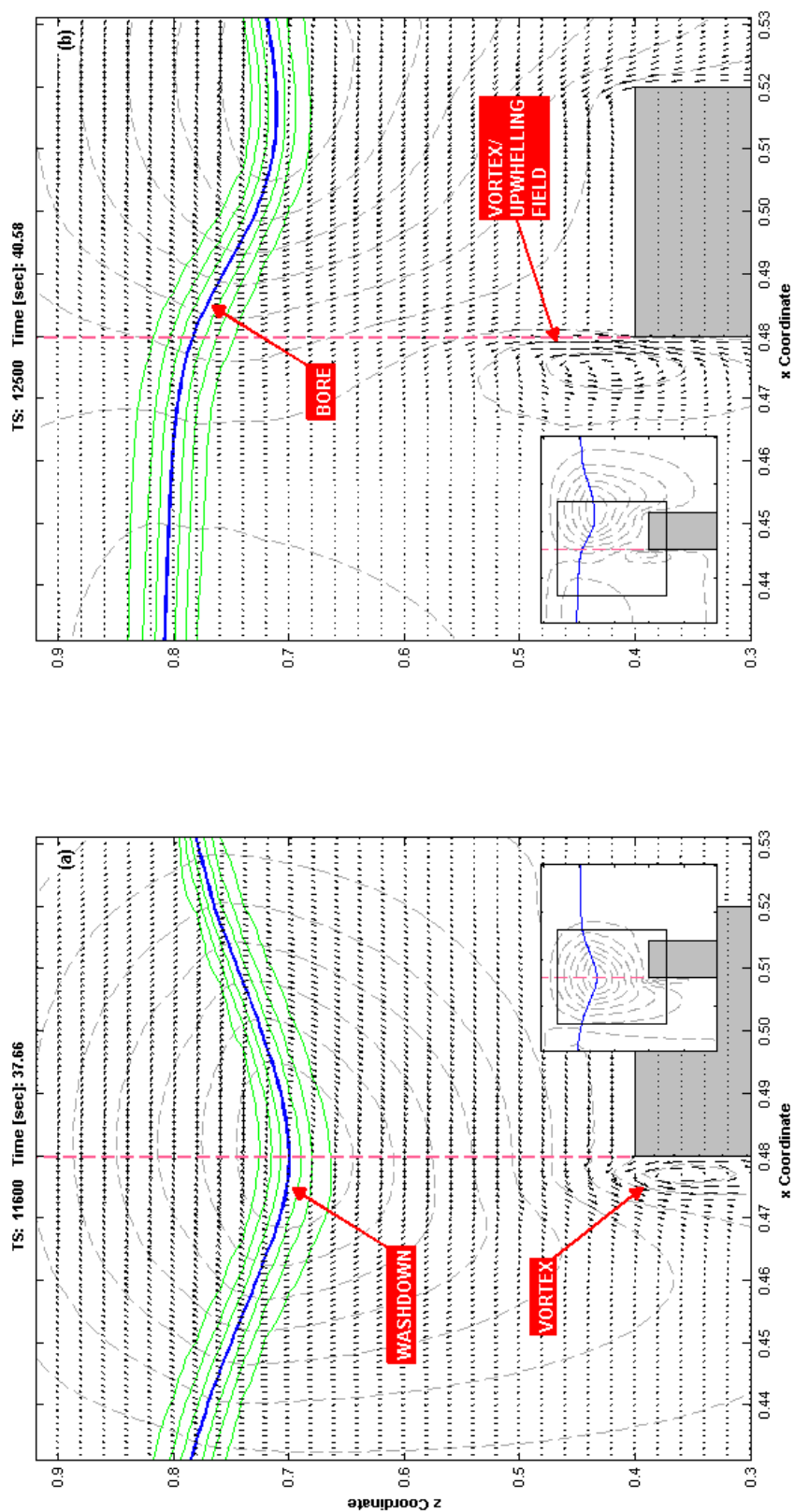


Figure 70. Selected details of a non-dimensional numerical simulation between an elevation-type ISW and an isolated rectangular obstacle showing "moderate interaction" (Table 14). The vertical dashed line corresponds to the position of the theoretical turning point plane defined by $h_1 = h_2$. Insets within each figure show the relative location of the ISW to the obstacle at the time step indicated. Vectors in the velocity field are shown as streamlines contours (dashed lines). (a) Onset of shoaling/breaking first defined by "wash-down." (b) "Breaking" of the ISW defined by the overturning of the pycnocline.

Triangular Obstacle. The time series depicted in Figure 71 once again shows a well developed, depression-type ISW of mode-1 at TS 8500 approaching an isolated triangular obstacle. The triangular form can be used as an analogue for an isolated MOR. For the purposes of this simulation, the obstacle again is twice as long as it is high; it is essentially in the form of an isosceles triangle. The apex of the triangle defines plane of the theoretical turning point. The blocking parameter ζ is equal 1.5 so “full interaction” can (theoretically) be expected between the obstacle and the incoming ISW during this particular simulation trial.

The first frame in the simulation sequence shown in Figure 71a indicates that the streamline contours have not encountered the obstacle. By about TS 8900, the simulation shows that the most distal streamline contour associated with the advancing ISW has begun to encounter the obstacle as that orbital is beginning to show signs of distortion. Evidence of the onset of a full encounter between the wave front defined by the pycnocline and the obstacle is not readily apparent until about TS 17,000 in the numerical simulation. At about this time, there are signs of ISW entrainment by virtue of wash-down (albeit slight) of the pycnocline, and thus “wave breaking.” Further pycnocline “wash-down” is apparent between TS 109,000 and TS 111,000 of the simulation.

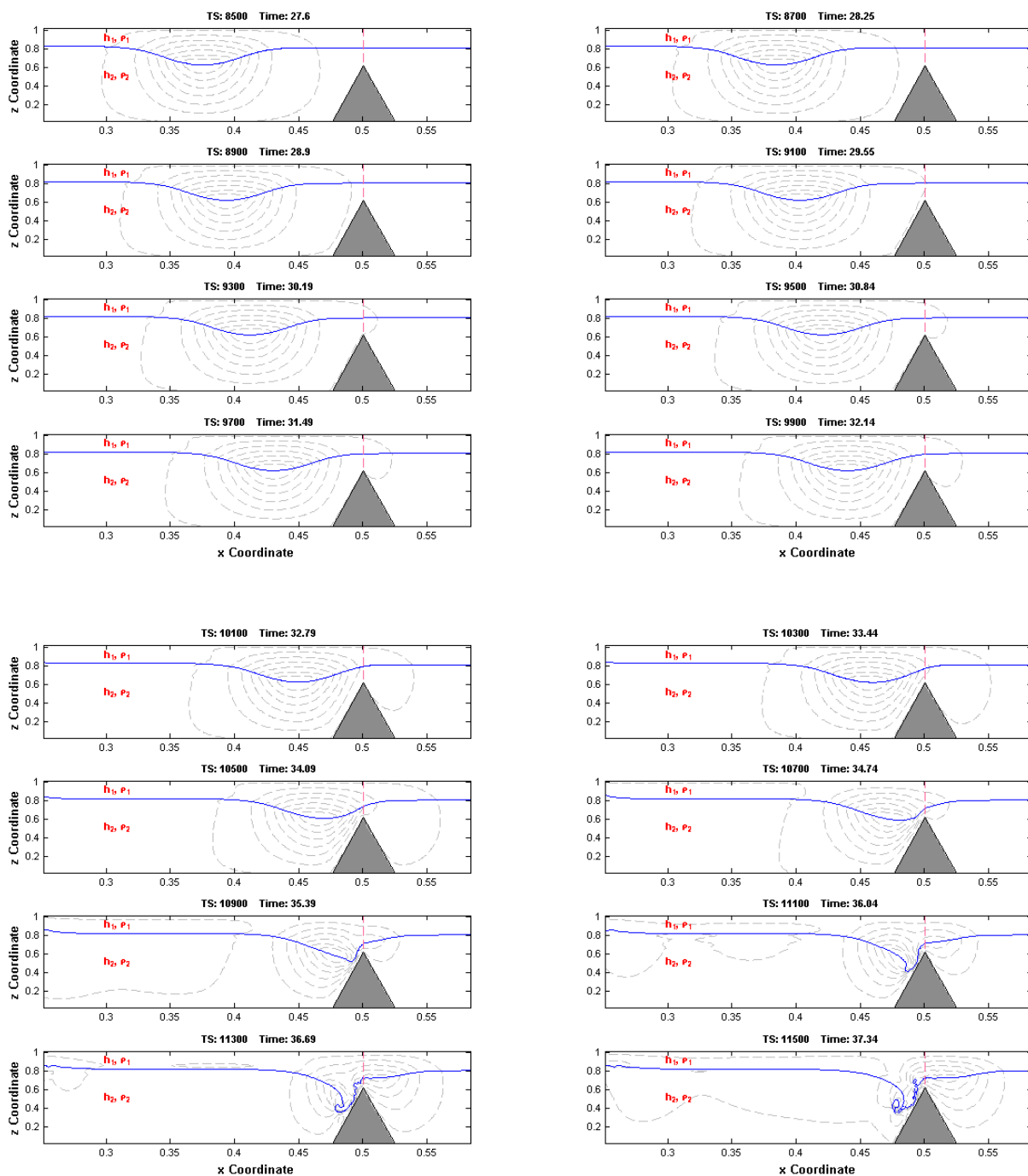


Figure 71a. Non-dimensional numerical simulation showing an encounter between a depression-type ISW and an isolated triangular obstacle. The vertical dashed line corresponds to the position of the theoretical turning point defined by $h_1 = h_2$. $Re = 6.247e4$, $Fn = 0.075$, and $Q = 24$.

By about TS 113,000, the evolution of the breaking ISW is entering a new phase. The pycnocline is beginning to develop signs of “roll-over” – that is to say the crest of the ISW is beginning to overturn onto itself or “break.” This feature is consistent with the next phase of the wave-breaking progression described earlier in this dissertation.

What is also apparent during this phase of the simulation is that the collision between the ISW and the triangular obstacle once again produces a lesser, reflected internal wave. The presence of this “artifact” is revealed by the collection of streamline contours that begin to form on the incident side of the obstacle, again as predicted by as predicted by Sugimoto, Hosokawa, and Kakutani (1987). See TS 119,000 (Figure 71b). In subsequent time steps, it is clear that the reflected ISW is now best described as a poorly-defined train of turbulence along the pycnocline whose polarity is opposite to that of the original incoming ISW. See TS 133,000. Lastly, it is worth noting that although some portion of the turbulent wave train is transmitted beyond the obstacle, the energetics of this hydrodynamic feature appear to diminish as it passes through the plane of the theoretical turning point, as discussed below.

Figure 71b. Continued.

Figures 71c and 71d show the remaining time steps of the numerical simulation depicting an encounter between an ISW of depression and an isolated triangular obstacle. These exhibits illustrate that the transmitted ISW that has advanced to a location well-beyond the position of the obstacle. These exhibits also reveal that there has been some decay in the speed of this transmitted wave by virtue of both a decline in the number of streamline contours as well as an increase in their relative spacing. Moreover, consistent with the trial involving the rectangular topographic obstacle, there is once again no evidence of a reversal of the polarity of the ISW following an encounter with the triangular obstacle. Plots of the velocity vectors contained in Figure 72 confirm that there is about a 40 percent decline in the wave speed following the encounter but the ISW polarity remains unchanged.

Additional insights concerning the interaction between an ISW and an isolated topographic obstacle can be obtained from the examination of higher-resolution figures. Appendix G contains a sequence of higher-resolution time series plots of the wave breaking sequence depicted in Figure 71, including the introduction of velocity vectors. The two principal steps in the ISW-breaking progression have been reproduced in the other simulations associated with this research and are shown in Figure 73. They include the “wash-down” phase (at TS 10,700) and the “breaking” phase (at TS 11,100).

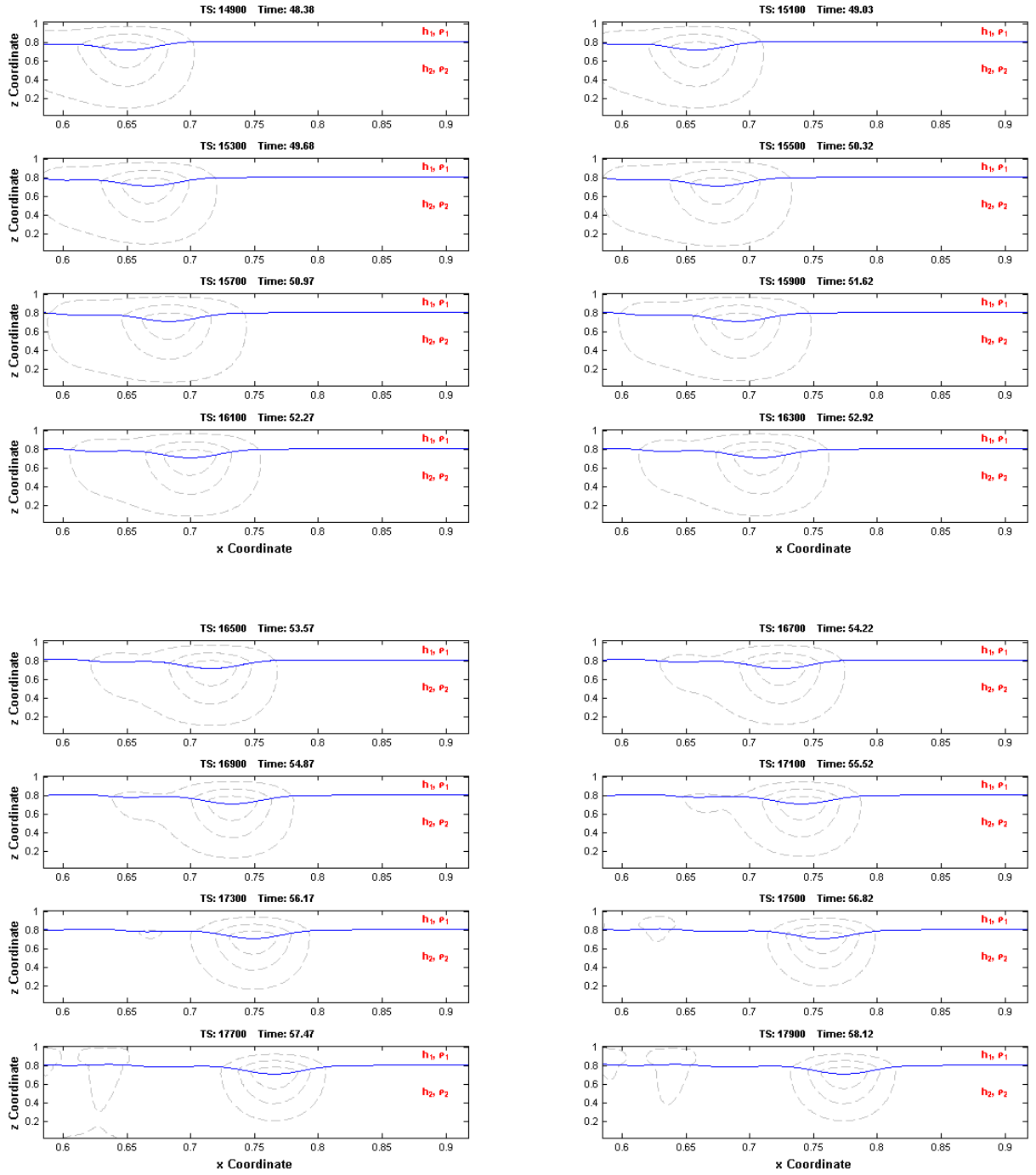


Figure 71c. Continued.

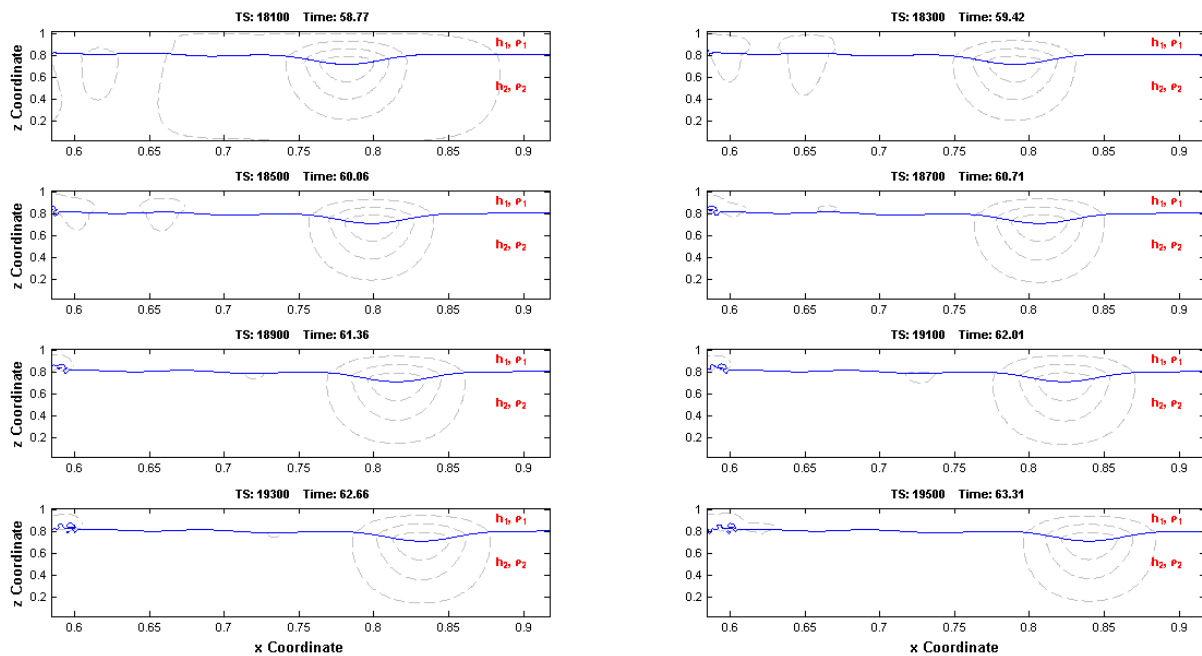


Figure 71d. Continued.

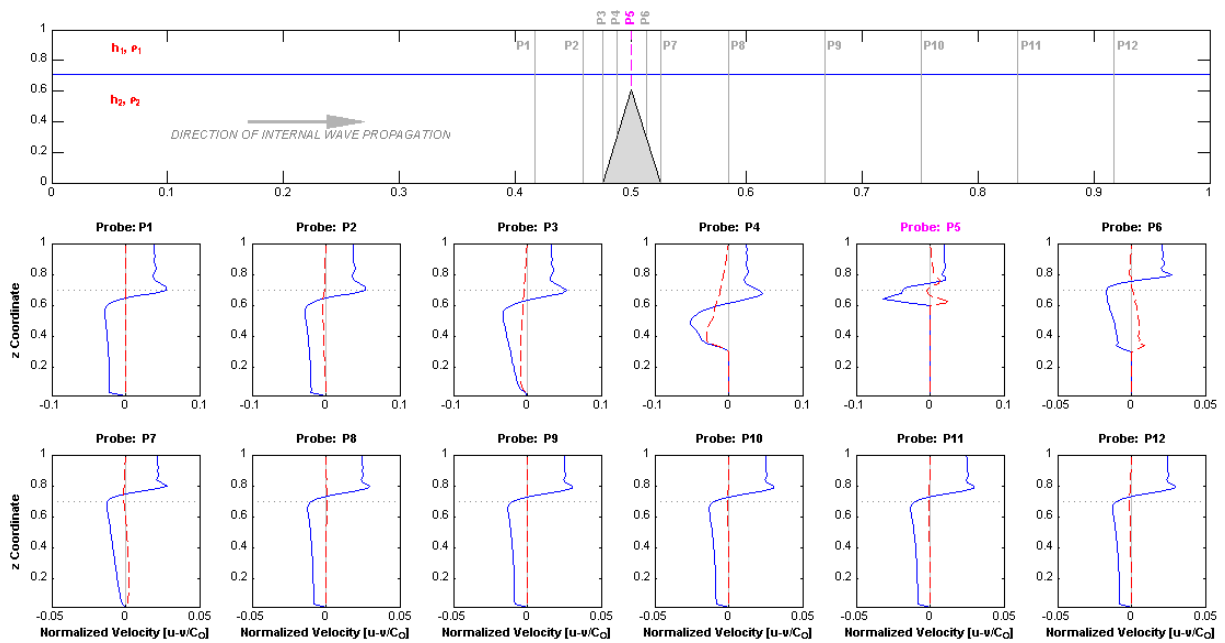


Figure 72. Time series plots of normalized velocity vector profiles for a depression-type ISW at 12 uniformly-spaced locations during an encounter with an isolated triangular obstacle. Horizontal velocity vectors are blue (or solid) lines. Vertical velocity vectors are red (or dashed) lines. The pycnocline elevation is depicted by a dotted line.

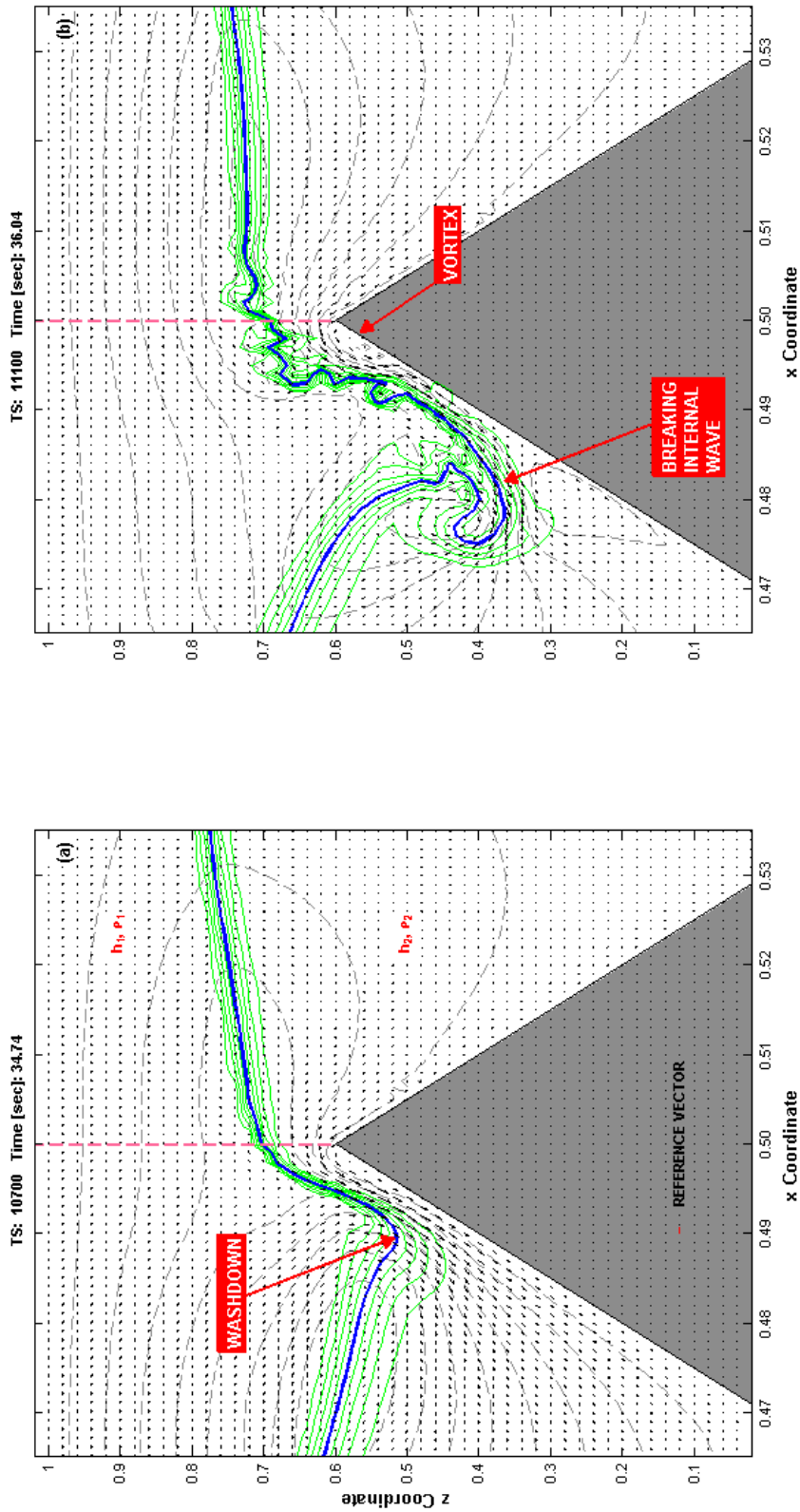


Figure 73. Selected details of a non-dimensional numerical simulation between an elevation-type ISW and an isolated triangular obstacle depicted in Figure 71 showing “full interaction” (Table 14). The vertical dashed line corresponds to the position of the theoretical turning point plane defined by $h_1 = h_2$. Vectors in the velocity field are shown as streamlines (dashed lines). (a) Onset of shoaling/breaking defined by “wash-down.” (b) “Breaking” of the ISW defined by the overturning of the pycnocline.

The physical configuration of the numerical simulation depicted in Figure 71 was such that the encounter between the ISW and the triangular obstacle evoked “full interaction” between the two. The magnitude of the blocking parameter ζ was approximately 0.8. To provide another perspective on how an ISW would hydrodynamically interact with this type of topographic shape, the simulation was repeated but under a different dimensional arrangement yielding different value for the blocking parameter ζ . Figures 74 and 75 show essentially the same non-dimensional simulation depicted in Figure 71 but configured in such a way as to illustrate, respectively, “moderate” and “weak interaction” with the topographic obstacle. The “moderate interaction” simulation (blocking parameter $\zeta = 0.5$) essentially generated all four phases of the wave breaking progression (Figure 74). As predicted by theory, the “weak interaction” simulation (blocking parameter $\zeta = 0.39$) produced on a modest wash-down feature and a questionable bore-like feature (Figure 75) suggesting little or no interaction.

What distinguishes the “moderate” and “weak interaction” simulations from the so-called “full interaction” simulation is the location of the pycnocline relative to the obstacle. In the “full interaction” simulation, the pycnocline has migrated to a position relatively close to the obstacle as a result of entrainment (shoaling). In the “moderate interaction” simulation, there is even more physical

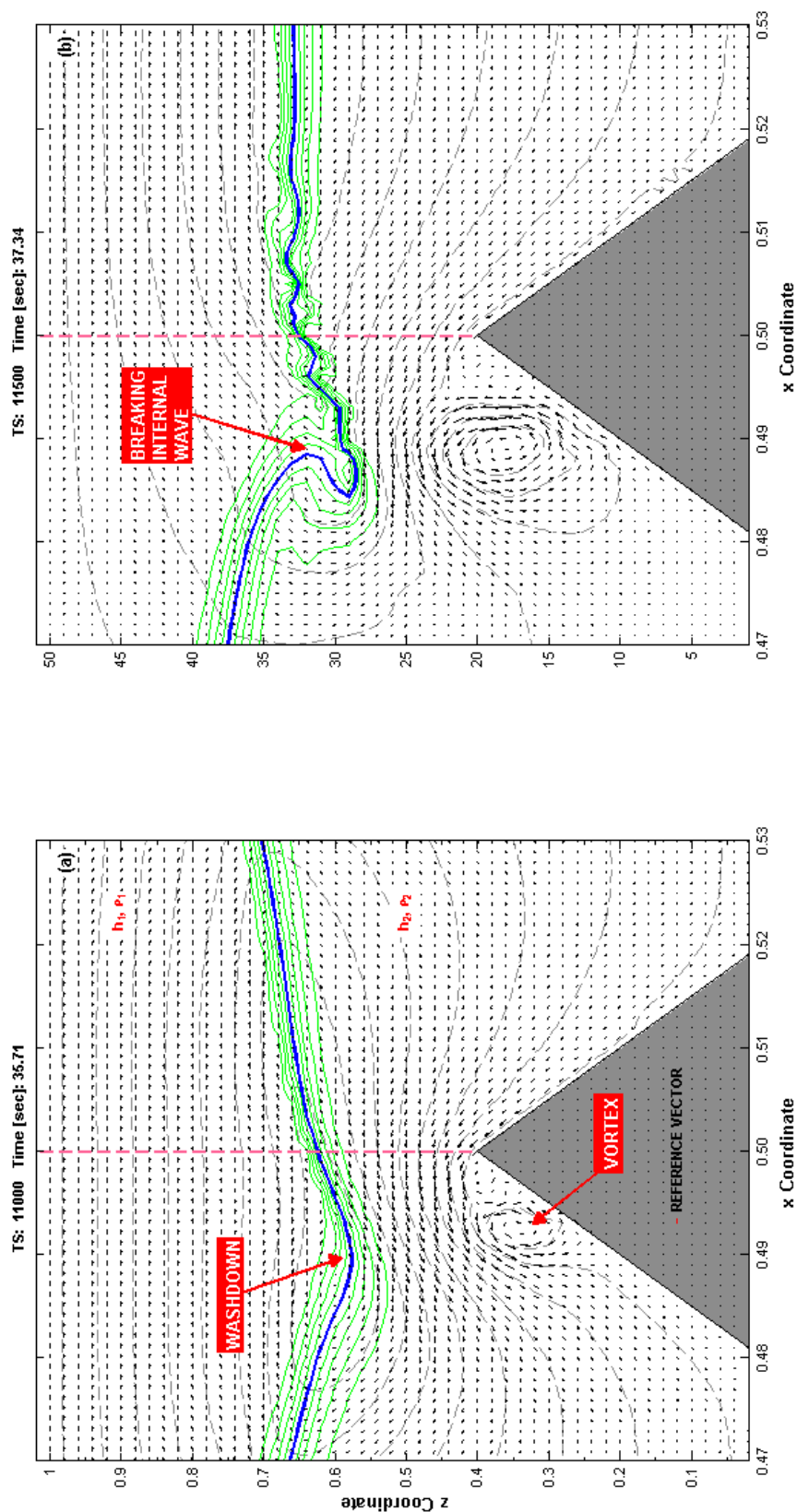


Figure 74. Selected details of a non-dimensional numerical simulation between an elevation-type ISW and an isolated triangular obstacle displaying “moderate interaction” (Table 14). The vertical dashed line corresponds to the position of the theoretical turning point plane defined by $h_1 = h_2$. Vectors in the velocity field are shown as are streamline contours (dashed lines). (a) Onset of shoaling/breaking defined by “wash-down.” (b) “Breaking” of the ISW defined by the overturning of the pycnocline.

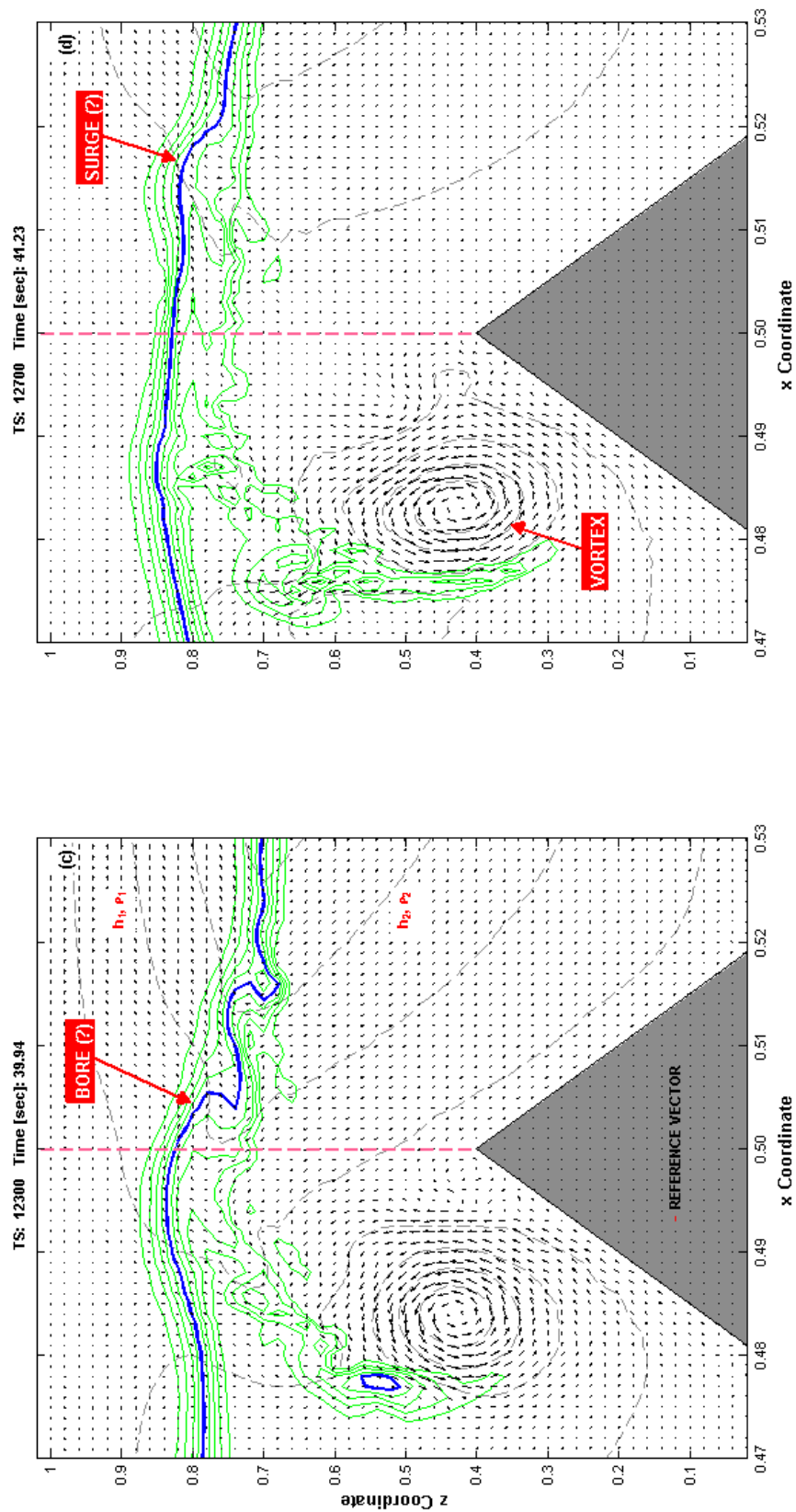


Figure 74. Continued. (c) Example of likely bolus/bore-like feature advancing beyond the plane of the theoretical turning point (vertical dashed line). (d) Example of likely internal wave surge.

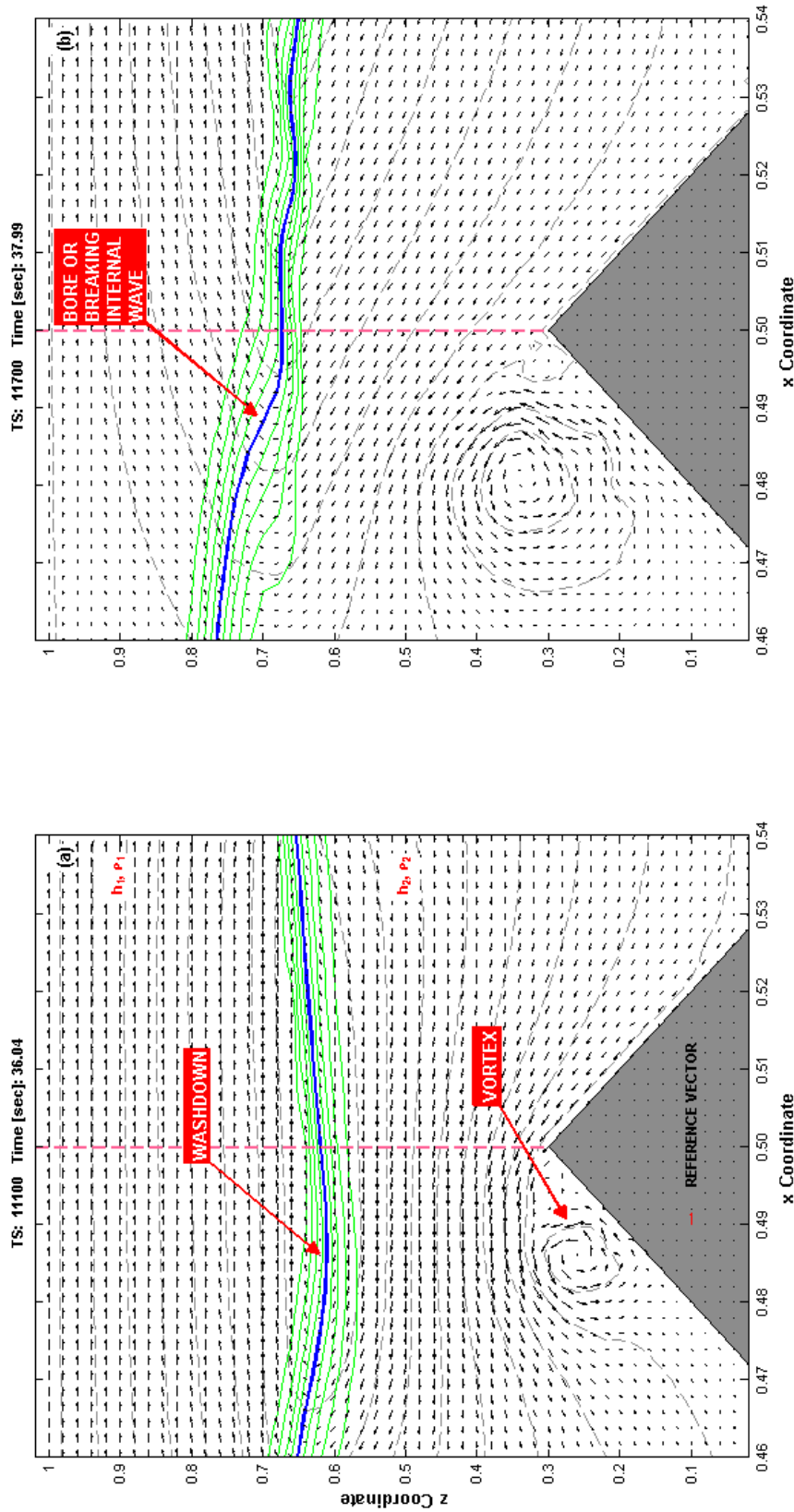


Figure 75. Selected details of a non-dimensional numerical simulation between an elevation-type ISW and an isolated triangular obstacle showing weak interaction (Table 14). The vertical dashed line corresponds to the position of the theoretical turning point plane defined by $h_1 = h_2$. Vectors in the velocity field are shown as are streamline contours (dashed lines). (a) Onset of shoaling/breaking defined by “wash-down.” (b) “Breaking “of the ISW.

separation between the pycnocline and the obstacle (Figure 74), suggesting a lesser degree of hydrodynamic communication (in the form of shoaling) between the two. Consistent with theory (Table 14), the “weak interaction” simulation (Figure 75) illustrates yet even more physical separation between the pycnocline and the obstacle implying that the presence of the topographic obstacle has little, if any, influence of the propagation of the ISW.

4.3.2 Quantitative Effects of Topographic Obstacles on ISWs

The numerical simulation trials depicted in Section 4.3.1 were intended to illustrate how ISWs interact with submerged topographic obstacles. The types of obstacle types selected for the simulations (Figure 47) were considered representative of the isolated topographic forms likely to be found in a marine setting. Although the simulations provided a reasonable physical representation of the wave breaking progression process, there is a qualitative aspect to these interactions that deserves some attention.

It was mentioned earlier that a key parameter controlling wave-breaking behavior in depression-type ISWs is the blocking parameter ζ (equation 4.10). Cheng (2006) has suggested that there is another variable that can also be used to evaluate wave breaking behavior. It is the nonlinear [blocking] parameter α_{NL}

and it can be expressed as ³³:

$$\alpha_{NL} = \frac{a_i}{h_2} \quad (4.12)$$

When considering both equations 4.10 and 4.11, researchers have been able to characterize the interactions as “weak,” “moderate,” or “strong” (i.e., “breaking”). In general, as the magnitude of the blocking parameters increase, the effect an obstacle’s relative height has on an internal wave’s behavior becomes more pronounced resulting in some moderation in the wave’s properties. Some of these effects will be examined in the following pages of this dissertation.

To evaluate the moderating influence a topographic obstacle has on ISW properties, 36 numerical simulation trials representing different modeling configurations were conducted using an isolated triangular obstacle. Results from these simulations are presented in Figures 76 through 78. In Figure 76, the effect of the non-linear parameter on the normalized amplitude of the transmitted ISW, following its encounter with the triangular obstacle, is illustrated. Figure 76(a) shows the numerical simulation trial results compare

³³ Not to be confused with the K-dV nonlinear coefficient α cited earlier in equation 2.2.

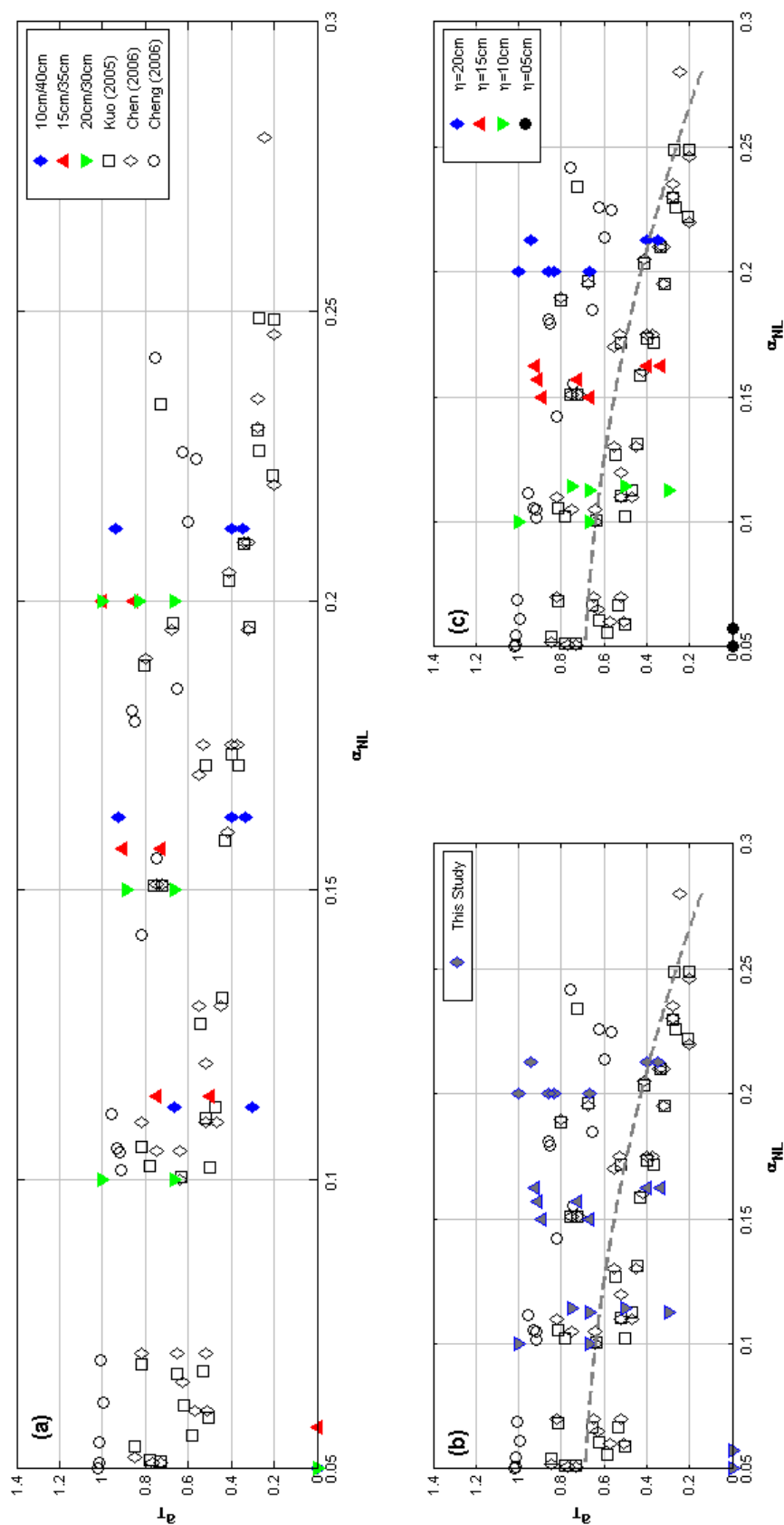


Figure 76. Normalized amplitude of transmitted internal wave vs. nonlinear parameter a_{NL} for simulated 50cm-deep wave tank trials involving an isolated triangular obstacle. Plots show data for 36 numerical simulation trials. (a) Comparison to Kuo (2005), Chen (2006), and Cheng (2006) experimental wave tank trials. (b) Comparison to MATLAB-generated best-fit curve of Kuo (2005) Chen (2006), and Cheng (2006) data. (c) Numerical simulations differentiated by magnitude of potential well depth η .

to experimental data collected by Kuo (2005), Chen (2006), and Cheng (2006). The trend of those experimental data can be approximated using a MATLAB-generated best-fit curve in Figure 76(b). This 2nd order polynomial curve indicates an inverse relationship between the magnitude of the transmitted wave amplitude and the non-linear parameter. When considering the best-fit curve, the results from the 36 numerical simulation trials are generally in good agreement with the normalized experimental data reported in the literature. As indicated by Figure 76(b), the 36 numerical simulation trial results straddle the best-fit curve. In general, the slope of the best-fit curve suggests that wave speed is sensitive to a change in the magnitude of the blocking parameter. This exhibit also suggests that for every unit change in the non-linear parameter, there is a six-fold decline in the wave speed. As the height of the obstacle is increased, there is a corresponding decline in the amplitude of the transmitted ISW.

To better understand which particular simulation configuration produced results that closely-matched the MATLAB-generated best-fit curve, data from the 36 numerical simulation trials are differentiated according to magnitude of the potential well depth η in Figure 76(c). This figure shows that for those numerical simulation trials based on either $\eta = 10$ cm or $\eta = 15$ cm, simulation results closely match the overall trend of the best-fit curve of the normalized

data. This observation would comport with Grue et al. (1999) who noted good correspondence between experimental results and theory for low-amplitude ISWs where $0.4 < \frac{a}{h_2} < 0.5$. When considering this exhibit, the other issue to consider is that under certain system configurations, the numerical solution may have associated with it non-linearities that are unavoidable, hence the lack of correlation between some of the experimental data in the literature and the results of certain simulation configurations (the 10 cm/40 cm simulation) as well as the occurrence of some outliers (simulations where $\eta = 20$ cm). These nonlinearities are once again likely attributable to the influence of the rigid-lid assumption.

The effect of the non-linear parameter α_{NL} on ISW speed following its encounter with the triangular obstacle is shown in Figure 77. Figure 77(a) shows the normalized amplitude of the transmitted ISW for 36 numerical simulation trials in relation to experimental data obtained by Cheng (2006). Figure 77(b) shows how these data compare to a MATLAB-generated best-fit 2nd order polynomial curve corresponding to the overall trend of those data. Once again, the simulation results are in good agreement with the best-fit curve. The slope of this curve indicates that the normalized wave speed is inversely proportional to the magnitude of the non-linear parameter. To understand which particular simulation configuration produces results that might be in

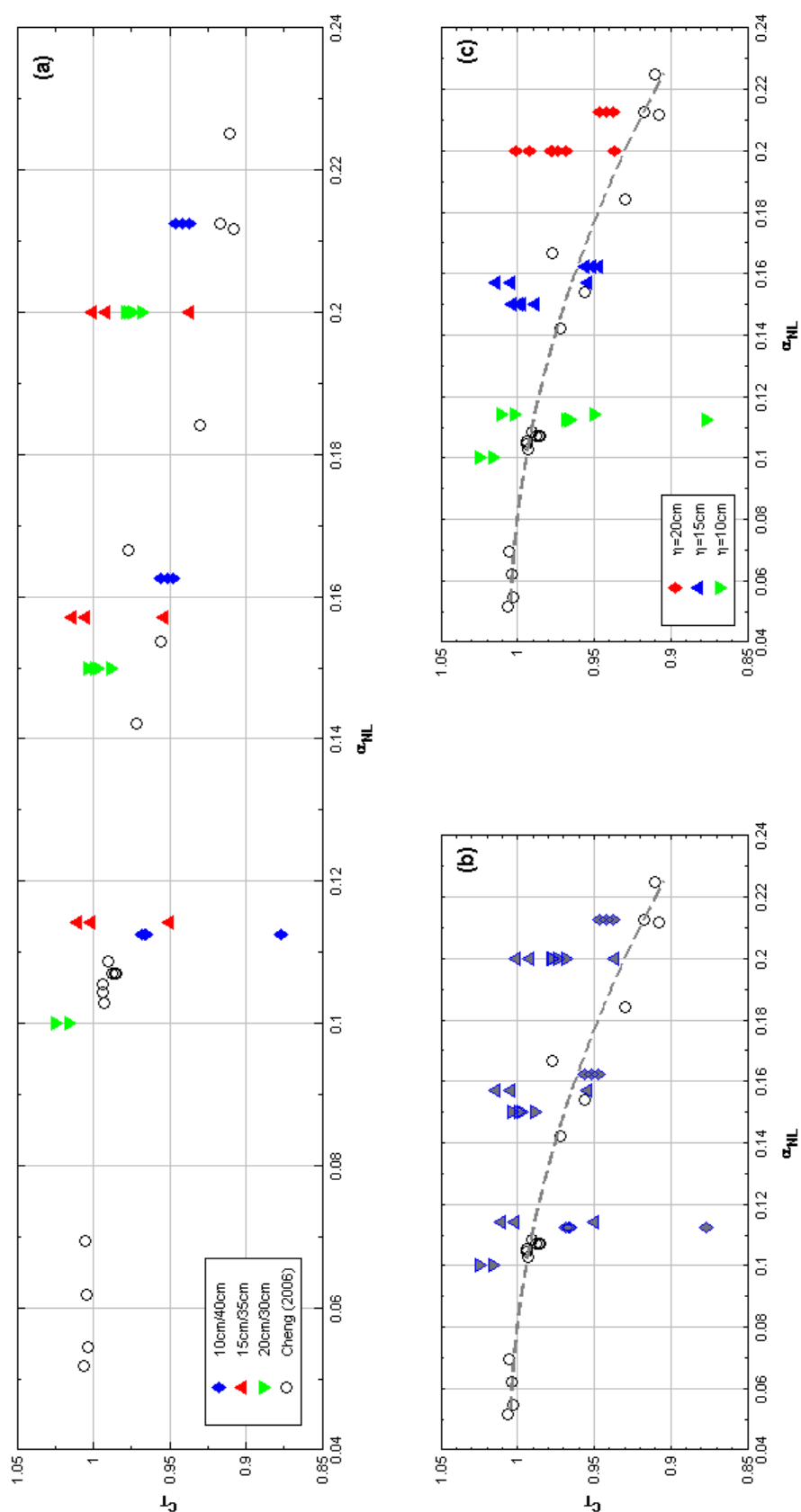


Figure 77. Normalized wave speed for a transmitted ISW vs. nonlinear parameter α_{NL} for simulated 50 cm-deep wave tank trials involving an isolated triangular obstacle. Plots show data for 36 numerical simulation trials. (a) Comparison to Cheng (2006) experimental wave tank trials. (b) Comparison to MATLAB-generated best-fit curve of Cheng (2006) data. (c) Numerical simulation trials differentiated by magnitude of potential well depth η .

closest agreement with the best-fit curve, the data from the 36 numerical simulation trials are presented in such a way in Figure 77(c) to allow them to be differentiated according to the magnitude of the potential well depth η . This exhibit shows that for those numerical simulations based on either $\eta = 10$ cm or $\eta = 15$ cm, results are produced that closely match the overall trend of the best-fit curve as well as the predictions of Grue et al. (1999) concerning small-amplitude ISWs in experimental settings.

The numerical simulation trial results depicted in Figures 73 through 75 illustrate the effects of the nonlinear parameter α_{NL} on ISW properties following an encounter with an isolated triangular obstacle. The next two exhibits in this dissertation illustrate the effect such encounters might have on ISW energy transmission. Figure 78 compares the normalized transmitted wave energy E_p to the nonlinear parameter. For this study, transmitted wave energy is defined as:

$$E_p = \frac{E_{incident} - E_{transmitted}}{E_{incident}} \quad (4.13)$$

Figure 78(a) shows the normalized wave energy associated with the transmitted ISW for 36 numerical simulation trials in relation to experimental data collected by Cheng (2006) for both triangular and trapezoidal

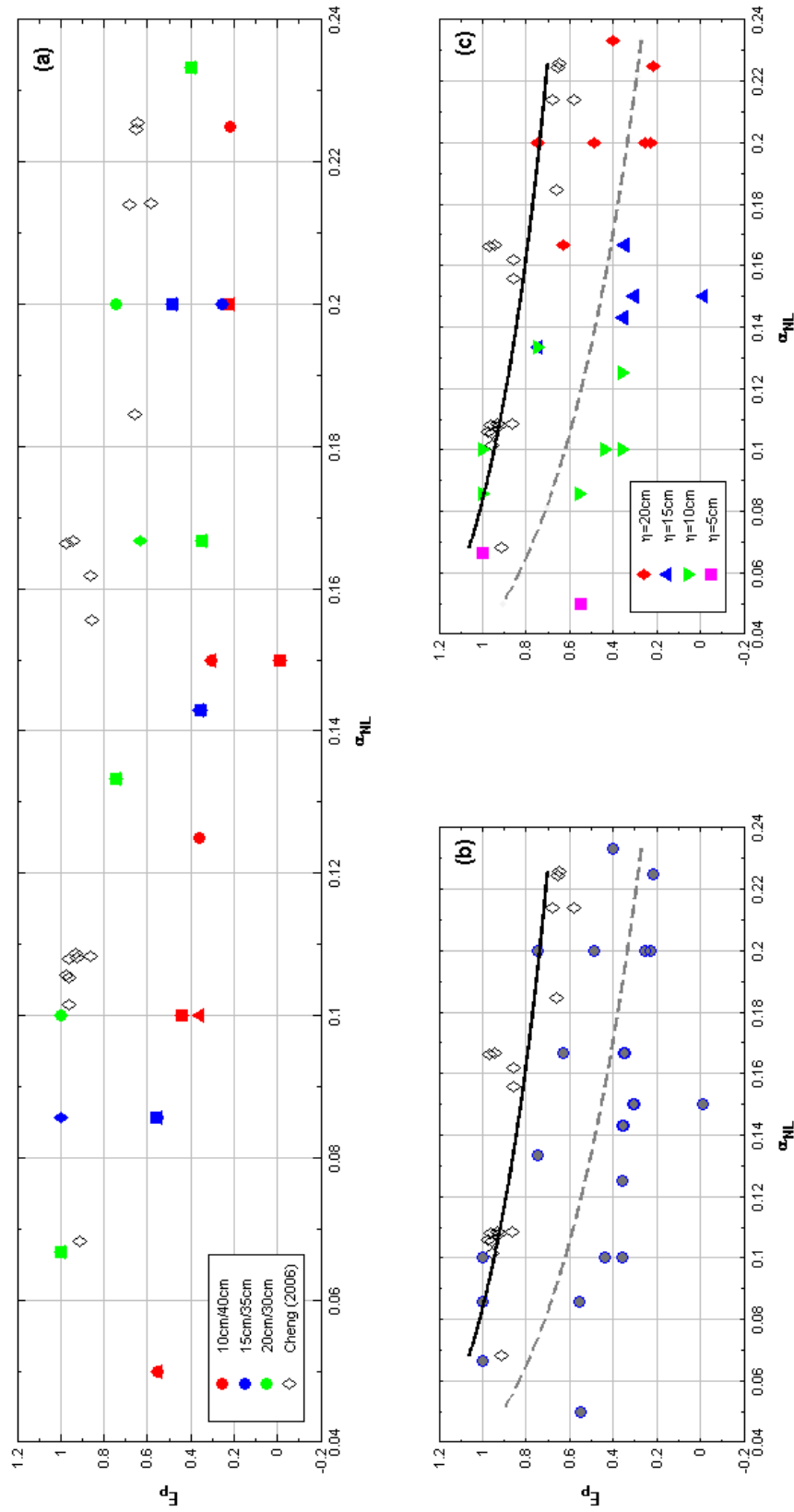


Figure 78. Normalized energy for a transmitted ISW vs. nonlinear parameter α_{NL} for simulated 50 cm-deep wave tank trials involving an isolated triangular obstacle. Plots show data for 36 numerical simulation trials. (a) Simulation results are compared to Cheng (2006) experimental wave tank trials that involved both triangular and trapezoidal obstacles. (b) MATLAB-generated best-fit curve of Cheng (2006) data depicted by solid line; dashed line corresponds to MATLAB-generated best-fit curve for simulations performed for this study. (c) Numerical simulation trials differentiated by magnitude of potential well η .

obstacles.³⁴ In Figure 78(b), the numerical simulation data are shown in relation to a MATLAB-generated best-fit curve corresponding to the trend of the Cheng (2006) data. This 2nd order polynomial defining this curve generally indicates an inverse relationship between the magnitude of the transmitted wave energy and the nonlinear parameter.

However, unlike the data plots of the transmitted wave amplitude and transmitted wave speed, the normalized plot of the transmitted wave energy indicates that while some of the simulation results rest on (or are coincident with) the best-fit curve, many fall below it. A second best-fit curve (corresponding to a dashed line) has been added to Figure 78(b) to show the trend of the data from the 36 numerical simulation trials. Both best-fit curves display the same general trend suggesting that the numerical simulation trials have accurately captured the basic physics of the interactions between the ISW and an isolated topographic obstacle. The disparity in the relative positions of the two curves reflects likely differences between experimental data acquired from wave tank trials from “data” acquired through an abstracted numerical simulation, in 2D, using a digital computer code. The reader is reminded that through the abstraction/modeling process, it is not possible to mathematically

³⁴ A trapezoid can be used as another geometric variant for a seamount type of topographic obstacle.

capture (or account) for some of the hydrodynamic process expected to occur in concert with the wave translating physically through a wave tank in a 3D environment. Another plausible explanation is that certain system configurations have a tendency to enhance non-linearities in the computer simulation more so than others.

An alternative perspective on the influence of obstacle height on ISW transmission can be obtained by examining the blocking parameter ζ . Unlike the nonlinear parameter α_{NL} , which relies on two variables (equation 4.11), the blocking parameter ζ (equation 4.10) is defined using four variables — wave amplitude, obstacle height, and the respective fluid layer depths. Figure 79 is a scatter diagram that shows how the blocking parameter ζ affects the amount wave energy transmitted following an encounter with a topographic obstacle. In Figure 79(a), results from the 36 numerical simulation trials are shown in relation to normalized experimental data collected by Kuo (2005), Chen (2006), and Cheng (2006). The data shown in this figure are limited to an encounter between depression-type ISWs and an isolated triangular obstacle. The distribution of the experimental data suggests a tightly-clustered, linearly-trending distribution which implies that an increase in the blocking parameter ζ magnitude produces a corresponding decrease in the amount of ISW energy

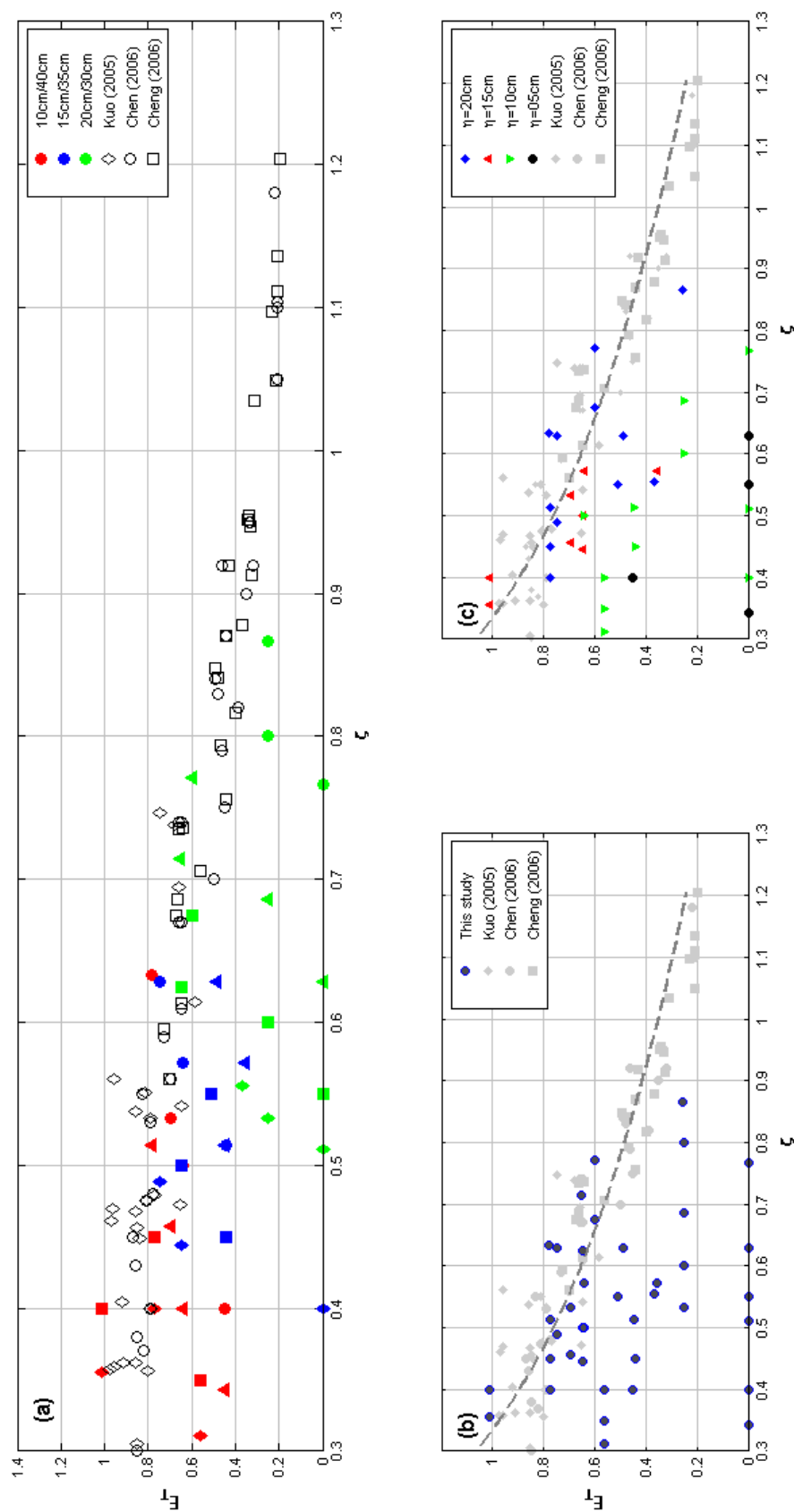


Figure 79. Normalized transmitted wave energy for an ISW vs. blocking parameter ζ for simulated 50 cm-deep wave tank trials involving an isolated triangular obstacle. (a) Simulation results are compared to experimental wave tank trials Kuo (2005), Chen (2006), and Cheng (2006). (b) Comparison to MATLAB-generated best-fit curve of Kuo (2005) and Cheng (2006) data.

transmitted. The trend for the statistics attributed to the numerical simulations is somewhat less apparent by virtue of their less-clustered distribution.

The trend of the data are more clearly revealed when they are fitted with MATLAB-generated best-fit curves. Figure 79(b) shows how the two data sets compare when best-fit curves are added — in this particular example, the best-fit curves are straight lines that indicate generally positive correlation. Two points are noteworthy concerning this exhibit. The first point is that the distribution of the simulation data generally falls above and slightly behind the more-linear trending distribution of experimental data. The second is that the slope of the best-fit line for the simulation data (solid line) is higher than the slope for the experimental data (dashed line) suggesting a higher rate of energy loss when the magnitude of the blocking parameter ζ increases. Overall, it can be concluded that the numerical simulation trials conservatively approximate the results obtained by other experimentalists as they underestimate those results.

A slightly different perspective on ISW energy transmission can be obtained by considering the wave energy transmission coefficient. This coefficient E_T can be defined as:

$$E_T = \frac{E_{Transmitted}}{E_{Incident}} \quad (4.14)$$

Figure 80 compares the wave energy transmission coefficient to the blocking parameter ζ . Comparing those variables allows for isolated topographic obstacles to be indexed according to their ability to attenuate wave energy. Figure 80(a) compares the results from the 36 numerical simulation trials in relation once again to comparable data collected by Kuo (2005), Chen (2006), and Cheng (2006). Figure 80(b) shows how the simulation data compare to MATLAB-generated best-fit curves. This logarithmic curve indicates an inverse relationship between the magnitude of the transmitted wave energy and the blocking parameter ζ . As the magnitude of the blocking parameter ζ increases, the amount of transmitted internal wave energy decreases.

What is conspicuous about this particular exhibit is that a several of the calculated estimates from the simulations rest on the abscissa, suggesting that no energy is transmitted as a result of the internal wave's encounter with the topographic obstacle. Although this might be true, another plausible explanation rests with the resolution capability of the finite difference method itself and the limitation of the numerical method to capture system variations that are smaller than the size of the grid spacing and thus beyond the resolution capability of the computer code.

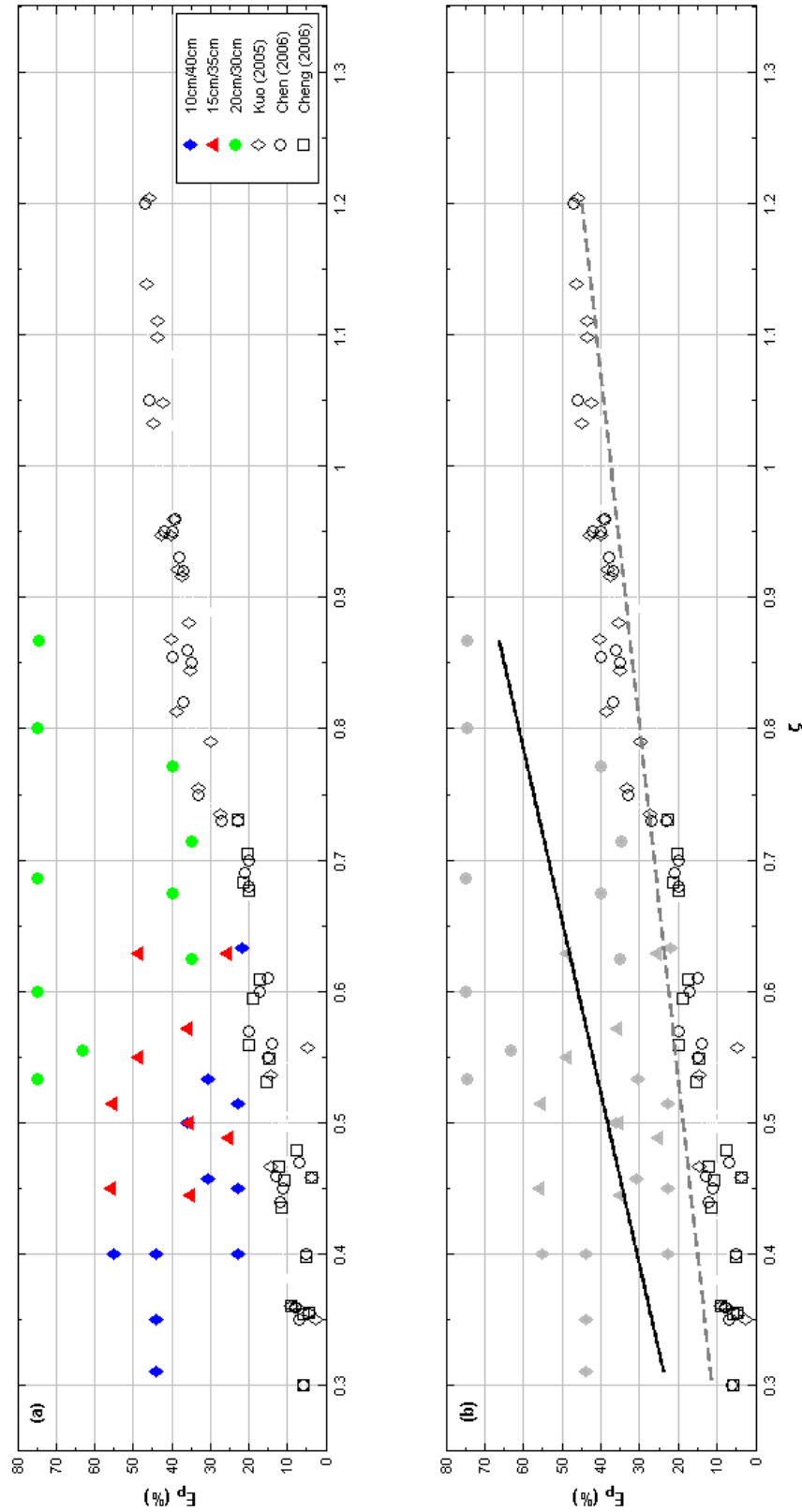


Figure 80. Wave energy transmission coefficient vs. blocking parameter ζ for simulated 50 cm-deep wave tank trials involving an isolated triangular obstacle. (a) Simulation results are compared to Kuo (2005), Chen (2006), and Cheng (2006) experimental wave tank trials. (b) Comparison to MATLAB-generated best-fit curves. (c) Numerical simulation trials differentiated by magnitude of potential well depth η .

4.3.3 Static Stability vs. Dynamic Instability

Earlier in this dissertation, it was mentioned that the artificial formation of an ISW, using a potential well as part of the numerical simulation, results briefly in a transient phase of wave development during which time there is the formation of K-H-like billows corresponding to dynamic instability within the fluid. These billows form when the more dense fluid overlies the less dense fluid. When they grow large enough, the billows collapse into turbulence and turbulent mixing. Also, the numerical simulation reveals that when an ISW interacts with a submarine obstacle, the entrainment process (i.e., “wash-down,” “breaking,” “bore formation,” and “surge”) results in conditions conducive to hydrodynamic instability resulting in wave-breaking phenomena and the production of K-H-like billows.

The question thus arises as to whether there might be an additional (quantitative) expression of instability in the simulation aside from an evaluation of the changing geometries of the pycnocline, isopycnals, velocity vectors, and the like. The evaluation of the Richardson number in both time and space provides another opportunity to evaluate the behavior of the ISW in the presence of topographic obstacles.

The ocean tends to be strongly stratified with a less-dense layer of water generally resting over a more-dense water layer. This generally accounts for the

well-defined deep ocean pycnocline illustrated in earlier Figure 10. As ocean currents tend to be weak and dominated by shear flow, turbulent mixing is intermittent and generally rare in a marine setting owing to the stabilizing influence of buoyant forces (Munk 1966). Along the boundaries of the oceans, mixing is driven primarily by topographic influences (Kunze and Llewellyn-Smith 2004). When turbulent mixing does take place in the open ocean, it can usually be attributed in large measure to (breaking) internal waves (Garrett and Munk 1979, Gregg 1980, Munk 1981). The measure of the stability of a stratified fluid system such as that described above can be expressed in terms of the Richardson number. This number (defined by equation 2.11) represents the resistance of a fluid parcel within a 2D water column to external perturbations. Mathematically, it describes the ratio of stabilizing buoyant forces the destabilizing shear forces caused by a velocity gradient that varies with depth.

Based on classic papers by Miles (1961) and Howard (1961), for an ideal 2D Boussinesq fluid that is stably-stratified, a linear stable threshold for steady horizontal shear flows holds that the respective fluid layers are stable everywhere in the water column when $Ri \geq 0.25$. When conditions are such that $0.25 > Ri > 0$, dynamic instability dominates the system. When these conditions exist, an exponential growth in turbulence can occur at the density interface producing K-H vortices. Eventually, the vortices grow into interfacial waves that

overturn and break. When the Richardson number is less than zero, the system is not stably-stratified; the upper fluid layer h_1 is heavier than the lower fluid layer h_2 and buoyant instability prevails.

Another perspective on the potential for turbulence and turbulent mixing within a stratified system is to examine the extent to which the water column might be statically stable. Oceanographers frequently rely on the evaluation of the normalized density gradient E_D , as represented by the following equation:

$$E_D \approx -\frac{1}{\rho} \frac{d\rho}{dz} \quad (4.15)$$

where E_D can be related to the Richardson number (equation 2.11) through the Brunt-Väisälä frequency (equation 2.14):

$$N^2 = gE_D \quad (4.16)$$

Vertical stability within the water column can be defined when $E_D > 0$ indicating that a less-dense fluid layer rests above a more-dense fluid layer. This condition is the most common density configuration encountered in nature. When $E_D < 0$, the system is vertically unstable suggesting just the opposite scenario — a more-dense fluid layer rests above a less-dense fluid layer thus encouraging strong vertical mixing (or gravitational overturning) due to the influence of buoyant forces. Various combinations of the physical processes and conditions identified in Table 2 can produce a vertically unstable density profile.

When $E_D = 0$, the system is neutrally stable owing to the relative densities of the two fluid layers being approximately the same.

Numerical simulations allow for the interrogation of the computational domain to determine the nature of the stability conditions. In this regard, calculation of both the Richardson number and the normalized density gradient, temporally as well as spatially, can provide additional insights regarding the hydrodynamics of the system. The next series of exhibits show an estimated Richardson number and the normalized density gradient in relation to some examples of ISW/topographic obstacle interactions described earlier in this dissertation. These exhibits were selected as they show examples of “strong,” “moderate,” and “weak” internal-wave/obstacle interaction (Table 14). The simulation exhibits are limited to trials involving both an isolated rectangular obstacle (Figures 81 and 82) as well as an isolated triangular obstacle (Figures 83 through 85). In the exhibits that follow, three stability “states” are depicted graphically:

State	Condition	Symbol
Richardson or K-H instability	$0.0 < Ri < 0.25$	■
Buoyant stability	$E_D > 0$	○
Buoyant instability	$E_D \leq 0$	◆

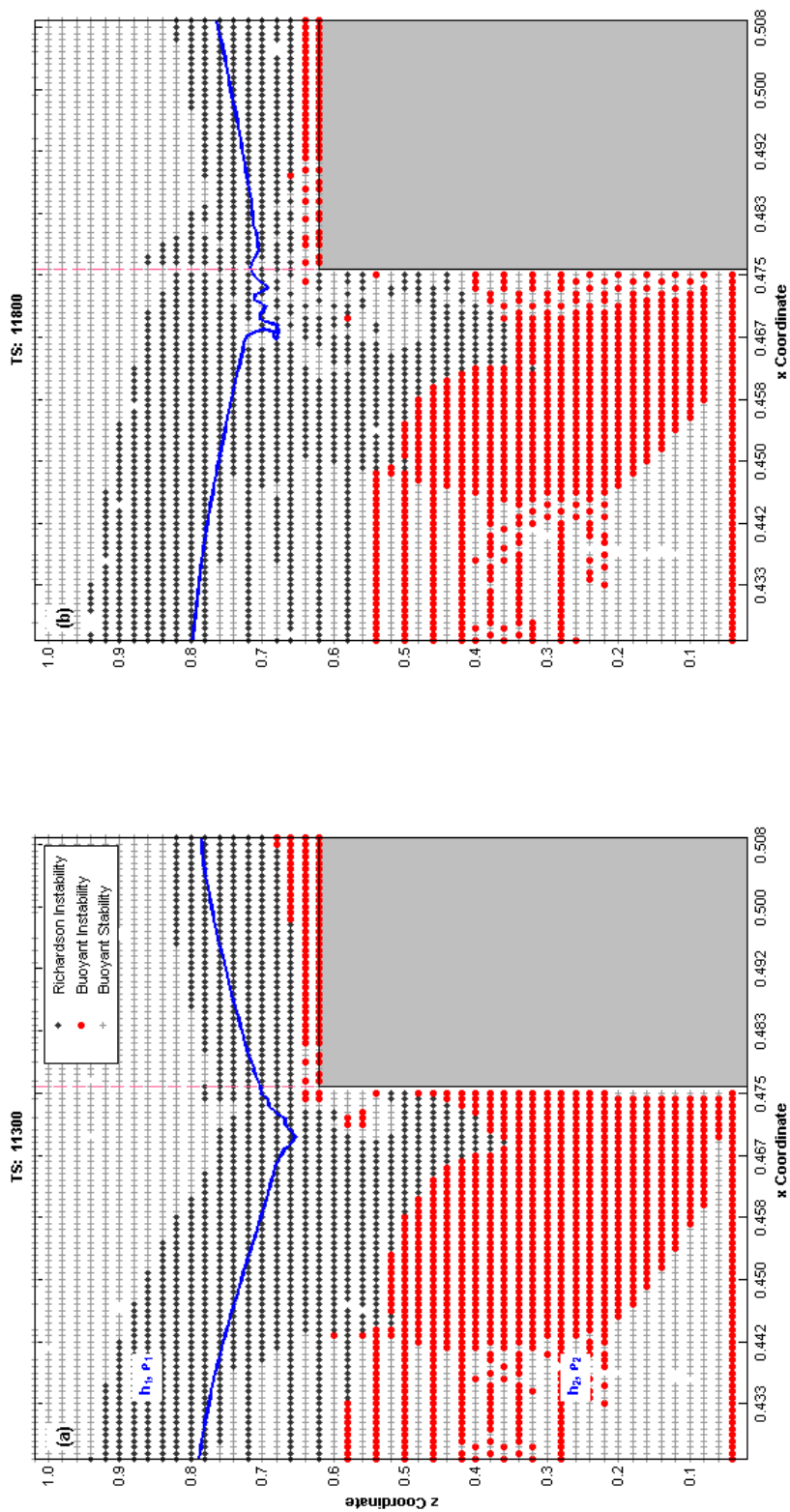


Figure 81. Spatial distribution of localized instability resulting in “full interaction” (Table 14) between an isolated rectangular obstacle and an ISW. (a) “Wash-down” phase. (b) “Breaking” phase. $Fn = 0.68$. Exhibit corresponds to numerical simulation trial shown earlier in Figure 67.

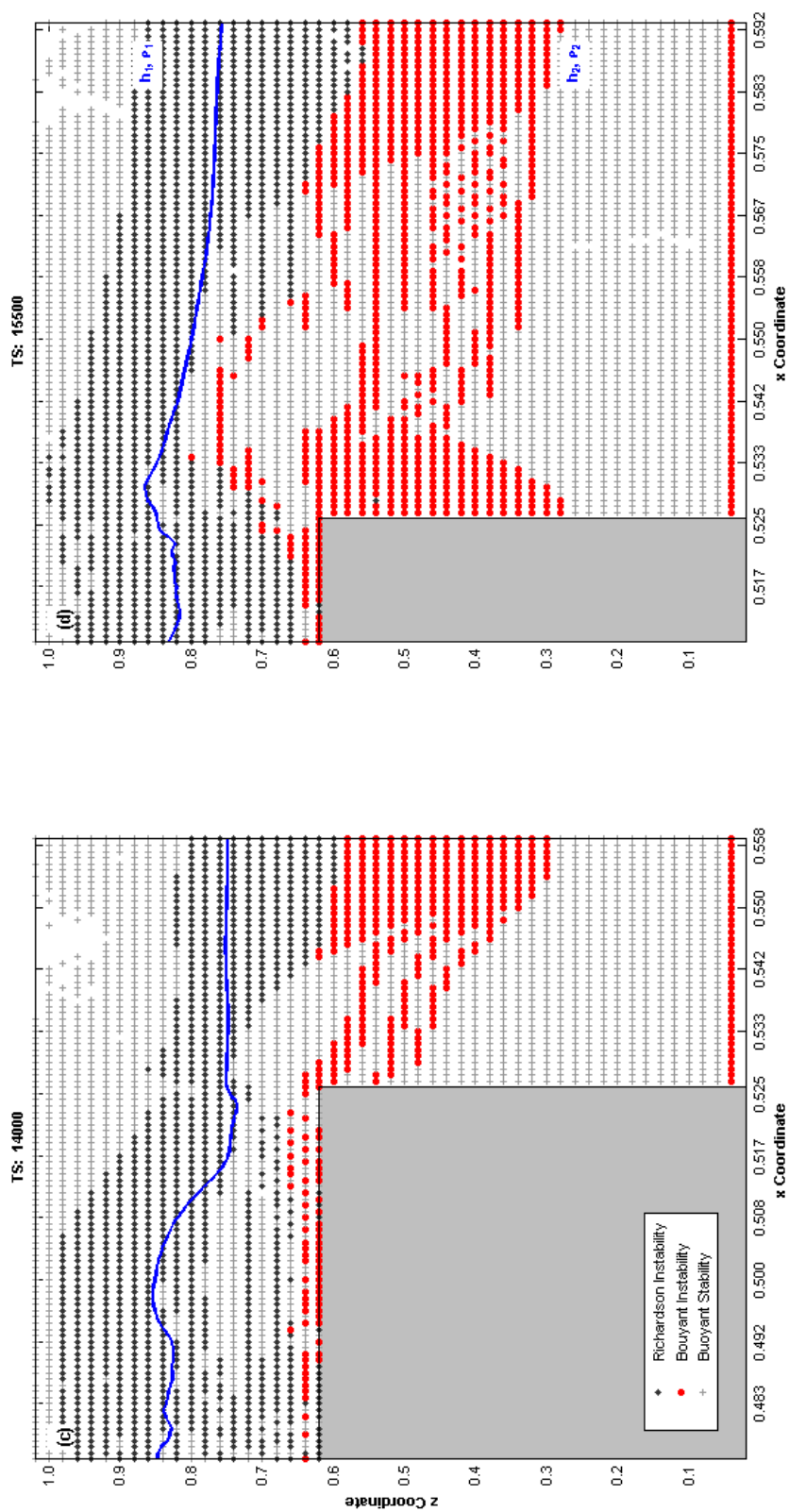


Figure 81. Continued. (c) “Bore formation” phase. (d) “Surge” phase.

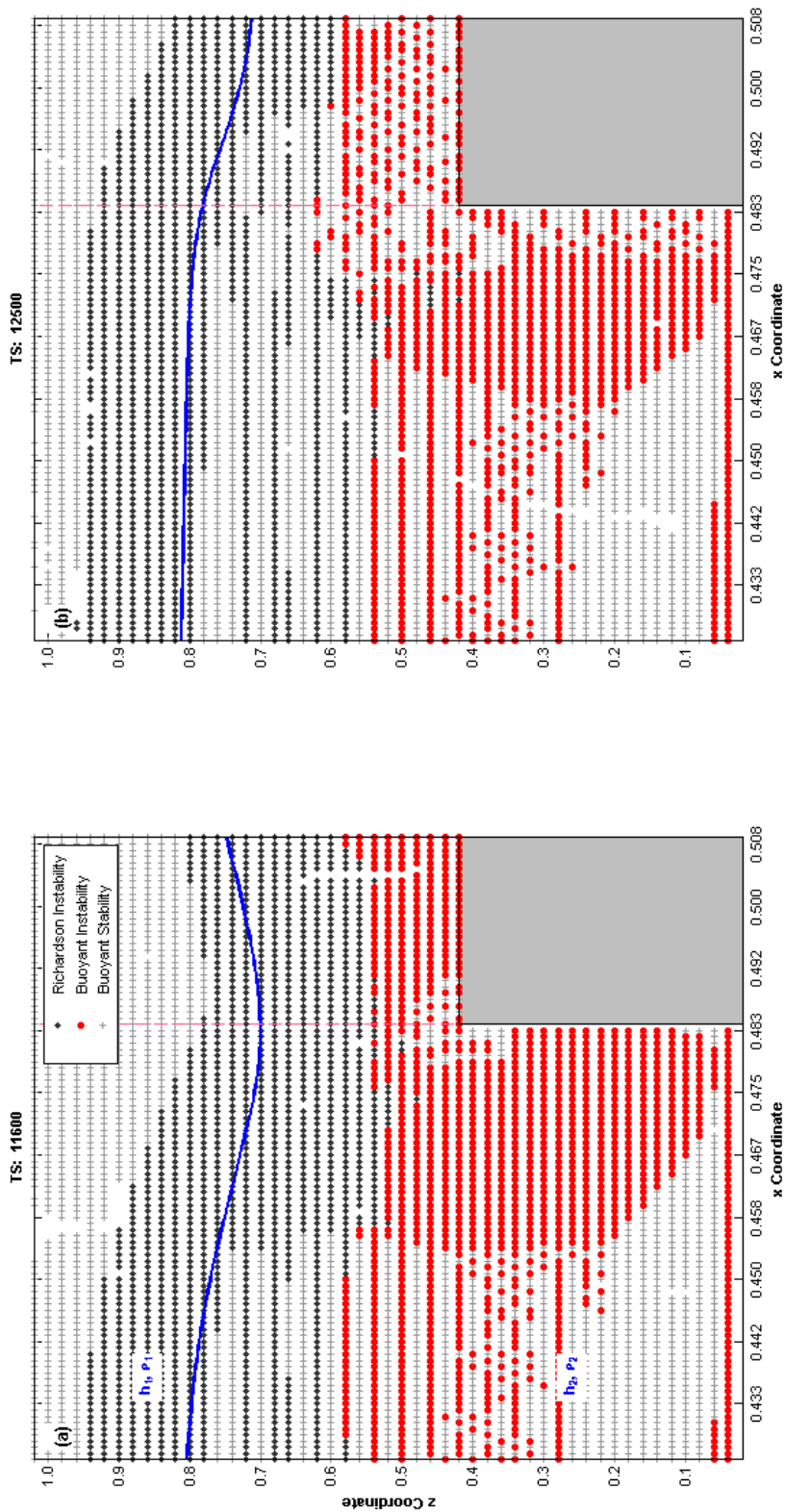


Figure 82. Spatial distribution of localized instability resulting in “weak interaction” (Table 14) between an isolated rectangular obstacle and an ISW. Solid line corresponds to the pycnocline. (a) “Breaking” phase. (b) “Wash-down” phase. $Fn = 0.68$.

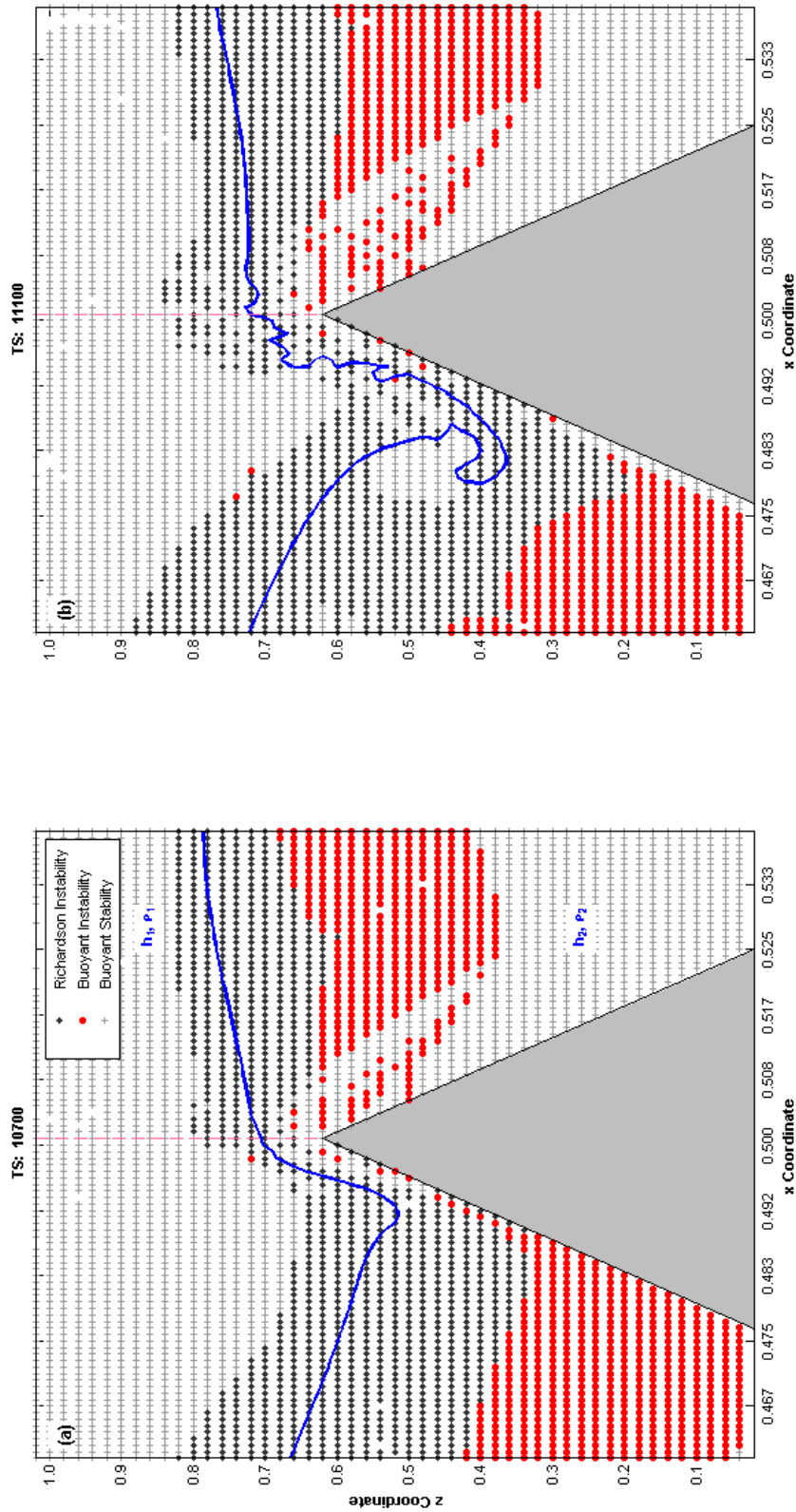


Figure 83. Spatial distribution of localized instability resulting in "full interaction" (Table 14) between an isolated triangular obstacle and an ISW. Solid line corresponds to the pycnocline. (a) "Breaking" phase. (b) "Wash-down" phase. $Fr = 0.68$. Exhibit corresponds to numerical simulation trial shown earlier in Figure 73.

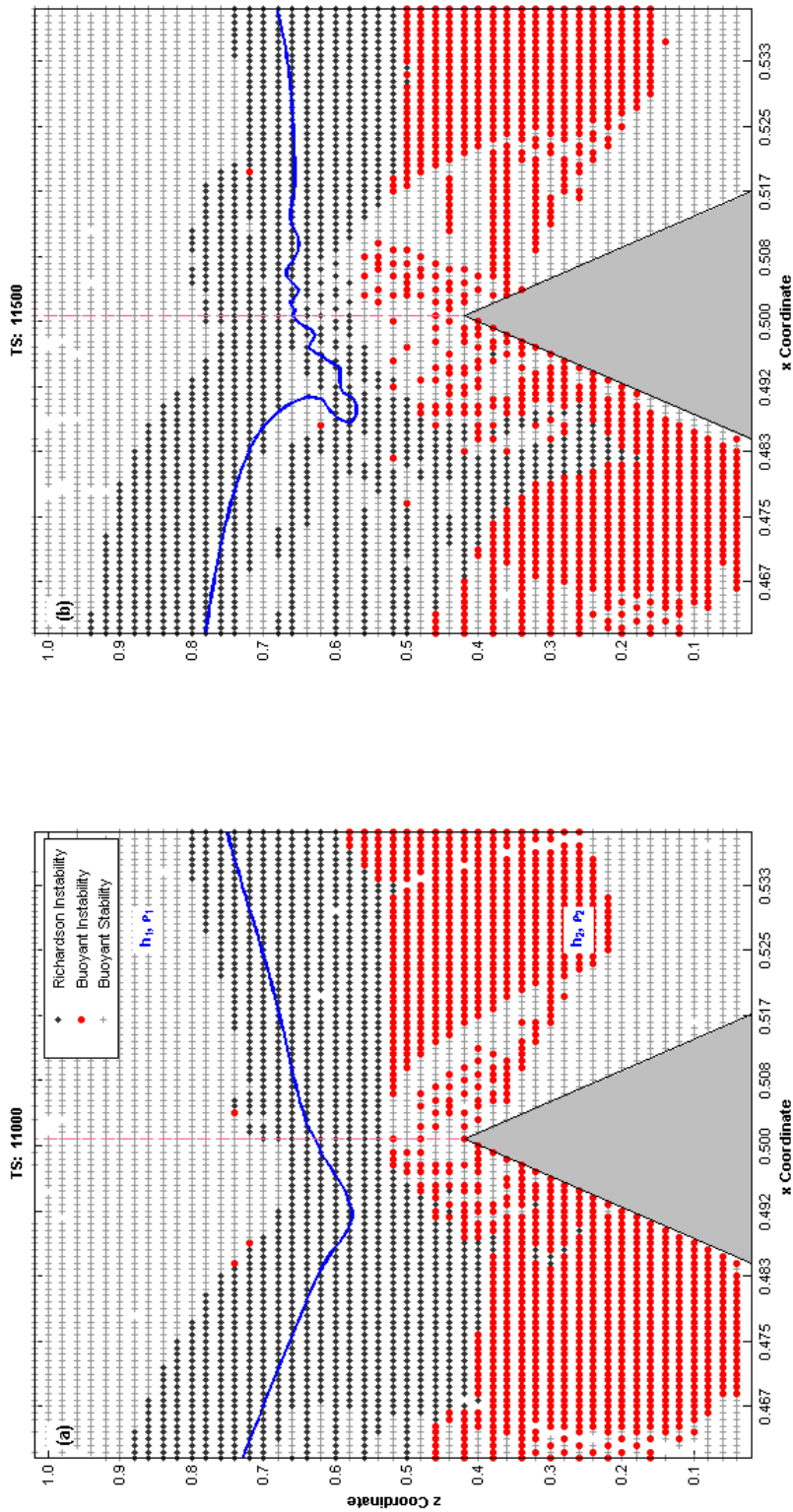


Figure 84. Spatial distribution of localized instability resulting in “moderate interaction” (Table 14) between an isolated triangular obstacle and an ISW. Solid line corresponds to the pycnocline. (a) “Breaking” phase. (b) “Breaking” phase. $Fn = 0.68$. Exhibit corresponds to numerical simulation trial shown earlier in Figure 74.

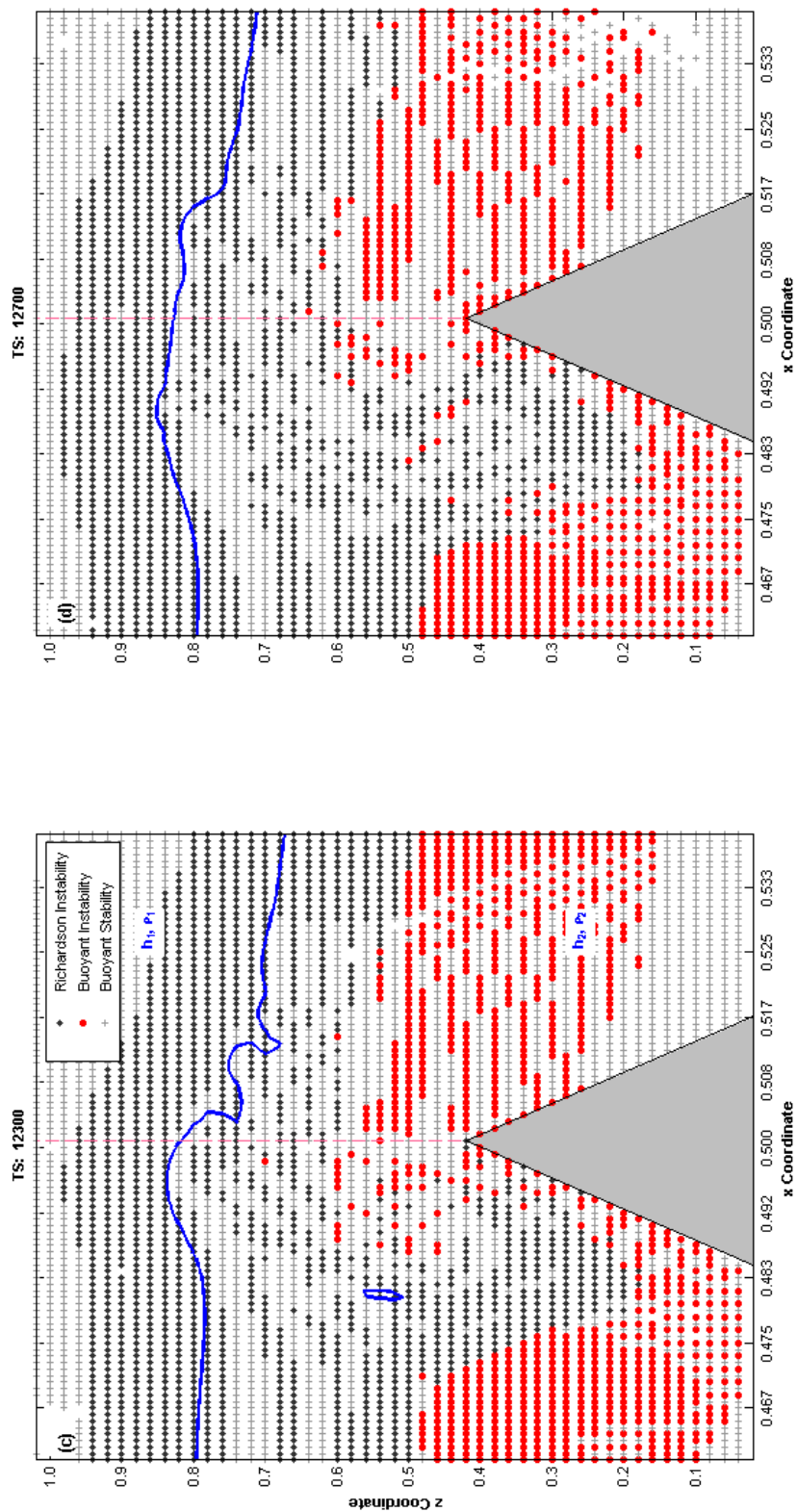


Figure 84. Continued. (c) “Bore formation” phase. (d) “Surge” phase.

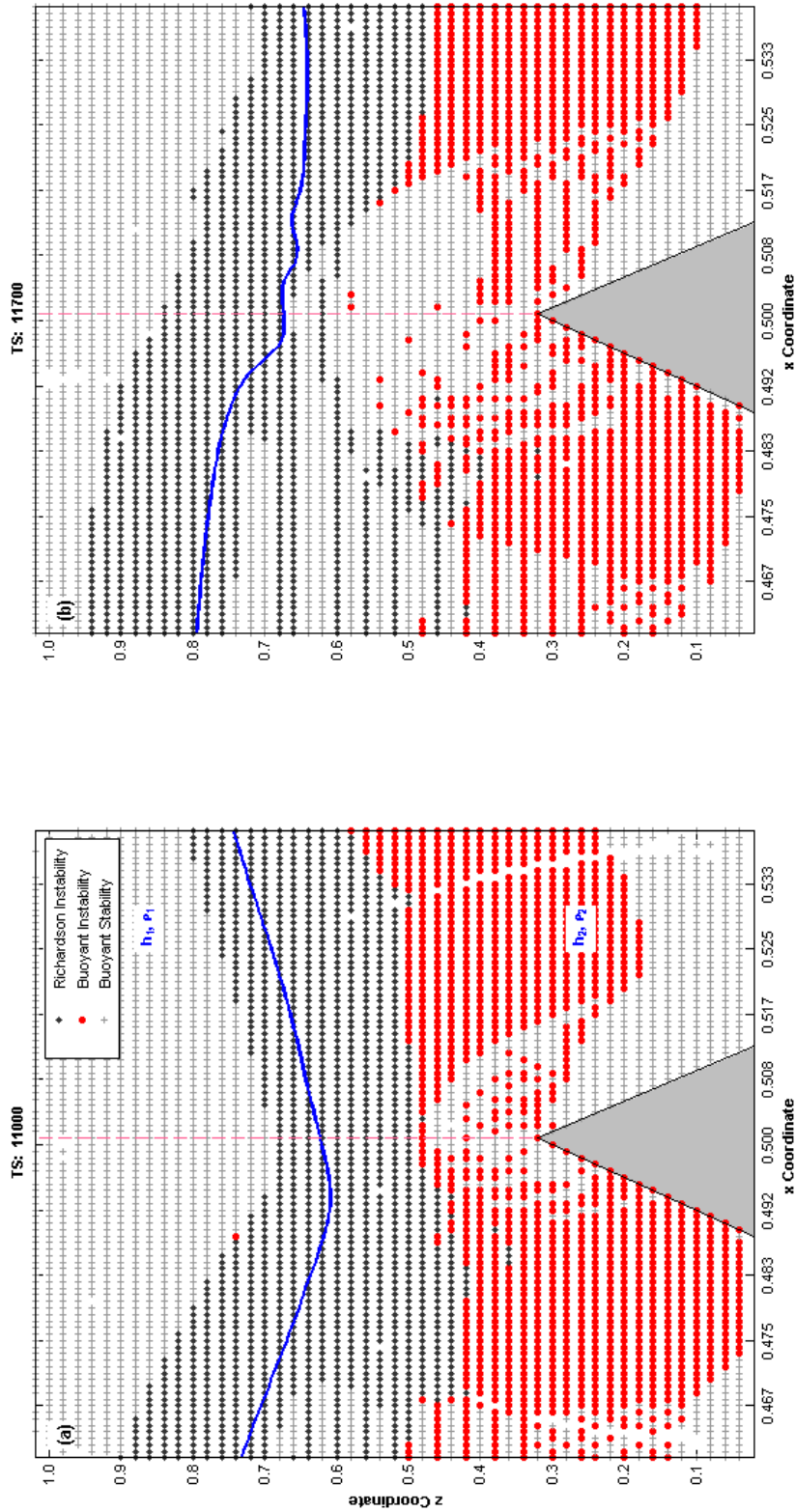


Figure 85. Spatial distribution of localized instability resulting in “weak interaction” (Table 14) between an isolated triangular obstacle and an ISW. Solid line corresponds to the pycnocline. (a) “Breaking” phase. (b) “Breaking” phase. $Fh = 0.68$. Exhibit corresponds to numerical simulation trial shown earlier in Figure 75

As a general observation, both sets of exhibits show the formation of zones of instability representing all three stability states. The region of Richardson instability is generally confined to locations immediately above and below the pycnocline. The zone of Richardson instability also closely matches the geometry of the pycnocline, particularly when the simulation shows evidence of breaking- like behavior — e.g., “wash-down,” “pycnocline overturning,” “bore formation,” or “surge.” A zone of buoyant instability can be observed along the leeward face of the advancing ISW in both fluid layers. An extensive zone of buoyant instability occurs in association with the Richardson instability zone, but this feature is limited to the lower h_2 fluid layer, and appears to occur proximally to the ISW. The balance of the computational domain is occupied by stably-buoyant fluid at locations generally distal to the advancing ISW.

A single layer of buoyant instability can be observed along the bottom of the computational domain, just above the **B2** boundary (Figure 24). This feature is a numerical artifact reflecting how the boundary conditions along this surface were defined. See Table 10.

Once the ISW encounters the obstacle and wave “breaking” occurs; the simulations show a turbulent zone along the upwind face of the obstacle where all three stability states exist, albeit randomly, within the lower h_2 fluid layer.

Once the ISW has passed beyond the location of the obstacle, the simulation results indicate that hydrodynamically quiescent conditions return, suggesting a buoyant stability state or $E_D > 0$.

CHAPTER V

CONCLUSIONS AND RECOMMENDATIONS

5.1 Conclusions

The key focus of the research was to examine how ISWs interact with topographic obstacles and examine how their properties changed when different obstacle geometries are encountered. The examination of ISW behavior was accomplished by 2D simulations, using a FORTRAN-based computer code employing numerical methods that relied on a simplified model of a 3D experimental wave tank. The analytical approach relied on a linearized approximation of the Navier-Stokes and continuity equations to derive equations for vorticity and stream function. These equations were solved using a finite difference numerical scheme with appropriate boundary conditions. The numerical results were post-processed using an academic version of MATLAB to obtain summary data and graphs. Approximately 120 numerical simulation trials were conducted as part of this research. The 2D computational results

obtained were compared to the 3D experimental results reported in the literature.

- This research was able to successfully generate a mode-1 ISW of both elevation and depression. Once the wake-generated internal waves reached steady state, it was possible to measure the wave's properties (e.g., amplitude and energy) and compare those to data in published studies. The numerical simulation trial results generally agreed with experimental studies.
- The finite difference solutions for 2D ISWs displayed a variety of hydrodynamic phenomena associated with this type of fluid flow. These solutions and key measures derived from them compare favorably with both qualitative and quantitative information reported in the scientific literature.
 - For example, this research successfully reproduced certain ISW behaviors observed and reported such as: wave breaking, K-H like features, polarity reversal, wave reflection, and the production of multiple boluses.
 - As for the quantitative results, the numerical simulations were in substantial agreement with the empirical data for some parameter ranges. A lack of agreement in some cases is likely due to (a) the artifacts of the numerical method employed or possibly (b) the

inability of this 2D simulation to represent three-dimensional effects observed experimentally.

- The simulations involving simple geometric forms, representing physiographic features that might be found in a marine setting and likely to interact with an interfacial wave, was useful in reproducing ISW phenomena reported in the literature. Such simulations provide a useful exploratory tool in the evaluation of basic ISW properties observed in the field or re-created in an experimental setting.
- Depending on the type of obstacle geometry encountered, different ISW responses were generated by these simulations.
 - Simulations involving isolated topographic obstacles were influenced in large measure by the magnitude of either the nonlinear parameter α_{NL} or the blocking parameter ζ . When the interaction between and ISW and an isolated obstacle was strong, a portion of the incoming was reflected rather than transmitted.
 - Simulations involving the so-called short-slope scenario demonstrated the full range of the wave-breaking progression. The key steps in this progression included “wash-down,” “breaking,” “bore,” and “surge.”

- Changes in streamline orbital geometry were observed well-before there were any discernable changes in the geometry of the pycnocline.
- Simulations involving monolithic-like obstacles (shelf, slope-shelf, and extended-slope) successfully produced reversals in ISW polarity.

5.2 Recommendations

The number of papers published evaluating ISW behavior in an experimental wave tank setting exceeds those investigations based solely on numerical simulations. Any one of the six geometric modeling scenarios evaluated in Sections 4.3.1 and 4.3.2 of this dissertation merit further detailed study as a way of advancing the state of knowledge concerning ISW behavior. To this end, investigations based on computer simulations of hydrodynamic phenomena in the past have proven to be an efficient and effective research tool (e.g., Vlasenko and Hutter 2002) and their utility to the study of ISW behavior merits further evaluation. Nevertheless, questions have been raised by both practitioners and lay-people alike about the physical representativeness of numerical solutions.

- Computer models simulating the hydrodynamic behavior of fluids have been available for many years. Despite their widespread availability,

there have also been questions raised about the reliability of such models in general (e.g., Oreskes, Shrader-Frechette, and Belitz 1994, Oreskes 2000). Spedding (2003) explores some of the issues associated with comparing experimental result with numerical simulations. Eisenberg et al. (1999) have provided some general recommendations with respect to how to improve the reliability of computer-based models. Coleman and Stern (1997), Roache (1998), and Coleman (1998) discuss how to address (and improve) the reliability of CFD-based computer code results.

- In spite of its utility, the finite difference method can be computationally inefficient. For the purposes of this dissertation, the simulations required an extensive computational capacity that frequently exceeded the potential of the computing environment used. Finite element methods, such as boundary-fitted techniques, requiring fewer computational cells (and computer capacity), might introduce computational efficiencies and produce results with fewer numerical errors. Lagrangian approaches may also lead to enhancements in computational precision as well as in the elimination of numerical artifacts.
- Previous empirical investigations of ISW behavior were conducted in 3D environments that also included 3D obstacles. Undoubtedly, some of the

differences in the simulation results are due to dimensionality. Other differences between these results and the 3D investigations may be due to artifacts created by the experimental configurations themselves, such as, differences in fluid types used in the experiments, wave tank widths, aspect ratio of the obstacles selected, and boundary effects such as wave reflection. Bourgault and Richards (2007) have previously questioned the validity of 3D wave tank experiments when it comes to modeling ISW behavior.

- Validation/verification studies, calibrating 3D wave tank research results with actual large-scale field data, would improve confidence in the use numerical simulations in this area of scientific inquiry.
 - As an additional line of investigation, it would be useful to explore under what parametric conditions a 2D simulation could be used to provide an adequate representation of a 3D wave tank experiment. Questions have been raised previously about the representativeness of “traditional” 2D-approaches to internal wave modeling (e.g., Sherwin et al 2002).
- In their 1973 paper, Emery and Gunnerson proposed seven different classes (morphologies) for breaking ISWs. Numerical simulations might represent an effective investigational approach to better understand what parameters can give rise to those seven different wave breaking classes. In this regard,

the calculation of the internal *Iribarren number*³⁵ may prove to be useful to differentiate the respective classes as part of any numerical simulation (e.g., Aghsaee, Boegman, and Lamb 2010).

³⁵ The Iribarren number ξ_{in} was first proposed by Iribarren and Nogales (1949) as a means of distinguishing between breaking and non-breaking waves on a plane beach. Mathematically, this number can be expressed as

$$\xi_{in} = \frac{\tan_b}{\sqrt{a_i / L_w}}$$

where \tan_b , a_i , and L_w represent the boundary slope, is the incoming wave amplitude, and the wavelength, respectively .

APPENDIX A EXAMPLE MATHCAD® SPREADSHEET

MATHCAD CALCULATOR: Constants Calculator for C_0 , R_e , and F_n

$\rho_1 := 999 \frac{\text{kg}}{\text{m}^3}$	fresh water	$h_1 := 5\text{cm}$
$\rho_2 := 1030 \frac{\text{kg}}{\text{m}^3}$	salt water	$h_2 := 15\text{cm}$
		$d := h_1 + h_2$
$\Delta\rho := \rho_2 - \rho_1$		$d = 0.2\text{m}$

$\Delta\rho = 31 \frac{\text{kg}}{\text{m}^3}$ gamma

Reference Velocity C_0

$$C_0 := \sqrt{\left[\frac{g \cdot (\rho_2 - \rho_1)}{\rho_2} \right] \left[\frac{(h_1 \cdot h_2)}{h_1 + h_2} \right]}$$

$C_0 = 0.105 \frac{\text{m}}{\text{s}}$

Kinematic Viscosity @ 20°C

$\nu := 1.00410^{-6} \frac{\text{m}^2}{\text{s}}$

$L = 12.0\text{m}$

Time

$t := \frac{L}{C_0}$

$t = 114.063\text{s}$

Reynolds Number R_e

$R_e := \frac{(C_0) \cdot d}{\nu}$

$R_e = 2.096 \times 10^4$

Richardson Number R_i

$R_i := \frac{g \cdot d}{C_0^2}$

$R_i = 177.204$

Froude Number F_n

$F_n := \frac{(C_0)}{\sqrt{g \cdot d}}$

$F_n = 0.075$

$F_{n1} := \frac{1}{\sqrt{R_i}}$

$F_{n1} = 0.075$

APPENDIX B

DETAILS OF NUMERICAL SIMULATION INVOLVING A SHELF-LIKE TOPOGRAPHIC OBSTACLE

The exhibits contained in this appendix depict the details of an interaction between a mode-1 depression-type internal wave and a shelf-like obstacle shown earlier in Figure 50. The non-dimensional simulation is shown in-progress, at TS 3400, just prior to the onset of shoaling (breaking). The normalized velocity vector field (black arrows), the streamline contours (dashed lines), and the pycnocline (solid blue line) are shown on each figure. Multiple isopycnals, shown as green lines about the pycnocline, provide additional information on the character of the density interface during the simulation. The theoretical turning point plane is the vertical dashed line located on the slope portion of the obstacle at a point defined by the fluid depth condition corresponding to $h_1 = h_2$. The non-dimensional time step interval for each figure is equal to 200.

At TS 3800, the simulation shows that internal wave has yet to encounter the obstacle. The streamline contours are widely-spaced

suggesting relatively uniform flow in this portion of the computational domain. The isopycnals are closely packed about the pycnocline suggesting a sharp density interface at this point in the simulation.

At about TS 11,000 (the first figure in this appendix), distortion of the streamline contours in the vicinity of the obstacle's face can be observed, suggesting the onset of shoaling. By about TS 12,000, the streamline contours are now clearly refracted in such a way as to mirror the face of the obstacle. As for the velocity field, between time steps 11,000 and 11,400 or so, the simulation shows that a localized cell of turbulence (a vortex) has begun to form within the h_2 fluid layer along the face of the obstacle. Based on the orientation of the velocity vectors, this vortex appears to be fed by flow occurring along the top of the obstacle by fluid within the same density horizon. By TS 12,000 of the simulation, the vortex has become well-defined, with the velocity vectors indicating a strong counter-clockwise flow pattern, opposite in flow to that of the advancing internal wave.

At TS 12,400 in the simulation, the pycnocline is beginning to deflect downward, in the vicinity of the obstacle face. This downward deflection is analogous to “wash-down” or “backwash” phenomena commonly associated with the initial phase of wave breaking. By TS 12,800, wash-down has driven the pycnocline to its lowest point of entrainment. With respect to this

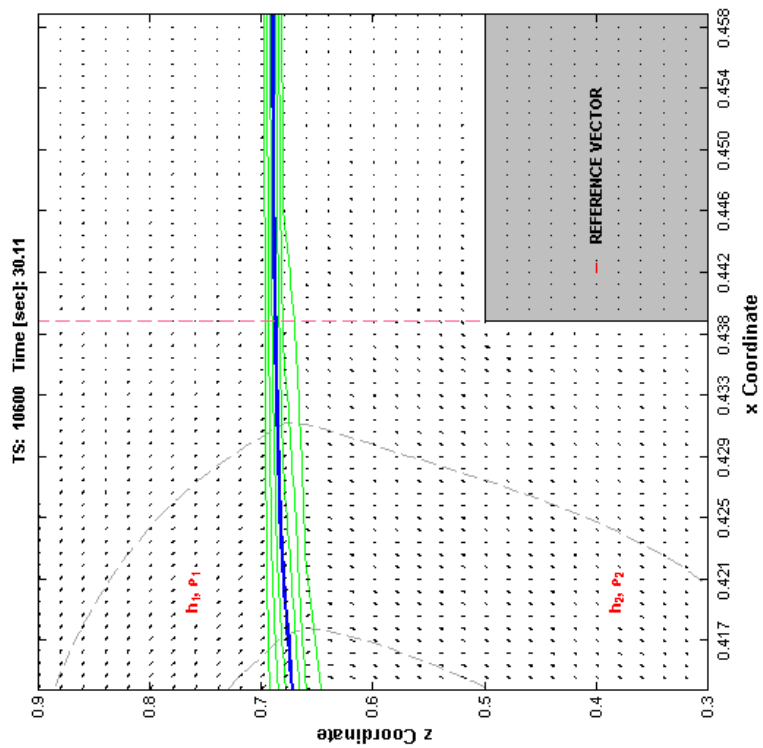
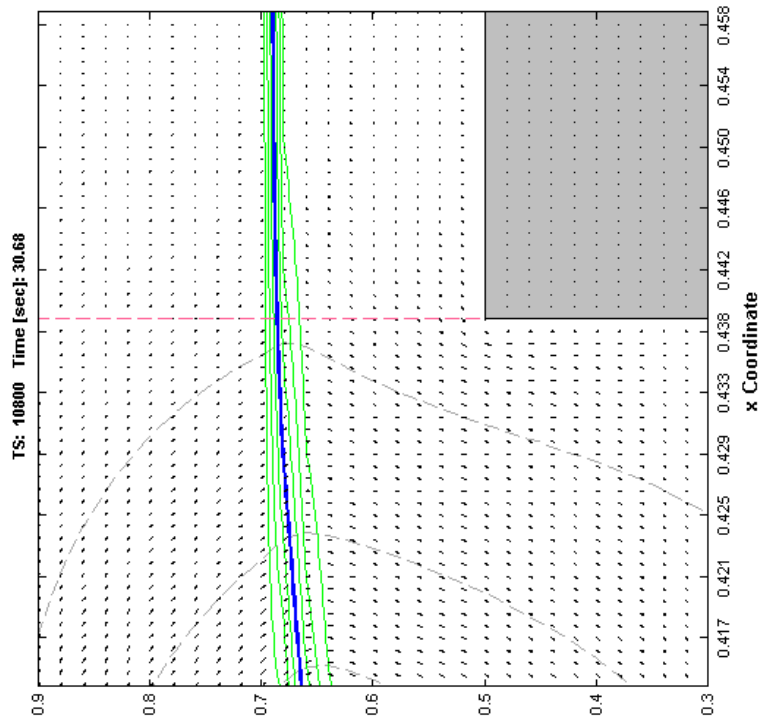
feature, the wash-down phenomena depicted in the simulation occurs along an imaginary vertical plane that is in approximate alignment with what is now a well-defined (and growing) clockwise cell of turbulent flow. These features are in close proximity to the vertical plane defining the theoretical turning point. This location corresponds to the fluid depth condition where $h_1 = h_2$. Careful review of the simulation at TS 12,800 shows that the lowest point of pycnocline entrainment (“wash-down”) is in general alignment with those velocity vectors defining the earlier-described vortex.

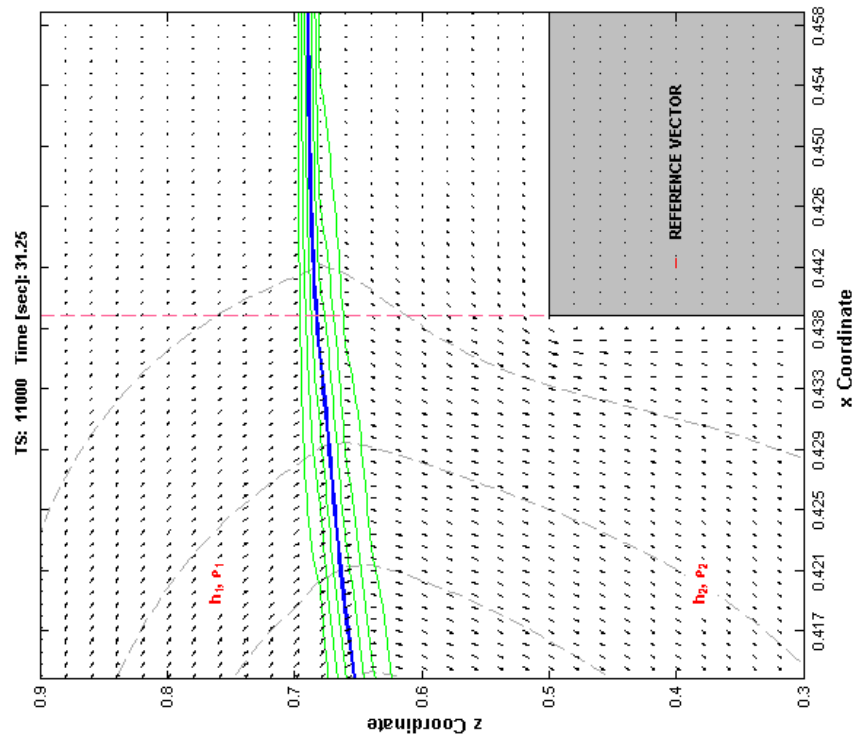
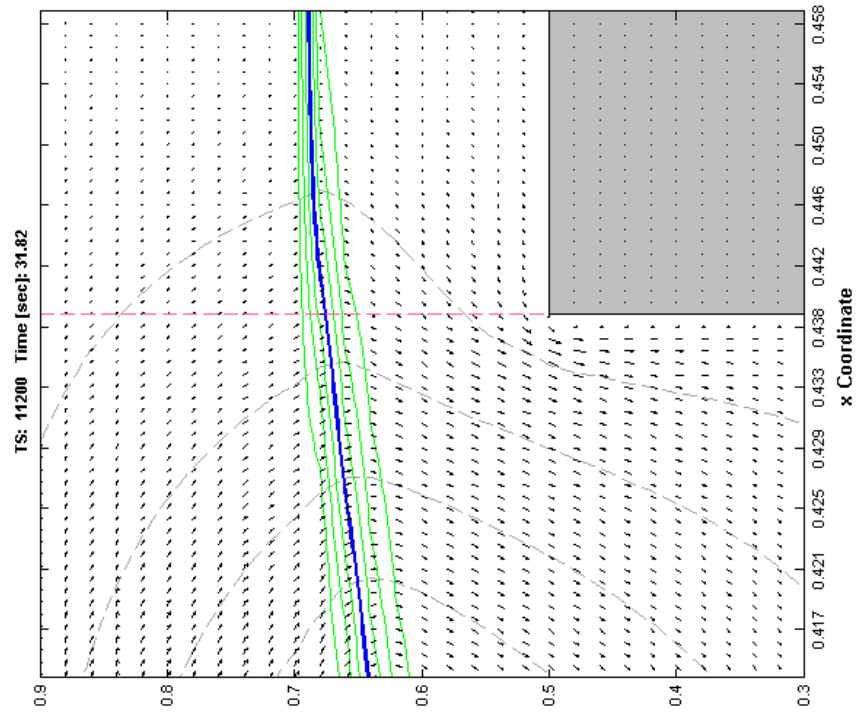
As the wash-down phase continues to progress, there is a pronounced increase in the magnitude of the flow in the h_2 fluid layer between the pycnocline and the horizontal face of the obstacle. The increase in fluid flow in this area is evident by the relative size (magnitude) of the velocity vectors in comparison to other velocity vectors also visible in the computational domain. By TS 13,000, this vector field appears to bifurcate (separate) in the vicinity of the pycnocline entrainment point. One component of the velocity field trends upwards whereas the other component appears to feeding into the existing turbulent flow cell (or gyre) that has remained semi-stationary at this general location.

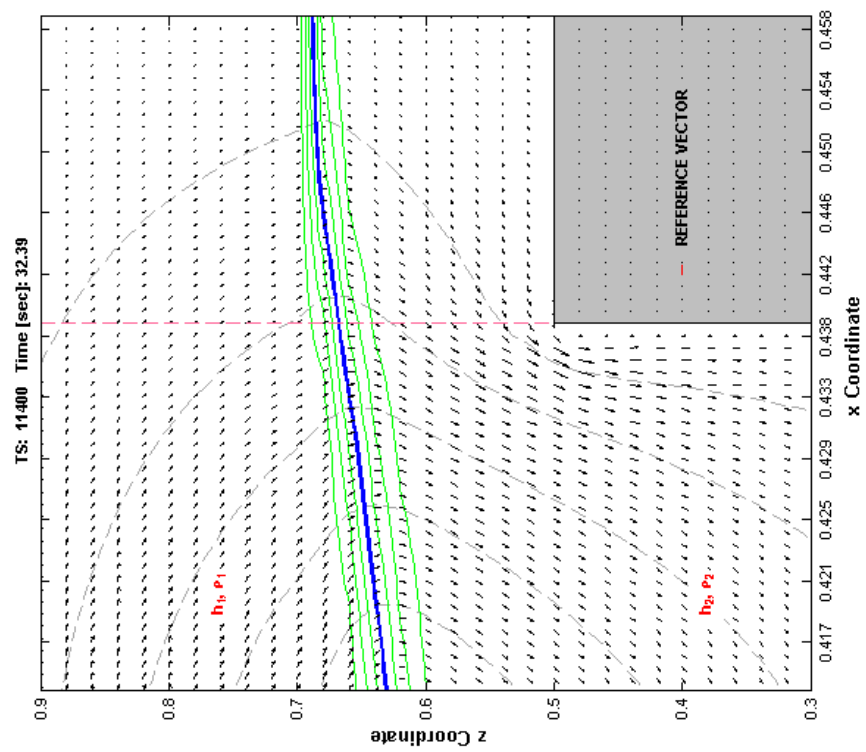
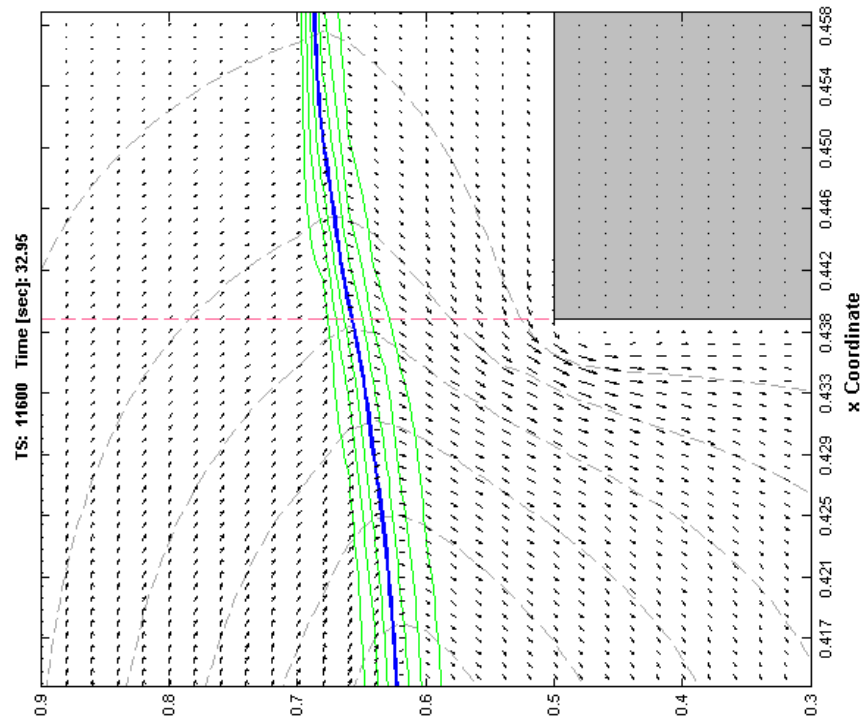
By about TS 13,600, the character of the velocity field is such that there is quasi-stationary vortex at the face of the obstacle. The growth in the

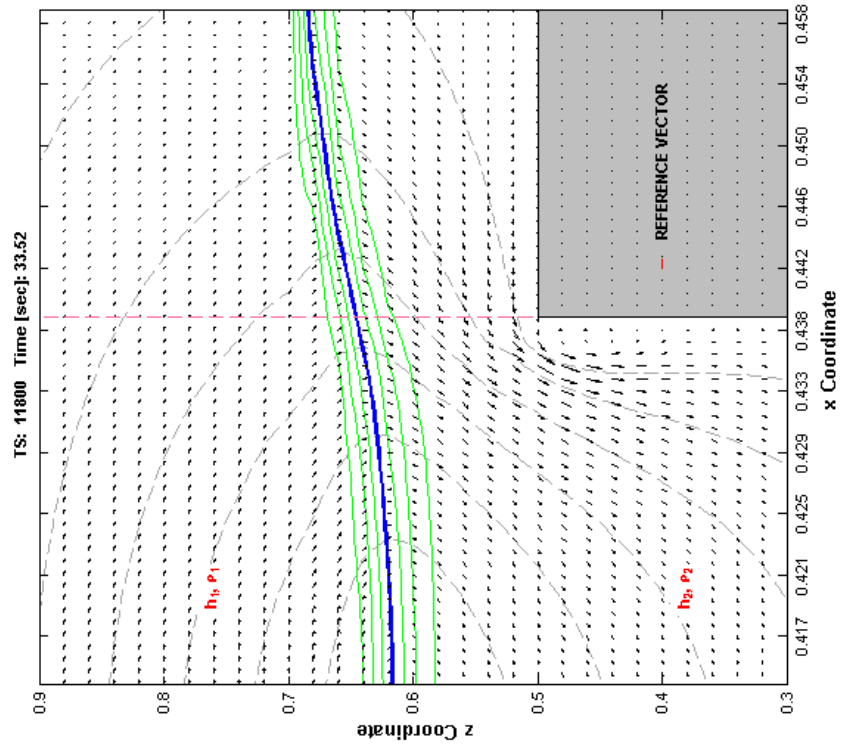
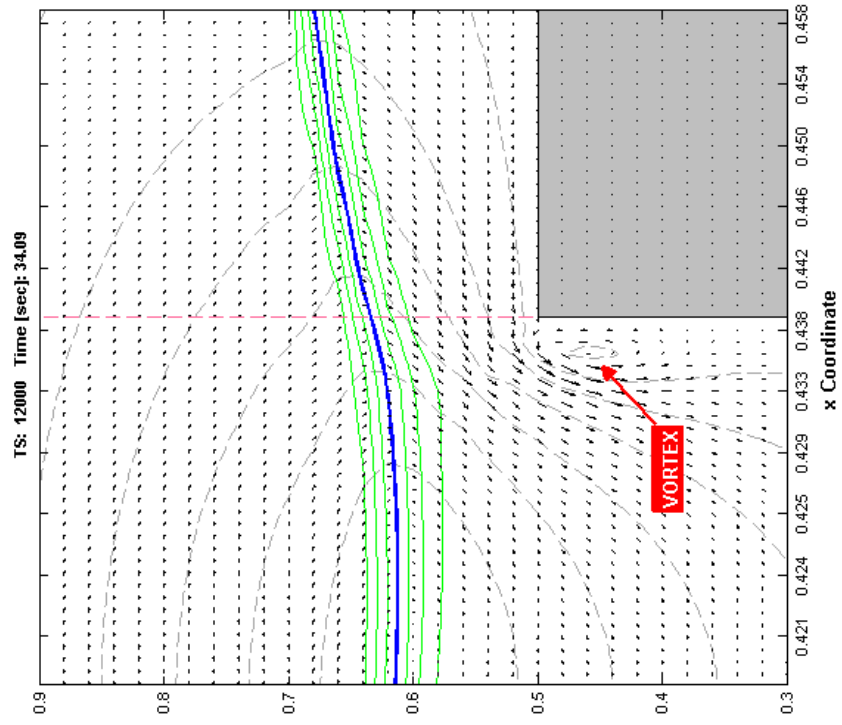
size of the flow field associated with this vortex appears to be a key factor contributing to the elevation (lifting) and advancement of the pycnocline up over the obstacle in a manner similar to that water advancing over a nappe or a weir. In subsequent time steps in the simulation, the pycnocline appears to be transitioning into a bore, aided in part by the quasi-stationary vortex that is now producing mostly vertically-directed flow.

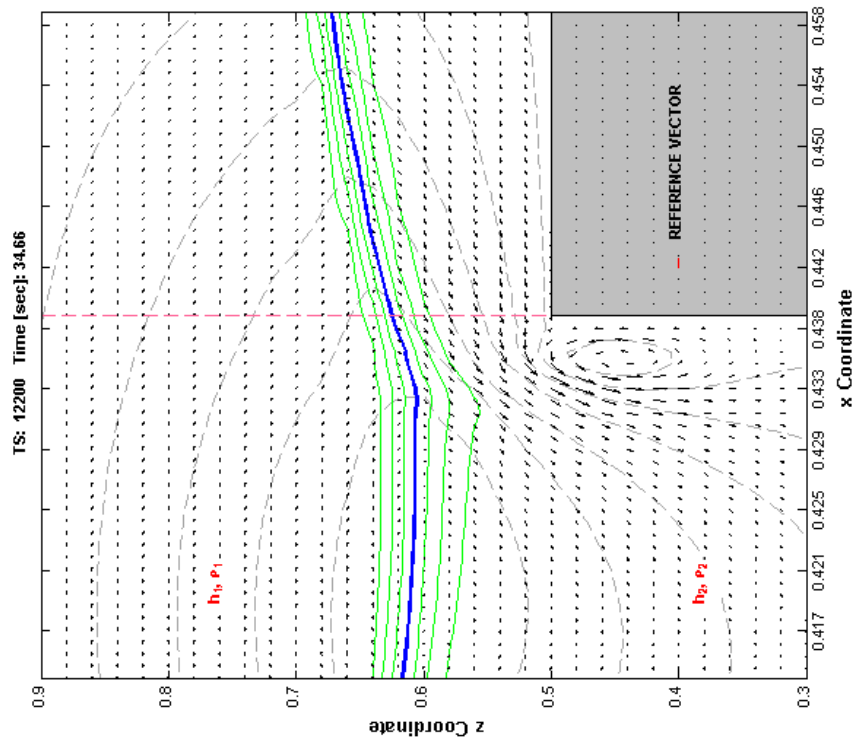
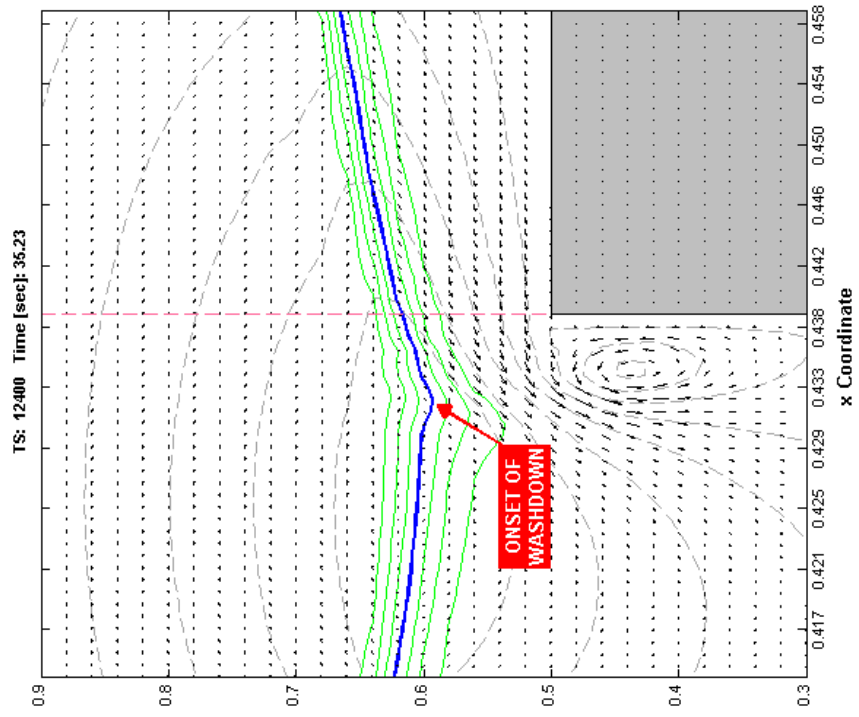
By TS 14,800, the pycnocline has evolved into a clearly-defined bore, driven in part by a well-developed velocity plane of upwelling flow. Later, at about TS 15,600, the arrangement of the velocity vectors at the crest of this bore, along the leading face of the pycnocline, indicates that there are two flow patterns present — one clockwise and the other counter-clockwise. See circled area in the exhibit. As shown in earlier Figure 44, this bore later evolves into an elevation-type internal wave in subsequent stages of the numerical simulation.

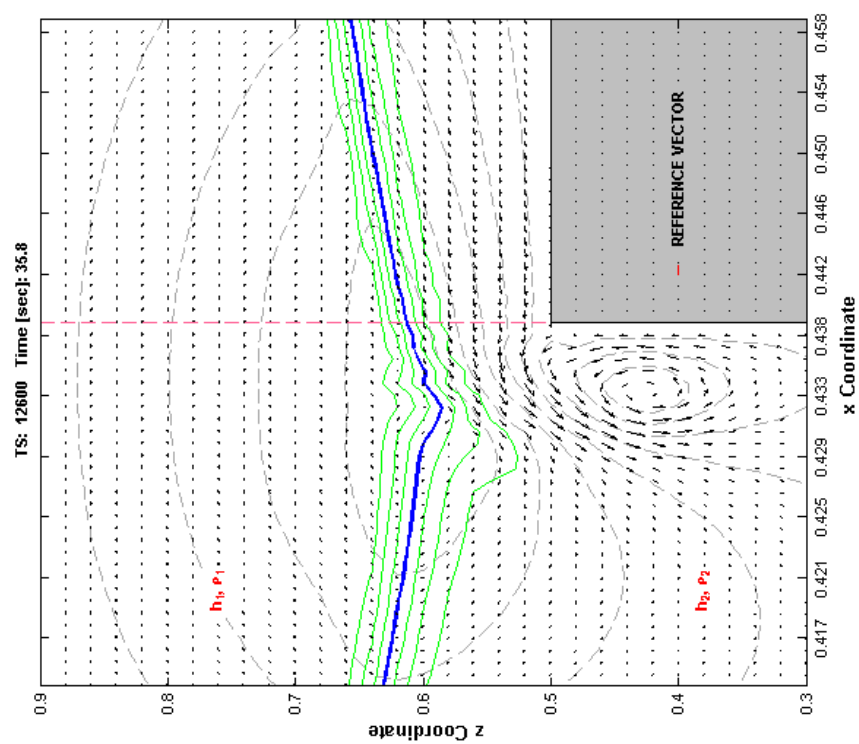
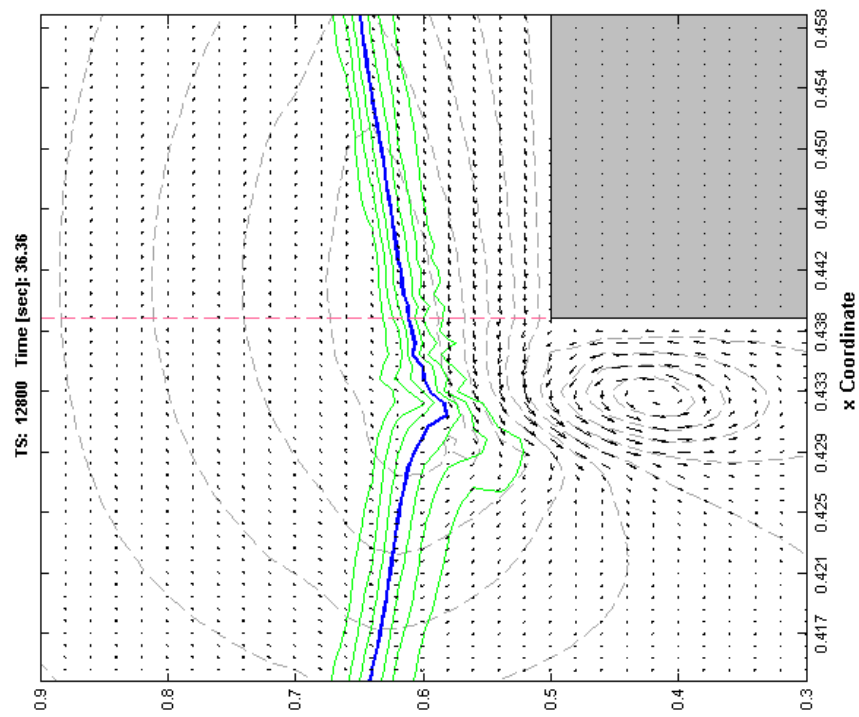


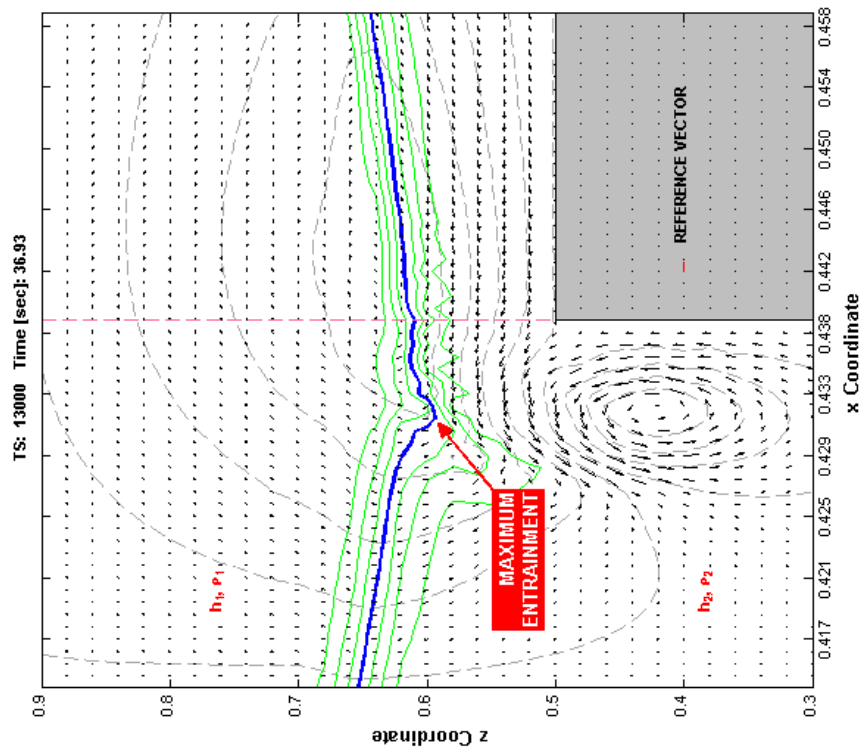
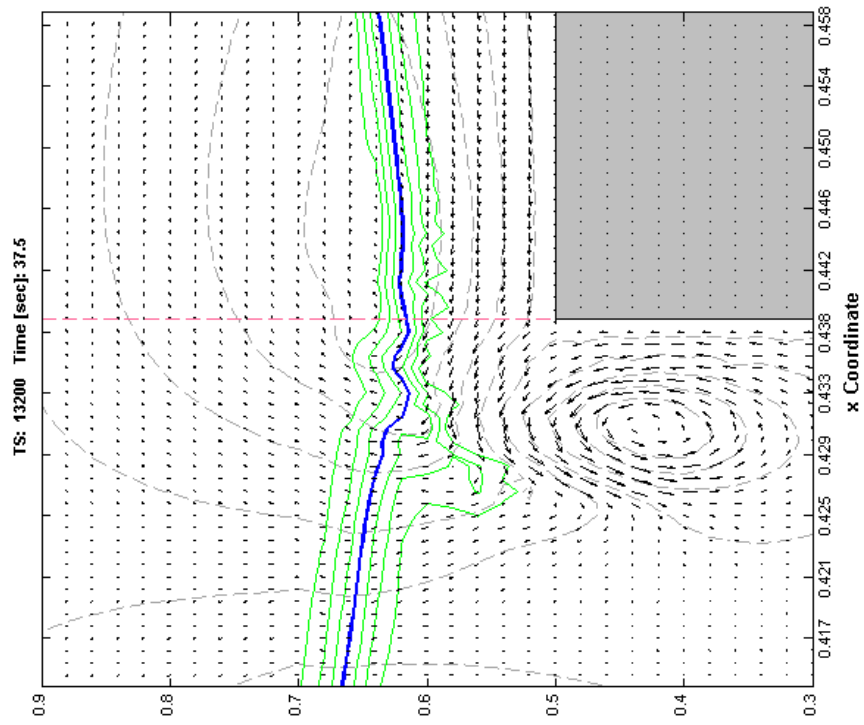


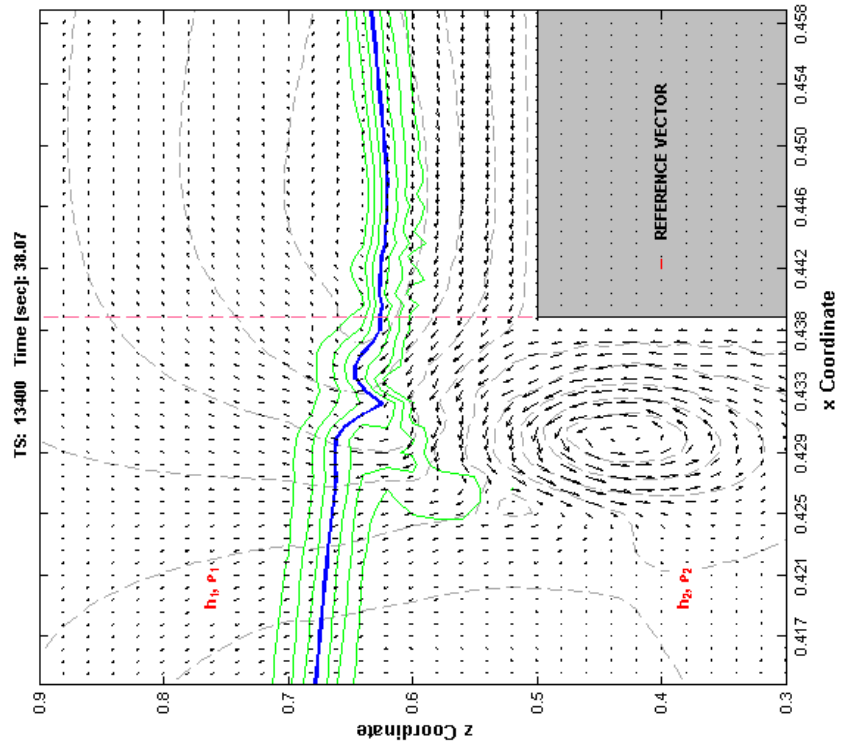
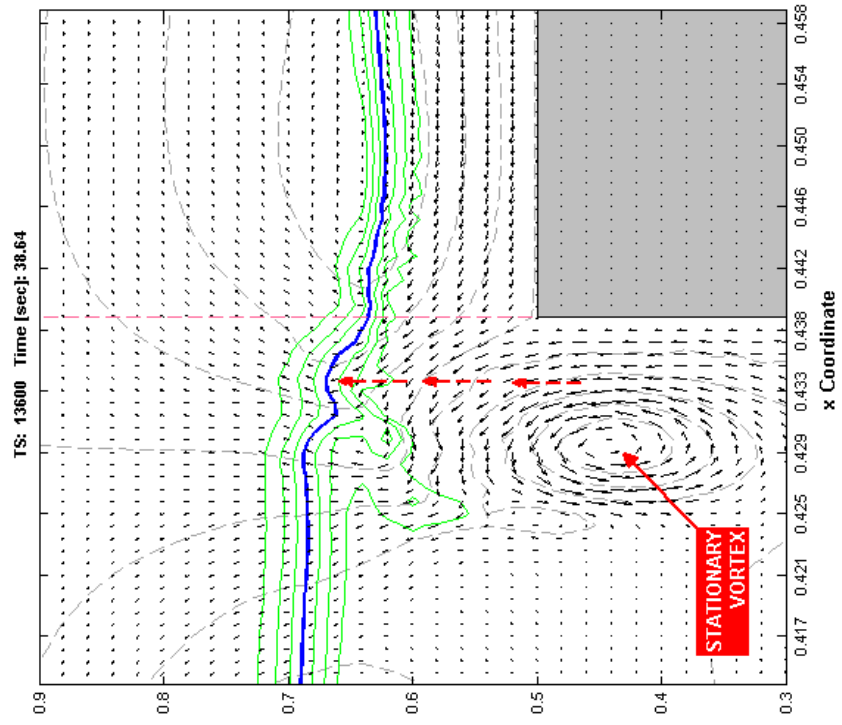


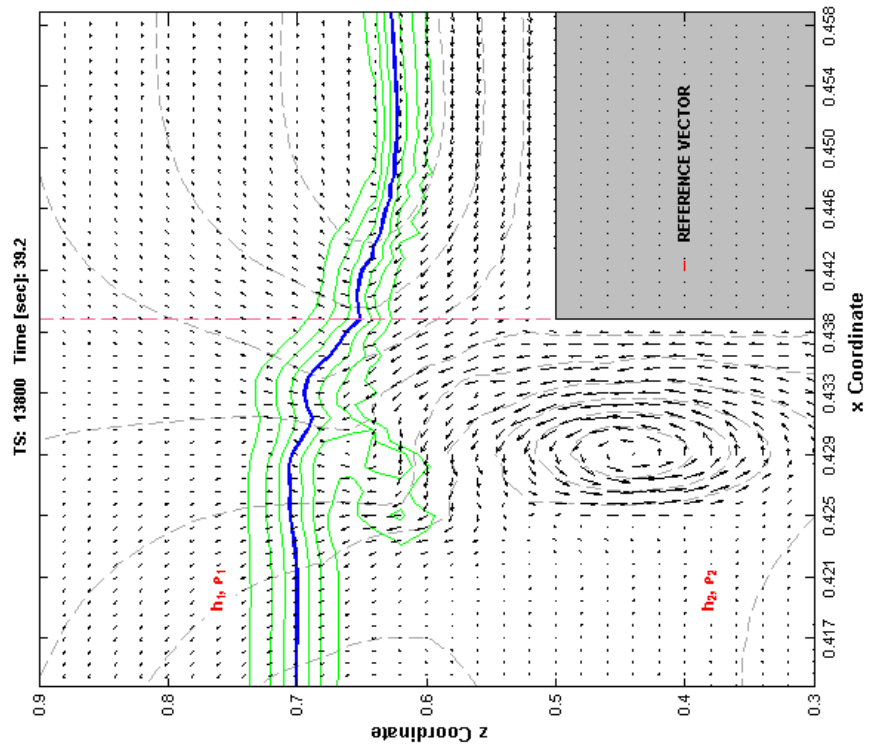
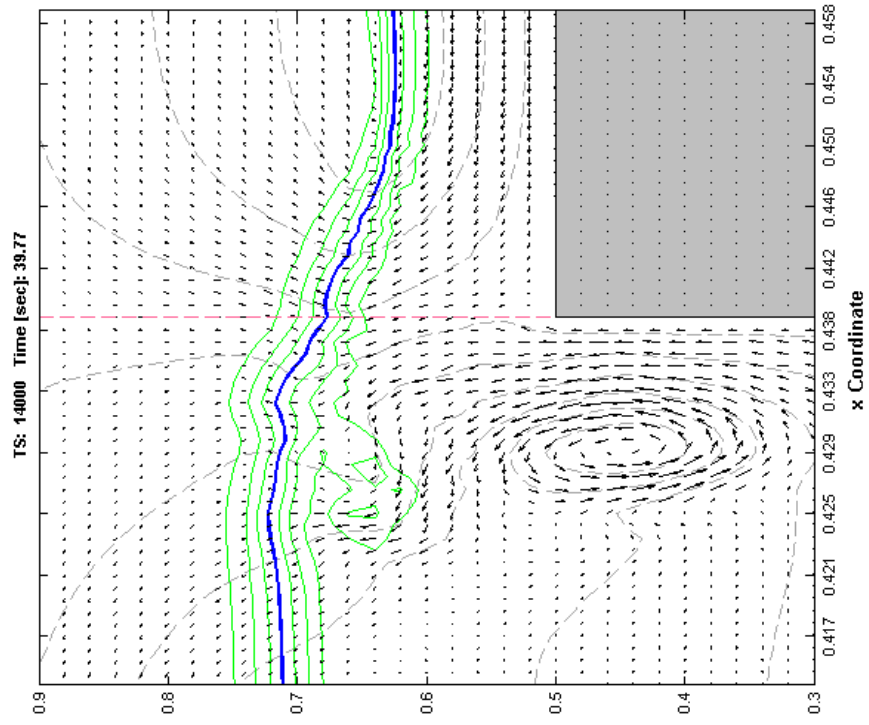


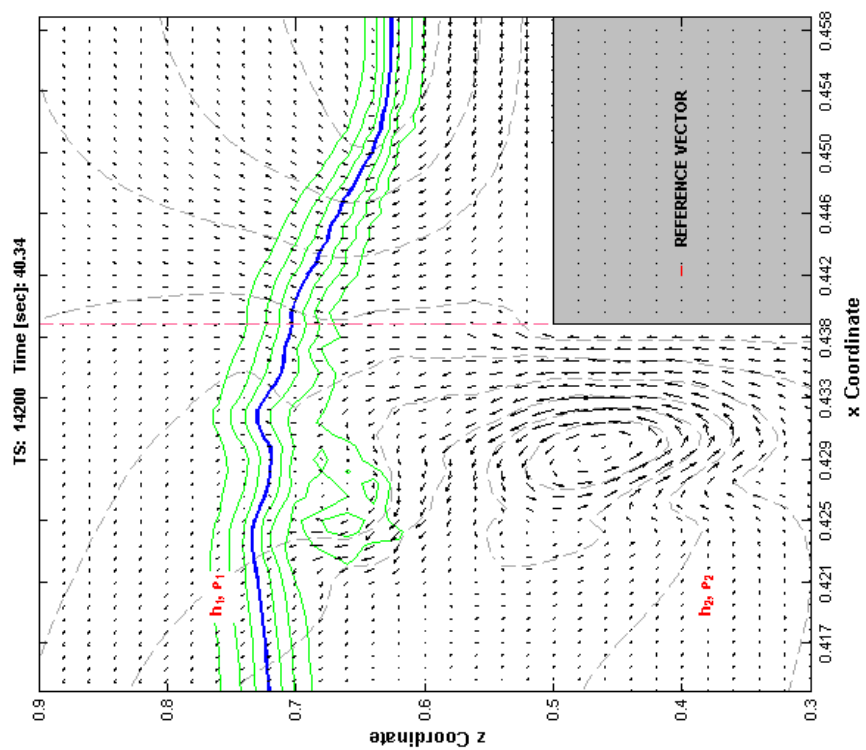
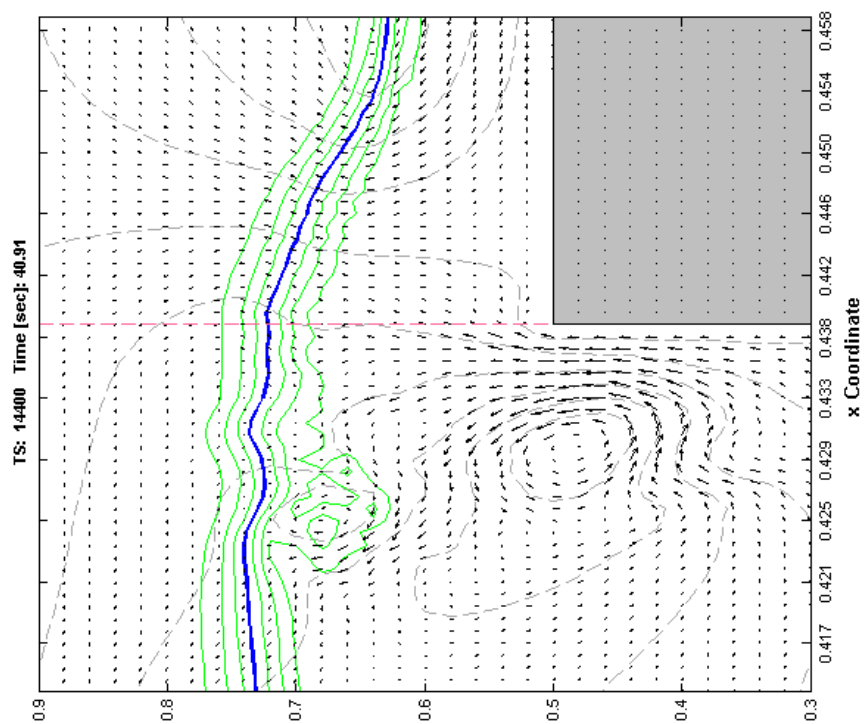


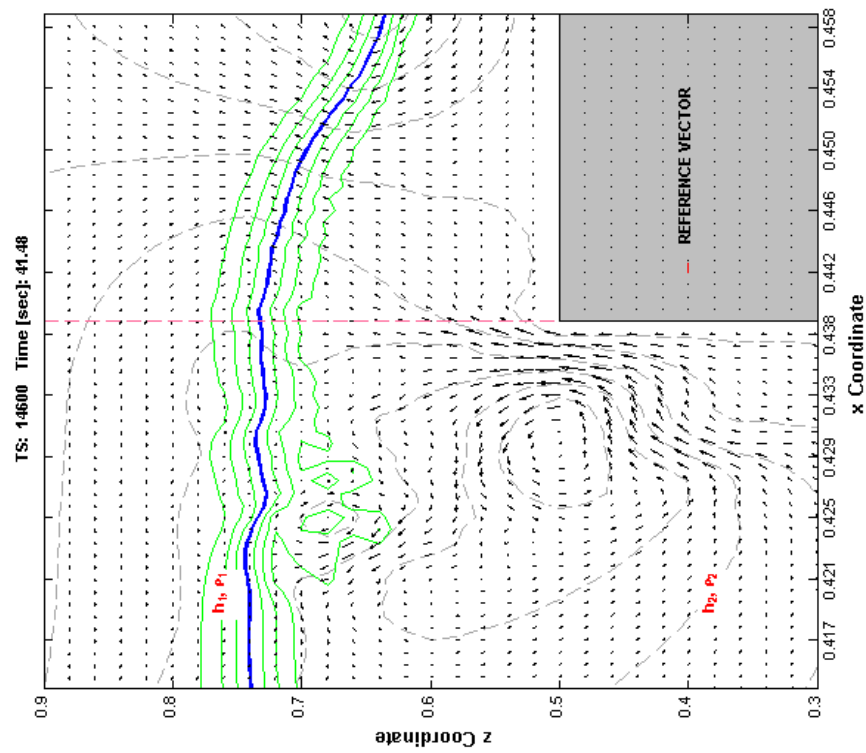
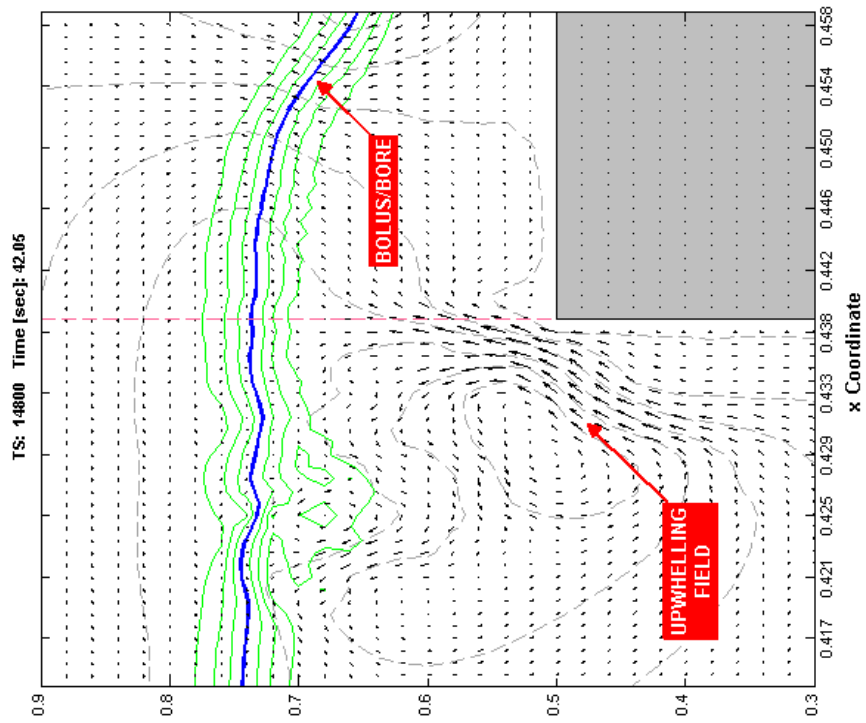


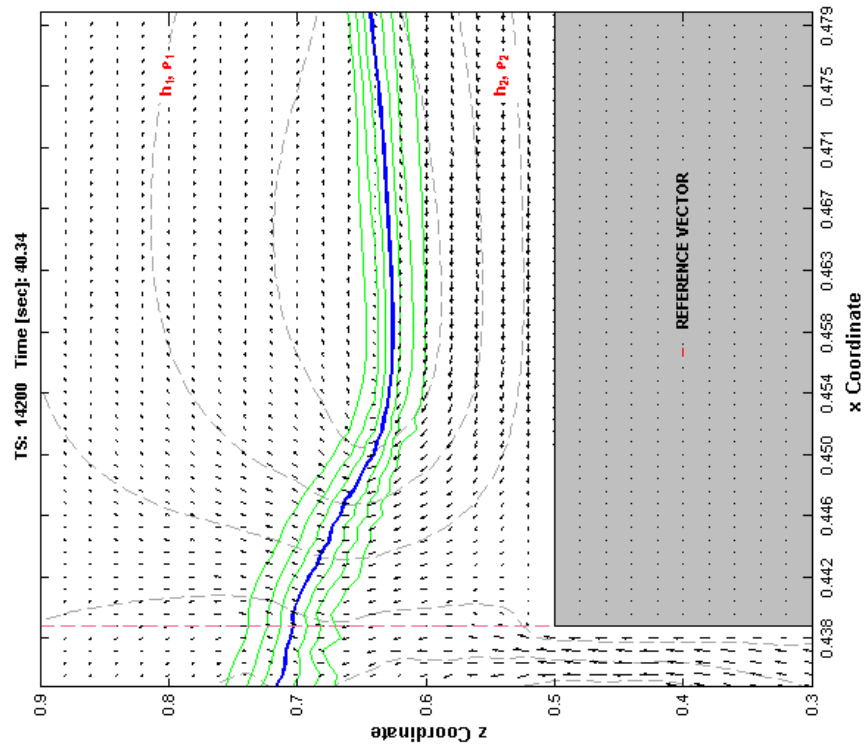
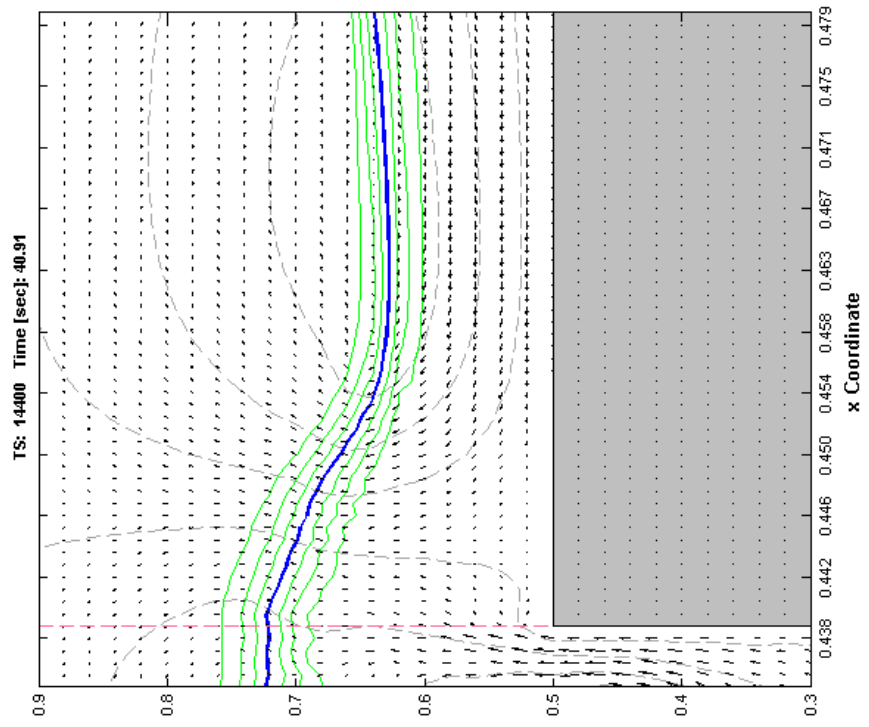


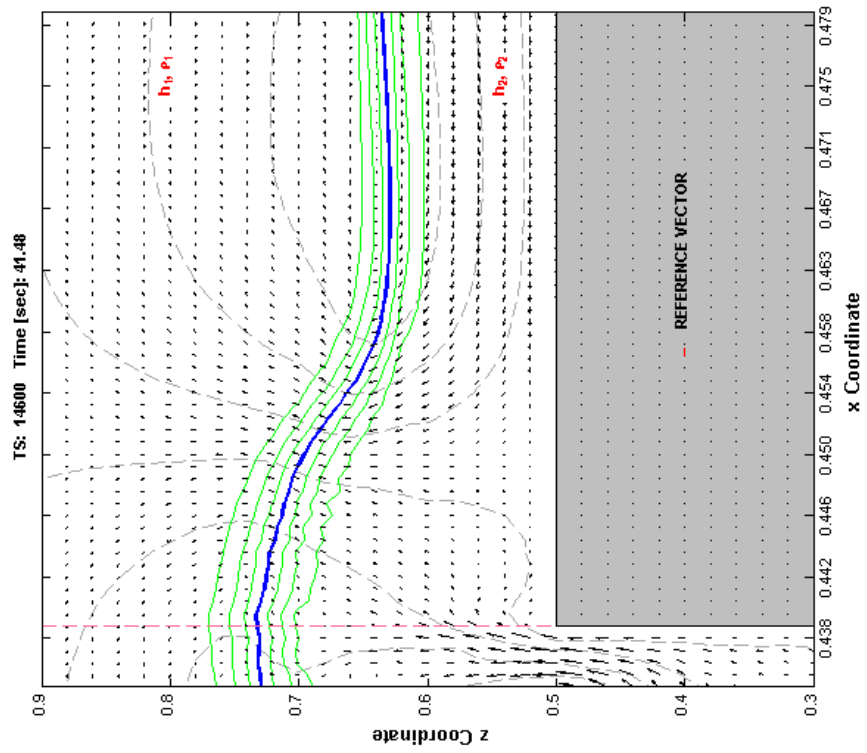
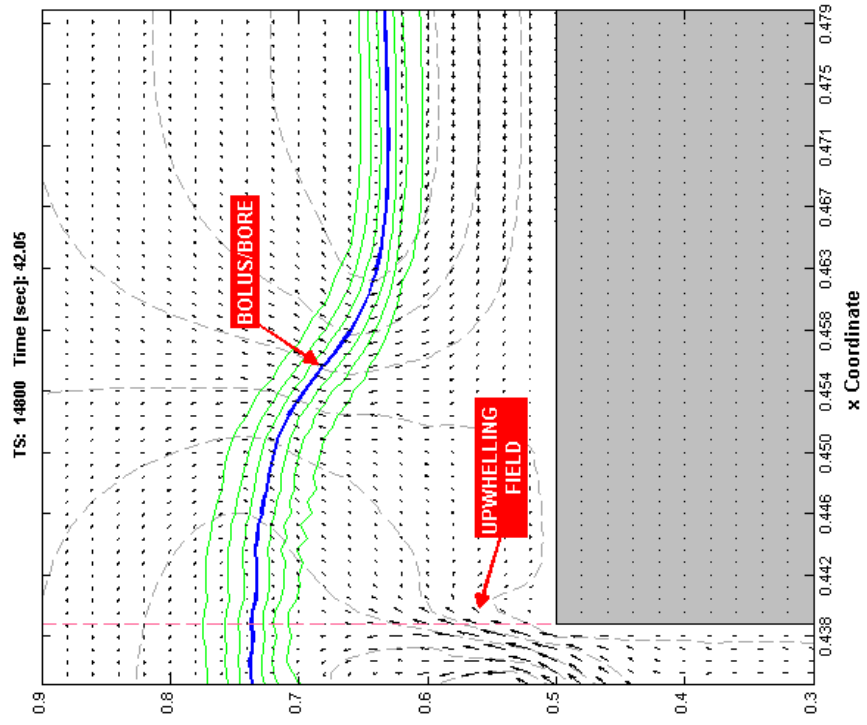


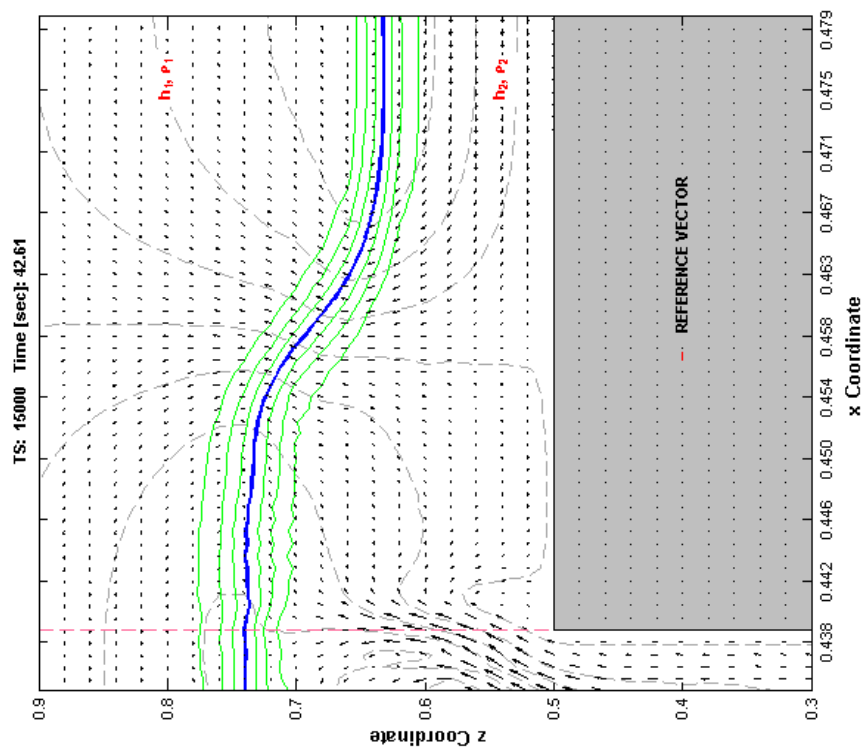
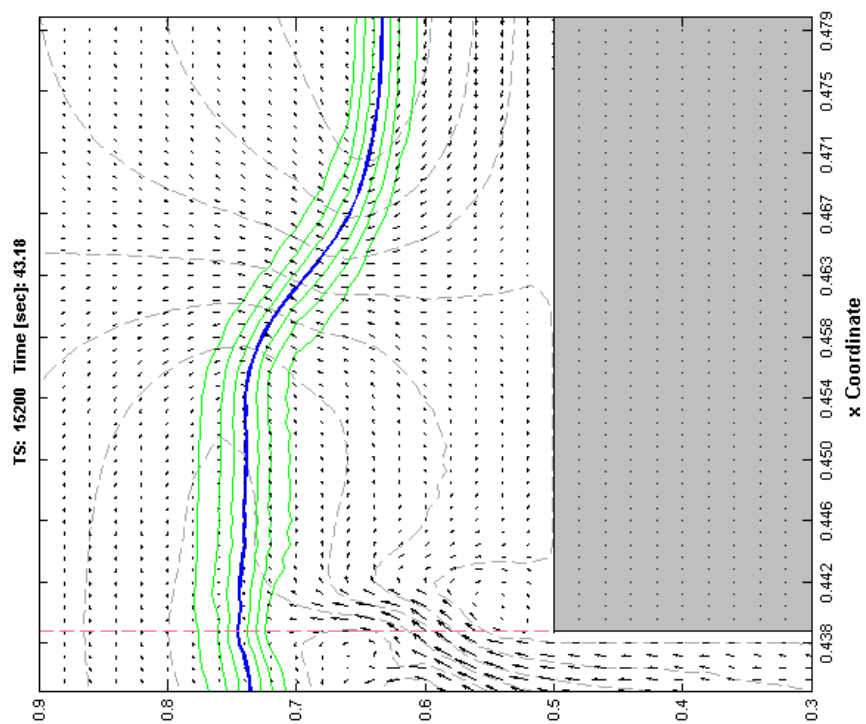


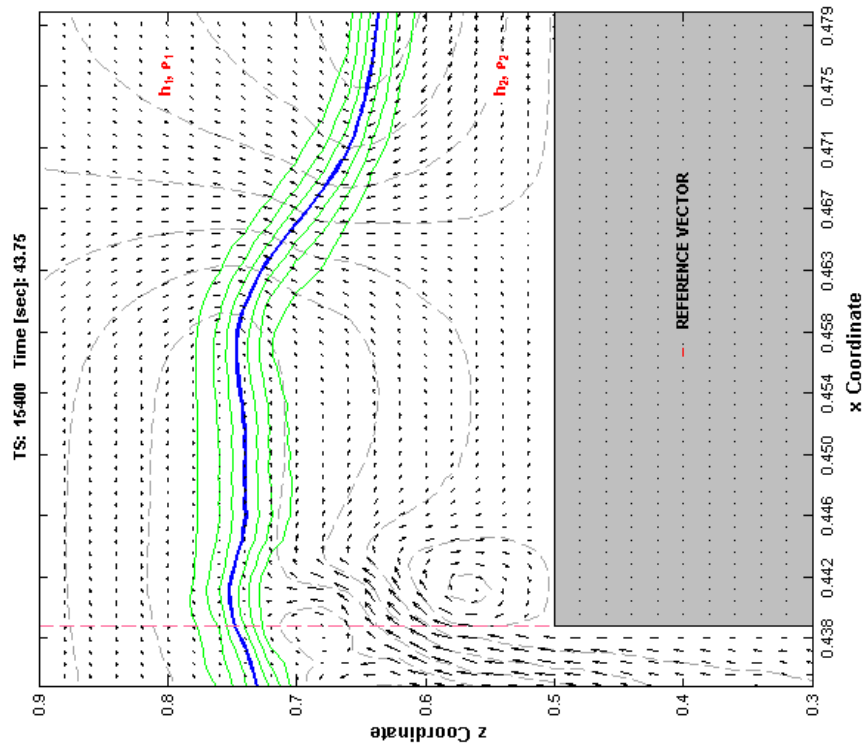
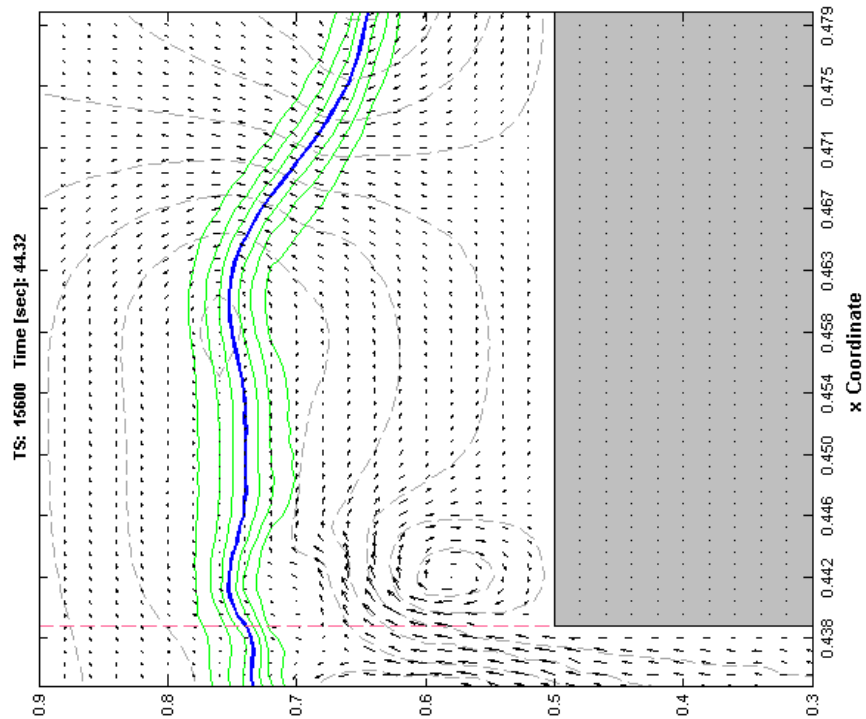


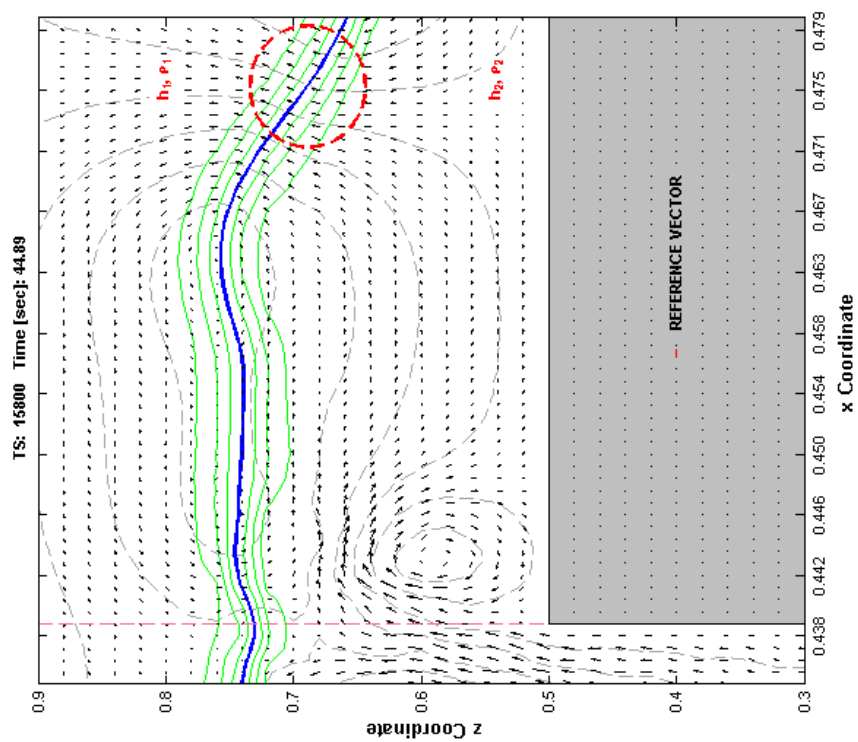
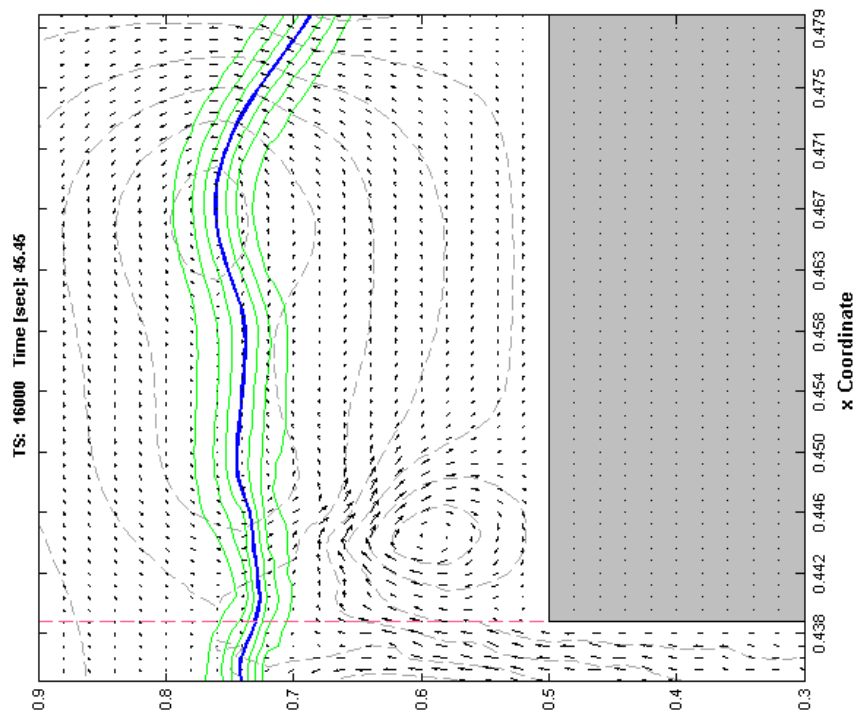












APPENDIX C

DETAILS OF NUMERICAL SIMULATION INVOLVING A SLOPE-SHELF TOPOGRAPHIC OBSTACLE

The exhibits contained in this appendix depict the details of an interaction between a mode-1 depression-type internal wave and a shelf-like obstacle shown earlier in Figure 53. The non-dimensional simulation is shown in progress at TS 3400, just prior to the onset of shoaling (breaking). The normalized velocity vector field (black arrows), the streamline contours (dashed lines), and the pycnocline (solid blue line) are shown on each figure. Multiple isopycnals, shown as green lines about the pycnocline, provide additional information on the character of the density interface during the simulation. The theoretical turning point plane is the vertical dashed line located on the face of the slope portion of the obstacle at a point defined by the fluid depth condition where $h_1 = h_2$. The non-dimensional time step interval for each figure is equal to 200.

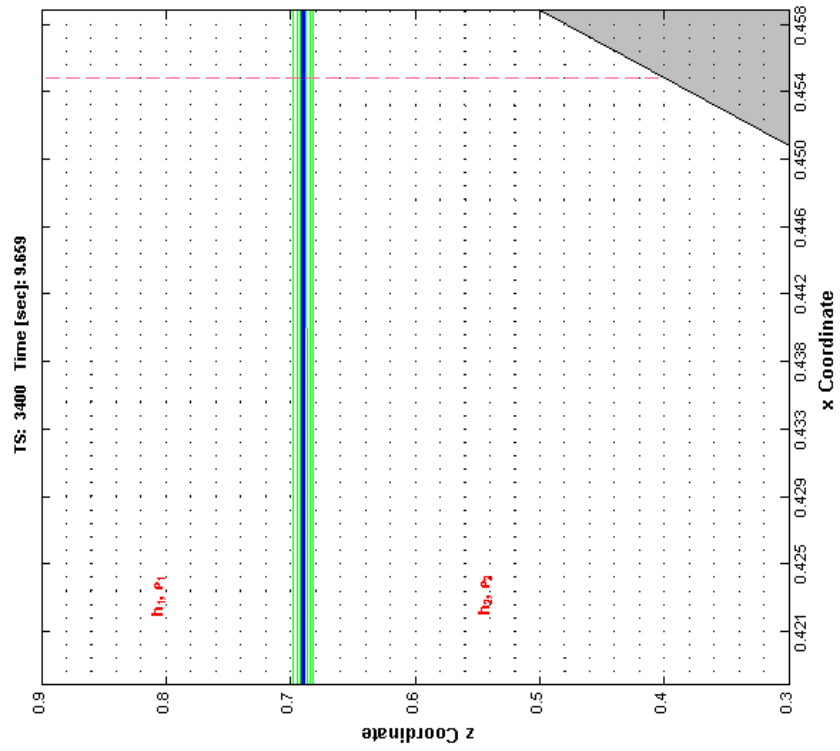
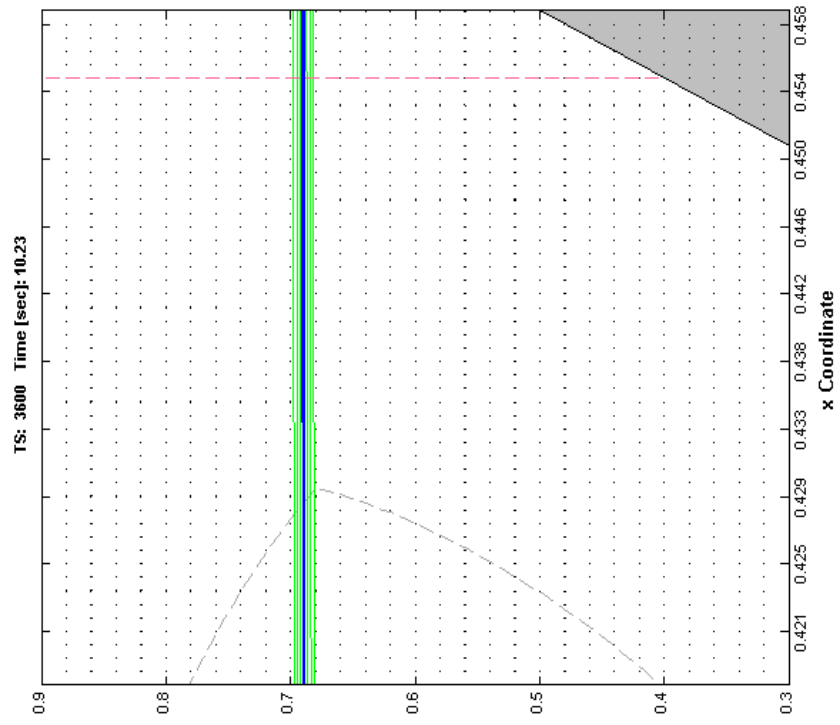
At TS 3400, the simulation shows that advancing internal wave has yet to encounter the obstacle. As the internal wave is a depression-type, the velocity field demonstrates a clockwise flow pattern about the pycnocline.

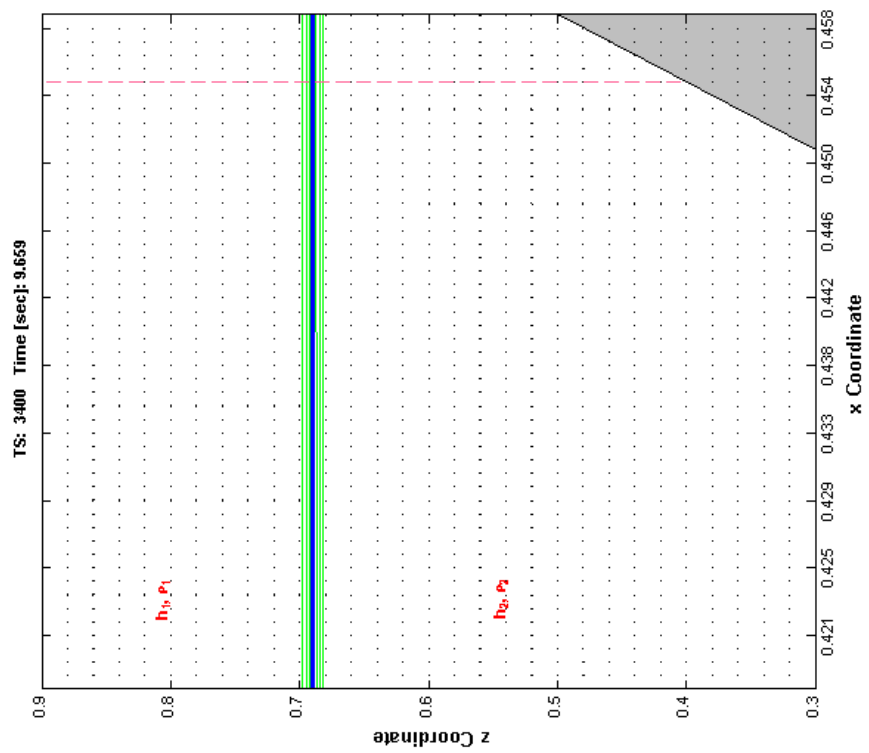
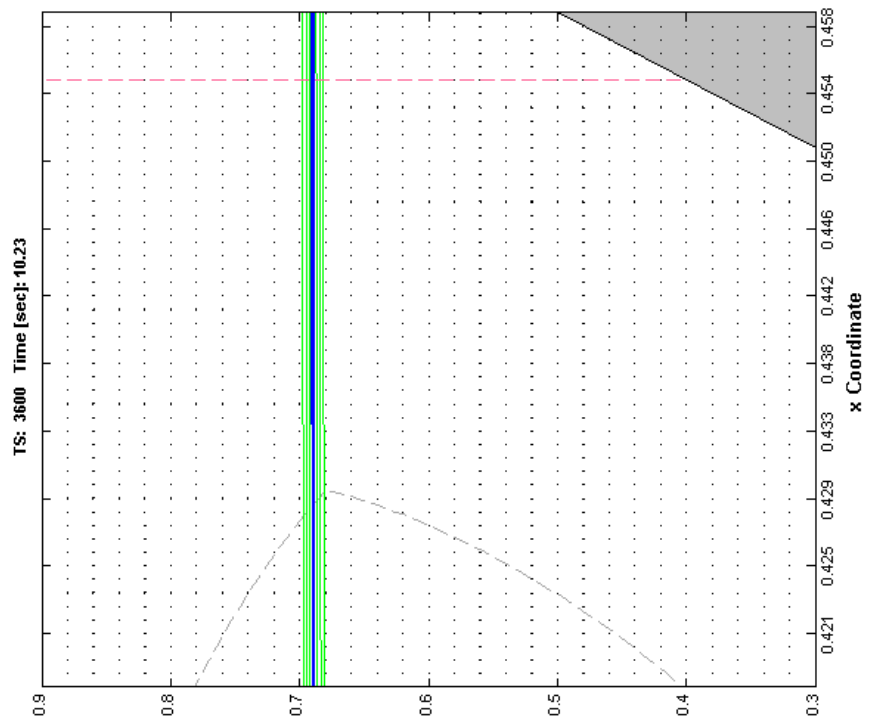
The streamline contours themselves are widely-spaced suggesting relatively uniform flow in this portion of the computational domain. The isopycnals are closely packed about the pycnocline suggesting a sharp density interface at this point in the simulation.

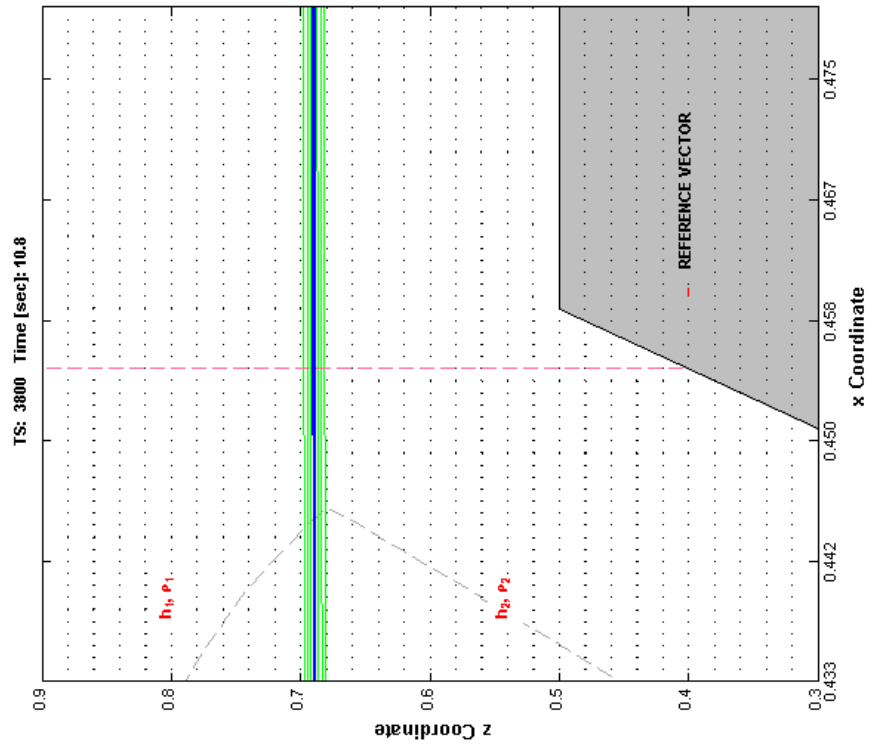
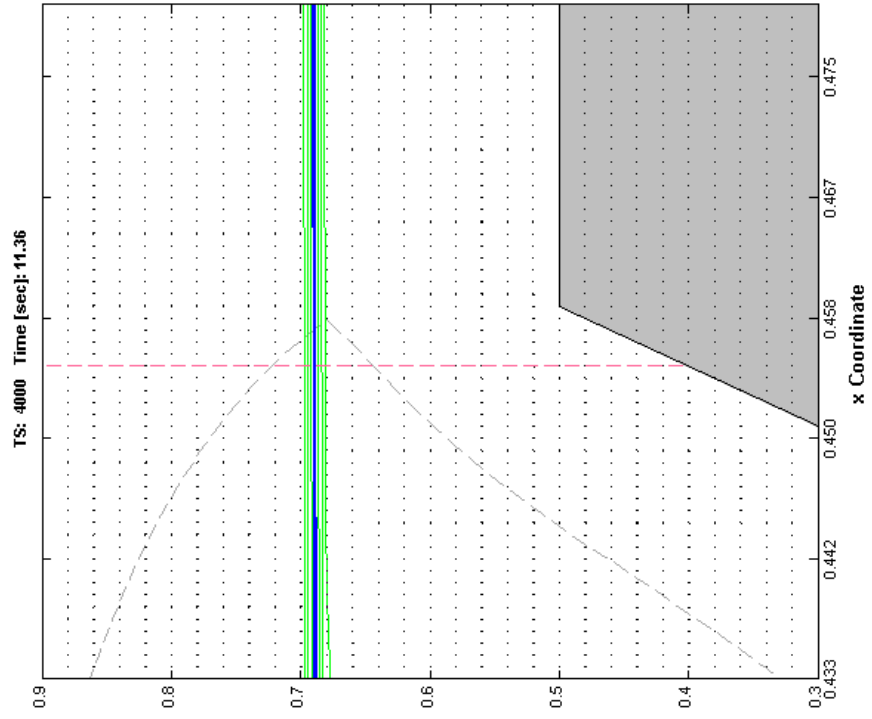
At about TS 4000, distortion of the streamline contours in the vicinity of the obstacle's face can be observed, suggesting the onset of shoaling. By about TS 5000, the streamline contours are now clearly refracted in such a way as to outline the shape of the obstacle. As for the velocity field, between TS 5400 and TS 6000 or so, the simulation shows that a localized cell of turbulence (a vortex or gyre) has formed within the h_2 fluid layer along the face of the obstacle, near its crest. Based on the arrangement of the velocity vectors, the vortex appears to be fed by fluid flow along the top of the obstacle. By TS 6200 of the simulation, the vortex has become well-defined, with the velocity vectors indicating a strong counter-clockwise flow pattern, but opposite in flow direction to that of the advancing internal wave. At this point in the simulation, the trough of the pycnocline is at the approximate location of the theoretical turning point plane. As the internal wave is a

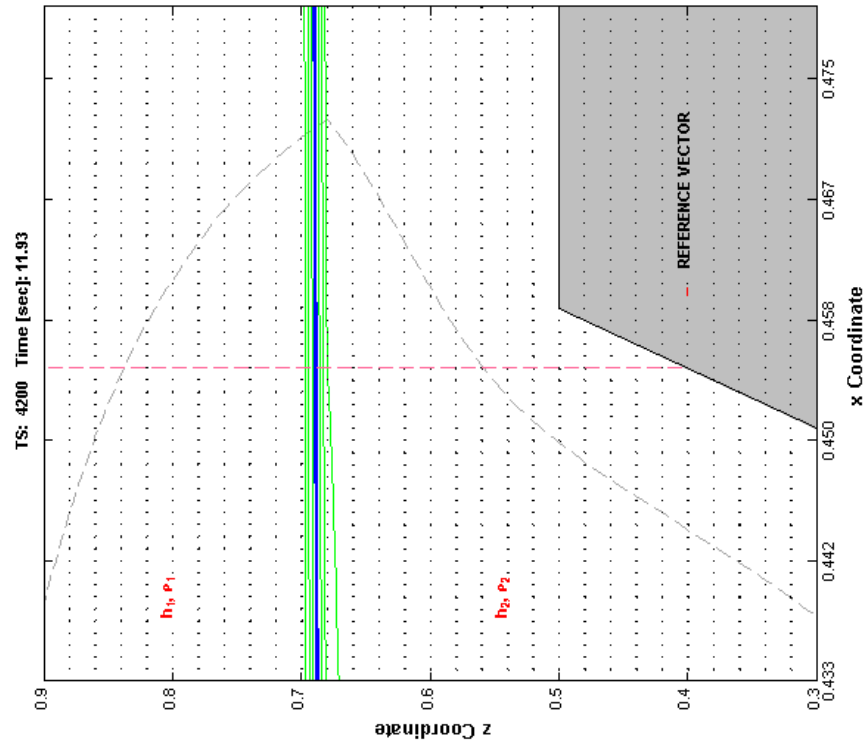
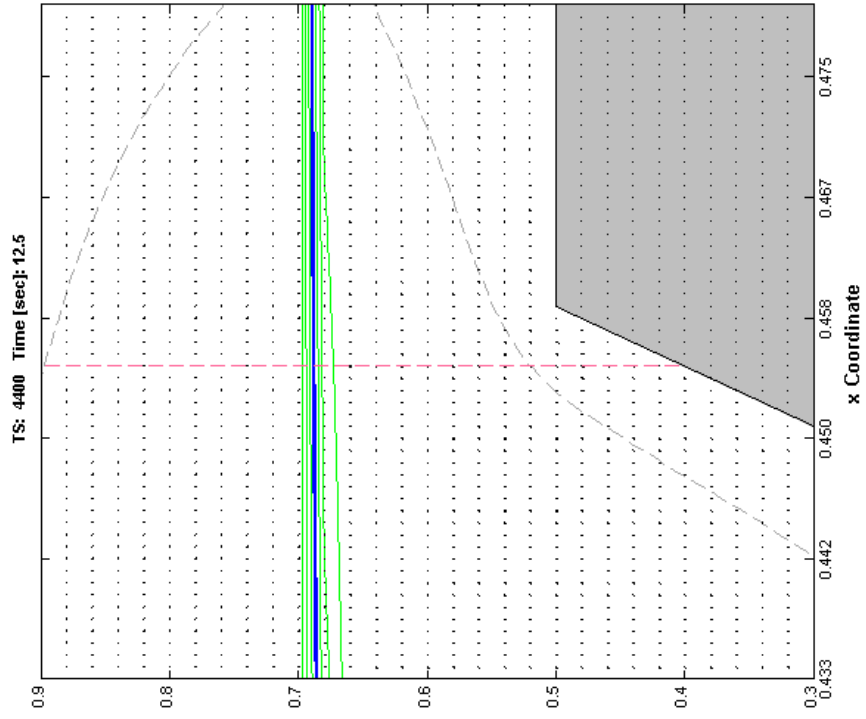
depression-type, the velocity field demonstrates a clockwise flow pattern about the pycnocline.

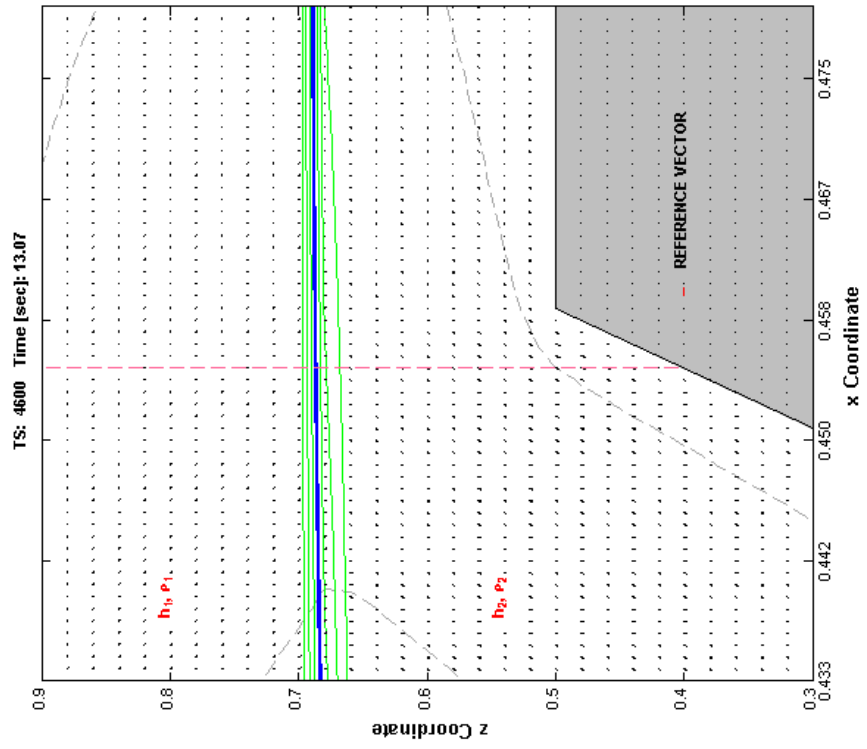
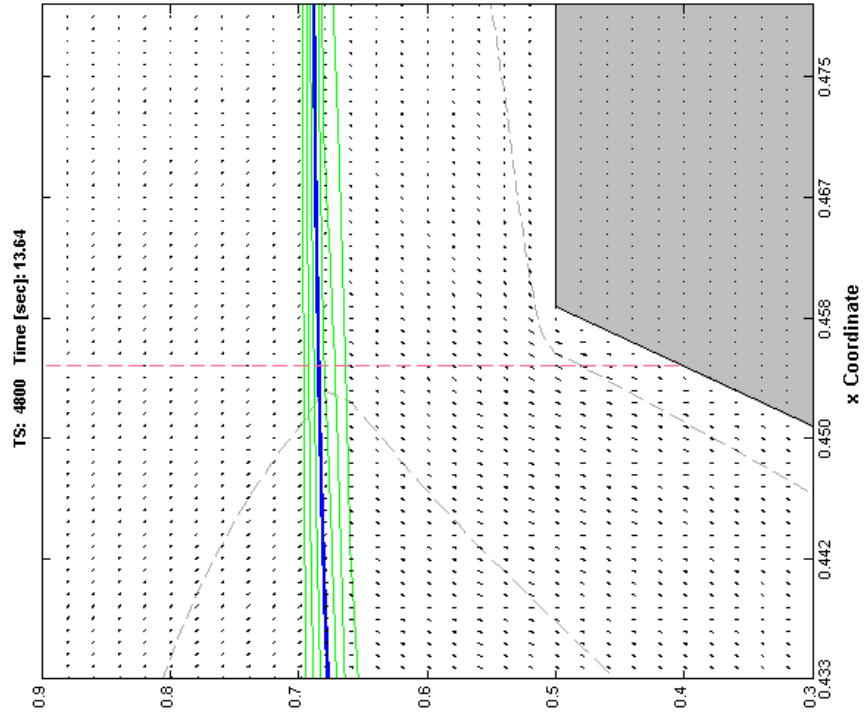
For the balance of the simulation (through TS 7600), the internal wave continues to advance through the computational domain. However, as can be seen in, the simulation did not produce any of the shoaling-like features that might be expected.

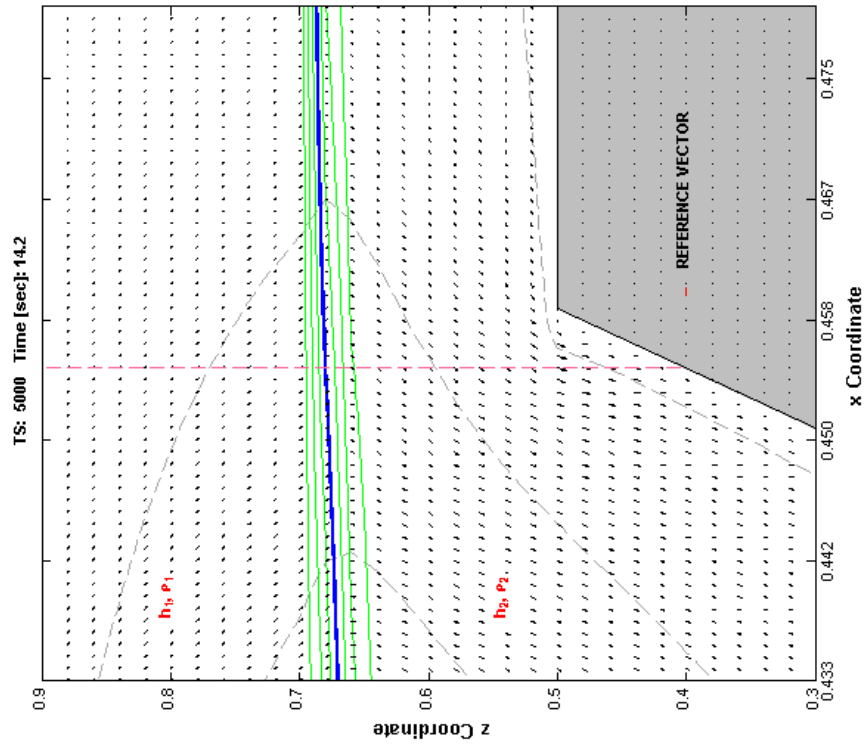
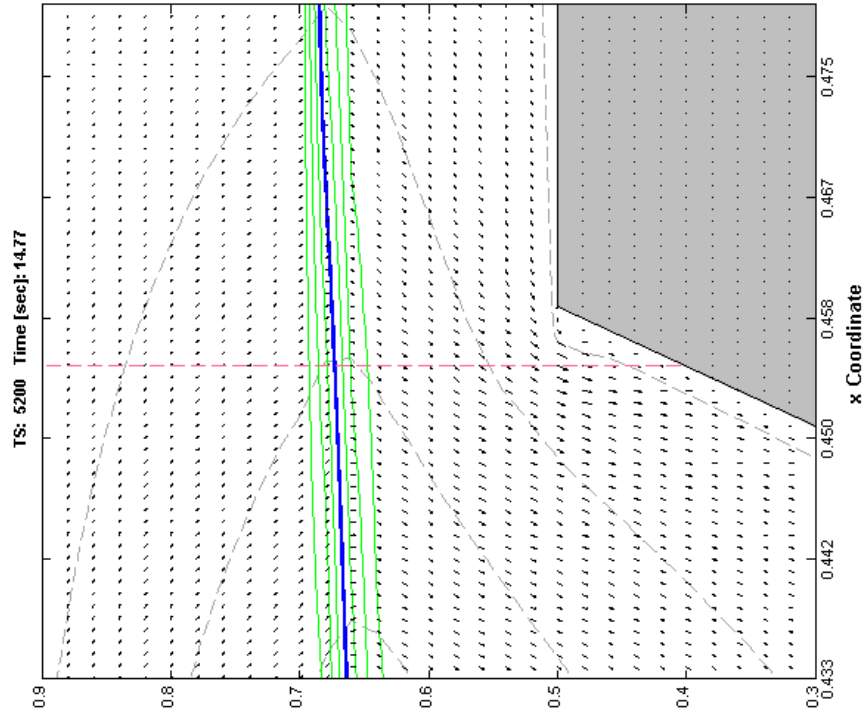


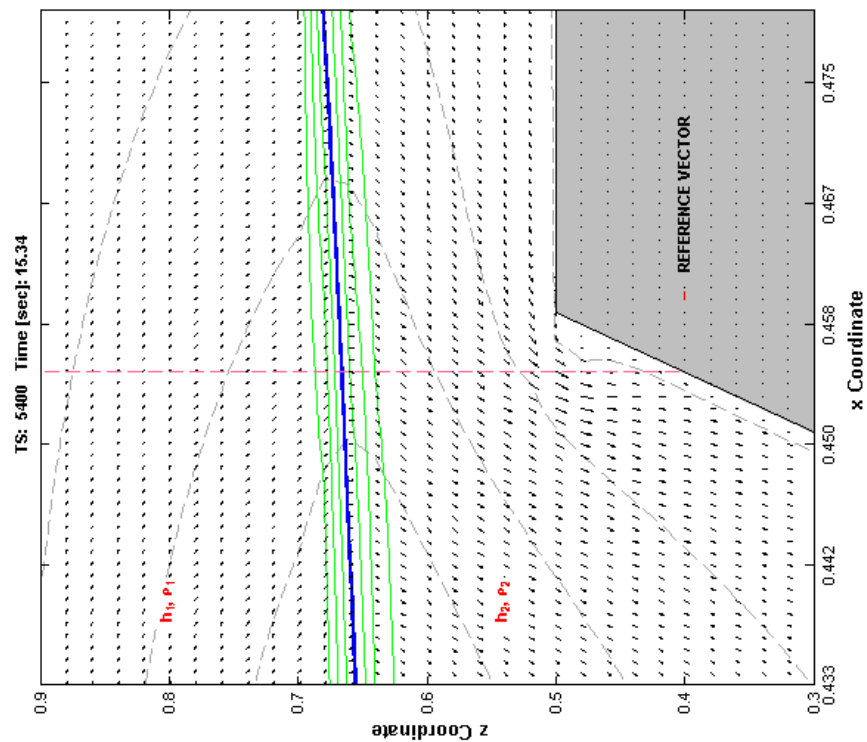
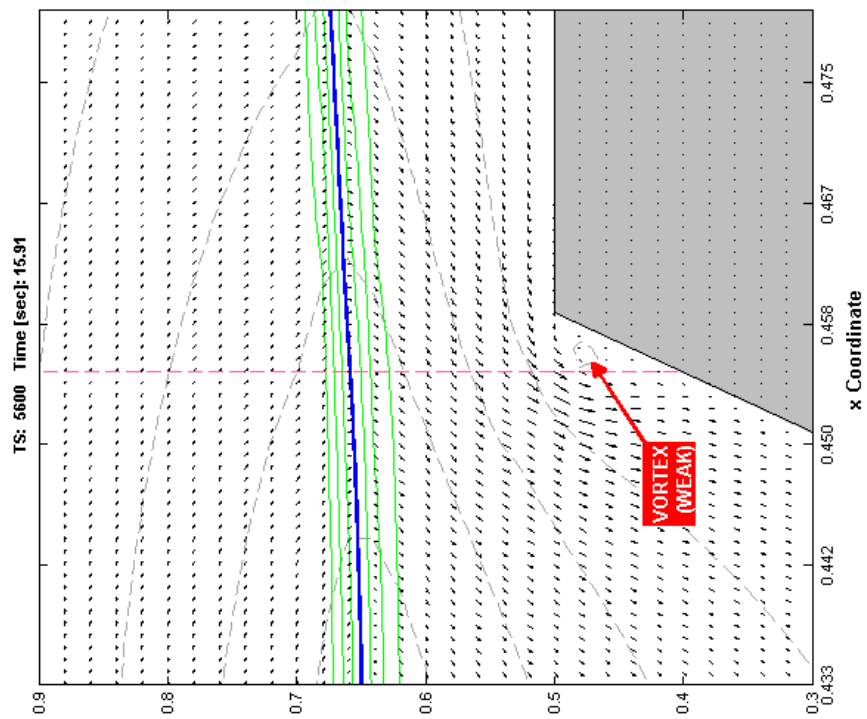


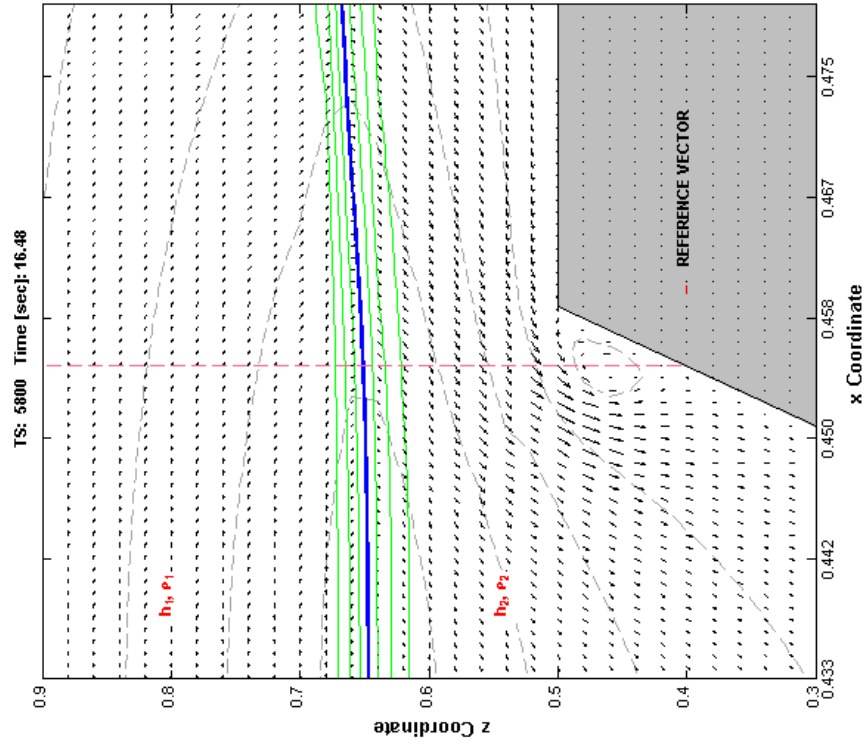
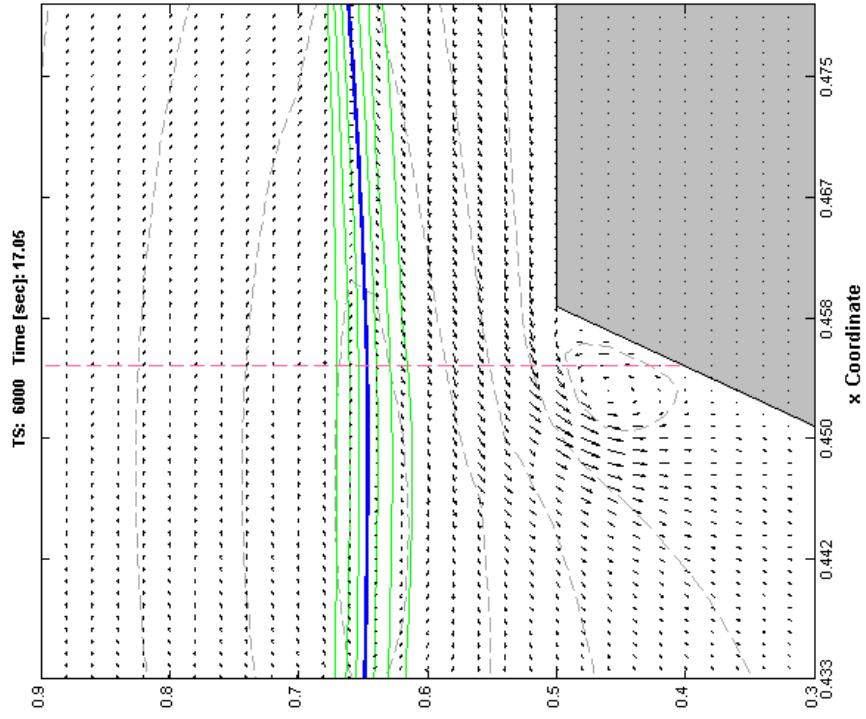


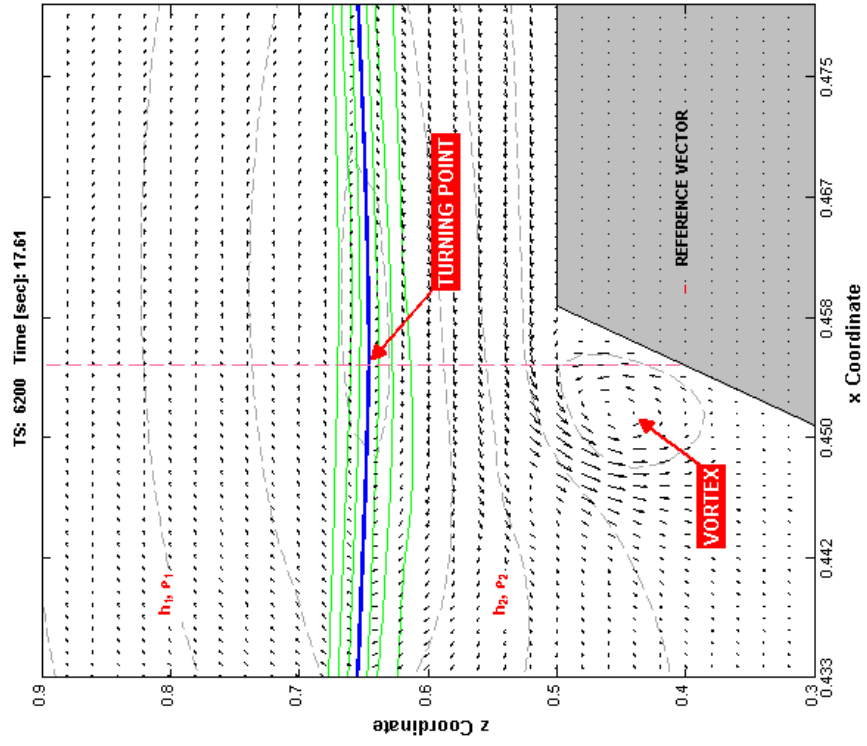
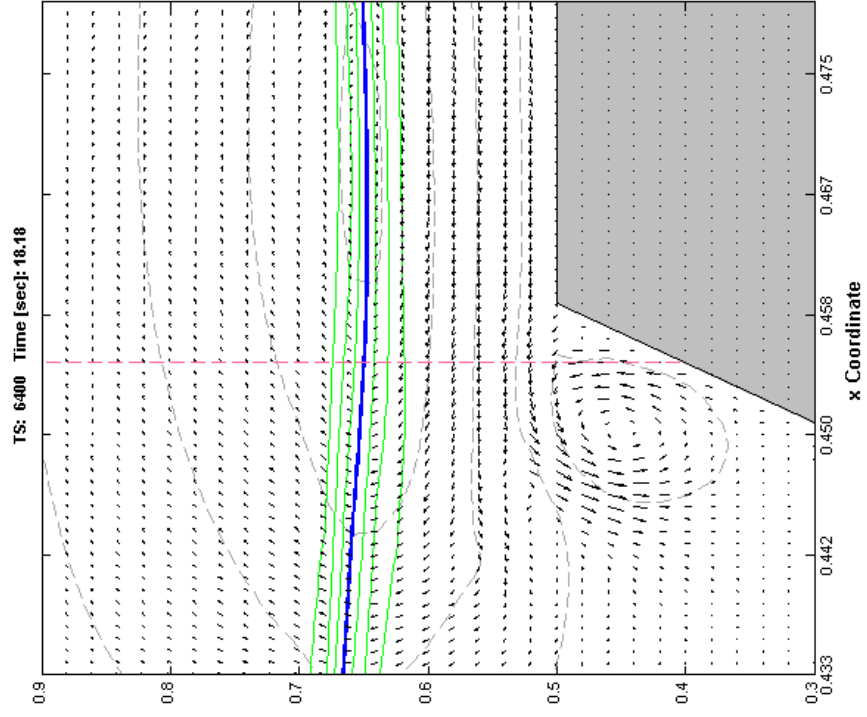


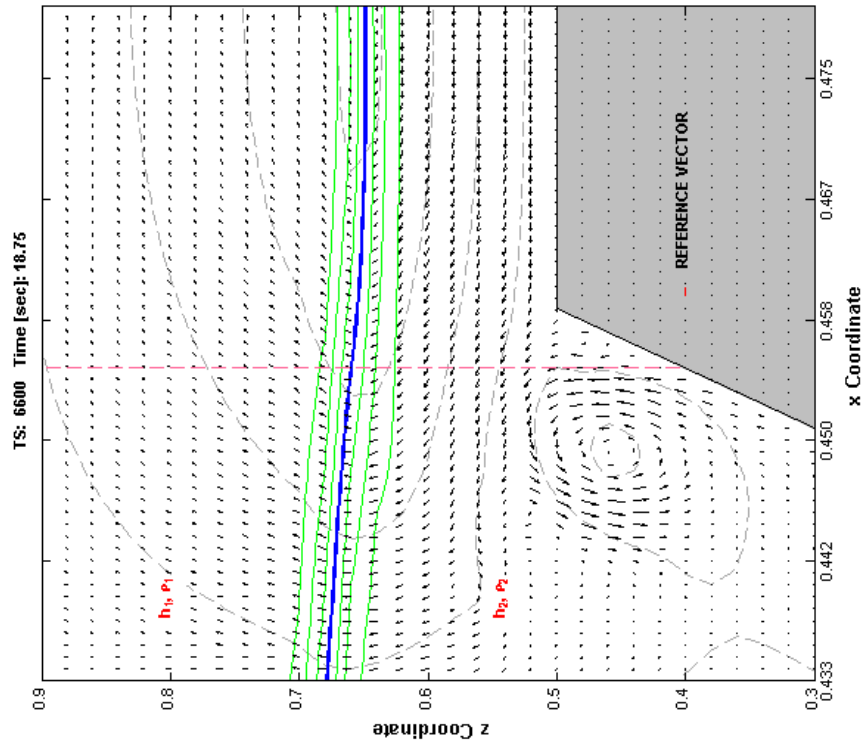
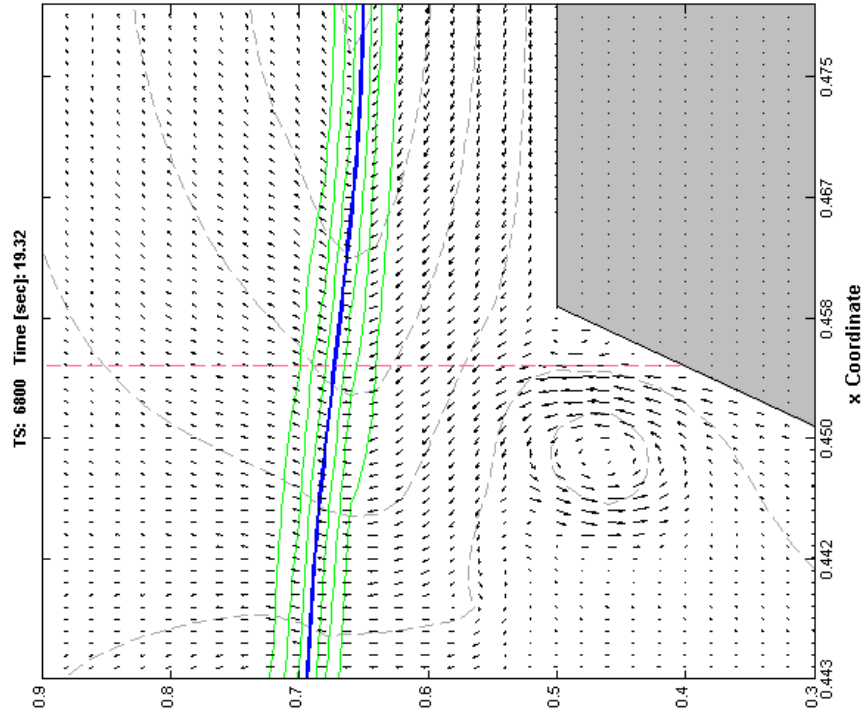


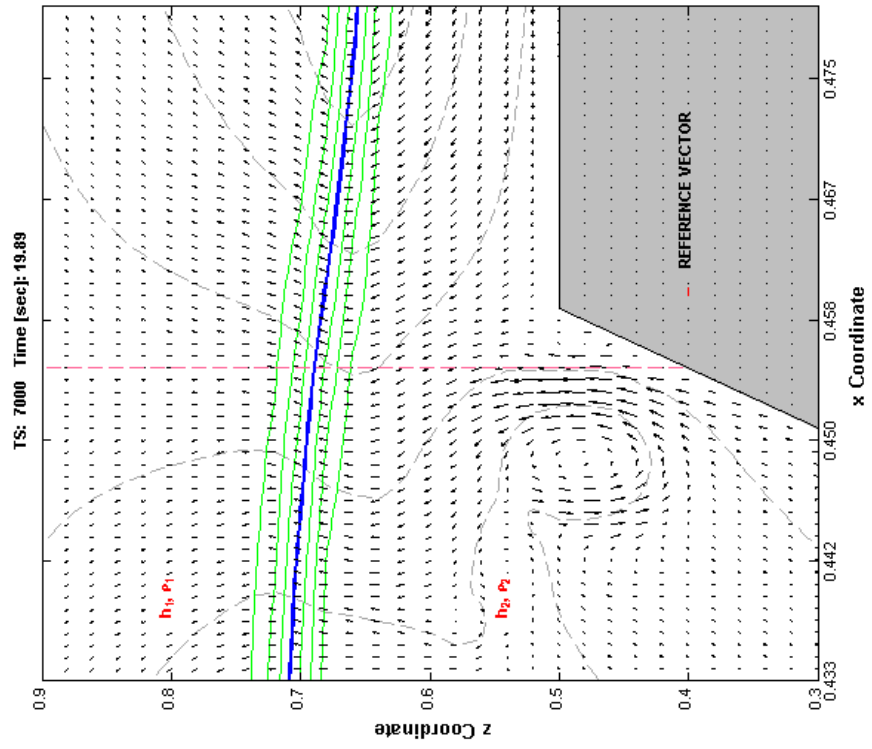
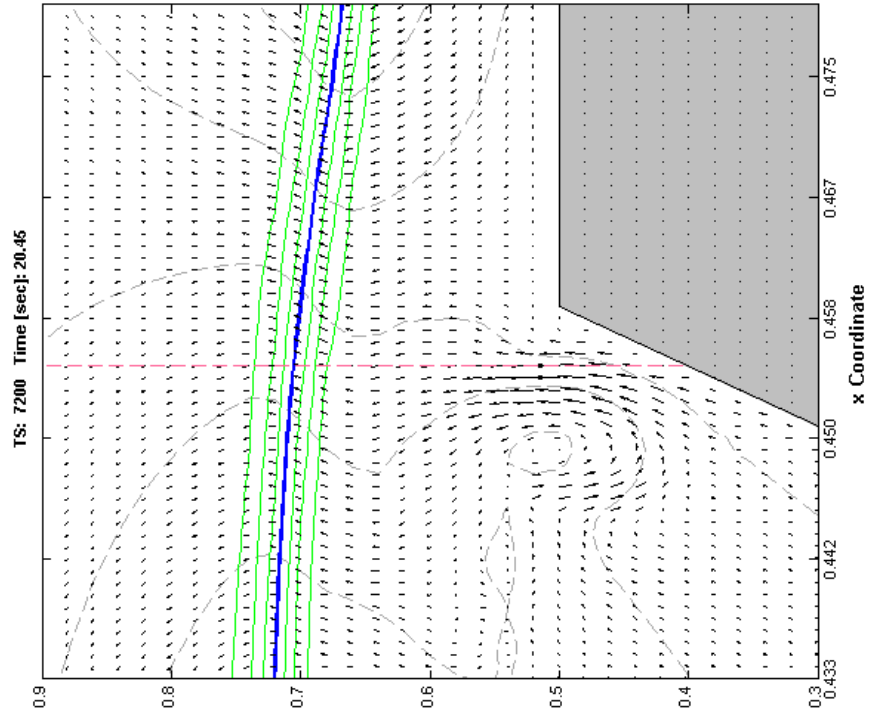


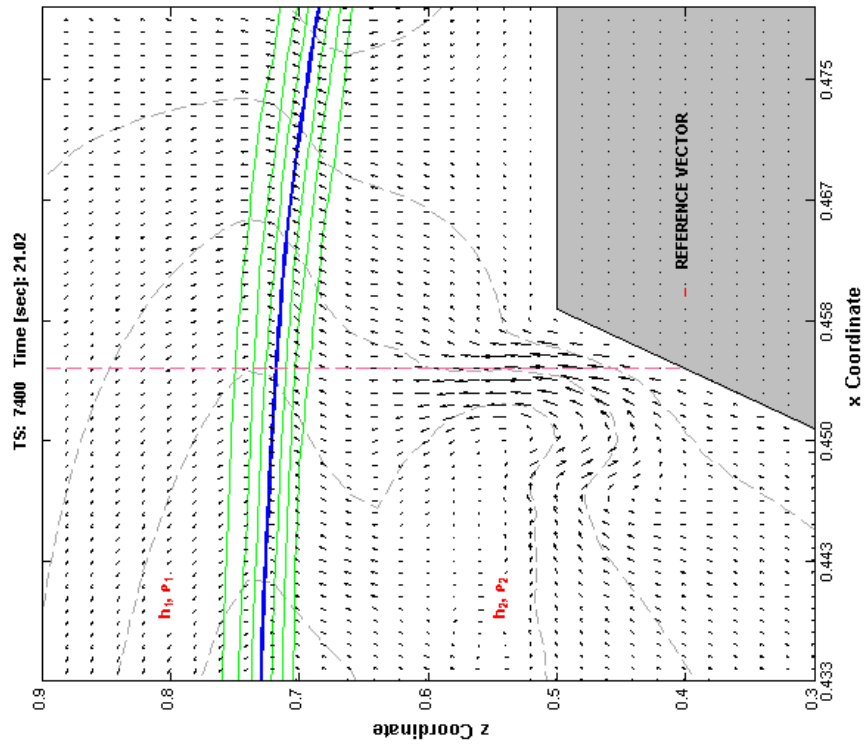
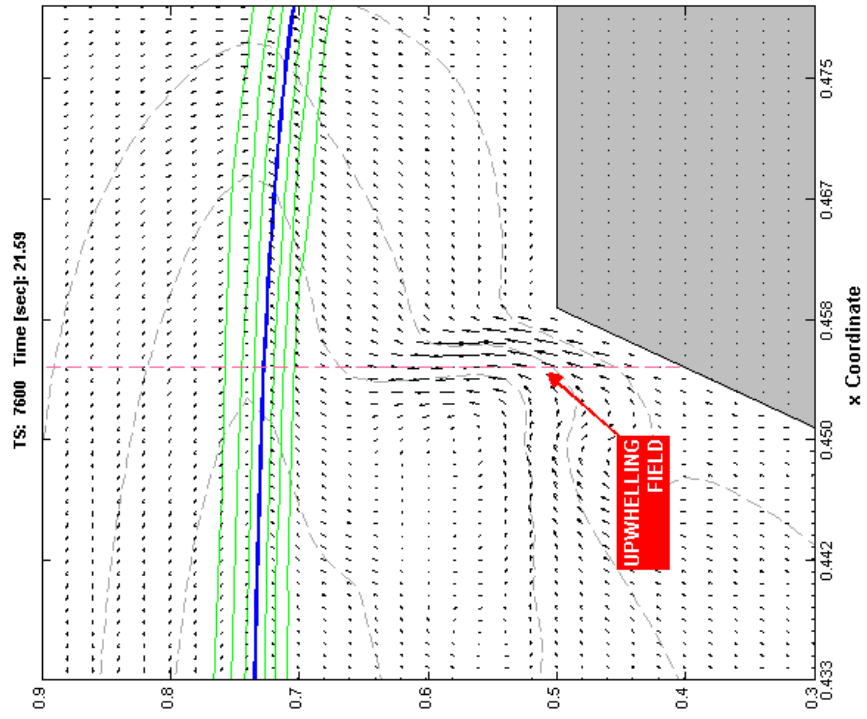


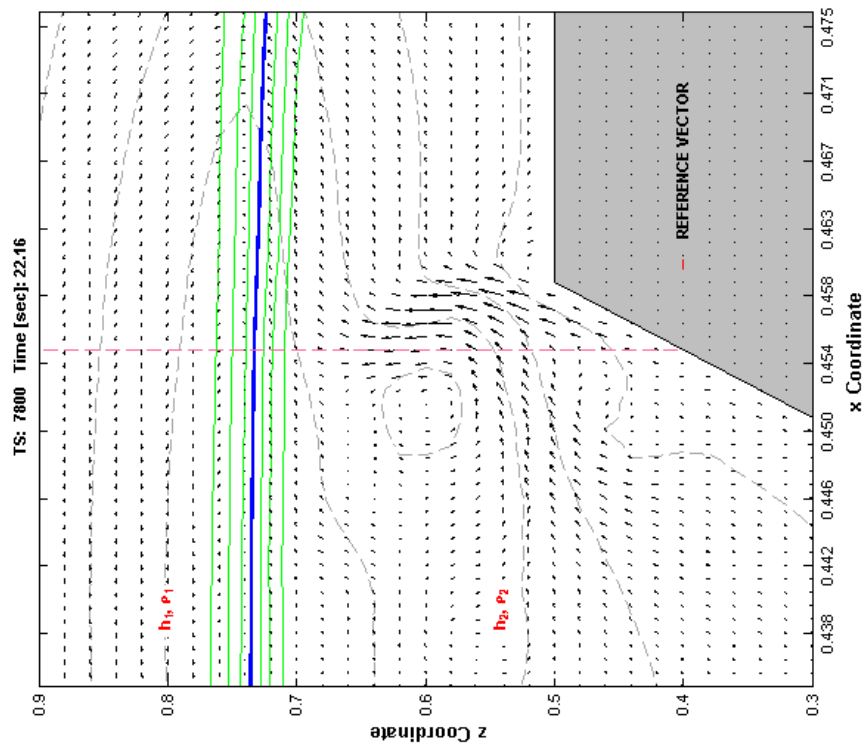
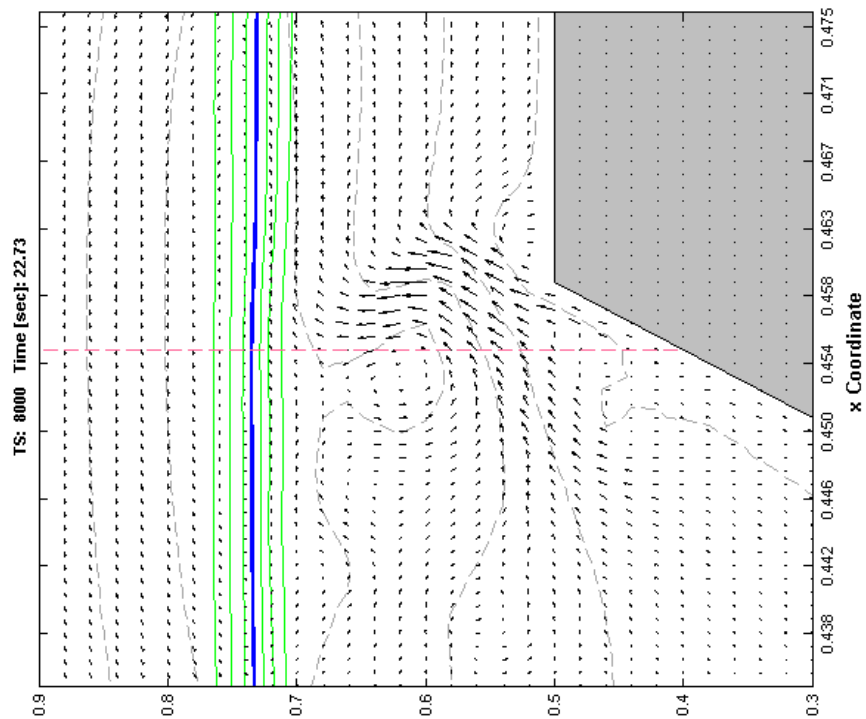












APPENDIX D

DETAILS OF NUMERICAL SIMULATION INVOLVING AN EXTENDED SLOPE-TYPE TOPOGRAPHIC OBSTACLE

The exhibits contained in this appendix depict the details of an interaction between a mode-1 depression-type internal wave and an extended (uniform) slope-type obstacle shown earlier in Figure 57. The non-dimensional simulation is shown in progress at TS 18,000 just prior to the onset of shoaling/breaking. As the intent of this particular simulation scenario was to illustrate how the internal wave polarity transformation sequence proceeds when the plane of the theoretical turning point is encountered, the illustrations capturing this transformation are limited to the pycnocline (solid blue line) and the theoretical turning point plane itself — the vertical dashed line corresponding to the fluid depth condition where $h_1 = h_2$. Supplemental isopycnals about the pycnocline are shown in green providing additional information on the character of the density interface during the simulation. Also shown is the location of the static pycnocline at time zero, prior to the initiation of the simulation, as a reference point. The non-dimensional time step interval for each figure is equal to 1000.

At about TS 18,000, the simulation shows that internal wave has yet to encounter the face of the obstacle as the wave itself is still enjoys a relatively symmetric profile. The theoretical turning point plane is on the far right margin of the figure. As was the case with the other simulations conducted as part of this research, the leading internal wave is followed by a lesser transient wave train.

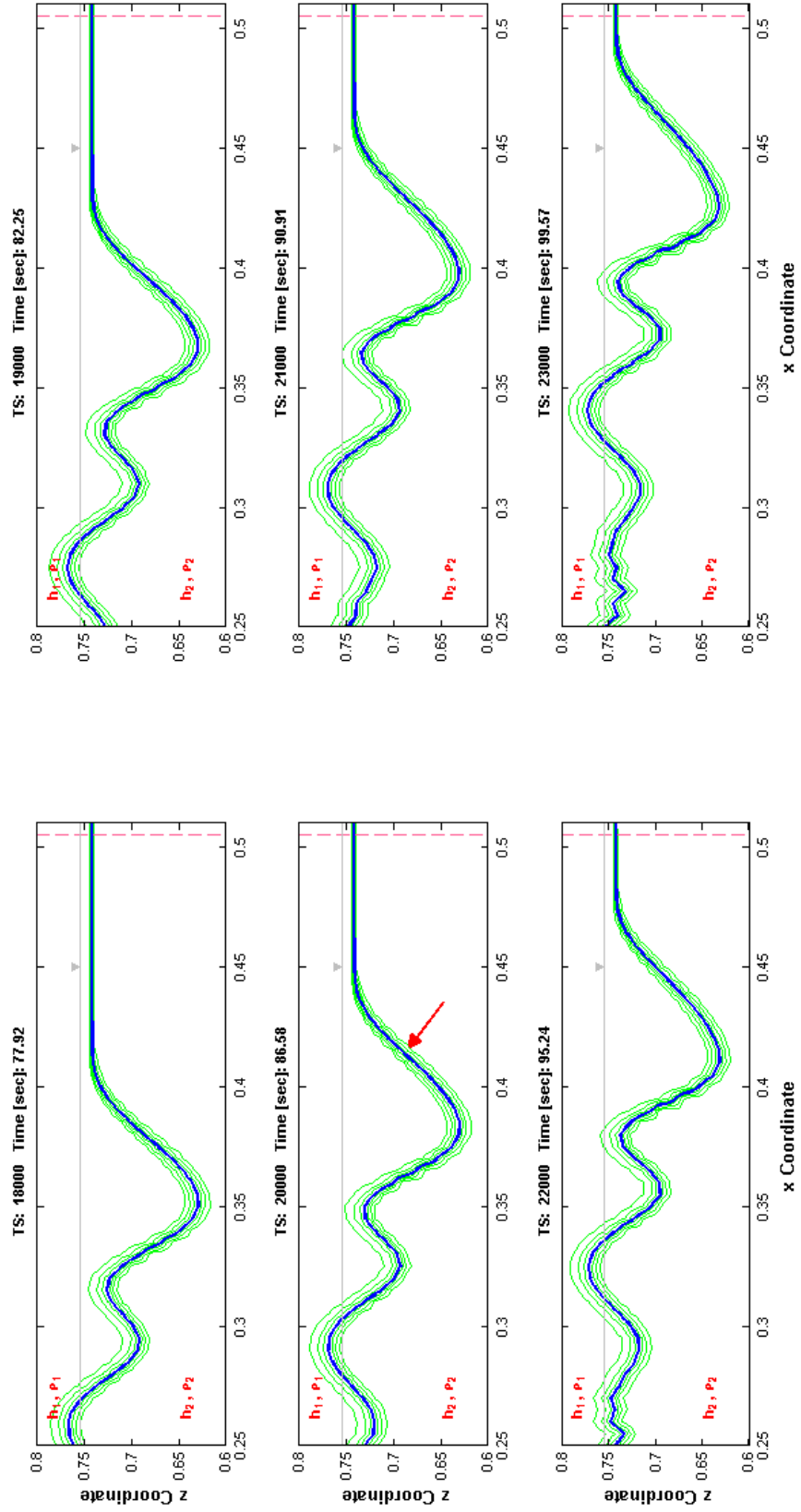
At about TS 20,000 in the simulation, asymmetry in the pycnocline profile is becoming apparent as the internal wave begins to encroach on the location of the theoretical turning point plane, suggesting the onset of shoaling. As illustrated in subsequent time steps, the internal wave's symmetry continues to decay as the wave front approaches the turning point plane. The nature of this decay is best characterized by the leading face of the wave appearing to level-out (horizontally) through the course of the simulation whereas the trailing-end of the wave appears to be rotating (vertically) up and forward, gaining elevation. While this transformation is taking place, the collection of lesser waves comprising the transient internal wave train are becoming more pronounced to the point that two (2) distinct internal waves of elevation can be observed to have formed. This development would correspond to about TS 26,000 in the simulation sequence. These and subsequent elevation-type internal waves appearing in

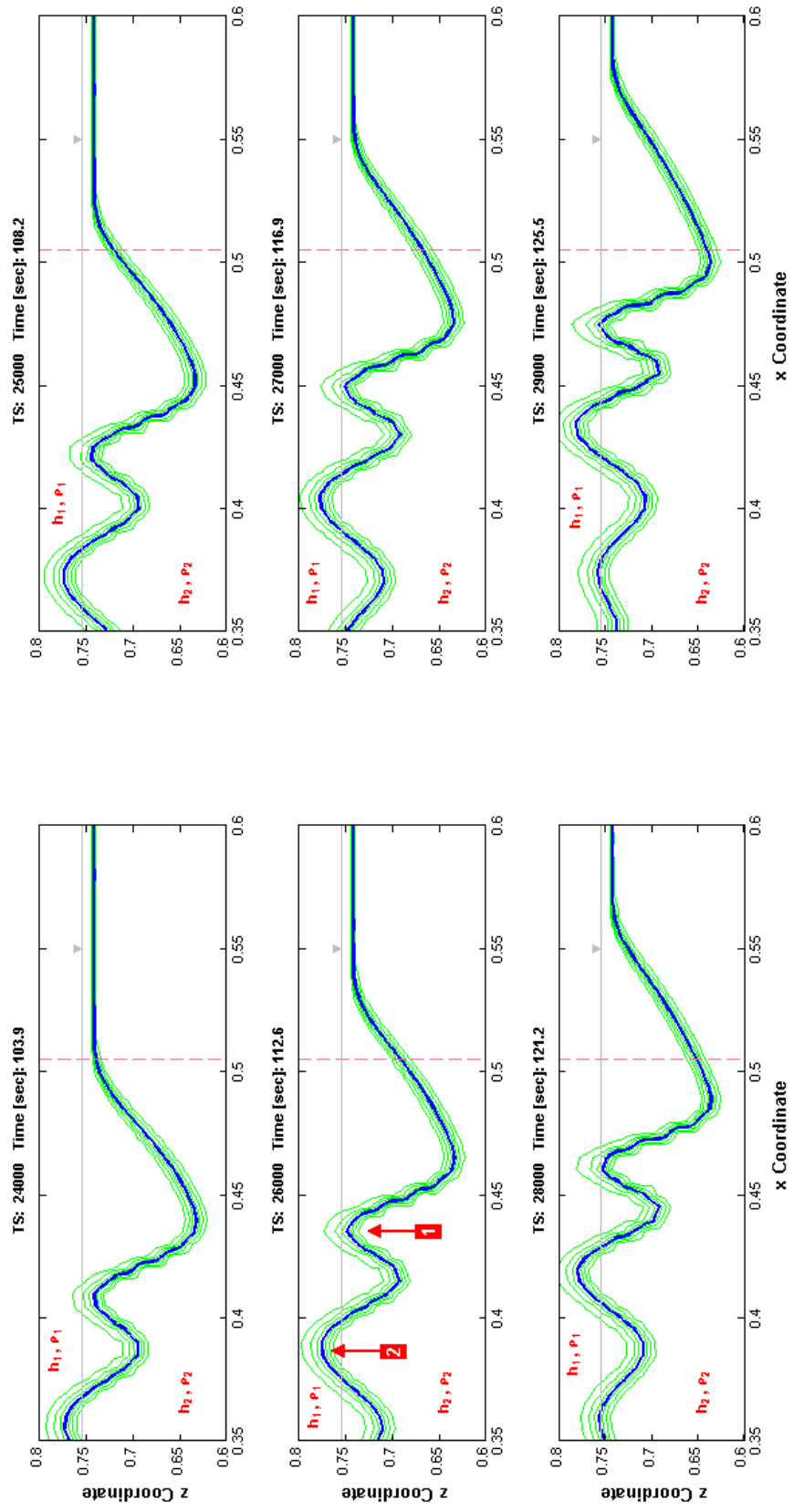
the simulation have been annotated in the exhibits using Arabic numbers – 1, 2, 3, and so on.

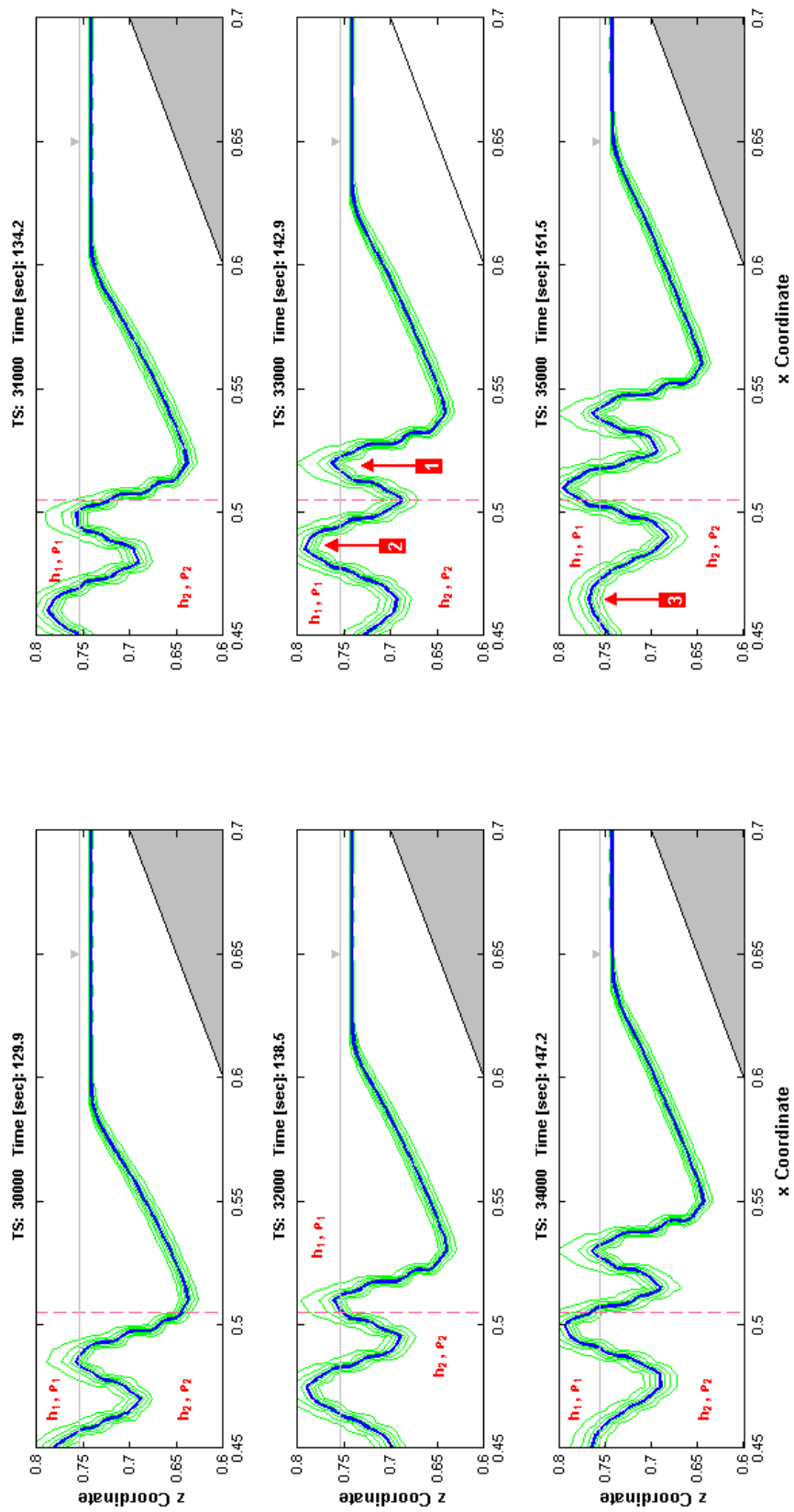
By about TS 29,000, the trough of the leading depression-type internal wave has reached the approximate location of the theoretical turning point plane. What is noteworthy about this phase of the simulation is that the emerging elevation-type internal waves associated with the dispersive internal wave train appear to be growing at the expense of the leading internal wave — which itself now appears to be decaying. By about TS 33,000, the simulation now appears to be dominated by two secondary, elevation-type internal waves that are well-formed and whose crests have risen above the level of the static density interface. By TS 35,000, a third elevation-type internal wave is apparent in the simulation and is beginning to form.

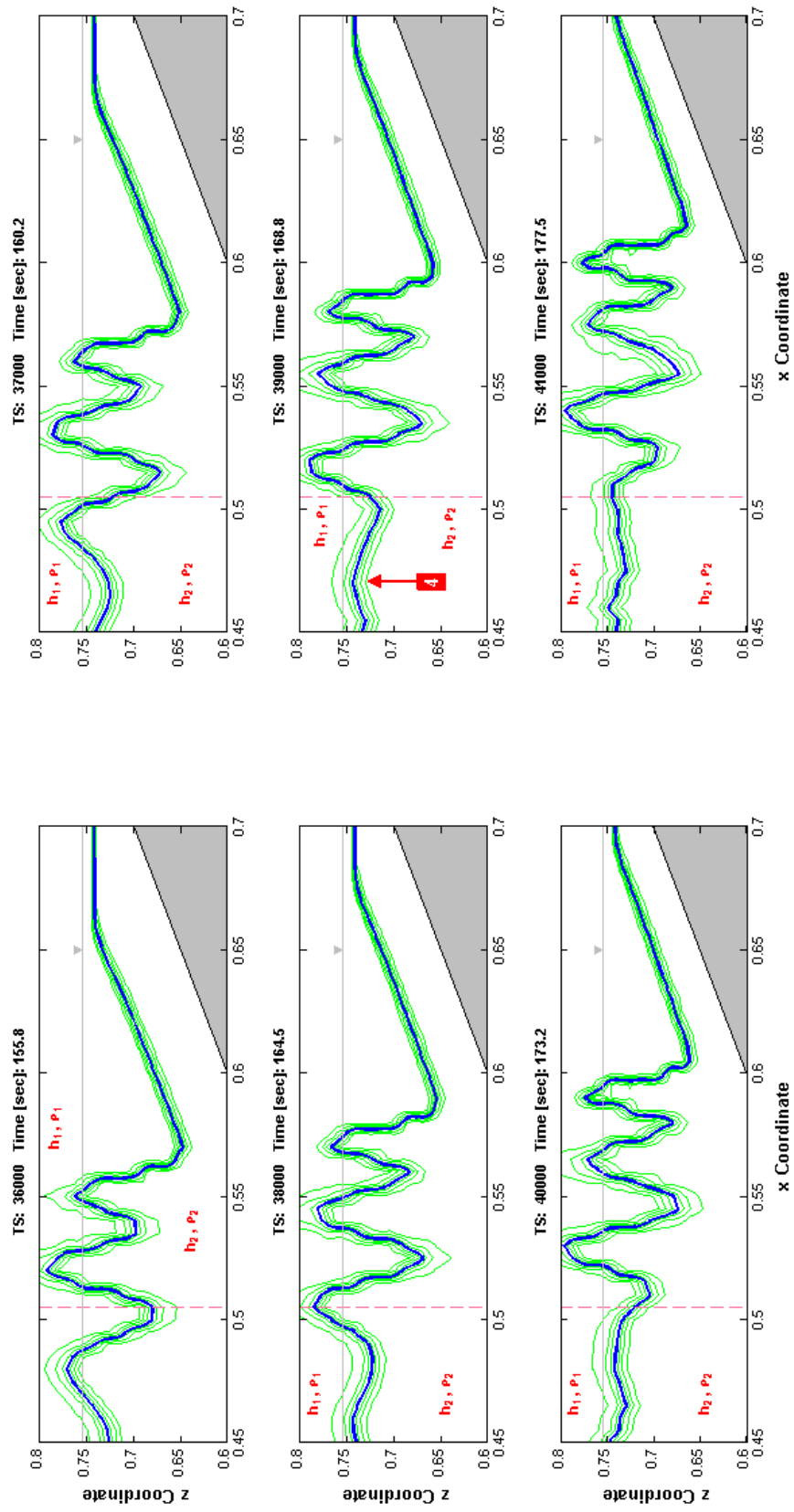
In subsequent time steps, additional secondary elevation-type internal waves associated with the disperse wave train continue to form as the wave train progresses up the slope of the obstacle, past the theoretical turning point plane. At TS 39,000, a forth elevation-type internal wave begins to take form in the simulation; by TS 43,000, this additional internal wave is separate and distinct. Additional secondary elevation-type internal waves appear in subsequent time steps — a fifth at TS 47,000, a sixth at TS 48,000,

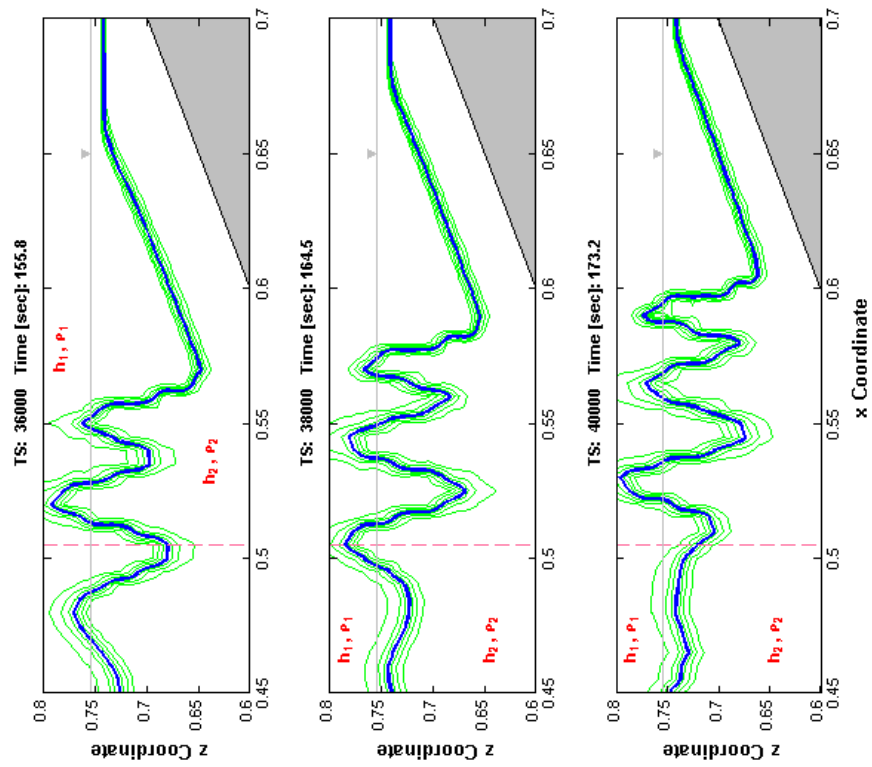
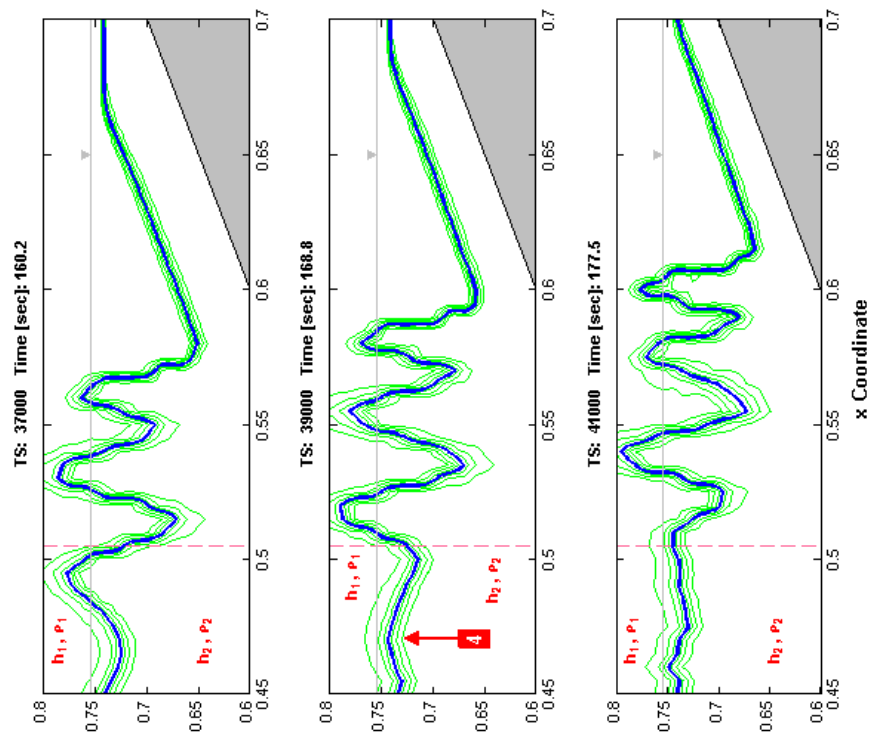
a seventh at TS 49,000, an eight at TS 51,000, and so on. What is also apparent in the simulation is that this collection of lesser internal waves (or boluses - ?) appears to march-up the face of the slope, as noted by the arrow. This aspect of the simulation comports with observations made by Bourgault et al. (2006). For example, between TS 54,000 and TS 59,000, the internal wave at the front of the wave train can be observed advancing up-slope.

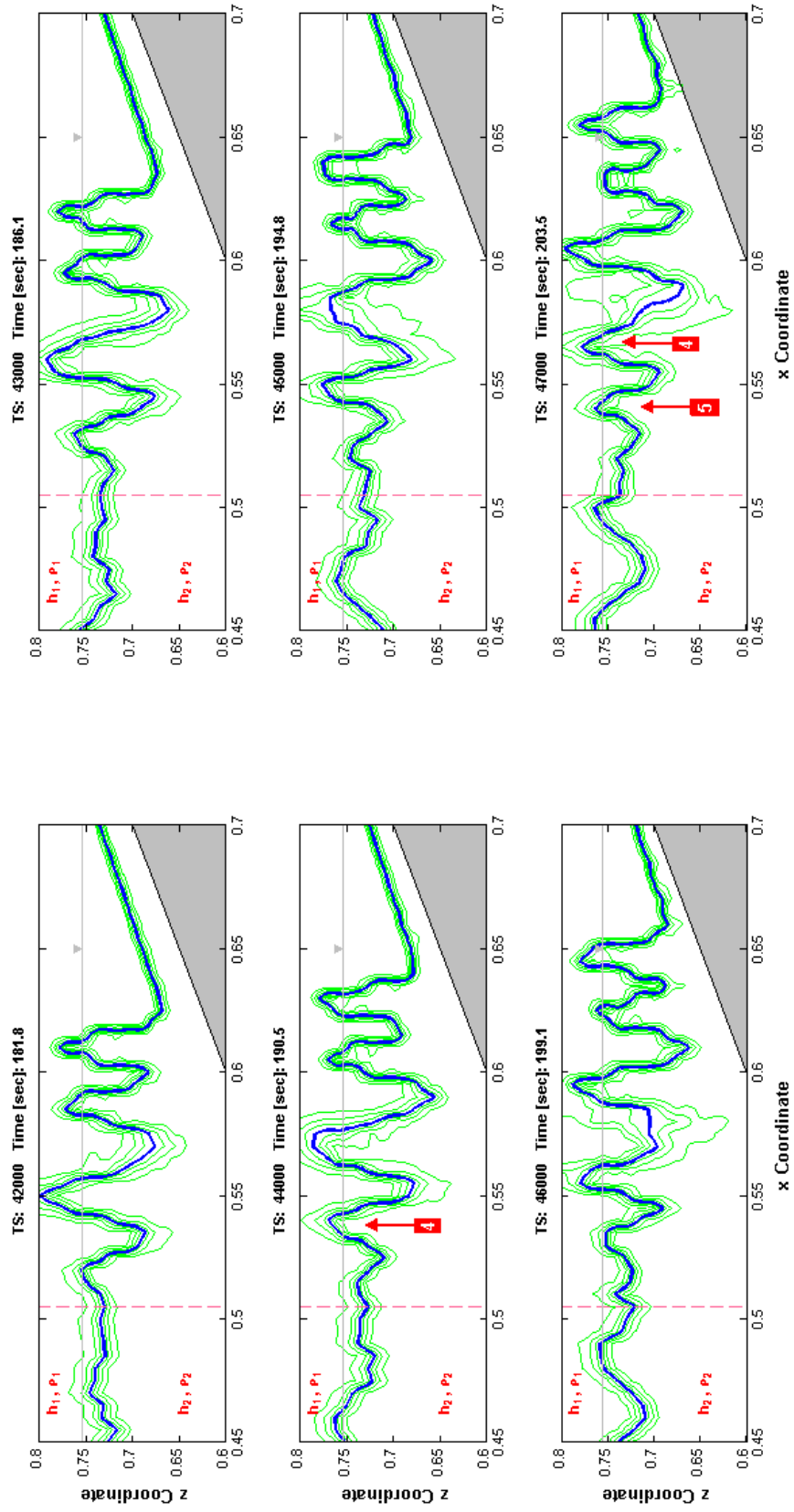


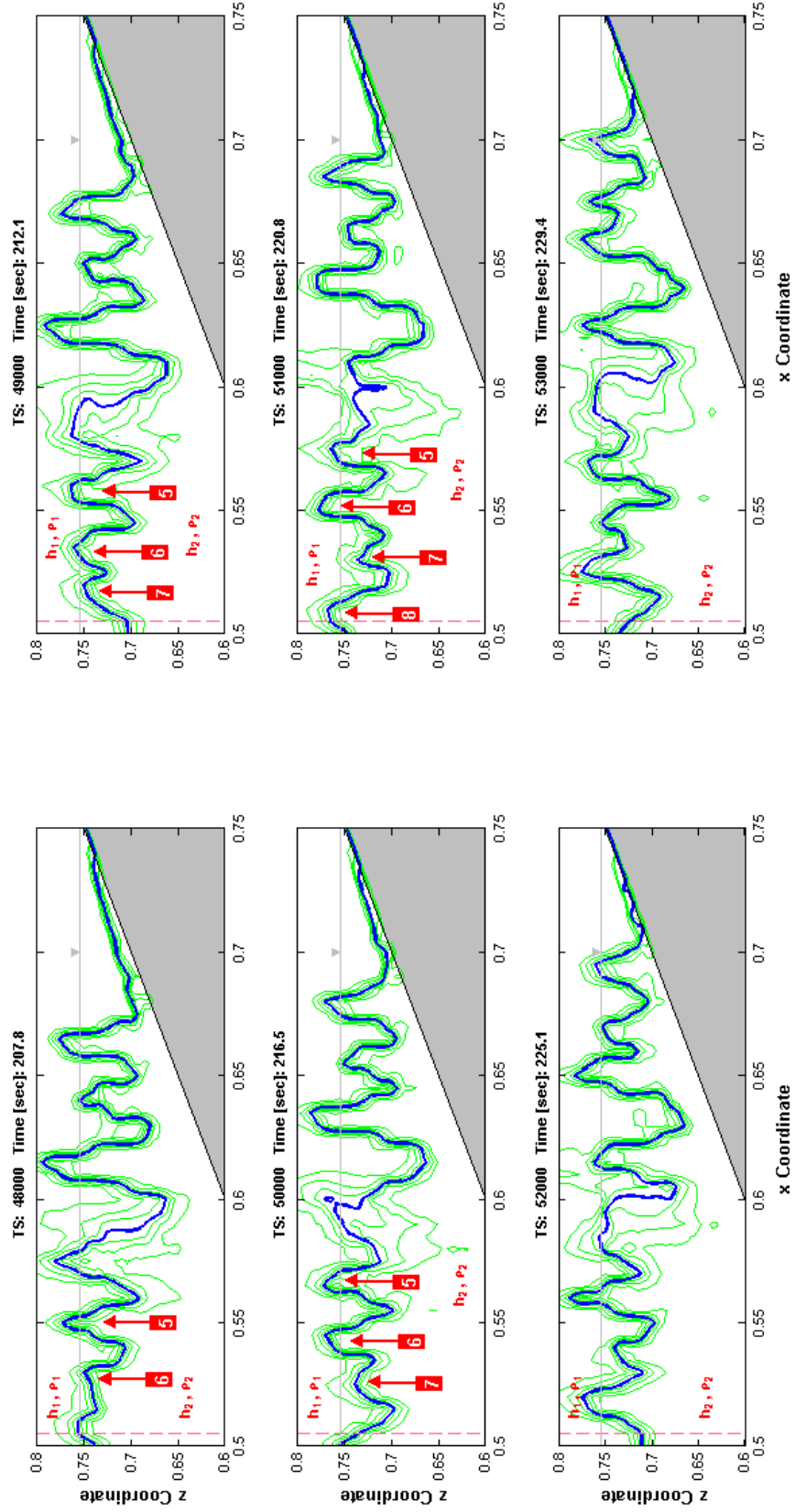


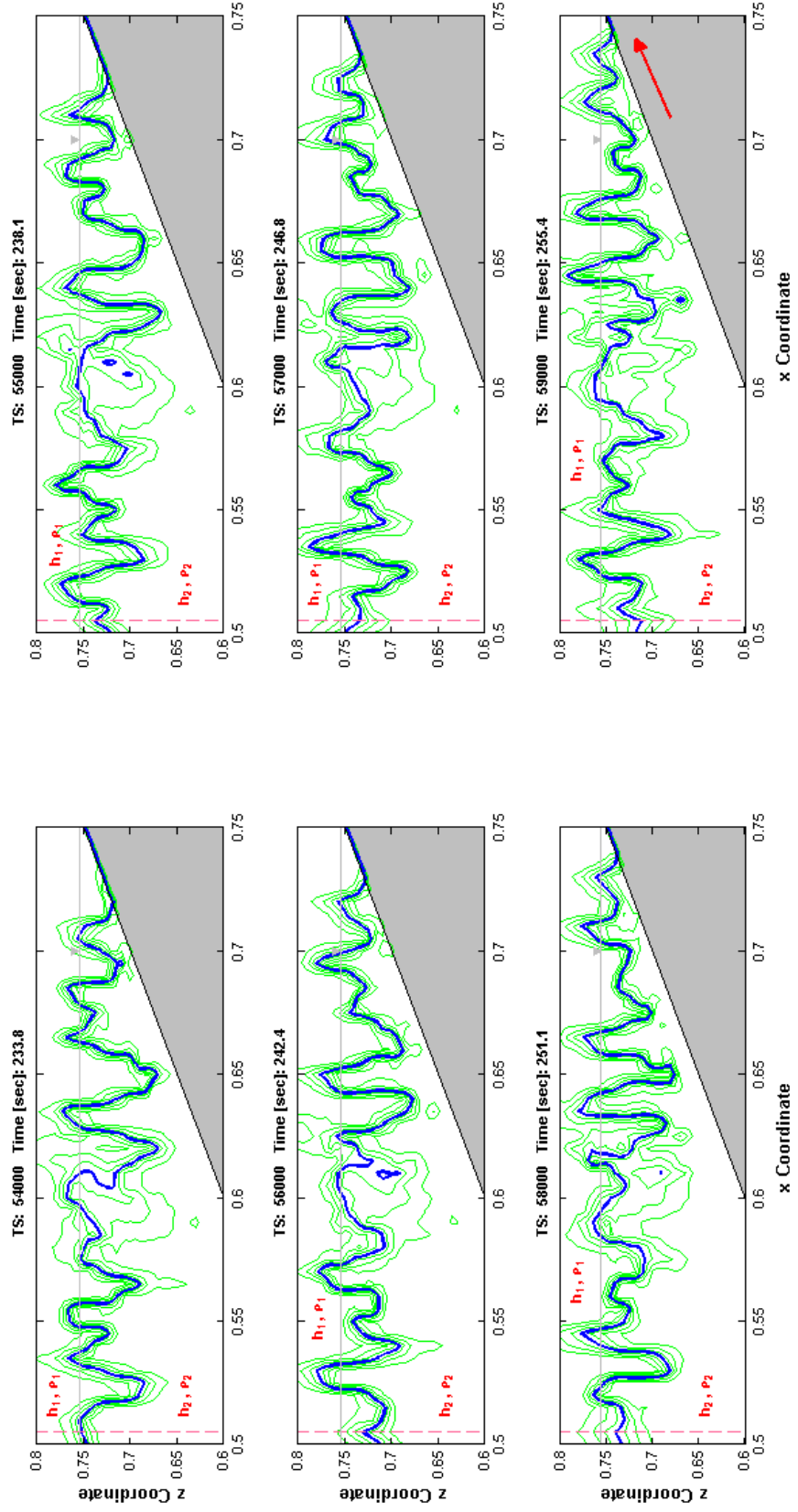












APPENDIX E

DETAILS OF NUMERICAL SIMULATION INVOLVING A SHORT SLOPE- TYPE TOPOGRAPHIC OBSTACLE

The exhibits contained in this appendix depict the details of an interaction between a mode-1 depression-type internal wave and an extended slope-type obstacle shown earlier in Figure 62. The intent of this particular simulation scenario was to replicate the shoaling-breaking progression sequence described by Michallet and Ivey (1999). The figures in the simulation show the non-dimensional simulation in progress at TS 18,800. At this point in the simulation, the internal wave has yet to encounter the obstacle, just prior to the onset of the theoretical shoaling-breaking progression. These figures show the normalized velocity vector field (black arrows), the streamline contours (dashed lines), and the pycnocline (solid blue line). To provide some context for each figure, inset maps also show the position of the internal wave relative to the topographic obstacle. The non-dimensional time step intervals equal to 200.

Prior to TS 19,000, the simulation shows that the advancing internal wave has yet to encounter the obstacle as the wave's profile is relatively symmetric. The velocity vectors show that the flow field is in the clockwise direction, consistent with a depression-type internal wave. The theoretical turning point plane, defined by the fluid depth condition corresponding to $h_1 = h_2$, is on the far right margin of the figure. As was the case with the other simulations conducted as part of this research, the inset maps show that the leading internal wave is followed by a lesser transient internal wave train.

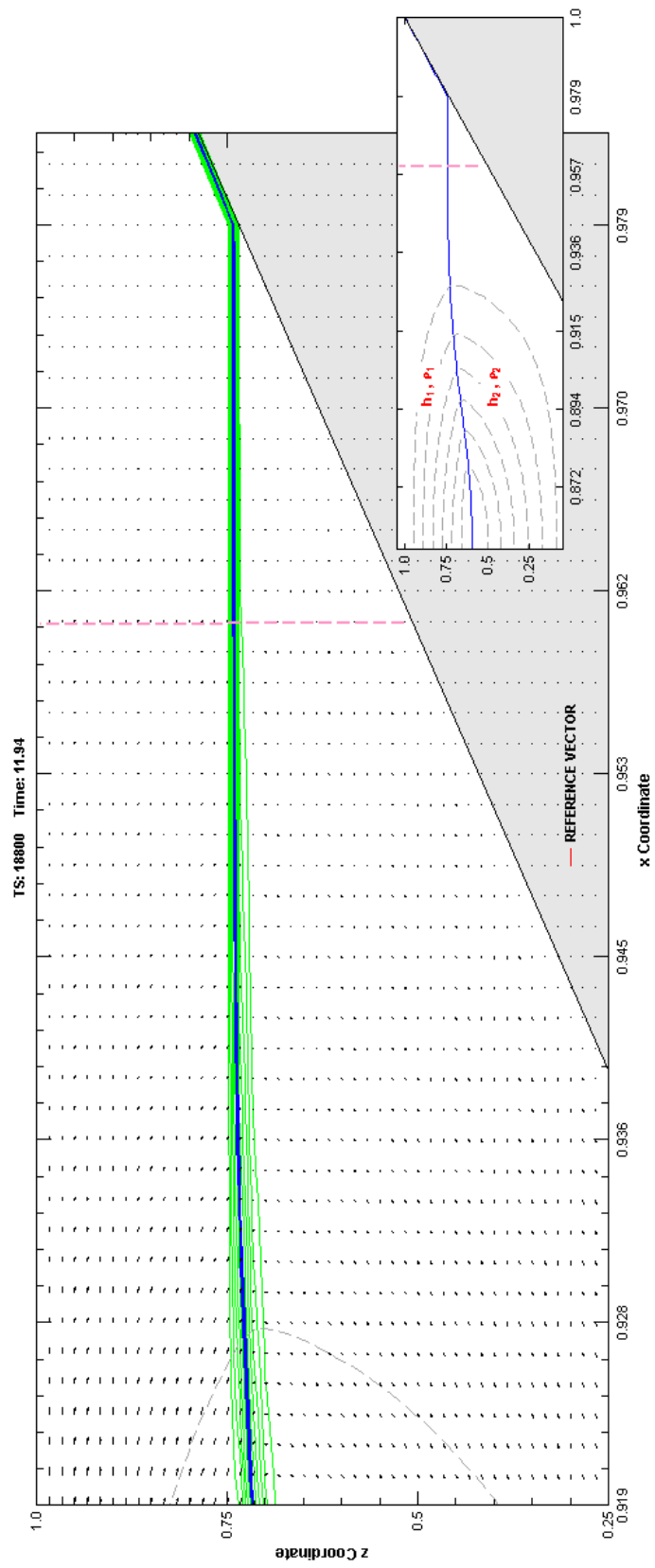
Recalling the simulation involving an extended-slope type obstacle described earlier in this dissertation (both Section 4.3.1.3 and Appendix D), as the internal wave approaches the obstacle, it becomes entrained and ultimately appears to slide or wash down the slope ("backwash"). At about TS 19,800 in this simulation, the profile of the pycnocline and the arrangement of the streamline contours begin to demonstrate some asymmetry in their geometry suggesting the onset of shoaling. As this occurs, the relative size of the velocity vectors is also growing suggesting that the speed on the internal wave is increasing. The increase in wave speed is confirmed by a decrease in the spacing of the streamline contours. As illustrated in subsequent time steps, the elevation of the pycnocline continues to decay as the wave front approaches the plane of the theoretical turning point. Fluid velocities in the h_2 fluid layer continue to increase as the

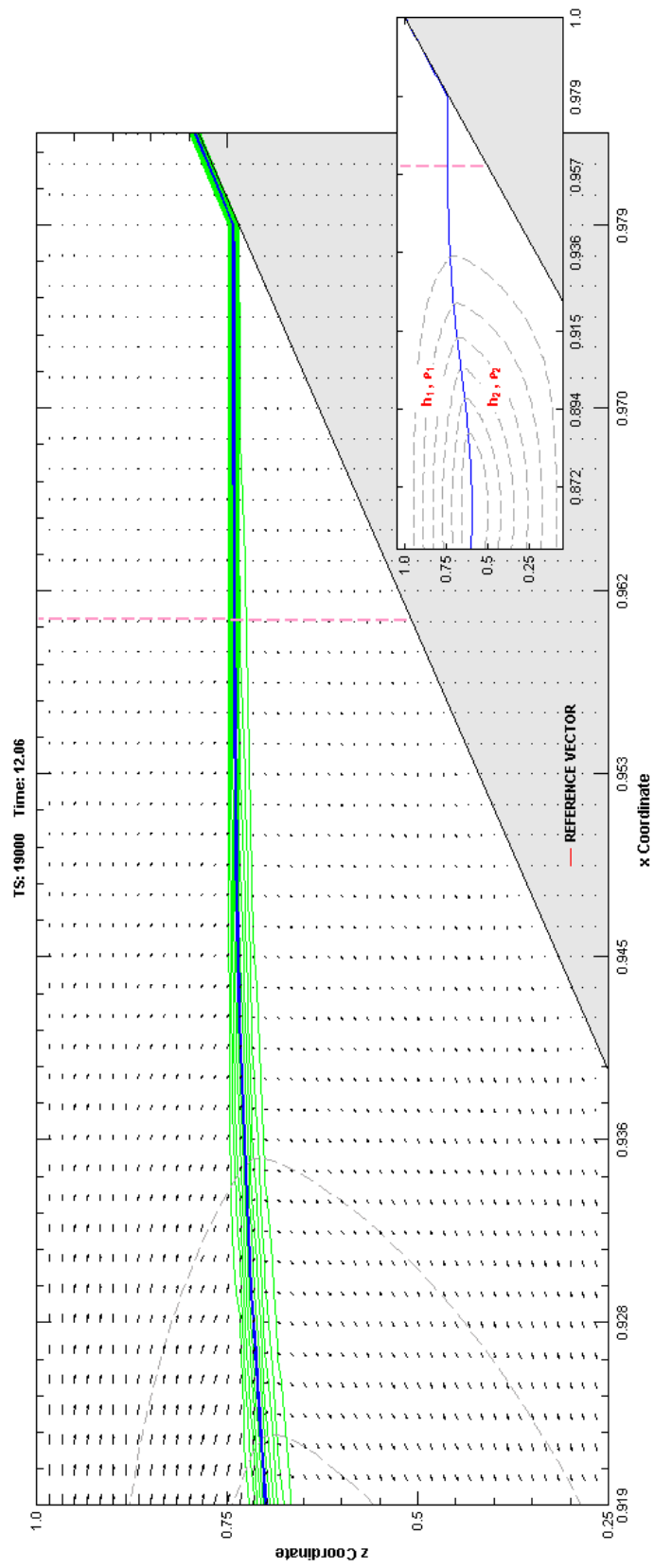
elevation of the pycnocline descends. This increase can be observed by the magnitude (length) of the velocity vectors in this region of the computational domain. At about TS 21,100, the pycnocline has reached its lowest point of descent marking the end of the “wash-down” phase of shoaling/breaking. Hence, a local “minima.” It is also worth noting that with the exception of the density interface along the pycnocline trough, the velocity vectors have diminished in magnitude, suggesting momentary “stagnation” of the system and the beginning of a new phase in the wave breaking progression.

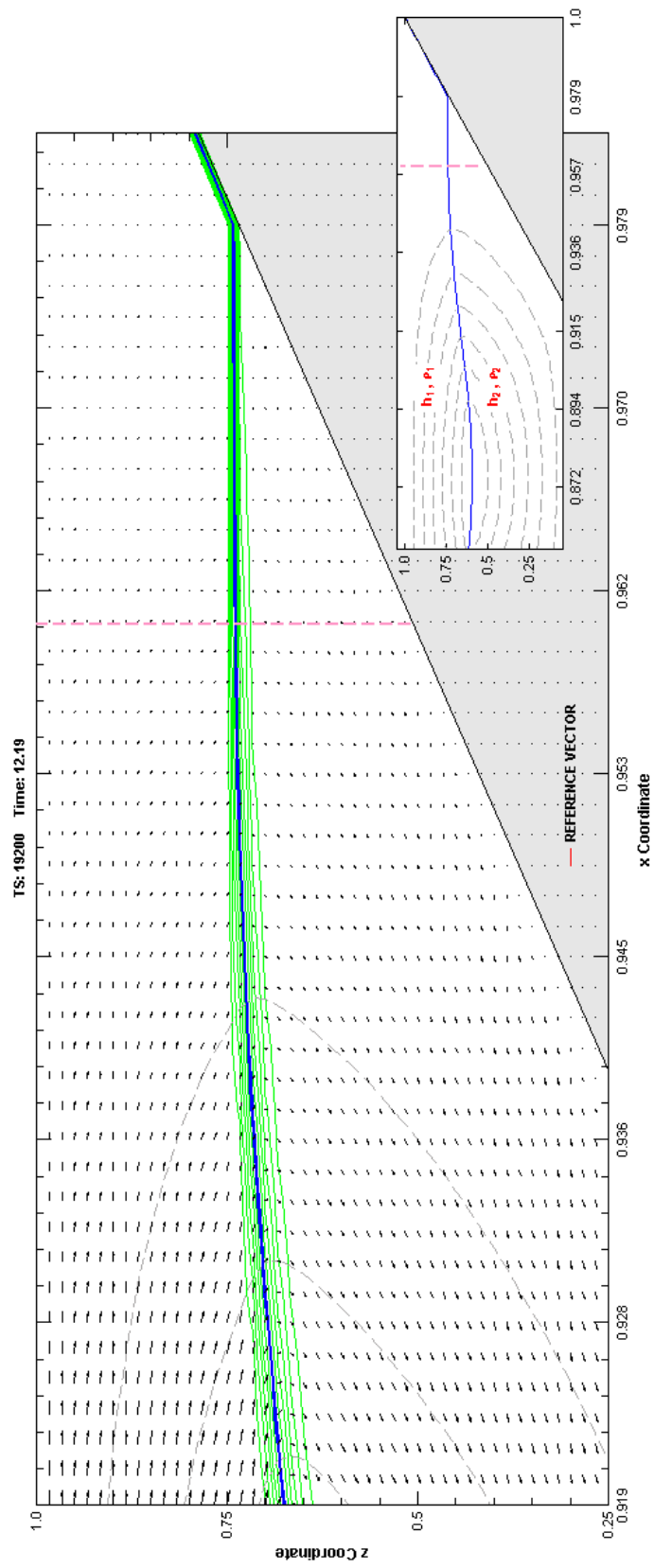
From this local “minima,” the trailing end of the internal wave begins to advance up-slope and grow as it proceeds. Through the next several time steps in the simulation, a wave-like feature begins to take form. Ultimately, this wave-like form becomes unstable and rolls-over onto itself. At this point in the simulation — about TS 21,600, the internal wave appears to break. Soon thereafter, at about TS 21,800, a K-H “cat’s eye” -like feature (Figures 14 and 15) forms revealing a localized area of turbulence. Also of interest at this point in the simulation is a change in the character of the velocity vectors. They have assumed a change in polarity. They are now flowing in a clockwise direction, and are also growing in magnitude as the simulation proceeds. It may be concluded that the apparent “stagnation” period described above appears to represent the approximate time in the simulation at which the velocity vectors reverse their polarity.

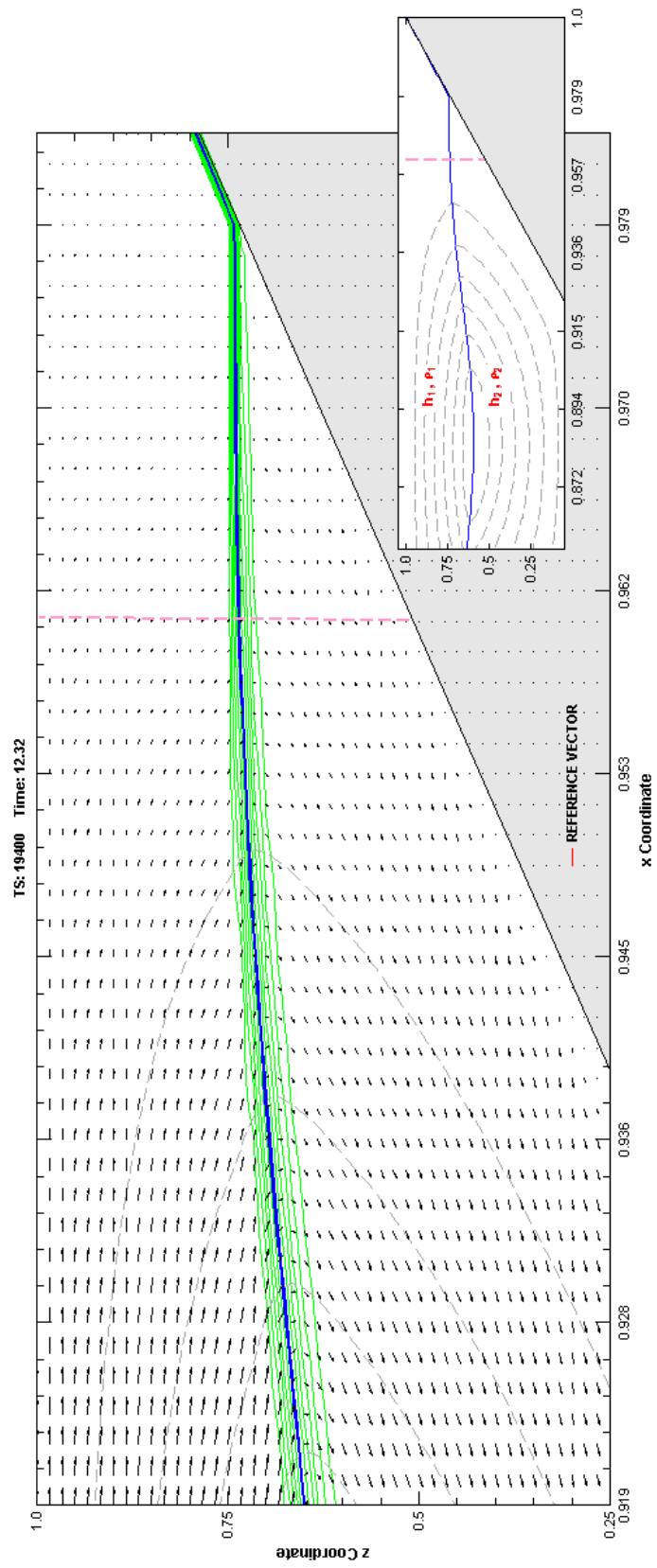
It is during this phase of the simulation that it can be observed that the internal wave is also undergoing an additional transformation as the wave front travels up the slope of the obstacle. There is an increase in the magnitude of the velocity vectors which now appear to favor a counter-clockwise flow orientation that is responsible for essentially “pushing” the pycnocline up-slope. By about TS 23,800, the wave front defined by the pycnocline has formed bore or bolus.

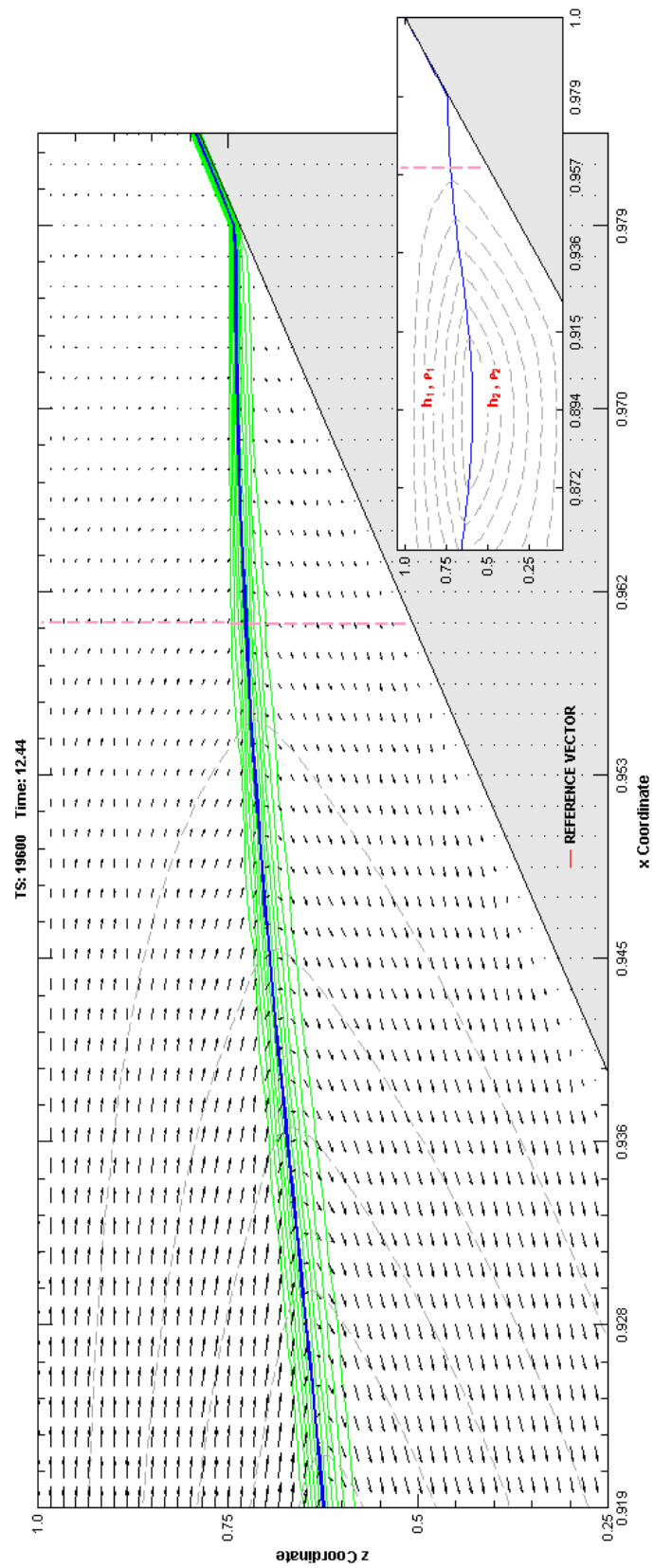
For the balance of the simulation, the bore continues to advance up the obstacle slope until reaching a maximum point of vertical ascent. This surge phase appears to reach its greatest vertical ascent at about TS 25,000.

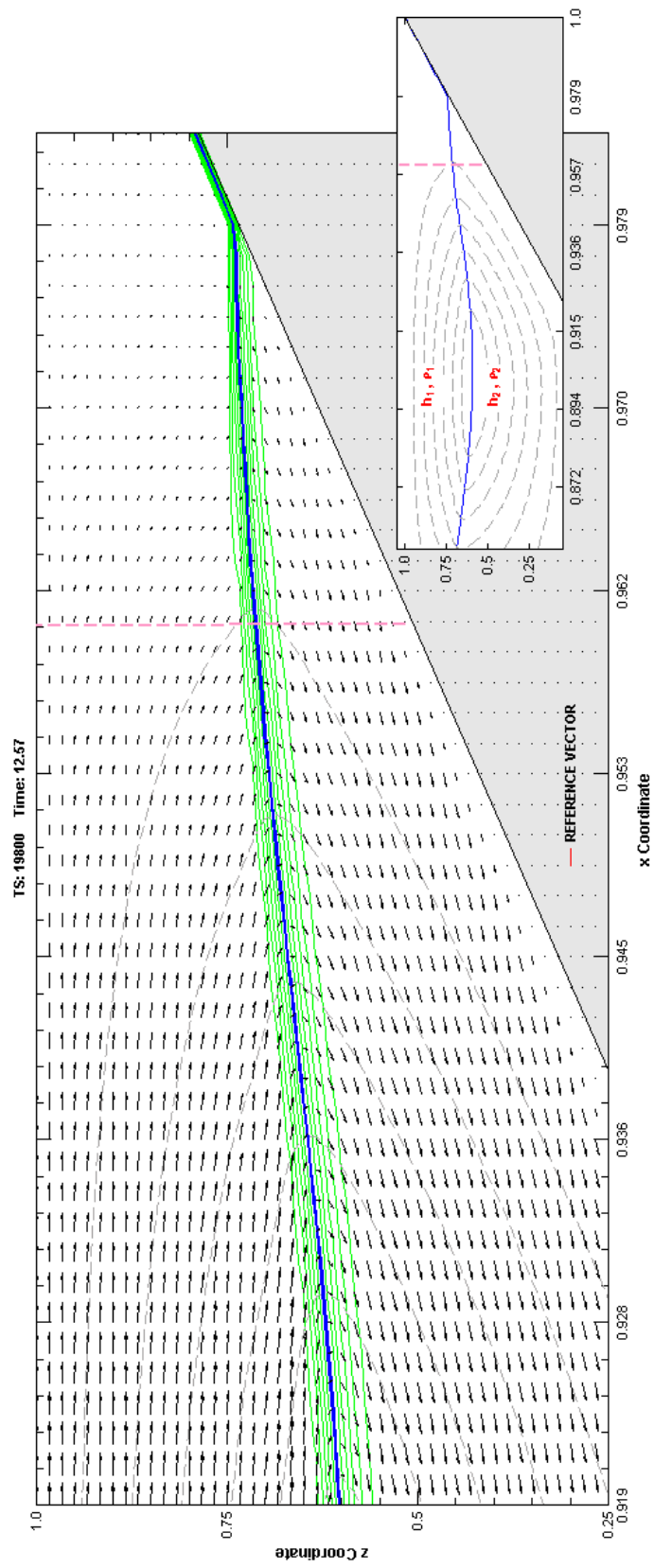


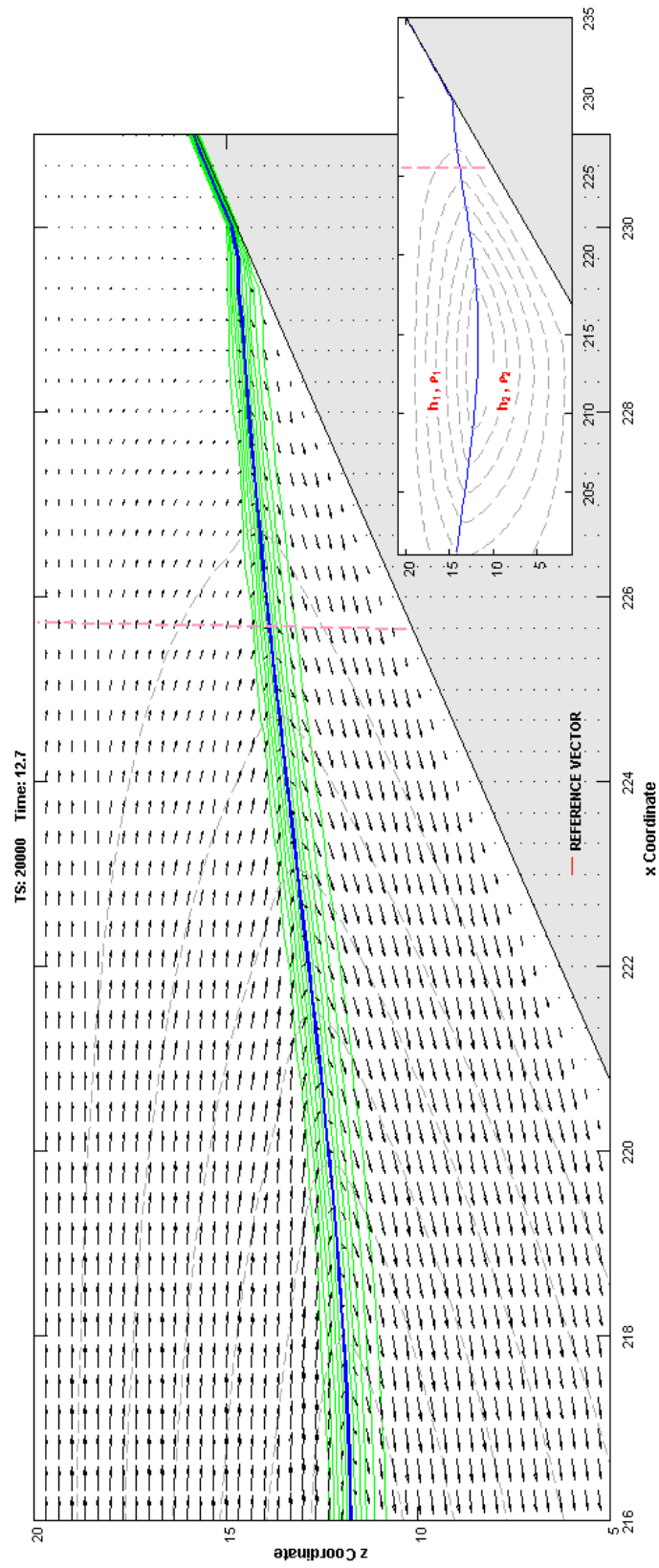


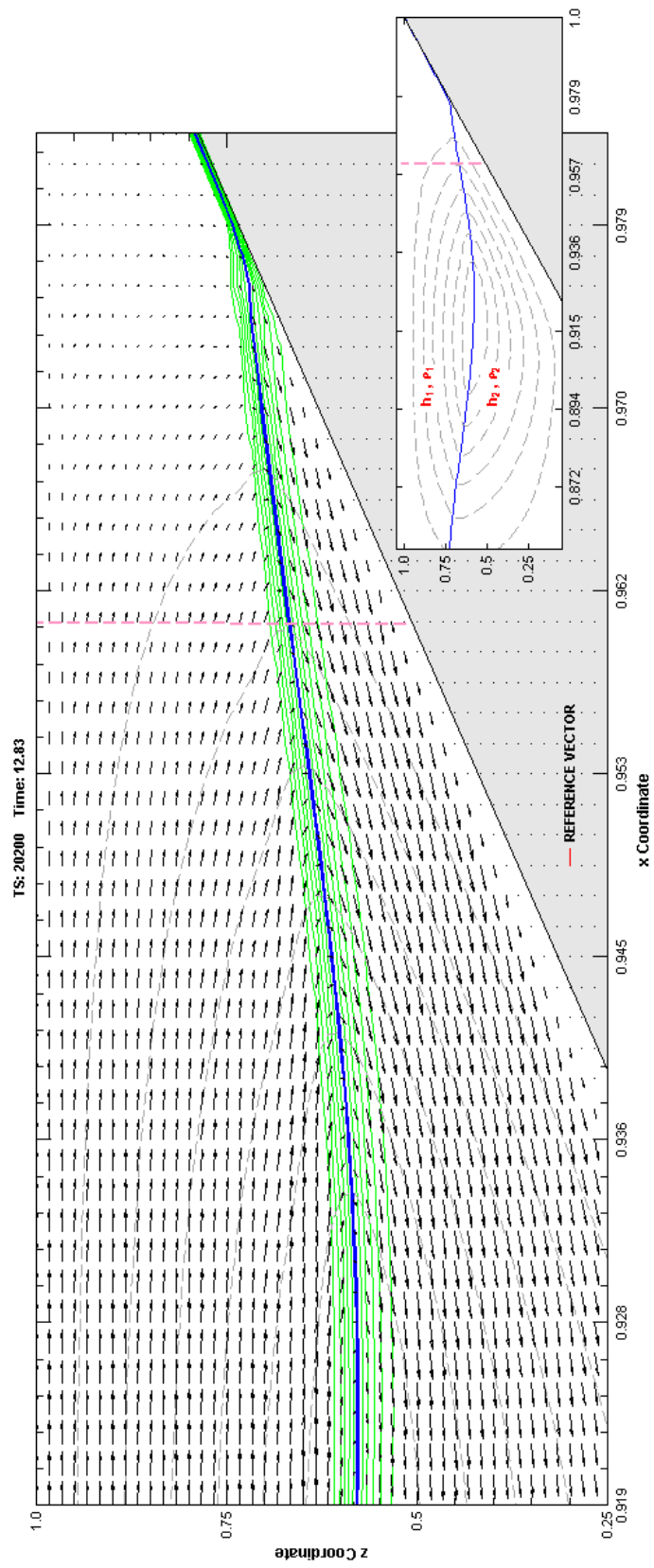


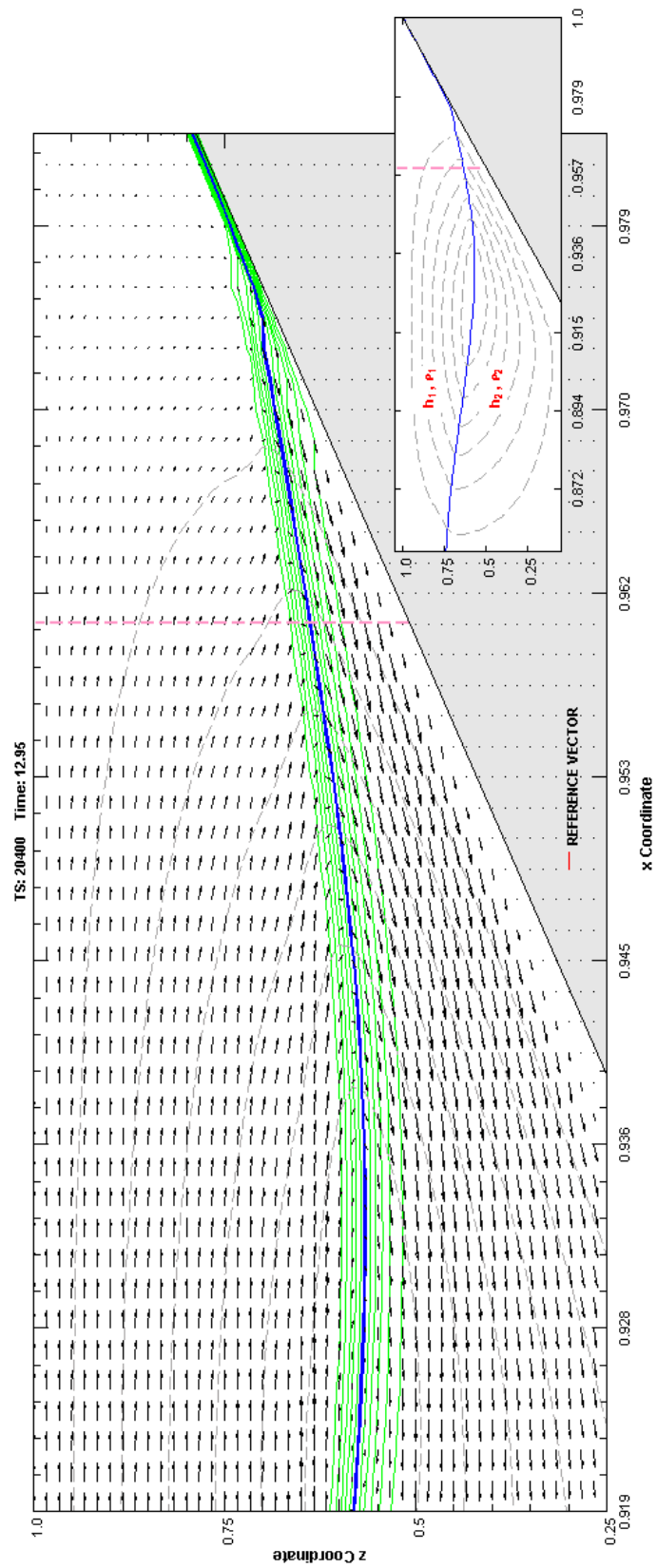


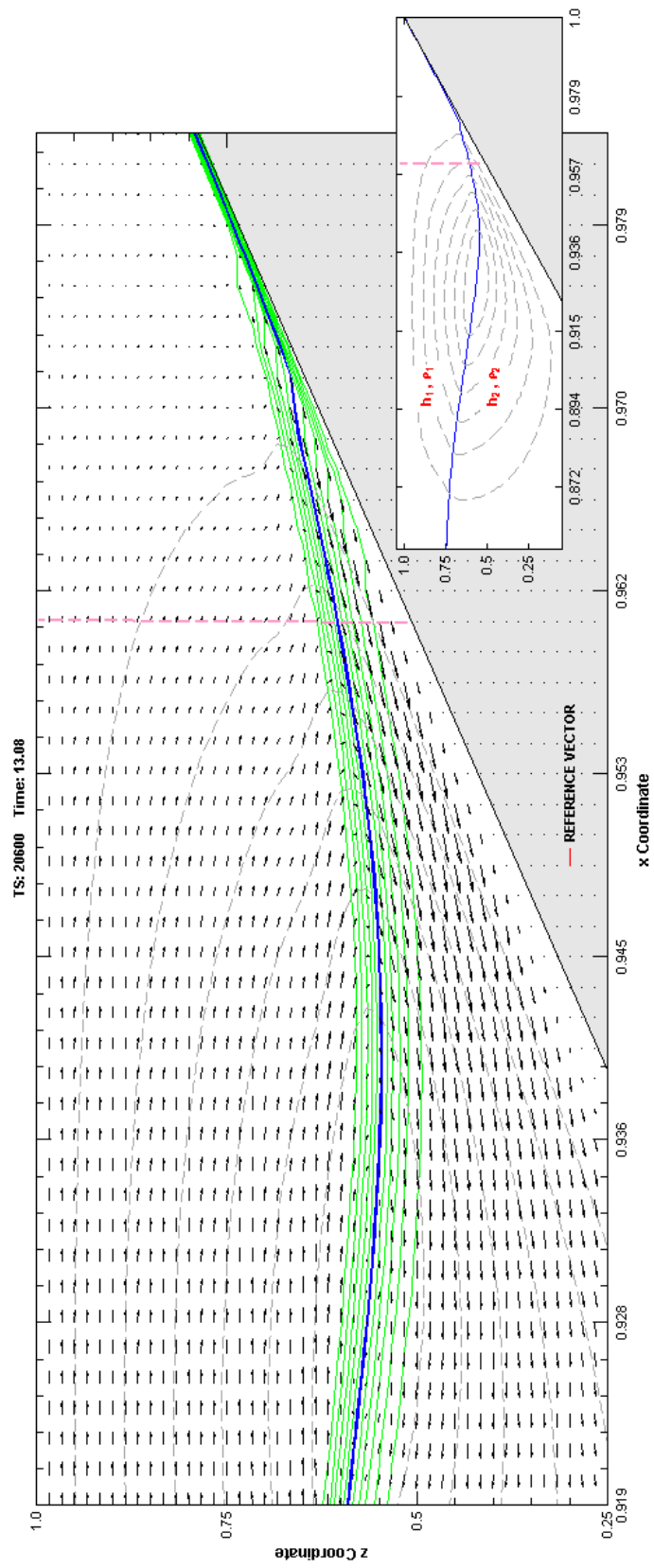


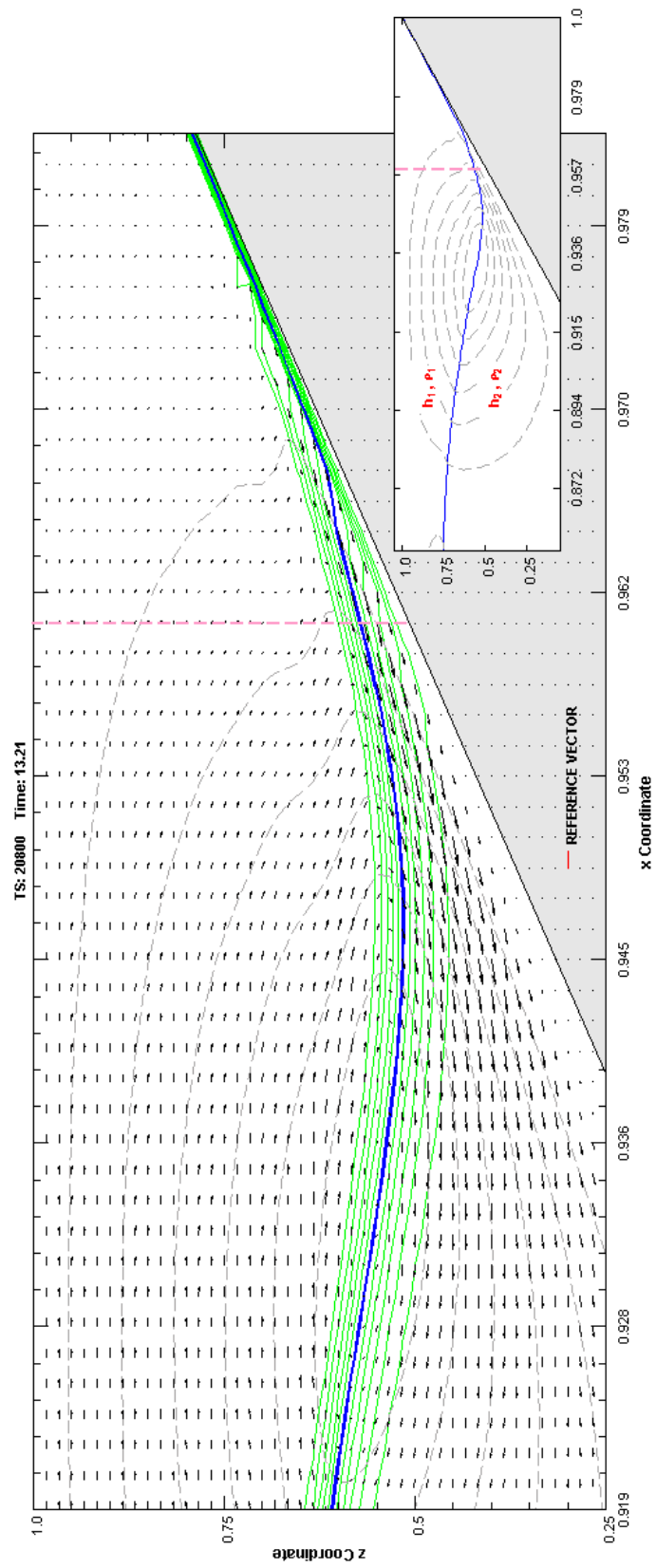


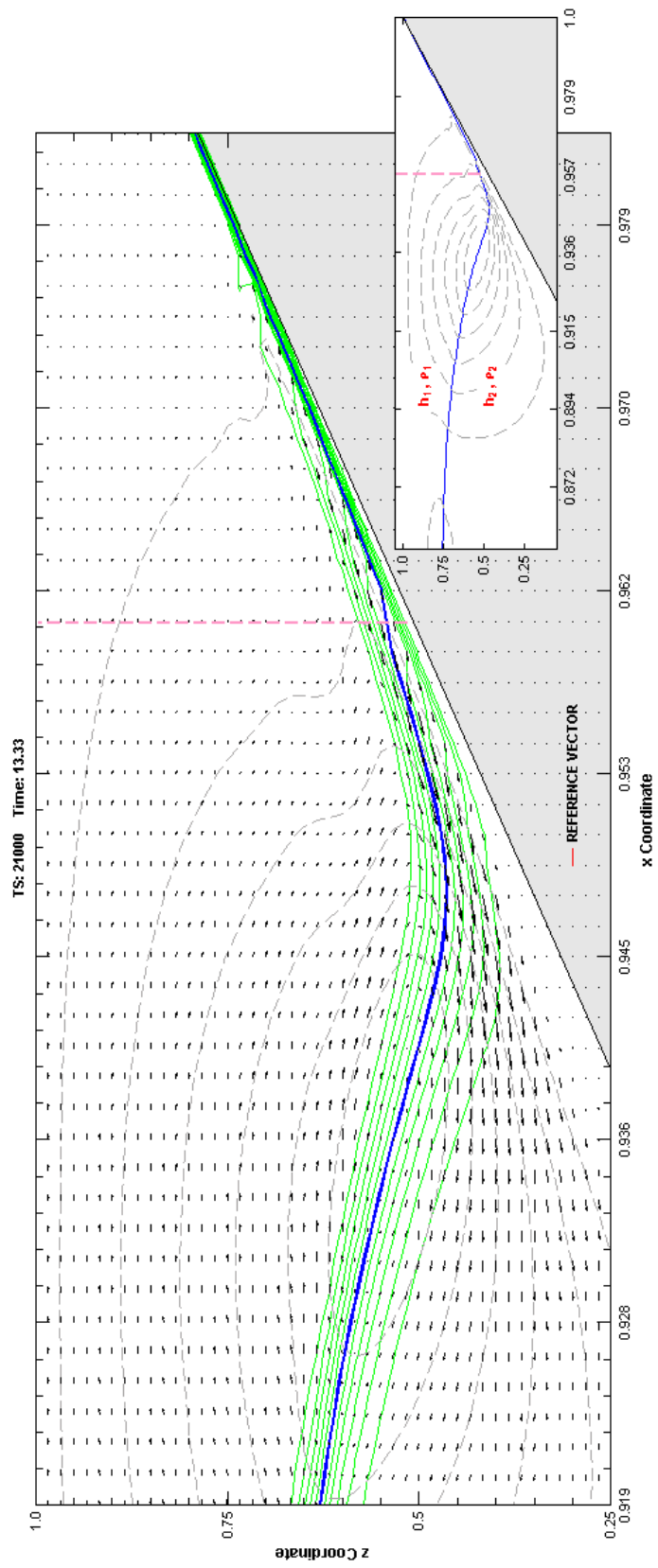


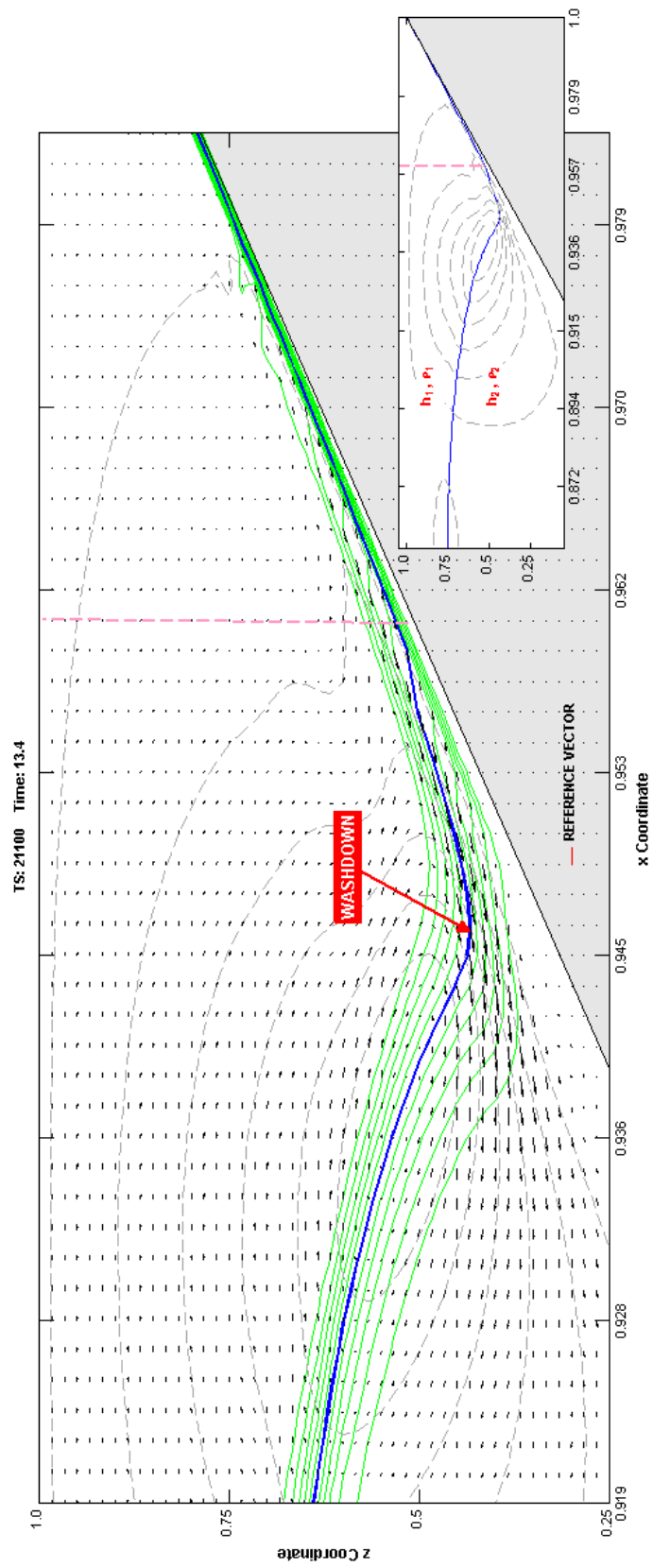


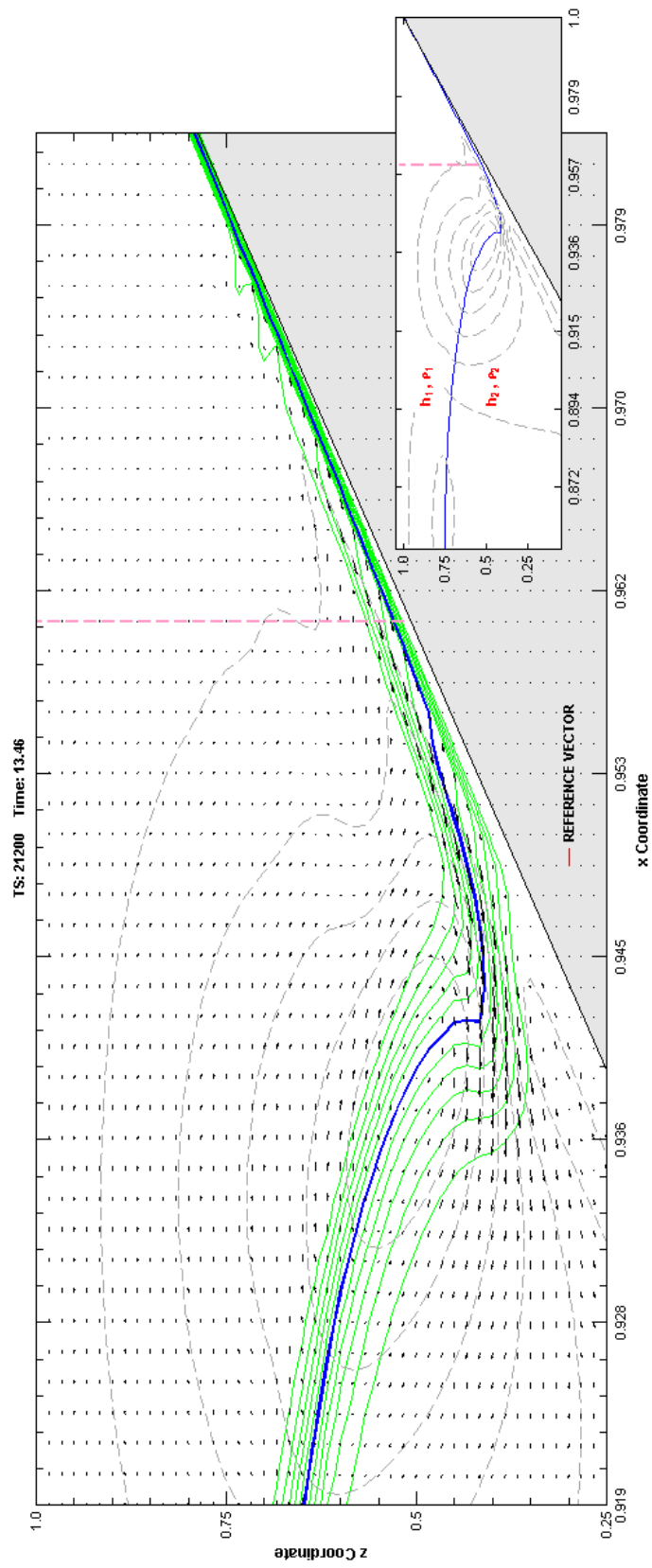


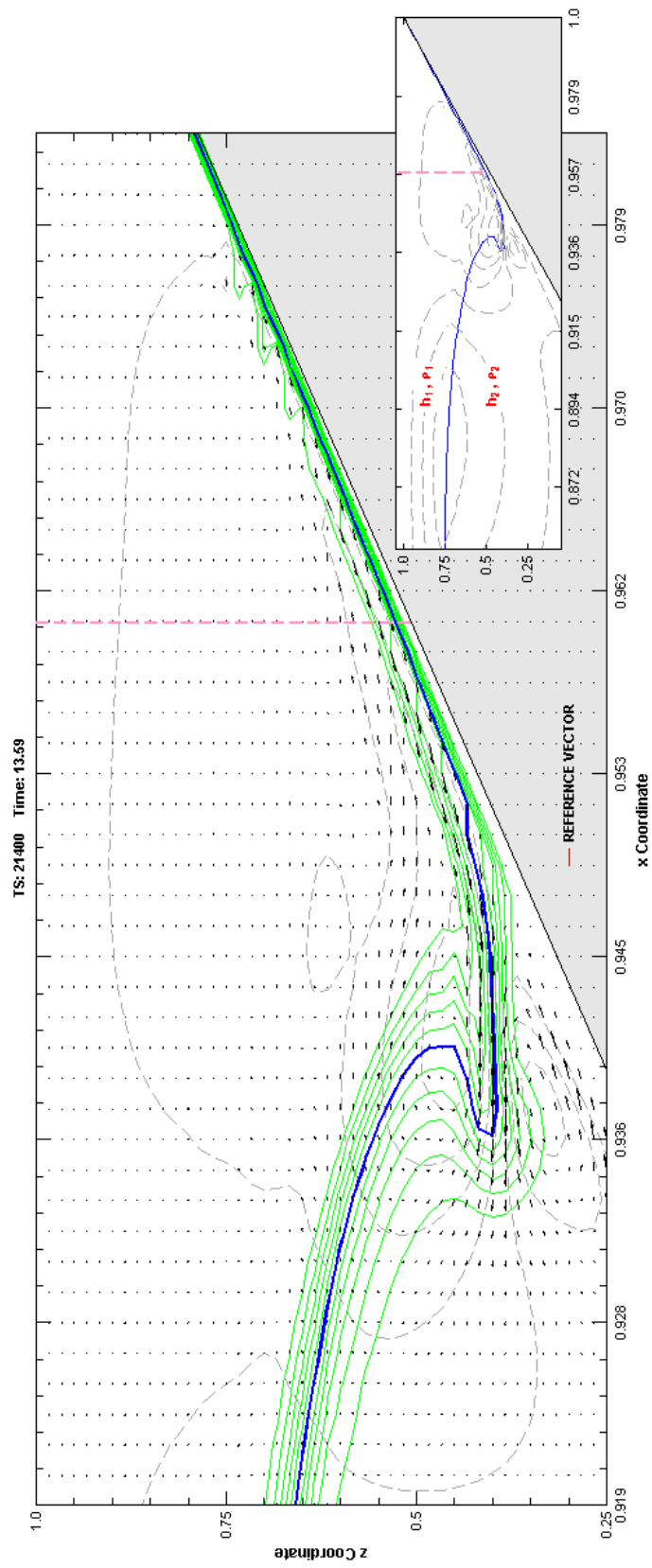


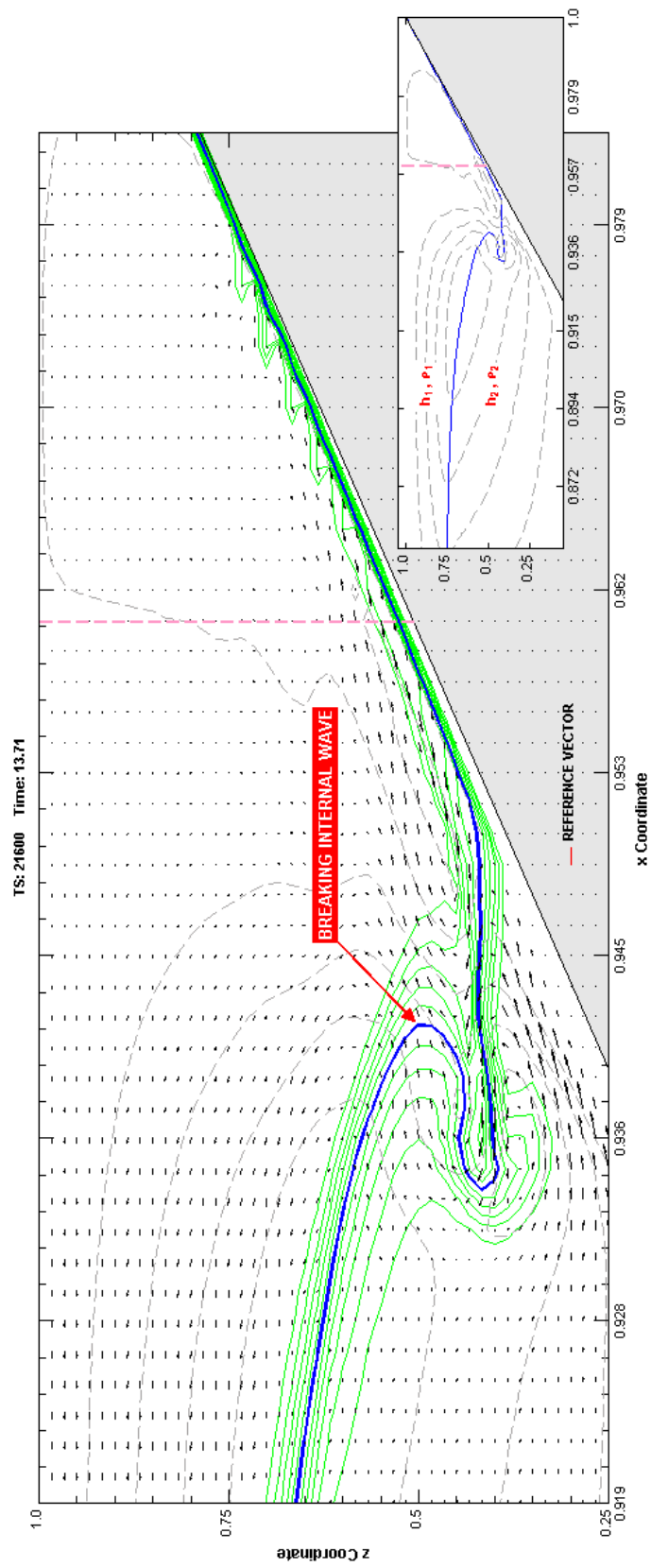


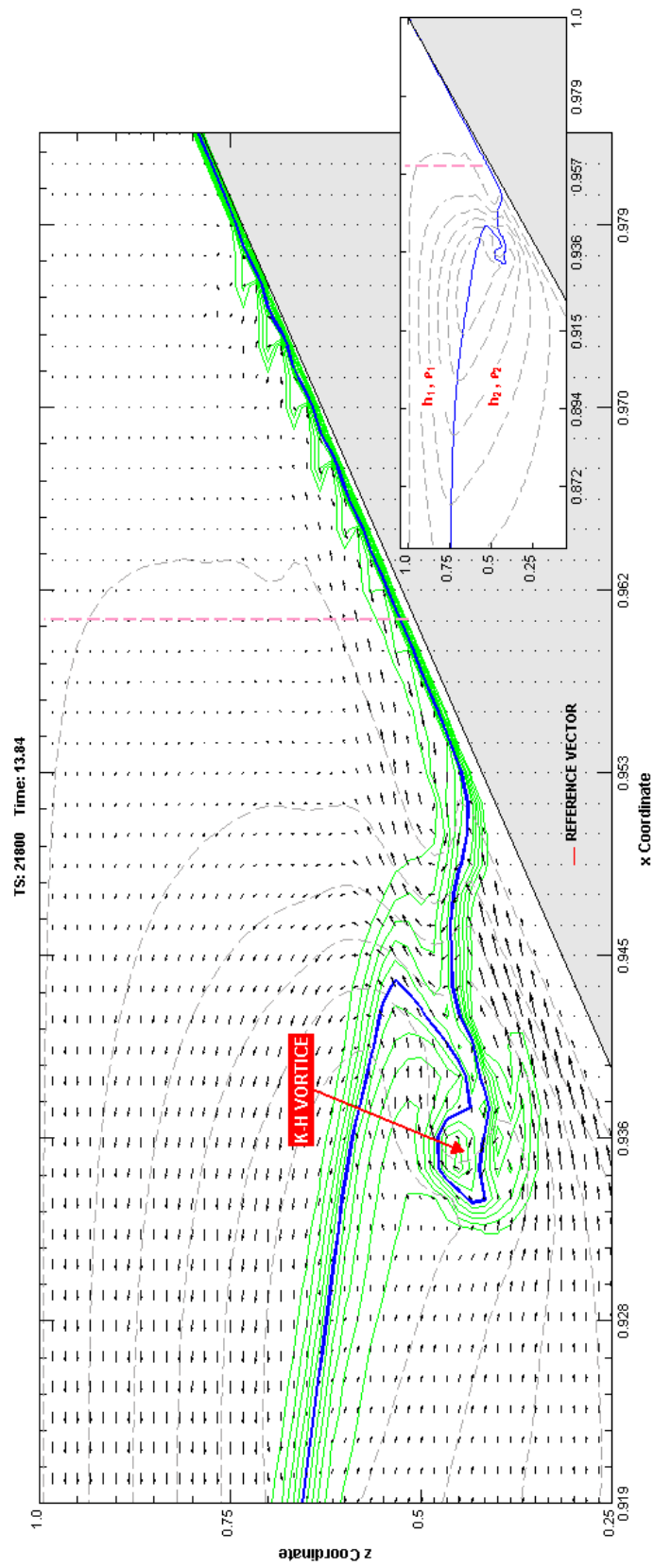


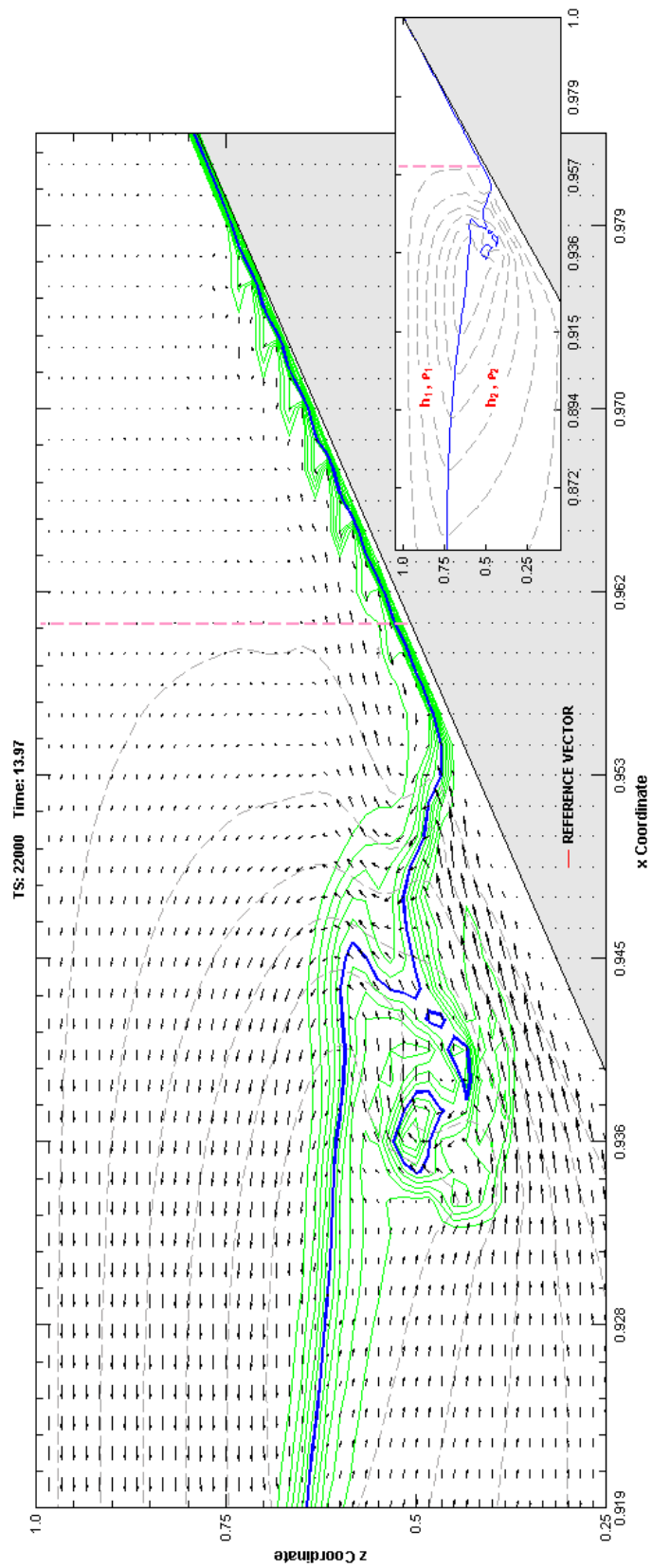


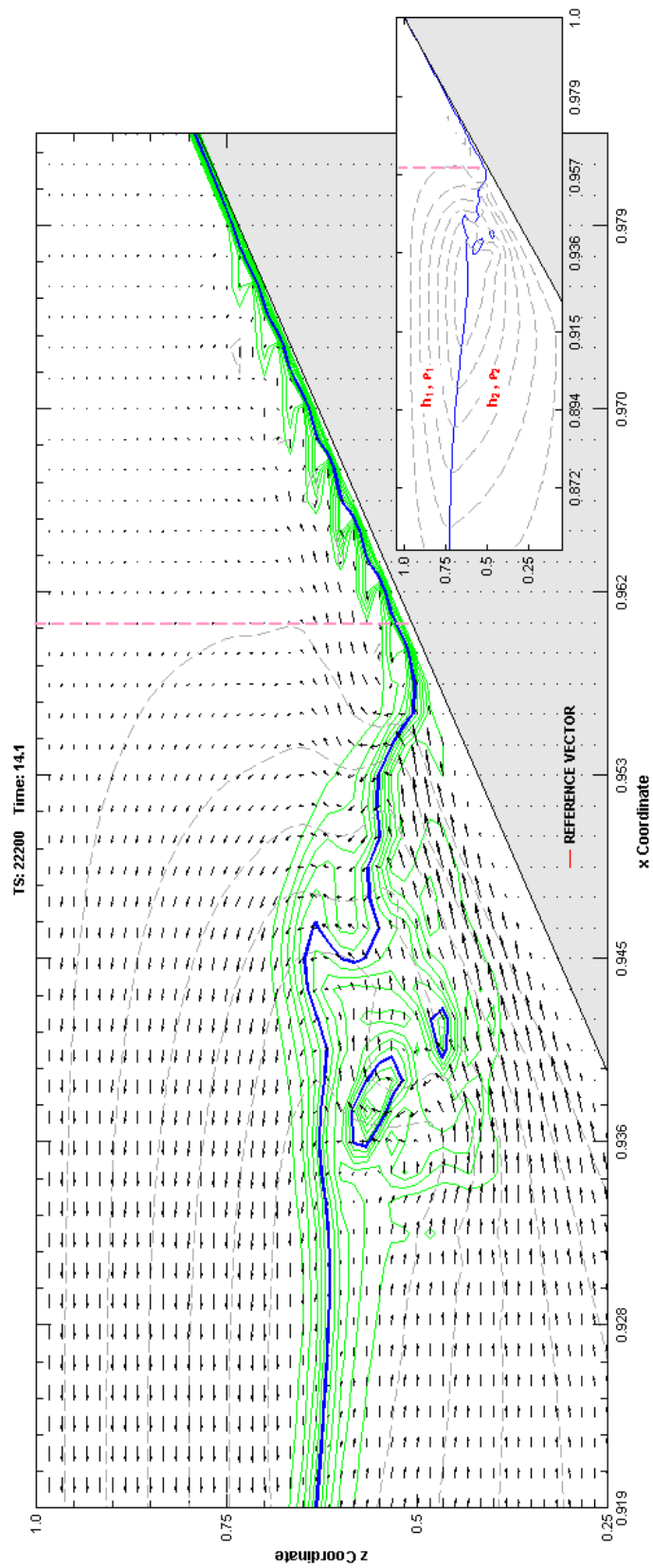


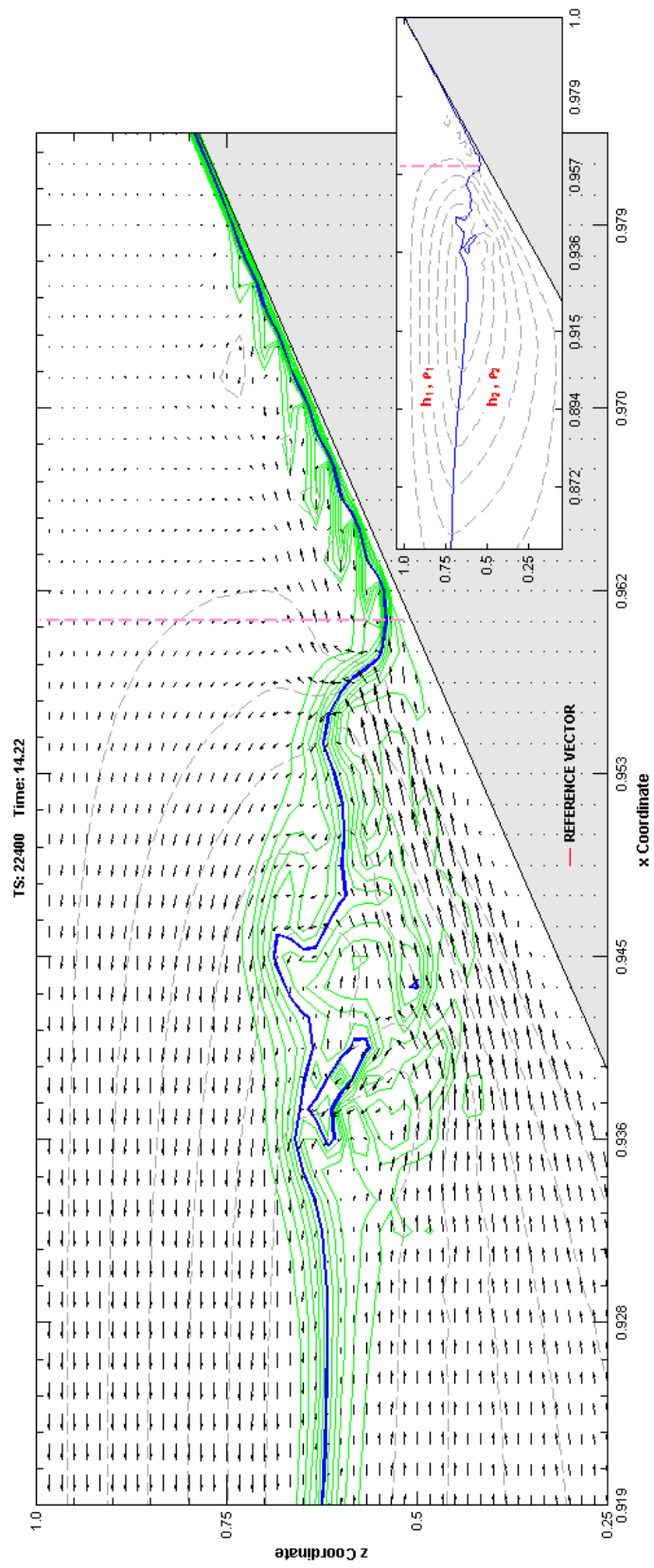


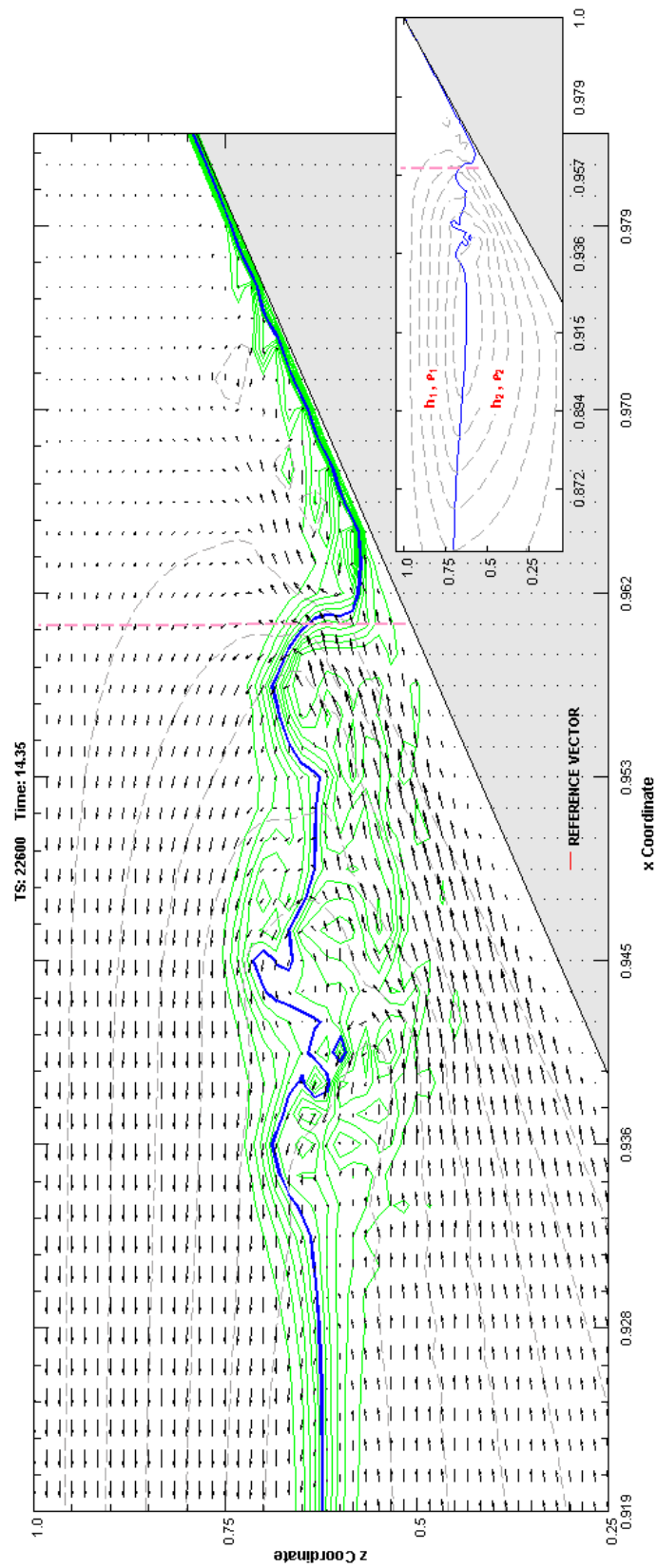


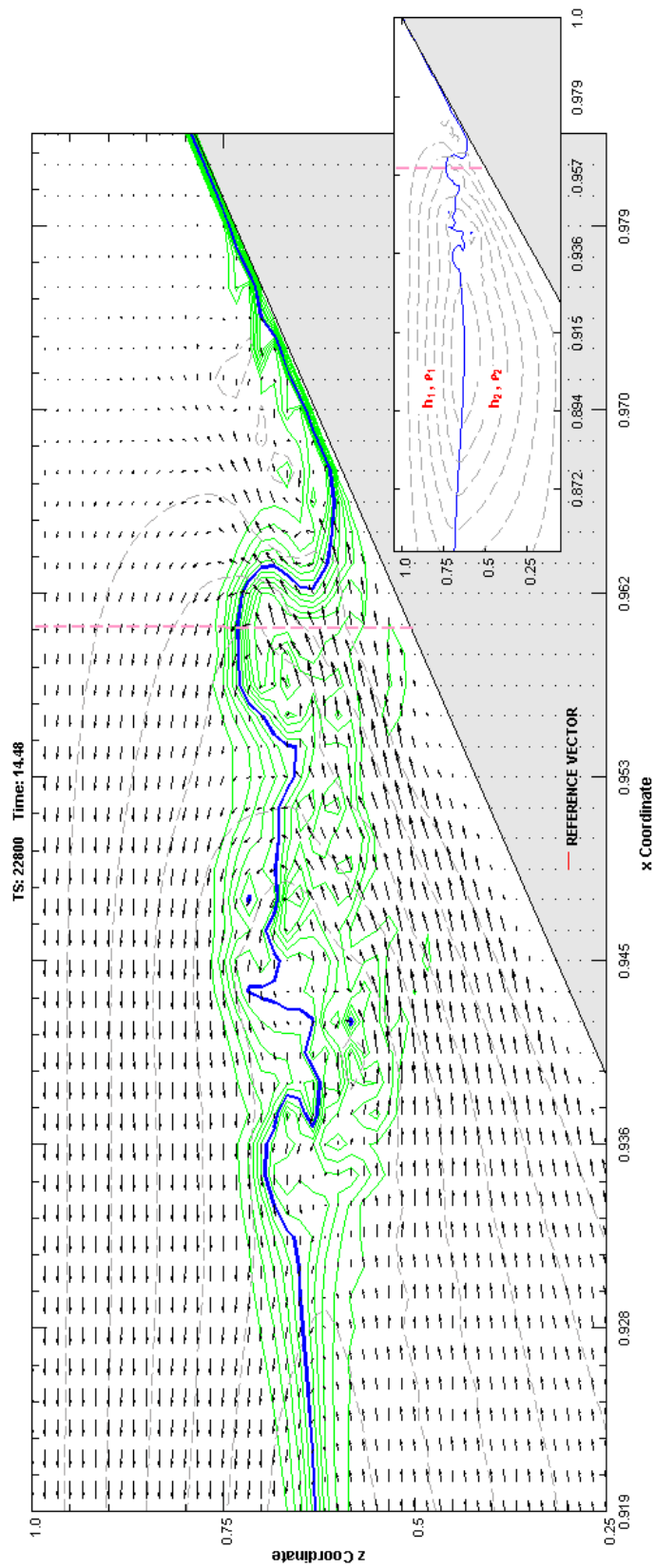


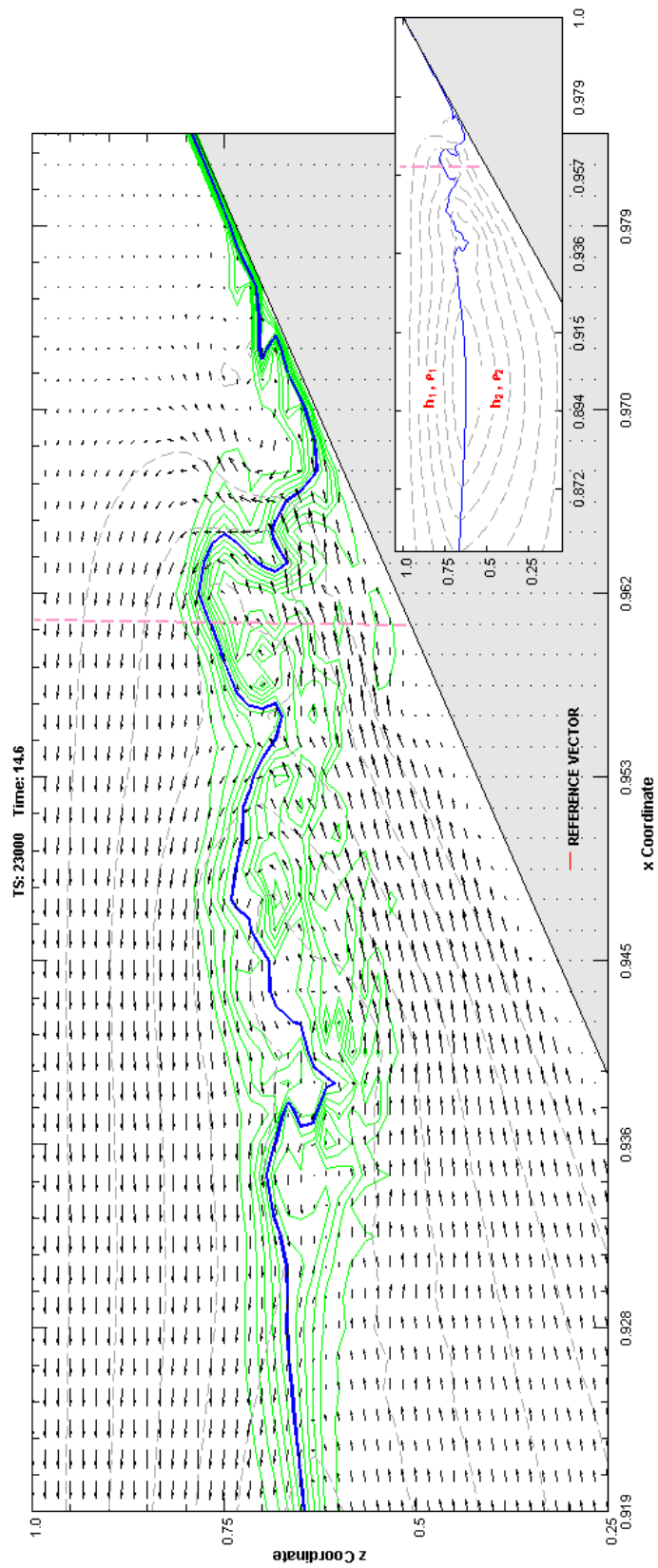


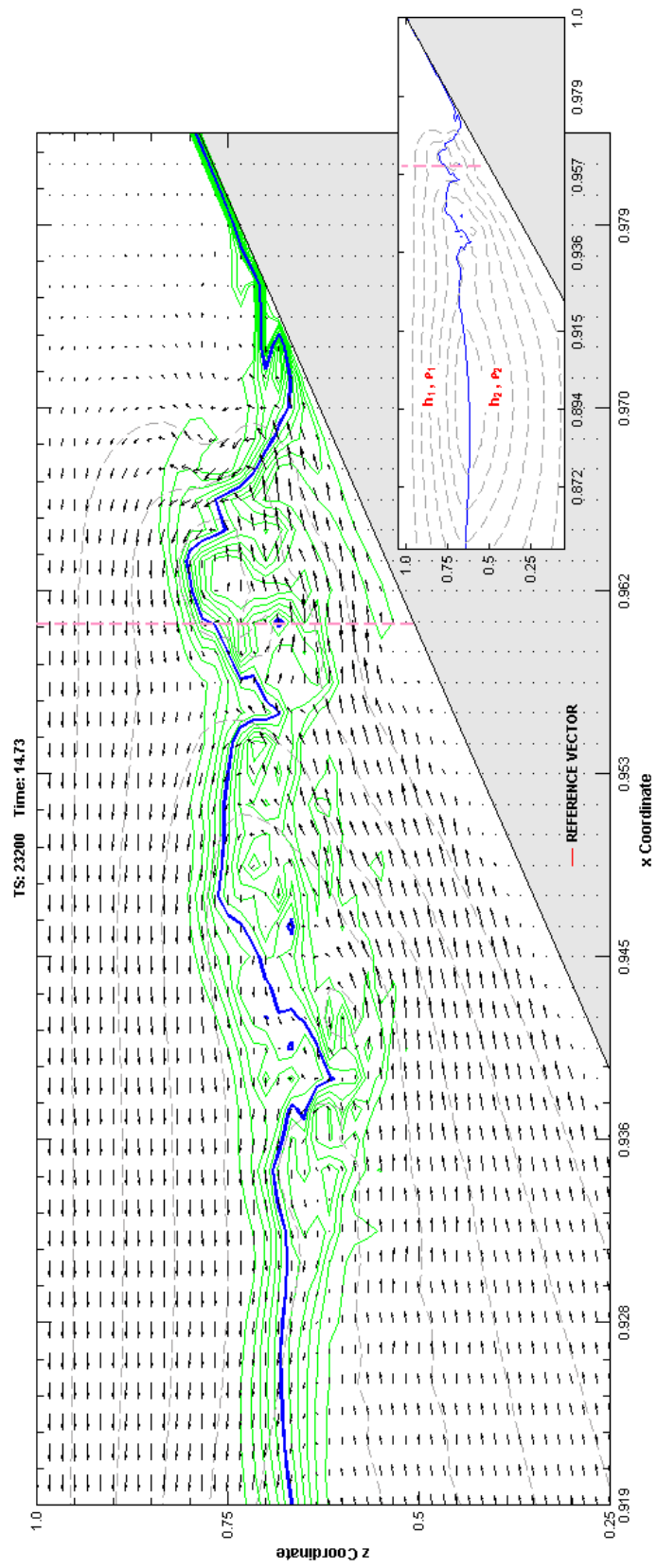


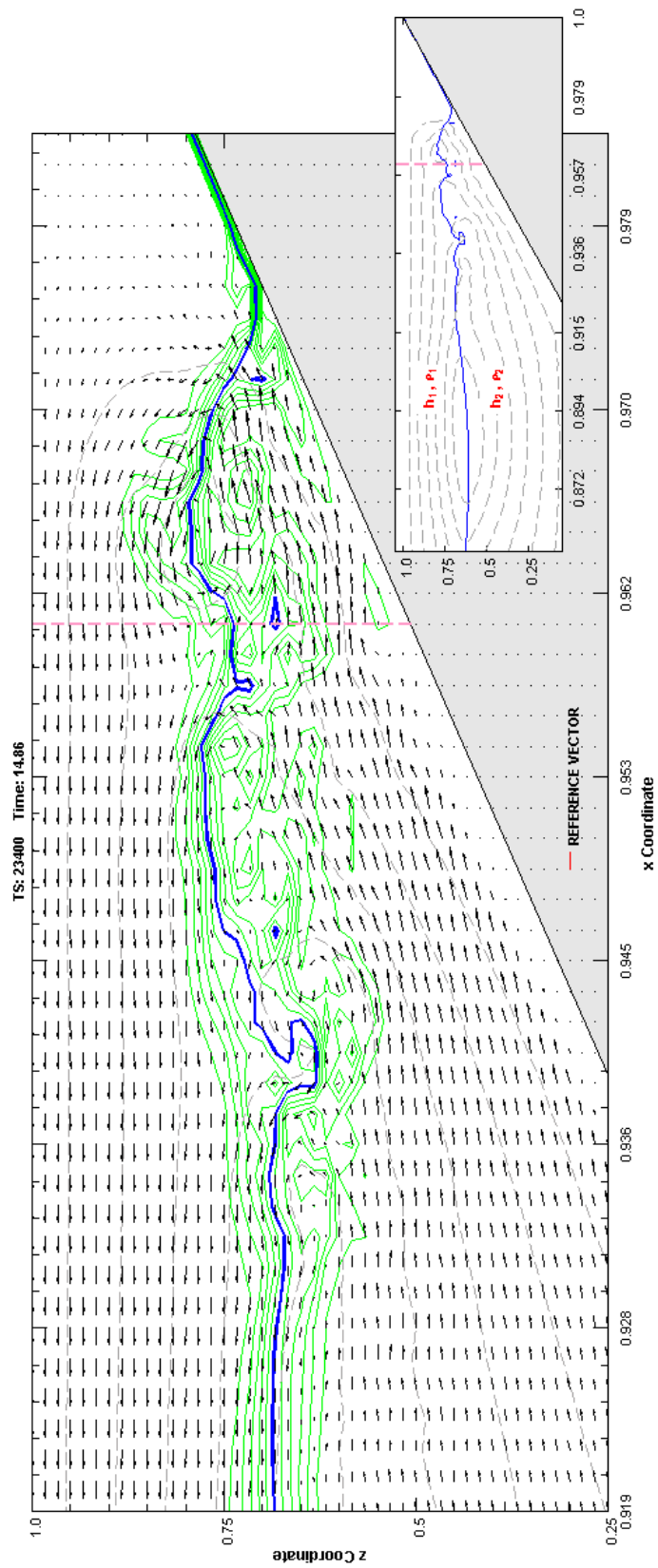


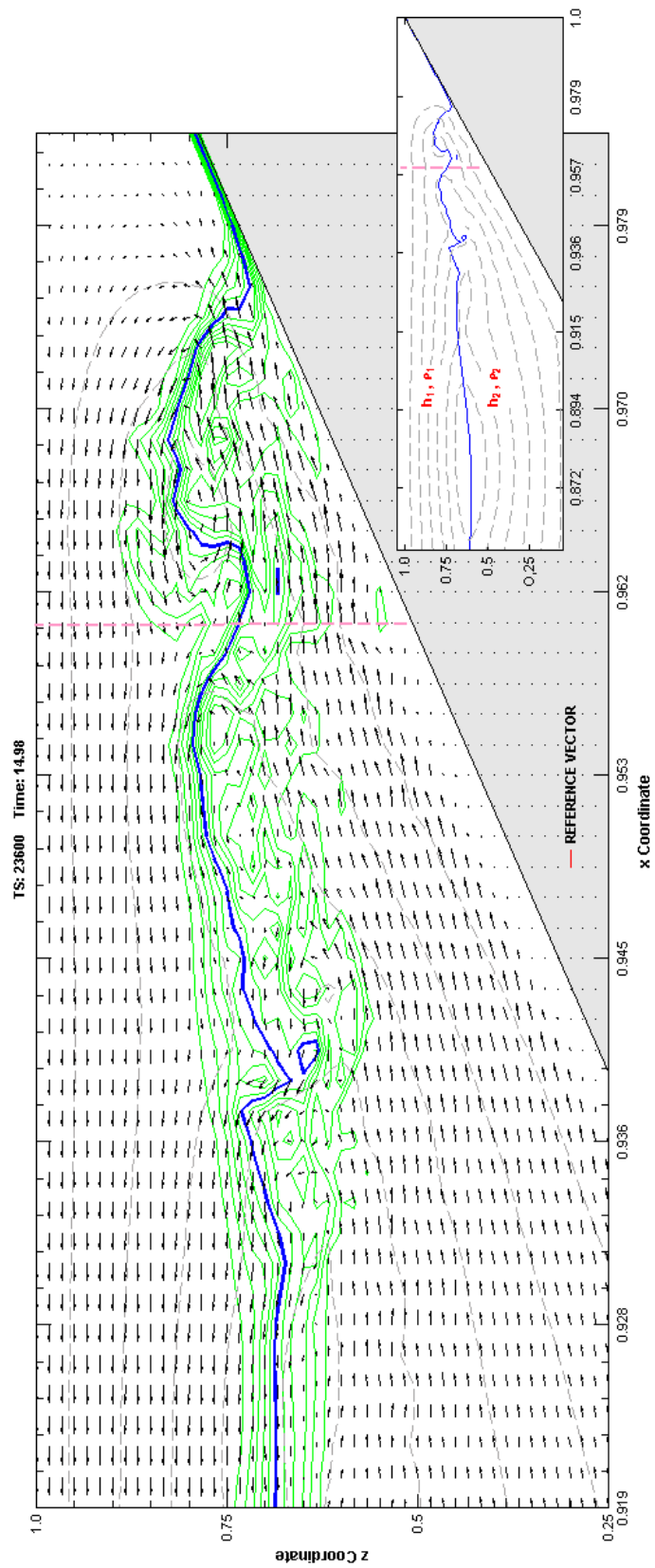


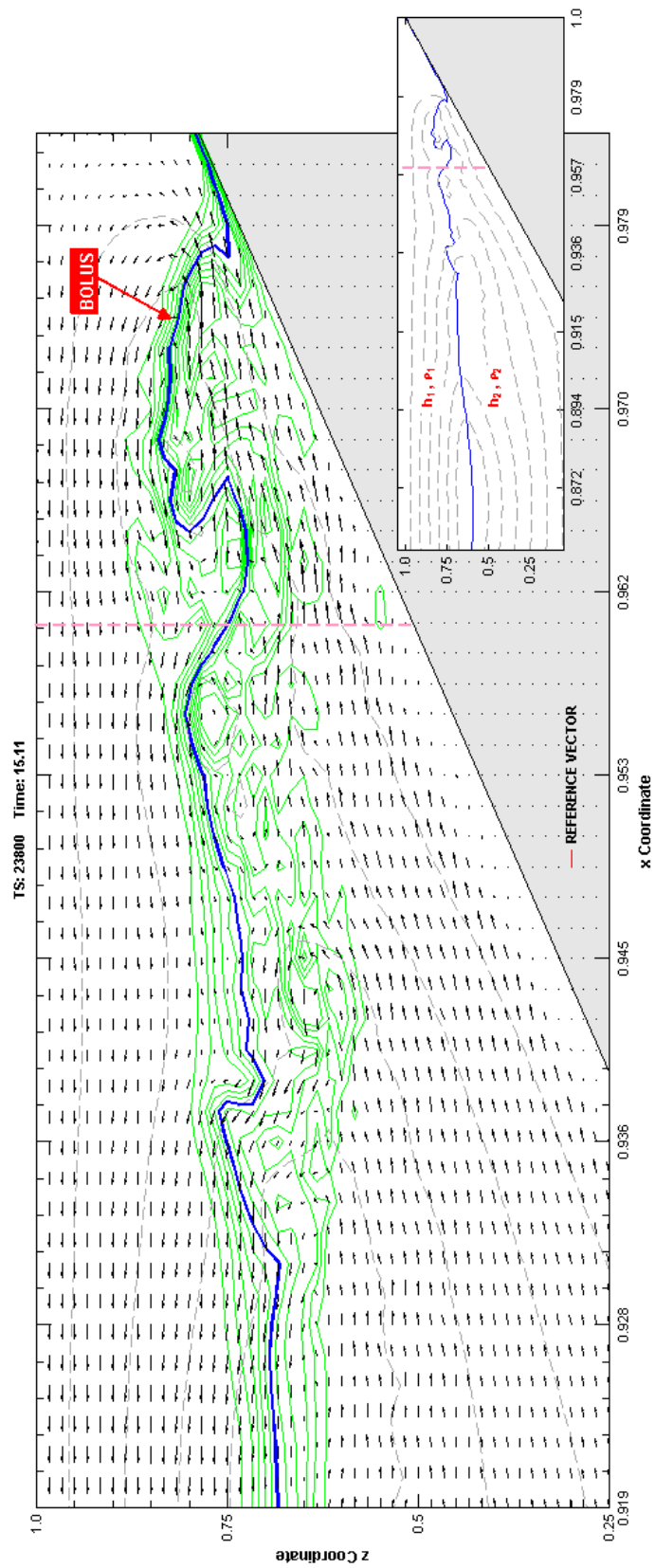


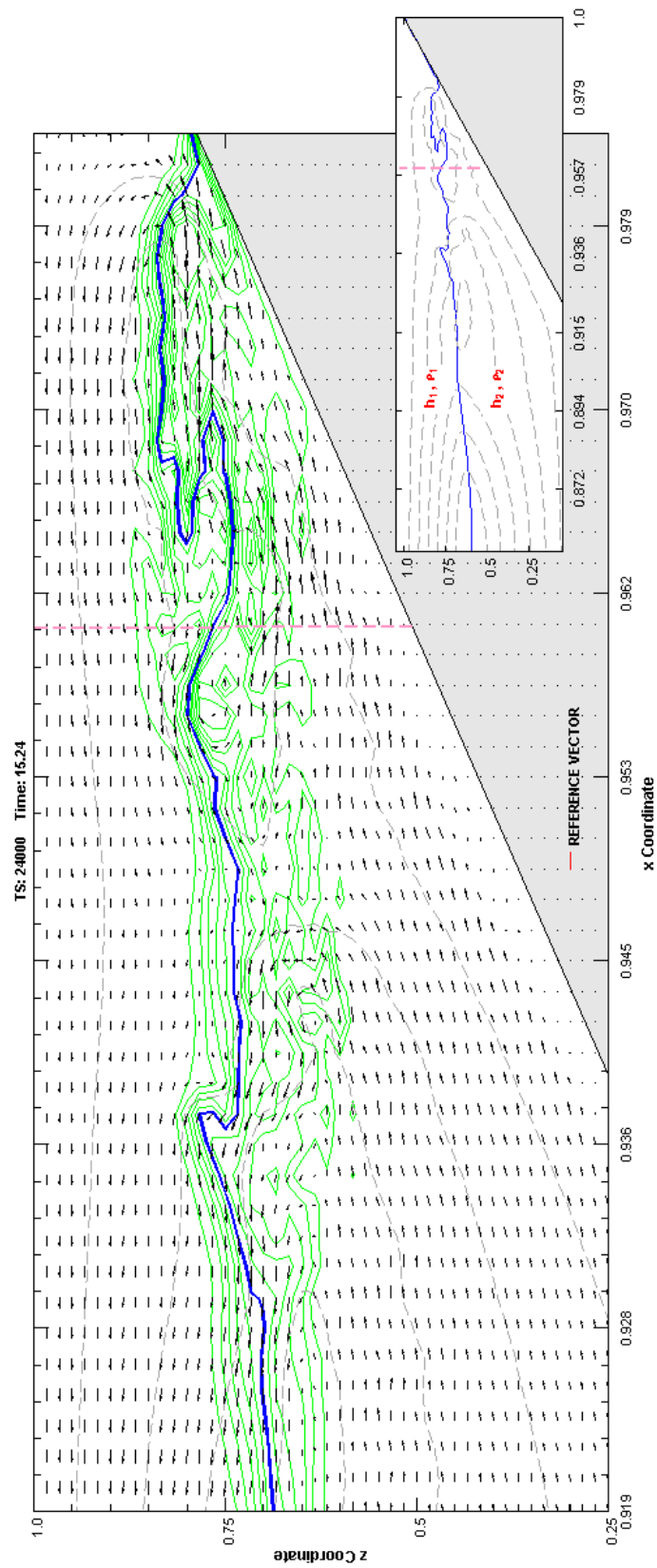


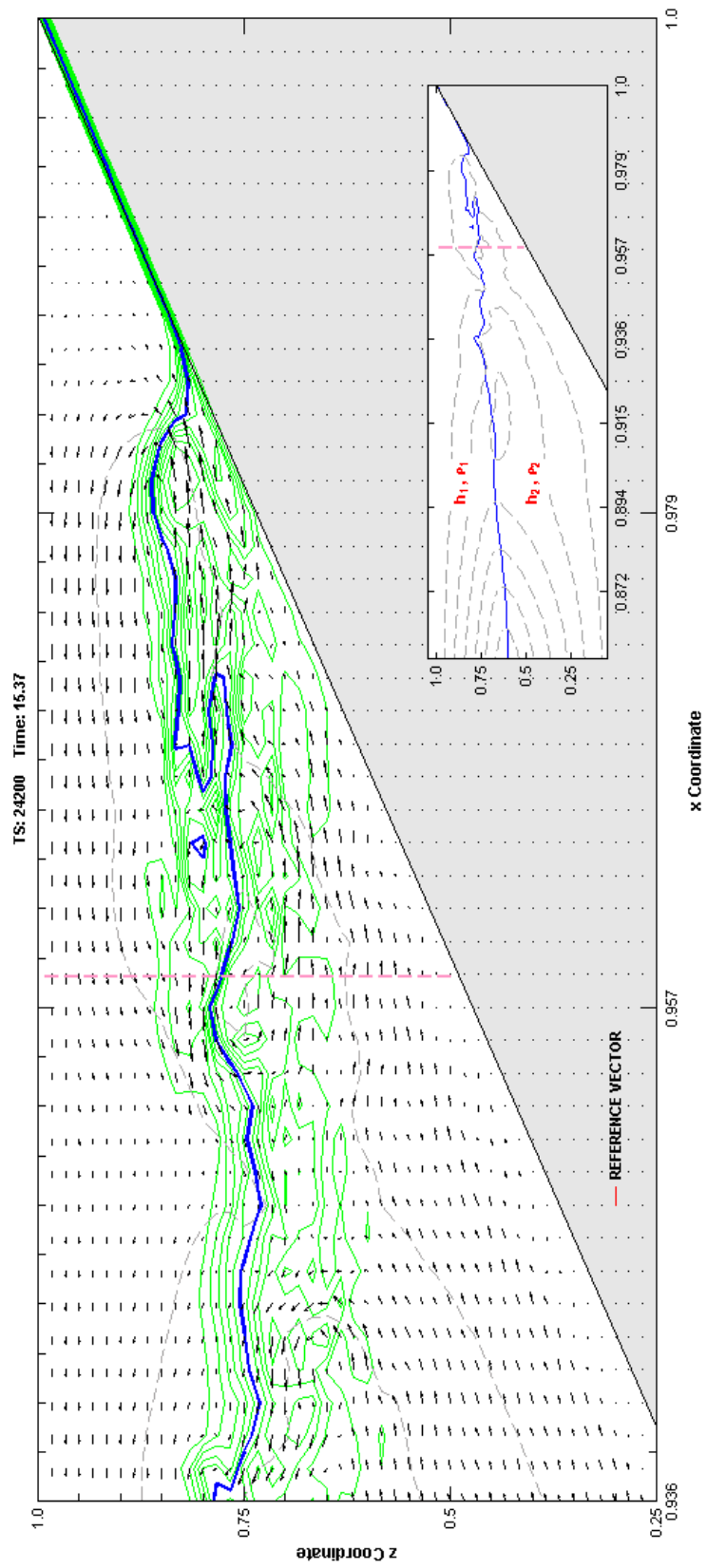


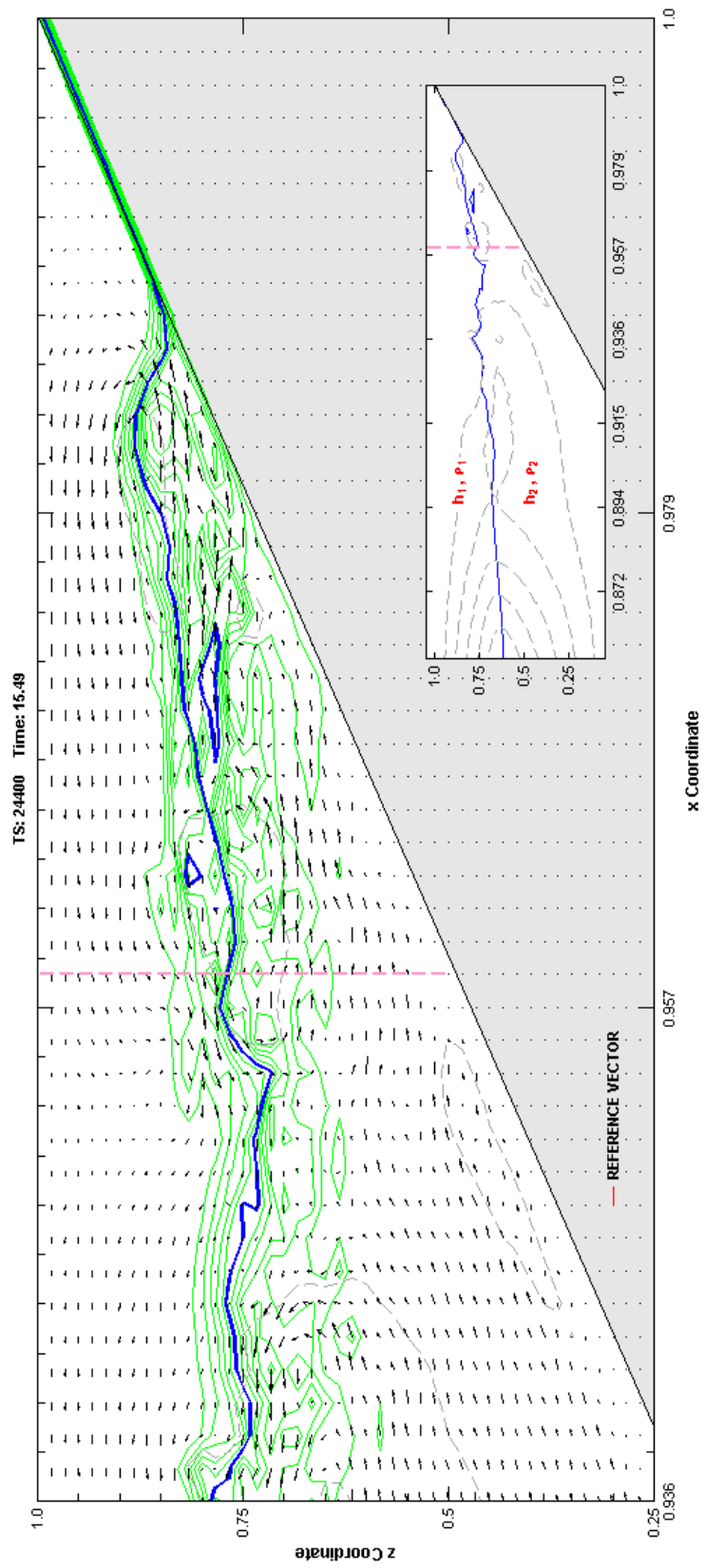


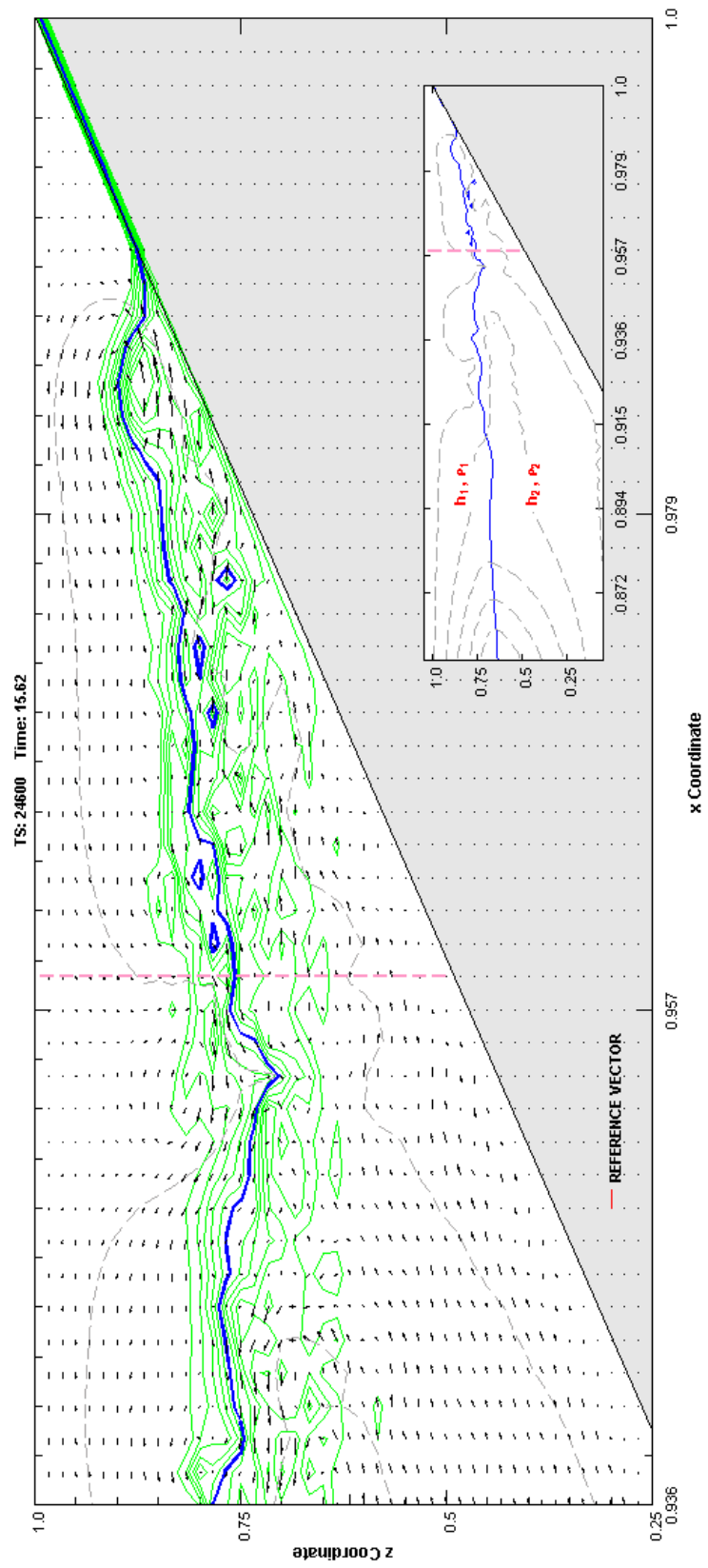


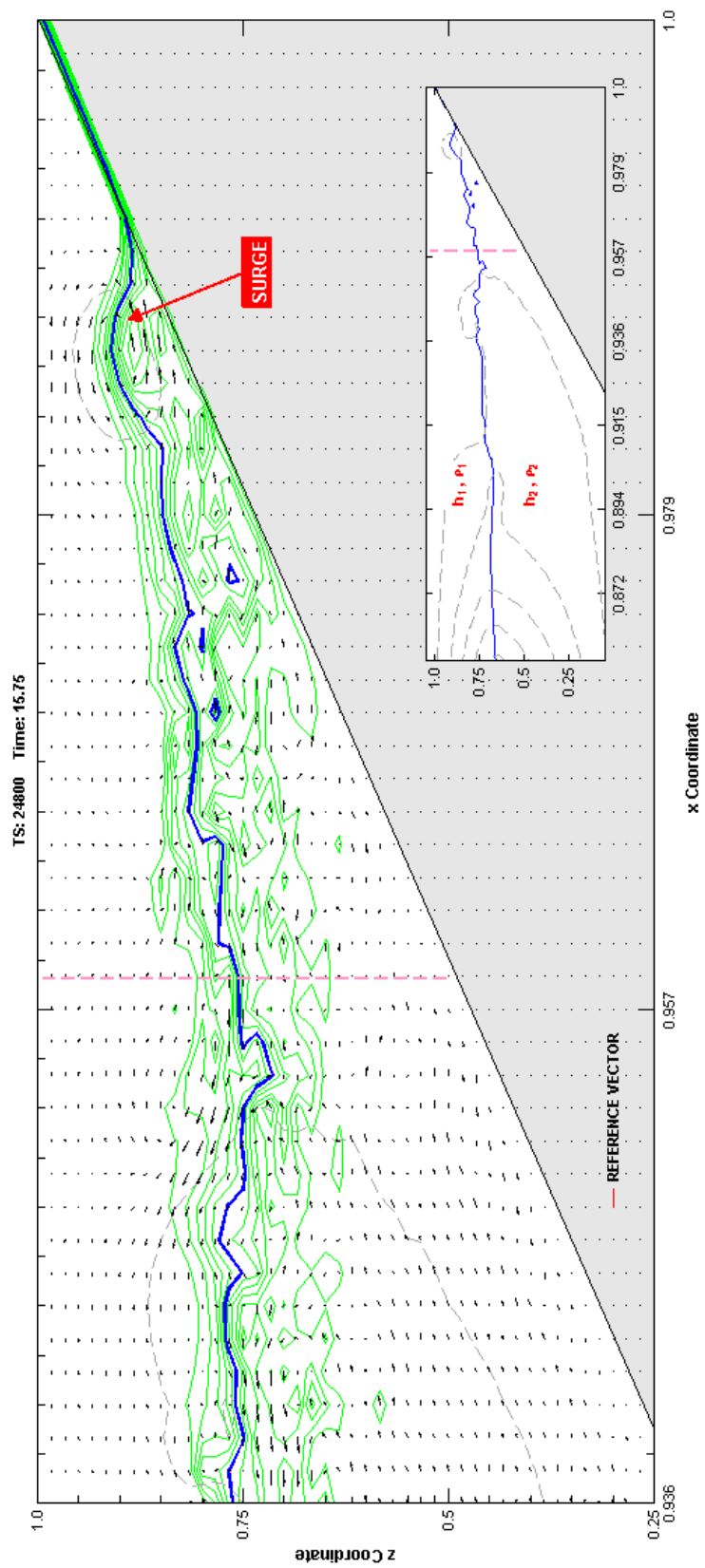


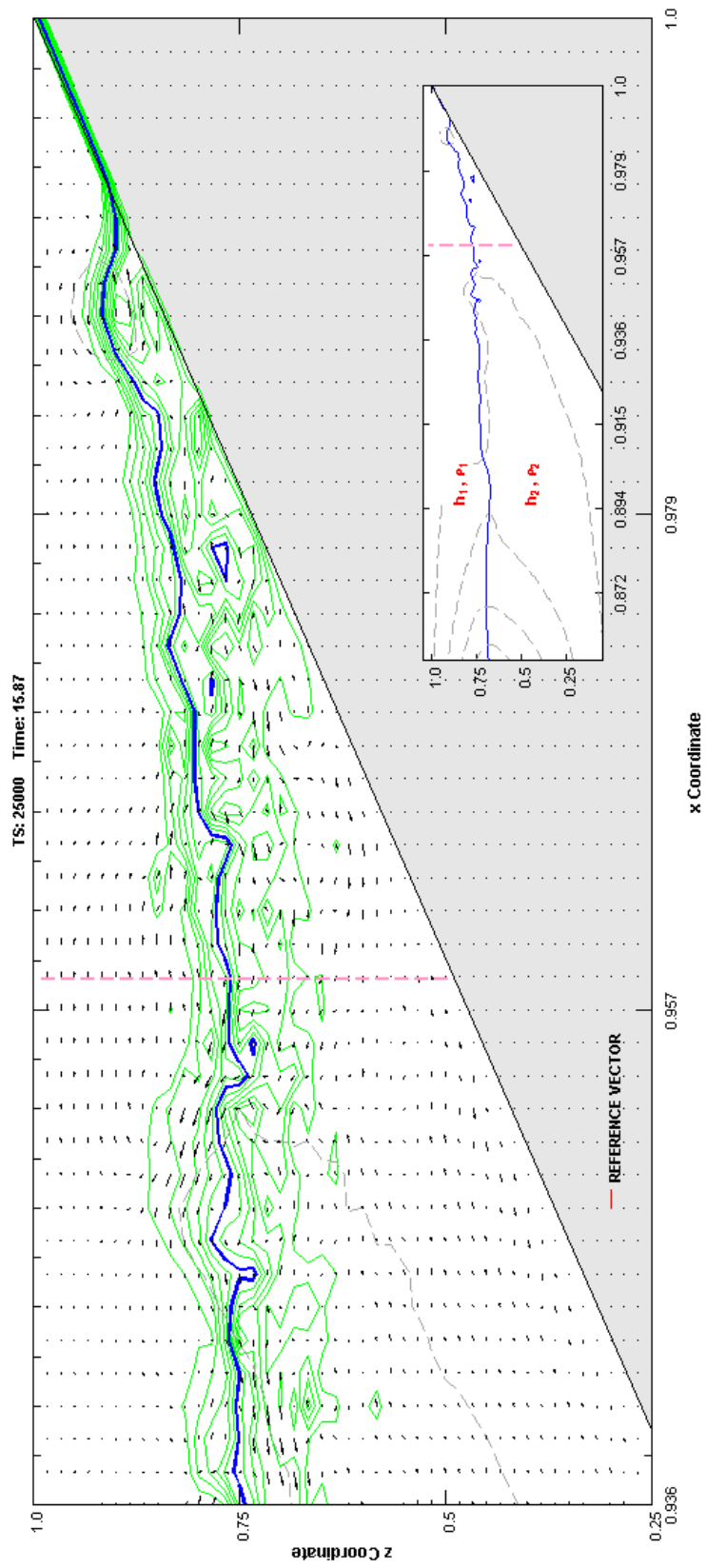


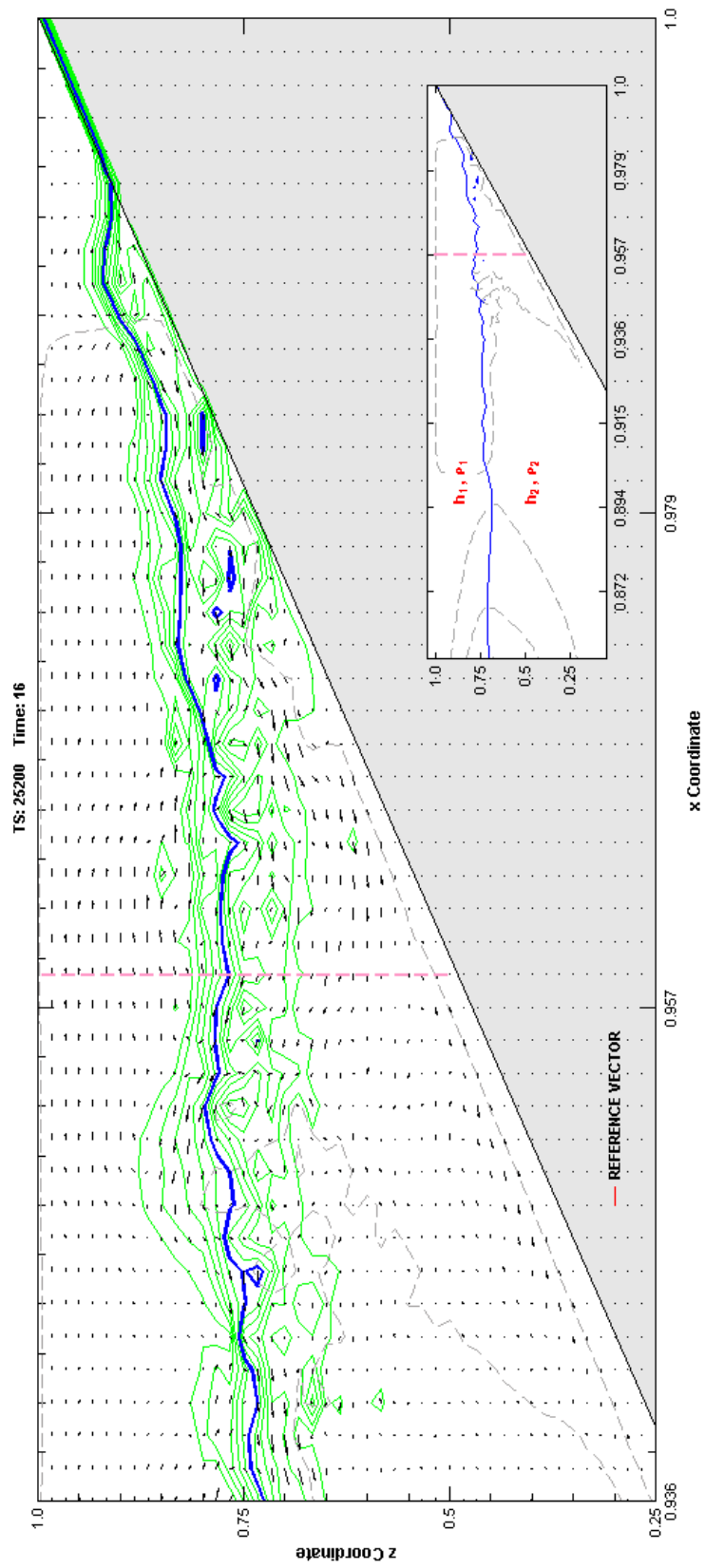


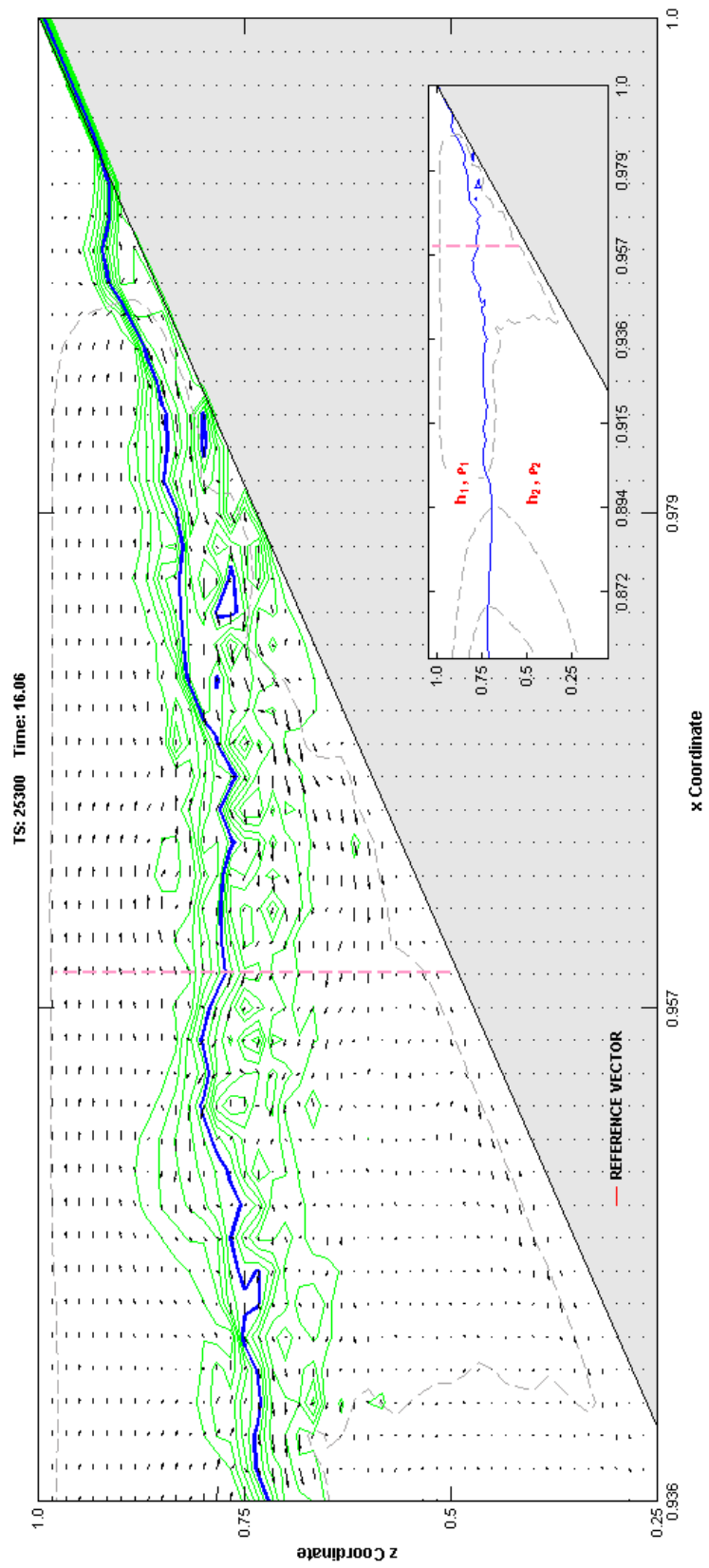


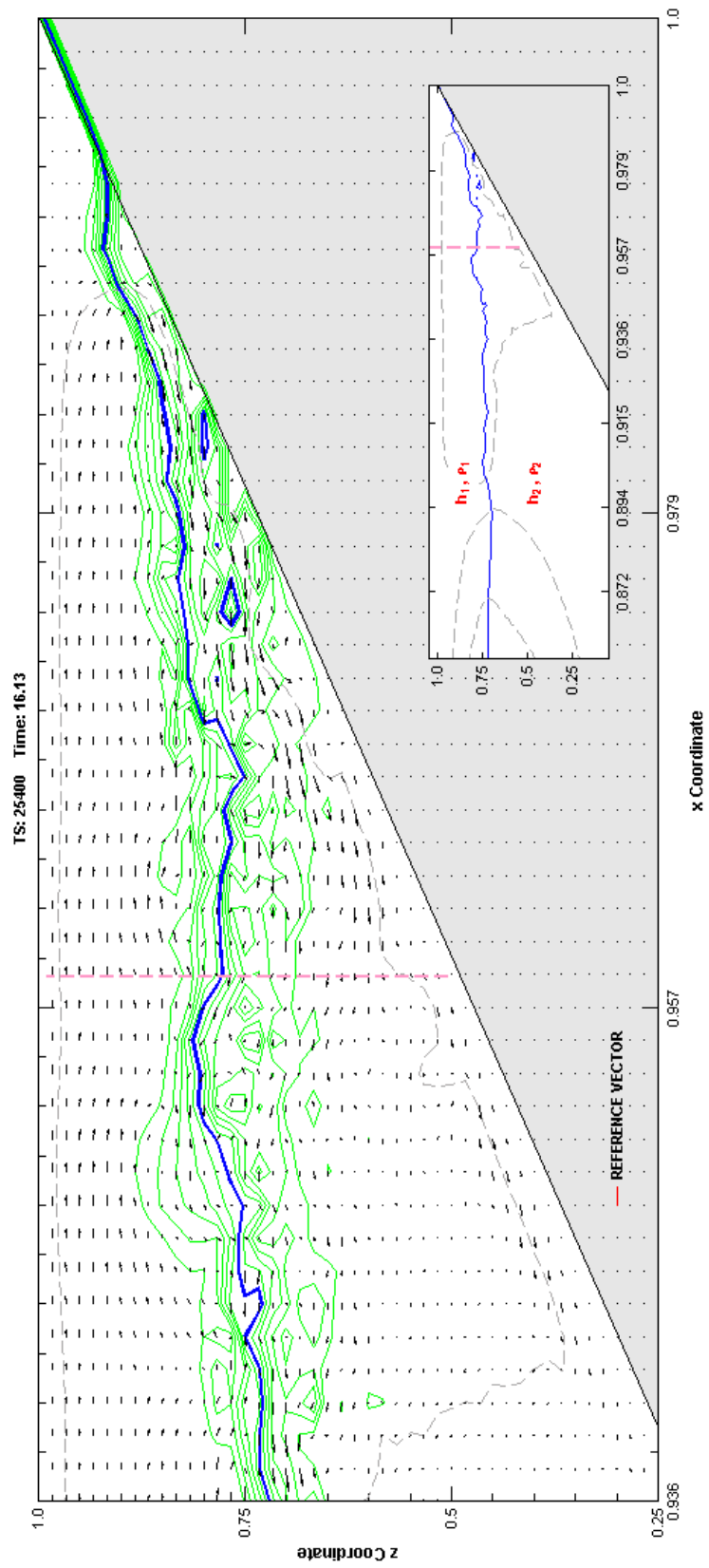


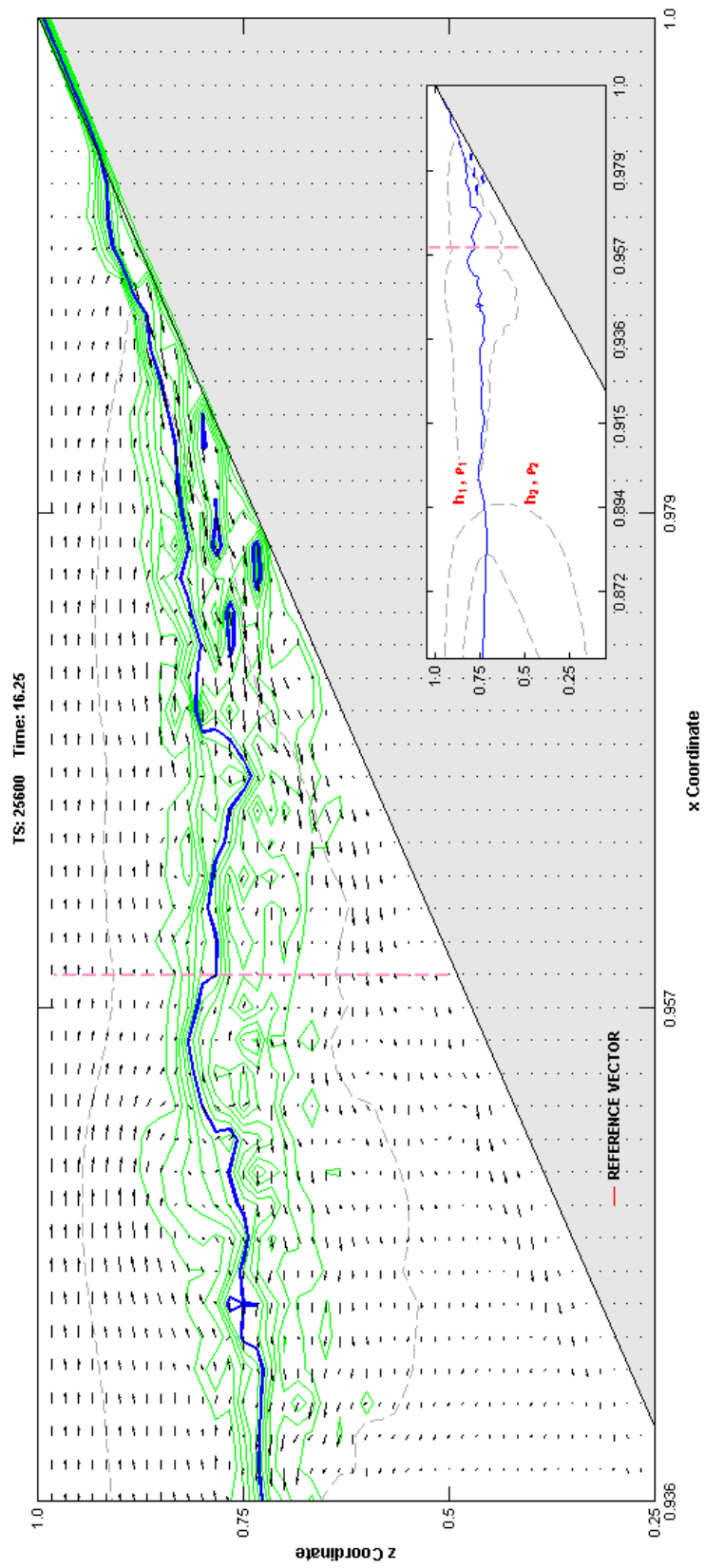












APPENDIX F

DETAILS OF REFLECTED INTERNAL WAVE

The discussions concerning the numerical simulations between ISWs and various types of topographic obstacles described in this dissertation have focused primarily on how the internal wave behaves as a result of its interaction with different types of topographic features. Although there are observable changes in the internal wave's properties stemming from its interaction with a submarine obstacle, the simulations have generally demonstrated that the internal wave continues to advance more-or-less through the stratified fluid system in spite of the encounter. One aspect of these interactions though that has not been discussed to any extent in this dissertation concerns internal wave reflection.

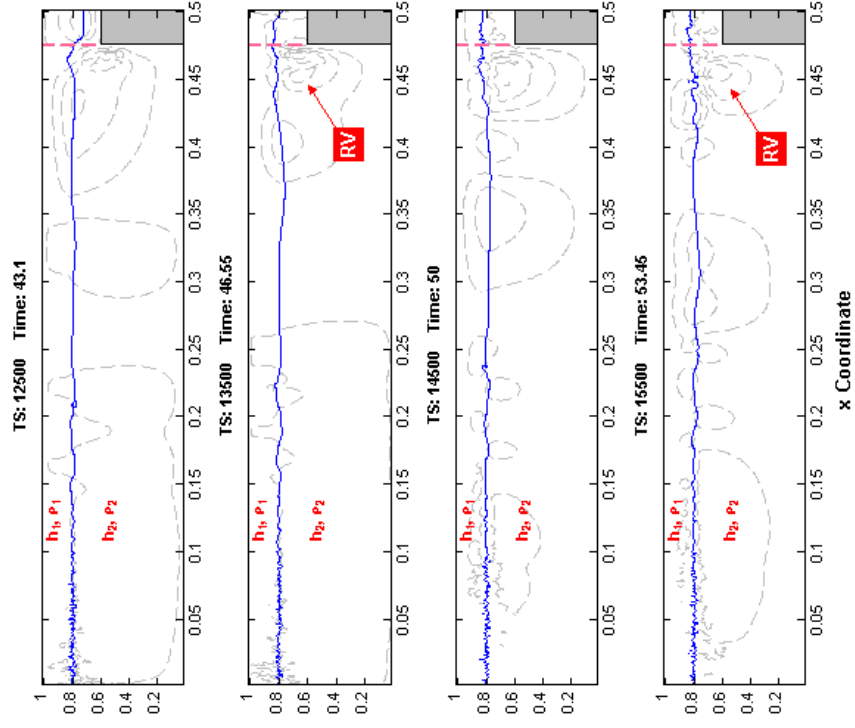
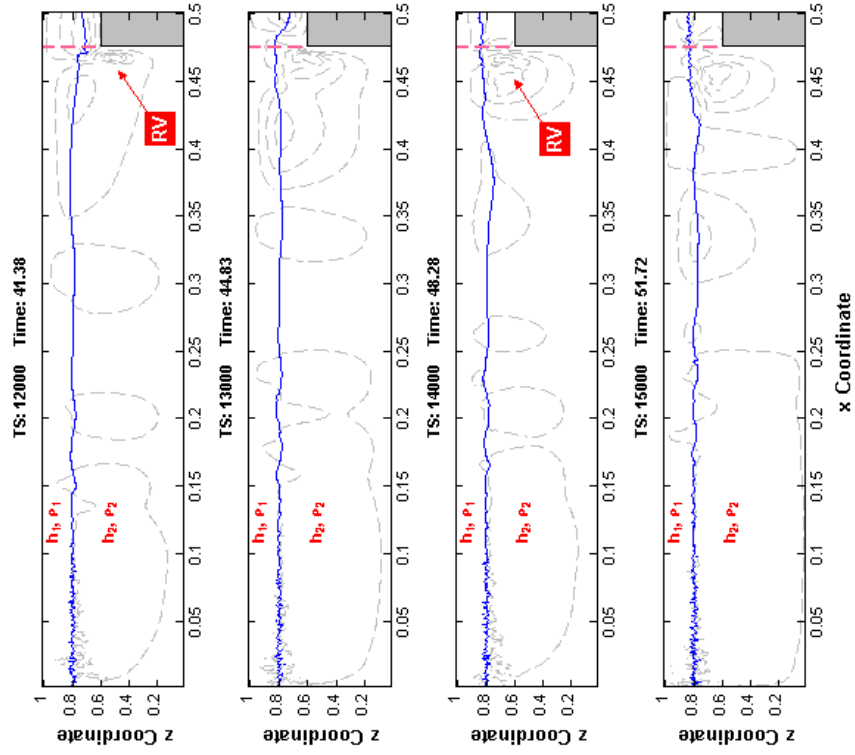
It is well known that when a wave encounters a non-yielding surface, it will reflect or bounce-back in the direction from which it came. In general, the angle at which the wave leaves the reflecting surface is equal to the angle at which the wave approaches that surface. When examining those simulations in this dissertation which involved what is essentially a surface

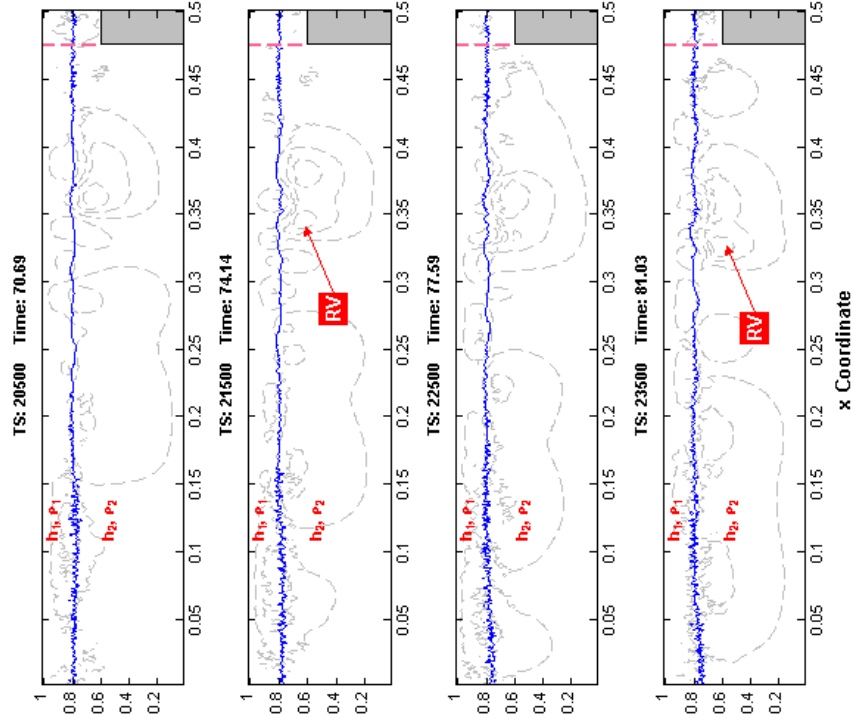
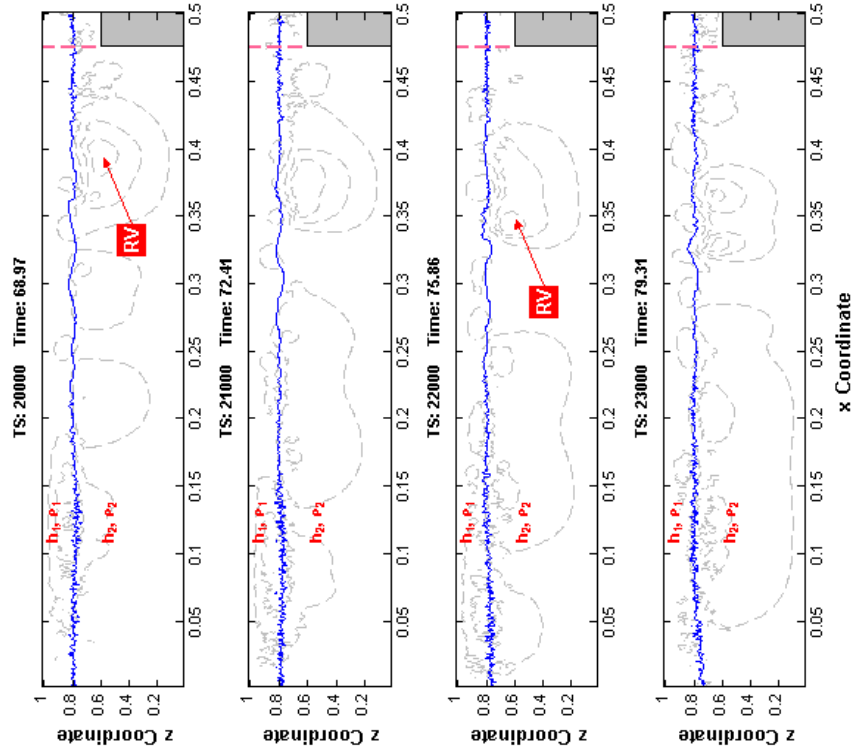
normal to the plane of the advancing ISW — the shelf-only and single rectangular obstacle scenarios — it was observed that some portion of the advancing wave train was reflected back in the direction of propagation. The numerical simulation involving a single rectangular obstacle provides a good example of this phenomenon.

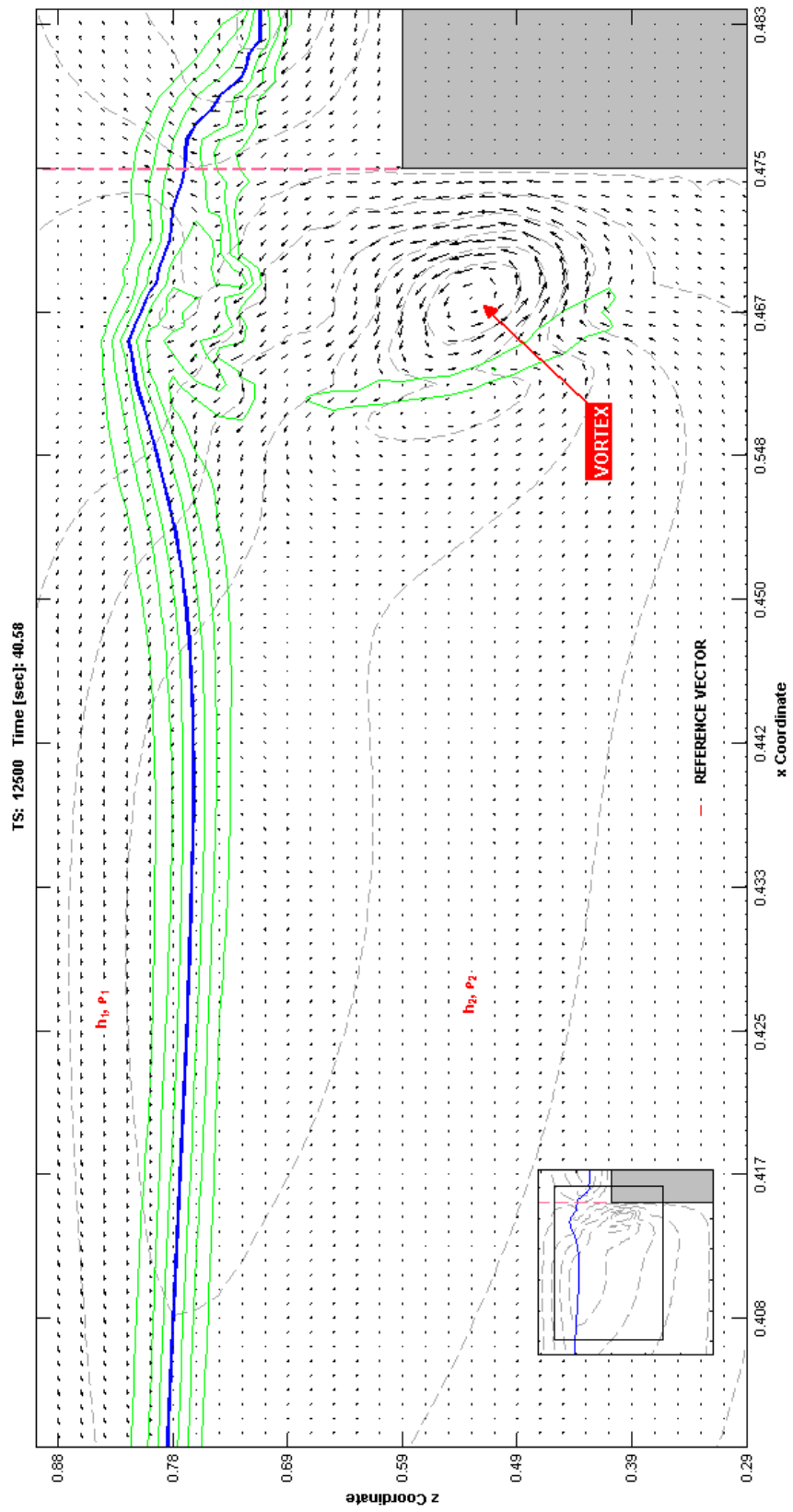
The time series depicted earlier in Figure 67 shows a well developed, depression-type ISW of mode-1 approaching a single rectangular obstacle, interacting with the obstacle, and then continuing to advance through the computational domain for the balance of the simulation. Closer inspection of the time series of exhibits in Figure 67a also shows that some portion of the ISW is reflected back in the direction of propagation through the course of the simulation. This reflection can be identified by virtue of the bifurcation of the streamline contours. Some of these contours remain along the upwind face of the obstacle and can be observed at subsequent time steps migrating or reflecting back towards the generation point. The exhibits in this appendix are intended to examine these reflected artifacts of the simulation in a more detail.

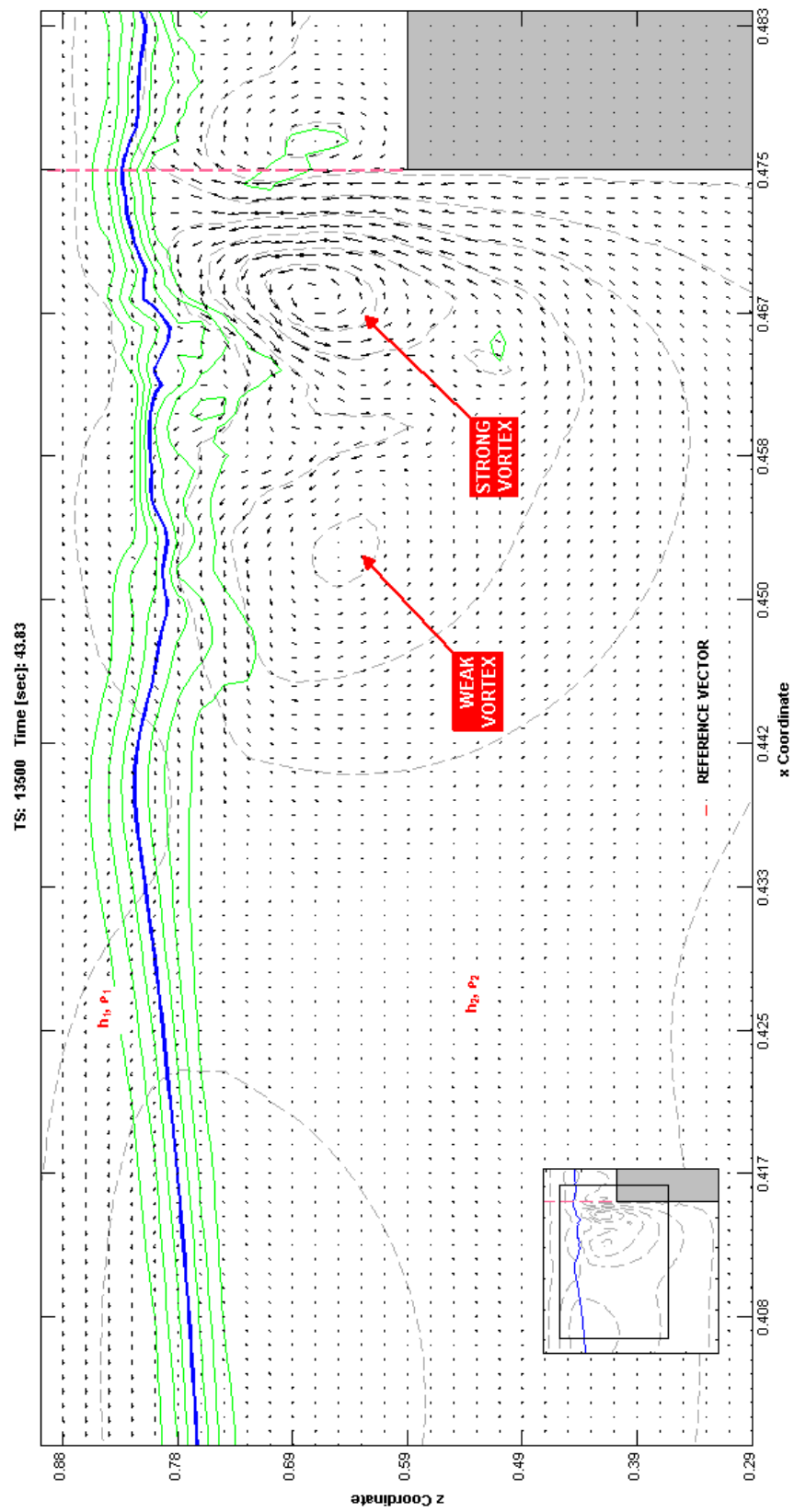
The first series of figures in this appendix show how the artifacts of the internal wave/obstacle interaction coalesce as a reflected vortex (designated as **RV** in the exhibits), beginning about TS 12,000, and then migrating

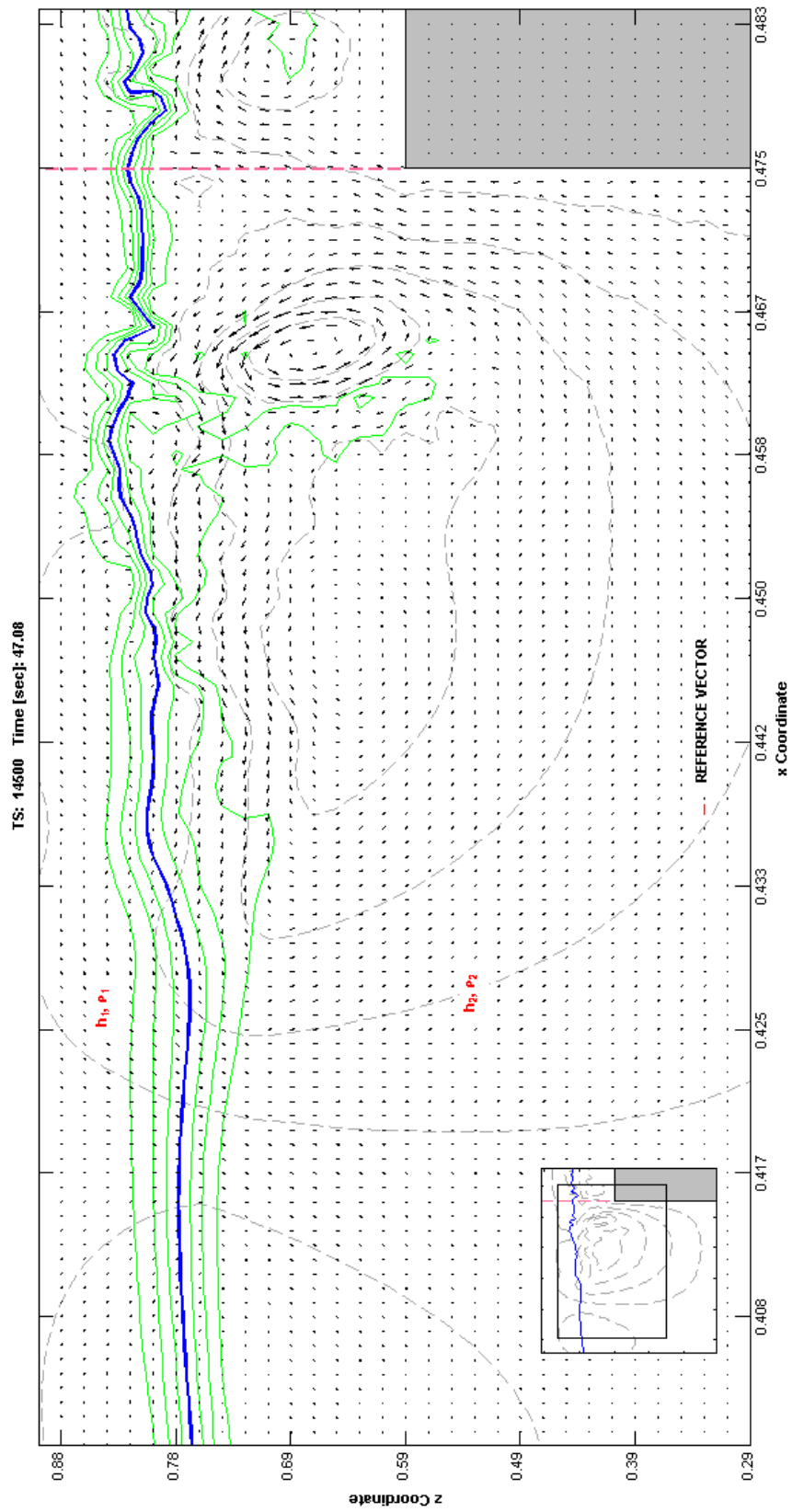
backwards in subsequent time steps. By TS 20,500, the reflected vortex identified has formed into a well-defined collection of streamlines. With the addition of velocity vectors, the detailed (higher-resolution) series of exhibits found later in the appendix reveal that the reflected collection of streamlines have a flow pattern orientation opposite to that of the original (incident) depression-type internal wave. See TS 15,000. The flow pattern for the “reflected” ISW velocity vectors is counter-clockwise whereas the velocity vector flow pattern for the incident ISW is clockwise. In a few cases, multiple vortices can be observed in the detailed exhibits. See TS 13,500, 16,000 and TS 17,000.

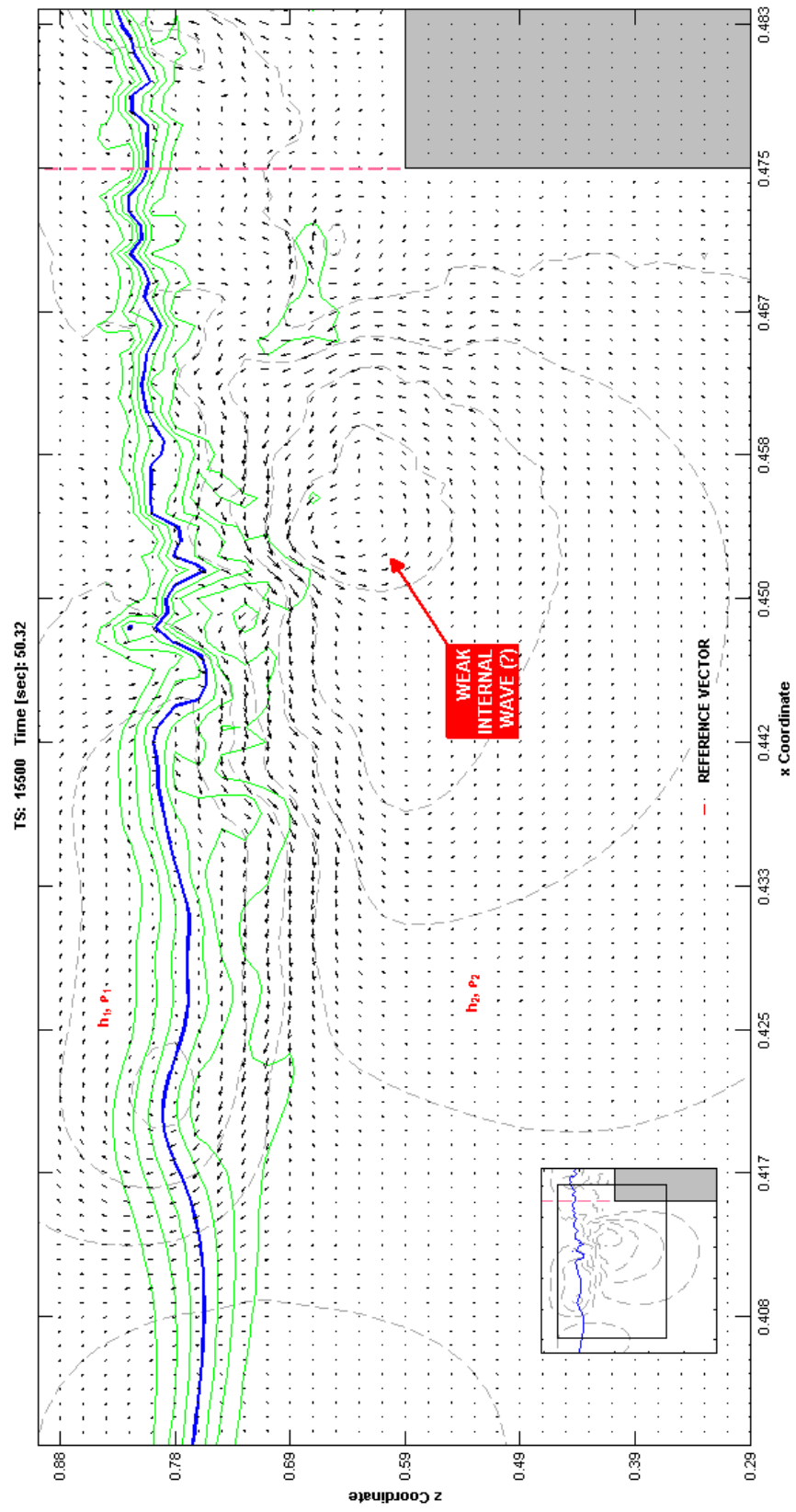


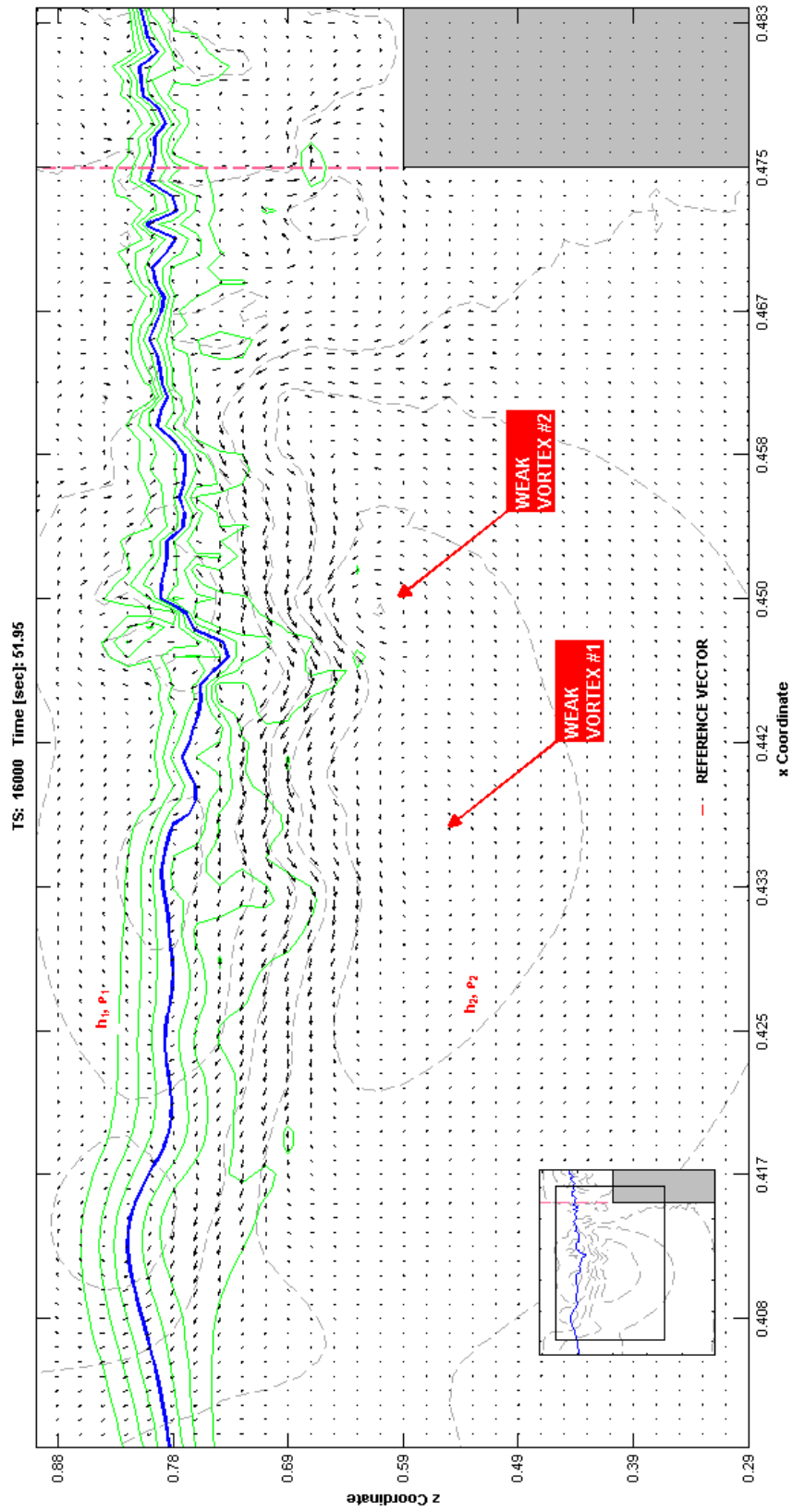


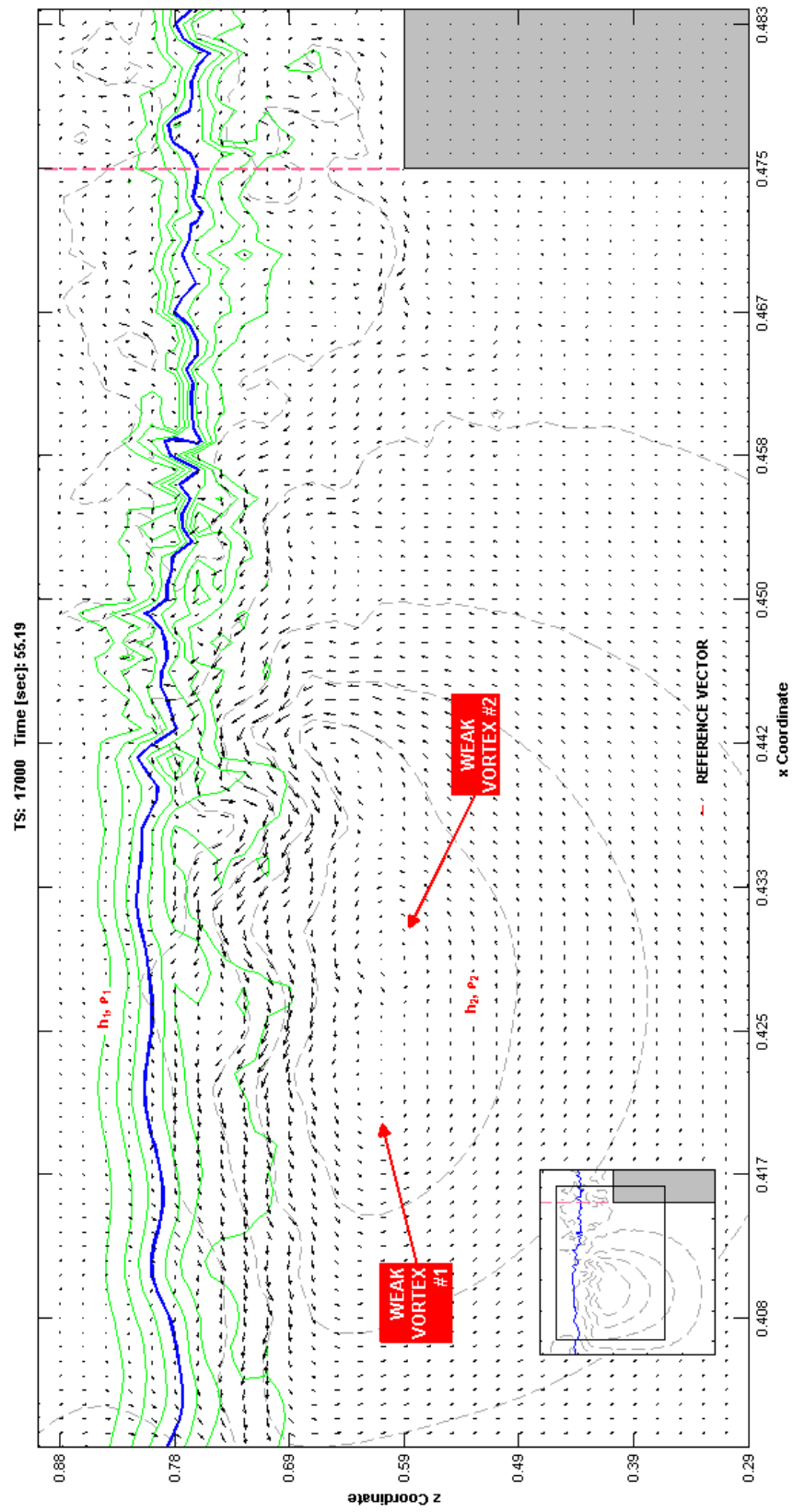


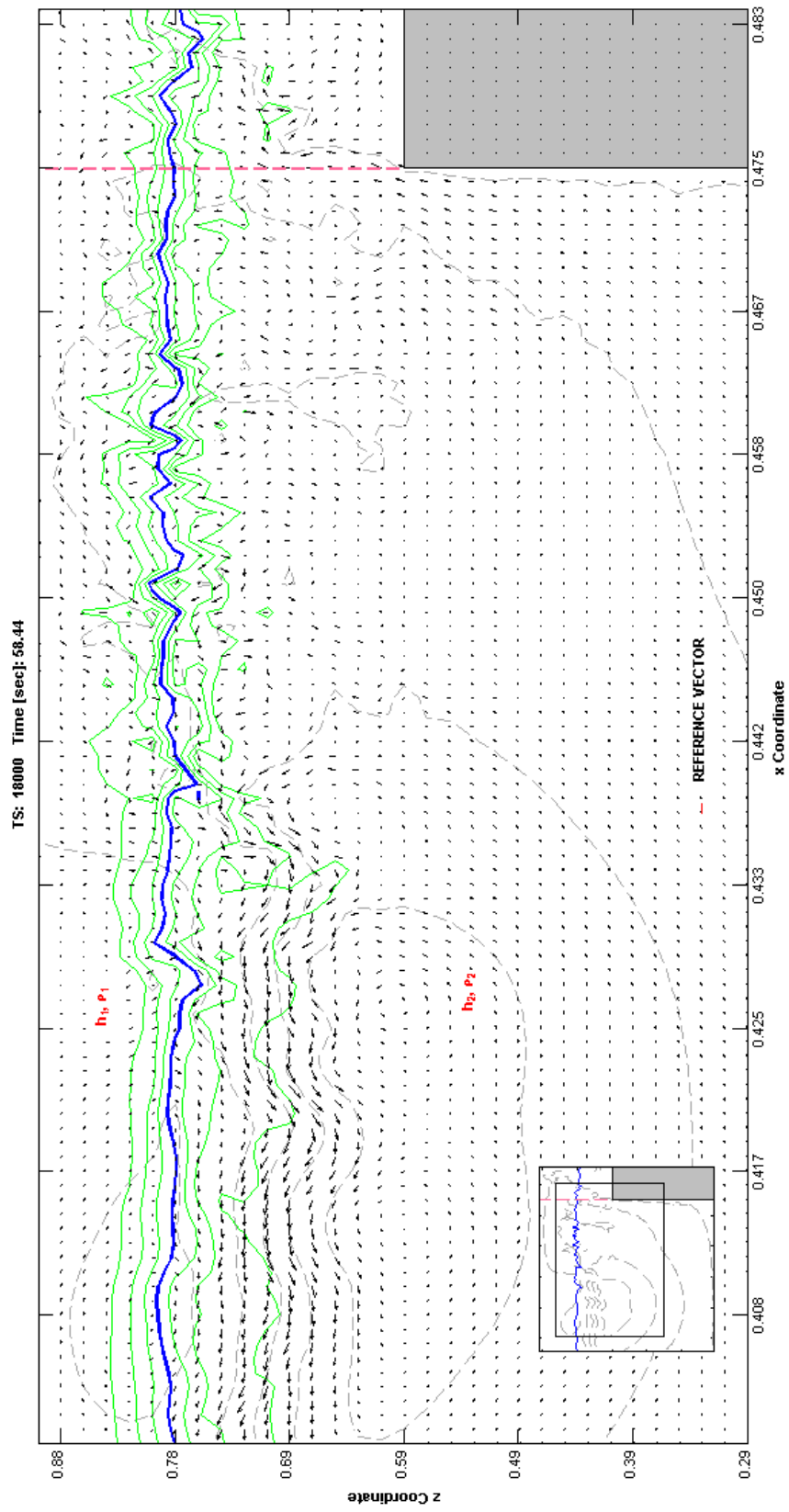












APPENDIX G

DETAILS OF NUMERICAL SIMULATION INVOLVING AN ISOLATED TRIANGULAR TOPOGRAPHIC OBSTACLE

The exhibits contained in this appendix depict the details of an interaction shown earlier in Figure 73 between a mode-1 depression-type internal wave and an isolated triangular obstacle. The non-dimensional simulation shown herein is in progress at TS 9900 just prior to the onset of the shoaling/breaking progression. As the intent of this particular simulation scenario was to illustrate how the internal wave polarity transformation sequence proceeds when the plane of the theoretical turning point is encountered, the illustrations capturing this transformation are limited to the pycnocline (solid blue line) and the theoretical turning point plane itself — the vertical dashed line corresponding to the depth condition of $h_1 = h_2$. Multiple isopycnals about the pycnocline are shown in green providing additional information on how the profile of the density interface changes during the simulation. Lastly, each detailed figure in the simulation sequence (whose non-dimensional time step is equal to 200) includes a smaller inset

plot illustrating the location of the overall internal wave in relation to the obstacle.

At TS 9900, the simulation shows that internal wave is just beginning to encounter the obstacle. Although the wave itself is still enjoys a relatively symmetric profile, the outermost streamline contour is just beginning to distort in response to the obstacle.

At TS 103,000 in the simulation, asymmetry in the pycnocline profile is now becoming apparent as the internal wave begins to encroach on the location of the theoretical turning point plane. As noted earlier in this dissertation, this change would suggest the onset of shoaling. The streamline contours are now clearly refracted in such a ways as to mirror the face of the obstacle. As illustrated in subsequent time steps, the internal wave's symmetry continues to decay as the wave front approaches the hypothetical turning point plane. By TS 107,000, as a result of wash-down, the pycnocline has been driven to its lowest point of entrainment.

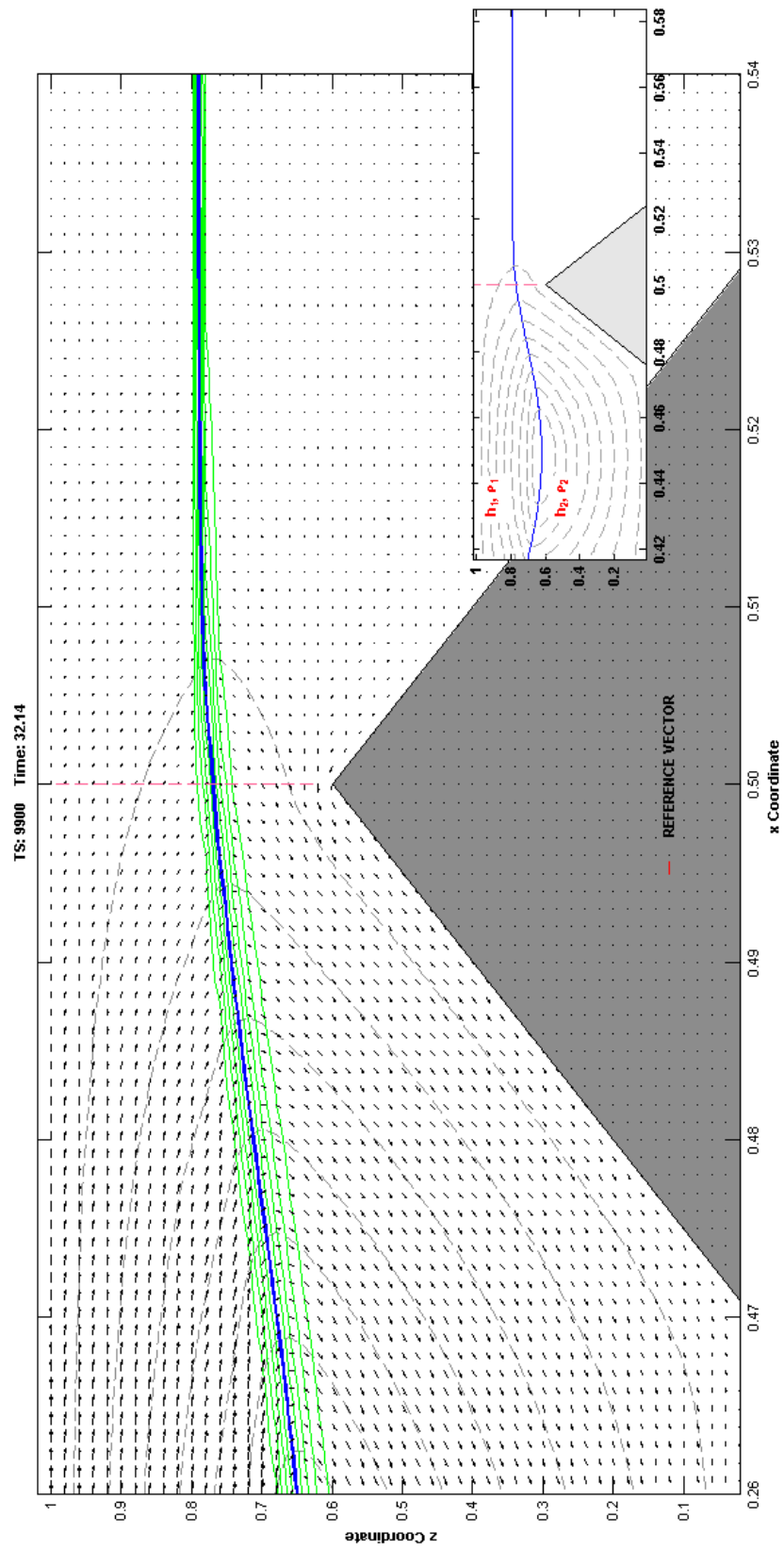
It is also worth noting that as the wash-down phase progresses, there is a pronounced increase in the magnitude of the flow in the h_2 fluid layer, in a region between the pycnocline and the downwind face of the obstacle. In a manner of speaking, the streamline contours can be observed colliding with

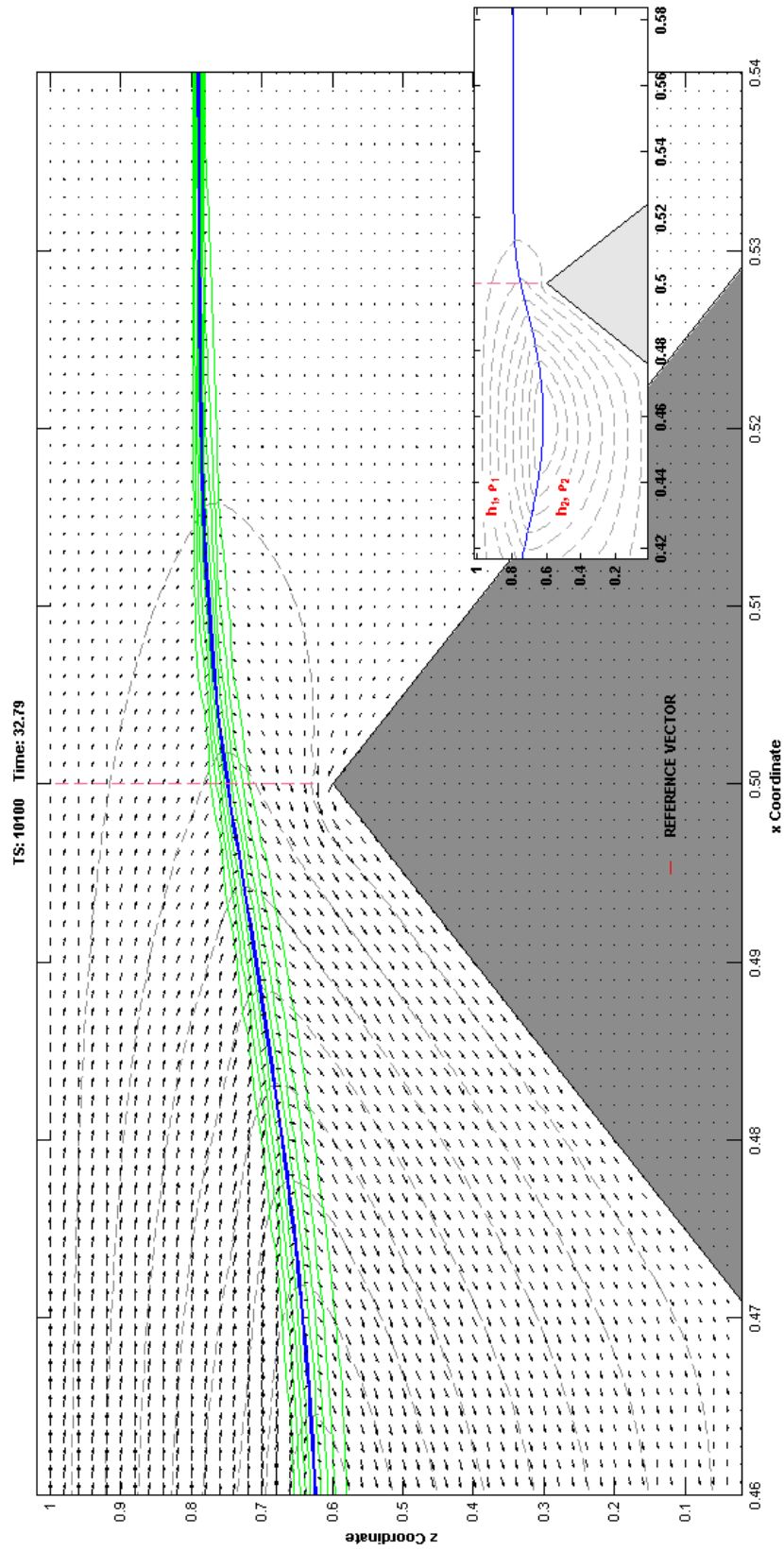
the obstacle. This increase in contour density would suggest an increased flux in this region of the flow field. This increased flux can be seen in the relative magnitude of the velocity vectors within the h_2 fluid layer along the face of the obstacle.

By about TS 111,000, the shoaling progression has produced a breaking internal wave. What had been the trailing leg of the internal wave has advanced forward through the course of the simulation and now appears to have rolled-over onto what had been the entrained portion of the pycnocline (e.g., the wave front at earlier TS 107,000) forming a K-H-like “cats-eye” (Figures 14 and 15). Soon thereafter, by about TS 113,000, the character of the velocity field in this area is such that there are now multiple vortices along the face of the obstacle. The growth in the size of this turbulent flow field appears to be a key factor contributing to the advancement of the internal wave over the obstacle. The turbulent flow field appears to elevate (lift) the pycnocline up over the obstacle in a manner similar to that water advancing over a nappe or a weir. By TS 117,000, a well-defined upwelling zone has formed downwind of the theoretical turning point plane. In later time steps, this upwelling zone of turbulent flow appears to form a portion of the pycnocline into a bulbous-like feature. However, there is no evidence that the shoaling progression produces a bore, as had been the case with some of the other simulations described in this dissertation. The incident internal

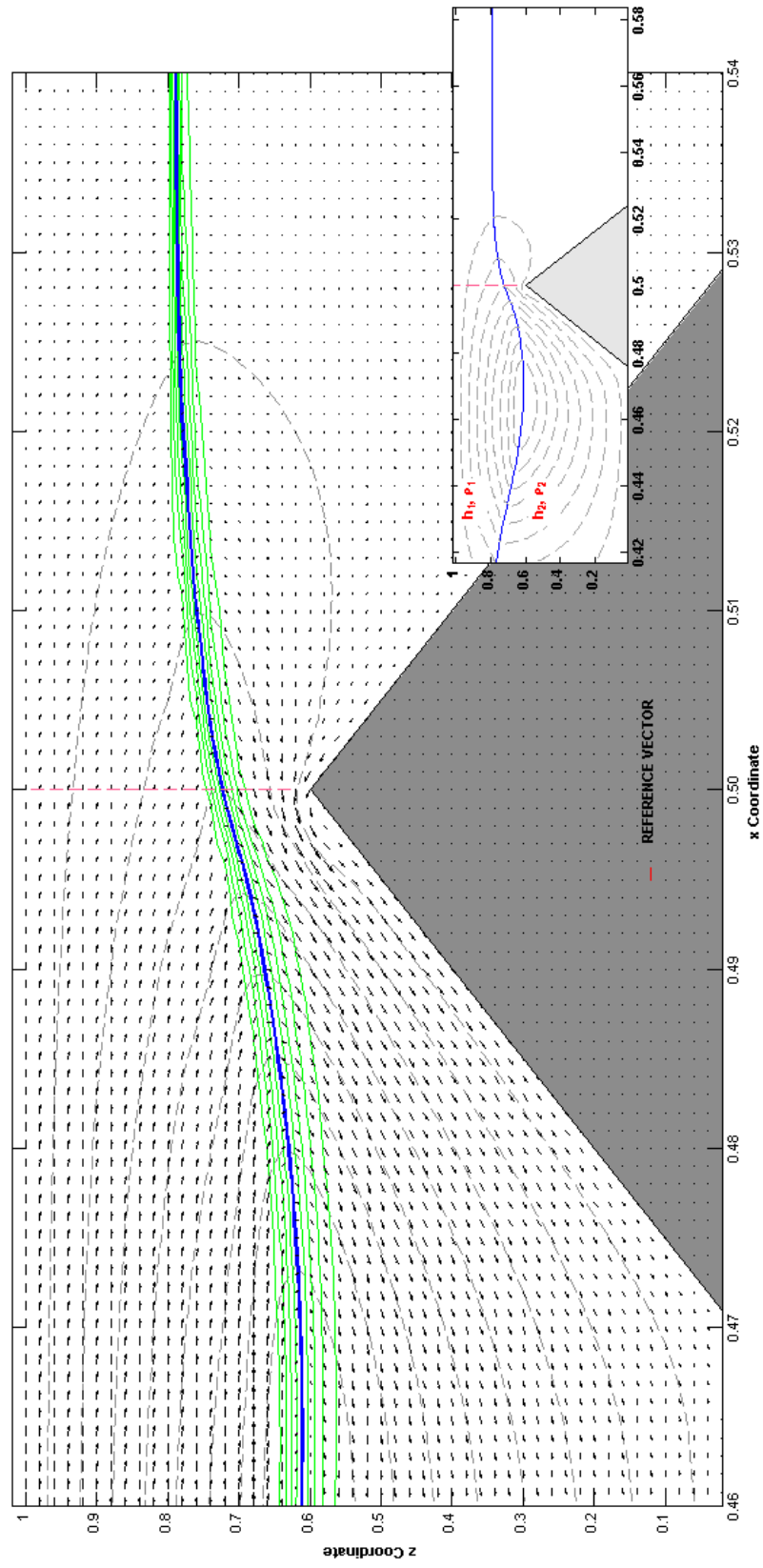
wave, although now diminished in amplitude by virtue of its encounter with the obstacle (as expressed by the magnitude of the nonlinear [blocking] parameter α_{NL}), has been transmitted over the obstacle to a new position along its downwind face. The ISW's overall position in the computational domain during the simulation is illustrated in the inset figure that accompanies each exhibit.

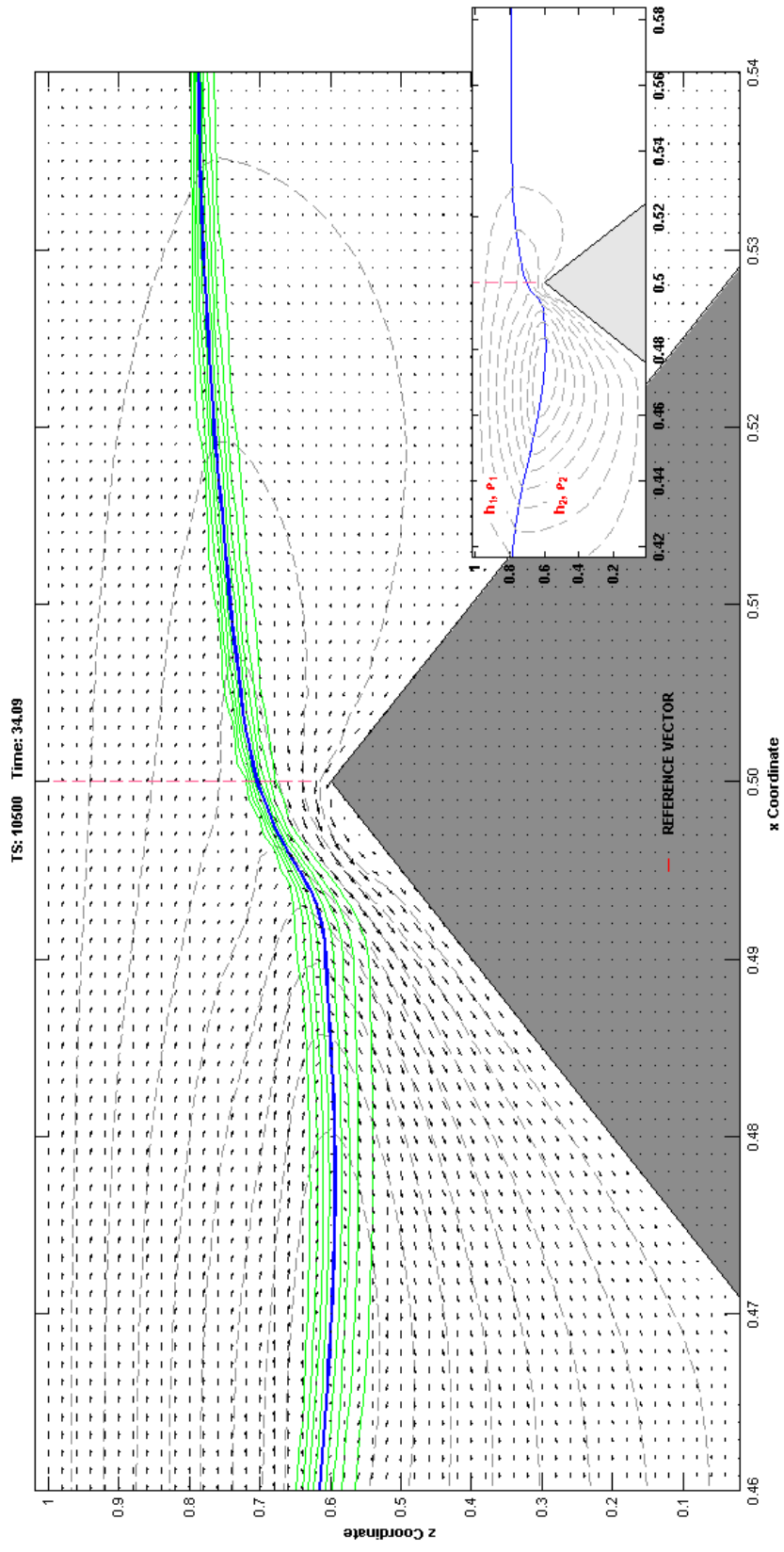
Recalling earlier Figure 73, the ISW continues to advance through the computational domain. As illustrated in the remaining exhibits, it can be observed that the upwelling zone of turbulent flow continues to persist along the downwind face of the obstacle. At TS 119,000, a well-developed vortex has formed along the downwind face of the obstacle. At TS 121,000, there is the suggestion in the simulation that a reflected internal wave has formed. The orientation of the velocity vectors indicates a counter-clockwise flow pattern, implying the pending formation of an elevation-type internal wave. Exhibits corresponding to subsequent time steps — TS 125,000, TS 130,000, TS 135,000, and TS 140,000 — reveal that a counter-clockwise flow field characteristic of an elevation-type internal wave has developed as a result of the earlier collision between the depression-type ISW and the isolated triangular obstacle.

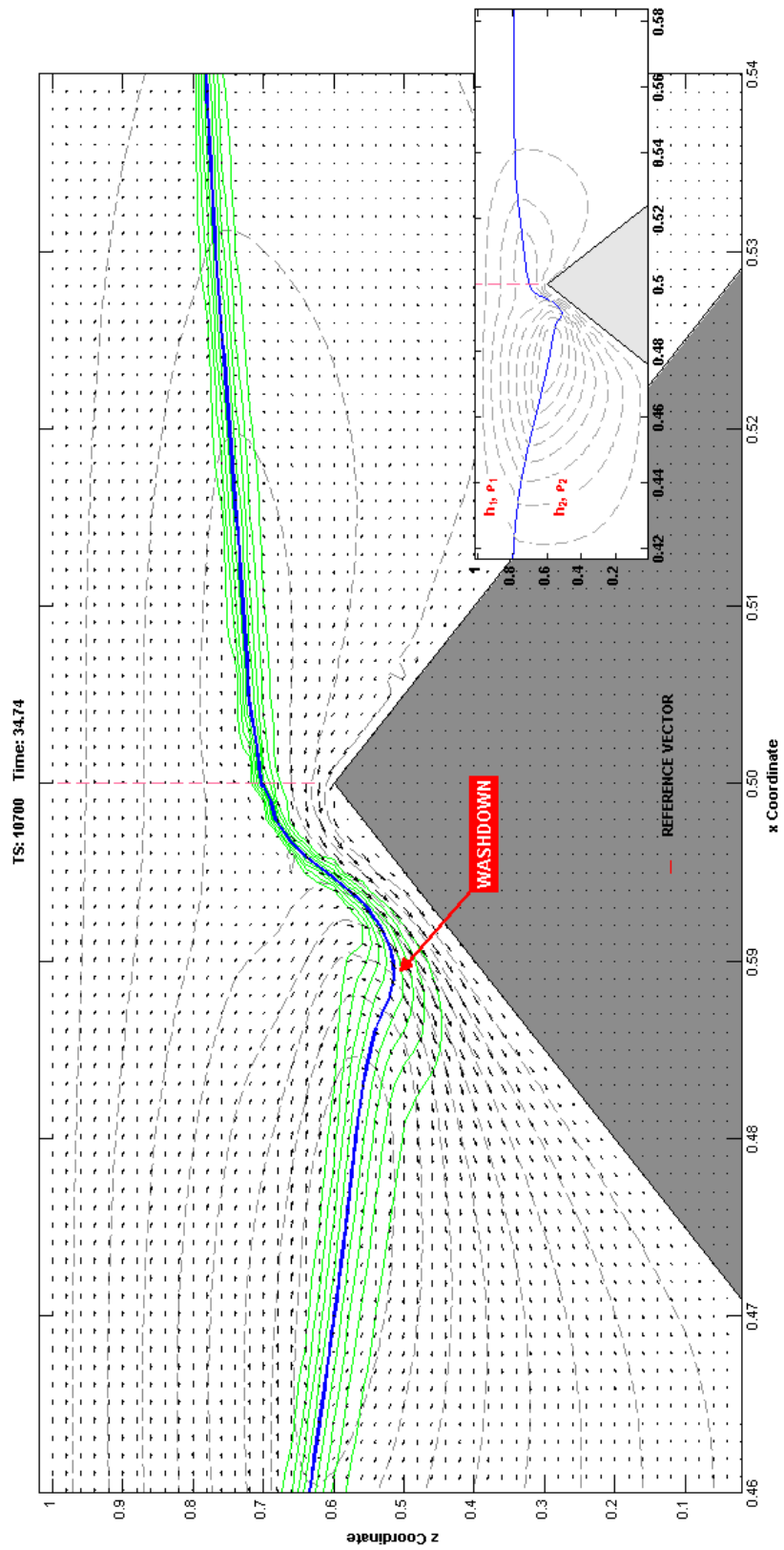


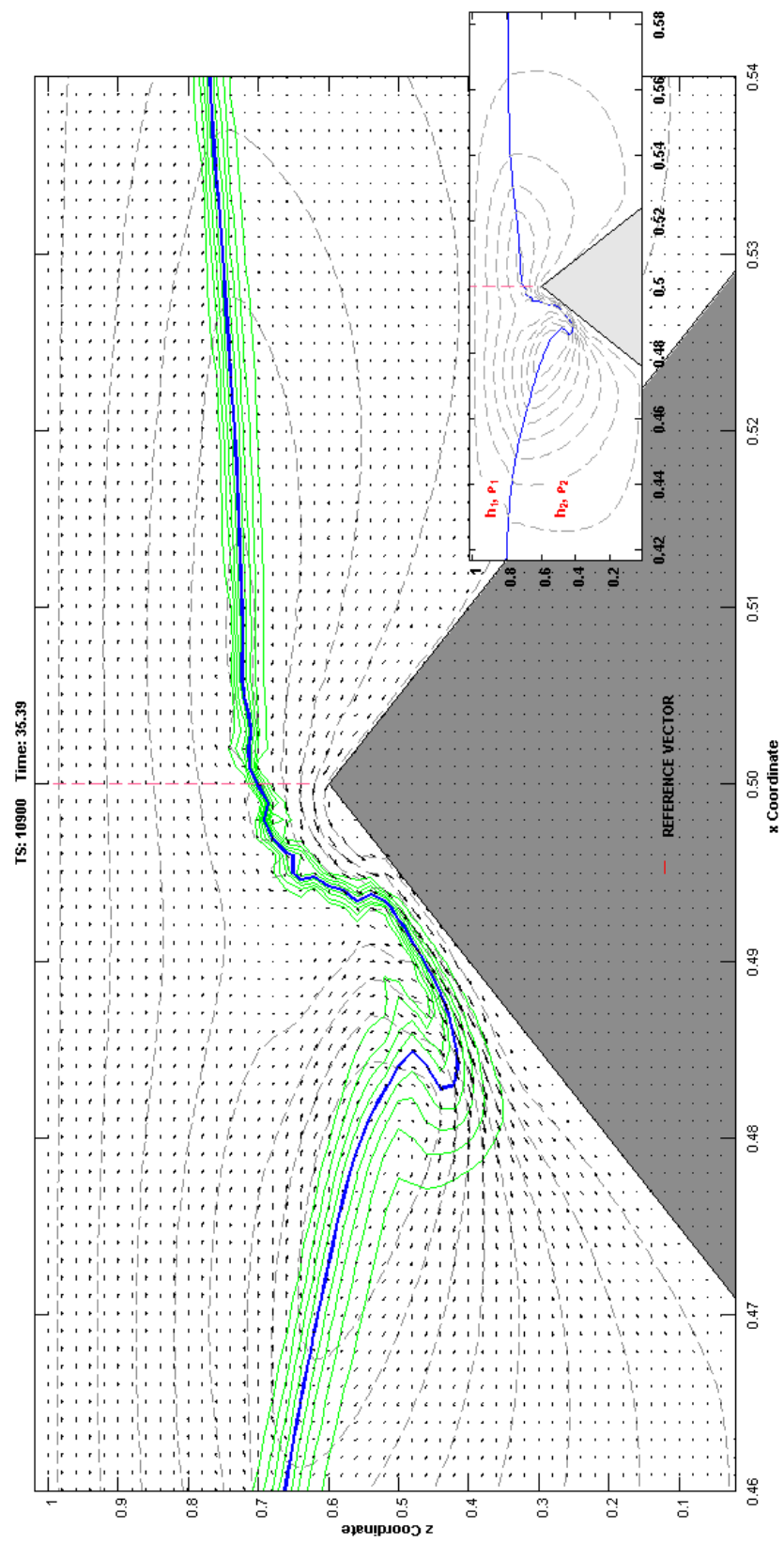


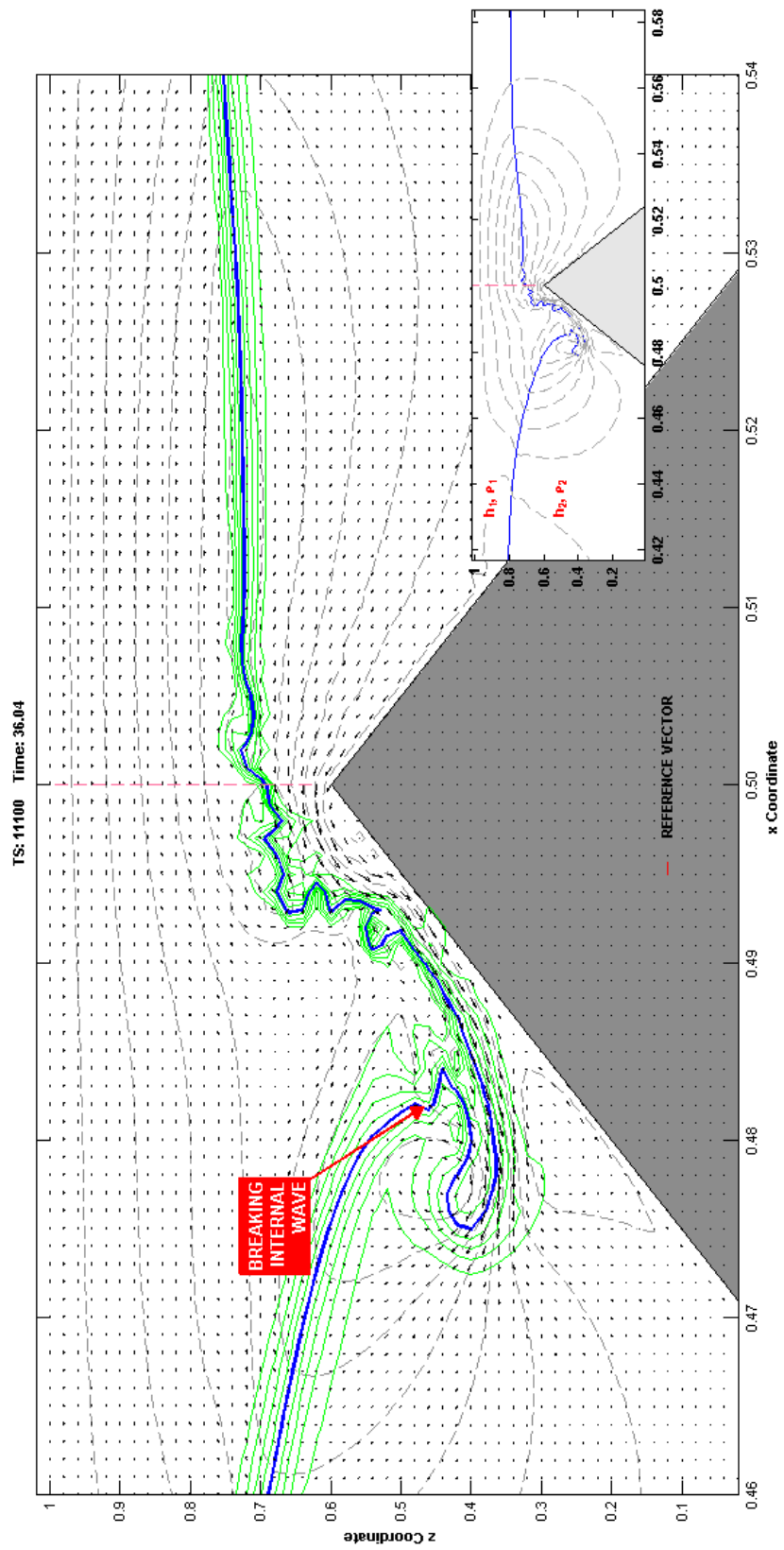
TS: 10300 Time: 33.44

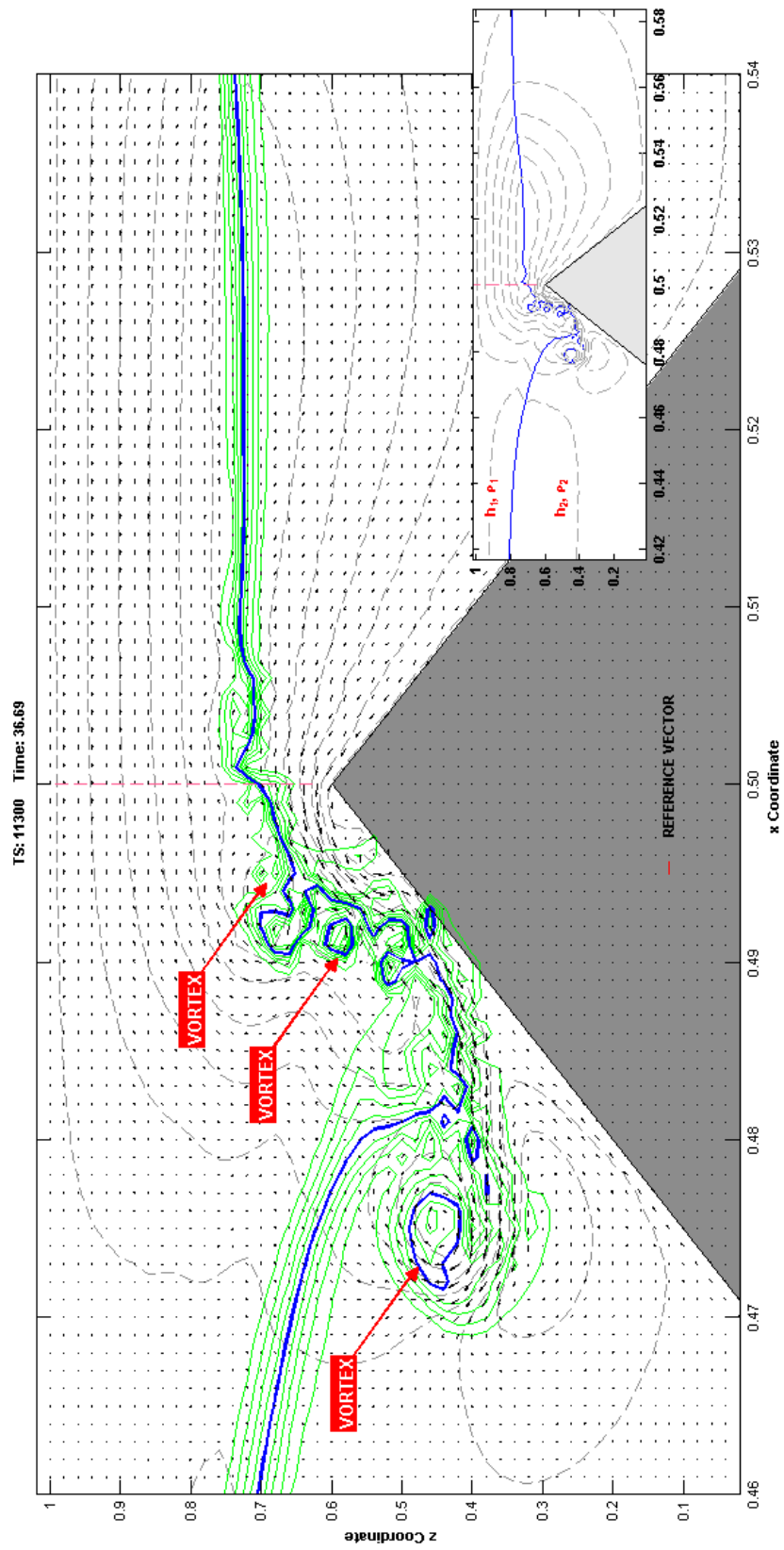


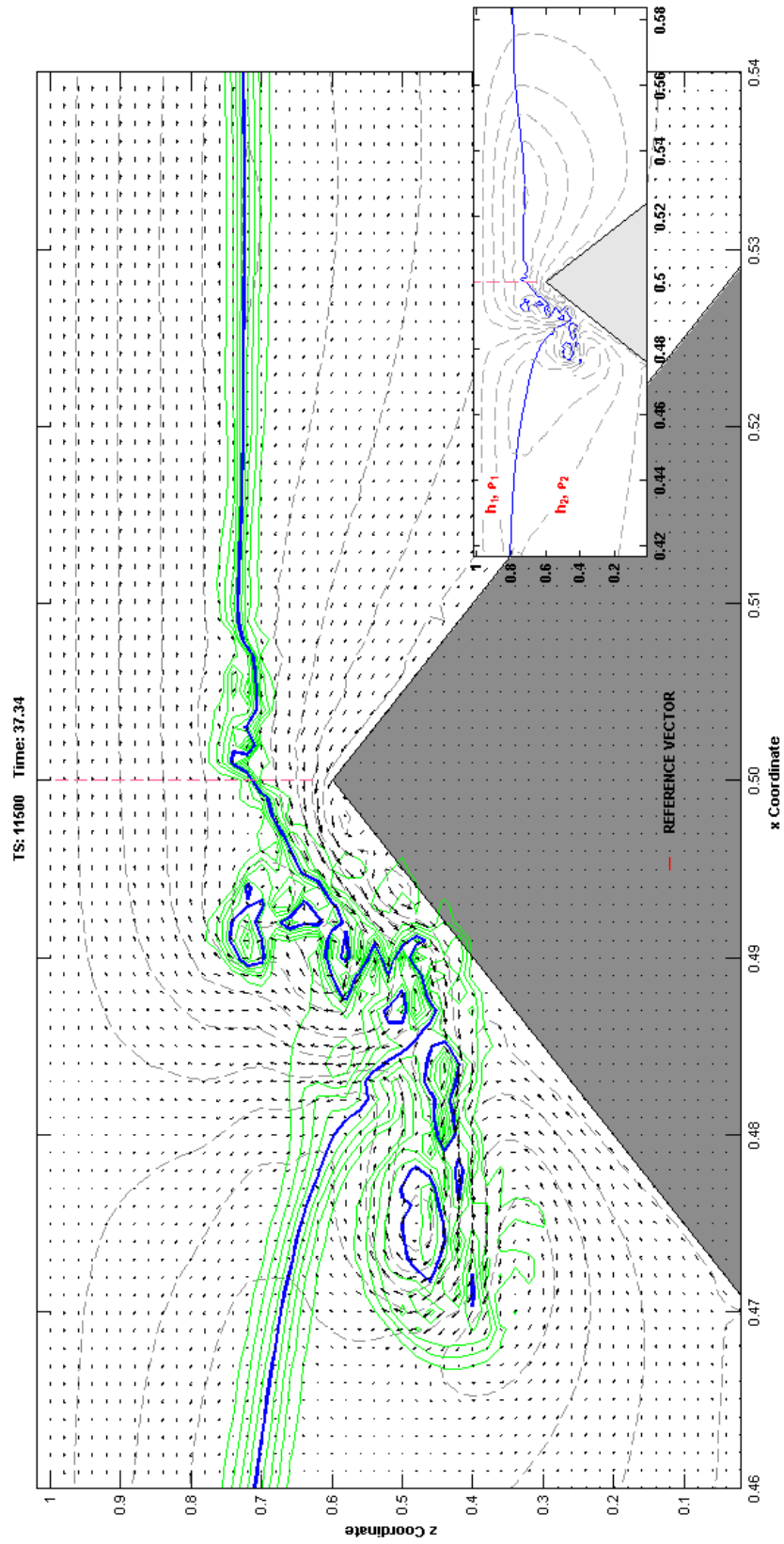


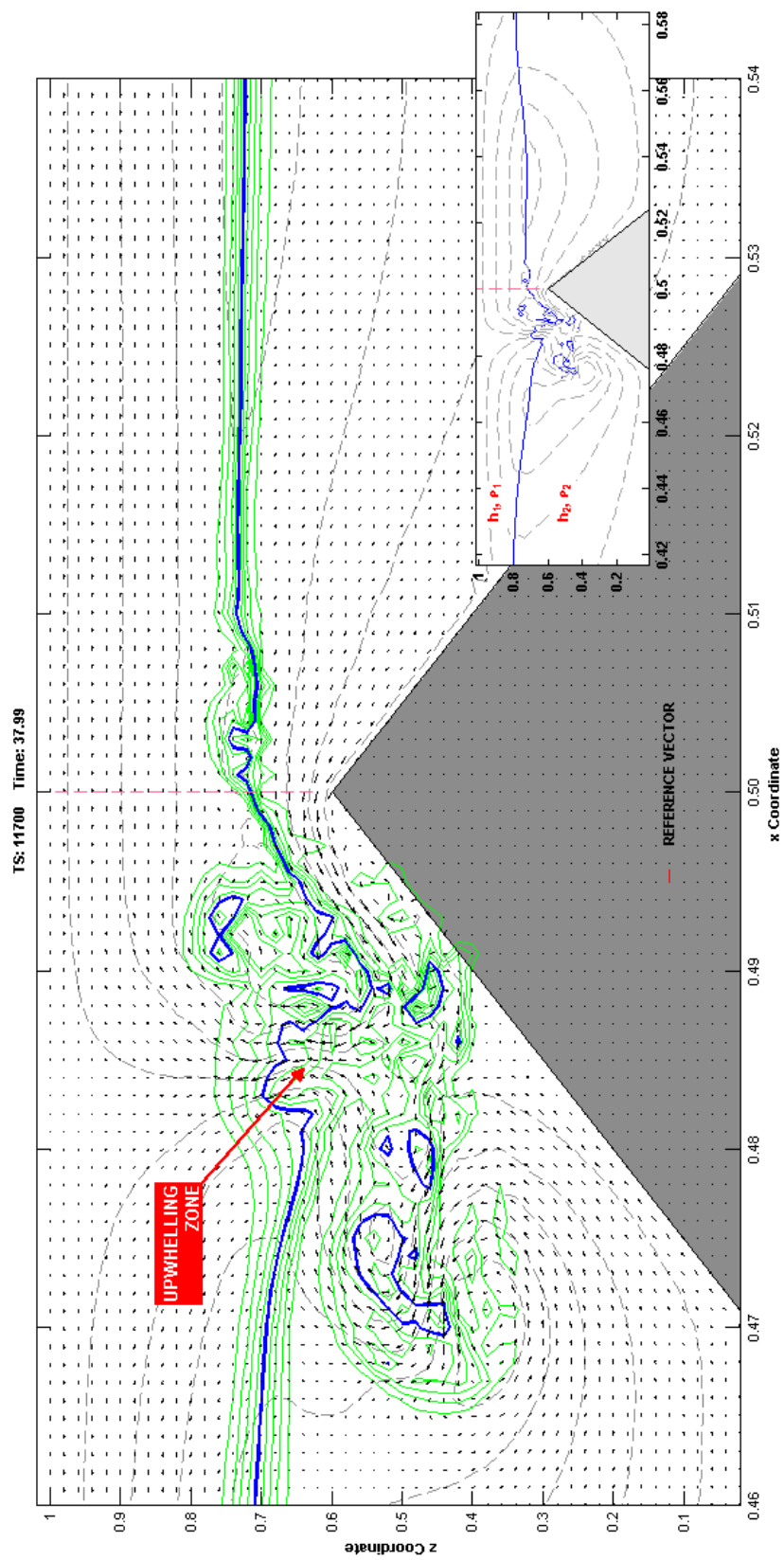


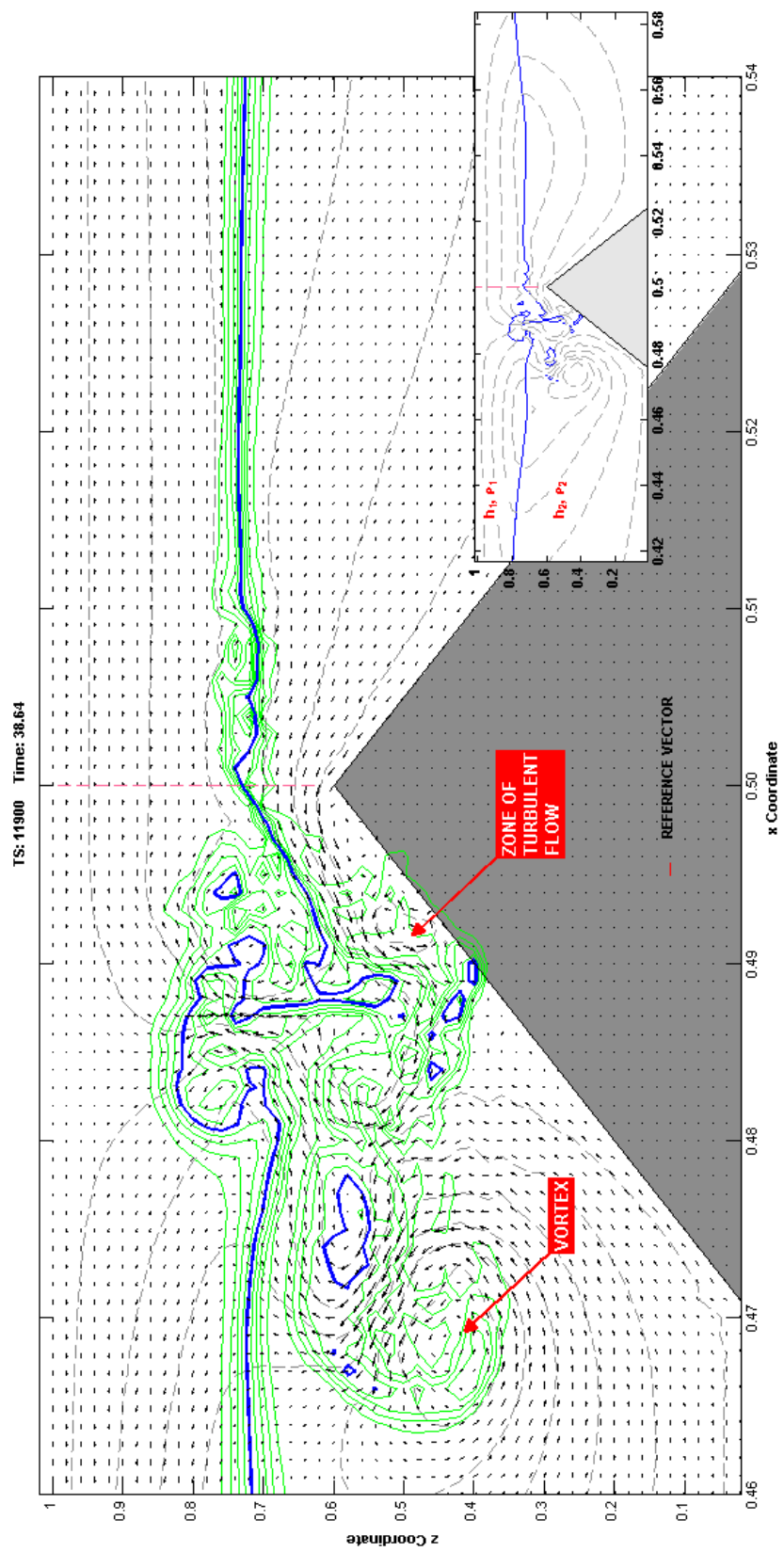


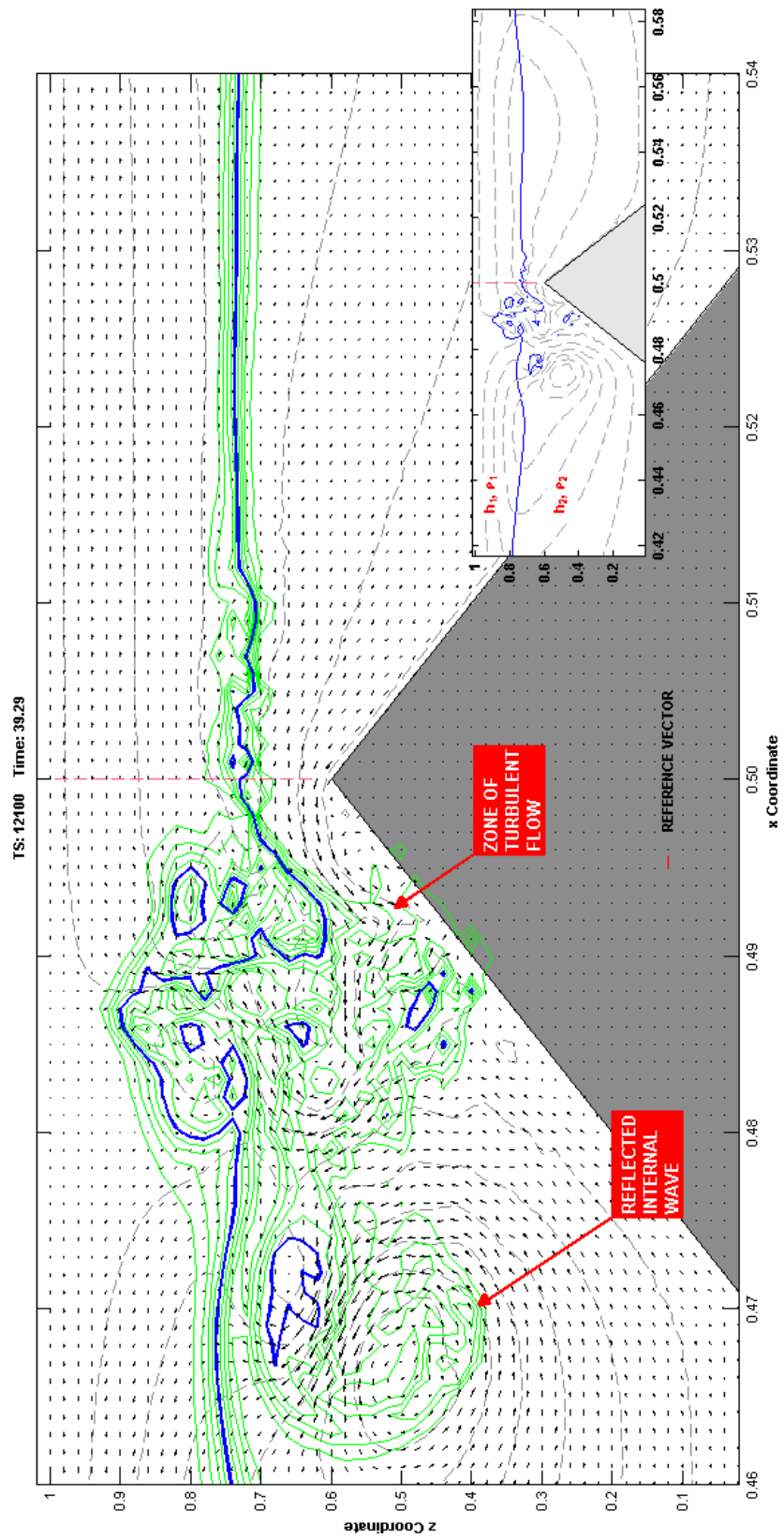


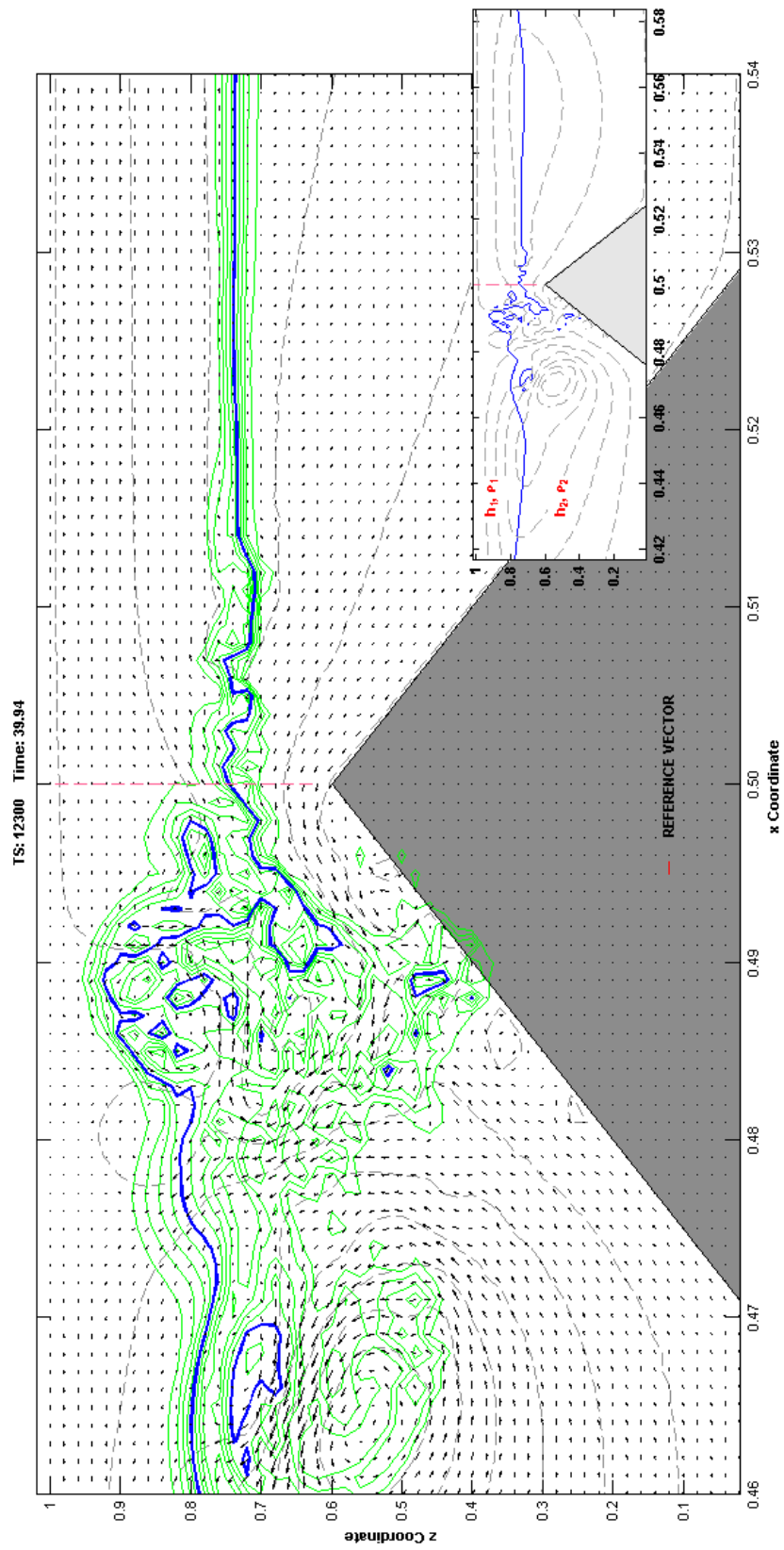


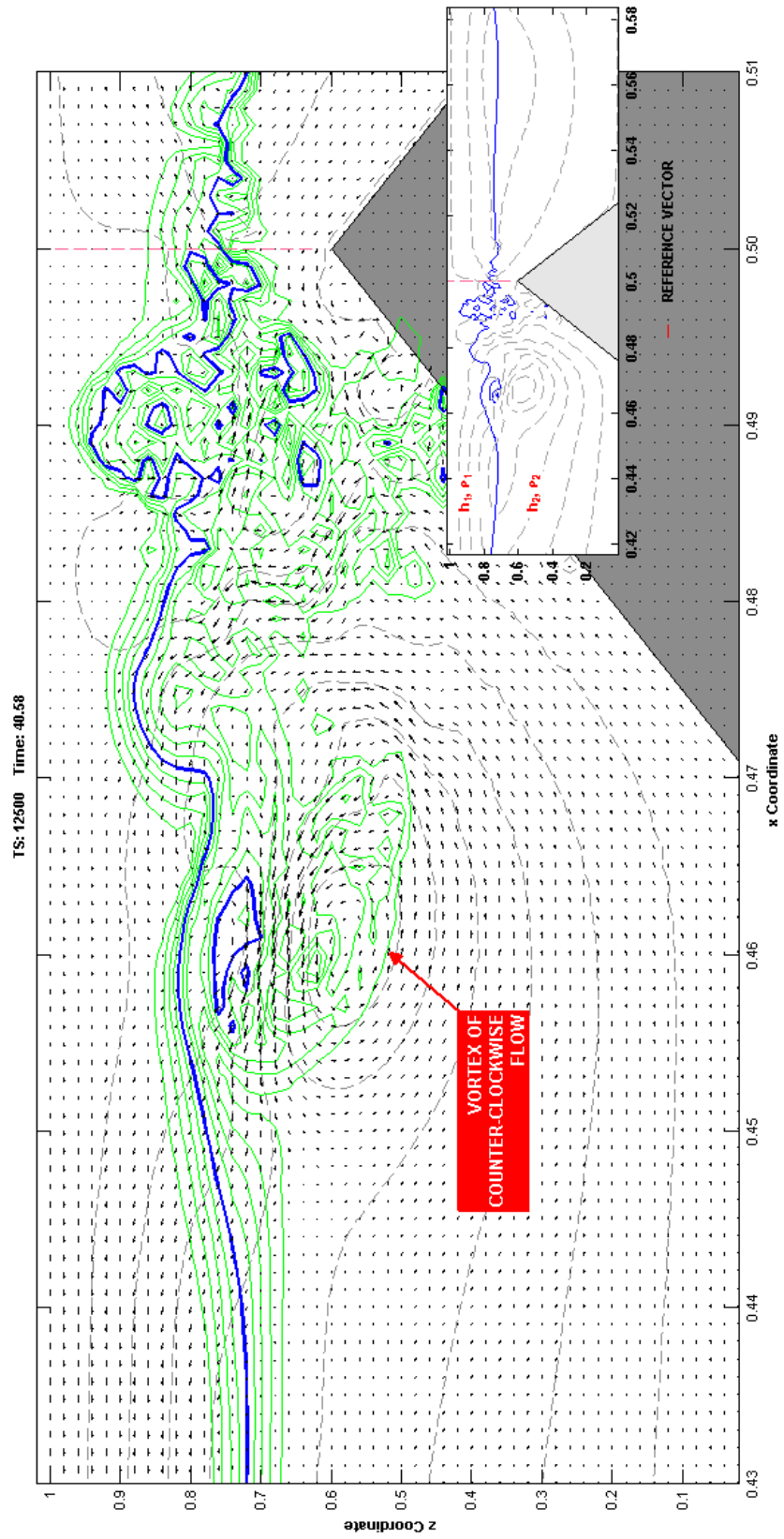


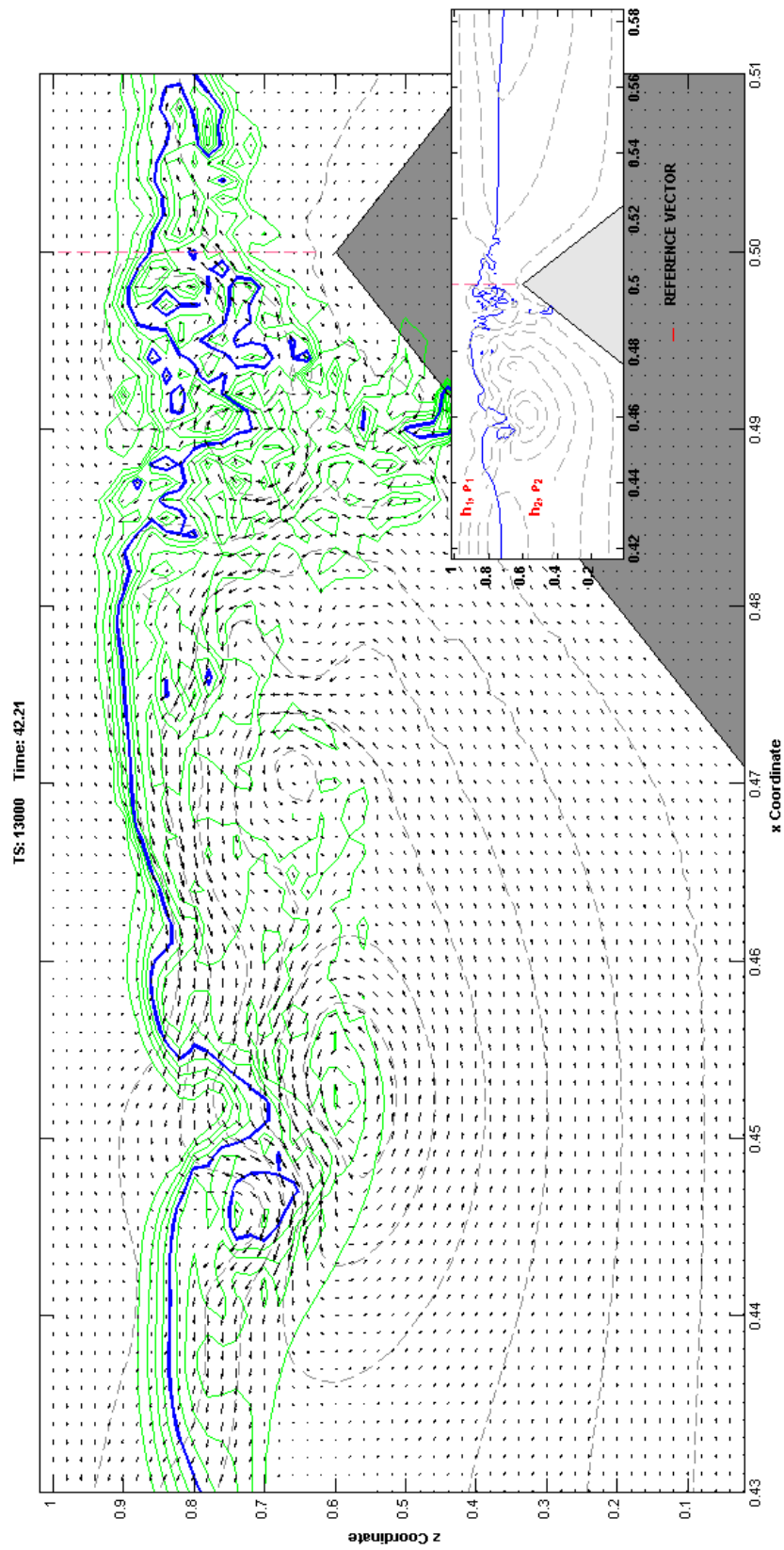


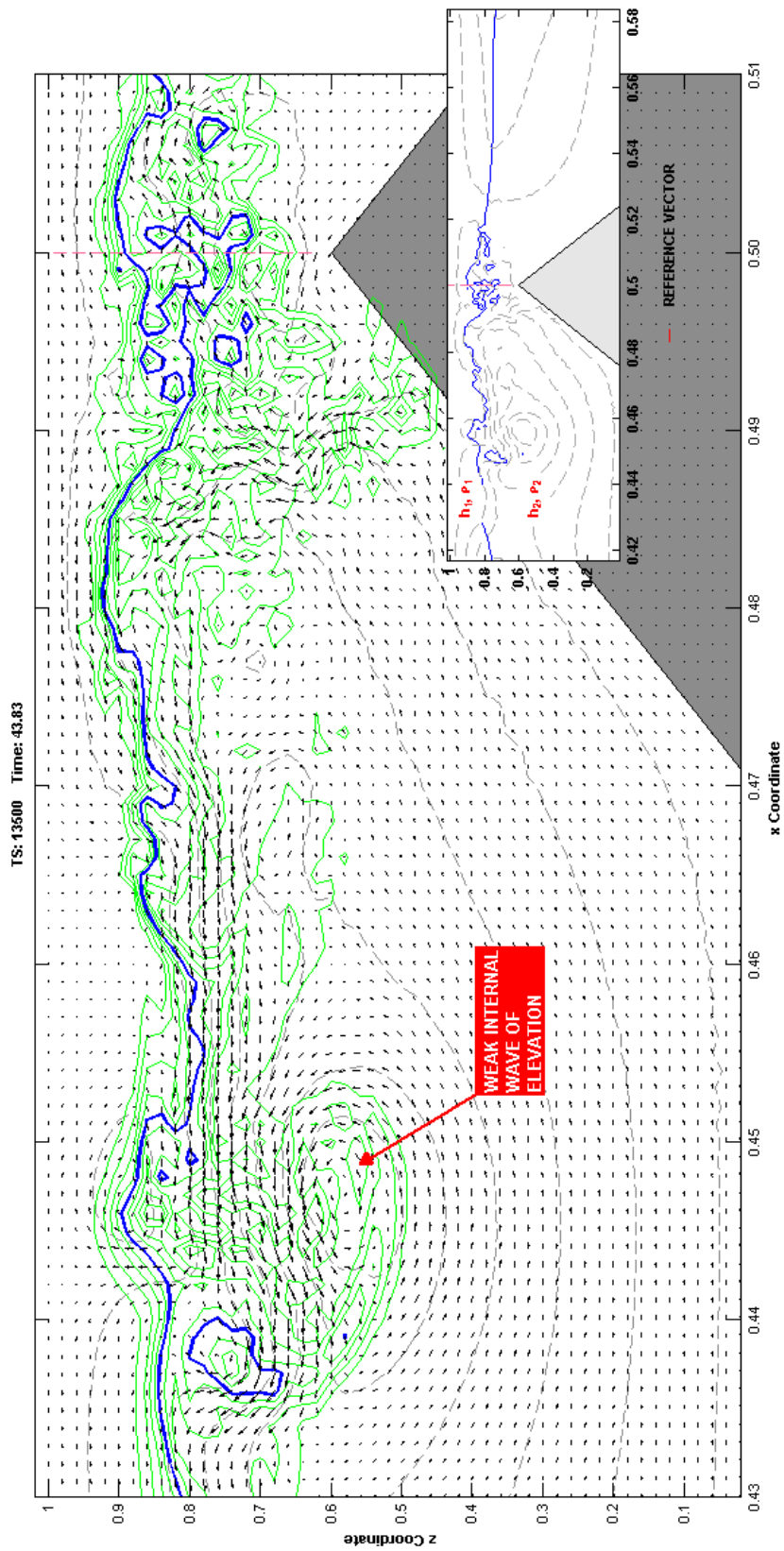


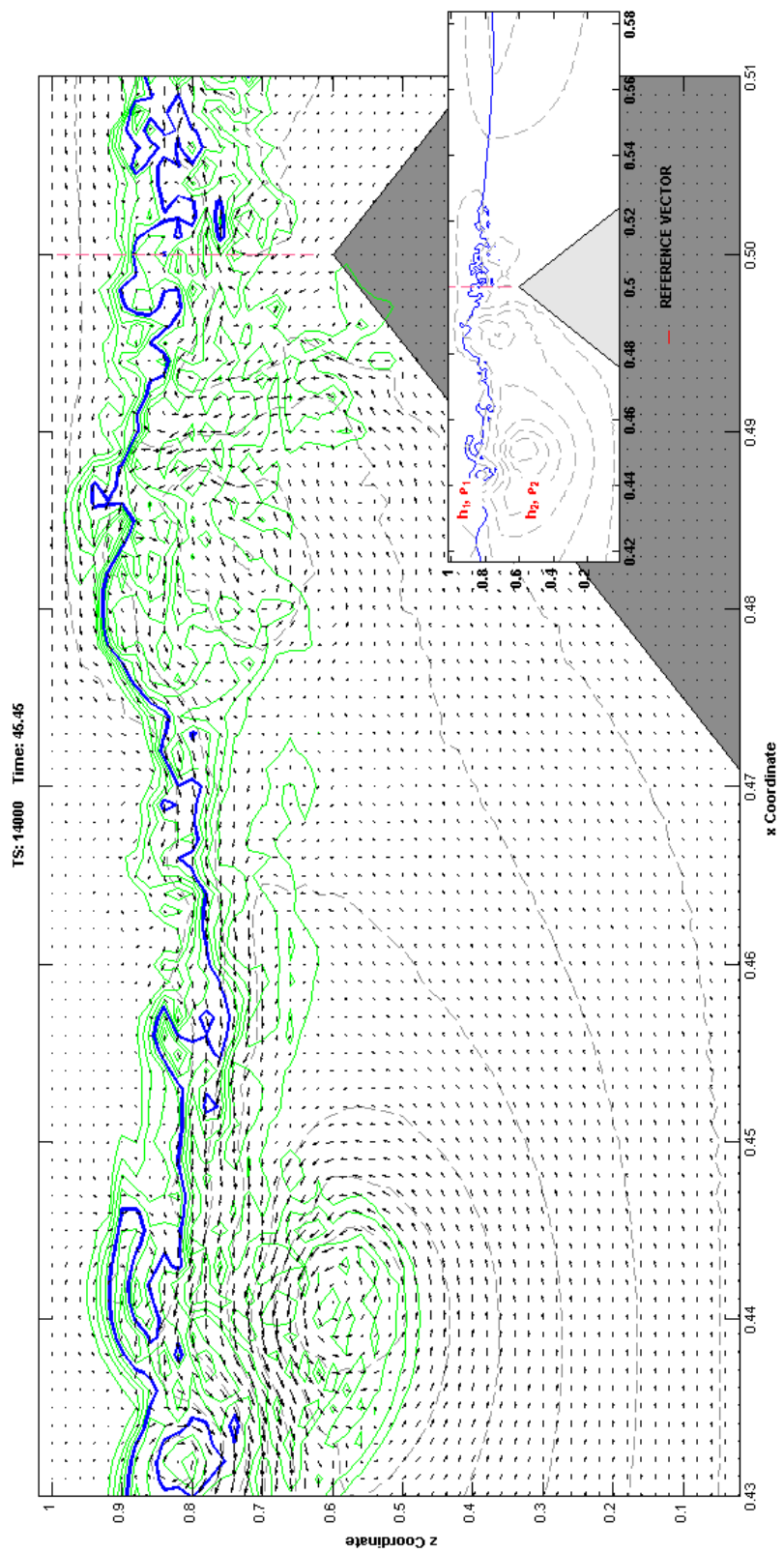












REFERENCES

- Abdullah, A.J. 1954. The atmospheric solitary wave. *Bull. Amer. Meteorol. Soc.* **10**: 515–518.
- Ager, D. 1993. *The New Catastrophism. The Importance of the Rare Event in Geologic History*. Cambridge (UK): Cambridge University Press.
- Aghsaee, P., L. Boegman, and K.G. Lamb. 2010. Breaking of shoaling internal solitary waves. *J. Fluid Mech.* **659**: 289-317.
- Aguilar, D.A., and B.R Sutherland. 2006. Internal wave generation from rough topography. *Phys. Fluids* **18** : 066603. doi:10.1063/1.2214538.
- Airy, G.B. 1845. Tides and waves. *Encyclopedia Metropolitana*, section **392**: 241–396.
- Alpers, W. 1985. Theory of radar imaging on internal waves. *Nature* **314**, no. 6008 (March 21): 245–247.
- Amante, C. and B. W. Eakins, 2009, ETOPO1 1 Arc-Minute Global Relief Model: Procedures, Data Sources and Analysis. NOAA Technical Memorandum NESDIS NGDC-24. Boulder: U.S. Department of Commerce.
- Arnberger, H., and E. Arnberger. 2001. *The Tropical Islands of the Indian and Pacific Oceans*. Vienna: Austrian Academy of Sciences Press.
- ANSYS FLUENT Release 13. 2010. Canonsburg, PA (USA): ANSYS, Inc.

- Apel, J. 2002. Oceanic internal waves and solitons. In *An Atlas of Internal Solitary-like Waves and their Properties*, ed. C.R. Jackson and J.R. Apel. Rockville: Global Ocean Associates.
- . H.M. Byrne, J.R. Proni, and R.L. Charnell. 1975. Observations of oceanic internal and surface waves from the Earth Resources Technology Satellite. *J. Geophys. Res. (Oceans)* **80**, no. C6: 865–881.
- . J.R. Holbrook, A.K. Liu, and J.J. Tsai. 1985. The Sulu Sea internal soliton experiment. *J. Phys. Oceanogr.* **15**, no. 12 (December): 1625–1651.
- . L.A. Ostrovsky, Y.A. Stepanyants, and J.F. Lynch. January 2006. *Internal Solitons in the Ocean*. Woods Hole Oceanographic Institute, WHOI-2006-04.
- Ariyaratnam, J. 1998. Investigation of slope stability under internal wave action. Eng. (Hons.) thesis, Dept. of Environmental Eng., University of Western Australia, Australia.
- Arthur, R.S. 1954. Oscillations in sea temperature at Scripps and Oceanside piers. *Deep-Sea Res. (1953)* **2**, no. 2 (January): 107–121.
- Atwater, B.F., M.-R. Satoko, S. Kenji, T. Yoshinobu, U. Kazue, and D.K. Yamaguchi. 2005. *The Orphan Tsunami of 1700: Japanese Clues to a Parent Earthquake in North America*. Seattle: The University of Washington Press.
- Babkov, A.I. 1973. The results of interpreting internal wave measurements from vertical aerial photography (in Russian). In *Sb. Aerofotos'yenka – methodizucheniya prirodnoy sredy*. Leningrad: Izd-vo nauka.
- Baines, P. 1973. The generation of internal tides by flat-bump topography. *Deep Sea Res. Oceanogr. Abstr.* **20**:179–205.

- . 1974. The generation of internal tides over steep continental slopes. *Philos. Trans. R. Soc. London* **A277**: 27–58.
- . 1982. On internal tide generation models. *Deep Sea Res. Part A*. **29**, no. 3 (March): 307–338.
- . 1984. A unified description of two-layer flow over topography. *J. Fluid Mech.* **146**: 127–167.
- . 1986. Tides, internal waves, and near-critical bottom motions (Chapter 2). In *Baroclinic Processes on Continental Shelves*, ed. C.N.K. Moores. Washington, D.C.: American Geophysical Union.
- Bais, S. 2005. *The Equations – Icons of Knowledge*. Cambridge: Harvard University Press.
- Balmforth, N.J., G.R. Ierley, and W.R. Young. 2002. Tidal conversion by subcritical topography. *J. Phys. Oceanogr* **32**, no. 10 (October): 2900–2914.
- Bartsch-Winkler, S., and D.K. Lynch. 1988. Catalog of Worldwide Tidal Bore Occurrences and Characteristics. Circular no. 1022. Washington, D.C.: U.S. Geological Survey.
- Bascoum, W. 1980. *Waves and Beaches*. Garden City: Anchor Press/Doubleday. [Revised edition.]
- Batchelor, G.K. 1967. *An Introduction to Fluid Dynamics*. Cambridge (UK): Cambridge University Press.
- Bazin, H. 1865. Recherches expérimentales su la propogation des ondes [Experimental research regarding the propagation of waves]. *Mémoires présentés par drivers Savants à l'Académie des Sciences France* **19**: 495–644.

- Bell, T. 1975. Topographically-generated internal waves in the open ocean. *J. Geophys. Res.* **80**, no. 3: 320–327.
- Berntsen, J. 2008. Notes on different aspects of internal waves – including references. Unpublished manuscript dated March 13, 2008, downloaded from the Internet at <http://folk.uib.no/nmajb/waves.pdf>. Department of Mathematics, University of Bergen, Bergen, Norway.
- Betz, F., and H.H. Hess. 1942. The floor of the North Pacific Ocean. *Geog. Rev.* **32**, no. 1 (January):99–116.
- Biesel, F. 1952. Study of wave propagation in water of gradually varying depth. In *Proceedings of the NBS Semicentennial Symposium on Gravity Waves Held at the NBS held in Washington, D.C., June 18-19, 1951*, Washington, D.C.: National Bureau of Standards Circular 521.
- Bjerknes, V. and others. 1933. *Physikalische Hydrodynamik*. Berlin: J. Springer.
- Boegman, L., G.N. Ivey, and J. Imberger. 2005. The degeneration of internal waves in lakes with sloping topography. *Limnol. Oceanogr.* **50**, no. 5: 1620–1637.
- Bogucki, D., and C. Garrett. 1993. A simple model for the shear-influenced decay of an internal solitary wave. *J. Phys. Oceanogr.* **23**, no. 8 (August): 1767–1776.
- Bourgault, D., and D.E. Kelly. 2003. Wave-induced boundary mixing in a partially mixed estuary. *J. Mar. Res.* **61**, no. 5 (September 1): 553–576.
- . M.D. Blokhina, R. Mirshak, and D.E. Kelley. 2007. The fate of a shoaling internal solitary wavetrain. *Geophys. Res. Lett.* **34**, L03601, doi:10.1029/2006GL028462.

- . and C. Richards. 2007. A laboratory experiment on internal solitary waves. *Amer. J. Phys.* **75**, no. 7 (July): 666–670.
- . D.E. Kelley, and P.S. Galbraith. 2008. Turbulence and boluses on an internal beach. *J. Mar. Res.* **66**, no. 5 (September): 563–588.
- Boussinesq, J. 1872. Théorie des ondes et des remous qui se propagent le long d'un canal rectangulaire horizontal, en communiquant au liquide contenu dans ce canal des vitesses sensiblement pareilles de la surface au fond [Theory of the waves and eddies that propagate themselves alongside a horizontal rectangular channel, while communicating to the contained liquid in this speed noticeably similar canal of the surface to the bottom]. *Journal de Mathématiques Pures Appliquées* **17**, no. 17: 55–108.
- . 1877. Essai sur la théorie des eaux courantes [Tests on common water theories]. *Mémoires présentés par divers Savants à l'Académie des Sciences France* **23**:1–680.
- . 1903. *Théorie Analytique de la Chaleur [Analytical Theory of Heat]*. Vol. II. Paris: Gauthier-Villars.
- Brink K.H. 1989. The effect of stratification on seamount-trapped waves. *Deep Sea Res. Part A* **36**, no. 6 (June):825–844.
- . 1991. Coastal-trapped waves and wind driven currents over the continental shelf. *Annu. Rev. Fluid Mech.* **23**:389–412
- Briscoe, M. 1975. Internal waves in the ocean. *Rev. Geophys. Space Phys.* **13**, no. 3 (July): 591–598, 636–645.
- . 1975. Introduction to collection of papers on oceanic internal waves. *J. Geophys. Res.* **80**, no. 3: 289–290.

- . 1984. Oceanography: Tides, solitons, and nutrients. *Nature* **312**, no. 15 (November 1): 15.
- Broad, W.J. 2010. In deep sea, waves with a familiar curl. *New York Times*, sec. D ["Science"], p. D3, April 20.
- Bullough, R.K. 1988. The wave 'par excellence,' the solitary, progressive wave of great equilibrium of the fluid – An early history of the solitary wave. In *Solitons*, ed. M. Lakshmanan, 150-281. New York: Springer.
- Cacchione, D.A., L.F. Pratson, and A.S. Ogston. 2002. The shaping of continental slopes by internal waves. *Science* **296**, no. 5568 (April 26): 724–727.
- . and L.F. Pratson. 2004. Internal tides and the continental slope. *Amer. Sci.* **92**, no. 2 (March-April): 130–137.
- Campbell, D. 1989. Introduction to nonlinear phenomena. In *Lectures in the Sciences of Complexity*, ed. D.L. Stein, 3–105. Redwood City, California: Addison-Wesley.
- Carsola, A.J., and E.B. Callaway. 1962. Two short-period internal wave frequency spectra in the sea off southern California. *Limnol. Oceanogr.* **VII**, no. 2 (April): 115–120.
- Carter, G.S., M.C. Gregg, and R.-C Lien. 2005. Internal waves, solitary-like waves, and mixing on the Monterey Bay shelf. *Cont. Shelf Res.* **25**, nos. 12-13 (August): 1499–1520.
- Cartwright, D.E. 1999. *Tides: A Scientific History*. Cambridge, United Kingdom: Cambridge University Press.

- Chandrasekhar, S. 1961. The stability of superimposed fluids: The Kelvin-Helmholtz instability (Chapter XI). In *Hydrodynamic and Hydromagnetic Stability*. London: Oxford/Clarendon.
- Chanson, H. 2009. Current knowledge in hydraulic jumps and related phenomena. A survey of experimental results. *Eur. J. Mech. B/Fluids* **28**: 191–210
- . 2010. Tidal bores, aegir and pororoca: The geophysical wonders. In Proceedings of the 17th Congress of IAHR Asia and Pacific Division, Auckland, New Zealand, February 21-24 2010. ed., B. Melville, G. De Costa, and T. Swann. The University of Auckland: International Association of Hydro-Environment Engineering and Research—Asia and Pacific Division. [Preprint]
- Chapman, D.C. 1989. Enhanced subinertial diurnal tides over isolated topographic features. *Deep Sea Res. Part A* **36**, no. 6 (June):815–824.
- Chen, C.-Y., J.R.-C. Hsu, C.-W. Chen, H.-H. Chen, C.-F. Kuo, and M.-H. Cheng. 2007. Generation of internal solitary wave by gravity collapse. *J. Mar. Sci. Technol.* **15**, no. 1: 1–7.
- Chen, H.H. 2004. Experimental study on the propagation and reflection of internal solitary wave from a uniform slope. M.Sc. thesis, National Sun Yat-sen University, Kaohsiung, Taiwan R.O.C.
- Chen, P. 2006. Laboratory Experiments on Internal Wave Evolution on Uniform Slopes and Topographic Sills. PhD diss., National Sun Yat-sen University, Kaohsiung, Taiwan R.O.C.
- Cheng, M.-H., 2006. Numerical modeling for internal solitary wave evolution on variable topography. M.Sc. thesis, National Sun Yat-sen University, Kaohsiung, Taiwan R.O.C.

- Chhibber, S., G. Apostolakis, and D. Okrent, 1992. A Taxonomy of Issues Related to the Use of Expert Judgments in Probabilistic Safety Studies. *Reliab. Eng. Syst. Saf.* **38**, nos. 1–2: 27–45.
- Chow, C.-Y. 1983. *An Introduction to Computational Fluid Mechanics*. New York: John Wiley and Sons, 1979. Corrected reprint. Boulder: Seminole Press.
- Coleman, H.W., and W.G. Steele. 1995. Engineering application of experimental uncertainty analysis. *AIAA J.* **33**, no. 10 (October): 1888–1896.
- Colton, J.B., Jr. 1972. *Short-term variations in estimates of chlorophyll abundance*. International Commission for the Northwest Atlantic Fisheries, Research Bulletin no. 9.
- Colvocoresses, A.P. 1974. *Remote Sensing Platforms*. Circular no. 693. Washington, D.C.: U.S. Geological Survey.
- COMSOL Multiphysics Modeling and Engineering Simulation Software. 1998. Version 4.1. Stockholm, Sweden: COMSOL AB.
- Courant, R., K. Friedrichs, and H. Levy. 1967. On the partial difference equations in mathematical physics. *Bell Sys. Tech. J.* **11**, no. 2 (March): 215–234. [English translation of 1928 paper appearing in *Mathematische Annalen* **100**, 32–74.]
- Cox, C., and W. Munk. 1954. Measurement of the roughness of the sea surface from photographs of the Sun's glitter. *J. Opt. Soc. Amer.* **44**, no. 11 (November): 838–850.
- Craik, A. D. D. 2004. The origins of water wave theory. *Annu. Rev. Fluid Mech.* **36**: 1–28.

- . 2005. George Gabriel Stokes on water wave theory. *Annu. Rev. Fluid Mech.* **37**: 23–42.
- Criminale, W. O., Jr. 1973. On breaking of internal gravity waves. In International Association for Hydraulic Research and the Academy of Sciences of the U.S.S.R. *International Symposium on Stratified Flows held in Novosibirsk, August 29-31, 1972*, 175–192. New York: American Society of Civil Engineers.
- Cushman-Roisin, B., and J-M. Beckers 2009. *Introduction to Geophysical Fluid Dynamics*. New York: Academic Press.
- Dalkey, N., and O. Helmer. 1963. An experimental application of the Delphi Method to the use of experts. *Management Science* **9**, no. 3 (April): 458–467.
- Daly, R.A. 1936. Origin of submarine canyons. *Am. J. Sci. Series 5*, **31** (June): 401-420
- Daniel, C., F.S. Wood, and J.W. Gorman. 1971. *Fitting Equations to Data – Computer Analysis of Multifactor Data for Scientists and Engineers*. New York: John Wiley and Sons.
- Darrigol, O. 2003. The spirited horse, the engineer, and the mathematician: Water waves in the nineteenth-century hydrodynamics. *Arch. Hist. Exact Sci.* **58**, no. 1 (November): 21–95.
- Davis, J.C., and U.C. Herzfeld, ed. 1993. *Computers in Geology: 25 Years of Progress*. Studies in Mathematical Geology, vol. 5. New York: Oxford University Press.
- Defant, A. 1959. Über interne Gezeitenwellen und ihre Stabilitätsbedingungen [About internal tidal waves and their stability conditions]. *Arch. Meteor. Geophys. Bioklimatol. Ser. A*, no. 1: 39–1.

- . 1961. “Internal Waves (Chapter XVI)” in *Physical Oceanography*. vol. 2. New York: Pergamon.
- Dickey, T. 1990. Physical-optical-biological scales relevant to recruitment in large marine ecosystems. In *Large Marine Ecosystems: Patterns, Processes, and Yields*, ed. K. Sherman, L.M. Alexander, and B.D. Gold, 82-98. Washington, D.C.: American Association for the Advancement of Sciences.
- . 1991. The emergence of concurrent high-resolution physical and bio-optical measurements in the upper ocean and their applications. *Rev. Geophys.* **29**, no. 3: 383–413.
- . 2003. Emerging ocean observations for interdisciplinary data assimilation systems. *J. Mar. Sys.* **40-41** (April): 5-48.
- Dietz, R.S. 1947. Aerial photographs in the geologic study of shore features and processes. *Photogram. Eng.* **14**, no. 4: 537–545.
- Doel, R.E., T.J. Levin, and M.K. Marker. 2006. Extending modern cartography to the ocean depths: military patronage, Cold War priorities, and the Heezen-Tharp mapping project, 1952-1959. *J. Hist. Geog.* **32**, no. 2 (July): 605–626.
- Drazin, P.G. 2002. *Introduction to Hydrodynamic Stability*. Cambridge Texts in Applied Mathematics, no. 32. Cambridge (UK): Cambridge University Press.
- Egbert, G.D., and R.D. Ray. 2000. Significant tidal dissipation of tidal energy in the deep ocean inferred from satellite altimeter data. *Nature* **405** (June 15): 775–778.
- Eisenberg, N.A., M.P. Lee, M.V. Federline, S. Wingefors, J. Andersson, S. Norrby, B. Sagar, and G. Wittmeyer. 1998. Review of performance

- assessment model validation literature. In *Regulatory Perspectives on Model Validation in High-level Radioactive Waste Management Programs: A Joint NRC/SKI White Paper*. Washington, D.C.: U.S. Nuclear Regulatory Commission/Swedish Nuclear Power Inspectorate. NUREG-1636/SKI Report 99:2.
- Ekman, V.W. 1904. On dead water, ed. F. Nansen. *Norwegian North Polar Expedition, 1893-1896, Scientific Results*. London: Longmans.
- El-Sabh, M.I., R. Glombitza, and O.M. Johannessen. 1971. On the vertical fluctuations of hydrochemical parameters in the Gulf of St. Lawrence, 1969. McGill University, manuscript No. 19. Montreal: Marine Sciences Center.
- Elmore, W.C., and M.A. Heald. 1969. *Physics of Waves*. New York: McGraw-Hill.
- Emery, K. 1956. Deep standing internal waves in California basins. *Limnol. Oceanogr.* **1**, no. 1 (January): 35–41.
- . 1965. Characteristics of the continental shelves and margins. *AAPG Bull.* **49**, no. 9 (September): 1379–1384.
- . and C.G. Gunnerson. 1973. Internal swash and surf. *Proc. Nat. Acad. Sci. U.S.A.* **70**, no. 8 (August): 2379–2380.
- Emmerson, G.S. 1977. *John Scott Russell: A Great Victorian Engineer and Naval Architect*. London: Murray.
- Eriksen, C.C. 1978. Measurements and models of fine structure, internal gravity waves, and wave breaking in the deep ocean. *J. Geophys. Res.* **83**, no. C6 (June 20): 2989–3009.

- Ernshaw, S. 1847. The mathematical theory of the two great solitary waves of the first order. *Trans. Cambridge Philos. Soc.* **8**: 326–341.
- Etnoyer, P.J., J. Wood, and T.C. Shirley. 2010. How large is the seamount biome (BOX 12)? *Oceanog.* **23**, no. 1 (March): 206–209.
- Ezyfit Version 2.30. Paris, Université Paris-Sud11, Laboratoire Fluides, Automatique et Systèmes Thermiques (FAST): F. Moisy, February 5, 2009. [Freeware application developed for MATLAB.]
- Farmer, D. 1980. Tidal interactions of stratified flow with a sill in Knight Inlet. *Deep Sea Res. Part A* **27**, no. 3-4 (April): 239–246.
- . and J.D. Smith. 1978. Nonlinear waves in a fjord. In *Hydrodynamics of Estuaries and Fjords: Proceedings of the 9th International Liège Colloquium on Ocean Hydrodynamics*, ed. J.C.J. Nihoul. Elsevier Oceanography Series Volume 23. Amsterdam: Elsevier North-Holland.
- . and L. Armi. 1999. The generation and trapping of solitary waves over topography. *Science* **283**, no. 5399 (January 8): 188–190.
- Fedorov, K. N., and A.I. Ginsburg, eds. 1992. *The Near-surface Layer of the Ocean*. Utrecht, The Netherlands: VSP BV.
- Ferziger, J.H., and M. Perić. 2002. *Computational Methods for Fluid Dynamics*. 3rd revised ed. Berlin: Springer-Verlag.
- Fischer, W.A. (ed.). 1975. History of Remote Sensing (Chapter 2). In *Manual of Remote Sensing*, ed. R.G. Reeves, vol. 2. Falls Church: American Society of Photogrammetry.
- Fisher, R.A. 1932. *Statistical Methods for Research Workers*. 4th ed. Edinburgh: Oliver & Boyd.

- Fjeldstad, J.E. 1933. Interne welle [Internal waves]. *Geofysiske Publikasjoner. Geophysica Norvegica* **10**, no. 6: 1–35.
- FLOW-3D. 2010. Santa Fe, NM (USA): FLOW Science.
- Fraser, D.M., R. Pillay, L. Tjatindi, and J.M. Case. 2007. Enhancing the learning of fluid mechanics using computer simulations. *J. Eng. Educ.* **96**, no. 4 (October): 381–388.
- Fromm, J.E. 1963. A method for computing non-steady, incompressible viscous fluid flows. Report no. LA-2910. Los Alamos: Los Alamos Scientific Laboratory.
- . and F.H. Harlow. 1963. Numerical solution of the problem of vortex street development. *Phys. Fluids* **7**, no. 6 (July): 975–982.
- Froude, W. 1862. *On the rolling of ships. Appendix 2: On the dynamical structure of oscillating waves [Read at the Second Session of the Institution of Naval Architects, March 1, 1861]*. Ed. Transactions of the Institution of Naval Architects. London (West Strand): Parker, Son, and Bourn.
- Fu, L.-L, and B. Holt. 1982. *Seasat Views Oceans and Sea Ice with Synthetic-Aperture Radar*. Pasadena: National Aeronautics and Space Administration. Jet Propulsion Laboratory, JPL Publication 81–120.
- Galperin, B., S. Sukoriansky, and P.S. Anderson. 2007. On the critical Richardson number in stability stratified turbulence. *Atmos. Sci. Lett.* **8**, no. 3 (September): 65–69.
- Galvin, C.J., Jr. 1968. Breaker type classification on three laboratory beaches. *J. Geophy. Res. (Solid Earth)* **73**, no. 12 (15 June): 3651–3659.

- Gardner, C.S., J.M. Greene, M.D. Kruskal, and R.M. Miura. 1967. Method for solving the Korteweg-de Vries equation. *Phys. Rev. Lett.* **19**, no. 19 (November 6): 1095–1097.
- Gargett, A. 1976. Generation of internal waves in the Strait of Georgia, British Columbia. *Deep-Sea Res. Oceanogr. Abstr.* **23**, no.1 (January): 17–20.
- . and B.A. Hughes. 1972. On the interaction of surface and internal waves. *J. Fluid Mech.* **52**: 197–181.
- Garrett, C. 2003. Ocean science: Internal tides and ocean mixing. *Science* **301**, no. 5641 (September 26): 1858–1859.
- . and W. Munk. 1972. Oceanic mixing by breaking internal waves. *Deep-Sea Res. Oceanogr. Abstr.* **19**, no. 12 (December): 823–832.
- . and W. Munk. 1972. Space-time scales of internal waves. *Geophys. Fluid Dyn.* **2**: 225–264.
- . and W. Munk. 1975. Space-time scales of internal waves: A progress report. *J. Geophys. Res.* **80**, no. 3: 291–297.
- . and W. Munk. 1979. Internal waves in the ocean. *Annu. Rev. Fluid Mech.* **11**: 339–369.
- . and L. St. Laurent. 2002. Aspects of deep ocean mixing. *J. Oceanogr. Soc. Japan* **58**, no. 1: 11–24.
- . and E. Kunze. 2007. *Internal tide generation in the deep ocean*. *Annu. Rev. Fluid Mech.* **39**: 57–87.
- . and P. Müller, ed. 2007. *Extreme Events – Proceedings of the 15th 'Aha Huliko'a, Hawaiian Winter Workshop held in Manoa, January 23–26, 2007*. Honolulu: University of Hawaii.

- Gerkema, T. 1996. A unified model for the generation and fission of internal tides in a rotating ocean. *J. Marine Res* **54**, no. 3 (May): 421–450.
- . and J.T.F. Zimmerman. 1995. Generation of nonlinear internal tides and solitary waves. *J. Phys. Oceanogr.* **25**, no. 6 (June): 1081–1094.
- Gerstner, F.G. 1802. *Theory of Waves*. Institute of Engineering Research, Waves Research Laboratory, no. 3, issue 339. Berkeley: University of California. [1954 English translation of “*Theorie der Wellen*.”]
- Gould, W.J. 1971. Spectral characteristics of some deep ocean current record from the eastern North Atlantic. *Philos. Trans. R. Soc. London* **A270**, no. 1206 (November 4): 437–450.
- Gregg, M. 1973. The microstructure of the ocean. *Sci. Amer.* **228**, no. 2 (February): 65–77.
- . 1980. Microstructure patches in the thermocline. *J. Phys. Oceanogr.* **10**, no. 6 (June): 915–943.
- . 1991. The study of mixing in the ocean: A brief history. *Oceanogr.* **4**, no. 1 (April): 39–45.
- Grue, J., H.A. Friis, E. Palm, and P.-O. Rusås. 1997. A method for computing unsteady fully nonlinear interfacial waves. *J. Fluid Mech.* **351**, no. 2: 223–252.
- . A. Jensen, P.-O. Rusås, and J.K. Sveen. 1999. Properties of large-amplitude internal waves. *J. Fluid Mech.* **380**: 257–278.
- Guo, Y., J.K. Sveen, P.A. Davies, J. Grue, and P. Dong. 2004. Modeling the motion of an internal solitary wave over a bottom ridge in a stratified fluid. *Environ. Fluid Mech.* **4**, no. 4: 415–441.

- Harlow, F.H. 1955. A Machine Calculation Method for Hydrodynamic Problems. Report no. LAMS-1956. Los Alamos: Los Alamos Scientific Laboratory.
- . 1987. PIC [Particle-in-Cell] and its Progeny - *Los Alamos National Laboratory Workshop on Particle Methods in Fluid Dynamics and Plasma Physics held in Los Alamos, April 13-15, 1987*. Report CONF-8704168-1. Los Alamos: Los Alamos Scientific Laboratory.
- . and A.A. Amsden. 1970. Fluid Dynamics: An Introductory Text. Report no. LA-4100. Los Alamos: Los Alamos Scientific Laboratory (May).
- . and E. Fromm. 1965. Computer experiments in fluid dynamics. *Sci. Amer.* **212**, no. 3 (March): 104–110.
- . and J.E. Welch. 1965. Numerical calculation of time-dependent viscous incompressible flow of fluid with free surface. *Phys. Fluids* **8**, no. 12 (December): 2182–2189.
- . J.P. Shannon, and J.E. Welch. 1965. Liquid waves by computer. *Science* **149**, no. 3688 (September 3): 1092–1093.
- Haurwitz, B. 1954. The occurrence of internal tides in the ocean. *Arch. Meteor. Geophys. Bioklimatol. Serie. A* **7**, no. 1 (June): 406–424.
- Haury, L.R., M.G. Briscoe, and M.H. Orr. 1979. Tidally generated internal wave packets in Massachusetts Bay. *Nature* **278**, no. 5702 (March 22): 312–317.
- Heezen, B.C. 1960. A rift in the ocean floor. *Sci. Amer.* **203**, no. 4 (October): 98–110.

- . M. Tharp, and M. Ewing. 1959. The North Atlantic Ocean. In *The Floors of the Ocean*. GSA Special Paper 65. Boulder: Geological Society of America.
- . and M. Tharp. 1977. *World Ocean Floor Panorama*. Scale: 1:23,230,300. 1 sheet. New York: Lamont-Doherty Geological Observatory of Columbia University.
- Heirtzler, J.R. 1968. Sea-floor spreading. *Sci. Amer.* **219**, no. 6 (December): 60–70.
- . P.T. Taylor, R.D. Ballard, and R.L. Houghton. 1977. A visit to the New England Seamounts. *Amer. Sci.* **65**, no. 4: 466–472.
- Helfrich, K.R. 1992. Internal solitary wave breaking and run-up on a uniform slope. *J. Fluid Mech.* **243**: 133–154.
- . and W.K. Melville. 1986. On long nonlinear internal waves over slope-shelf topography. *J. Fluid Mech.* **167**: 285–308.
- . and W.K. Melville. 2006. Long nonlinear internal waves. *Annu. Rev. Fluid Mech.* **38**: 395–425.
- Helland-Hansen, B., and W. Ekman. 1909. The Norwegian Sea. Its Physical Oceanography Based Upon the Norwegian Researches 1900-1904. Report on Norwegian Fishery and Marine-Investigations 11, nos. 1 and 2. Kristiania (Norway): Det Mallingske Bogtrykkeri.
- Heller, V., J. Unger, and W. Hagar. 2005. Tsunami run-up—A hydraulic perspective. *J. Hydr. Eng.* 131, no. 9 (September): 743–747.
- Hess, H.H. 1946. Drowned ancient islands of the Pacific Basin. *Am. J. Sci.* **244** (November): 772–791.

- Heywood, K.J., E.D. Barton, and J.H. Simpson. 1990. The effects of flow disturbance by an oceanic island. *J. Marine Res* **48**, no. 1 (February): 55–73.
- Hibiya, T. 1986. Generation mechanism of internal waves by tidal flow over a sill. *J. Geophys. Res. (Oceans)* **91**, no. C6: 7697–7708.
- . 2004. Internal wave generation by tidal flow over a continental shelf. *J. Oceanogr. Soc. Japan* **63**: 637–643.
- Hickey, B.M. 1995. Coastal submarine canyons. In, ed. P. Müller and D. Henderson, 199–206. Honolulu: University of Hawaii.
- Hildebrand, F.B. 1968. *Finite-Difference Equations and Simulations*. Englewood Cliffs: Prentice-Hall.
- Hirt, C.W., B.D. Nichols, and N.C. Romero. 1975. SOLA – A Numerical Solution Algorithm for Transient Fluid Flows. Report no. LA-5852. Los Alamos: Los Alamos Scientific Laboratory.
- Holloway, P.E., and M.A. Merrifield. 1999. Internal tide generation by seamounts, ridges, and islands. *J. Geophys. Res.* **104**: 25,937–25,952.
- Hora, S.C., and R.L. Iman. 1989. Expert Opinion in Risk Analysis: The NUREG-1150 Methodology. *Nucl. Sci. Eng.* **102**, no. 4: 323–331.
- Hotchkiss, F.S., and C. Wunsch. 1982. Internal waves in Hudson Canyon with possible geological implications. *Deep Sea Res. Part A.* **29**, no. 4 (April): 415–422.
- Howard, L.N. 1961. Note on a paper of John W. Miles. *J. Fluid Mech.* **10**, no. Part 4: 509–512.
- . and S.A. Maslowe. 1973. Stability of stratified shear flows. *Boundary-Layer Meteorol.* **4**, no. 1-4 (April): 511–523.

- Hsu, M.-K, A.K. Liu, and C. Liu. 2000. A study of internal waves in the China Seas and Yellow Sea using SAR. *Cont. Shelf Res.* **20**, no. 4-5 (March): 389–410.
- Hughes, B.A. 1985. The effect of internal waves on surface wind waves 2. Theoretical analysis. *J. Geophys. Res. (Oceans)* **83**, no. C1: 455–465.
- Hunter, R.L., and C.J. Mann, eds. 1989. Techniques for determining probabilities of events and processes affecting the performance of geologic repositories: Literature review. NUREG/CR-3964, vol. 1. Washington, D.C.: U.S. Nuclear Regulatory Commission. [Prepared by the Sandia National Laboratory.]
- Ichiye, T. 1950. On stationary internal waves caused by the bottom configuration [in Japanese]. *J. Oceanogr. Soc. Japan* **6**, no. 1: 1–7.
- . 1966. Annotated bibliography on internal waves. *J. Oceanogr. Soc. Japan* **22**, no. 5: 201–222.
- Imberger, J. 1987. Introduction to papers from the IUTAM Symposium on mixing in stratified fluids. *J. Geophys. Res.* **92**, no. C5 (May 15): 5229.
- Ingmanson, D.E., and W.J. Wallace. 1973. *Oceanology: An Introduction*. Belmont: Wadsworth.
- Iribarren, C.R., and C. Nogales. 1949. Protection des ports [Protection of ports]. In *Proceedings of the 17th International Navigation Congress, Lisbon, Portugal, December 1949*. Section 2, comm. 4: 31–80.
- Iversen, H.W. 1951. Waves in shoaling water. In *Manual of Amphibious Oceanography*, ed. R.L. Wiegel. Washington, D.C.: Office of Naval Research.

- Ivey, G.N., P. de Silva, and J. Imberger. 1995. Internal waves, bottom slopes, and boundary mixing. In *Topographic Effects in the Ocean – Proceedings of the 8th 'Aha Huliko'a, Hawaiian Winter Workshop held in Manoa, January 17-20, 1995*, ed. P. Müller and D. Henderson, 199–206. Honolulu: University of Hawaii.
- Jackson, C.R. 2004. *An Atlas of Internal Solitary-like Waves and their Properties*. 2nd ed. Alexandria: Global Ocean Associates.
- . 2009. An empirical model for estimating the geographic location of nonlinear internal solitary waves. *J. Atmos. Oceanic Technol.* **26**, no. 10 (October): 2243–2255.
- Jacoby, W.R. 1981. Modern concepts of earth dynamics anticipated by Alfred Wegener. *Geology* **9**, no. 1 (January): 25–27.
- Kao, T. and H.-P. Pao. 1980. Wake collapse in the thermocline and internal solitary waves. *J. Fluid Mech.* **97**: 115–127.
- . F.S. Pan, and D. Renouard. 1985. Internal solitons on the pycnocline: Generation, propagation, shoaling and breaking over a slope. *J. Fluid Mech.* **159**: 19–53.
- . H.-P. Pao, and C. Park. 1978. Surface intrusions, fronts, and internal waves: A numerical study. *J. Geophys. Res. (Oceans)* **83**, no. C9: 4641–4650.
- Kaufman, W.J., III, and L.L. Smarr. 1993. *Supercomputing and the Transition of Science*. New York: W.H. Freeman.
- Kaup, D.J., and A.C. Newell. 1978. Solitons as particles, oscillators, and in slowly changing media: A singular perturbation theory. *Philos. Trans. R. Soc. London* **A361**: 413–446.

- Keating, B.H., P. Fryer, R. Batiza, and G.W. Boehlert. ed. 1987. *Seamounts, Islands, and Atolls*. Geophysical Monograph, vol. 43. Washington, D.C.: American Geophysical Union.
- Keller, J.B. 1948. The solitary wave and periodic waves in shallow water. *Commun. Pure Appl. Math.* **1**, no. 4 (December): 323–329.
- Keulegan, G. 1948. Gradual damping of solitary wave. *J. Res. Nat. Bur. Stand.* **40** (June): 487–498. [Research Paper RP1895]
- . 1953. Characteristics of internal solitary waves. *J. Res. Nat. Bur. Stand.* **51**, no. 3 (September): 133–140. [Research Paper RP2442]
- . 1959. Energy dissipation in standing waves in rectangular basins. *J. Fluid Mech.* **6**: 33–50.
- Kinsman, B. 1965. *Wind Waves — Their Generation and Propagation on the Ocean Surface*. Englewood Cliffs: Prentice-Hall.
- Knickerbocker, C.J., and A.C. Newell. 1980. Internal solitary wave near a turning point. *Phys. Lett. A* **75**, no. 5 (February 4): 326–330.
- Koch, C., and H. Chanson. 2008. Turbulent mixing beneath an undular bore front. *J. Coastal Res.* **24**, no. 4 (July): 999–1007.
- . 2009. Turbulence measurements in positive surges and bores. *J. Hydraulic Res.* **47**, no. 1 (January): 29–40.
- Komar, P.D. 1976. *Beach Processes and Sedimentation*. Englewood Cliffs: Prentice-Hall.
- Koop, C.G., and G. Butler. 1981. An investigation of internal solitary waves in a two-fluid system. *J. Fluid Mech.* **112**: 225–251.

- Korteweg, D.J., and G. de Vries. 1895. On the change of the form of long waves advancing in a rectangular canal and on a new type of long stationary waves. *Philos. Mag.* **39**: 422–433.
- Kunze, E., L.K. Rosenfeld, G.S. Carter, and M.C. Gregg. 2002. Internal waves in Monterey submarine canyon. *J. Phys. Oceanogr.* **32**, no. 6 (June): 1890–1913.
- . and S.G. Llewellyn-Smith. 2004. The role of small-scale topography in turbulent mixing of the global ocean. *Oceanogr.* **17**, no. 1 (2004): 55–64.
- Kuo, C.-F. 2005. Experimental study on the evolution and effect of bottom obstacle on internal solitary wave. M.Sc. thesis. Kaohsiung, Taiwan R.O.C.
- LaFond, E. 1959. Sea surface features and internal waves in the sea. *Indian J. Meteorol. Geophys.* **10**, no. 4 (October): 415–419.
- . 1961a. Internal waves in shallow water. *J. Mar. Res.* **19**, no. 1: 33–39.
- . 1961b. Internal wave motion and its geological significance. In *Mahadevan Volume: A Collection of Geological Papers*. Hyderabad (India): Osmania Univ. Press, pp. 61–77.
- . 1962. Internal Waves (Chapter 22). In *The Sea. Ideas and Observations on Progress in the Study of the Seas*, ed. M.N. Hill. New York: Interscience.
- . and C.P. Rao. 1954. *Vertical oscillations of tidal periods in the temperature structure of the sea*. Visakhapatnam, India: Andhra University, Memoirs, vol. 1.

- Lahey Fortran 90 Version 4.0. 1997. Incline Village, NV: Lahey Computer Systems, Inc.
- Lamb, H. 1932. *Hydrodynamics*. 6th ed. Cambridge, UK: Cambridge University Press. [Dover Press (New York) reprint of original 1879 publication.]
- Lamb, K.G. 1994. Numerical experiments of internal wave generation by strong tidal flow across a finite amplitude bank edge. *J. Geophys. Res. (Oceans)* **99**, no. C1: 843–864.
- Lapidus, L., and G.F. Pinder. 1982. *Numerical Solution of Partial Differential Equations in Science and Engineering*. New York: Wiley-Interscience.
- Laplace, P-S Marquis de. 1776. Recherches sur quelques points du système du monde (XXV-XXVII). *Académie (Royale) des Sciences, Mémoires (de physique et de mathématiques)* **9**, no. 88: 75–182.
- Lavelle, W., and C. Mohn, 2010. Motion, commotion, and biophysical connections at deep ocean seamounts. *Oceanogr.* **23**, no. 1 (March): 90–103.
- Lawrence, D. 1999. Mountains under the sea: Marie Tharp's maps of the ocean floor shed light on the theory of continental drift. *Mercator's World* **4**, no. 6 (November/December): 36–43.
- Lee, O.S. 1961. Observations on internal waves in shallow water. *Limnol. Oceanogr.* **6**, no. 3: 312–321.
- Ledwell, J.R., E.T. Montgomery, K.L. Polzin, L.C. St. Laurant, R.W. Schmidt, and J.M. Toole. 2000. Evidence of enhanced mixing over rough topography in the abyssal ocean. *Nature* **403** (January 30): 179–182.

- Legg, S., and K.M.H. Huijts. 2006. Preliminary simulations of internal waves and mixing generated by finite amplitude tidal flow over isolated topography. *Deep Sea Res. Part II* **53**, nos. 1–2 (January):140–156.
- . and J. Klymak. 2008. Internal hydraulic jumps and overturning generated by tidal flow over a tall steep ridge. *J. Phys. Oceanogr.* **38**, no. 9 (September): 1949–1964.
- Leichhter, J.J., S.R. Wing, S.L. Miller, and M.W. Denny. 1996. Pulsed delivery of subthermocline water to Conch Reef (Florida Keys) by internal tidal bores. *Limnol. Oceanogr.* **41**, no. 7: 1490–1501.
- Leone, C., H. Segur, and J.L. Hammack. 1982. Viscous decay of long internal solitary waves. *Phys. Fluids* **25**, no. 6 (June): 942–944.
- Levine, M.D. 1983. Internal waves in the ocean: A review. *Rev. Geophys.* **21**, no. 5: 1206–1216.
- Li, H., and H. Yamazaki. 2001. Observations of a Kelvin-Helmholtz billow in the ocean. *J. Oceanogr. Soc. Japan* **57**, no. 6 (December): 709–721.
- Li, X., P. Clemente-Colón, and K.S. Friedman. 2000. Estimating oceanic mixed-layer depth from internal wave evolution observed from Radarsat-1 SAR. *Johns Hopkins APL Tech. Digest* **21**, no. 1 (January–March): 130–135.
- Lighthill, J. 1978. *Waves in Fluids*. Cambridge, UK: Cambridge University Press.
- Liu, C.-T., R. Pinkel, J. Klymak, M.-K. Hsu, H.-W. Chen, and C. Villanoy. 2006. Nonlinear Internal Waves from the Luzon Strait, *Eos Trans. AGU.* **87**, no. 42 (October 17): 491–451.

- Long, R.R.. 1953. Some aspects of the flow of stratified fluids: I. A theoretical investigation. *Tellus* **5**, no. 1 (February):42–58.
- . 1954. Some aspects of the flow of stratified fluids: II. Experiments with a two-fluid system. *Tellus* **5**, no. 2 (May):97–115.
- . 1955. Some aspects of the flow of stratified fluids: II. Continuous density gradients. *Tellus* **7**, no. 3 (August):341–357.
- . 1956. Solitary waves in the one- and two-fluid systems. *Tellus* **8**, no. 4 (November): 460–471.
- . 1965. On the Boussinesq approximation and its role in the theory of internal waves. *Tellus* **17**, no. 1 (February): 46–52.
- . 1971. The steepening of long, internal waves *Tellus* **24**, No. 2 (April): 88–99.
- . 1972. Stratified Flow in *The Illustrated Experiments in Fluid Mechanics: The NCFMF Book of Film Notes*. National Committee for Fluid Mechanics Films. Cambridge (MA): The MIT Press.
- Lowman, P. D., Jr. 1999. Landsat and Apollo: The forgotten legacy. *Photogram. Engin. Remote Sens.* **65**, no. 10 (October): 1143–1147.
- Lui, A.K., Y.S. Chang, M.-K Hsu, and H.K. Liang. 1998. Evolution of nonlinear internal waves in the South China Seas. *J. Geophys. Res.* **103**, no. C4: 7995–8008.
- Lynch, D.K. 1982. Tidal bores. *Sci. Amer.* **247**, no. 4 (October): 146–156.
- Malandain, M.M. 1988. La Seine au Temps du Mascaret [The Seine River at the Time of the Mascaret]. *Le-Chasse-Marée* **34**: 30–45.

- Martin, A., S.A. Walker, and W.J. Easson. 1998. An experimental investigation of solitary internal waves. In *Proceedings of the 17th Internal Conference on Offshore Mechanical and Arctic Engineering held in Lisbon, Portugal, July 5–9, 1998*. New York: American Society of Mechanical Engineers.
- Mason, M.A. 1952. Some observations of breaking waves. In *Proceedings of the NBS Semicentennial Symposium on Gravity Waves Held at the NBS held in Washington, D.C., June 18-19, 1951*, Washington, D.C.: National Bureau of Standards Circular 521.
- MATLAB® and SIMULINK® - Student Version 7.7.0.471 (R2008b). 2008. Natick, MA (USA): The Mathworks.
- Matsuno, T., T. Hibiya, S. Kanari, and C. Kobayashi. 1997. Small scale internal waves and turbulent fluctuations near the continental shelf break in the East China Sea. *J. Oceanogr. Soc. Japan.* **53**, no. 3: 259–269.
- Maury, M.F. 1861. *The Physical Geography of the Sea and its Meteorology*. New York: Harper.
- Maxworthy, T. 1979. A note on the internal solitary waves produced by tidal flow over a three dimensional ridge. *J. Geophys. Res.* **84**, no. C1: 338–346.
- . 1980. On the formation of nonlinear internal waves from the gravitational collapse of mixed regions in two and three dimensions. *J. Fluid Mech.* **96**, no. 1: 47–64.
- McBirney, A.R. 1963. Factors governing the nature of submarine volcanism. *Bull. Volcanol.* **26**, no. 1: 455–469.
- . 1971. Oceanic volcanism: A review. *Rev. Geophys.* **9**, no. 3: 523–556.

- McCowan, J. 1891. On the solitary wave. *Philos. Mag.* **32**, series 5: 45–58.
- McKenzie, P. 1958. Rip-current systems. *J. Geol.* **66**, no. 2 (March): 103–113.
- Melville, W.K., and K.R. Helfrich. 1987. Transcritical two-layer flow over topography. *J. Fluid Mech.* **178**: 31–52.
- Mei, C.C., and P.L.-F. Liu. 1993. Surface waves and coastal dynamics. *Annu. Rev. Fluid Mech.* **25**: 215–240.
- Menard, W. 1964. *Marine Geology of the Pacific*. New York: McGraw-Hill.
- . 1986. *Islands*. New York: W.H. Freeman.
- . and S.M. Smith. 1966. Hypsometry of ocean basin provinces. *J. Geophys. Res.* **71**, no. 18: 4305–4325.
- Meyer, M.A., and J.M. Booker. 1989. Eliciting and analyzing expert judgment – A practical guide. NUREG/CR-5424. Washington, D.C.: U.S. Nuclear Regulatory Commission. [Prepared by the Los Alamos National Laboratory.]
- Michallet, H., and E. Barthélemy. 1998. Experimental study of interfacial solitary waves. *J. Fluid Mech.* **366**: 159–177.
- . and G.N. Ivey. 1999. Experiments on mixing due to internal solitary waves breaking on uniform slopes. *J. Geophys. Res. (Oceans)* **104**, no. C6 (June 15): 13,467–13,477.
- Midorikawa, K. 1977. The effect of tidal currents on internal waves. *J. Oceanogr. Soc. Japan.* **33**: 311–319.
- Miles, J. 1961. On the stability of heterogeneous shear flow. *J. Fluid Mech.* **10**: 96–508.

- . 1963. On the stability of heterogeneous shear flow. Part 2. *J. Fluid Mech.* **16**: 209–227.
- . 1980. Solitary waves. *Annu. Rev. Fluid Mech.* **12**: 11–43.
- . 1981. The Korteweg – de Vries equation: An historical essay. *J. Fluid Mech.* **106**: 131–147.
- Monaghan, J.J., and A. Kos. 2000. Scott Russell's wave generator. *Phys. Fluids* **12**, no. 3 (March): 622–630.
- Monin, A.S., V.M. Kamenkovich, and V.G. Kort. 1977 [1974]. *Variability of the Oceans*. Trans. J.J. Lumley. New York: Wiley-Interscience.
- Mortimer, C.H. 1952. Water movements in lakes during summer stratification; Evidence from the distribution of temperature in Windermere (with an appendix by M.S. Longuet-Higgins). *Philos. Trans. R. Soc. London* **B236**, no. 635 (May 6): 355–398.
- Moum, J. D.M. Farmer, W.D. Smyth, L. Armi, and S. Vagle. 2003. Structure and generation of turbulence at interfaces strained by internal solitary waves propagating shoreward over the continental shelf. *J. Phys. Oceanogr.* **33**, no. 10 (October): 2093–2112.
- . J.D. Nash, and J.M. Klymak. 2008. Small-scale processes in the coastal ocean: Varicose waves (inset by E. Shroyer). *Oceanogr.* **21**, no. 4 (December): 22–33.
- Müller, P. and D. Henderson. ed. 1991. *Dynamics of Oceanic Internal Gravity Waves — Proceedings of the 6th 'Aha Huliko'a Hawaiian Winter Workshop held in Manoa, January 15-18, 1991*. Honolulu: University of Hawaii.

- . and D. Henderson. ed. 1995. *Topographic Effects in the Ocean – Proceedings of the 8th 'Aha Huliko'a Hawaiian Winter Workshop held in Manoa, January 17-20, 1995*. Honolulu: University of Hawaii.
- . and D. Henderson. ed. 1999. *Dynamics of Oceanic Internal Gravity Waves, II – Proceedings of the 11th 'Aha Huliko'a Hawaiian Winter Workshop held in Manoa, January 17-20, 1999*. Honolulu: University of Hawaii.
- . and R. Pujale. ed. 1984. *Internal Gravity Waves and Small-Scale Turbulence – Proceedings of the 2nd 'Aha Huliko'a Hawaiian Winter Workshop held in Manoa, January 17-20, 1984*. Honolulu: University of Hawaii.
- Murray, H.W. 1941. Submarine mountains in the Gulf of Alaska. *Bull. Geol. Soc. Am.* **52**, no. 3 (March):333–362.
- Munk, W.H. 1941. Internal waves in the Gulf of Mexico. *J. Mar. Res.* **4**, no. 1 : 81–91.
- . 1966. Abyssal recipes. *Deep Sea Res. Oceanogr. Abstr.* **13**, no. 4 (August): 707–730.
- . 1981. Internal waves and small-scale processes. In *Evolution of Physical Oceanography: Scientific Surveys in Honor of Henry Stommel*, ed. B.A. Warren and C. Wunsch, 265–291. Cambridge (MA): MIT Press.
- . and C. Wunsch. 1998. Abyssal recipes II: Energetics of tidal and wind mixing. *Deep Sea Res. Part I* **45**, no. 12 (December): 1977–2010.
- Mutel, C.F. 1998. *Flowing through Time: A History of the Iowa Institute of Hydraulic Research*. Iowa City: Iowa Institute of Hydraulic Research.

- Nagashima, H. 1971. Reflection and breaking of internal waves on a sloping beach. *J. Oceanogr. Soc. Japan*. **27**, no. 1 (February): 1–6.
- Nash, J.D., and J.N. Moum. 2005. River plumes as a source of large-amplitude internal waves in the coastal ocean. *Nature* **437**, no. 7057 (September 15): 400–403.
- National Academy of Sciences. 1975. *Proceedings of Numerical Models of Ocean Circulation Symposium, Durham, New Hampshire, October 17–20, 1975*. Ocean Science Committee of the Ocean Affairs Board. Washington, D.C.: National Academy Press.
- National Academy of Sciences, Commission on Physical Sciences, Mathematics, and Applications. 1993. *Statistics and Physical Oceanography*. Washington, D.C.: National Academy Press.
- National Academy of Sciences, Commission on Geosciences, Environment, and Resources. 2000. *50 Years of Ocean Discovery: National Science Foundation 1950–2000*. Washington, D.C.: National Academy Press.
- National Research Council. 1963. Ocean Wave Spectra. In *Proceedings of a Conference Sponsored by the U.S. Naval Oceanographic Office and the National Academy of Sciences held in Easton, Maryland, May 1–4, 1961*, Garden City: Prentice-Hall.
- Newell, A.C. 1983. The history of the soliton. *J. Appl. Mech.* **50** (December): 1127–1138.
- Niwa, Y., and T. Hibiya. 2001. Numerical study of the spatial distribution of the M₂ internal tide in the Pacific Ocean. *J. Geophys. Res.* **106**: 22,441–22,449.
- Nycander. 2005. Generation of internal waves in the deep ocean by tides. *J. Geophys. Res.* **110**, no. C10028: doi:10.1029/2004JC002487.

- Oberkampf, W.L., F.G. Blottner, and D.P. Aeschliman. 1995. Methodology for computational fluid dynamics code verification/validation. In *26th AIAA Fluid Dynamics Conference held in San Diego, CA, June 19-22, 1995*, Paper 95-2229, Reston (VA): The American Institute of Aeronautics and Astronautics.
- Oberkampf, W.L., and F.G. Blottner. 1998. Issues in computational fluid dynamics code verification and validation. *AIAA J.* **36**, no. 5 (May): 687–695.
- Oberkampf, W.L., and T.G. Trucano. 2002. *Verification and validation in computational fluid dynamics*. SAND2002-0529. Albuquerque: Sandia National Laboratories.
- Oreskes, N. 2000. Why Believe a Computer? Models, Measures, and Meaning in the Natural World. In *The Earth Around Us - Maintaining a Livable Planet*, ed. J.S. Schneiderman, 70–82. New York: W.H. Freeman and Co.
- . K. Shrader-Frechette, and K. Belitz. 1994. Verification, validation, and confirmation of numerical models in the earth sciences. *Science* **263**, no. 5147 (February 4): 641–646.
- Orr, M.H., and P.C. Mignerey. 2003. Nonlinear internal waves in the South China Sea: Observation of the conversion of depression internal waves to elevation internal waves. *J. Geophys. Res.* **108**, no. C3 (March): 3064. doi:10.1029/2001JC001163
- Osborne, A., T.L. Burch, and R.I. Scarlet. 1978. The influence of internal waves on deep-water drilling. *J. Pet. Technol.* **30**, no. 10 (October): 1497–1504.

- . and T.L. Burch. 1980. Internal solitons in the Andaman Sea. *Science* **208**, no. 4443 (May 2): 451–460.
- Ostrovsky, L.A., and Y.A. Stepanyants. 1989. Do internal solitons exist in the ocean? *Rev. Geophys.* **27**, no. 3 (August): 293–310.
- Parametric Technology Corporation (PTC). 2007. Mathcad® version 14.0. Needham, MA.
- Patankar, S.V. 1980. *Numerical Heat Transfer and Fluid Flow*. Washington, D.C.: Hemisphere Publishing.
- Patrick, D.A., and R.L. Wiegel. 1955. *Amphibian tractors in the surf*. In *First Conference on Ships and Waves held in Hoboken, New Jersey, October 1955*, ed. J.W. Johnson, 397–422. Berkeley: Council on Wave Research.
- Pedlosky, J. 1979. *Geophysical Fluid Dynamics*. New York: Springer-Verlag.
- Peregrine, D.H. 1983. Breaking waves on beaches. *Annu. Rev. Fluid Mech.* **15**: 149–178.
- Perry, R.B., and G.R. Schimke. 1965. Large amplitude internal waves observed off of the Northwest coast of Sumatra. *J. Geophys. Res.* **70**, no. 10: 2319–2324.
- Pétrélis, F., S. Llewellyn-Smith, and W.R. Young. 2002. Tidal conversion at a submarine ridge. *J. Phys. Oceanogr.* **36**, no. 6 (June): 1053–1071.
- Philips, O.M. 1966. “Internal waves (Chapter 5)” in *The Dynamics of the Upper Ocean*. Cambridge: Cambridge University Press.
- Pielou, E.C. 2001. *The Energy of Nature*. Chicago: University of Chicago Press.

- Pierson, W.J., Jr., G. Neuman, and R.W. James. 1958. Practical methods for observing and forecasting ocean waves by means of wave spectra and statistics. Publication No. 603. Washington, D.C.: Naval Hydrographic Office.
- Pineda, J. 1991. Predictable upwelling and the shoreward transport of planktonic larvae by internal tidal bores. *Science* **253**, no. 5019 (August 2): 548-549.
- . 1994. An internal tidal bore regime at near shore stations along western U.S.A.: Predictable upwelling within the lunar cycle. *Cont. Shelf Res.* **15**, no. 8 (July): 1023–1041.
- Polzin, K.L., J.M. Toole, J.R. Ledwell, and R.W. Schmitt. 1997. Spatial variability of turbulent mixing in the abyssal ocean. *Science* **276**, no. 5309 (April 4): 93–96.
- Pond, S., and G.L. Pickard. 1983. *Introductory Dynamical Oceanography*. Kidlington (UK): Elsevier Butterworth-Heinemann.
- Pratson, L.F., and W.F. Haxby. 1983. What is the slope of the U.S. continental slope? *Geology* **24**, no. 1 (January): 3–6.
- . 1997. Panoramas of the seafloor. *Sci. Amer.* **276**, no. 6 (June): 82–87.
- Pretor-Pinney, G. 2010. *The Wave Watcher's Companion – From Ocean Waves to Light Waves via Shock Waves, Stadium Waves, and All the Rest of Life's Undulations*. New York: Perigee/Penguin.
- Proudman, J. 1916. On the motion of solids in a liquid possessing vorticity. *Proc. R. Soc. Lond. A* **92**: 408-424.
- Pugh, D.T. 1987. *Tides, Surges, and Mean Sea-Level*. Chichester (UK): John Wiley & Sons.

- Rankine, W.J.M. 1863. On the exact form of waves near the surface of deep water. *Philos. Trans. R. Soc. London* **153**: 127–128.
- Rattray, M., Jr. 1960. On the coastal generation of internal tides. *Tellus* **12** (1): 54–62.
- Ray, R.G. 1960. *Aerial Photographs in Geologic Interpretation and Mapping*. Professional Paper, no. 373. Washington, D.C.: U.S. Geological Survey.
- Rayleigh, Lord (J. W. Strutt). 1876. On waves. *Philos. Mag.*, Ser. **5**, no. 1: 257–259.
- . 1877. On progressive waves. *London Math. Soc.* **9**, no. 1: 21–26.
- Reid, J.L. 1956. Observations of internal tides in October 1950. *Trans. AGU* **37**: 278–286.
- Reidy, M.S. 2008. *Tides in History: Ocean Science and Her Majesty's Navy*. Chicago: Univ. Chicago Press.
- Roache, P. 1972. *Computational Fluid Dynamics*. 1976. Albuquerque: Hermosa Publishers. [Revised printing]
- . 1997. Quantification of uncertainty in computational fluid dynamics. *Annu. Rev. Fluid Mech.* **29**: 123–160.
- . 1998. *Fundamentals of Computational Fluid Dynamics*. Albuquerque: Hermosa Press.
- . 1998. *Verification and Validation in Computational Science and Engineering*. Albuquerque: Hermosa Press.
- Roberts, J. 1975. *Internal Gravity Waves in the Ocean*. New York: Dekker.

- Roden, G.I., B.A. Taft, and C.C. Ebbesmeyer. 1982. Oceanographic aspects of the Emperor Seamounts region. *J. Geophys. Res. (Oceans)* **87**, no. C12: 9537–9552.
- Rogers, A.D. 1994. The biology of seamounts. *Adv. Mar. Biol.* **30**: 305–350.
- Roth, M.W., M.G. Briscoe, and C.H. McComas. 1981. Internal waves in the upper ocean. *J. Phys. Oceanogr.* **11**, no. 9 (September): 1234–1247.
- Rottman, J.W., and F. Einaudi. 1993. Solitary waves in the atmosphere. *J. Atmos. Sci.* **50**, no. 14 (July): 2116–2136.
- Rouse, H. 1976. *Hydraulics in the United States, 1776-1976*. Iowa City: University of Iowa.
- Ronov, A.B., and A.A. Yaroshevsky. 1969. Chemical composition of the earth's crust. In *The Earth's Crust and Upper Mantle*, ed. P.J. Hart, Geophysical Monograph 13. Washington, D.C.: American Geophysical Union.
- Rudnick, D.L., T.J. Boyd, R.E. Brainard, G.S. Carter, G.D. Egbert, M.C. Gregg, P.E. Holloway, J.M. Klymak, E. Kunze, C.M. Lee, M.D. Levine, D.S. Luther, J.P. Martin, M.A. Merrifield, J.N. Moum, J.D. Nash, R. Pinkel, L. Rainville, and T.B. Sanford. 2003. From tides to mixing along the Hawaiian Ridge. *Science* **301**, no. 5631 (July 18): 355–357.
- Ryan, W.B.F., S.M. Carbotte, J.O. Coplan, S. O'Hara, A. Melkonian, R. Arko, R.A. Weissel, V. Ferrini, A. Goodwillie, F. Nitsche, J. Bonczkowski, R. Zemsky. 2009. Global multi-resolution topography synthesis. *Geochem. Geophys. Geosyst.* **10**, Q03014, doi:10.1029/2008GC002332.
- Saffarinia, K. 1991. Numerical and Experimental Study of the Interaction of an Internal Solitary Wave with a Slope-Shelf Topography. PhD diss., The Catholic University of America, Washington, D.C.

- . and T.W. Kao. 1996. A numerical study of the breaking of an internal soliton and its interaction with a slope. *Dyn. Atmos. Oceans* **23**, no. 1-4 (January): 379–391.
- Sandström, H. 1991. The origin of internal tides (A revisit). In *Tidal Hydrodynamics*, ed. B.B. Parker. New York: John Wiley & Sons.
- . J.A. Elliott, and N.A. Cochrane. 1989. Observing groups of solitary internal waves and turbulence with BATFISH and echo-sounder. *J. Phys. Ocean.* **19**, no. 7 (July): 987–997.
- Sapolsky, H.M. 1990. *Science and the Navy: The History of the Office of Naval Research*. Princeton: Princeton University Press.
- Scannapieco, E., and F.H. Harlow. September 1995. Introduction to Finite-Difference Methods for Numerical Fluid Dynamics. Report no. LA-12984. Los Alamos: Los Alamos National Laboratory.
- Scheidegger, A.E. 1963. *Principles of Geodynamics*. New York: Academic Press.
- Schlichting, H. 1968. *Boundary-Layer Theory*. New York: McGraw-Hill.
- Scott-Russell, J. 1838. Report on waves. In *Report of the Seventh Meeting of the British Association for the Advancement of Science held in Bristol, 1837*. London: John Murray.
- . 1845. Report on waves. In *Report of the Fourteenth Meeting of the British Association for the Advancement of Science held in York, September 1844*. London: John Murray.
- Senior Seismic Hazard Analysis Committee. 1995. Recommendations for Probabilistic Seismic Hazard Analysis: Guidance on Uncertainty and

- Use of Experts. UCRL-ID-122160. 2 vols. Livermore, California, Lawrence Livermore National Laboratory.
- Shand, J.A. 1953. Internal waves on Georgia Strait. *Trans. AGU* **34**, no. 6: 849–856.
- Shepard, F. 1973. *Submarine Geology*. 3rd ed. New York: Harper & Row.
- . and R.F. Dill. 1966. *Submarine Canyons and Other Sea Valleys*. Chicago: Rand McNally.
- . and N.F. Marshall. 1973. Currents along floors of submarine canyons. *Bull. AAPG* **57**, no. 2 (February): 244–264.
- Sherwin, T.J., V.I. Vlasenko, N. Stashchuk, D.R. Gus Jeans, and B. Jones. 2002. Along-slope generation as an explanation for some unusually large internal tides.. *Deep Sea Res. I.* **49**, no. 10 (October): 1787–1799.
- Shroyer, E.L., J. N. Moum, J. D. Nash, 2009: Observations of Polarity Reversal in Shoaling Nonlinear Internal Waves. *J. Phys. Oceanogr.* **39**: 691–701.
- Simmons, J.G. 1952. Outstanding aerial photographs in North America. *J. Geol.* **60**, no. 5 (September): 506.
- Small, C., 1998. Global systematics of mid-ocean ridge morphology. In *Faulting and Magmatism at Mid-Ocean Ridges*, ed. W.R. Buck, P.T. Delaney, J.A. Karson, and Y. Lagabriele, 1–24. AGU Geophysical Monograph 106. Washington, DC: American Geophysical Union.
- . and D.T. Sandwell. 1994. Imaging mid-ocean ridge transitions with satellite gravity. *Geology* **22**, no. 2 (February): 123–126.
- Small, J., and D.M. Farmer. 1977. Nonlinear internal waves and internal hydraulic jump in a fjord. In *Geofluidodynamical Wave Mechanics held*

- in Seattle, August 20–September 2*, by Applied Mathematics Group/Conference Board on the Mathematical Sciences. Seattle: University of Washington.
- . T.C. Sawyer, and J.C. Scott. 1999. The evolution of an internal bore at the Malin shelf break. *Ann. Geophysicae* **17**, no. 4: 547–565.
- Smith, C.B. 2006. *Extreme Waves*. Washington, D.C.: Joseph Henry Press.
- Smyth, W.D., and J.N. Moum. 2000. Length scales of turbulence in stably stratified mixing layers. *Phys. Fluids*. **12**, no. 6: 1327–1342.
- Sorensen, R.M. 1997. *Basic Coastal Engineering*. New York: Chapman and Hall.
- Spanier, J., and K.B. Oldham. 1987. *An Atlas of Functions*. Bristol (PA): Hemisphere Publishing Corp.
- Spedding, G.R. 2003. Comparing fluid mechanics models with experimental data. *Philos. Trans. R. Soc. London* **B238**: 1567–1576.
- St. Laurent, L., S. Stringer, C. Garrett, and D. Perrault-Joncas. 2003. The generation of internal tides at abrupt topography. *Deep-Sea Res. Part I* **50**: 987–1003.
- Staquet, C., and J. Sommeria. 2002. Internal gravity waves: From instabilities to turbulence. *Annu. Rev. Fluid Mech.* **34**: 559–593.
- Staudigel, H., and D.A. Clague. 2010. The geological history of deep-sea volcanoes. Biosphere, hydrosphere, and lithosphere interactions. *Oceangr* **23**, no. 1 (March): 58–71.
- Stern, F, R.V. Wilson, H.W. Coleman, and E.G. Paterson. 2001. Comprehensive approach to verification and validation of CFD

- simulations – Part 1: Methodology and procedures. *J. Fluids Eng.* **123**, no. 4 (December): 793–802.
- . M. Muste, M.-L. Beninati, and W.E. Eichinger. 1999. *Summary of experimental uncertainty assessment methodology with example*. IIHR Technical Report No. 406. Iowa City: The University of Iowa, Iowa Institute of Hydraulic Research.
- Stevens, C.L., E.R. Abraham, C.M. Moore, P.W. Boyd, and J. Sharples. 2005. Observations of small-scale processes associated with the internal tide encountering an island. *J. Phys. Ocean* **39**, no. 9 (September): 1553–1567.
- Stevick, P.T., L.S. Incze, S.D. Kraus, S. Rosen, N. Wolff, and A. Baukus. 2008. Trophic relationships and oceanography on and around a small offshore bank. *Mar. Ecol. Prog. Ser.* **363** (July 15): 15–28.
- Stokes, G.G. 1847. On the theory of oscillatory waves. *Trans. Cambridge Philos. Soc.* **8**: 441–455.
- Sugimoto, N., K. Hosokawa, and T. Kakutani. 1987. Reflection and transmission of a shallow-water soliton over a barrier. *J. Phys. Soc. Japan.* **56**, no. 8 (August): 2744–2754.
- Susanto, R.D., L. Mitnik, and Q. Zheng. 2005. Ocean internal waves observed in the Lombok Strait. *Oceanog.* **18**, no. 4 (December): 80–87.
- Sveen, J.K., Y. Guo, P.A. Davies, and J. Grue. 2002. On the breaking of internal solitary waves at a ridge. *J. Fluid Mech.* **469**, no. 25: 161–188.
- Sverdrup, H.U., M.W. Johnson, and R.H. Fleming. 1949. Waves and Tides (Chapter XIV). In *The Oceans – Their Physics, Chemistry, and Biology*. Tokyo: Prentice-Hall/Tuttle.

- Synolakis, C.E., 1987. The runup of solitary waves. *J. Fluid Mech.* **185**: 523–545.
- Tannous, A.G., and D.T. Valentine. 1989. Calculation of turbulent transport in a rectangular settling tank. In Proceedings of ASME International Computers in Engineering Conference and Exposition held in Anaheim, California, July 30-August 3, 1989. 1: 51–57, ed. D.R. Riley, T.J. Cokonis, G. Gabriel, G.L. Kinzel, K.K. Tamma, D.W. Bennett, M.F. Kinoglu, A.A. Busnaina, and W.J. Rasdorf, New York: American Society of Mechanical Engineers.
- Taylor, G.I. 1917. Motion of solids in fluids when the flow is not irrotational. *Proc. R. Soc. Lond. A* **93**:99-113.
- Taylor, J.R. 1997. *An Introduction to Error Analysis — The Study of Uncertainties in Physical Measurements*. 2nd ed. Sausalito: University Science Books.
- Thorpe, S. 1974. Statically unstable layers produced by overturning internal gravity waves. *J. Fluid Mech.* **260**: 333–350.
- . 1975. The excitation, dissipation, and interaction on internal waves in the deep ocean. *J. Geophys. Res.* **80**, no. 3 (January 30): 328–338.
- . 1987. Transitional phenomena and the development of turbulence in stratified fluids: A review. *J. Geophys. Res. (Oceans)* **92**, no. C5 (May 15): 5231–5248.
- . 2001. Internal wave reflection and scatter from sloping rough topography. *J. Phys. Oceanogr.* **31**, no. 2 (February): 537–553.
- . 2004. Recent developments in the study of turbulence. *Annu. Rev. Earth Planet Sci.* **32**: 91–109.

- . and A.J. Hall. 1974. Notes: Evidence of Kelvin-Helmholtz billows in Loch Ness. *Limnol. Oceanogr.* **19**, no. 6 (November): 973–976.
- Thurnherr, A.M., L.C. St. Laurent, K.G. Speer, J.M. Toole, and J.R. Ledwell. 2005. Mixing associated with sills in a canyon on the midocean ridge flank. *J. Phys. Oceanogr.* **35**, no. 8 (August):1370–1381.
- Tricker, R.A.R. 1965. *Bores, Breakers, Waves, and Wakes: An Introduction to the Study of Waves on Water*. New York: American Elsevier.
- Tufte, E. 1983. *The Visual Display of Quantitative Information*. Cheshire (CT): Graphics Press.
- . 1990. *Envisioning Information*. Cheshire: Graphics Press.
- . 1997. *Visual Explanations: Images and Quantities, Evidence and Narrative*. Cheshire: Graphics Press.
- Turner, J.S. 1973. *Buoyancy Effects in Fluids*. Cambridge: Cambridge University Press.
- Ufford, C.W. 1947. Internal waves in the ocean. *Trans. AGU* **28**: 79–86.
- Valentine, D.T. 1987. Comparison of finite difference methods to predict passive contaminant flow. In *Proceedings of ASME International Computers in Engineering Conference and Exposition held in New York, New York, August 9–13, 1987*. 3:263–269, ed. R.E. Fulton, New York: American Society of Mechanical Engineers.
- van Haren, H., and L. Gostiaux. 2010. A deep-ocean Kelvin-Helmholtz billow train. *Geophys. Res. Lett.* **37** (February 6): L03605. doi:10.1029/2009GL041890.
- Vastano, A.C., and B.A. Warren. 1976. Perturbations to the Gulf Stream by Atlantis II Seamount. *Deep-Sea Res.* **23**, no. 8: 681–694.

- Venayagamoorthy, S.K., and O.B. Fringer. 2006. Numerical simulations of the interaction of internal waves with a shelf break. *Phys. Fluids* **18**, no. 7 (July): 076603. doi:10.1063/1.2221863.
- Visual MODFLOW Premium. 2010. Waterloo, Ontario (Canada): Schlumberger Water Services.
- Vlasenko, V., and K. Hutter. 2002. Numerical experiments on the breaking of solitary internal waves over a slope-shelf topography. *J. Phys. Oceanogr.* **32**, no. 6 (June): 1779–1793.
- . and W. Alpers. 2005. Generation of secondary internal waves by the interaction of an internal solitary wave with an underwater bank. *J. Geophys. Res.* **110** (February 22): C02019. doi:10.1029/2004JC002467.
- Wahr, J. 1995. Earth tides. In *Global Earth Physics - A Handbook of Physical Constants*, ed. T.J. Ahrens. AGU Reference Shelf 1. Washington, D.C.: American Geophysical Union.
- Wallace, B.C., and D.L. Wilkinson. 1988. Run-up of internal waves on a topographic sill in a two-layered system. *J. Fluid Mech.* **191**: 419–442.
- Warn-Varnas, A.C., S.A. Chin-Bing, D.B. King, and Z. Hallock. 2003. Ocean-acoustic solitary wave studies and predictions. *Surveys Geophysics* **24**, no. 1: 37–79.
- Wehausen, J.V., and E.V. Laitone. 1960. Surface Waves. In *Encyclopedia of Physics, vol. IX, Fluid Dynamics III*, ed. S. Flügge and C. Truesdale. Berlin: Springer-Verlag.
- Wei, G., J.T. Kirby, S.T. Grilli, and R. Subramanya. 1995. A fully nonlinear Boussinesq model for surface waves. Part 1. Highly nonlinear unsteady waves. *J. Fluid Mech.* **294**: 71–92.

- Wiegel, R. 1964. Waves in Shoaling Water (Chapter 7). In *Oceanographical Engineering*. Englewood Cliffs: Prentice-Hall.
- . 2006. Tsunami information sources. *Sci. Tsunami Hazards* **24**, no. 2: 58–178.
- Welch, J.E., F.H. Harlow, J.P. Shannon, and B.J. Daly. 1965. *The MAC Method – A Computing Technique for Solving Viscous, Incompressible, Transient Fluid Flow Problems Involving Free Surfaces*. Report no. LA-3425. Los Alamos: Los Alamos Scientific Laboratory. University of California.
- Wessel, P., and K. Hutter. 1996. Interaction of internal waves with a topographic sill in a two-layered fluid. *J. Phys. Oceanogr.* **26**, no. 1 (January): 5–20.
- . D.T. Sandwell, and S.-S. Kim. 2010. The global seamount census. *Oceanogr.* **23**, no. 1 (March): 24–33.
- Wesseling, P. 2004. *An Introduction to Multigrid Methods*. New York: John Wiley and Sons. [Corrected reprint of 1994 edition by Philadelphia: R.T. Edwards.]
- White, B.S., and B. Fornberg. 1998. On the chance of freak waves at sea. *J. Fluid Mech.* **355**: 113–138.
- White, M., and C. Mohn. 2002. Seamounts: A review of physical processes and their influence on the seamount ecosystem. Hamburg: Universität Hamburg, Institut für Hydrobiologie und Fischereiwissenschaft. European Commission, EVK3-CT-2002-00073-OASIS.
- Whitham, G.B. 1974. *Linear and Nonlinear Waves*. New York: Wiley–Interscience.

- Williams, R.S., Jr., and W.D. Carter, ed. 1976. *ERTS-1, A new window on our planet*. Professional Paper, no. 929. Washington, D.C.: U.S. Geological Survey.
- Wilson, J.T. 1963. Continental Drift. *Sci. Amer.* **208**, no. 2 (April):86-100.
- . 1965. A new class of faults and their bearing on continental drift. *Nature* **207** (July 24): 343–347.
- Wolanski, E., and E. Deleersnijder. 1998. Island-generated internal waves at Scott Reef, Western Australia. *Cont. Shelf Res.* **18**, no. 13 (November): 1649–1666.
- . P. Colin, J. Naithani, E. Deleersnijder and Y. Golbuu. 2004. Large amplitude, leaky, island-generated, internal waves around Palau, Micronesia. *Estuarine Coastal Shelf Sci.* **60**, no. 4(August):705–716.
- Wunsch, C., and R. Ferrari. 2004. Vertical mixing, energy, and the general circulation of the oceans. *Annu. Rev. Fluid Mech.* **36**: 281–314.
- Wyllie, P.J. 1971. *The Dynamic Earth: Textbook in Geosciences*. New York: John Wiley & Sons.
- Yasui, M. 1961. Internal waves in the open ocean – Internal waves of long periods in the ocean weather station 'Tango'. *Oceanogr. Mag. (Tokyo)* **12**, no. 2: 227–234.
- Yih, C.-S. 1969. Stratified flows. *Annu. Rev. Fluid Mech.* **1**: 71–110.
- . 1974. Wave motion in stratified fluids. In *Nonlinear Waves*, ed. S. Leibovich and A.R. Seebass, 263–290. Ithaca: Cornell University Press.
- Zabusky, N.J., and M.D. Kruskal. 1965. Interaction of "solitons" in a collisionless plasma and the recurrence of initial states. *Phys. Rev. Lett.* **15**, no. 6 (August 9): 240–243.

- Zaron, E.D., and J.N. Moum. 2009. A new look at Richardson number mixing schemes for equatorial ocean mixing. *J. Phys. Oceanogr.* **39**, no. 10 (October): 2652–2664.
- Zeilon, N. 1913. On the seiches of the Gullmar Fjord. *Svenska Hydrogi-Biologi Komm. Skrifter* **V**: 1–17.
- . 1934. Experiments on boundary tides: A preliminary report. *Göteborg Kungliga Vetenskaps-och Vitterhets-Samhälles Handlingar Femten Följden, Serien* **B3**, no. 10: 1–8.
- Zhang, H.P., B. King, and H.L. Swinney. 2008. Resonant generation of internal waves on a model continental slope. *Phys. Rev. Lett.* **100**, no. 24 (June 20): 244504-1 – 244504-4.
- Zheng, Q., X.-H. Yan, and V. Klemas. 1993. Statistical and dynamical analysis of internal waves on the continental shelf of the middle Atlantic Bight from space shuttle photographs, *J. Geophys. Res. (Oceans)* **98**, no. C5: 8495–8504.
- Ziegenbein, J. 1969. Short internal waves in the Strait of Gibraltar. *Deep Sea Res. Oceanogr. Abstr.* **16**, no. 5 (November): 479–487.
- Zhao, Z., V.V. Klemas, Q. Zheng, and X.-H. Yan, 2003. Satellite observation of internal solitary waves converting polarity. *Geophys. Res. Lett.* **30**, no. 19, doi:10.1029/2003GL018286
- . and M.H. Alford. 2006. Source and propagation of internal solitary waves in the northeastern South China Sea. *J. Geophys. Res.* **111**, C11012: doi:10.1029/2006JC003644.
- Zuosheng, Y., K.O. Emery, and X. Yui. 1989. Historical development and use of thousand-year-old tide-prediction tables. *Limnol. Oceanogr.* **34**, no. 5 (July): 953–957.